

Journal of ASTM International
Selected Technical Papers STP 1545
**Durability of Building and Construction
Sealants and Adhesives: 4th Volume**

JAI Guest Editor:
Andreas T. Wolf



ASTM International
100 Barr Harbor Drive
PO Box C700
West Conshohocken, PA 19428-2959

Printed in the U.S.A.

ASTM Stock #: STP1545

Library of Congress Cataloging-in-Publication Data

ISBN: 978-0-8031-7531-0

ISSN: 2154-6673

Copyright © 2012 ASTM INTERNATIONAL, West Conshohocken, PA. All rights reserved. This material may not be reproduced or copied, in whole or in part, in any printed, mechanical, electronic, film, or other distribution and storage media, without the written consent of the publisher.

Journal of ASTM International (JAI) Scope

The JAI is a multi-disciplinary forum to serve the international scientific and engineering community through the timely publication of the results of original research and critical review articles in the physical and life sciences and engineering technologies. These peer-reviewed papers cover diverse topics relevant to the science and research that establish the foundation for standards development within ASTM International.

Photocopy Rights

Authorization to photocopy items for internal, personal, or educational classroom use, or the internal, personal, or educational classroom use of specific clients, is granted by ASTM International provided that the appropriate fee is paid to ASTM International, 100 Barr Harbor Drive, P.O. Box C700, West Conshohocken, PA 19428-2959, Tel: 610-832-9634; online: <http://www.astm.org/copyright>.

The Society is not responsible, as a body, for the statements and opinions expressed in this publication. ASTM International does not endorse any products represented in this publication.

Peer Review Policy

Each paper published in this volume was evaluated by two peer reviewers and at least one editor. The authors addressed all of the reviewers' comments to the satisfaction of both the technical editor(s) and the ASTM International Committee on Publications.

The quality of the papers in this publication reflects not only the obvious efforts of the authors and the technical editor(s), but also the work of the peer reviewers. In keeping with long-standing publication practices, ASTM International maintains the anonymity of the peer reviewers. The ASTM International Committee on Publications acknowledges with appreciation their dedication and contribution of time and effort on behalf of ASTM International.

Citation of Papers

When citing papers from this publication, the appropriate citation includes the paper authors, "paper title", J. ASTM Intl., volume and number, Paper doi, ASTM International, West Conshohocken, PA, Paper, year listed in the footnote of the paper. A citation is provided as a footnote on page one of each paper.

Preface

What Impact Do Design Choices in the Building Industry Have on Our Destiny?

The global population of *Homo sapiens* reached four billion in 1974, five billion in 1987, six billion in 1999, and seven billion by the end of October 2011. It continues to soar at a rate of 1.1 percent per year and is expected to reach eight billion sometime within the time frame of 2025-2027, and nine billion around mid-century¹.

Whilst the population has increased by a factor of about 2.7 during the past 60 years, the global annual primary energy consumption has grown by a factor of 4.5, a trend bearing the signs of a typical *runaway process*. A worry compounding this symptom is that only a small share of the global population, some 1.2 billion people (approximately 15 percent of the total population) located in the OECD countries, accounts for the lion's share (47 percent) in global energy consumption^{2,3}. The developing countries are now eagerly adopting this historically '*proven formula*' for success.

The biosphere, and hence the environment, of planet Earth is self-regulating. If humankind is not capable of simultaneously halting or reversing population growth whilst drastically reducing its average footprint of energy consumption per capita, this *runaway process* will result in an environmental implosion, which will be aided by increasing demand for water, productive land (food) as well as waste generation⁴. The ensuing starvation and environmental disasters will drastically decimate our population to a level that again can be sustained by Earth's fragile (and then damaged) environment. Assuming that we are able to quickly and effectively minimize our impact on the environment, we are still facing an environmental bottleneck in this century.

¹Anonymous, *Real time World Statistics*, online at: <http://www.worldometers.info/world-population/>

²Anonymous, *Key World Energy Statistics 2011*, International Energy Agency (IEA), Paris, 2011, available for download at: http://www.iea.org/textbase/nppdf/free/2011/key_world_energy_stats.pdf

³Anonymous, *BP Statistical Review of World Energy*, 2011, available for download at: http://www.bp.com/assets/bp_internet/globalbp/globalbp_uk_english/reports_and_publications/statistical_energy_review_2011/STAGING/local_assets/pdf/statistical_review_of_world_energy_full_report_2011.pdf

⁴Anonymous, *The Little Green Data Book*, The World Bank, Washington, D.C., 2011, online at: <http://data.worldbank.org/products/data-books/little-data-book/little-green-data-book>

Impact of Buildings on the Environment and the Way Forward

One of the principal needs essential for the human race to survive is subsistence, which relies on an unconditional availability of food and shelter. The services involved in the operation of ‘modern shelters’, i.e., residential and commercial buildings — lighting, heating in the winter, cooling in the summer, water heating, electronic entertainment, computing, refrigeration, and cooking — require a staggering amount of energy. The energy required for the operation of buildings in the U.S.⁵ alone corresponds to 42 EJ (1 Exajoule = 10^{18} Joule) or about 1 Giga-ton-oil-equivalent (1 toe = 41.87 GJ). This accounts for almost 40 percent of the total U.S. energy use. This amount is equivalent to the energy released by about 670,000 atomic bombs of the ‘Little Boy’ type dropped over Hiroshima on August 6, 1945, a bomb that exploded with an energy of about 15 kilotons of TNT (63 TJ).

In addition to the operational energy employed during use, buildings embody the energy used in the mining, extraction, harvesting, processing, manufacturing and transport of building materials as well as the energy used in the construction and decommissioning of buildings. This embodied energy, along with a building’s operational energy, constitutes the building’s life-cycle energy and carbon dioxide (CO₂) emissions footprint.

Energy efficiency of buildings has been on the agenda of many governments during the past 20 years. However, in order to effectively shrink the ecological footprint of our buildings, we must seek ways to ‘decarbonize’ our energy sources, i.e., we have to shift from the burning of fossil fuels to energy sources that do not release additional CO₂ to the atmosphere. Renewable energy sources, such as wind, hydro, tide and wave, geothermal, photovoltaic and thermal solar, biomass fuels, as well as synthetic fuels produced, for instance, by genetically modified algae or bacteria or by the Fischer-Tropsch process from existing atmospheric CO₂ are likely to play an increasingly important role in the future energy mix^{6,7}. However, this shift towards more benign and renewable energies does not imply that energy efficiency is off the agenda. On the contrary, we have to strengthen our efforts directed at making our buildings more energy efficient. Finally, we have to consider ways of dematerializing as well as rematerializing our buildings. Dematerialization is a

⁵Anonymous, Energy Efficiency Trends in Residential and Commercial Buildings, U.S. Department of Energy, 2008, available for download at: http://apps1.eere.energy.gov/buildings/publications/pdfs/corporate/bt_stateindustry.pdf

⁶Schattenberg, P., “Ancient Algae: Genetically Engineering a Path to New Energy Sources?”, ScienceDaily, July 11, 2011, online at: <http://www.sciencedaily.com/releases/2011/07/1107111164533.htm>

⁷Jess, A., Kaiser, P., Kern, C., Unde, R.B., von Olshausen, C., “Considerations Concerning the Energy Demand and Energy Mix for Global Welfare and Stable Ecosystems”, *Chemie Ingenieur Technik*, Vol. 83, No. 11, 2011, pp. 1777–1791.

reduction in the bulk (mass) of hardware and the associated embodied energy used in the construction of buildings (“doing more with less”), while rematerialization is the reuse or recycling of building materials at the demolition stage. Both dematerialization and rematerialization recognize that there are finite limits to the amount of materials we can extract from our planet.

The amount of carbon dioxide emissions that construction can influence is substantial. A British report, published in autumn 2010, estimates that construction-related CO₂ emissions account for almost 47 percent of total carbon dioxide emissions of the United Kingdom⁸. The previously cited U.S. EPA report estimates that buildings in the United States contribute 38.9 percent of the nation’s total carbon dioxide emissions. Due to the energy inefficiency of the existing housing stock, CO₂ emissions generated during use of buildings in the U.K. account for over 80 percent of total CO₂ emissions. Previous life-cycle energy analyses have repeatedly found that the energy used in the operation and maintenance of buildings dwarf the energy embodied in building materials. For example, Cole and Kernan⁹, in 1996, as well as Reepe and Blanchard¹⁰, in 1998, found that the energy of operation was between 83 to 94 percent of the 50-year life cycle energy use. Even for new, highly efficient office buildings located in China, where currently considerably less energy is being consumed by the operation of buildings when compared to the U.S.A. or Western Europe, operational energy accounts for 56 percent of the total life cycle energy¹¹.

Building construction and demolition are major contributors to the waste we generate. In a report issued in April 2009, the U.S. EPA estimates that 160 million tons of building-related construction and demolition (C&D) debris is generated in the U.S.A. annually, of which 8 percent is generated during new construction, 48 percent is demolition debris, and 44 percent is

⁸Anonymous, *Estimating the Amount of CO₂ Emissions that the Construction Industry can Influence - Supporting material for the Low Carbon Construction IGT Report*, Ministerial Correspondence Unit, Department for Business, Innovation & Skills, London, United Kingdom, 2010, available for download at: <http://www.bis.gov.uk/assets/biscore/business-sectors/docs/e/10-1316-estimating-co2-emissions-supporting-low-carbon-igt-report>

⁹Cole, R. and Kernan, P. “Life-cycle Energy Use in Buildings”, *Building & Environment*, Vol. 31, No. 4, 1996, pp. 307–317.

¹⁰Reepe, P. and Blanchard, S., *Life Cycle Analysis of a Residential Home, Report 1998-5*, Center for Sustainable Systems, University of Michigan, 1998, available for download: <http://www.umich.edu/~nppcpub/research/lcahome/homelca.PDF>

¹¹Fridley, D., Zheng, N., and Zhou, N., “Estimating Total Energy Consumption and Emissions of China’s Commercial and Office Buildings”, Report LBNL-248E, Lawrence Berkeley National Laboratory, Berkeley, CA, USA, 2008, available for download at: <http://china.lbl.gov/publications/estimating-total-energy-consumption-and-emissions-chinas-commercial-and-office-building>

renovation waste. An estimated 20 to 30 percent of building-related C&D debris is recovered for processing and recycling. The materials most frequently recovered and recycled were concrete, asphalt, metals, and wood¹².

Regardless of one's personal opinion about the consequences of the above facts and statistics for the future of humanity, any rational thinker among us must appreciate the serious cost overhead associated with all this waste. In monetary terms, can the waste laden expenditures of the past continue to be expanded and sustained by humankind in the 21st Century?

21st Century Potential for Positive Change – Contributions by Sealants and Adhesives

What do the previous comments have to do with a book focused on the durability of building and construction sealants and adhesives?

Sealants and adhesives are at the interface between building materials and/or components and provide important functions, such as sealing, bonding, strengthening, movement accommodation, shock protection, fire retention, thermal or electrical insulation, and many others. These functions provide added value to the building and can enable a reduction in the building's ecological footprint. Below are just a few examples of the contributions that sealants and adhesives can make to the reduction of operational energy associated with a building:

- Energy-efficient ventilation achieved via controlled air and moisture flows (elimination of both 'infiltration' and 'exfiltration', the unintentional and uncontrollable flow of air through cracks and leaks in the building envelope).
- Improved thermal insulation of windows achieved by replacement of existing glazing by durable, sealed high performance insulating glass units.
- Renewable energy generation: Use of sealants and adhesives in the assembly and sealing of photovoltaic (PV) solar modules as well as during installation of building integrated photovoltaic solar panels (BIPV) in the building envelope.

The use of a structural sealant or adhesive may also allow redesign of a building component such that the dematerialization results in a reduction of the associated embodied energy of the component.

¹²Anonymous, *Buildings and their Impact on the Environment: A Statistical Summary*, Revised April 22, 2009, U.S. Environmental Protection Agency, Green Building Workgroup, available for download at: <http://www.epa.gov/greenbuilding/pubs/gbstats.pdf>

One example is the elimination of steel reinforcement bars in uPVC windows by bonding the glass panes to the uPVC frame as an alternative reinforcement measure. Experience gained with silicones in structural glazing and protective glazing systems and with polyurethanes in automotive direct glazing led to the development of these structurally bonded window systems. Obviously, the strength of the window then depends on the structural strength of the glass unit. However, glass has a good load bearing capability (stiffness) and can contribute considerably to the overall strength of the system. In addition to their environmental benefit (smaller carbon footprint), these constructions also offer functional benefits, such as leaner and more slender frame designs (the larger vision area results in increased light transmission via the window opening and provides improved natural lighting) as well as improved protective glazing properties (resistance to burglars, bomb blasts, hurricanes, earthquakes, avalanches, etc.)¹³. In this example, dematerialization is achieved by satisfying several product functions through one component (sealant) of the overall product (window).

A second example is the replacement of concrete beams by hybrid composite beams. These composite beams are one-tenth the weight of concrete, one-third the weight of steel, yet they are strong enough to replace structural concrete beams. Manufactured by filling fiberglass composite boxes with a concrete and steel arch, covered by composite tops secured using a two-part methacrylate adhesive, they show excellent environmental durability and are expected to have a useful life of at least 100 years, during which they need less maintenance than existing materials. Furthermore, due to their resilient, energy absorbing, construction, they provide seismic shock resistance¹⁴. The ‘dematerialized’ components mentioned here in the two examples can lower the carbon footprint of construction projects due to the reduction in their materials’ embodied energy, and the lower fuel usage needed to ship these lighter weight components.

Design Choices Involving Sealants and Adhesives in Building Construction and Their Impact on our Environmental Footprint

Whether sealants and adhesives will be seen from an ecological point of view as being part of the solution or part of the problem – especially when one considers recycling of materials and components at the renovation or demolition stage – depends largely on decisions made during the design phase.

¹³Wolf, A.T., “Sustainability Driven Trends and Innovation in Glass and Glazing”, 2009, available for download at: http://www.dowcorning.com/content/publishedlit/sustainability_driven_trends_and_innovation_in_glass_and_glazing.pdf

¹⁴Anonymous, “Attaching Hard-to-bond Construction Materials for Innovative Performance”, online at: <http://www.specialchem4adhesives.com/home/editorial.aspx?id=5505&lr=mas12184&li=10020918>

First, it should be recognized that, even if the design process itself had only a minor contribution to the cost of building, a considerable portion of the cost (as well as material and energy use) associated with later life cycle phases is committed at the design stage. It has been estimated that more than 80 percent of a product's environmental impact is determined during its design phase¹⁵, and it is likely that the same holds true for buildings. Therefore, it is essential to consider environmental aspects of the whole buildings as well as of the components and materials used from the first stages of design and development. Such an approach is generally termed 'Eco-innovation' or 'Design for Environment (DfE)'. The purpose of Design for Environment then is to design a building in such a way as to minimize (or even eliminate!) the environmental impacts associated with its life cycle. Design for Environment, as applied to buildings, typically focuses on energy efficiency and effectiveness, materials innovation, and recycling. While energy efficiency often is understood as addressing energy savings at the sub-system level, for instance in terms of the heating, ventilation and cooling (HVAC) system, energy effectiveness may be defined as producing the best overall results with the least amount of energy. Materials innovation addresses the need to develop new materials that allow construction of low embodied energy, light weight, and durable components which also meet the need for improved recyclability (which often is a challenge with composites) and have less environmental impact. Recyclability finally is considered at the design stage by 'Design for Deconstruction (DfD)'. Design for Deconstruction is an emerging concept that borrows from the fields of design for disassembly, reuse, remanufacturing and recycling in the consumer products industries^{16,17}. According to the ISO 14021:1999 standard "Environmental labels and declarations - Self-declared environmental claims (Type II environmental labeling)", the use of the term 'design to disassemble' refers to the design of a product that can be separated at the end of its life-time, in such a way its components and parts are reused, recycled, recovered as energy form, or in some other way separated from the remainders flow. The overall goal of Design for Deconstruction is to reduce pollution impacts and increase resource and economic efficiency in the adaptation and eventual removal of buildings, and recovery of components and materials for reuse, re-manufacturing and recycling. From

¹⁵ Knight, A., "The New Frontier in Sustainability – The Business Opportunity in Tackling Sustainable Consumption", BSR, San Francisco, USA, July 2010, available for download at: http://www.bsr.org/reports/BSR_New_Frontier_Sustainability.pdf

¹⁶ Guy, B. and Shell, S., *Design for Deconstruction and Materials Reuse*, available for download at: <http://www.recyclecddebris.com/rCDd/Resources/Documents/CSNDesignDeconstruction.pdf>

¹⁷ Steward, W.C. and Baum-Kuska, S.S., "Structuring Research for 'Design for Deconstruction'", *Deconstruction and Building Materials Reuse Conference*, 2004, available for download at: <http://citeseerx.ist.psu.edu/viewdoc/download?doi=10.1.1.195.573&rep=rep1&type=pdf>

an environmental point of view, building adhesives and sealants often face two contradicting requirements: On the one hand, these materials should be durable and resist the environmental stressors, such as sunlight, water, and heat; on the other hand, there is the need to easily separate substrates for recycling or repair. Recently, there has been increased interest in ‘Debonding on Demand’, which refers to the process of easily separating two adhered surfaces. Heat and light switchable adhesives have been developed, as well as primers that can act as a separation layer when activated by infrared or microwave radiation^{18,19,20}. Surely novel methods for Debonding on Demand will be developed in the near future and it will be interesting to see what the environmental durability of these sealants and adhesives will be.

Returning to the topic of dematerialization, it should be noted that less material use does not automatically imply less environmental impact. If the dematerialized product or component is inferior in quality and has a shorter usable life, then more replacements will be needed during the overall life of the building, and the net result likely will be a greater amount of waste in both production and use. Design for Dematerialization, therefore, must always be accompanied by Design for Reliability and Durability, i.e., designing a product or component to perform its task in a reliable, consistent manner, and ensuring that it will also have a long life span. From an environmental viewpoint, therefore, dematerialization should perhaps be better defined as the reduction in the amount of waste generated per unit of building product.

When considering Design for Durability, a fair question to ask is: What should be the design life of a building or a material or component used in the building? Clearly, there is a trade-off between the embodied energy in the building and its energy efficiency and effectiveness. Building components that are still far from being fully optimized in terms of their impact on energy efficiency should not last forever; rather they should be easily replaceable with new, more efficient components and easily recycled at the end of their life. Obviously, the corollary to this statement is that the higher the energy efficiency associated with a building component is, the higher its expected service life should be. The same holds true from an economic point of view: The higher the investment cost, the longer it takes to recover the invest-

¹⁸Jacobsson, D., “Strong Adhesion to Fragile Surfaces – Debonding on Demand”, online at: http://www.adhesivesmag.com/Articles/Green_Recycling/BNP_GUID_9-5-2006_A_1000000000000679822

¹⁹Manfrè, G. and Bain, P.S., “Debonding TEM technology for reuse and recycling automotive glazing”, *Glass Performance Days*, 2007, pp. 791–796, available for download at: <http://www.glassfiles.com/library/3/article1162.htm>

²⁰Anonymous, “Reversible glue ‘de-bonds’ at the touch of a button”, Royal Society of Chemistry (RSC), 2006, online at: <http://www.rsc.org/chemistryworld/News/2006/July/26070601.asp>

ment, the higher the durability of the component should be. Consequently, recyclability is more important for short-lived products and components than for more durable ones.

Another, very effective approach to dematerialization is moving from a product to a service orientation, i.e., using less material to deliver the same level of functionality to the building owner. After all, building owners and users are more interested in the value a product provides than in its physical presence. For example, the newly published ASTM Standard C 1736-11 “Practice for Non-Destructive Evaluation of Adhesion of Installed Weatherproofing Sealant Joints Using a Rolling Device” offers the sealant applicator an opportunity to move from installation contracts to product-oriented service contracts. Probably most applicators will initially view the concept of inspecting the quality of installed joint seals as challenging their reputation, possibly resulting in increased liability for them. However, when this inspection is offered as part of a periodic maintenance contract, sealant failures can be repaired locally and without replacing the entire installation. Such maintenance results in material savings as well as satisfied building owners (and facility managers), as the functionality of the seals is ensured and maintained at a high level, and, ultimately, also results in better and more stable relationships between sealant applicators and their clients due to the more frequent contacts and the higher value provided. Similarly, sealant manufacturers initially will be concerned that such service contracts will lead to decreasing sealant product sales. However, revenue models could be developed that allow extension of sealed joint warranties based on certification fees associated with the inspection of the building.

Choosing Energy Effectiveness Rather than Efficiency

In order to be energy effective, it is important to look at the Life-Cycle Analysis (LCA) to see what lifecycle stage (material production, manufacturing, use, end-of-life) has the greatest environmental impact. It is important to focus efforts first on this stage before dedicating time to the others. Operational energy reduction is a key priority, since the *most sustainable energy is energy saved*. Energy itself is not of particular interest, but rather is a means towards desired ends. Clients desire the services that energy can deliver, for instance, comfort, illumination, power, transportation - not energy by itself. Hence, maximum energy efficiency with minimal environmental impact is the architectural challenge that ultimately allows us to “have our cake and eat it too”. In this context, material choices that impact operational energy are important, while they are less significant for the energy spent in manufacturing, construction and demolition of the building.

Therefore, two of the key objectives in designing sustainable buildings are to lower the operational energy consumption and the life-cycle costs of the building. This should be achieved by:

- First, focusing on improving the performance of the building envelope in order to lower the energy demand, as the life span of the envelope is between 50 and 100 years. Commonsense already tells us to focus on things such as air tightness of the building envelope, the quality of the insulation and especially of the windows, and to avoid thermal bridges.
- The second priority then should be to avoid energy use, for instance, by using efficient appliances and through the increased use and conversion of energy embedded in natural day-lighting (the ultraviolet and infra-red fractions).
- Once this has been accomplished, the focus should shift towards the generation of energy from ‘renewable’ source, as the life span of these systems is in the 10-25 years range. This approach is also dictated by simple economic considerations, as more capital is needed for an oversized renewable energy system to compensate for a poorly designed building envelope or for inefficient appliances.

In building, the most technically appropriate materials will lower operational energy costs over the life cycle of a building and demonstrate excellent durability. For example, composite materials involving carbon fibers or ceramic compounds may have a relatively high embodied energy, but when they are used appropriately, they can save energy in a building’s use-phase due to their advanced physical properties, e.g., insulation, strength, stiffness, heat or wear resistance.

Choosing Wisdom over Intelligence

Energy effectiveness also requires ‘Intelligent Design’ – meant here as a consideration of all interactions at the highest system level and anticipating unexpected side-effects. For instance, some poor designs meant to improve energy efficiency of buildings have led to major problems in terms of comfort and health for the building occupants. As mentioned earlier, reducing air leakage from the building envelope and ductwork is typically among the most substantial improvements that can be made to reduce operational energy use. Sealing the building envelope leads to a reduction in the air exchanges previously achieved by ‘natural ventilation’. The desired effect is a reduction in the HVAC operational energy. However, when poorly designed, the undesired side-effect is an increase in potentially harmful volatile organics, radon, moisture and mold growth, with negative impact on the comfort and health of the building occupants. On the other hand, when properly planned by combining air tight envelopes with mechanical ventilation

systems having integrated heat exchangers, very low operational energy consumption can be achieved, down to the level of ‘passive house’ standard, while at the same time providing good air quality to the building occupants.

The challenges both designers and businesses face when moving from traditional design and production methods to ones that promote a sustainable future are huge. For the designer, it is important to appreciate, what building owners really want: *Sustainability, but not at the expense of performance and aesthetics!* Designers who balance and optimize the technical and aesthetic life-span requirements for a building product or component with the environmentally related characteristics and performance attributes can reduce the energy and materials dedicated to these requirements.

The adhesives and sealants industry as well as academia will choose wisely if they seek out the *environmental attributes* that can be delivered by their products with the key aim of lowering the operational energy consumption and the life-cycle costs of the building. Enhancing a product’s function and life span with the added benefit of improving its environmental profile and impact should be a key focus in future research and development efforts. More effort can be put into the design phase of building materials, such as adhesives and sealants, building components, building systems, and finally *the whole building* to truly achieve improved sustainability. As highlighted a number of times in this preface, durability and sustainability are related in different ways and at different levels. As an industry, will we choose wisely? Will we see more papers and presentations on this topic at one of the future Durability of Building and Construction Sealants and Adhesives symposia?

Maybe ‘Intelligent Design’ is not an adequate term anyway. Intelligence predicts the success of individuals without regard to the consequences of their success to others. Wisdom, however, reflects the ability to make adaptive decisions in a social context. It requires altruism, balanced judgment, competent reality testing, and a *consistent view of the big picture*. This is why wisdom, not intelligence, applies to the survival of species²¹.

What we must strive to achieve is sustainability, supporting the long-term ecological balance, certain in the knowledge that “*the most sustainable energy is the energy saved*”. ‘Wise Design’ takes this fundamental truth into account, and has the potential of truly living up to the expectations of Carolus Linnaeus, the father of modern biological classification (taxonomy), who in 1758 applied the name *Homo sapiens* (Wise Man) to our species.

Andreas T. Wolf
Wiesbaden, Germany

²¹Watson, D.E., *Is Homo sapiens sapiens a Wise Species?*, online at: [http://www.enformy.com/\\$homosap.html](http://www.enformy.com/$homosap.html)

Contents

Preface	vii
Overview	xvii
A Panel Discussion: ASTM Introduces C1736 Standard Practice for Non-Destructive Evaluation of Adhesion of Installed Weatherproofing Sealant Joints Using a Rolling Device	
A. T. Wolf	xxxi

Laboratory Testing and Specialized Outdoor Exposure Testing

Bond Strength Between Cast-in-Place Ultra-High-Performance-Concrete and Glass Fiber Reinforced Polymer Plates Using Epoxy Bonded Coarse Silica Sand	
D. Chen and R. El-Hacha	3
Characterization of Adhesive Joints for Hybrid Steel-Glass Beams by Means of Simplified Small Scale Tests	
M. Feldmann, B. Abeln, and E. Preckwinkel	26
Durability of Acrylic Sealants Applied to Joints of Autoclaved Lightweight Concrete Walls: Evaluation of Exposure Testing	
H. Miyachi, M. A. Lacasse, N. Enomoto, S. Murata, and K. Tanaka	47
In Situ Measurement of Compression Set in Building Sealants During Outdoor Aging	
G. T. Schueneman, C. G. Hunt, S. Lacher, C. C. White, and D. L. Hunston	70
Preliminary Evaluation of the Mechanical Properties and Durability of Transparent Structural Silicone Adhesive (TSSA) for Point Fixing in Glazing	
S. Sitte, M. J. Brasseur, L. D. Carbary, and A. T. Wolf	86
Adhesive Joints in Glass and Solar Engineering	
B. Weller and I. Vogt	124
Outline of Testing and Evaluation Program Used in Selection of Adhesives for Transparent Adhesive Joints in All-Glass Load-Bearing Structures	
B. Weller, F. Nicklisch, V. Prautzsch, and I. Vogt	152
A Systematic Approach to the Study of Accelerated Weathering in Building Joint Sealants	
C. C. White, D. L. Hunston, K. T. Tan, J. J. Filliben, A. L. Pintar, and G. Schueneman	177

Factors Influencing the Durability of Sealed Joints and Adhesive Fixations

Durability of Cold-Bent Insulating-Glass Units	
K. Besserud, M. Bergers, A. J. Black, L. D. Carbary, A. Mazurek, D. Misson, and K. Rubis	205
The Mechanism of Adhesion Improvement of Elastomeric Silicone Sealants to Difficult-to-Bond Polymeric Substrates Through Reactive or Interpenetrating Molecular Brushes	
W. S. Gutowski, G. Toikka, and S. Li	243
Mechanical Characteristics of Degraded Silicone Bonded Point Supports	
A. Hagl	266

Glass Unit Corner Loading—Key Parameter in Durability	
A. Hagl and O. Dieterich	286
Mechanisms of Asphalt Blistering on Concrete Bridges	
B. W. Hailesilassie and M. N. Partl	308
Ways of Improving the Interfacial Durability of Silicone Adhesives in Building Applications	
P. Vandereecken and I. Maton	331

Development of New Test Methods and Performance-Based Specifications

Attempt at Quantification of Surface Degradation and Evaluation of Relationship between Outdoor and Accelerated Exposure of Construction Sealants	
N. Enomoto, A. Ito, and K. Tanaka	343
Development of a Non-Destructive Evaluation Practice of Installed Weatherproofing Sealant Joints Using a Rolling Device—An Introduction to ASTM C 1736	
D. N. Huff	361
Weathering Evaluation of Structural Silicone Sealants used in Korea	
J. Jung, K. Hahn, and H. Lee	370
Evaluation of Sealed Joint Performance for the Selection of Sealants Suitable for Use in Autoclaved Lightweight Concrete Panels	
H. Miyauchi, M. A. Lacasse, S. Murata, N. Enomoto, and K. Tanaka	385
Potential of Dynamic-Mechanical Analysis Toward a Complementary Material and System Testing Approach for Structural Glazing	
C. Recknagel	404
A Test Method for Monitoring Modulus Changes during Durability Tests on Building Joint Sealants	
C. C. White, D. L. Hunston, and K. T. Tan	432

Field Experience with Sealed Joints and Adhesive Fixation

Moisture Sensitive Adhesives and Flooring Adhesive Failures	
P. E. Nelson and E. R. Hopps	447
Case Studies of Adhesive and Rigid Insulation Board Failures due to Moisture in Low Sloped Roofing Assemblies	
D. S. Slick, N. A. Piteo, and D. A. Rutila	456

Performance under Seismic Loads

Seismic Racking Test Evaluation of Silicone Used in a Four-Sided Structural Sealant Glazed Curtain Wall System	
K. A. Broker, S. Fisher, and A. M. Memari	473
Evaluation of the Structural Sealant for Use in Four-Sided Structural Sealant Glazing Curtain Wall System for a Hospital Building	
A. M. Memari, S. Fisher, C. Krumenacker, K. A. Broker, and R.-U. Modrich	505
A Review of the Behavior Structural Silicone Glazing Systems Subjected to a Mega-Earthquake	
E. Bull and J. Cholaky	529
Author Index	565
Subject Index	567

**LABORATORY TESTING
AND SPECIALIZED OUTDOOR
EXPOSURE TESTING**

Donna Chen¹ and Raafat El-Hacha²

Bond Strength Between Cast-in-Place Ultra-High-Performance- Concrete and Glass Fibre Reinforced Polymer Plates Using Epoxy Bonded Coarse Silica Sand

ABSTRACT: A significant amount of attention has been directed toward the use of fibre reinforced polymer (FRP) materials in structural applications, particularly as main components in hybrid structural members. As a result, the need for an effective connection mechanism that can maintain full composite action at the interface between adjacent dissimilar materials is critical in order to achieve optimum performance of the hybrid structural members. The objective of this experimental program was to investigate the bond performance between glass fibre reinforced polymer (GFRP) plates and cast-in-place Ultra-High-Performance- Concrete (UHPC) using epoxy bonded coarse silica sand aggregates at the bond interface. Both shear and tension tests were conducted using three different types of epoxy adhesives. The general effectiveness of the connection mechanism at the bond interface as well as the relative performance of each epoxy adhesive used were investigated. Analysis showed that, of the three epoxy adhesives tested, the specimens bonded at the interface between the UHPC and GFRP plates using the moisture tolerant epoxy adhesive intended for bonding of hardened concrete and steel performed the best.

KEYWORDS: fibre reinforced polymers, glass, Ultra-High-Performance-Concrete, bond, epoxy, silica sand, shear, tension

Manuscript received February 22, 2011; accepted for publication November 9, 2011; published online March 2012.

¹Dept. of Civil Engineering, Univ. of Calgary, 2500 Univ. Dr., Calgary, Alberta T2N 1N4, Canada, e-mail: dsmchen@gmail.com

²Dept. of Civil Engineering, Univ. of Calgary, 2500 Univ. Dr., Calgary, Alberta T2N 1N4, Canada, e-mail: relhacha@ucalgary.ca

Cite as: Chen, D. and El-Hacha, R., "Bond Strength Between Cast-in-Place Ultra-High-Performance- Concrete and Glass Fibre Reinforced Polymer Plates Using Epoxy Bonded Coarse Silica Sand," *J. ASTM Intl.*, Vol. 9, No. 3. doi:10.1520/JAI103836.

Copyright © 2012 by ASTM International, 100 Barr Harbor Drive, PO Box C700, West Conshohocken, PA 19428-2959.

Introduction

The potential uses of fibre reinforced polymers (FRPs) for structural applications have been explored in great detail since early 1970s [1]. More recently, research has focused on investigations relating to hybrid FRP structural members, which incorporate a combination of different FRP materials, conventional materials as well as other high performance materials, such as Ultra-High-Performance- Concrete, in specially designed cross sections in order to optimize the most advantageous qualities of each distinct material [2–5]. In order to achieve the best performance in these hybrid structural members, full composite action is required across the complete cross section. This has led to numerous investigations with the aim at determining and predicting the behaviour of different types of connection methods at various material interfaces [6–13].

The main objective of this particular research was directed towards the study of a particular type of connection mechanism used at the interface between glass FRP (GFRP) plates and cast-in-place UHPC. The connection mechanism used consisted of coarse silica sand aggregates bonded to the GFRP plate using an epoxy adhesive, similar to previous research performed in regards to bonding between GFRP and normal strength concrete [13]. Experimental testing and analysis were performed to evaluate the shear and tension strength at the GFRP-UHPC interface using this particular type of connection mechanism. Additionally, comparisons between the effectiveness of the connection mechanism using three different types of epoxy adhesives for aggregate bonding were made.

Materials

Glass Fibre Reinforced Polymer (GFRP)

The GFRP plates were fabricated using the pultrusion method, with internal glass rovings in the longitudinal direction and continuous strand glass mats or stitched reinforcements in the transverse direction. The GFRP plates were fabricated using a proprietary system with a combination of fibreglass reinforcements and thermosetting polyester resin. From the manufacturer's specifications the GFRP plates have a minimum tensile strength of 207 MPa, with a modulus of elasticity of 17.2 GPa [14]. Experimental testing using three tension coupon specimens in accordance with ASTM D3039-00 [15] provided values for the ultimate tensile strength as 230 ± 44 MPa, with the value for the modulus of elasticity equal to $18\,689 \pm 2927$ MPa.

Ultra-High-Performance- Concrete (UHPC)

The UHPC used is a proprietary concrete product with metallic short fibers. According to the manufacturer's specifications, the ultimate compressive strength at 28 days is expected to range between 150 to 180 MPa with a strength after 24 h equal to approximately 30 MPa [16]. Though supplementary heat treatment administered to the UHPC could allow the compressive strength to exceed 200 MPa [16], this procedure was not performed on the UHPC used in this experimental program. Similarly, the manufacturer's specifications provided values for the modulus of elasticity

equal to between 50 and 60 GPa [16]. Experimental testing, in accordance with ASTM C469-94 [17], using three UHPC cylinders determined the compressive strength to be 131 ± 12 MPa and the modulus of elasticity to be $52\,559 \pm 7102$ MPa. Splitting tests performed in accordance with ASTM C496-96 [18] showed the tensile strength of the UHPC to be equal to 24 ± 2 MPa.

Epoxy Adhesives

Three different types of epoxy adhesives were used. The first epoxy type A (a moisture insensitive epoxy adhesive intended for bonding between hardened concrete and steel) has a reported tensile strength of 48 MPa, tensile elongation limit of 1.9 %, and a modulus of elasticity equal to 3726 MPa [19]. Epoxy type B (intended for use in conjunction with Carbon FRP fabrics in wet lay-up strengthening systems) is reported to have a tensile strength of 72.4 MPa, tensile elongation of 5.0 %, and a modulus of elasticity of 3180 MPa [20]. Epoxy type C (a moisture tolerant, high strength, high modulus epoxy adhesive, intended for vertical and overhead applications), according to manufacturer's specifications, has a tensile strength of 30 MPa, ultimate tensile strain of 1.5 %, and a modulus of elasticity equal to 3800 MPa [21].

Test Specimens

In order to investigate the bond behaviour between the cast-in-place UHPC and the GFRP plate, it was decided to subject the bond interface to two distinct types of load configurations, one under pure shear load and the other under pure tension load. Two different types of specimens were designed for each loading configuration.

Preparation of Bond Interface

The bond interface for all of the specimens tested, for both shear and tension specimens, were prepared in a similar fashion. The bond surface of the GFRP plate was first coarsened using a Grit 60 belt sander followed by manual coarsening using a heavy duty sanding stone. A thin layer of epoxy (approximately 1 mm in thickness) was then applied to the coarsened surface. Coarse silica sand aggregates, with diameters ranging from 4.5 to 9.0 mm, were distributed evenly overtop of the epoxy to achieve an aggregate density of approximately 4 kg/m^2 . The applied aggregate density is in agreement with experimental results obtained in similar research [13]. The coarse silica sand aggregates were gently pressed downwards onto the GFRP plate to ensure good bonding. The plates with the bonded sand aggregates were allowed to cure undisturbed for 7 days prior to casting of the UHPC onto the bond interface. Figure 1 includes photographs showing different stages during the preparation of the specimens.

Double-Lap Shear Test Specimens

Three specimens for each type of epoxy adhesive used were fabricated, with nine specimens in total. It was decided to determine the shear bond strength



FIG. 1—Fabrication of test specimens.

using double-lap shear specimens, due to the reduction in possible load eccentricities and misalignments during testing. The dimensions of the double shear test specimens are shown in Fig. 2. The instrumentation used for each specimen included ten strain gauges, with locations shown in Fig. 3, and two linear strain conversion transducers (LSCTs), which perform similarly to linear variable displacement transducers (LVDTs). The two LSCTs were used to measure the

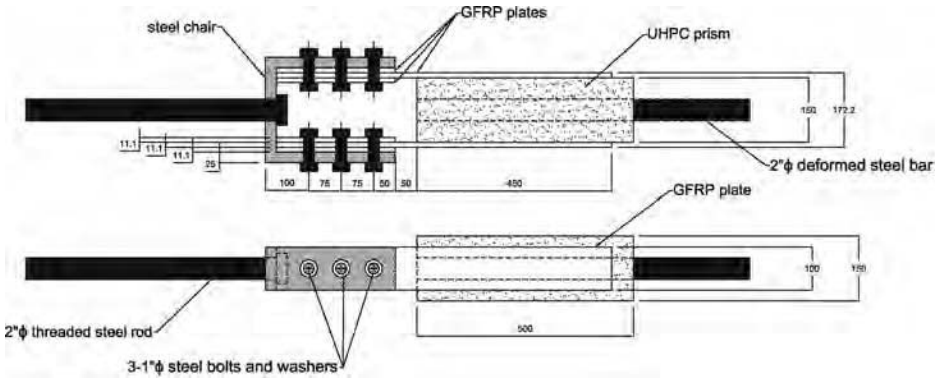


FIG. 2—Dimensions for double-lap shear test specimens.

differential displacement between the GFRP plate and the UHPC prism on each side. A photograph of the final load setup is shown in Fig. 4.

For the purpose of clarity, experimental results as well as discussion of analysis in this paper will refer to the end of the double shear test specimens with the protruding steel bar as the “fixed end”; the opposite end, which will be attached to the steel chair shown in Fig. 4, will be referred to as the “free end.” In a similar fashion, the side with strain gauges SG-1 to SG-5 will be referred to as the “east side,” whereas the side with strain gauges SG-6 to SG-10 will be called the “west side.”

Tension Pull-out Specimens

Similar to the double-lap shear test specimens, three specimens were fabricated for each type of epoxy adhesive, resulting in a total of nine specimens. The

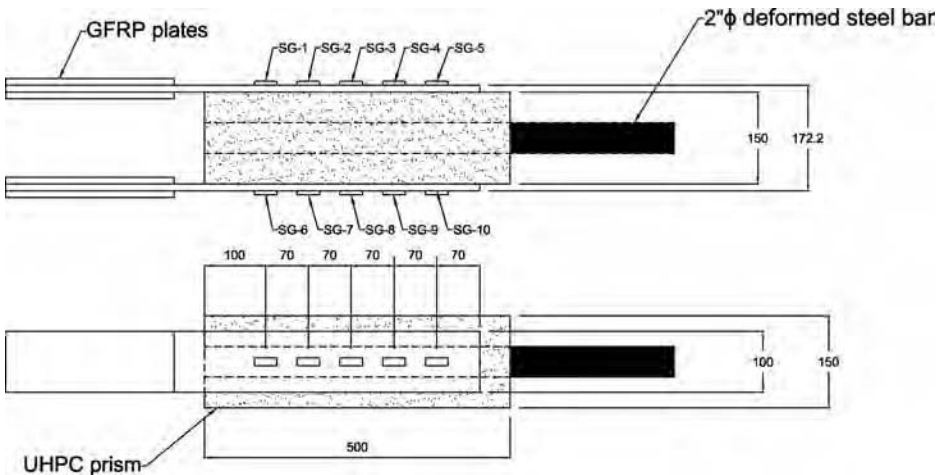


FIG. 3—Location of strain gauges on double-lap shear test specimens.



FIG. 4—Double-lap shear specimen testing load setup.

dimensions for each specimen are shown in Fig. 5, with the load setup provided in Fig. 6. To prepare the specimens for testing, circular cuts were made with diameters of 50 mm. The cuts were initiated from the outer surface of the GFRP plate until an approximate depth of 5 mm into the UHPC layer was achieved. Steel discs, with a diameter of 50 mm and prepared with threaded holes through its center, were then bonded onto the outer surface of the GFRP plate. Through optimization arrangement, five individual pull-out tests were able to be performed on each specimen made, as shown in Fig. 5. The primary focus of these tests was the determination of the ultimate pull-out load as well as the

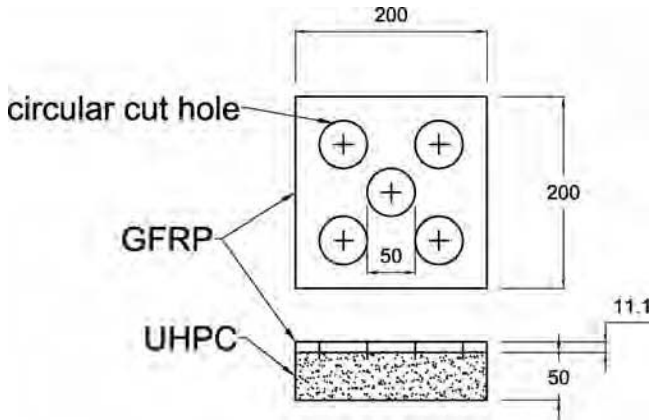


FIG. 5—Dimensions for tension pull-out test specimens.

mode of failure; therefore, only one load cell was used for data collection without the use of any strain gauges or LSCTs.

Experimental Results

Double-Lap Shear Tests

All of the specimens were tested until failure. The shear stress at the bond interface at the time of failure were calculated using

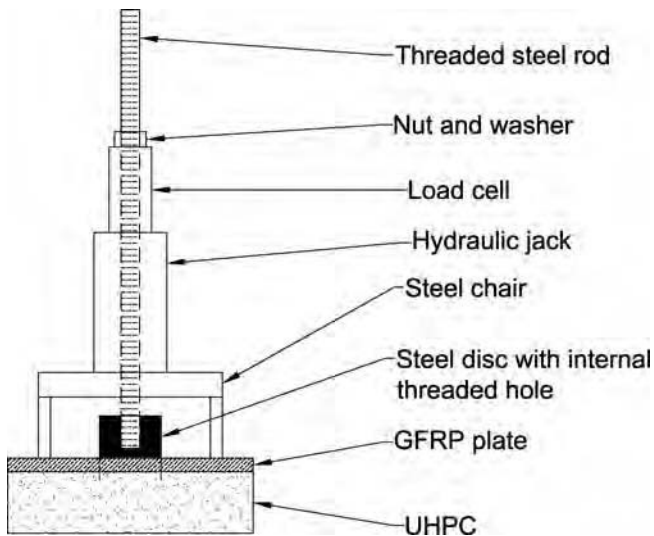


FIG. 6—Tension pull-out specimen testing load setup.

$$\tau = \frac{P}{2lw} \quad (1)$$

where:

τ = the shear stress at each bond interface (MPa),

P = the recorded ultimate applied load (N),

l = the length of effective bond area (mm), equal to 450 mm for this experiment and,

w = the width of effective bond area (mm), equal to 100 mm for this experiment.

In Table 1 a summary of the experimental results is provided; in addition, the specific side of the specimen that experienced failure is shown as being either east or west, which were defined previously in "Double-Lap Shear Test Specimens." In the case of the specimens using epoxy type A, failure did not occur due to debonding between the GFRP and the UHPC. Instead, shear failure in the GFRP plates at the connection with the steel chair occurred. As can be seen in Table 1, the side of the specimen that experienced failure was not stated for the specimens using epoxy type A. Accordingly, the shear strength at the bond interface was provided as a lower limit, due to the fact that had shear failure not occurred at the connection a higher applied load would have been reached. The failure for the specimens that used epoxy types B or C for bonding of the coarse silica sand aggregates occurred predominantly in the epoxy adhesive layer, though some fracturing of the aggregates were seen along the interface for the specimens that used epoxy type C for aggregate bonding. In conjunction with the values for maximum shear strength, comparison of the failure modes for the specimens with epoxy types B and C shows that the epoxy type B provided greater bonding between the UHPC and the coarse silica sand aggregates, where it maintained a consistent bond strength equal to or greater than the fracture strength of the aggregates. Photographs showing the failure of representative specimens under shear load for all three types of epoxy adhesive used are shown in Fig. 7.

TABLE 1—*Experimental results of double shear test specimens.*

Epoxy Type	Specimen	Failure Side	Maximum Applied Load, kN		Shear Strength, MPa	
			Data	Average	Data	Average
A	A-1	...	157.63	$>165.36 \pm 28.17$	>1.75	$>1.84 \pm 0.31$
	A-2	...	196.57		>2.18	
	A-3	...	141.87		>1.58	
B	B-1	East	169.17	173.67 ± 12.08	1.88	1.93 ± 0.13
	B-2	West	187.35		2.08	
	B-3	East	164.48		1.83	
C	C-1	West	82.91	81.00 ± 4.90	0.92	0.90 ± 0.05
	C-2	East	84.65		0.94	
	C-3	East	75.43		0.84	



FIG. 7—Photographs at failure for double shear test specimens.

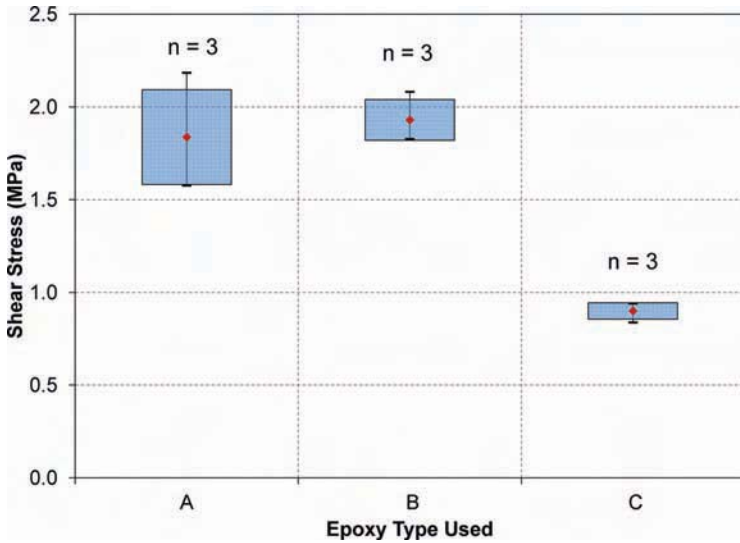


FIG. 8—Distribution and variance of shear strength for different types of epoxy used for coarse silica sand bonding.

The distribution and variance for the shear strength of the individual double shear test specimens are shown in Fig. 8, with the $\pm\sigma$ range represented by the box and the actual experimental minimum and maximum values indicated by the capped vertical lines. It can be observed in Fig. 8 that the specimens that used epoxy type A for aggregate bonding at the interface provided the highest shear resistance. In order to ascertain if the results obtained from the specimens with the three different types of epoxy adhesives were statistically different, a single factor ANOVA (analysis of variance) test was performed, with the results shown in Table 2. By comparing the F value with the value for F_{crit} , it is evident that F is substantially greater than F_{crit} . The result from the ANOVA analysis indicates that the average shear strength provided by the specimens using the three different epoxy adhesive types were statistically different from one another within a 95 % confidence level.

Tension Pull-out Tests

A summary of the ultimate applied tension load for all of the specimens tested is shown in Table 3. The maximum tensile strength of each specimen was determined using

TABLE 2—ANOVA F -test results for double shear test specimens.

Source of Variation	SS	df	MS	F	P Value	F_{crit}
Between groups	1.95	2	0.97	24.58	0.001288	5.14
Within groups	0.24	6	0.040			

TABLE 3—*Experimental results of tension pull-out test specimens.*

Specimen	Epoxy Type A		Epoxy Type B		Epoxy Type C	
	Load, kN	Stress, MPa	Load, kN	Stress, MPa	Load, kN	Stress, MPa
1	9.2	4.5	10.7	5.3	3.1	1.5
2	6.7	3.3	8.5	4.2	1.6	0.8
3	7.6	3.7	7.7	3.8	1.1	0.5
4	... ^a	... ^a	3.4	1.7	1.7	0.8
5	2.7	1.3	3.4	1.7	4.8	2.4
6	4.4	2.2	1.4	0.7	1.3	0.7
7	12.3	6.1	13.4	6.6	1.0	0.5
8	2.9	1.4	2.9	1.4	4.0	2.0
9	2.5	1.2	3.7	1.8	2.6	1.3
10	3.1	1.5	6.7	3.3	2.8	1.4
11	2.2	1.1	7.8	3.8	0.4	0.2
12	2.7	1.3	11.7	5.8	0.4	0.2
13	2.6	1.3	3.8	1.9	0.4	0.2
14	5.6	2.8	7.6	3.7	2.2	1.1
15	... ^a	... ^a	13.5	6.6	7.8	3.8

^aAccidental movement during steel disc bonding process prevented these specimens from being tested.

$$\sigma = \frac{4P}{\pi d^2} \quad (2)$$

where:

σ = the shear stress at each bond interface (MPa),

P = the recorded ultimate applied load (N) and,

d = the diameter of the bonded area (mm), equal to 50 mm for this experiment.

Failure of the specimens that used epoxy types A and B under pull-out tension forces occurred as a combination of both separation in the epoxy layer as well as fracturing of the bonded aggregates. In the case of the specimens that used epoxy type C for bonding of the aggregates, the bulk of the failure occurred in the epoxy layer with very little to no fracturing of the aggregates. Representative photographs showing the failure of the three different types of tension pull-out specimens are shown in Fig. 9. The distribution and variance of the tension strength provided by the specimens are shown in Fig. 10, which shows that epoxy type B provided the highest resistance to tension pull-out forces. The F -test ANOVA results for the tension pull-out tests are shown in Table 4. Similar to the conclusion made in "Double-Lap Shear Tests" for the double shear test specimens, the value for F was noticeably greater than the value for F_{crit} , leading to the conclusion that the average tension strength provided by the three different epoxy adhesive types were statistically different from one other.

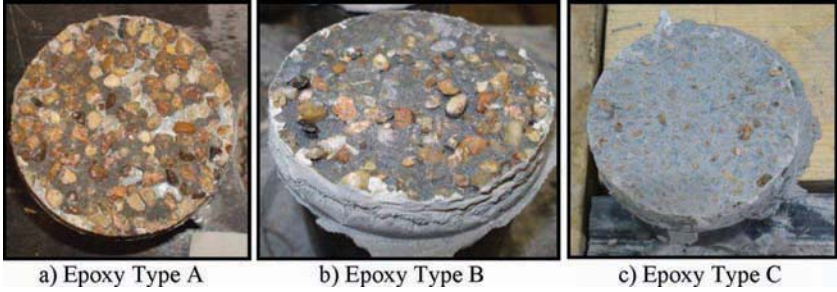


FIG. 9—Photographs at failure for tension pull-out specimens.

Discussion and Analysis

Shear Interface Bond Slippage Behaviour

In order to investigate in detail the bond behaviour at the shear interface for the double shear test specimens, the bond slippage behaviour along the interface was characterized using two different methods. The first method used the data collected from the LSTs according to Eqs 3 to 5, while the second method used the data collected from the strain gauges, according to Eqs 6 to 8 [13]. The total slippage between the GFRP and the UHPC can be determined by the summation of strain differences between adjacent strain gauges over the length of the bond. This value would then be comparable to the differential movement indicated by

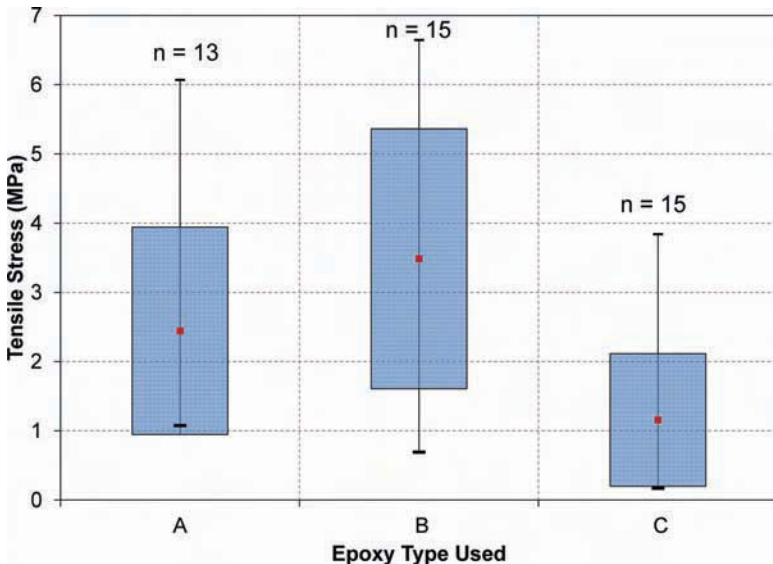


FIG. 10—Distribution and variance of tension strength for different types of epoxy used for coarse silica sand bonding.

TABLE 4—ANOVA *F*-test results for tension pull-out test specimens.

Source of Variation	SS	df	MS	F	P Value	F _{crit}
Between groups	105342	2	52671	8.52	0.000827	3.23
Within groups	247253	40	6181			

the LSCT readings, allowing for proper comparisons to be made between the two methods.

Method 1

$$\delta_E = \mu_E \quad (3)$$

$$\delta_W = \mu_W \quad (4)$$

$$\delta_{\text{ave}} = \frac{\mu_E + \mu_W}{2} \quad (5)$$

where:

μ_E, μ_W = the LSCT readings from the east and west sides, respectively (mm) and δ_{ave} = the measured slip (mm).

Method 2

$$d_E = \int_0^L \varepsilon(x) dx \cong \sum_1^5 \varepsilon_{i,E} \Delta L_i \quad (6)$$

$$d_W = \int_0^L \varepsilon(x) dx \cong \sum_6^{10} \varepsilon_{i,W} \Delta L_i \quad (7)$$

$$d_{\text{ave}} = \frac{d_E + d_W}{2} \quad (8)$$

where:

d_E, d_W = the integrated deformation on the east and west sides, respectively (mm),

$\varepsilon_{i,E}, \varepsilon_{i,W}$ = the reading at strain gauge i on the east and west sides, respectively ($\mu\varepsilon$),

ΔL_i = the average centre-to-centre spacing between gauge i and the adjacent gauges $i - 1$ and $i + 1$ and,

d_{ave} = the average integrated deformation (mm).

The shear interface slippage behaviour exhibited for all of the specimens, determined using both the methods described in the section, are shown in Figs. 11, 12, and 13 for the specimens using epoxy types A, B, and C, respectively, at the bond interface. The shear interface slippage behaviour was shown for the

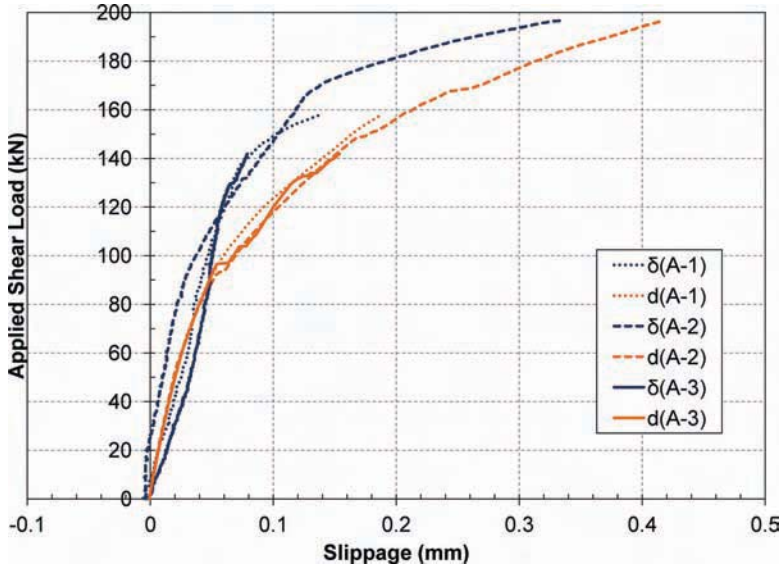


FIG. 11—Shear interface slippage behaviour for double shear test specimens with epoxy type A at the bond interface.

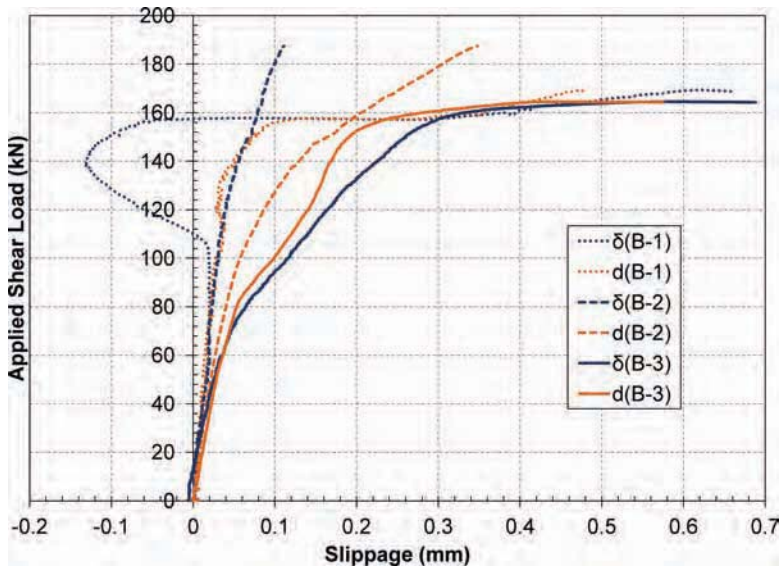


FIG. 12—Shear interface slippage behaviour for double shear test specimens with epoxy type B at the bond interface.

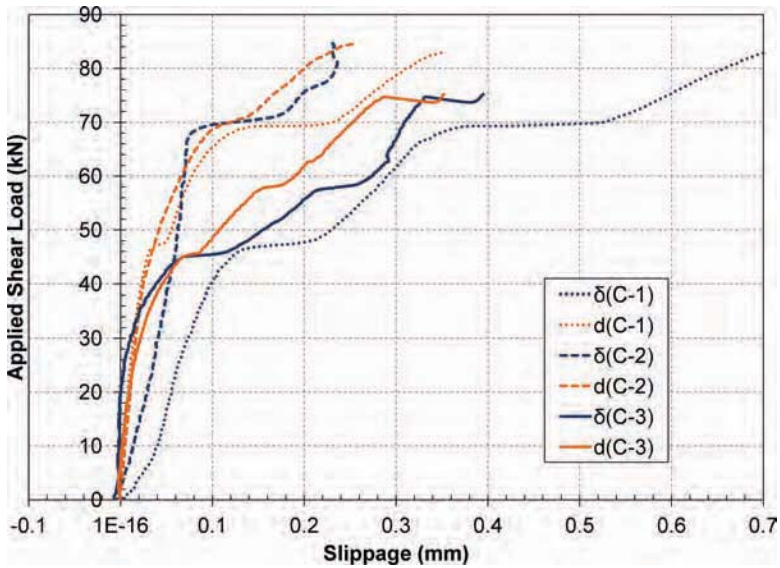


FIG. 13—Shear interface slippage behaviour for double shear test specimens with epoxy type C at the bond interface.

side that experienced failure, as indicated earlier in Table 1, using Eqs 3, 4, 6, and 7 where applicable. In the case of the specimens that used epoxy type A at the bond interface, where bond failure did not occur, the average slippage calculated from Eqs 5 and 8 were used for analysis. Comparison between the two methods used to determine the shear slippage behaviour at the interface showed mixed findings and correlations, where the results determined using methods 1 and 2 were represented using darker and lighter lines, respectively. For epoxy type A, the trend exhibited by the three specimens in Fig. 11 showed moderate consistency within the results obtained from each of the two methods; however, when comparing the values obtained between the two methods, there were noticeable differences where significant divergence in the trend were noted when the applied load exceeded approximately 100 kN, which is equal to a bond shear strength of 1.11 MPa. In the case of the specimens that used epoxy type B at the bond interface, initial observations showed that extremely large discrepancies were present in Fig. 12 when comparing the results from the two methods. More specifically, there were irregular portions in the curves, shown by the portions where the amount of slippage at the interface appeared to be decreasing with increased loading, which may have been caused by accidental slippage in the mounting apparatus of the LSCTs. Upon closer inspection, it can be seen that by ignoring the irregular portions, the characteristic features of both the darker and lighter curves (locations of dramatic slope changes) for each specimen occurred at approximately the same load level. This demonstrates that consistent similarities were exhibited in the load-slippage behaviour of the specimens using epoxy type B. In Fig. 13 the shear interface slippage behaviours

obtained using both methods for specimen C-2 were nearly identical. In the case of the other two specimens that used epoxy type C for bonding of the coarse silica sand aggregates, visible horizontal offsets were present though the distinctive features in the trend were seen to occur at the same load levels, similar to the observation made in regards to Fig. 12. Direct comparison of the load-slippage behaviour obtained through the use of the three different types of epoxy adhesives is shown in Fig. 14, which used the shear interface slippage curves determined using method 2 due to the fact that it provided more consistent and regular trends. In general, it was confirmed that the specimens that used epoxy types A and B showed better performance than the specimens that used epoxy type C.

Shear Strain Profiles

The shear strain profiles for each of the specimens using epoxy types A, B, and C are shown in Figs. 15–17, Figs. 18–20 and Figs. 21–23, respectively. For Figs. 15–17 the shear profiles provided are for the side of the double shear test specimens that experienced the highest shear strain. In all of the specimens shown in Figs. 18–23, the uppermost curves, representing the shear strain profiles at failure, have a downward concave shape in contrast with the convex shape exhibited by all of the other shear strain profile curves. This deviation in the shape of the curve is expected at the onset of debonding failure, due to the fact that the initiation of separation between the GFRP plate and the UHPC prism starting from the free end would cause an instantaneous drop in shear strain in SG-1 and SG-6 relative to SG-2 and SG-7, respectively, as a result of the sudden

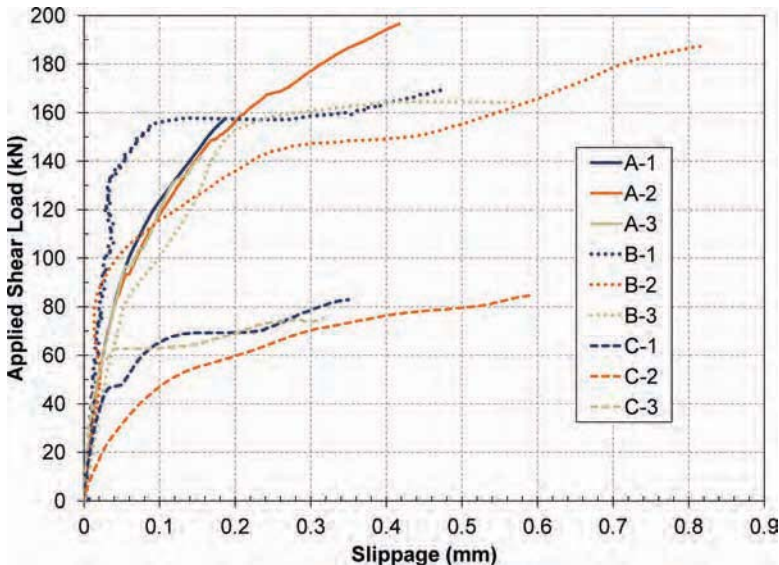


FIG. 14—Shear interface slippage behaviour comparison for all epoxy adhesive types used.

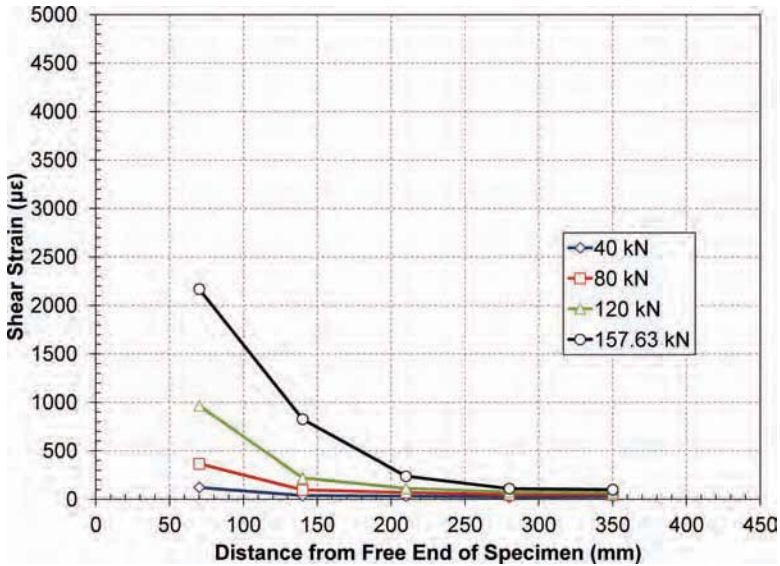


FIG. 15—Shear strain profiles for specimen A-1.

release of fixed constraint. Therefore the strain data values collected by SG-1 and SG-6 at failure are not representative of the peak shear strain reached at those locations at the instant directly prior to debonding. In general, the shear strain profiles exhibited load-strain trends similar to a polynomial relationship

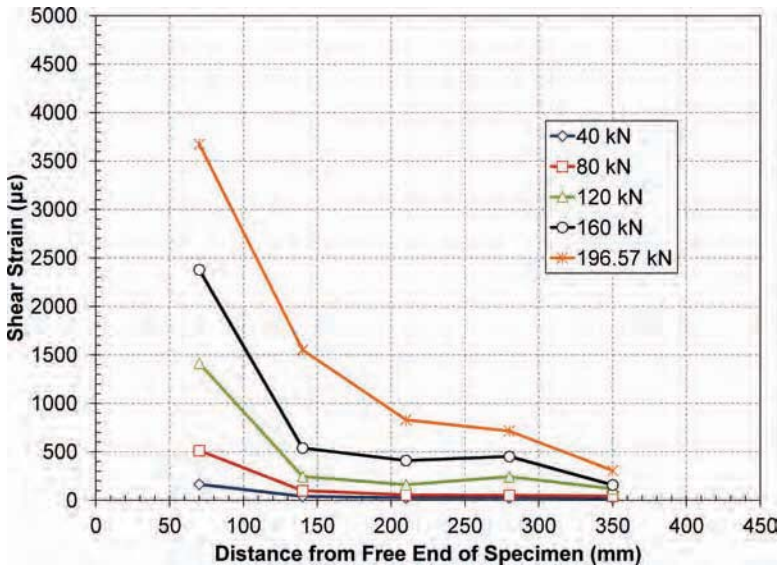


FIG. 16—Shear strain profiles for specimen A-2.

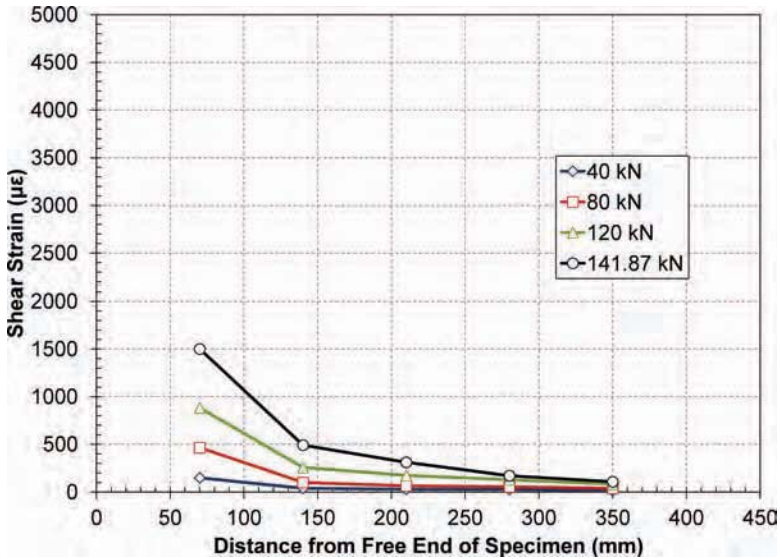


FIG. 17—Shear strain profiles for specimen A-3.

($y = Ax^2 + Bx + C$) closer to the free end while the trend is better described by a power relationship ($y = Ax^n + C$) closer to the fixed end. This is due to the changes in shear strain over the length of the bonded area, where the rate of strain increase is very stagnant at a distance from the free end but changes dramatically as the distance decreases.

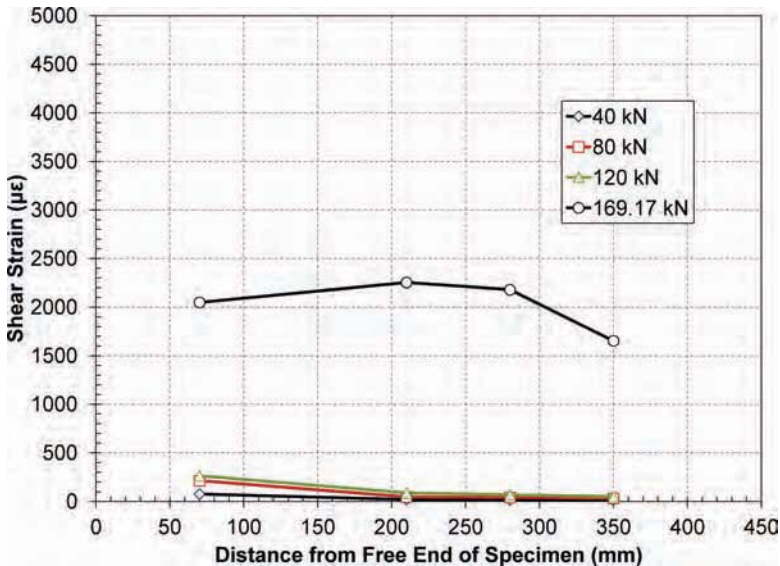


FIG. 18—Shear strain profiles for specimen B-1.

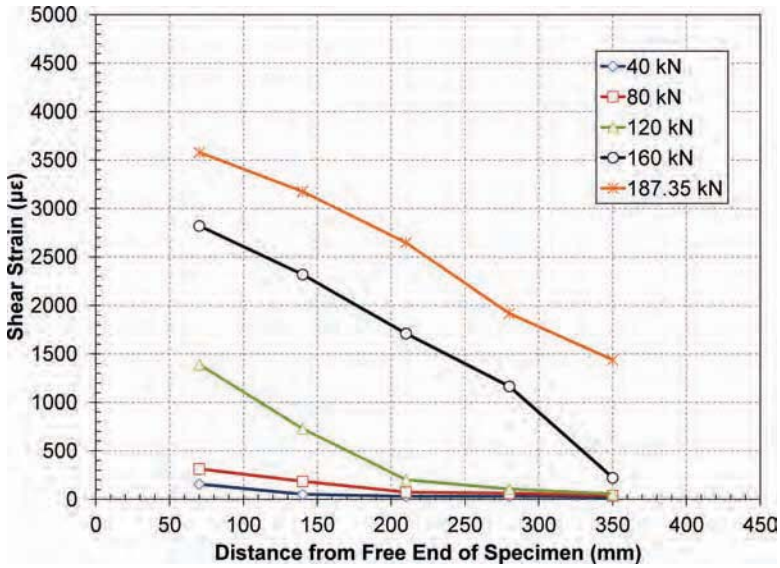


FIG. 19—Shear strain profiles for specimen B-2.

Summary of Relative Performance

The relative performance of the three different types of epoxy adhesives used for bonding of the coarse silica sand aggregates from both double shear testing as well as tension pull-out testing is summarized in Table 5, where the higher

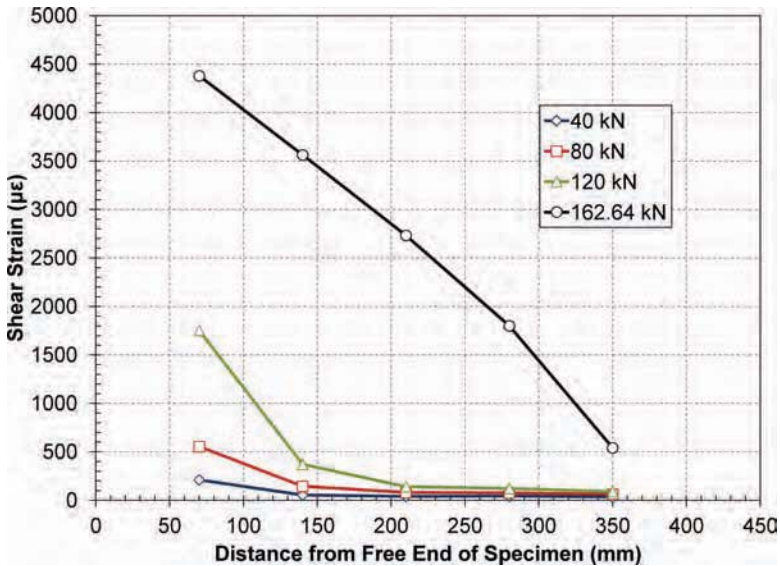


FIG. 20—Shear strain profiles for specimen B-3.

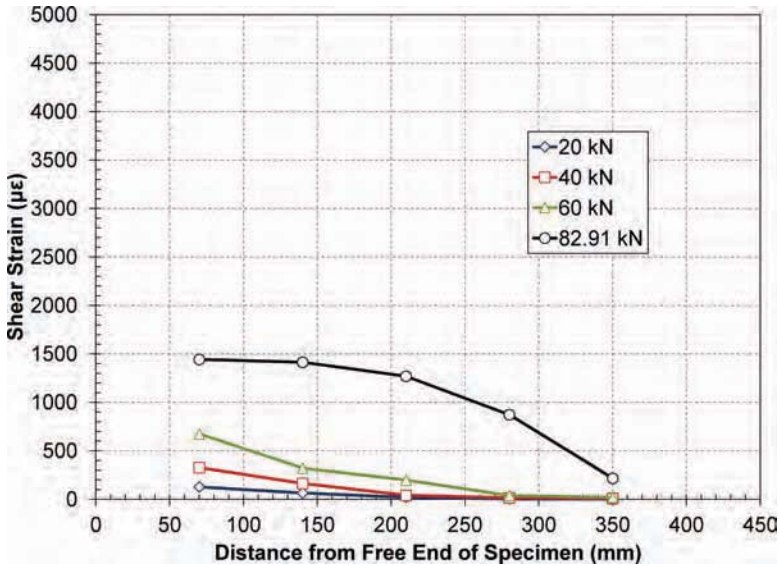


FIG. 21—Shear strain profiles for specimen C-1.

ranking is associated with the smallest number. While experimental error is to be expected for all research to be performed in a laboratory environment, the analysis conducted did show good consistency within each subgroup examined. Overall, it was evident that epoxy types A and B performed better than epoxy

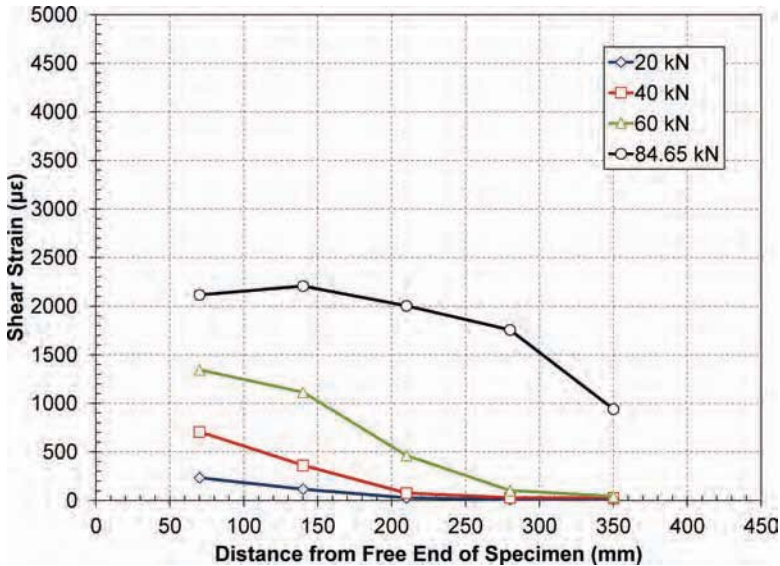


FIG. 22—Shear strain profiles for specimen C-2.

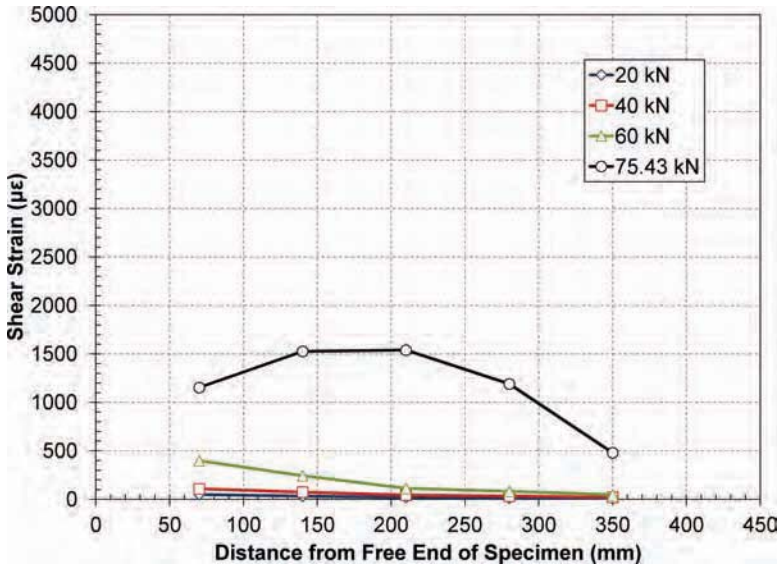


FIG. 23—Shear strain profiles for specimen C-3.

type C. Though epoxy type A performed better under shear loading, with epoxy type B showing higher performance under tension loading, it must be taken into account that the specimens with epoxy type A did not reach their full shear capacity at the interface due to premature shear failure at the bolted connections. Comparison between the distribution of data values collected from the shear and tension tests also showed greater consistency and smaller variance during the shear testing. From these results, epoxy type A was chosen as the epoxy adhesive for bonding of the coarse silica sand aggregates at the GFRP-UHPC interface, where the specimens demonstrated the best and most reliable performance under both shear and tension loading.

Conclusions

From the results obtained in this experimental program, the following conclusions were made:

TABLE 5—Relative performance of epoxy adhesives in double shear and tension pull-out tests.

Epoxy Type	Double Shear Test	Tension Pull-out Test
A	1	2
B	2	1
C	3	3

- Specimens using epoxy type A for bonding the coarse silica sand aggregates at the bond interface performed best during the double shear bond testing, where testing was interrupted by premature connection failure without any interface debonding.
- Specimens using epoxy type B for bonding the coarse silica sand aggregates at the bond interface performed best during tension pull-out testing.
- Failure in the specimens with epoxy type A and B occurred due to a combination of aggregate fracture as well as separation in the epoxy layer rather than solely in the epoxy layer, as was the case for the specimens using epoxy type C.
- Shear interface slippage behaviour is better represented using strain values obtained along the length of the specimen rather than differential displacement between the UHPC prism and the GFRP plate due to the higher number of data points used in the assessment of the load-slippage behaviour as well as the elimination of potential shifts in the mounting apparatus that could influence the data collected.

Acknowledgments

The writers would like to thank the following companies for their generous donations of materials used: Fyfe Co. LLC, Lafarge Canada, Hardwire LLC, and Sika Canada Inc. In addition, we would like to acknowledge the University of Calgary as well as the Natural Sciences and Engineering Research Council of Canada (NSERC) for their financial support towards this research.

References

- [1] Holloway, L. C., "A Review of the Present and Future Utilisation of FRP Composites in the Civil Infrastructure With Reference to Their Important In-Service Properties," *Constr. Build. Mater.*, Vol. 24, 2010, pp. 2419–2445.
- [2] Deskovic, N., Triantafyllou, T. C., and Meier, U., "Innovative Design of FRP Combined With Concrete: Short-Term Behaviour," *J. Struct. Eng.*, Vol. 121, 1995, pp. 1069–1078.
- [3] Cheng, L. and Karbhari, V. M., "Steel-Free Hybrid FRP Stiffened Panel-Concrete Deck System," *7th International Symposium on Fiber Reinforced Polymer Reinforcement for Reinforced Concrete Structures*, KS City, KS, Nov 5–7, 2005.
- [4] Honickman, H. and Fam, A., "Investigating a Structural Form System for Concrete Girders Using Commercially Available GFRP Sheet-Pile Sections," *J. Compos. Constr.*, Vol. 13, 2009, pp. 455–465.
- [5] Hai, N. D., Mutsuyoshi, H., Asamoto, S., and Matsui, T., "Structural Behavior of Hybrid FRP Composite I-Beam," *Constr. Build. Mater.*, Vol. 24, 2010, pp. 956–969.
- [6] Chajes, M. J., Finch, W. W., Jr., Januszka, T. F., and Thomson, T. A., Jr., "Bond and Force Transfer of Composite Material Plates Bonded to Concrete," *ACI Struct. J.*, Vol. 93, 1996, pp. 208–217.
- [7] Keller, T. and Gürtler, H., "Design of Hybrid Bridge Girders With Adhesively Bonded and Compositely Acting FRP Deck," *Compos. Struct.*, Vol. 74, 2006, pp. 202–212.
- [8] Keller, T. and Gürtler, H., "Composite Action and Adhesive Bond Between Fiber-Reinforced Polymer Bridge Decks and Main Girders," *J. Compos. Constr.*, Vol. 9, 2005, pp. 360–368.

- [9] Cho, K., Cho, J. R., Chin, W. J., and Kim, B. S., "Bond-Slip Model for Coarse Sand Coated Interface Between FRP and Concrete From Optimization Technique," *Comput. Struct.*, Vol. 84, 2006, pp. 439–449.
- [10] Correia, J. R., Branco, F. A., and Ferreira, J. G., "Flexural Behaviour of GFRP-Concrete Hybrid Beams With Interconnection Slip," *Compos. Struct.*, Vol. 77, 2007, pp. 66–78.
- [11] Ferracuti, B., Savoia, M., and Mazzotti, C., "Interface Law for FRP-Concrete Delamination," *Compos. Struct.*, Vol. 80, 2007, pp. 523–531.
- [12] Yun, Y., Wu, Y. F., and Tan, W. C., "Performance of FRP Bonding Systems Under Fatigue Loading," *Eng. Struct.*, Vol. 30, 2008, pp. 3129–3140.
- [13] Cho, J. R., Cho, K., Park, S. Y., Kim, S. T., and Kim, B. S., "Bond Characteristics of Coarse Sand Coated Interface Between Stay-In-Place Fibre-Reinforced Polymer Formwork and Concrete Based on Shear and Tension Tests," *Can. J. Civ. Eng.*, Vol. 37, 2010, pp. 706–718.
- [14] EXTREN Fibreglass structural shape, Strongwell Corporation, 2009.
- [15] ASTM D3039/D3039M-00, 2000, "ASTM. Standard Test Method for Tensile Properties of Polymer Matrix Composite Materials," *Annual Book of ASTM Standards*, Vol. 15.03, ASTM International, West Conshohocken, PA.
- [16] Ducal Fiche de Caractéristiques Techniques (25 June 2007, revision 2), http://www.ductal-lafarge.com/wps/portal/ductal/6_2-Products_and_technical_datasheet (Last accessed 3 Sep. 2010).
- [17] ASTM C469-94, 1994, "ASTM. Standard Test Method for Static Modulus of Elasticity and Poisson's Ratio of Concrete in Compression," *Annual Book of ASTM Standards*, Vol. 14.02, ASTM International, West Conshohocken, PA.
- [18] ASTM C496-96, 1996, "ASTM. Standard Test Method for Splitting Tensile Strength of Cylindrical Concrete Specimens," *Annual Book of ASTM Standards*, Vol. 14.02, ASTM International, West Conshohocken, PA.
- [19] Sikadur 32 HI-MOD product data sheet (Edition 7.1.2008) from <http://ca01.webdms.sika.com/files/show.do?documentID=103> (Last accessed 3 Sep. 2010).
- [20] Tyfo S saturant epoxy product sheet, from <http://www.fyfeco.com/products/pdf/tyfo%20s%20epoxy.pdf> (Last accessed 16 Dec. 2009).
- [21] Sikadur 330 product data sheet (Edition 07.2007) from <http://ca01.webdms.sika.com/files/show.do?documentID=95> (Last accessed 3 Sep. 2010).

M. Feldmann,¹ B. Abeln,² and E. Preckwinkel³

Characterization of Adhesive Joints for Hybrid Steel-Glass Beams by Means of Simplified Small Scale Tests

ABSTRACT: In the recent past there have been calls for transparent and filigree structures in the building industry. Therefore, glass plays an increasing role not only in a classic way, as a space enclosing element, but also more and more in terms of offering load carrying functions. Glass beams for façade elements or floor girders, glass columns, or bracing façade elements are examples of this. To realize such architecturally attractive structures, bonded hybrid steel-glass elements have been developed in which each material is used in an optimized way according to its material properties. Promising examples for such bonded structures are I-beams in which steel flanges and glass webs are connected by linear adhesive bonds. The shear force is carried by the glass web, whereas the bending capacity of the hybrid beam is significantly increased by slender steel flanges compared to the pure glass pane. The shear forces between steel and glass are sustained only by the adhesive between them. In order to maximize the exploitation of both steel and glass, the adhesive on the one hand has to ensure an adequate stiffness but on the other hand has to be flexible enough to allow for a reduction or redistribution of local stress peaks, as well as other constraints such as thermal dilatation. However, the load-bearing capacity of such beams is governed, besides by the mechanical and geometrical characteristics of the

Manuscript received June 9, 2011; accepted for publication October 28, 2011; published online December 2011.

¹Professor, Dr.-Ing., Institute for Steel Structures, RWTH Aachen Univ., Aachen, Germany, Mies-van-der-Rohe-Str. 1, 52074 Aachen.

²Dipl.-Ing., Institute for Steel Structures, RWTH Aachen Univ., Aachen, Germany, Mies-van-der-Rohe-Str. 1, 52074 Aachen, e-mail: abeln@stb.rwth-aachen.de

³Dipl.-Ing., Institute of Steel Construction, Dortmund Univ. of Technology, Dortmund, Germany, August-Schmidt-Straße 6, 44227 Dortmund, e-mail: Eva.Preckwinkel@tu-dortmund.de

Cite as: Feldmann, M., Abeln, B. and Preckwinkel, E., "Characterization of Adhesive Joints for Hybrid Steel-Glass Beams by Means of Simplified Small Scale Tests," *J. ASTM Intl.*, Vol. 9, No. 1. doi:10.1520/JAI104079.

Copyright © 2012 by ASTM International, 100 Barr Harbor Drive, PO Box C700, West Conshohocken, PA 19428-2959.

adhesive joint, by aging, temperature, and creeping. In this contribution, an approach is shown for characterizing the adhesive joints for hybrid steel-glass beams by means of simplified small-scale tests. Standardized specimens (block shear and tension bulk specimens) and small-scale push-out tests are used to derive adequate mechanical values for analytical and numerical calculations, allowing one to draw conclusions regarding the general load carrying behavior of large-scale hybrid steel-glass beams. The results show that full-scale hybrid steel-glass beams, especially those with butt splice bonded and U-bonded geometries, are feasible using new structural adhesives, predominantly elasto-plastics such as polyurethanes or epoxy resins.

KEYWORDS: hybrid steel-glass beams, structural glazing, adhesive technology, small- and large-scale tests, structural behavior

Introduction

In the recent past there have been calls for transparent and filigree structures in the building industry. Therefore, glass plays an increasing role, not only in a classic way as a space enclosing element, but also more and more in terms of offering load carrying functions. As a comparatively new development, hybrid or all-glass structures are the topic of recent research projects [1–4] in which glass forms the main supporting structure, such as glass beams for façade elements and floor girders, glass columns, or bracing façade elements. The brittle glass behavior and a small tolerance toward stress peaks in contrast to the characteristics of plastic and ductile steel require some targeted design appropriate for both materials involved. For these contemporary transparent and load bearing structures, bonded hybrid steel-glass elements are suitable; in these, each material is used in an optimized way according to its material properties.

Promising examples for such bonded structures are I-beams consisting of steel flanges and glass webs that are connected by linear adhesive bonds [5]. In particular, load-bearing elasto-plastic and stiff adhesives are the focus of research, as these are considered as an enhancement to the general accepted and multiple applied silicones in façade structures.

In such beams, the shear force is carried by the glass web, whereas the bending capacity of the hybrid beam compared to that of the pure glass pane is significantly increased by slender and hardly perceptible steel flanges. The shear forces between steel and glass are sustained only by the adhesive between them. In order to maximize the exploitation of steel and glass, the adhesive on the one hand has to ensure an adequate stiffness and carrying capacity but on the other hand has to be flexible enough to allow for a reduction or redistribution of stress peaks. At the same time, the mechanical characteristics of the joint could be strongly influenced by aging, temperature, and creeping, governing the overall load-bearing capacity of such beams.

Systematic Approach and Design Procedure

The geometry, stiffness, and load carrying capacity of the adhesive joint are of central significance for the structural behavior of the hybrid beam. This implies

detailed knowledge of the mechanical values and the durability of the adhesives. Particularly, discontinuities in the boundary areas require a closer examination.

The aim of the INNOGLAST project [5,6] is to derive simple design recommendations for bonded hybrid steel-glass beams, taking into consideration the common safety specifications of glass and thus avoiding extensive finite element calculations. In order to achieve this, a systematic approach was chosen, which is shown in Table 1.

The basis for this approach is the knowledge of the slip and elongation characteristics of the adhesive joint (Table 1, I) arising from the context of the building structure, defining the structural and geometrical requirements for the adhesive joint. Depending on the connection type (Table 1, II), slip differential equations [7] are a useful means to determine the slip-strain behavior. In the next step, appropriate adhesives are chosen (Table 1, III) and the mechanical values are determined (Table 1, IV), and these are then carried over to small-scale push-out tests (Table 1, V–VI) and verified by large-scale component tests (Table 1, VII). Finally, design recommendations are derived (Table 1, VIII).

In the following, the detailed approaches for the choice of appropriate adhesive systems and the derivation of suitable mechanical values are presented, in particular with respect to durability and realistic bonding geometries.

Requirements for the Adhesive Joint

As a result of this (still ongoing) research, it has become apparent that structural bonded joints should be divided into different connection classes that describe their carrying behavior clearly in order to design them according to the static relevance of the bonded connection. Hence the working group “Adhesive Bonding” of the German Professional Association for Structural Glazing (FKG) is currently creating a guideline for the fabrication and monitoring of bonded connections in structural glazing [8]. Figure 1 shows the general structural classification. The draft guideline proposes the division of bonded connections in continuous and discontinuous joints. Accordingly, continuous joints are assemblies or components such as hybrid bonded beams or structural glazing elements [9,10] that offer, due to their plane or distinctive linear bonding geometry or because of their structural integrity, a more ductile and redundant behavior. In opposite discontinuous joints are cross sections, connections, or details such as point fittings [11] and lap joints that show a brittle behavior as a result of their punctual or small bonding surface without structural redundancy. In Ref [5], small-scale push-out tests represent discontinuous joints and component tests represent continuous joints.

Surfaces and Materials

Surface preparation and pretreatment are essentially necessary for the durability of bonded joints. However, in civil engineering, which shows considerable tolerance and surface contamination compared to the automotive or aviation industry, the effort, extent, and benefit of preparation methods must be well

TABLE 1—Systematic approach within the INNOGLAST project [5].

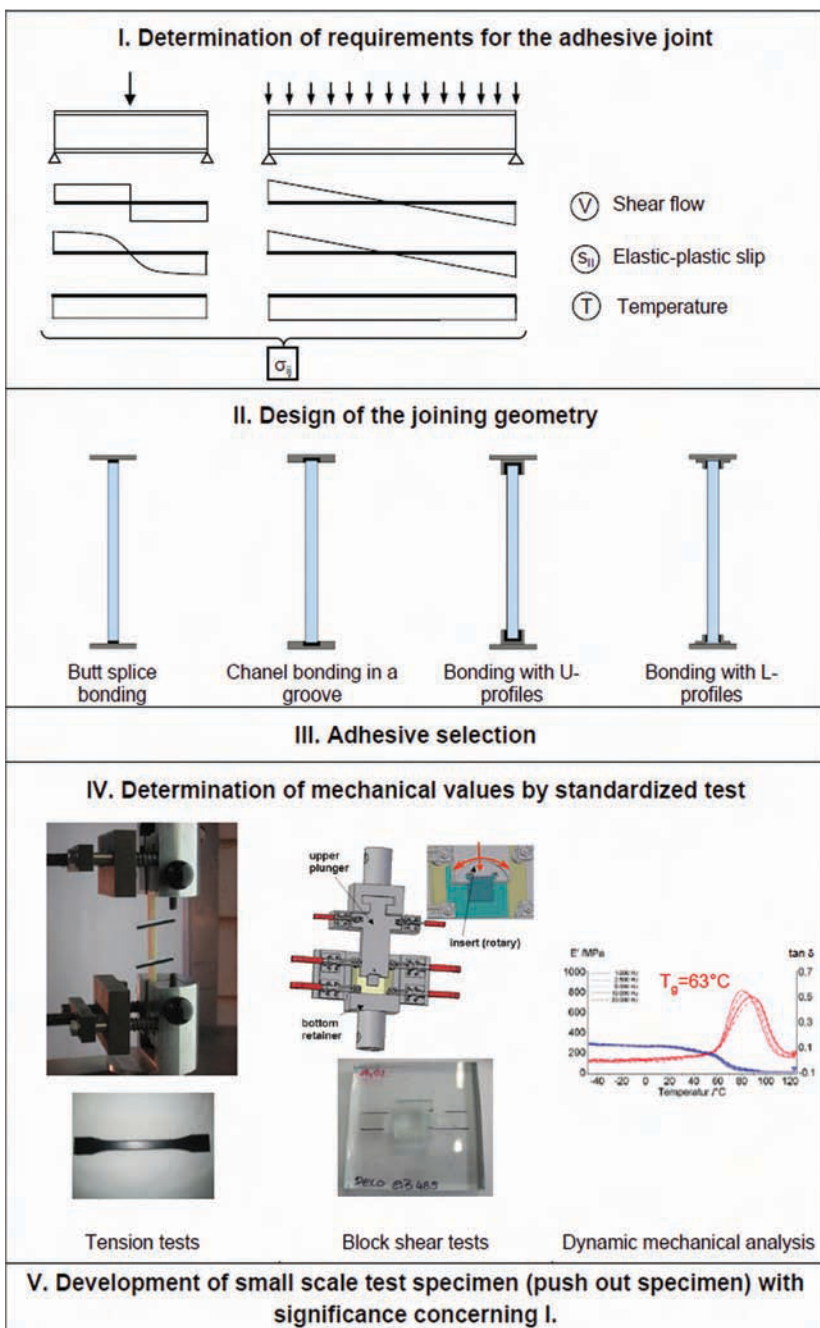
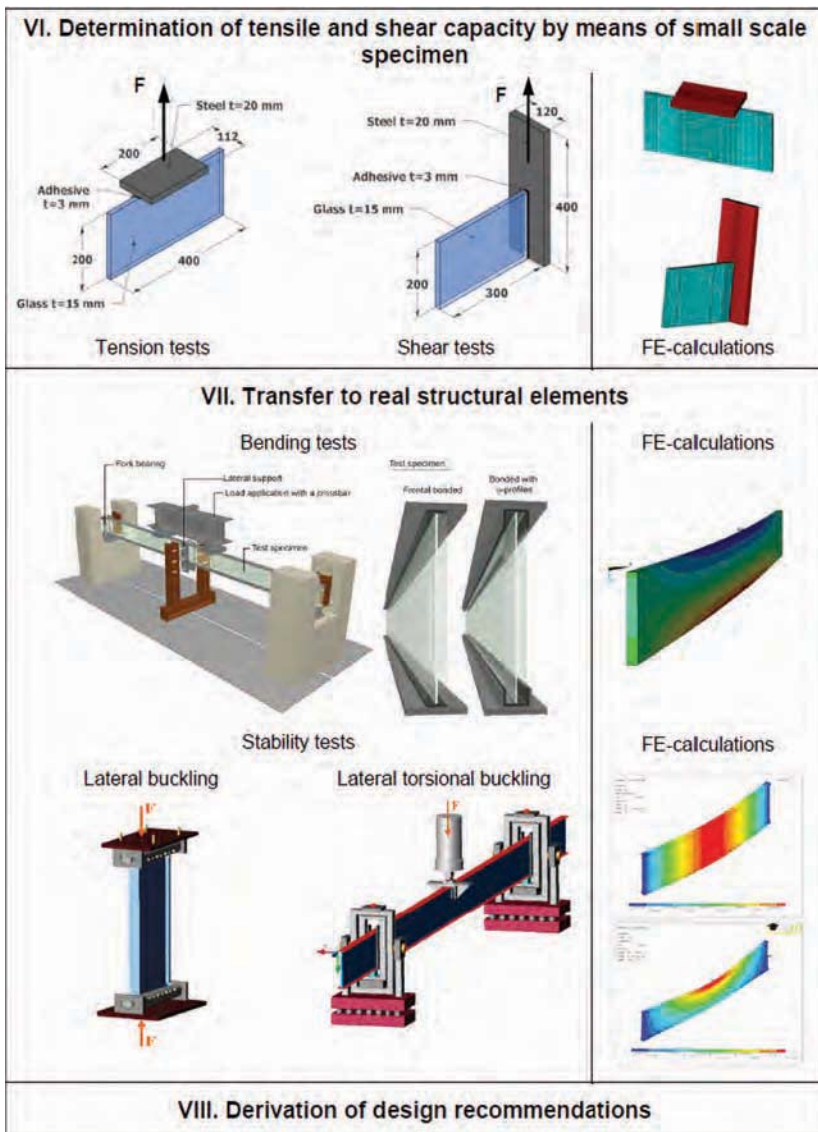


TABLE 1—Continued



balanced. Therefore, only associated adhesive-primer systems identified by the producers were used in order to avoid additional disturbing factors such as the general applicability and compatibility of primer and surface treatments.

In the case of adhesive with a low or medium shear modulus, carbon steel grade S235 was applied for the flanges, and for stiff epoxy resins steel grade S355 was used. The glass webs for small-scale tests consisted of toughened

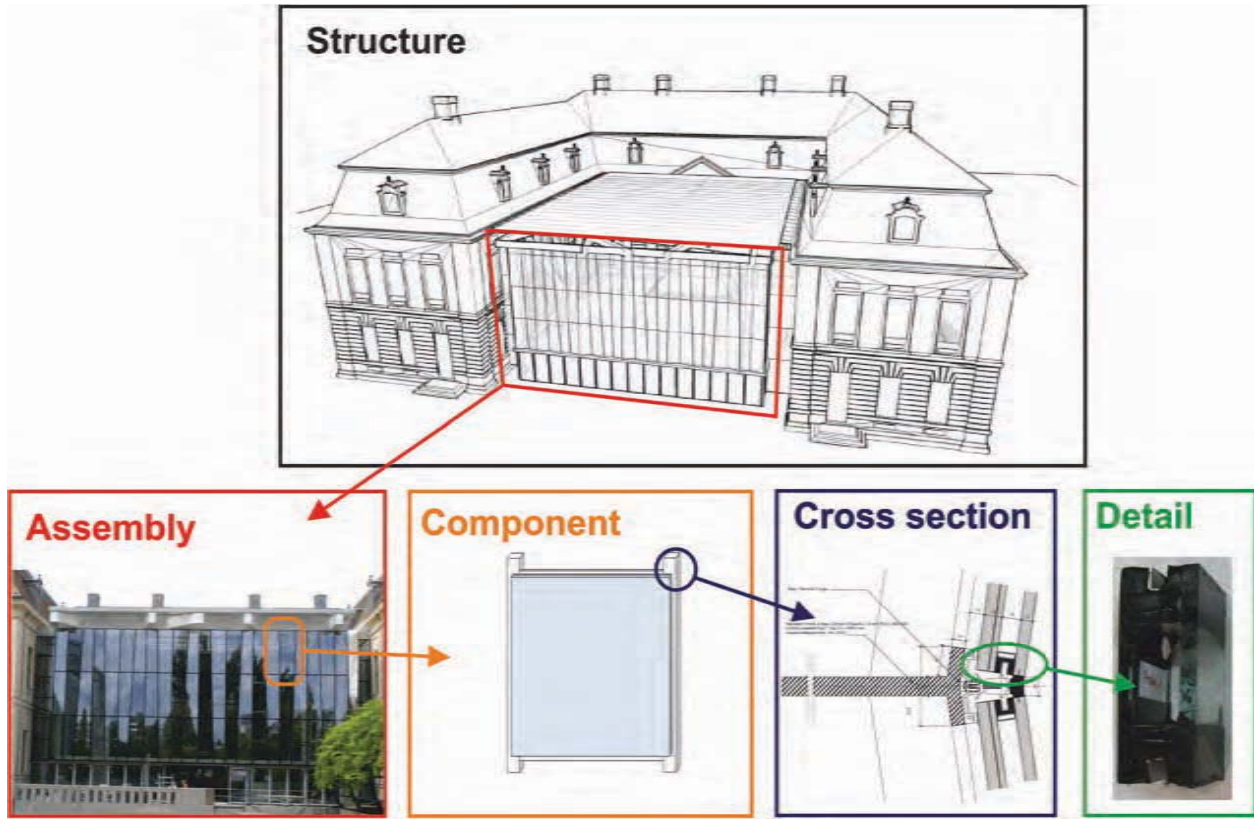


FIG. 1—Classification of building structures [8].

safety glass, and for component large-scale tests it consisted of laminated safety glass due to safety aspects that will be demanded by building authorities. All steel surfaces were sandblasted to cleanliness 2 1/2 [12–14]; glass surfaces were wiped, degreased, furnished with primer, evaporated, and bonded directly.

Adhesive Selection

In addition to the mechanical properties, the selection of adhesives is ruled by a lot of other factors, which, according to Ref [8], can be categorized in terms of product requirements, loads and actions, resistances related to aging, durability, and other factors.

Product requirements involve aspects regarding the type of substrate (steel, glass), thicknesses, tolerances, surfaces (contamination, grease, oil), coatings (screen print, zinc), pre-treatments (primer, activator), connection type (structural, dis-/continuous, sealing, assembling), production conditions (on-site, workshop, laboratory), application behavior (viscosity, pot life), and processing properties (curing mechanism, mixing).

Loads and actions can be static, strain-rate, or temperature dependent; creeping; and relaxation or dynamic. Another significant load is summarized by exposure classes, which include effects from climate change, weathering, corrosion, and ultraviolet (UV) light.

The resistance to aging and temperature is strongly influenced by durability aspects such as the projected life cycle, compatibility (polyvinyl butyral (PVB) foils), inspection, and reparability.

Other issues are economical (costs), architectural (color, visual attraction), or constructional ones that determine the adhesive selection.

Therefore, mechanical values are not always the only decisive selection criterion.

Concerning bonded hybrid beams, the adhesive selection firstly depends on the bonding geometry (Table 1, II), which has to ensure the bubble-free filling of joints and complete curing and guarantee protection from UV radiation and weathering, which would lead to a considerable strength decrease or loss of adhesion. Butt joints and connections with U-profiles seem to be the most promising in this regard. Additionally, the cured bonded joint has to meet static and constructional requirements such as the following:

- Load transfer of shear forces.
- Compensation of fabrication tolerances.
- Reduction of stress peaks.
- Compensation of constraint forces due to possible thermal expansion.

In particular, the adhesive thickness is one of the decisive factors for the load bearing behavior and stiffness of the adhesive joint. In the past, numerous research projects revealed that every adhesive has an optimal thickness (for most adhesives it is between 0.05 and 0.2 mm) at which the load bearing behavior and carrying capacity are best [15]. For the large-scale hybrid steel-glass beams developed within the INNOGLAST project, it was not possible to achieve adhesive thicknesses smaller than 3 mm without avoiding steel-glass contact due to the tolerances of the thin steel flanges and glass fins of at least 4 m in

length. Smaller adhesive thicknesses of about 1 mm would increase the stiffness significantly and lead to higher ultimate loads and beam stiffnesses, but from a manufacturing point of view they are not achievable in practice. However, the main advantage of these high thicknesses is the high temperature compensation capability for temperature differences between steel and glass, even for very stiff adhesives. Therefore, in all cases an adhesive thickness of 3 mm was used.

Based on these considerations, seven cold-hardening (room temperature) adhesives were selected, most of them two-component structural adhesives: one two-component high-strength epoxy resin with high temperature resistance, four two-component polyurethanes with different strengths, one UV-curing acrylate, and, as a reference, a two-component silicone generally applied for structural sealant glazing. These adhesives were selected in such a way as to include both very stiff adhesive systems with high Young's moduli and strength values and flexible adhesive systems with low strengths and stiffnesses. Adhesives with minor temperature resistance were generally avoided, as were adhesives with limited pot life or viscosity and those with a curing mechanism unsuitable for linear steel-glass connections, such as warm- or humidity-curing systems.

Beyond that, the choice of adhesives was made with regard to potential "inside" and "outside" application, which means the adhesives should withstand weathering, UV radiation, cleaning agents, and temperature changes without any relevant change of their mechanical properties or any loss of bearing capacity. Not all of the four joining geometries (Table 1, II) are well suited for each adhesive; thus the advantages and disadvantages must be checked for each application. In addition to the required bonding length, high workmanship and optical criteria are of particular importance.

Determination of Mechanical Values of the Adhesives

In a first approach, the mechanical properties of the selected adhesives are determined by carrying out small-scale tests using standardized specimens (Table 1, IV):

- Determination of tension strength, Young's modulus, and Poisson's ratio by means of dumbbell specimens according to DIN EN 527 [16].
- Aging of block shear specimen through the immersion test (six-week water bath at 60°C [17]).
- Determination of shear modulus, shear strength, and shear stress-sliding behavior by pressure block shear tests of aged and unaged glass specimens according to EN ISO 13445 [18].
- Differential scanning calorimetry to obtain the temperature behavior, including the glass transition temperature.

The tension tests are performed on dumbbell specimens (specimen type 1A) using a universal testing machine with a video extensometer. In a first approach, the tests are carried out as displacement-controlled with rates of 1.0 mm/min.

For the intended shear tests, usually thick steel or aluminum adherents, according to DIN EN 14869-2 [19], are used. Because of the need to test glass substrates, the geometries mentioned in EN 14869 are not applicable; therefore,

within the INNOGLAST project [5] the shear values were determined using a modified block shear test [20] according to EN ISO 13445.

It is important to note that for the evaluation of test results, the failure mode of the tested shear specimens must be similar, which means that the predominant failure mode must be cohesive, occurring in the adhesive layer or near the boundary layer. That is why the use of hybrid steel-glass bonded joints should be consciously discarded for the tests in order to avoid mixed steel-glass bonds, with which the failure cannot always be allocated clearly to the steel or glass surface, potentially making the failure ambiguous.

The immersion tests are performed according to DIN 53287 [17]. The test is defined by a six-week water storage in 60°C demineralized water. After six weeks the specimens are removed from the water bath and cured in a climate chamber. The aged specimens are then subjected to shear tests. The results are compared to the shear test results of unaged specimens.

Table 2 gives an overview of the important mechanical values of the selected adhesives as determined by the tests mentioned above. Figure 2 shows the change of shear moduli determined in block shear tests on unaged specimens and aged specimens after six weeks of water bath immersion. In the diagram, mean values and 5% fractiles are displayed. Especially for the high-strength epoxy resins and polyurethane adhesives, there is a significant decrease of stiffness and strength after aging; in the case of K02, the specimen even showed considerable embrittlement. However, when the silicone K07, which is commonly used for structural glazing applications, is compared with high-performance polyurethane (K05, K06), it becomes evident that there are modern adhesive systems with adequate stiffness, strength, and ductility. These adhesives offer good aging resistance together with a stiffness and strength at least five times higher than that for silicones. Even if the durability still must be further verified and conferred on building purposes, new possibilities for dimensioning and load transfer by adhesive connections are possible.

TABLE 2—Characteristics and mechanical values of the selected adhesives (strengths and strains are log-normal distributed 5% fractile values).

Adhesive	K01	K02	K03	K04	K05	K06	K07
Adhesive system	EP	PU	PU	AC	PU	PU	SI
Components	2	2	2	1	2	2	2
Pot life, min	90	10	90	1 (UV)	15	30	10
Tension strength, MPa	27.3	9.3	7.9	9.3	4.2	6.3	0.9
Elongation at break, %	3.3	26	0.5	74	30	111	76
Young's modulus, MPa	1499	231	1906	314	16.5	20	2.4
Unaged shear strength, MPa	18.6	12.9	2.7	6.3	6.7	3.7	1.4
Unaged shear modulus, MPa	242	128	146	63	5.4	3.4	1.1
Glass transition temperature, °C	60	25	43	—	−61	−83	−90

Note: EP, epoxy resin; PU, polyurethane; AC, acrylates; SI, silicone

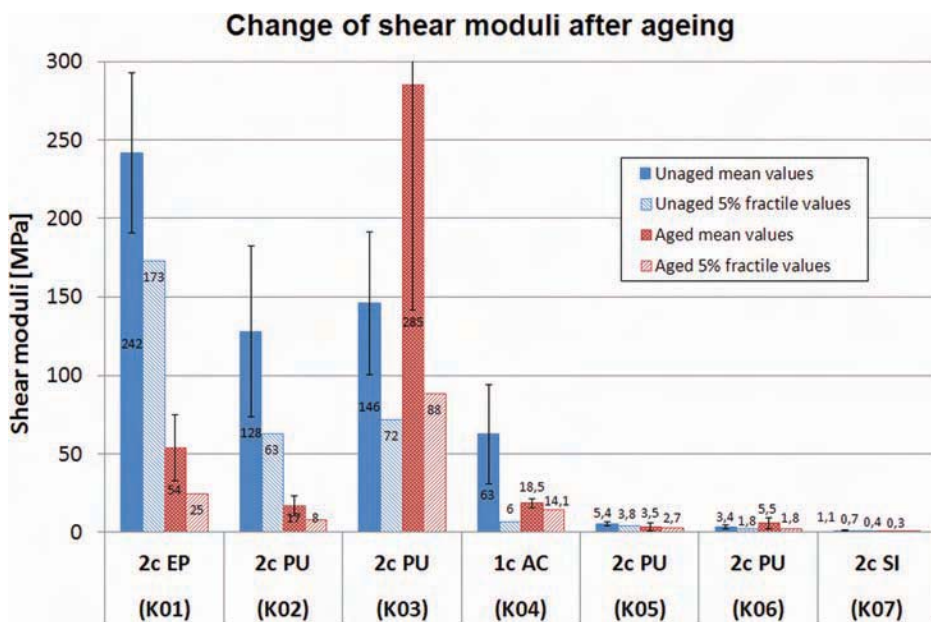


FIG. 2—Change of shear moduli before and after aging as determined by block shear tests.

For the following finite element (FE) modeling of the push-out and component tests, the standardized tests described above showed restrictions regarding the precision with which they could be used as input values for finite element method. In particular, the block shear tests revealed non-neglectable bending moments due to the single lapped geometry and their eccentricity. The resulting peel stresses significantly affected the shear stress-strain curve, thus preventing simple shear tests.

Therefore, the approach has been modified, resulting in a changed test setup and test control. The tension tests then have been performed with a Zwick Z100 universal testing machine with touching high-precision extensometers. All tests have been performed as strain-controlled with varying strain rates (0.0033/0.033/0.33/3.33 1/Min.) in order to cover the rate dependency, in particular for common façade application (<1 Hz).

The shear tests have been carried out on modified thick adherent test specimens made of steel and glass using the same strain rate as for the tension tests, in order to compare the results of both load types. The resulting characteristic values have been used as input values for Drucker-Prager material laws in the case of stiff, elasto-plastic adhesives (epoxy resins, some polyurethanes) and have been verified with butt-joint tests. With Drucker-Prager material laws, the influence of the hydrostatic state of stress and yielding can be considered. The modeling of visco-elastic adhesives (silicones, most polyurethanes) has been done using Mooney-Rivlin, Arruda-Boyce, Neo-Hookean, or Ogden, and in most cases Arruda-Boyce and Neo-Hookean fit best.

Additionally, the influence of the surface (steel or glass surface) has been taken into account in order to secure this strategy. This modified approach is still ongoing and will be finished by the end of this year [21].

Small-Scale Component Tests

In order to derive reliable design methods to predict the adhesives' strength behavior via continuum mechanical analyzing methods, various small-scale push-out tests were carried out. For the standardized tests (Table 1, IV), the load carrying behavior is treated separately for shear and tension loading (Table 1, VI). The tests take into account different adhesives and additionally the geometric influence of different joining geometries (Table 1, II). The general transfer of characteristic values determined by standardized characteristic tests (Table 1, IV) on bulk material or simple shear connections to small-scale components also has been investigated.

When the force-deflection behaviors of different joining geometries for the same load case (either shear or tension) are compared, it becomes evident that bonded connections with U- and L-profiles and butt splice joints and channel bondings have very similar structural behavior in terms of stiffness, strength, and ductility. Figure 3 shows results for the two-component polyurethane (K05) using the four joining geometries in Table 3, which are representative of the tested flexible adhesives. Connections with U- and L-profiles hereby show a considerable increase of strength and stiffness in comparison with butt splice and

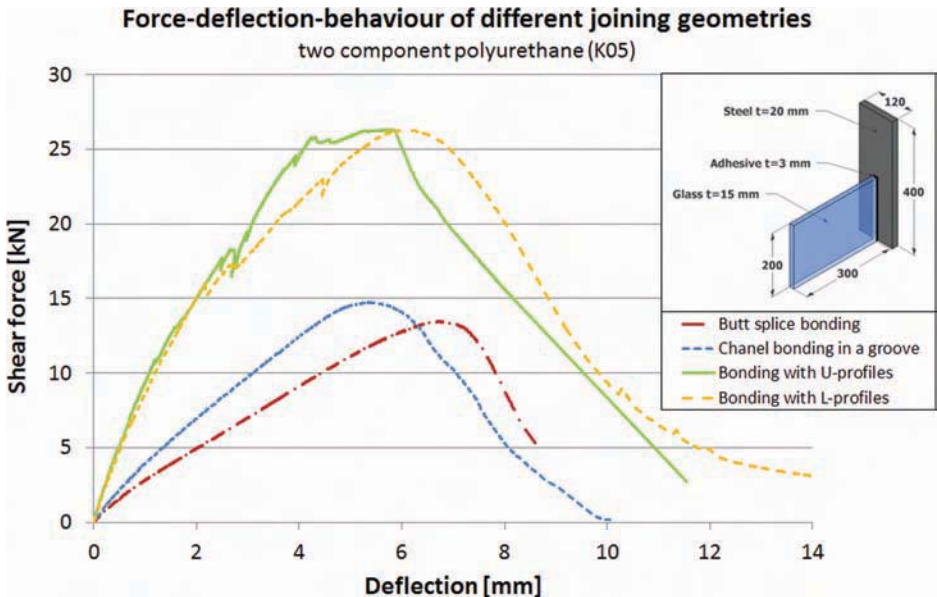
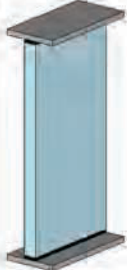





FIG. 3—Force-displacement behavior for two-component polyurethane (K05) subjected to shear loading using different adhesive geometries (Table 3).

TABLE 3—Relative performance of different adhesive geometries (refer to Table 1 and 2).

Adhesive geometry	Butt splice bonding 	Chanel bonding in a groove 	Bonding with U-profiles 	Bonding with L-profiles 
Adhesive surface	+	++	+++	+++
Producibility	+++	++	+	+
Appearance	++	+++	+	+
Controllability	+++	++	+	+
Ductility	+	++	+++	+++
Resistance	+	++	+++	+++

channel bonded connections. The bonding geometry (U-shaped joint with three flanks versus butt joint) substantially determines the constraint of the lateral expansion, which, for the U- and L-shaped geometries, leads to a visible stiffening effect. The higher carrying capacity for the U-shaped joints results from the enlarged adhesive surface.

For simple shear loading, Fig. 4 shows that the stiffness of the push-out specimen can be reproduced by the standardized tests very well, whereas for simple tension loading this is not successful (see Fig. 5). In both figures the maximum loads of small-scale tests are generally higher due to scale effects.

Thus it is explicable that the results of the standardized block shear and tensions tests, which in the beginning of the INNOGLAST project are expected to be mechanical simple tests, cannot be transferred to large-scale component tests for every type of loading. The block shear test with significant bending effects in particular does not present a simple shear test.

In fact, most adhesives show a quasi-isotropic material behavior for small strains in the elastic region, but depending on the type of adhesive the state of stress and the following yielding and failure—in particular for elasto-plastic

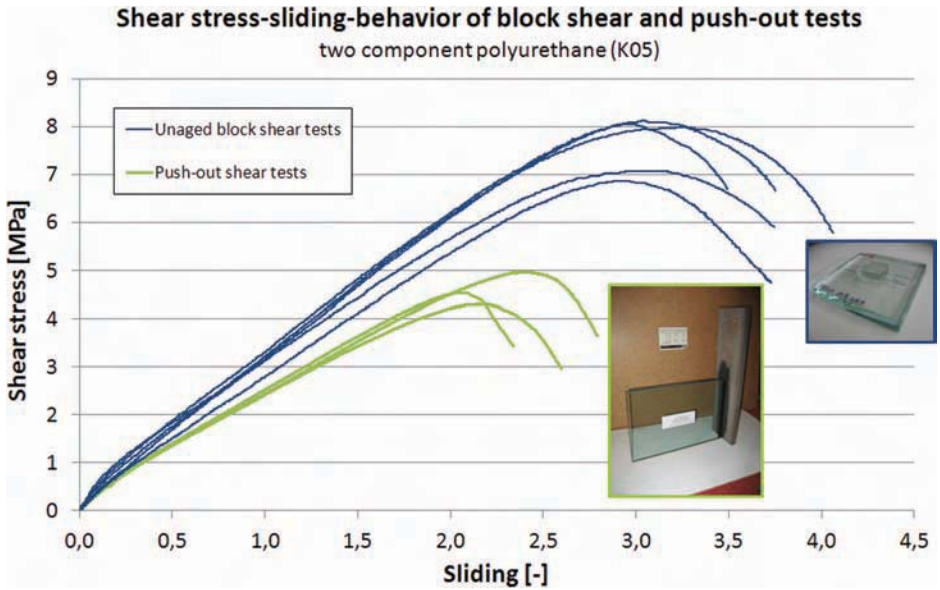


FIG. 4—Stress-strain behavior of standardized specimen and component tests subjected to shear loading.

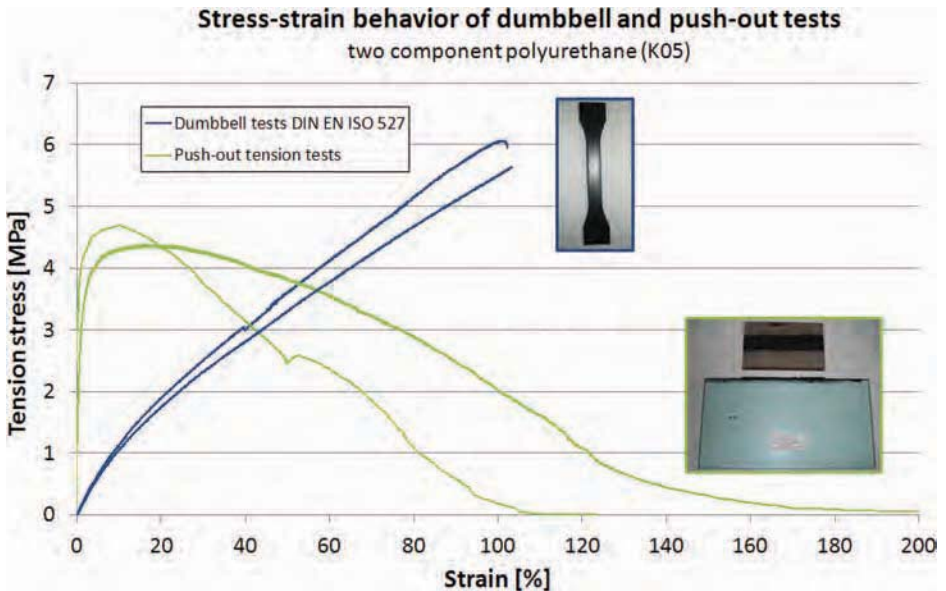


FIG. 5—Stress-strain behavior of standardized specimen and component tests subjected to tension loading.

adhesives—is predominantly determined by the hydrostatic stress portion (see Eq (1))

$$\begin{pmatrix} \sigma_{11} & \sigma_{12} & \sigma_{13} \\ \sigma_{21} & \sigma_{22} & \sigma_{23} \\ \sigma_{13} & \sigma_{32} & \sigma_{33} \end{pmatrix} = \begin{pmatrix} \sigma'_{11} & \sigma'_{12} & \sigma'_{13} \\ \sigma'_{21} & \sigma'_{22} & \sigma'_{23} \\ \sigma'_{13} & \sigma'_{32} & \sigma'_{33} \end{pmatrix} + \begin{pmatrix} \sigma_m & 0 & 0 \\ 0 & \sigma_m & 0 \\ 0 & 0 & \sigma_m \end{pmatrix} \quad (1)$$

Spatial state of stress
Deviator (deformation)
Spheric tensor (volumetric change)

To characterize this hydrostatic stress effect, simple tension tests, simple shear tests, and butt joint tests with constraint lateral expansion are performed; see the section “FE Modeling” and Fig. 9.

Due to the existing compressibility of elasto-plastic, stiff adhesives, the influence of the hydrostatic state of stress for these adhesives is larger than that for flexible, visco-elastic adhesives with approximately incompressible behavior (volume constancy), such as silicones or visco-elastic polyurethanes.

Based on the pronounced restraint of the lateral expansion, the push-out tests reveal a multiaxial state of stress (caused by a uniaxial state of strain), whereas the standardized tension tests offer a state of uniaxial stress. This fact must be considered for the FE calculations, choosing appropriate material laws and flow rules, e.g., with Drucker-Prager or Schlimmer-Mahnken [22].

For these mechanical reasons, and also for other important reasons, following the evaluation in Table 3, not all of the four joining geometries are quite applicable for all adhesives. Major differences have been found in the area of the adhesive surface, the quality of work, the controllability, and the aesthetic appearance of the bonded joint. Indeed, bonded joints realized with U- or L-profiles proved to be more sustainable and more ductile due to the redistribution capacity from the frontal part to the flanks of the bonded joint. However, for these two geometries the disadvantages regarding production predominate, especially when they are being applied to large components. Here only casting with low viscosity adhesives is applicable. Focusing in particular on simplicity while taking into account all relevant criteria gained within this project, the butt joints turn out to be the most promising ones.

Large-Scale Component Tests

Building on the standardized adhesive tests described in the section “Determination of Mechanical Values of the Adhesives” and the small-scale push-out tests discussed in the section “Small-Scale Component Tests,” the bearing behavior was studied via large-scale component tests. As the effectiveness of the load transfer through the adhesive connection mainly depends on the length of the hybrid beam, a span of 4 m was chosen for constructional aspects. Figure 6 shows the test setup of the four point bending test. Within the test series, the cross-sectional dimensions were kept constant, and only the adhesive varied, using the adhesives K01, K05, and K07 from Table 2. The hybrid beams were displacement controlled loaded until glass breakage, and it became obvious that the carrying capacity significantly rises with increasing shear stiffness of the adhesive (see Fig. 7). The calculation of stresses at midspan shows that the different bearing

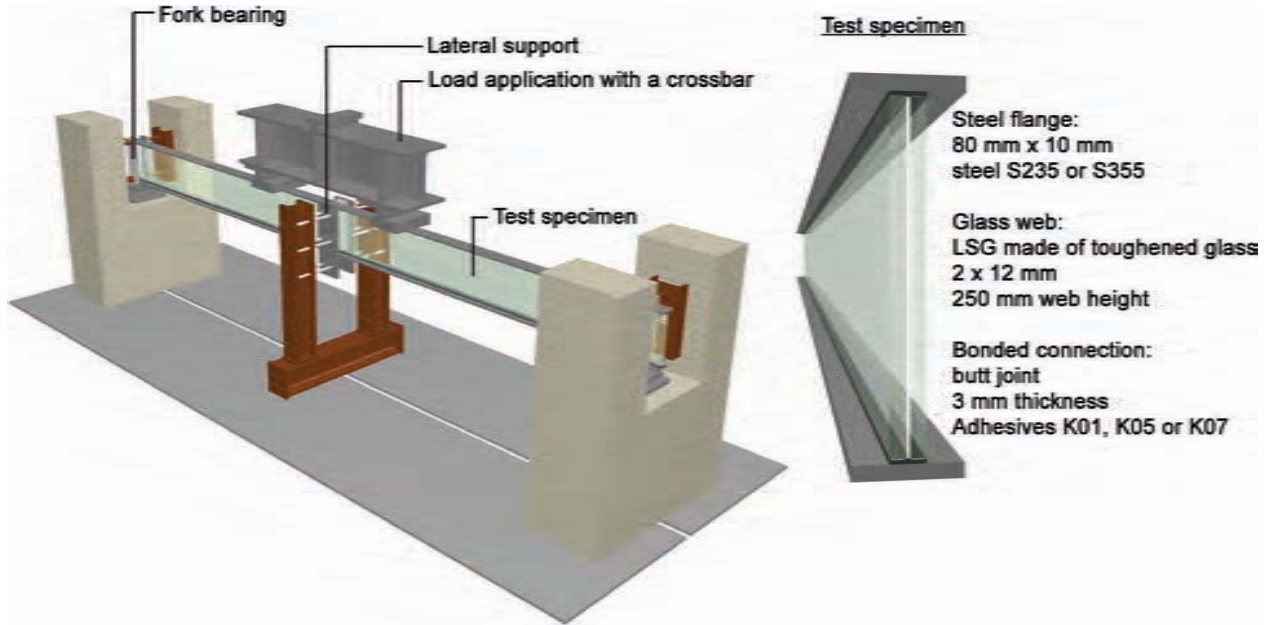


FIG. 6—Test setup of large-scale tests.

Failure loads of large scale component tests

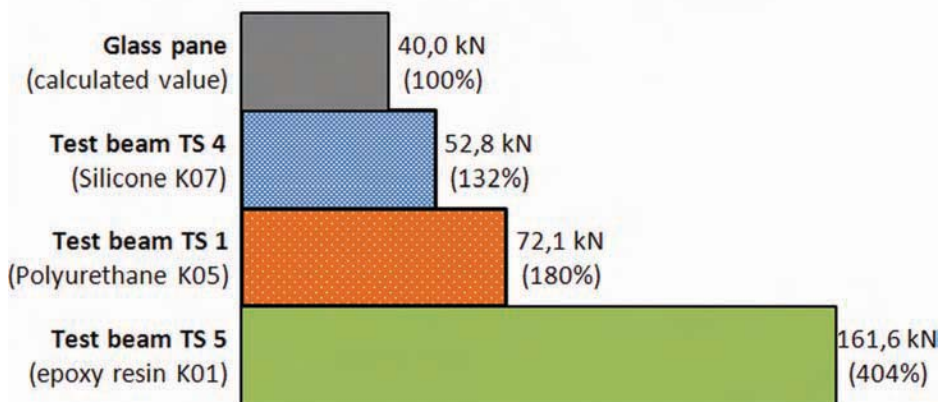


FIG. 7—Failure loads of large-scale tests.

capacities are directly related to the normal forces in the flanges, as moments in web and flanges are almost similar.

The large-scale tests were recalculated using analytical and numerical methods (see the section “Modeling and Design”), assuming a linear deflection behavior of the adhesive connection. These linear approaches are in good accordance with the tests. Figure 8 compares the linear shear stiffness of the large-scale tests with the stiffness of the block shear tests (see the section “Determination of Mechanical Values of the Adhesives”). The shear stiffnesses of tests TS4 and TS5 match the secant stiffness of the associated block shear tests very well; the rather small discrepancy in TS1 is the result of a discovered inferior bonding quality of the component test.

Modeling and Design

Analytical Modeling

Because of their bonded connection, hybrid steel-glass beams offer a specific bearing behavior that needs to be considered in analytical calculations. Hereby the load transfer mainly depends on the shear stiffness of the adhesive connection. The size of the composite action between steel and glass specifies the normal force that can be transferred to the steel flanges and thus defines the bearing capacity of the beam. Appropriate methods are based either on the sandwich theory [23] or on approaches according to Möhler [24] or Pischl [25]. Within the analytical investigations of INNOGLAST on bonded steel-glass beams, these three methods were modified (sandwich theory in Ref [26], Möhler or Pischl theory in Ref [27]) and used for the design of steel-glass beams. Especially, approaches according to Möhler and Pischl have been established for segmented wooden structures with flexible connections for years and have led to reliable results that are easy to calculate for practical applications. The basis of the

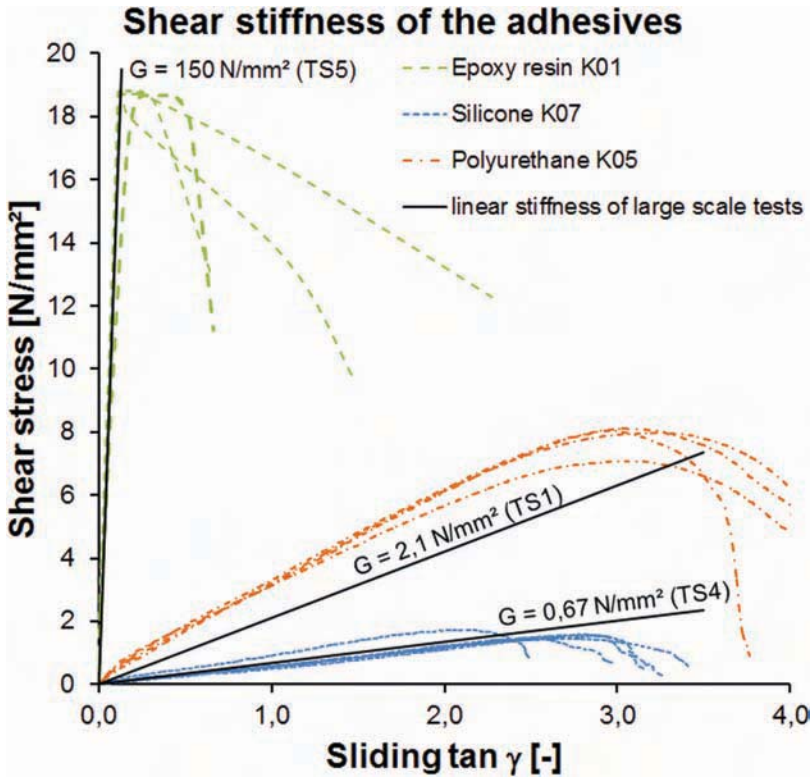


FIG. 8—Comparison of the adhesives' deformation behavior in block shear tests and large-scale component tests.

Möhler approach is the calculation of effective beam stiffnesses, whereas the Pischl method directly assigns the normal force to the flanges. The disadvantage of all simplified methods is the lack of knowledge of the detailed multi-axial stress distribution within the adhesive connection; here only smooth distributions result.

FE Modeling

On the basis of the results described in the section "Determination of Mechanical Values of the Adhesives," non-linear FE calculations of the push-out tests were performed. One of the project's aims was the choice of adequate material laws to describe the structural adhesive behavior of the connection of characteristic tests on standardized specimens for each of the adhesive systems (epoxy resin, polyurethane, silicone). Both hyper-elastic material laws on the basis of elastic potential (Mooney-Rivlin, Yeoh, Ogden) and a micro-mechanical chain model according to Arruda-Boyce were used; in general these are able to characterize the rubber-like behavior of soft adhesives adequately. For elastic-plastic adhesives it becomes apparent according to Fig. 9 that FE calculations on the basis of von-Mises

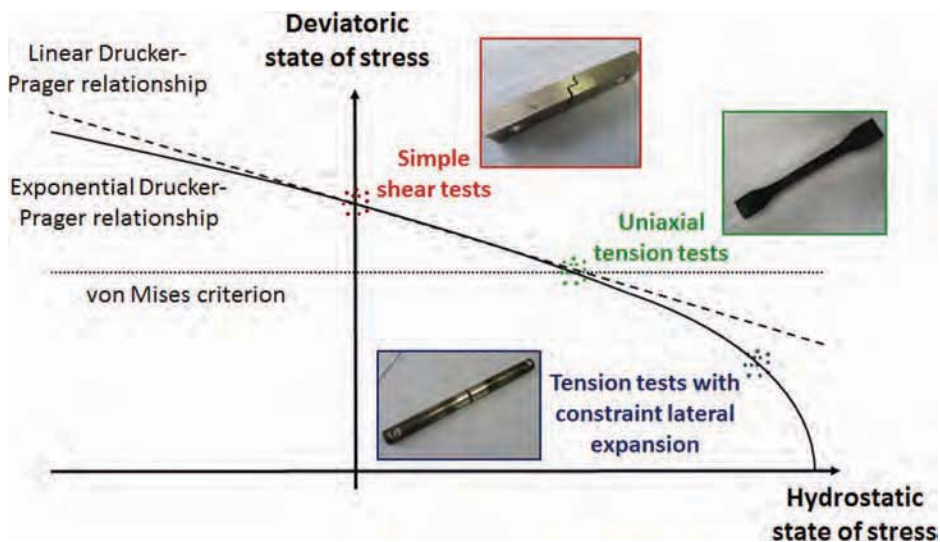


FIG. 9—Approach for determination of failure criteria based on mechanical values from simple basic tests.

equivalent stresses cannot provide sufficient results for the flow behavior of adhesives, especially under tension loading. An improved approximation for building purposes can be achieved with a linear or exponential Drucker-Prager or Mohr-Coulomb relationship. A comparatively new approach according to Schlimmer and Mahnken [22] has not been applied here due to the complex determination of input parameters by characteristic tests, its focus on crash simulation, and the missing implementation in commercial FE software.

As for the analytical method, the FE calculation of component tests using linear modeling of the adhesive behavior describes the test results very well. Here plastic calculations are not expedient at this time because as a first approach the plastic limit shall be far from being reached due to safety reasons. So for typical applications of hybrid beams, analytical models and dimensioning tables [5] based on linear calculations now are available that can replace complex FE calculations. Thus pilot projects or first applications of such hybrid steel-glass beams for building purposes can be both simplified and accelerated.

Summary and Future Prospects

The aim of the extensive testing program within the INNOGLAST project [5] was the derivation of analytic and numerical design approaches for dimensioning bonded hybrid steel-glass beams for roofing or façade beams. Such approaches are now available as pre-dimensioning tables, design tables, and graphs [5]. Here special attention is focused on the bonded joint that substantially contributes to the carrying capacity of the elastic composite section. On that score, appropriate adhesives were examined and their mechanical values

were determined, and these values then were carried over to realistic joint geometries in small-scale push-out tests.

The general applicability of this design approach was verified by large-scale component tests, including bending tests and stability pre-tests for flexural buckling and lateral torsional buckling.

The results of the investigations of the adhesives especially show a high carrying capacity and good elasticity for polyurethanes. Although the application of polyurethanes for automotive glazing has been almost uniform and well established for years, they are uncommonly used for structural glazing today. In contrast, epoxy resins offer a substantially higher level of carrying capacity. But their brittleness goes along with possible stress peaks, which explains why their application for structural glazing on the basis of the current state of research is recommended only after careful design.

In parallel to the ongoing research on bonded joints in steel or façade structures, a draft of a guideline regarding the fabrication and monitoring of bonded connections in structural glazing has been introduced by the FKG and will be continuously developed and filled with content. This draft has already been adapted to the general form of the European Standards, which is based on the three columns “products,” “design,” and “execution.” With an existing European regulation for structural silicone glazing according to ETAG 002 [28], the scope of the guideline draft emphasizes bonded joints outside existing product rules (see Fig. 10). As briefly described here in the sections “Requirements for the Adhesive Joint” and “Adhesive Selection,” the envisaged bonded connections will be classified in eight main categories that allow for a distinct definition of different design cases.

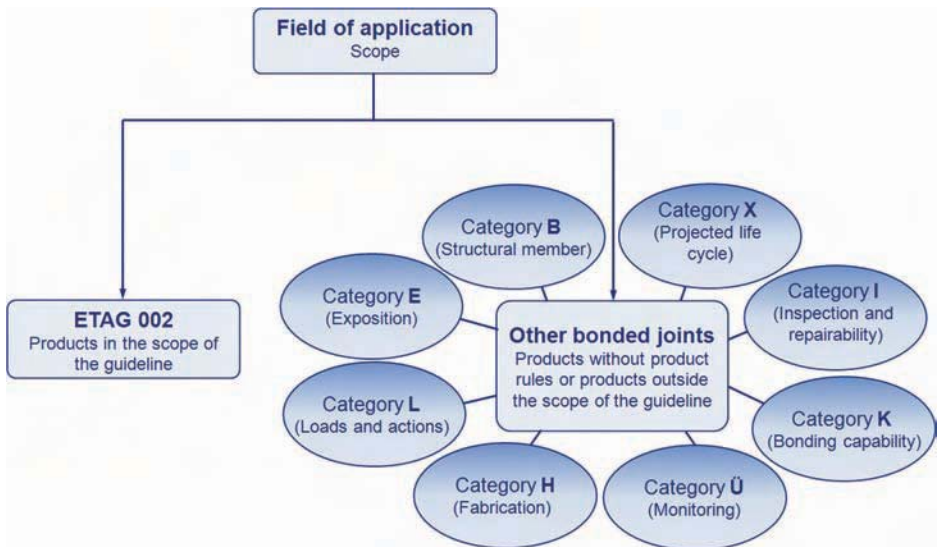


FIG. 10—Main categories for classifying bonded joints of structural glazing.

In addition, safety concepts have to be developed in order to ensure a reliable design procedure and a durable building structure.

Acknowledgments

The research project “Development of innovative steel-glass structures in respect to structural and architectural design (INNOGLAST)” was funded by the Research Fund for Coal and Steel (RFCS) (No. RFCS-CT-2007-00036). Sincere thanks are given to the European Commission, particularly to the Steel Technical Group TSG 8, and to the research partners for their good cooperation.

References

- [1] Bucak, Ö., Hagl, A., Held, B., and Bues, M., “Adhesively Bonded Connections in Structural Civil Engineering,” *Report No. 17040255*, Research Project of the German Federation of Industrial Research Associations (AiF), Köln, Germany, 2007 (in German).
- [2] Geiß, P. L., Kötter, M. P., Bucak, Ö., and Bues, M., “Partially Transparent Load Bearing Hybrid Structures (3TVB),” *Report No. 15058N*, Research Project of the German Federation of Industrial Research Associations (AiF), Köln, Germany, 2010.
- [3] Sedlacek, G., Feldmann, M., Naumes, J., and Wellershoff, F., “Development of Optimum Hybrid Steel-Glass Beams in Respect to Structural and Architectural Criteria,” *Final Report*, Aachen, 2005.
- [4] Wellershoff, F., “Utilization of Glazing for the Bracing of Building Envelopes,” Ph.D. thesis, RWTH Aachen University, Issue 57, 2006 (in German).
- [5] Feldmann, M., Ungermann, D., Abeln, B., Baitinger, M., and Preckwinkel, E., “Development of Innovative Steel-Glass Structures in Respect to Structural and Architectural Design (INNOGLAST),” *Report No. RFCS-CT-2007-00036*, Research Project of the European Research Fund for Coal and Steel, Brussels, Belgium, 2007–2010.
- [6] Abeln, B. and Preckwinkel, E., “Development of Hybrid Steel-Glass Beams,” *Stahlbau*, Vol. 80, No. 4, 2011, pp. 218–225.
- [7] Gesella, H., “Prediction of the Crack Propagation for Shear Studs in Composite Beams Under Cyclic Loading,” Ph.D. thesis, RWTH Aachen Univ., Issue 68, 2009 (in German).
- [8] German Professional Association for Structural Glazing working group, “Adhesive Bonding,” “Guideline for Fabrication and Monitoring of Bonded Connections in Structural Glazing,” Fachverband Konstruktiver Glasbau (FKG), Köln, Germany, 2010.
- [9] Feldmann, M., Pilsl, M., and Langosch, K., “The New Glass Courtyard of the Jewish Museum in Berlin—An Innovative Façade with Special Technical Requirements,” *Stahlbau*, Vol. 77, Suppl.1, 2008, pp. 34–41.
- [10] Feldmann, M., Pilsl, M., Baitinger, M., and Gesella, H., “The Steel and Glass Façade—The New Citroën-Show Room in Paris,” *Stahlbau*, Vol. 75, No. 6, 2006, pp. 409–414.
- [11] Feldmann, M., Pilsl, M., and Segura, C. C., “Strength of Bearing Connections in Toughened Glass Plates for the Structural Use,” *Stahlbau*, Vol. 77, No. 1, 2008, pp. 17–25.

- [12] Feldmann, M., Völling, B., Geßler, A., Wellershoff, F., Geiß, P.-L., and Wagner, A., "Adhesive Bonding for Steel Construction," *Stahlbau*, Vol. 75, No. 10, 2006, pp. 834–846.
- [13] Minten, J., Sedlacek, G., Paschen, M., Feldmann, M., and Geßler, A., "SPS—An Innovative Method for the Repair and Refurbishment of Orthotropic Deck-Plates of Steel-Bridges," *Stahlbau*, Vol. 76, No. 7, 2007, pp. 438–454.
- [14] Feldmann, M., Sedlacek, G., and Gessler, A., "A System of Steel-Elastomer Sandwich Plates for Strengthening Orthotropic Bridge Decks," *Mech. Compos. Mater.*, Vol. 43, No. 2, 2007, pp. 183–190.
- [15] Habenicht, G., *Adhesive Bonding: Basics, Technologies, Applications*, 5th ed., Springer-Verlag, Berlin, 2006 (in German).
- [16] DIN EN ISO 527, 1996, "Plastics—Determination of Tensile Properties," Deutsches Institut für Normung e.V. (DIN), Berlin, Germany.
- [17] DIN 53287, 2005, "Testing of Adhesives for Metals and Adhesively Bonded Metal Joints. Determination of the Resistance to Liquid," Deutsches Institut für Normung e.V. (DIN), Berlin, Germany.
- [18] DIN EN ISO 13445, 2006, "Determination of Shear Strength of Adhesive Bonds between Rigid Substrates by the Block-Shear Method," Deutsches Institut für Normung e.V. (DIN), Berlin, Germany.
- [19] DIN EN 14869-2, 2004, "Structural Adhesives—Determination of Shear Behavior of Structural Bonds. Part 2: Thick Adherents Shear Test," Deutsches Institut für Normung e.V. (DIN), Berlin, Germany.
- [20] Geiß, P. L., Wagner, A., and Luhn, R., "Influence of Surface Pre-Treatments on the Longterm Durability of Bonded Glass Joints (Proglazing)," *Report No. 14.776 BG/1*, Research Project of the German Federation of Industrial Research Associations (AiF), Köln, Germany, 2006–2008.
- [21] Abeln, B., Ph.D. thesis, RWTH Aachen Univ. (in preparation).
- [22] Brede, M., Hahn, O., Schlimmer, M., Dilger, K., Mahnken, R., Matzenmiller, A., Thoma, A., and Gumbusch, P., "Development of Methods to Simulate High Strength Adhesive Joints with Sheet Steel at Crash Conditions for Vehicle Construction," *Project P 676*, Research Association Steel Application FOSTA, Germany, 2008.
- [23] Völling, B., "Analytical Calculation of Sandwich Structures by Means of Residual Stress Solutions," Ph.D. thesis, RWTH Aachen University, Issue 62, 2007 (in German).
- [24] Möhler, K., "On the Behavior of Beams and Compressions Struts with Compound Sections and Flexible Connection Devices," Habilitation, University of Technology Karlsruhe, 1956 (in German).
- [25] Pischl, R., "Calculation of Wooden Beams based on the Elastic Composite Theory," Ph.D. thesis, Graz University of Technology, 1966 (in German).
- [26] Patetta, S., "Development of Design Tables and Diagrams for Hybrid Steel-Glass Beams Subjected to Bending," diploma thesis, RWTH Aachen University, 2009 (in German).
- [27] Flinterhoff, A., "Structural Behavior of Bonded Steel-Glass Composite Structures under Bending," diploma thesis, Dortmund University of Technology, 2002 (in German).
- [28] ETAG 002, 1998, "Guideline for European Technical Approval for Structural Sealant Glazing Systems," European Organization for Technical Approvals, Brussels.

Hiroyuki Miyauchi,¹ Michael A. Lacasse,² Noriyoshi Enomoto,³ Shigeki Murata,⁴ and Kyoji Tanaka⁵

Durability of Acrylic Sealants Applied to Joints of Autoclaved Lightweight Concrete Walls: Evaluation of Exposure Testing

ABSTRACT: In Japan acrylic sealants are traditionally the sealant products of choice when specified for use between autoclaved lightweight concrete (ALC) panels. Although, in general terms, the mechanisms of the deterioration of acrylic sealants are well known its long-term durability to outdoor exposure has not, however, been fully investigated. The research described in this paper focuses on the change in the properties and deterioration of acrylic sealant products when exposed to outdoor testing. The two stage project consisted of (i) on-site investigations of deteriorated acrylic sealants that had been placed in external joints of ALC-clad buildings; and (ii) outdoor exposure testing of different types of acrylic sealant in three climate regions located in Japan. The results of the work from the first stage of the study revealed the following. Two-sided adhesion joint configurations installed in deep panel ALC cladding were more reliable than three-sided adhesion joints used for thin panel ALC cladding from the viewpoint of the durability of the

Manuscript received June 4, 2011; accepted for publication October 10, 2011; published online December 2011.

¹Assistant Professor, Dr. of Eng., Chungnam National Univ., Dept. of Architectural Engineering, Daejeon 305 764, South Korea (Corresponding author), e-mail: miyauchi@cnu.ac.kr

²Senior Research Officer, Ph.D., P. Eng., National Research Council Canada, Institute for Research in Construction, Ottawa, K1A0R6, Canada.

³Scientific Committee Member, Dr. of Eng., Japan Sealant Industry Association, Tokyo 101 0041, Japan.

⁴Scientific Committee Member, ALC Association, Tokyo 101 0047, Japan.

⁵Emeritus Professor, Dr. of Eng., Tokyo Institute of Technology, Kanagawa 226 8503, Japan.

Cite as: Miyauchi, H., Lacasse, M. A., Enomoto, N., Murata, S. and Tanaka, K., "Durability of Acrylic Sealants Applied to Joints of Autoclaved Lightweight Concrete Walls: Evaluation of Exposure Testing," *J. ASTM Intl.*, Vol. 9, No. 1. doi:10.1520/JAI104063.

Copyright © 2012 by ASTM International, 100 Barr Harbor Drive, PO Box C700, West Conshohocken, PA 19428-2959.

sealed joint installed in actual buildings. Most fractures of the sealed joint could be characterized as failure in peel (or thin layer cohesive failures), in which the sealant ruptured at the interface with the ALC substrate to which it was applied. Additionally, in 47 of 62 locations surveyed, surface cracks were apparent on the coating that had been applied to protect the sealant. The second stage of the project focused on the degree of deterioration of coated and non-coated acrylic sealants subjected to outdoor exposure testing in a cold, a warm, and a subtropical climate. Results from this stage showed that aging of the sealant, as determined by the degree of surface cracking, expectedly depended on the local temperature and the respective degree of exposure to solar radiation. It was determined that the longer the exposure period, the lower the tensile performance of the acrylic sealants. The elongation of three-sided adhesive joint configurations after 5 years exposure testing decreased remarkably and their maximum elongation was less than 50 %. A significant number of sealed joints after 5 years of exposure had ALC substrate failure.

KEYWORDS: Sealant, autoclaved lightweight concrete, wall panel, durability, exposure testing

Introduction

The “Housing Quality Assurance Act” [1] was established in 2000 in Japan and, as a consequence, a ten year warranty period was imposed on industries producing and installing waterproofing systems. Sealed joints installed in buildings form part of a building façade’s waterproofing system and thus require long-term performance and it is therefore necessary to verify the durability of currently available sealed joint systems. In Japan when considering performance standards and specifications for sealed joint systems, the performance of sealants is regulated by two test methods: (i) “Sealants for Sealing and Glazing in Buildings” (JIS A 5758) [2], and (ii) “Testing Methods of Sealants for Sealing and Glazing in Buildings”(JIS A 1439) [3].

The primary specification and guideline documents that respectively provide for the material, design, and construction of sealed joints include: “Public Construction Standard Specifications” [4] and “The Construction Work Supervision Guideline” [5]; both of these documents are regulated by the Ministry of Land, Infrastructure, Transport and Tourism of Japan. The Architectural Institute of Japan also provides the “Recommendation for Design of Joints and Jointing for Control of Water and Air Penetration in External Walls” [6]. The performance regulations for the design and installation of sealed joints in building and constructed works have been established to improve the long-term performance of such products used both in government building assets and those of the private sector.

Sealed joint systems designed for use in ALC (autoclaved lightweight aerated concrete) panels have, for a considerable time, followed construction practices as provided for external walls of industrial buildings. Likewise, acrylic sealant products have been used in Japan for ALC panel joints for a significant

time, and perhaps elsewhere around the globe, because: (i) coatings can readily be applied to these products (thus prolonging their aesthetic performance); (ii) their initial tensile strength is low thus offering a reduced risk to premature tensile failure of the ALC panel substrate; and (iii) this sealant type can be installed in conditions where the substrate may be moist or, indeed, wet. However, a systematic verification concerning the long term performance of acrylic sealants used in ALC panel structures which have been exposed to up to 30 years of aging has not yet been done. Consequently, a study was undertaken to investigate the condition of deteriorated sealed joints of buildings clad with ALC panels such that some basic information on the actual condition and degree of deterioration of aged sealed joints could be obtained. Following the information gained from this study, a subsequent work was initiated that focused on the exposure of acrylic sealed joints that were tested to evaluate their mode of degradation and the likelihood of achieving long-term performance.

Degradation of Sealed Joints Installed on Panels of an ALC-Clad Building

Outline of Investigation

An outline of the investigation of sealed joints installed on panels of an ALC-clad building is shown in Table 1. The ALC panels on the building consist of two basic types that may be classified according to the depth of the panel, specifically: (i) The deep ALC panel, for which the depth of the ALC panel cladding is 100 mm, and (ii) the thin ALC panel where the ALC panel depth may be 35, 37, or 50 mm deep. The deep ALC cladding panels are typically used for homes, commercial buildings, or factories having steel frame construction whereas the thin ALC panels are normally used for homes or on low-rise buildings having wood frame construction. In this study, the buildings for which the investigations were completed, all of which were constructed over ten years ago, were inspected in respect to the type of sealants used in the joints, the degree of degradation of the sealants, and their respective strength characteristics were subsequently determined from laboratory testing. The joint types that had been used for the deep ALC panels or the thin ALC panels are shown in Table 2. As may be seen in Table 2, the deep ALC cladding panels used two-sided working joints whereas the thin ALC panels used three-sided non-working joints. Given that the short side of the joint length along the deep ALC panel deforms to a greater extent than that of a joint on the long side of the panel, it was determined that the representative panel joint would be a two-sided adhesion joint having a width of 10 mm. On the contrary, the joint for the thin ACL panel was considered a three-sided adhesion joint of 7 mm width.

Results of Investigation

Results of Deteriorated Sealed Joints—The sealant product condition is provided in terms of a qualitative assessment of the extent of damage and the classification of sealed joints between ALC panels and are shown in Table 3. In buildings aged over 20 years, all sealed joint products were one component

TABLE 1—*Outline of investigation concerning ALC building.*

Location	Hokkaido, Tokyo, Kobe, Kagawa	
Panel type	Building age: 10 years	
	Deep panel type: ALC panel with 100 mm wall depth	-Structure: steel frame construction, -Panel fixing method: Rocking panel fixing system -Sealed joint: Two-sidedadhesion joint
	Thin panel type: ALC panel with 50 mm wall depth	-Structure: steel or wood frame construction, -Panel fixing method: screw fastening system -Sealed joint: Three-sidedadhesion joint
	ALC panel with 35(37) mm wall depth	-Structure: wood frame construction, -Panel fixing method: Fastening system by screws -Sealed joint: Three-sidedadhesion joint
Research method	Sampling of sealants from actual external wall in 4 regions	
Evaluation parameters	-Visual inspection on the surface of sealants with coating material (deterioration, crack condition) -Hardness of sealants, tensile stress of sealants	

TABLE 2—Sealed joint types.

Two-sided adhesion joint		Three-sided adhesion joint	
Long side joint	Short side joint	Long side joint	Short side joint

TABLE 3—Sealant inspection results.

Elapsed years	Sealant type ^a	Depth of ALC wall panel									Total
		100 mm			50 mm			35(37) mm			
		Two-sided adhesion joint			Three-sided adhesion joint						
		○ ^b	Δ ^b	× ^b	○ ^b	Δ ^b	× ^b	○ ^b	Δ ^b	× ^b	
5-9	AC-1	1	0	0	2	0	0	2	0	0	5
	PU-2	5	0	0							5
10-14	AC-1				9	1	0	6	2	0	18
	PU-2	2	0	0	1	0	0				3
15-19	AC-1	3	0	0	3	0	0	10	0	0	16
	PU-2	3	0	0	1	1	0				5
20-21	AC-1				5	0	0	5	0	0	10
	PU-2										0
Total		14	0	0	21	2	0	23	2	0	62

Note: Δ=Slight (partial) damage on sealed joint; ×=Damage on sealed joint in many places.

^aAC-1:1 component acrylic sealant, PU-2:2 component urethane sealant.

^b○: No damage on sealed joint.

acrylic sealants; inspection results are reported for acrylic sealants at four intervals, the first between 5 and 9 years, thereafter at 10-14 years, 15-19 years, and 20-21 years. Whereas for buildings less than 20 years of age only two component urethane sealants had been used for the sealed joints; inspection results are only reported for intervals of 5-9 years, 10-14 years, and 15-19 years. Because the amount of anticipated movement in the sealed joint between the deep ALC panels was large, a two component urethane sealant was used as a working joint given its capacity to accommodate movement.

There was no evidence of any complete damage to the sealed joint (symbol: ×), regardless of the depth of the panel, however partial failure (symbol: Δ) of the sealed joint was observed (4 damages out of 62 total) in four locations in thin panels, specifically, the ALC panel having a 50 mm depth had partial damage (symbol: Δ) evident for one acrylic (1 damage out of 20) and one urethane sealant (1 damage out of 3), and the ALC panels with 35 (37) mm wall depth had partial damage for two acrylic joints (2 damages out of 25).

Crack Conditions of Sealed Joint—Examples of damaged sealant products applied to joints of ALC panels are shown in Fig. 1. All damaged sealed joints (symbol: Δ) were those occurring in thin ALC panels and for joints having three-sided adhesion. Of those joints having three-sided adhesion, 2 damaged joints were evident for 50 mm deep panels and another 2 damaged joints for 35 mm deep panels. In both instances, cohesive failure occurred at the center of the

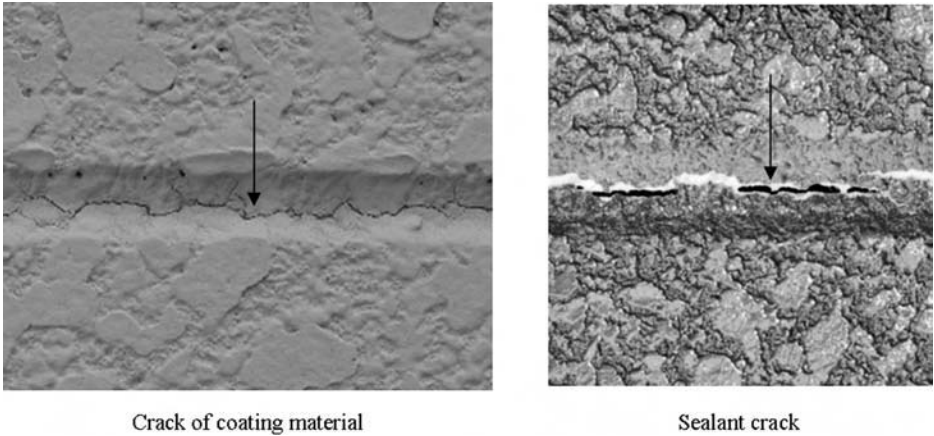


FIG. 1—Crack condition of sealed joints.

sealed joint and where cracks were observed. In 47 of the 62 sealed joints inspected cracks were evident on the surface coating material (i.e., damage evident to 47/62); these cracks did not depend on the movement of the structure or the type of sealant to which they were applied. The coating material has, in fact, a reduced performance in accommodating deformation as compared to that of sealants. It was also evident that the sealed joints along the short side of the panel have significantly more cracks than joints along the longer side of the panel. It is thought that the degree of expansion and contraction of the joint along the short side of the panel is greater than that along the longer side of the panel.

Test Results of Basic Properties—The hardness [7] and tensile strength [3] of a 17 year old sealant product used in the joints of a wood frame constructed home were measured by a testing machine. The hardness of the sealed joint was measured with a Shore Type A hardness meter (JIS K 6253). The value for the hardness of the sealant was approximately 60 Shore A on both sides of the sealed joint. An unaged sealant of the same product type was estimated to be 20 Shore A when first installed (Table 6). The change in hardness of the aged product appears to confirm, therefore, the degradation of the sealants over time.

The tensile test for the sealed joint was carried out using a special jig, as shown in Fig. 2. Fourteen tensile test specimens were evaluated; the maximum tensile stress ranged between 0.36 and 0.73 N/mm² with the mean value being 0.54 N/mm². The elongation at maximum load ranged between 7 and 21 % and provided a mean value of 15 %. Most sealed joint fractures were characterized as failures in peel (or thin layer cohesive failures), in which the sealant fractured at the interface between the sealant and the ALC substrate. The maximum elongation at fracture of the sealed joint extended from 53 to 223 % with a mean value of 117 %.

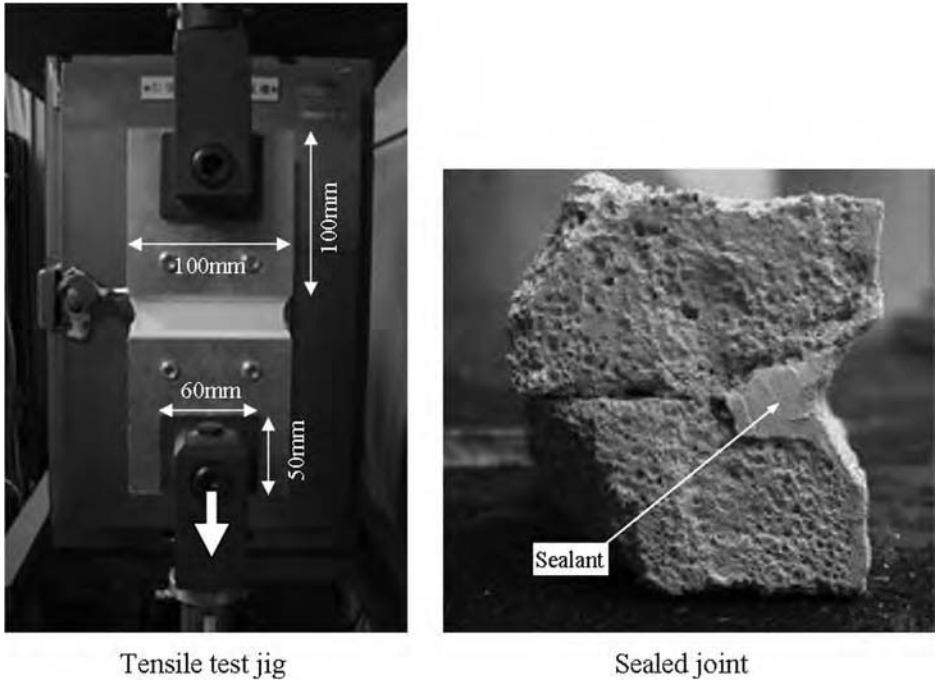


FIG. 2—Tensile test and sample specimen.

Outdoor Exposure Tests

Outline of Outdoor Exposure Test

As described in Table 4, the outdoor exposure tests were carried out at three different locations in Japan over a 5 year period; each location had a different climate. Control specimens were also prepared to which the sealants exposed to the different climates were compared; these were kept in indoor laboratory conditions, as described in Table 4. The evaluation parameters included the: (i) effect of climate conditions (e.g., ultraviolet radiation, temperature, and moisture load), (ii) the effect of the joint type between ALC panels, and (ii) the effect of the sealant and coating material types.

Test Specimens and Test Methods

Test Specimens—The specimens are shown in Fig. 3 and the items inspected over the course of the outdoor exposure test are shown in Table 4. The joint types include: a two-sided adhesion joint (joint width: 10 mm, joint depth: 8 mm) and a three-sided adhesion joint (joint width and depth: 7 mm with a small 1 mm gap at mid-width and the base of joint). Low density (1.1 g/cm^3) one component acrylic sealant commercially available Japanese products were those

TABLE 4—*Test parameters.*

	Item	Conditions
Test specimen	Sealant	Acrylic sealants (Type A, Type B, Type C)
	Coating material	With coating, without coating
	Joint type	Two-sided adhesion joint, three-sided adhesion joint
	Curing time	4 weeks indoor environment room at $20 \pm 3^{\circ}\text{C}$
Exposure test	Exposure location	Rikubetsu Climate: Cold climate area Place: Rikubetsu exposure testing site (October 17, 2001)
		Yokohama Climate: Warm climate area Place: Roof at Tokyo Institute of Technology (Nov. 6, 2001)
		Miyako Island Climate: Subtropical climate area Place: Japan Weathering test center (Nov. 6, 2001)
		Indoor room Climate: No degradation Place: Room (Temp. $23 \pm 2^{\circ}\text{C}$)(October 17, 2001)
		Evaluated exposure periods

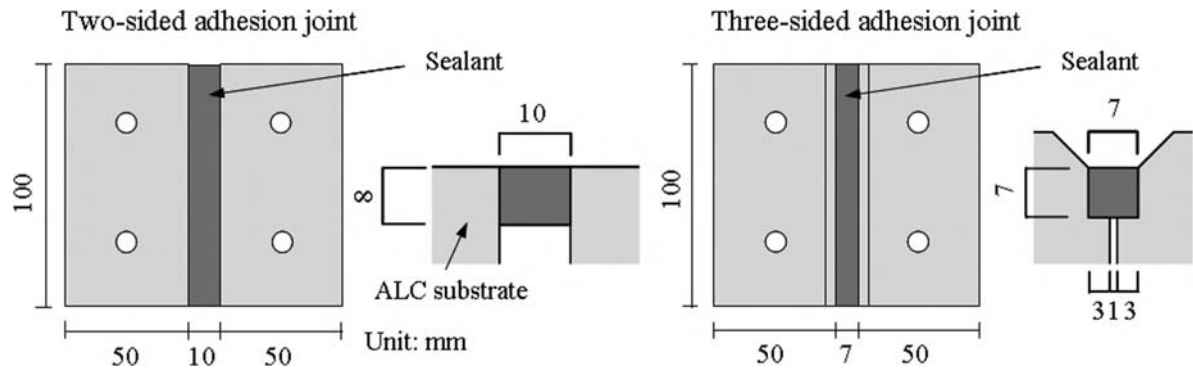


FIG. 3—Test specimen.

subjected to tests. The effect of coating materials was evaluated and the test specimens were prepared both with and without a coating material applied to the exterior surface of the joint. All sides of the ALC substrate, with the exception of that surface on which the sealant was applied, were coated with one component silicone sealant in order to protect the substrate from water absorption when exposed to the outdoors. The test specimens were cured indoors at $23 \pm 2^\circ\text{C}$ for 4 weeks before starting the outdoor exposure test. Three test specimens were used in evaluating each test parameter.

Exposure Test Method—As shown in Fig. 4, the geographical locations of the exposure testing sites for Rikubetsu, Yokohama, and Miyako Island are evidently quite different and consequently, the local climate conditions vary greatly from one location to another. The test specimens placed in the outdoor exposure site at these three locations were set up on testing tables inclined at 45° (Fig. 4). On the contrary, test specimens prepared as control specimens were cured in a darkroom with no sunlight and maintained at a temperature of $23 \pm 2^\circ\text{C}$ over the test period.

Figure 5 shows the outdoor temperature conditions at the three outdoor exposure sites over a selected exposure period in October. The mean value for the maximum outdoor temperature over a five year period for the warmest exposure site (Miyakojima Island) was 29.4°C ; whereas, the mean value for the minimum outdoor temperature over five years for this same exposure site was 18.2°C . On the other hand, Rikubetsu is an exposure site where temperature differences are large and the mean value for the maximum temperature over five years was 18.6°C and the corresponding minimum temperature was -9.6°C . Therefore, the sequence of exposure sites in order of decreasing thermal exposure severity is as follows: Miyakojima Island > Yokohama > Rikubetsu.

Evaluation Method for Degradation of Sealed Joints—The degree of degradation of the sealed joint is evaluated by observation of the surface of the sealed joint, with use of the hardness meter (Shore Type A), along with tensile tests. Moreover, the tensile tests were carried out by fixing the test specimen to a special jig (Fig. 2). The tensile rate of deformation was 5 mm/min and the test temperature was $23 \pm 2^\circ\text{C}$.

Results of Outdoor Exposure Tests

Surface Condition of Sealed Joints—Fig. 6 shows the surface condition of the sealed joints after 5 years of outdoor exposure at the different exposure site locations. In Table 5 results of the aging (staining due to dirt pickup) and degree of cracking from the outdoor exposure tests are presented. As might be expected, the degree of aging (dirt pickup) of test specimens after 5 years of exposure is greater than that at the onset of the exposure period (0 year) and after 2 years exposure, in particular, the degree of dirt pickup of test specimens exposed to the Yokohama climate is the greatest. It is thought that dust is more prevalent on the surface of sealants at the Yokohama exposure site because this site is close to a highway. However, it was not possible to confirm the differences in

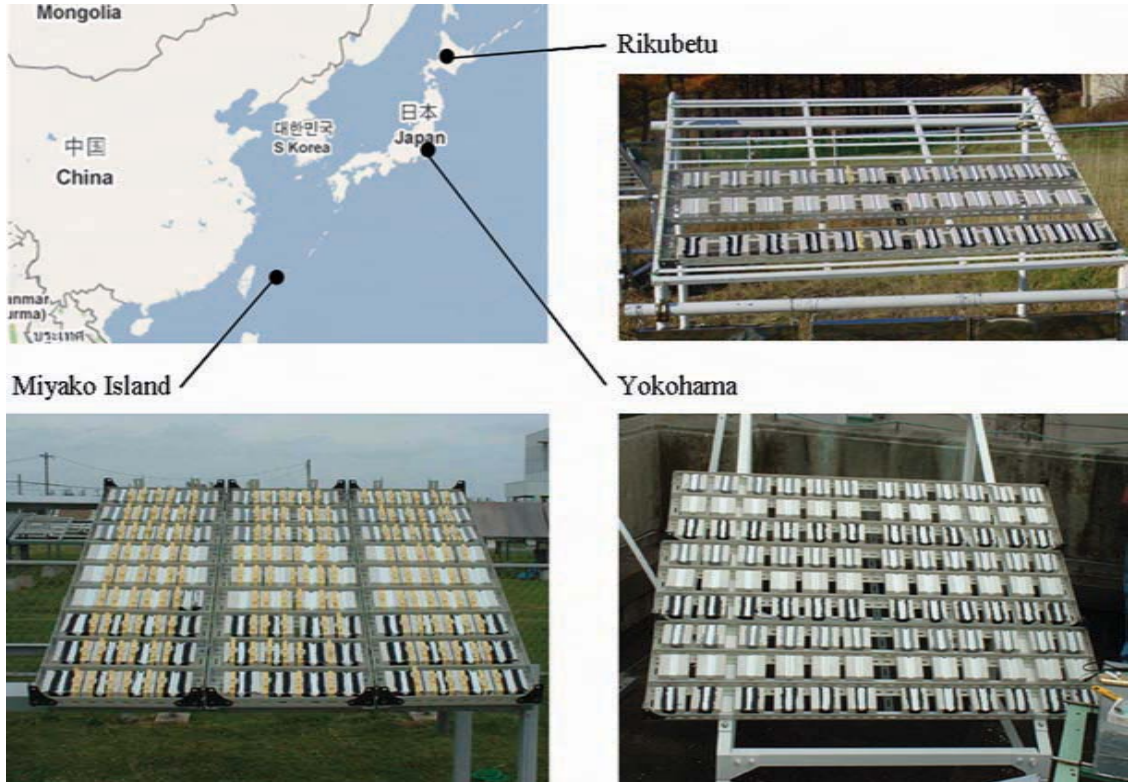


FIG. 4—Location of outdoor exposure test.

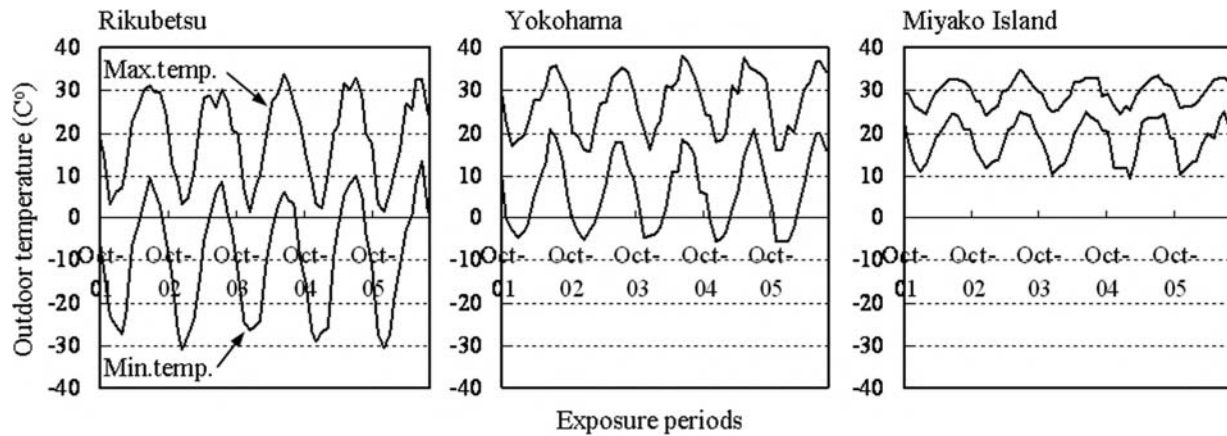


FIG. 5—Temperature conditions at the three exposure site locations.

Sealants	Coating	Joint type	Rikubetu	Yokohama	Miyako Island
Type A	Without	2			
		3			
	With	2			
		3			
Type B	Without	2			
		3			
	With	2			
		3			
Type C	Without	2			
		3			
	With	2			
		3			

FIG. 6—Outdoor exposure test results after 5 years.

TABLE 5—Aging (dirt pick-up) and crack condition from outdoor exposure testing.

Sealants	Coating	Joint type	Aging (Stain), years									Cracks, years								
			Rikubetsu			Yokohama			Miyako			Rikubetsu			Yokohama			Miyako		
			0	2	5	0	2	5	0	2	5	0	2	5	0	2	5	0	2	5
Type A	Without	2	0	1	3	0	1	3	0	0	1	0	0	1	0	1	2	0	1	1
		3	0	1	2	0	1	2	0	0	1	0	0	1	0	1	2	0	1	1
	With	2	0	0	1	0	2	3	0	0	1	0	0	1	0	0	1	0	0	1
		3	0	0	1	0	2	3	0	0	0	0	2	2	0	2	2	0	2	2
Type B	Without	2	0	1	2	0	3	3	0	1	1	0	0	0	0	0	0	0	0	0
		3	0	1	3	0	3	3	0	1	1	0	0	0	0	0	0	0	0	0
	With	2	0	0	2	0	2	4	0	1	1	0	0	0	0	1	0	0	1	1
		3	0	0	2	0	2	3	0	1	1	0	2	2	0	1	1	0	2	2
Type C	Without	2	0	1	1	0	3	3	0	0	0	0	0	0	0	0	0	0	0	0
		3	0	1	2	0	3	3	0	0	1	0	0	0	0	0	0	0	0	0
	With	2	0	1	3	0	3	4	0	1	1	0	0	1	0	0	1	0	2	2
		3	0	1	1	0	3	4	0	1	1	0	0	2	0	2	2	0	2	2

Note: Aging (Stain) degree: 0 to 5 scale: 0 = none, 5 = severe. Crack condition 0: No crack, 1: Slight cracking, 2: Large crack, 3: Through crack.

the degree of dirt pickup by the presence or absence of coating applied to the exterior surface of joint specimens. As for the rate of occurrence of cracks on sealed joints, it was evident that test specimens exposed at the Miyako Island and the Yokohama sites were high. The rate of occurrence of cracks of coated sealant products for three-sided adhesion joints was greater than that of products in joints having two-sided adhesion.

Hardness Measurement Results of Sealed Joints—The hardness of sealed joints exposed to the different exterior climate conditions is shown in Table 6. The results indicate that the longer the exposure period to which the specimens were subjected, the greater the value of hardness of the sealed joint product. As for the importance of the exposure site with respect to the aging and hardening of the sealant, the results indicate the following order, in decreasing order of hardness value: Miyakojima (52 Shore A hardness) > Yokohama (49 Shore A hardness) > Rikubetsu (39 Shore A hardness). The results also indicated that the hardness of sealed joints without a coating was greater than that of joint products with a coating.

Tensile Test Results—Fig. 7 shows the maximum tensile stress obtained for two- and three-sided adhesion joint specimens that had been coated with paint for outdoor exposure testing. The differences between the two- and three-sided adhesion joint specimens in respect to values achieved for maximum tensile stress and maximum percent elongation arise because three-sided adhesion joints bring about greater internal stress to the joint as compared to two-sided joints. In essence, three-sided joints are capable of accommodating less movement as compared to 2-sided joints and, for the same degree of movement, give rise to both higher bond and internal stress. The results revealed that the longer the exposure period, the greater the tensile stress achieved in the sealant specimens. The location of the exposure site affected the severity of the exposure conditions and consequently the degree of aging and resulting tensile stress of the aged products. It was determined, on the basis of results from tensile tests, that the order of exposure severity starting with the most severe exposure location and proceeding toward less severe exposure locations was: Myakojima > Yokohama > Rikubetsu. The tensile stress achieved for three-sided adhesion joint specimens was greater than that of two-sided adhesion joints. Figure 8 shows the maximum elongation achieved of sealed joints in tension; results indicate that the longer the exposure period, the lower the degree of elongation of the sealed joint specimen.

Considering the differences in elongation achieved for three-sided as compared to two-sided joint specimens, the degree of elongation of three-sided adhesion joint specimens was remarkably smaller after two years exposure and additionally, after 5 years of exposure testing the maximum elongation was less than 50 % at all exposure locations, whereas that of the two-sided joints all exceeded 50 % elongation. The results did not confirm that differences existed amongst the various three-sided adhesion joint specimens and neither were these affected by the severity of conditions at the different exposure sites.

TABLE 6—Hardness of sealant for outdoor exposure testing.

Sealants	Coating	Joint type	Hardness, years								
			Rikubetsu			Yokohama			Miyako Island		
			0	2	5	0	2	5	0	2	5
Type A	Without	2	20	27	38	20	33	53	20	35	54
		3	20	30	38	20	34	56	20	42	55
	With	2	20	25	33	20	30	51	20	33	45
		3	20	28	41	20	32	51	20	32	53
Type B	Without	2	11	22	45	11	35	63	11	33	59
		3	11	29	45	11	33	47	11	39	60
	With	2	11	25	34	11	33	46	11	32	40
		3	11	30	38	11	36	47	11	35	49
Type C	Without	2	8	25	42	8	27	51	8	31	52
		3	8	28	53	8	34	51	8	35	68
	With	2	8	22	24	8	24	33	8	27	42
		3	8	23	34	8	29	40	8	30	44
Average			13	26	39	13	32	49	13	34	52

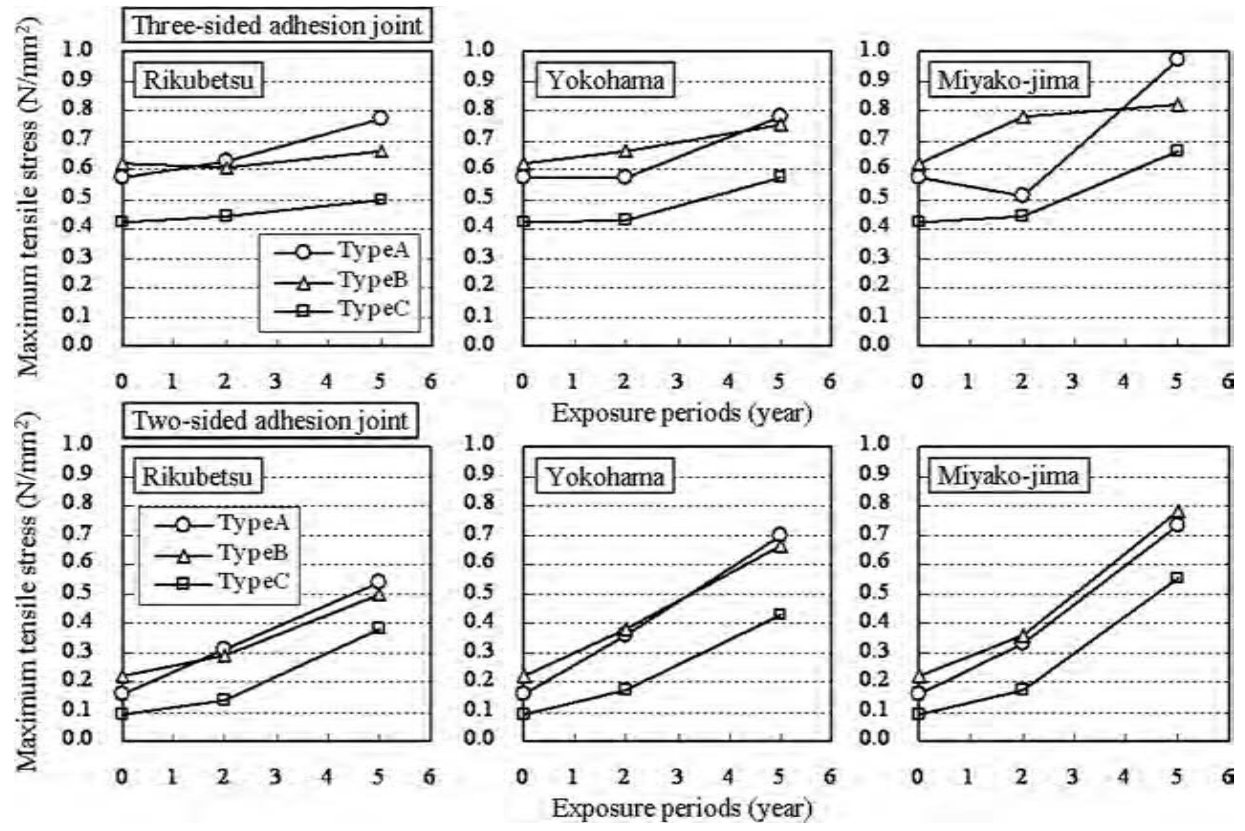


FIG. 7—Maximum tensile stress of sealants with painting material in outdoor exposure test.

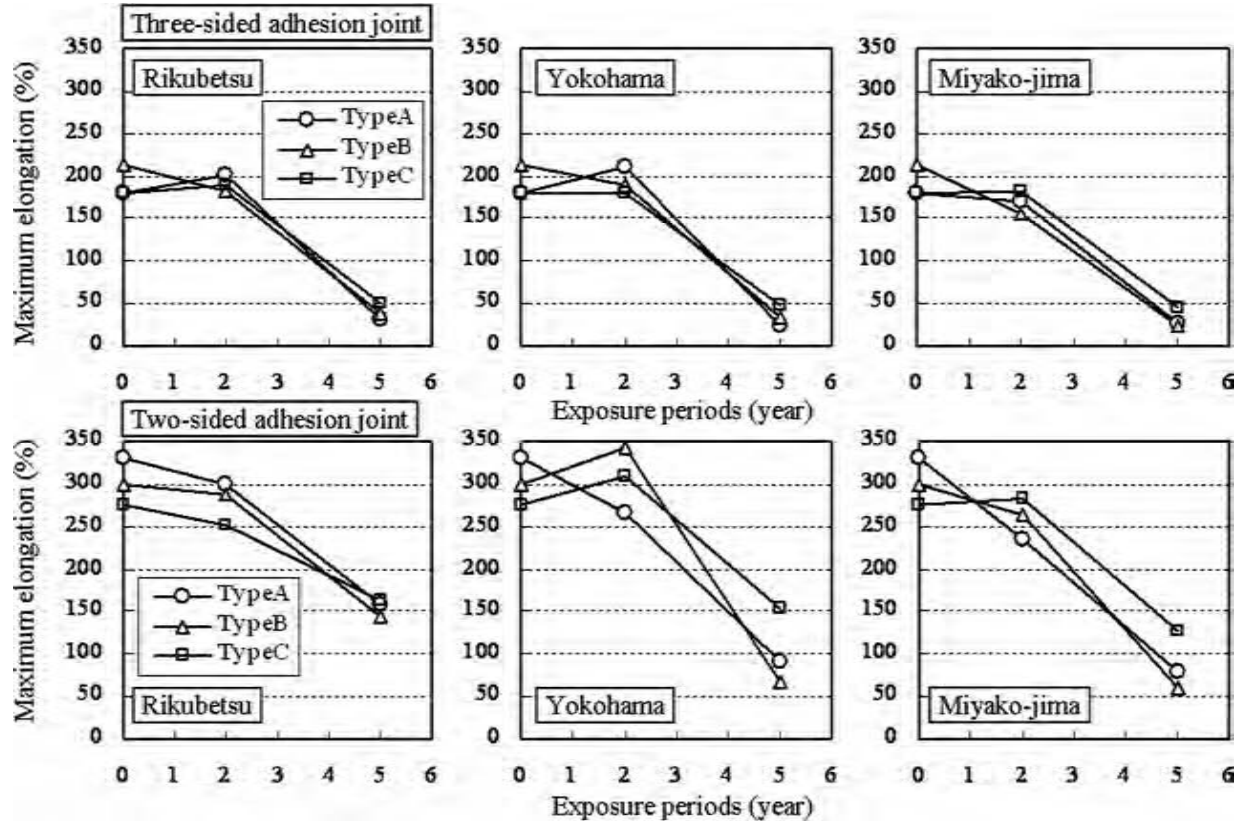


FIG. 8—Maximum elongation of sealed joints with painting material in outdoor exposure test.

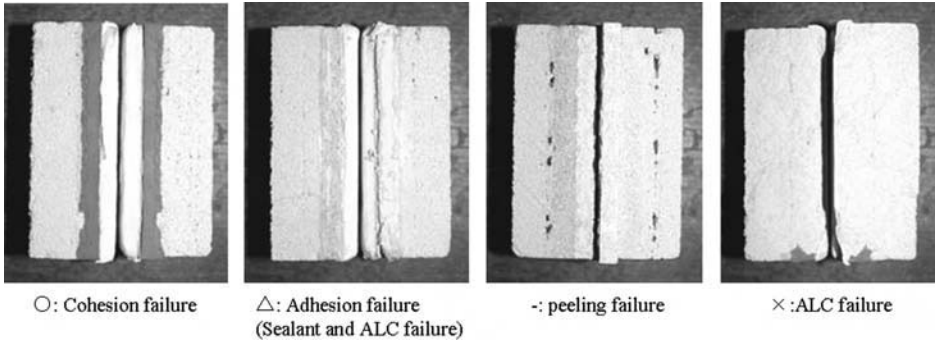


FIG. 9—Type of fracture of sealed joint.

However, the lower degree of elongation obtained for two-sided adhesion joint specimens varied in relation to the severity of the climate for which the least degree of elongation was obtained for the exposure location having the more severe exposure conditions; specifically, in order of more to least severe effects, this was: Miyakojima < Yokohama < Rikubetsu.

Figure 9 and Table 7 provide information on the type of failure of the sealed joint specimens in tensile tests; these could be classified into four types of failure: (i) cohesion failure (symbol: ○); (ii) mixed mode adhesive failure of the sealant and ALC substrate (symbol: △); (iii) failure in peel (symbol: -), and failure of the ALC substrate (symbol: ×). The sealed joint specimens used as control specimens and cured indoors in laboratory conditions all failed in cohesion (symbol: ○). On the contrary, the results confirmed that the sealed joint specimens after 2 years of exposure testing had mixed mode adhesion failure, exhibiting both sealant and ALC substrate failure (symbol: △) as well as failure in peel (symbol: -). It was also revealed that a considerable number of the sealed joint specimens after 5 years of exposure testing had failed at the ALC substrate (symbol: ×). The value of the 50 % modulus of the sealed joint specimens having three-sided adhesion joints could not be measured because the failure of test specimens had already occurred at an elongation below 50 %.

Conclusions

The conclusions from this study are as follows:

- (1) Two-sided adhesion joints used for sealing deep ALC panels were more reliable than that of three-sided adhesion joints used for the thin ALC panel type from the viewpoint of durability and degradation of the sealed joint of ALC panels in actual buildings. The damage to three-sided adhesion joints used in thin ALC panels was confirmed from partial damage located at 4 locations of 62. The hardness of the acrylic sealant was approximately 60 Shore A for sealants used in the joints of a 17 year old building. As a result of the tension tests, the maximum tensile stress achieved was 0.36–0.73 N/mm² (mean value: 0.54 N/

TABLE 7—Fracture type form tensile testing.

Sealants	Coating	Joint type	Aging								
			Rikubetsu, years			Yokohama, years			Miyako Island		
			0	2	5	0	2	5	0	2	5
Type A	Without	2	○○○	○○○	△△△	○○○	○○○	○△×	○○○	○○○	○△△
		3	○○○	○○—	○△△	○○○	○○○	○××	○○○	○○○	△××
	With	2	○○○	○○○	○△△	○○○	○○△	△△△	○○○	○○○	△△×
		3	○○○	○○○	○○△	○○○	○○—	△××	○○○	○○△	△△△
Type B	Without	2	○○○	○○○	△××	○○○	○○○	×××	○○○	○○—	×××
		3	○○○	○○○	△△△	○○○	○○○	×××	○○○	○○△	×××
	With	2	○○○	○○○	○○○	○○○	○○○	×××	○○○	○○○	○△×
		3	○○○	○○○	△△△	○○○	○○△	○△×	○○○	○△△	○△×
Type C	Without	2	○○○	○○○	○○△	○○○	○○○	○○△	○○○	○○○	○○○
		3	○○○	○○△	○○△	○○○	○○○	○○△	○○○	○○○	○○△
	With	2	○○○	○○○	○○△	○○○	○○○	○○○	○○○	○○○	○△△
		3	○○○	○○○	○○△	○○○	○○△	○△△	○○○	○○○	○○△

Note: ○=Cohesion failure; △=Adhesion failure (Sealant and ALC failure); ×=ALC failure; —=peeling failure.

mm²). The maximum elongation at the fracture of the sealed joint was 53-223 % (mean value 117 %). Most fractures of sealed joint were thin layer cohesion failures where the sealant was fractured at the interface with the ALC substrate. In 47 of 62 specimens, cracks in the coating on the surface of the sealant were observed; however, these cracks did not penetrate into the depth of the sealant.

- (2) In regard to the results on the surface condition of a sealed joint after 5 years of outdoor exposure, the aging (degree of dirt pickup) and the extent of the occurrence of cracks depended on the environmental conditions apparent at any exposure location. In particular, the exposure site with the highest average monthly temperature (climate zone) had, in this study, the greatest effect on the durability of the sealed joint. The longer the exposure period of the sealed joint, the lower the durability of the sealed joint in respect to values obtained for the tensile stress and elongation. The degree of elongation of three-sided adhesion joints after 5 years of exposure was markedly decreased and its maximum elongation was less than 50 %. A number of sealed joints after 5 years of exposure testing had failure at the ALC substrate (symbol: ×).

Therefore, given that the maximum elongation observed for the acrylic sealant was less than 50 % and that the degree of movement accommodation of three-sided adhesion joints in ALC panels with such types of sealant is reduced, thereby increasing the likelihood of premature joint failure, it was determined that a suitable sealant for use on ALC substrates is a sealant having a greater degree of movement accommodation than acrylic sealants and also a product that has enhanced durability. Furthermore, in order to enhance the longevity of the sealed joints, it is recommended that for joints of ALC panel systems, the sealant products should be applied, as is usually the practice for other joints, as a two-sided joint.

Acknowledgments

This work was performed as part of the activities of the working group for the "Research of Sealants for Sealed ALC Panel Joints," conducted by the Tokyo Institute of Technology, Autoclave Lightweight aerated Concrete panels and the Japan Sealant Industry Association. This work was also supported by the Basic Science Research Program of the National Research Foundation of Korea (NRF) funded by the Ministry of Education, Science and Technology, Korea (Grant No. 2010-0011927). Some researchers were funded by the Korean Government and supported by the 2nd Korea Brain (BK21) foundation. The writers are grateful to all these parties for their support.

References

- [1] The Building Center of Japan, 2005, "The Housing Quality Assurance Act and Japan Housing Performance Indication Standards," Vol. 2004, p. 135, Japan.
- [2] JIS A 5758-2010, 2010, "Sealants for Sealing and Glazing in Buildings," Japanese Standards Association, Japanese Industrial Standards Committee, Japan.

- [3] JIS A 1439-2010, 2010, "Testing Methods of Sealants for Sealing and Glazing in Buildings," Japanese Industrial Standards Committee, Japan, p. 46.
- [4] Ministry of Land, Infrastructure, 2010, "Public Construction Standard Specifications," Japan, p. 447.
- [5] Ministry of Land, Infrastructure, Transport and Tourism, 2010, "The Construction Work Supervision Guideline," Japan, p. 1780.
- [6] Architectural Institute of Japan, 2008, "Recommendation for Design of Joints and Jointing for Control of Water and Air Penetration in External Walls," Japan, p. 357.
- [7] JIS K 6253-2006, 2006, "Rubber, Vulcanized or Thermoplastic—Determination of Hardness," Japanese Standards Association, Japanese Industrial Standards Committee, Japan, p. 32.

Gregory T. Schueneman,¹ Christopher G. Hunt,² Steven Lacher,³
Christopher C. White,⁴ and Donald L. Hunston⁴

In Situ Measurement of Compression Set in Building Sealants During Outdoor Aging

ABSTRACT: The durability of sealants is dictated by many factors such as joint design, surface preparation, application, formulation, joint movement, and weather. Among these factors the link between formulation (material behavior) and weathering durability is difficult to assess in short term tests. We attempt to address this challenge by monitoring changes in apparent modulus during exposure to outdoor weathering and cyclic strain. This is accomplished via custom built systems that apply cyclic strain to 16 samples simultaneously via programs that simulate wood (cold compression) and concrete/metal (hot compression) construction materials. A key finding of the research presented here is that changes in apparent modulus are primarily driven by underlying changes in the compression set, a potentially critical contributor to stress in structures during rapid temperature changes. Detection of the compression set is made possible by the in situ material property assessments used in this research. Aging tests that rely on offline evaluation of property changes may miss or underestimate this effect on the sealant's stiffness due to time delay and/or losing track of the original zero stress–zero strain state.

KEYWORDS: Building sealant, compression set, durability, outdoor aging, strain cycling, apparent modulus

Manuscript received June 14, 2011; accepted for publication October 10, 2011; published online December 2011.

¹Research Materials Engineer, Forest Products Laboratory, One Gifford Pinchot Dr., Madison, WI 53726 (Corresponding author), e-mail: gtschueneman@fs.fed.us

²Research Chemist, Forest Products Laboratory, One Gifford Pinchot Dr., Madison, WI 53726.

³Materials Engineer, Forest Products Laboratory, One Gifford Pinchot Dr., Madison, WI 53726.

⁴Scientist, National Institute of Standards, 100 Bureau Dr., Stop 1060, Gaithersburg, MD 20899.

Cite as: Schueneman, G. T., Hunt, C. G., Lacher, S., White, C. C. and Hunston, D. L., "In Situ Measurement of Compression Set in Building Sealants During Outdoor Aging," *J. ASTM Intl.*, Vol. 9, No. 1. doi:10.1520/JAI104142.

Copyright © 2012 by ASTM International, 100 Barr Harbor Drive, PO Box C700, West Conshohocken, PA 19428-2959.

Introduction

Sealants are a critical part of a structure's moisture and weather barrier envelope. Understanding and predicting the service life expectancy of sealants is necessary to prevent serious damage to the cosmetic and structural integrity of buildings and structures. Given this well recognized need, several challenges prohibit the direct assessment of such knowledge. One of the primary challenges is the difficulty in assessing the critical combinations of factors (environmental, displacement, fatigue, formulation, material property, etc.) that determine a sealant's durability in a well characterized service condition. Secondly, pass-fail tests address lifetime prediction by exposing materials to conditions much more severe than the conditions of use. Severe conditions are necessary based on a factor of safety approach and the short testing times desired. The approach taken in this research program is to conduct simultaneous outdoor weathering and cyclic strain aging of sealants while recording environmental conditions and changes in modulus via in situ measurements. This data set is intended to provide the means for obtaining a dosage versus damage model that may facilitate better predictions of service life for a given application and environment.

The outdoor exposure takes place in Madison, Wisconsin via a custom built computer controlled instrument named the Badger IIIa [1]. The advantage of this approach is that it provides active feedback on incremental material property changes as a function of weathering and cyclic strain dosage. The disadvantage of cyclic testing is having sufficient sample throughput to provide statistically significant data. The instrument we designed addresses this issue by applying controlled displacement to 16 sealant specimens simultaneously as a function of temperature. The applied displacement is computer controlled such that custom functions can be developed to fit a service environment. The functions are principally temperature based. Consequently, the specimens experience instantaneous and daily diurnal displacement cycles of a controlled magnitude and rate induced by temperature changes within set strain limits. Cycling is stopped once per week to run a stress relaxation profile allowing the calculation of the sealant's apparent modulus [2].

Compression set is a well-known phenomenon defined as the fraction of applied compressive strain remaining in the sealant after full compressive strain is removed. This, of course, is a time-dependent phenomenon, since upon removal of the compressive strain the sealant moves toward the original dimensions more slowly over time and may never recover its original shape. In most sealant testing, specimens are allowed to relax between the compression application and the measurement of properties. This has a very practical benefit, removing a time-dependent factor, making property measurements more repeatable. The sacrifice, however, is that information about the contribution of transient compression set to sealant properties is lost.

Herein we describe the results from two sealants exposed to five months of hot compression cycling and outdoor weathering on an instrument that was designed to enable the measurement of stress relaxation behavior and the calculation of apparent modulus immediately after stopping cyclic strain exposure.

This test protocol more closely simulates exposure conditions on buildings with exteriors that respond quickly to changes in temperature.

Experiment

Specimens: The sealant specimens are provided by the National Institute for Standards and Technology (NIST) in Gaithersburg, MD via their consortium of sealant companies who fabricate the specimens [3]. All chemical information (formulations, base chemistry, fillers, etc.) about the samples is hidden from the Forest Products Laboratory and NIST due to the blind nature of this study. Additionally, chemical analysis of the samples is not permitted. The sealants consist of Consortia C and ASTM round robin B (ASTM B). The Consortia C sealant is specially formulated to fail earlier than commercially available sealants. Per the limitations of this study, it is not known what formulation attribute was changed in order to achieve this intent. The ASTM B sealant is commercially available with a $\pm 25\%$ movement rating. The specimens consist of a pair of anodized 6063 aluminum blocks ($12.7 \times 12.7 \times 76.2$ mm) bonded together with sealant in the form of a $12.7 \times 12.7 \times 50.8$ mm bond line cured in conformance with ASTM C719-93 [4].

Strain Cycling: The custom built test machine shown in Fig. 1 consists of two parallel aluminum I-beams with up to 18 sealant specimens fixtured between them. The I-beams are driven by two captive stepper linear actuators (size 34, Hayden Kerk, Waterbury, CT) whose position is monitored by two linear variable differential transformers (model HSD 750 250-010, Macro Sensors, Pennsauken, NJ). The programmed displacement follows the temperature profile of polyvinylchloride (PVC) based durability engines in operation at NIST. The displacement (Δ , cm) versus temperature (T , °C) equation for such engines is given in Eq 1. Strain gauges were not applied to individual specimens. Thus, the values reported as strain are based upon the linear variable differential transformer position of the I-beam and are approximate

$$\Delta = -(T - 4.5)/105 \quad (1)$$



FIG. 1—Photograph of *Badger IIIa* with 18 sealant specimens.

The temperature is recorded from a thermocouple embedded in a piece of PVC pipe exposed to solar irradiation. The hot compression cycling displacement boundaries were set in this experiment such that +25 % strain occurred at -29°C and -25 % strain at 38°C , corresponding to climate norms for the Wisconsin test site. The load response to the applied displacement is independently measured for each specimen by S-type load cells (model SSM-AJ-250, Interface, Scottsdale, AZ).

Motion control, load cell conditioning, and data acquisition during testing was accomplished via a National Instruments (Austin, TX) Compact RIO (cRIO)-9073 integrated 266 MHz real time controller.

Once per week, displacement cycling was stopped and an apparent modulus cycle was run to check for changes in modulus as a result of weather and displacement aging; see Fig. 2. The cycle consisted of two peaks of approximately 15 % strain that act to remove the Mullins effects from the sealants followed by a 10 % estimated strain stress relaxation period [5]. The 15 % peaks remove any effects of filler bonds and secondary bonds that contribute to non-reversible stress-strain behavior. Thus, the stress relaxation period occurs at a lower strain than the first two peaks and is free of these effects.

The apparent modulus (E_a) is determined using a stress relaxation test proposed by NIST as a new ASTM International sealant test method [2]. The E_a is calculated via Eq 2, where t is time, λ is the extension ratio, L is the load, W is the specimen width, and B is the specimen thickness. Here, λ is calculated using Eq 3 where Δ is the displacement and h is the specimen height. This methodology is taken from the statistical theory of rubber elasticity [6,7]

$$E_a(t, \lambda) = 3L(t)/(WB(\lambda - \lambda^{-2})) \quad (2)$$

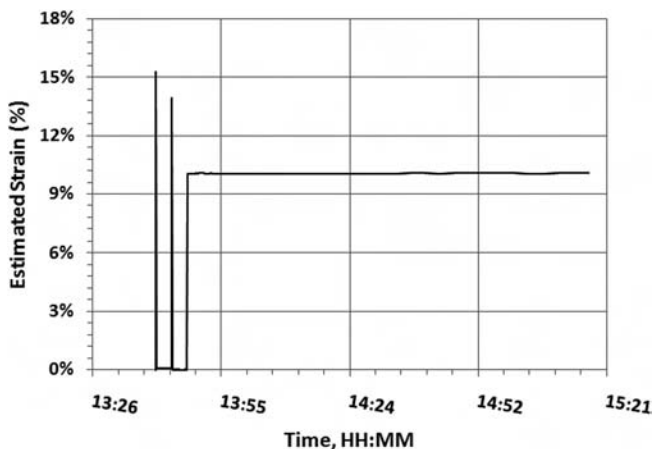


FIG. 2— E_a cycle taken on Jul. 6, 2006 consisting of two approximately 15 % strain Mullins peaks followed by a stress relaxation period at approximately 10 % tensile strain.

$$\lambda = 1 + \Delta/h \quad (3)$$

Weather: Solar irradiance, temperature, and relative humidity were recorded during outdoor exposure. Spectral irradiance is recorded via a Smithsonian SERC 18 scanning radiometer model, SR-18. This model records the UVB spectral irradiance in $\text{mW}/(\text{m}^2 \cdot \text{nm})$ and the Smithsonian uses a radiative transfer model to calculate the UVA and visible bands. Air temperature and relative humidity are recorded via a weather station. The test started in March and concluded in August of 2010. A lighting strike in April damaged the equipment resulting in the loss of approximately one month of weather data.

Results and Discussion

The cyclic loading applied to the sealant specimens due to a temperature change during the third week of July 2010 is shown in Fig. 3 for the ASTM B samples. Offsets between the three ASTM B replicates result from differences in the specimens as confirmed by offline tension and compression tests. The temperature change is the mirror image of the stress response due to outdoor exposure being run in hot compression mode. This mode simulates the displacement-temperature behavior of concrete or metal structures. This plot is typical of the exposure for all specimens with the magnitude and rate of change dependent on the weather. The variation in stress and temperature at the peak values is caused by a local variation in cloud cover inducing a rapid change in the temperature of the PVC pipe section acting to drive the computer controlled displacement.

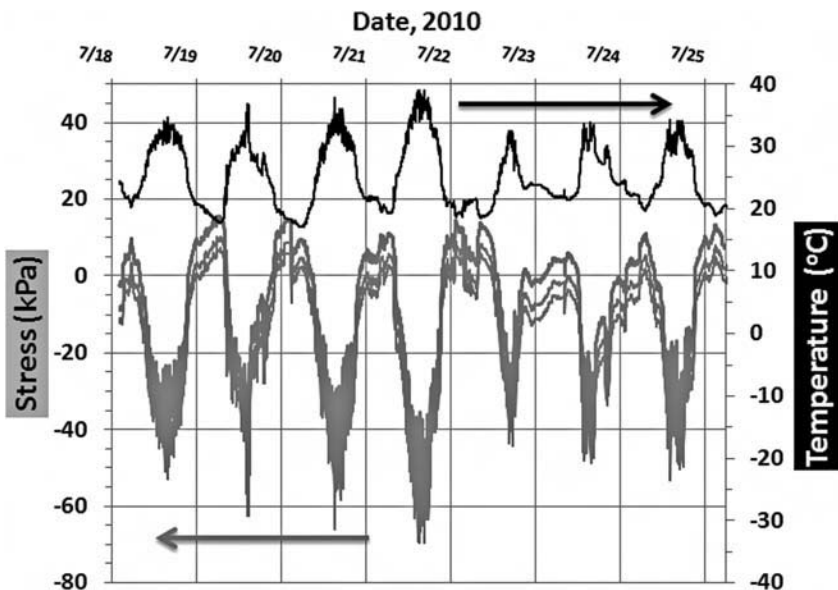


FIG. 3—Stress (left axis) and bulk temperature (right axis) versus time cycles that were recorded.

The total recorded ultraviolet A band (UVA, 315–399 nm) dosage from March 1 to Aug. 7, 2010 was 130 MJ/m². This value does not represent the total dosage due to a lightning strike in April where data was lost. It is estimated that an additional 30–40 MJ/m² could be added to the total dosage. The UVA band was tracked as opposed to the total UV band due to the detected ultraviolet B (UVB) dosage being of low intensity by comparison to the UVA values. The daily UVA dosage during aging varied considerably due to cloud cover. Overall, the accumulated UVA dosage increased linearly with time. The daily average air temperature and relative humidity values recorded at the Wisconsin test site are shown in Fig. 4. The spring temperature and humidity values varied widely. The average temperature started at below 0°C in early March and rose to 20°C by the end of the month with several cold periods in between. The average humidity varied considerably from 50 to 100 % during this time frame. Data loss due to the April lightning strike is responsible for the gap in the data from April 6 to April 21. The transition from spring to summer took place in May via a relatively uniform rise in average temperatures from 5 to 25°C. The daily average relative humidity (RH) during May continued to vary widely from 50 to 100 %. Starting in early June and continuing to August average temperatures achieved and maintained a consistent value of approximately 25°C. The RH during this time similarly became more consistent, ranging from 70–100 % with values clustered around an average of approximately 90 %. Comparing recorded weather data during the testing period with historical averages revealed that the high and low temperatures were above normal average high and low temperatures from

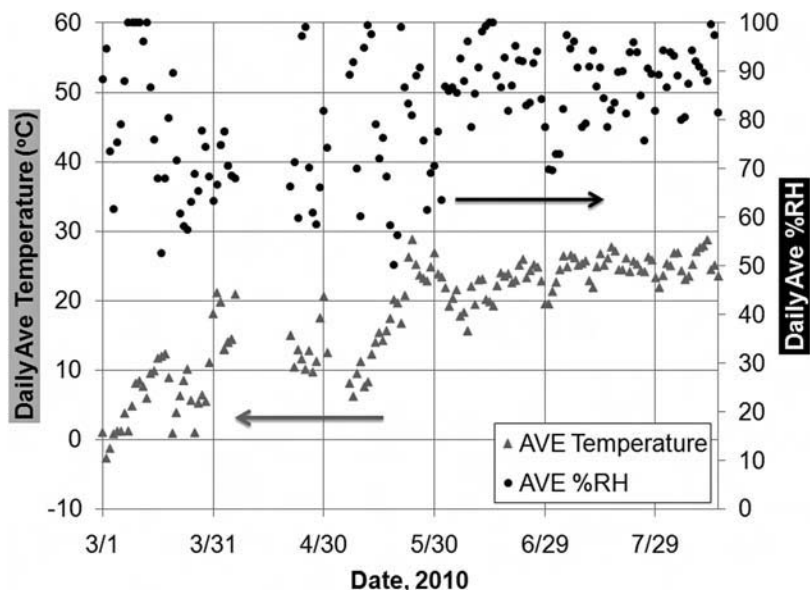


FIG. 4—Air temperatures (left axis) and RH (right axis) recorded at the Madison, WI exposure site from March through September of 2010.

March through August [8]. High temperatures recorded in May were near record highs [8]. The precipitation was double the normal amount during June and July 2010 for the south central region of Wisconsin that includes the Madison test site [8].

The mean strain (e_m) and daily strain ratio (e_r) resulting from the PVC temperature change (Eq (1)) are plotted in Figs. 5 and 6. The strain ratio and mean strain were calculated via Eqs. (4) and (5), respectively, where e_{min} is the day's minimum strain and e_{max} is the day's maximum compressive strain

$$e_r = e_{min}/e_{max} \quad (4)$$

$$e_m = (e_{max} + e_{min})/2 \quad (5)$$

The daily values of e_{min} and e_{max} are also plotted in Fig. 5 where they are indicated as bars radiating from the daily mean strain value. Not surprisingly, the mean strain values correspond to the average air temperature pattern shown in Fig. 3. The effect of solar heating variation due to cloud cover changes is reflected in the difference and variation in the maximum strain values shown in Fig. 5. The minimum strain typically occurred at night and hence is less variable on a day to day basis and is more in correspondence to the air temperature. The mean strain and max/min values vary considerably from April through mid-May. During this time, mean strain, minimum, and maximum values

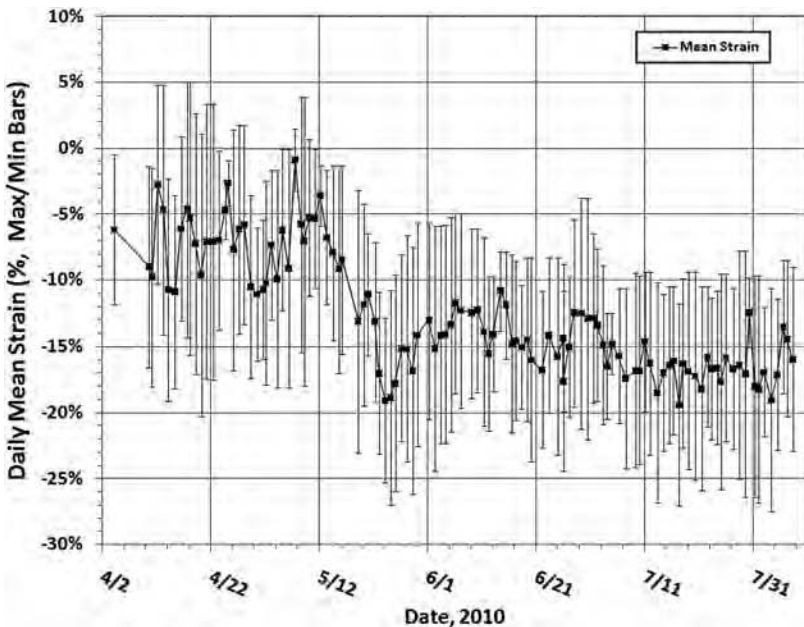


FIG. 5—Daily mean strain resulting from the diurnal PVC temperature change with error bars indicating the strain differential for each day.

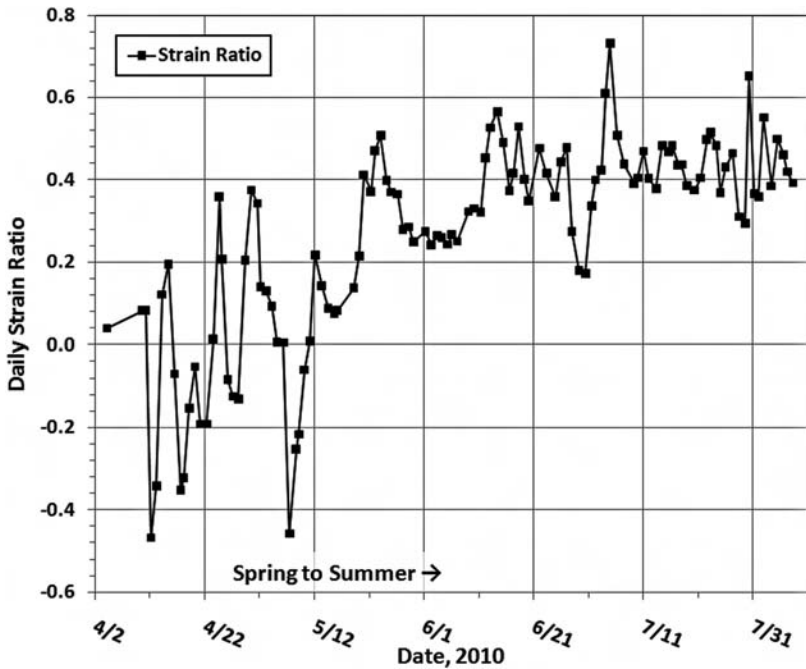


FIG. 6—The strain ratio resulting from the diurnal cycle.

varied from 0 to -11% , 5 to -6% , and -3 to -20% , respectively. Thus, there are day to day transitions from compression to tension strain exposure. As with the air temperature, the mean strain dropped during May from -5 to -20% with a recovery to -13% at the end of the month. The mean strain and its daily variability decreased as the temperature rose towards a relatively uniform value of -15% strain starting in June and gradually decreased through August. The minimum strain made a transition during this time to values less than -5% strain. Thus, the sealants experienced a constant state of compressive stress during the summer. The applied strain ratio increased during the seasonal transition from spring to summer and its variability between days decreased. Both trends are indicative of decreased daily temperature swings and hence, more stable strain patterns applied to the sealants during the summer. Additionally, the rising strain ratio reveals that during the summer the sealants are carrying more strain.

The strain ratio shown in Fig. 6, is commonly prescribed in uniform continuous cyclic fatigue testing as a means to set the predominate mode of exposure. Specifically, high values indicate that the samples will carry a large amount of strain during the fatigue exposure. This results in a combined fatigue and stress relaxation exposure in controlled strain testing, as used here, or fatigue and creep exposure in controlled load testing. Low strain ratio values induce a large delta strain in the samples during each cycle. Such cycles can result in temperature build up (not expected in this study), and an acceleration of any hysteresis

based damage mechanisms such as filler particle debonding, the Mullins effect, crazing, delamination, crack formation and growth, etc. The daily extremes represented in Fig. 6 are quite variable from March to mid-May indicating no consistent trend towards stress relaxation or hysteresis based exposure. The mean strain in Fig. 5 reveals a period of relatively low compression strain with variation from 0 to 11 % during this same period. This changed dramatically in mid-May to high positive strain ratios due to both extremes being compressive. This continued through August with a significantly lower variation.

The Ea cycle described in the experimental section is run on a weekly basis in order to track changes in apparent modulus during aging. The Badger's computer controlled stepper motors allow such measurements to take place without having to remove the specimens. The stress versus time responses from an Ea cycle run on Apr. 27, 2010 are shown in Figs. 7 and 8 for ASTM B and Consortia C sealants, respectively. During this time frame the Badger did not meet the programmed strain level of 15 % for the Mullins peaks, yet the peaks did sufficiently exceed the 10 % strain for the stress relaxation period used to calculate Ea. The error bars in these plots are the standard deviations among the sealant replicates. As previously stated, offline testing confirmed that the variations in ASTM B are due to sample variations. The offline tests on the Consortia C replicates revealed them to be relatively uniform. Therefore, the variation seen here is due to variations in the sample shape or shimming of the specimens during installation on the Badger resulting in slightly different applied strain values. The difference in error bar density is due to a difference in the sampling rate

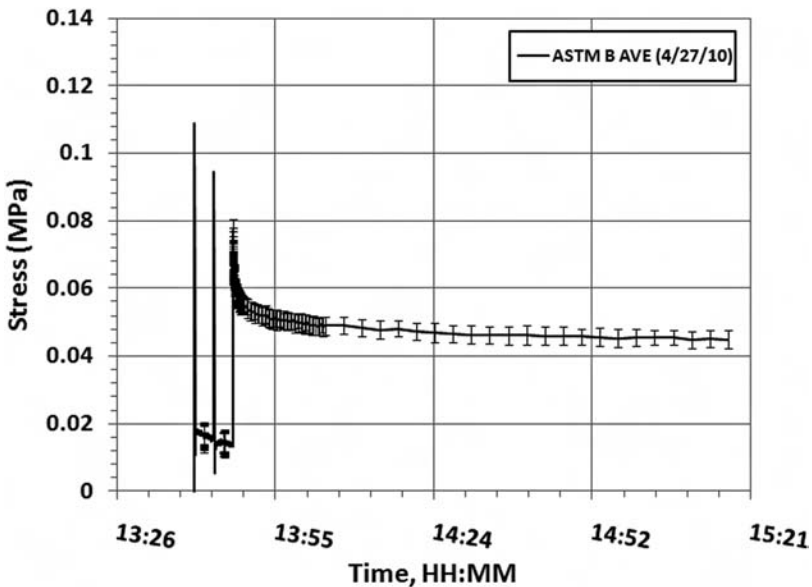


FIG. 7—Average stress for the three ASTM B sealant specimens resulting from the Ea cycle completed on Apr. 27, 2010.

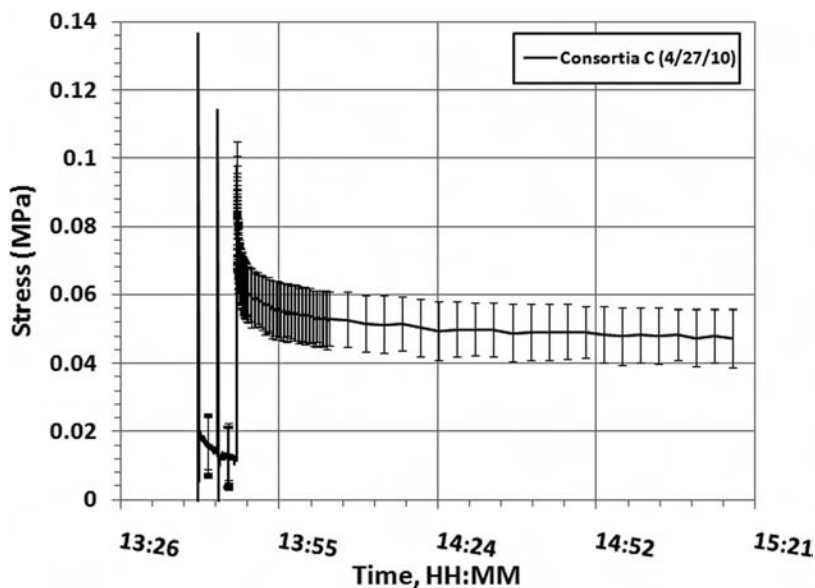


FIG. 8—Average stress for the three Consortia C sealant specimens resulting from the Ea cycle completed on Apr. 27, 2010.

during the Ea cycle. The time gaps after each Mullins peak are prescribed to be zero strain, allowing time for the samples to relax to zero stress, thereby alleviating any dynamic effects. Here, both sealants do not quite make it to zero stress at zero strain before the stress relaxation period begins.

The Ea versus stress relaxation time curves from April 13 to Aug. 3, 2010 are shown in Figs. 9 and 10 for the ASTM B and Consortia C sealants, respectively. A power law fit to the data resulted in high correlation coefficients and two parameters. The first parameter, the intercept at the Ea axis, acts as a good indication of the change in the overall stiffness of the sealants. The second parameter, an exponent, represents the time dependency of the sealant and how it changes during aging. Figure 9 shows that the Ea value at 5.8 ks increases by 62 % over the course of the experiment. The time dependent exponent decreased by 39 % indicating that the sealant exhibited less viscous behavior after aging.

Figure 10 shows that the Consortia C sealants underwent a 30 % increase in Ea at 5.8 ks as a result of outdoor aging. The increase in stiffness does not appear to be linear with aging time since the Ea values calculated on August 3 are lower than the values in June and late July. Such a phenomenon does not agree with the general concept of irreversible degradation or consumption of the chemical bond or other formulation additive. Since the formulations are not known to us and we are prohibited from chemical investigations, we cannot specifically comment on the chemical mechanisms that may be at work here. The power law fit exponent for Consortia C decreases by 42 % due to outdoor aging representing less time dependency and less viscous behavior.

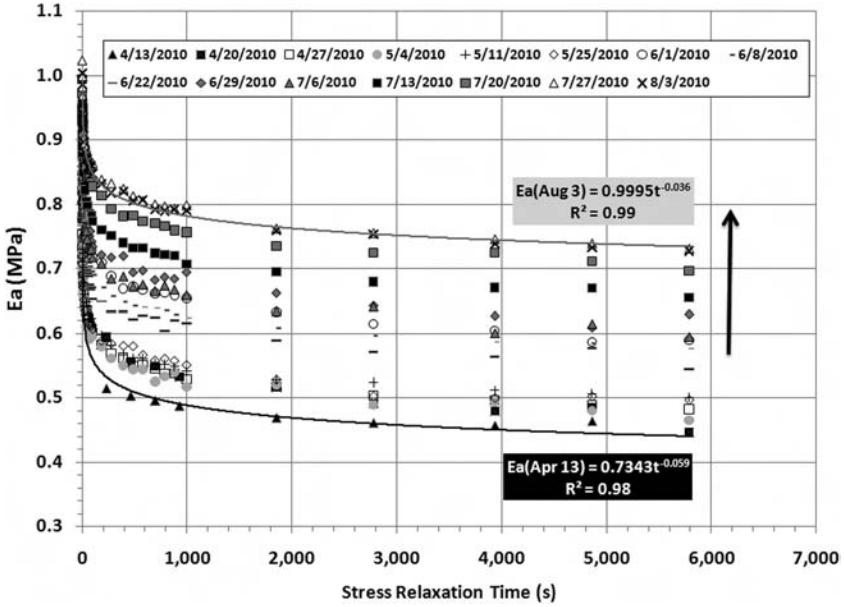


FIG. 9—Stress relaxation behavior of the ASTM B sealant from April 13 to Aug. 3, 2010.

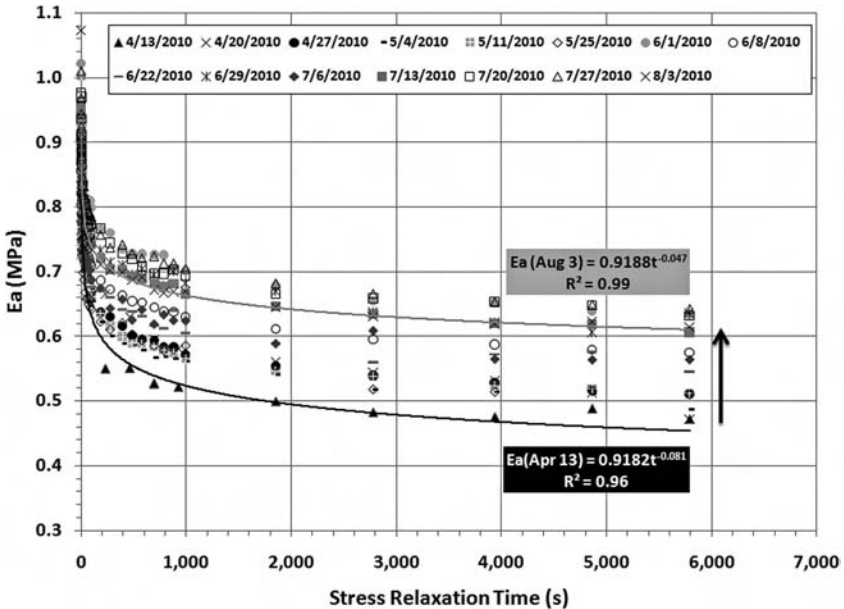


FIG. 10—Stress relaxation behavior of the Consortia C sealant from April 13 to Aug. 3, 2010.

The % change in E_a at 5.8 ks is plotted in Fig. 11 as a function of aging time for both sealants. Overall, there is a significant increase in E_a with time with occasional periods of reduction or recovery in E_a . Both sealants have increases and recovery in E_a that appear to be coincident in time indicating that the aging conditions applied to the sealants are inducing a similar type of change in the sealants. Also plotted in Fig. 11 is the strain ratio applied to the sealants during the aging time. The rise in E_a coincides with the transition in strain ratio to values greater than 0.2 where the samples begin experiencing compression 24 h a day. Comparing the change in E_a versus the applied strain ratio indicates a generally increasing E_a with strain ratio values at 0.2 and higher. Notable periods of decreasing E_a occur in contrast to this observation.

These observations led us to search for other factors that may affect E_a . This revealed that the non-zero stress level at zero strain observed in Figs. 7 and 8 as a fraction of the stress relaxation stress grows with aging time to become a significant fraction of the stress relaxation stress. This acts to unintentionally raise the starting stress for the stress relaxation period resulting in higher and higher E_a values. Since the non-zero stress at zero strain is positive, it is the result of a residual compressive strain in the sealants remaining from hot compression aging exposure. This effect is commonly referred to as the compression set. Figures 7 and 8 provide some evidence to support the hypothesis that the tensile load resulting from the compression set does relax with time. Unfortunately, the Mullins portion of the E_a cycle used during this research did not

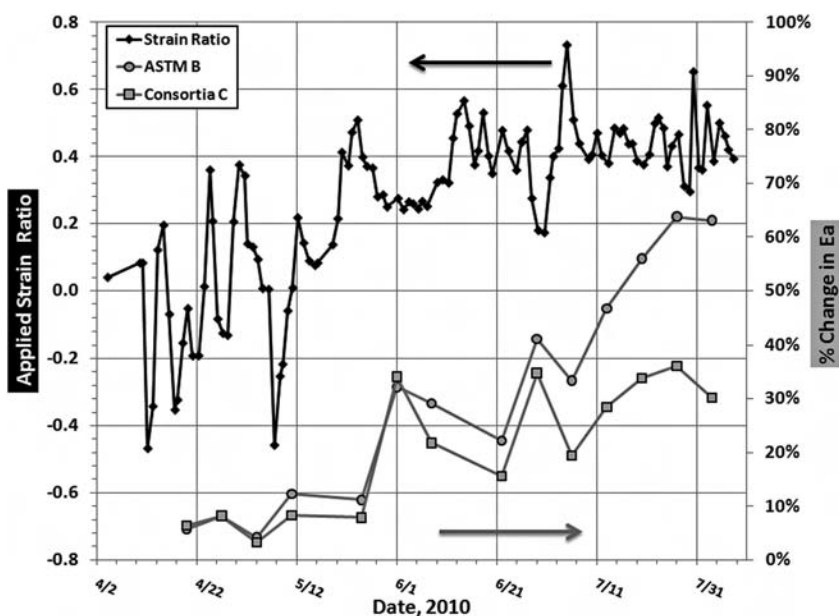


FIG. 11—Daily strain ratio resulting from temperature fluctuations (left axis) and % change in E_a (5.8 ks) for the ASTM B and Consortia C sealants as a function of outdoor exposure time.

hold at zero strain long enough to allow an accurate measurement of compression set relaxation time. The compression set value prior to the start of the stress relaxation period can instead be used to correct the E_a values calculated soon after the stress relaxation period has started. Figures 12 and 13 plot for sealants ASTM B and Consortia C, respectively, the compression set stress, the average stress relaxation stress at 100 s, and the corrected average stress relaxation stress at 100 s. The average stress relaxation stress are the values that would be used to calculate the apparent modulus at 100 s, $E_a(100)$. Subtracting the compression set stress from this value results in the corrected average stress relaxation stress at 100 s. Comparing the change in compression set stress with the stress relaxation stress over aging time makes it clear that the principal driving force behind the change in stress relaxation stress and the E_a values calculated from them is the compression set stress. It is not clear whether the compression set is temporary or permanent from these results. The contribution of the compression set stress is subtracted to yield a corrected stress relaxation at 100 s value. Figure 12 plots the corrected value for ASTM B versus aging time. This plot shows only minor deviations through Aug. 3 from the value measured on April 13. Applying the same analysis to the Consortia C sealant, Fig. 13 reveals a gradual decrease in corrected stress relaxation stress from April 13 to Aug. 3 to a value that is approximately 14.6 % lower. Given the variation among the Consortia C replicates, this result does not appear to translate to a significant change in stiffness calculated from this value. In short, after removing compression set effects from ASTM B and Consortia C sealants, we could detect no significant change in stiffness during aging.

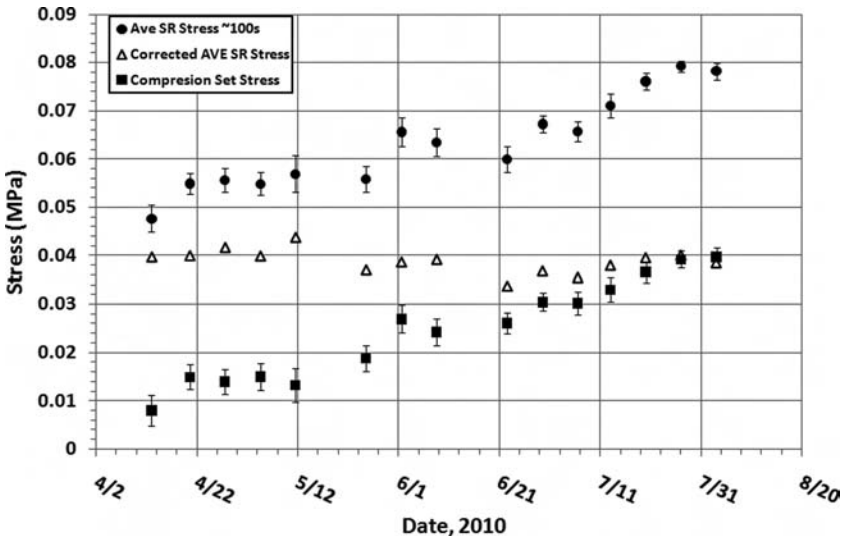


FIG. 12—Compression set stress, average stress relaxation stress at 100 s, and corrected average stress relaxation stress for ASTM B.

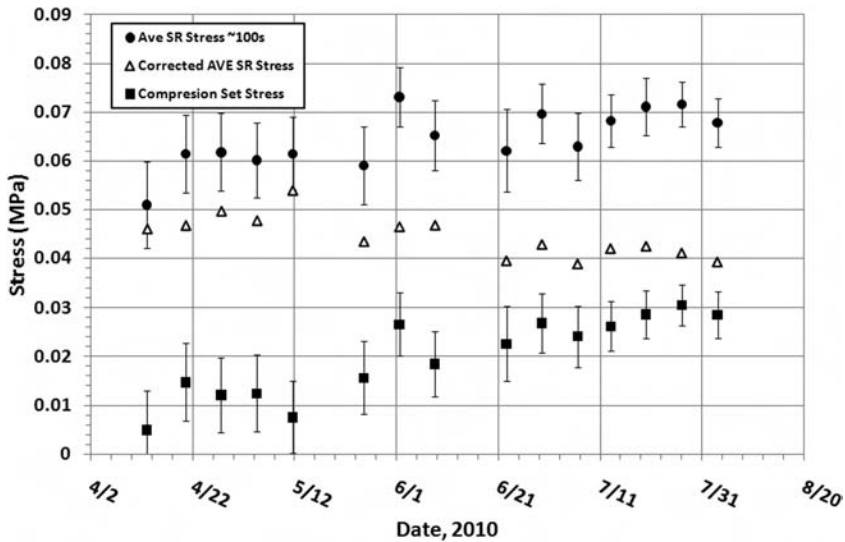


FIG. 13—Compression set stress, average stress relaxation stress at 100 s, and corrected average stress relaxation stress for Consortia C.

The change in the time dependent exponent of stress relaxation observed over the course of the experiment could also be explained by the compression set. Since some of the stress applied to the specimens originates with the compression set, the stress relaxation rate would be a combination of the stress relaxation of the applied load and the relaxation of the compression set. Even the small compression set apparent following the Mullins peaks in Figs. 7 and 8 suggest that the compression set relaxation is slower than the applied load relaxation that follows. In other words, the time dependent exponent for the relaxation of the compression set is smaller than the value for the applied load, and so the combined (measured) value decreases as the contribution of the compression set increases over the course of the experiment. There is also the possibility that a fraction of the compression set is permanent such that its overall relaxation halts prematurely.

While the specimens did not undergo a definitive change in stiffness during aging, the compression set has real implications on actual performance. Because of compression set, the effective stiffness of the sealants did increase and would act to restrict the movement of attached substrates to a proportional degree as if the sealant's modulus had indeed increased. Thus, similar sealants bonded to metal or cement substrates would impart greater stresses to the bond area after hot compression induced set than would be predicted by the original properties of the sealant. Such high stresses could precipitate failure well in advance of what short term accelerated testing may have predicted. Outdoor exposure tests that do not determine apparent modulus in situ such as the Badgers are more likely to miss this effect due to relaxation after sample recovery

and before offline testing is completed and/or if reference to the original zero strain/stress point is not tracked.

The measurement rate of the compression set and the severity of its contribution should be matched to the rate of movement of the building envelope. If a building moves very slowly, the finding presented here may not be important because the compression set may have time to relax during building movement, provided it is not permanent. Metal exterior cladding systems, however, have the potential to move very quickly. It is conceivable that during the summer, the sealants joining the metal skin of a building experience long periods of compression at high temperature, causing compression set. The arrival of a thunderstorm, and the wetting of the surface from rain, however, can cause a precipitous drop in surface temperature and hence, a fast opening of the joint. It is this kind of situation where the increased apparent stiffness from compression set will most likely exceed the bond strength of the sealant and result in failure. Clearly, sealants on highly absorbing (dark), thin cladding systems with high thermal transfer and expansion coefficients, such as metal skins, are most vulnerable to this kind of problem. Sealants intended for this kind of application should be tested to determine the extent and rate of recovery from compression set. When choosing a sealant, these values should be compared to the potential rate of the temperature change of the skin and hence the rate of movement of the joint.

Conclusions

The methodology and instrumentation developed and implemented in this experiment allowed the successful tracking of environmental exposure and strain dosage factors and the progressive change in sealant stiffness with reference to the original zero stress/strain state. The stiffness increases observed here are predominately, if not completely, due to a progressive compression set inducement. This gradual process creates the appearance of increasing stiffness in our strain controlled modulus measurements via a non-zero stress at the programmed or original zero strain-zero stress state. This process can be seen as an artifact that interferes with attempts to track real time changes in sealant properties during aging. An alternative view is that this is a real phenomenon that takes place in buildings and structures during prolonged high temperatures. A rapid transition to cooler weather after prolonged compression may result in exceeding the failure stress of the sealants due to unexpectedly high strain from compression set. If the sealant or its bond is already compromised due to aging or other factors, failure could result from such a combined effect. Therefore, the compression set may be a key factor in a sealant's durability and warrants further study. The methods used in this study are ideally suited to its detection and the monitoring of its effects. Short term accelerated weathering or outdoor aging approaches that are not long enough in duration to induce compression set or do not allow for in situ measurement of compression set and its effect on apparent modulus may miss or underestimate this important factor in service life prediction.

Acknowledgments

The writers wish to acknowledge Marshal Begel, David Eustice, Bob Foss, Will Kinney, William Nelson, and David Simpson of the Forest Products Laboratory for their essential contributions that made this work possible.

References

- [1] Williams, R. S., Lacher, S., Halpin, C., and White, C., "Evaluating Cyclic Fatigue of Sealants During Outdoor Testing," *Service Life Prediction of Polymeric Materials Global Perspectives*, J. W. Martin, R. A. Ryntz, J. Chin, and R. A. Dickie, Eds., Springer, New York, 2009, Chap. 9, pp. 129–151.
- [2] White, C. C., Tan, K. T., Hunston, D. L., and Williams, R. S., "Durability of Building Joint Sealants," *Service Life Prediction of Polymeric Materials Global Perspectives*, J. W. Martin, R. A. Ryntz, J. Chin, and R. A. Dickie, Eds., Springer, New York, 2009, Chap. 8, pp. 115–128.
- [3] See NIST Service Life Prediction of Sealant Materials Consortia web page, <http://slp.nist.gov/sealant/sslpmain.html>
- [4] ASTM C719, 1993 (2010), "Standard Test Method for Adhesion and Cohesion of Elastomeric Joint Sealants Under Cyclic Movement," *Annual Book of ASTM Standards*, ASTM International, Vol. 04.07, West Conshohocken, PA, pp. 88–93.
- [5] Mullins, L., "Softening of Rubber by Deformation," *Rubber Chem. Technol.*, Vol. 42, 1969, pp. 339–363.
- [6] Treloar, L. R. G., *Physics of Rubber Elasticity*, 3rd ed., Oxford Univ. Press, Oxford, 2002.
- [7] Ferry, J. D., *Viscoelastic Properties of Polymers*, 3rd ed., John Wiley & Sons, Inc., New York, 1980.
- [8] See Wisconsin State Climatology Office web page: <http://www.aos.wisc.edu/~sco.clim-history/7cities/madison.html>

Sigurd Sitte,¹ Michael J. Brasseur,² Lawrence D. Carbary,³
and Andreas T. Wolf⁴

Preliminary Evaluation of the Mechanical Properties and Durability of Transparent Structural Silicone Adhesive (TSSA) for Point Fixing in Glazing

ABSTRACT: The paper reports on the preliminary evaluation of a transparent structural silicone adhesive (TSSA) developed for point fixing in glazing, which combines high transparency, strong adhesion performance, thermal stability, and excellent weatherability. The transparent film adhesive is a heat curing one-part material that shows strong bonding to glass, metals, ceramics, and even plastics typically without primer. The paper presents information on the durability and physical properties of the new material and suggests a methodology for deriving static and dynamic design strength values for the new material based on creep rupture experiments as well as nondestructive dynamic load experiments using the stress whitening phenomenon observed with this material as the limit state. The paper further discusses material characterization and hyperelastic modeling used in the finite element analysis based on finite strain theory.

KEYWORDS: structural, silicone, film adhesive, point fixing, glazing

Introduction

Glass is widely used in contemporary architecture as transparent infill elements in the building envelope because of its aesthetic characteristics. The use of glass

Manuscript received June 1, 2011; accepted for publication July 26, 2011; published online August 2011.

¹AETS Professional, Dow Corning GmbH, D-65201 Wiesbaden, Hesse, Germany.

²AETS Professional, Dow Corning Corporation, Midland, MI 48686-0994.

³Industry Scientist, Dow Corning Corporation, Midland, MI 48686-0994.

⁴Senior Industry Scientist, Dow Corning GmbH, D-65201 Wiesbaden, Hesse, Germany (Corresponding author), e-mail: Andreas.Wolf@DowCorning.com

Cite as: Sitte, S., Brasseur, M. J., Carbary, L. D. and Wolf, A. T., "Preliminary Evaluation of the Mechanical Properties and Durability of Transparent Structural Silicone Adhesive (TSSA) for Point Fixing in Glazing," *J. ASTM Intl.*, Vol. 8, No. 10. doi:10.1520/JAI104084.

Copyright © 2011 by ASTM International, 100 Barr Harbor Drive, PO Box C700, West Conshohocken, PA 19428-2959.

also permits passage of light into the building, which is important for the well being of the building's occupants. The glass panes may be fixed to the supporting structure by either linear or point bearings. The linear supports attach the glass pane to the substructure on two, three, or four sides. In this system, the glass pane may either be retained on both faces in a glazing channel by a flexible gasket made from EPDM, chloroprene, silicone, or a similar material, or adhesively attached on one face by a structural glazing sealant. Point bearings can be classified into fixing clamps and point-fixed supports. The point-fixed supports are generally positioned in the vicinity of the corners of the glass pane and retain the glass pane either mechanically (metal bolts penetrating the glass) or adhesively [1,2]. Mechanical fixing of glass panes furnished with holes requires the designer to pay attention to the placement of the holes in order to meet the requirements of national standards. For instance, ASTM C 1048 Specification for Heat-Treated Flat Glass [3] specifies that the hole must be placed at a distance of at least 6.5 times the thickness of glass away from the corner. Furthermore, in order to deal with unavoidable stress concentrations around the fixing holes, heat strengthened or tempered glass must be used.

Bonded point-fixed supports have recently received increased attention, as in contrast to mechanical point supports they offer a number of advantages, such as no or less visibility from the exterior, a "smooth" transfer of the load into the glass pane (avoiding stress peaks), and the elimination of drilling holes into the glass [4–7]. Contrary to the glass panes, the adhesive fixing used in either linear or point bearings may experience both out-of-plane and in-plane loads, depending on whether the dead load of the glazing element is carried by mechanical setting blocks into the building envelope substructure. Based on the current state-of-the-art, the adhesive fixing of glazing elements in exterior (building envelope) applications is limited to structural silicone sealants and, more recently, to acrylic pressure-sensitive adhesive (PSA) coated structural foam tapes [8].

Structural silicone sealants have been used in linear adhesive fixing of glazing elements at a tertiary structural level since the 1960s [9]. The long-term experience with silicone sealants in this field has led to standardization of both the performance requirements on the structural adhesive sealants as well as the glazing designs [10,11]. The room-temperature-vulcanizing (RTV) structural silicone sealants used in linear fixing of glazing elements (structural silicone glazing) display a low Young's modulus (generally in the range of about 1.0–2.5 MPa in tension) and a high elongation at break (generally in the range of >100% when measured in tension on a tensile-adhesion joint with dimensions as defined in ISO 8339 [12]). The resulting joint design allows compensation of thermally induced movements and dimensional tolerances between the substrates, which is a necessity for linear structural bonded bearings. However, for adhesively bonded point-fixed bearings, a higher Young's modulus is desirable to achieve higher stiffness with a smaller bonding area that still allows carrying significant out-of-plane loads [6].

Recent studies have focused on the evaluation of photocured acrylics for this application; however, these materials still suffer from limitations, such as insufficient water resistance and application issues (watery thin viscosity),

which currently restrict their broader use in exterior (building envelope) applications [4,5]. Therefore, it would be highly desirable having a transparent silicone material available that combines the inherent durability of the siloxane polymers [13] with an improved strength, suitable for adhesive point fixing, and a simple application method.

This paper presents experimental data obtained on a one-part, heat-triggered addition-cure structural silicone film adhesive. It also discusses proposals for the development of design strength values for the material when exposed to dynamic or static loads.

Properties of the High-Strength Structural Silicone Film Adhesive (TSSA)

Cure Chemistry and Behavior

The structural silicone film adhesive is a one-part material that features a heat-activated addition-cure mechanism, as shown in Fig. 1.

The addition-cure mechanism causes no cure by-products (and no odor) to be evolved during the reaction. The film adhesive is cured at temperatures of 120–130°C for a period of 20–30 min between the substrates while applying a pressure, typically 0.15–1.3 MPa, in order to provide efficient wet-out on the substrate. The optimum cure conditions are achieved in an autoclave, such as those used in the production of laminated glass. Alternative production methods, such as prepressing (prior to heat cure) or vacuum-bagging (during heat cure) are currently being investigated.

The onset of cure occurs rather rapidly; however, the heat exposure time of 20–30 min is needed to achieve a uniform activation temperature and complete, homogeneous cure within the glass/glass or glass/metal assembly. The cure behavior of the film adhesive was characterized in a rotorless cure meter (oscillating die rheometer) under isothermal conditions at a temperature of 130°C (no preheat) and constant maximum strain (arc 3°) and constant oscillation frequency (100 cycles/min) for a total running time of 30 min [14]. The rheometry trace is shown in Fig. 2. After approximately 5 min at 130°C, the torque rapidly increases within about 2 min by a factor of 8 and after a total cure time of about 7–8 min, the torque value reaches about 80% of its final value. The steep increase in torque is an indication that the chemical reactions associated with the cross linking of the silicone film adhesive have begun.

The rheometer gives two important pieces of information: First is the maximum torque (T_f), which is a measure of the final set rigidity. Second is a value called T_{90} , the amount of time it takes for the torque to reach 90% of the maximum value. T_{90} is correlated to the material's setting time. At 130°C, T_{90} is reached after approximately 15 min of cure and T_f after about 30 min.

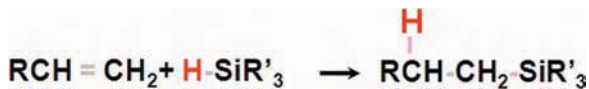


FIG. 1—Silicone addition cure reaction yielding no cure by-products.

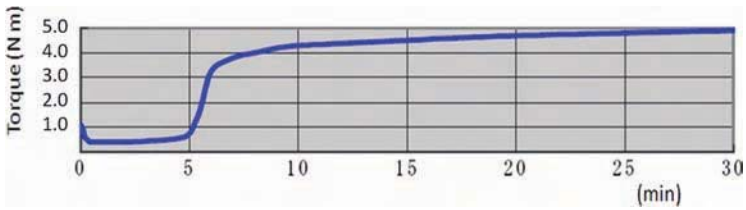


FIG. 2—Rheometry trace for silicone film adhesive cured at 130°C.

General Properties

The preformed film features a simple application, as it is easy to cut and apply, and can be stacked as multiple layers. After cure, the film adhesive has high transparency (see Fig. 3) as well as high tensile strength, strong adhesion performance, excellent thermal stability, and high weatherability, as reported earlier [15].

The film is optically clear, its transparency has a very low dependency on temperature (see Fig. 4), and its refractive index (1.41) sufficiently matches that of window glass (1.51–1.52) [16] so as not to cause optical distortions. Furthermore, the film has a low heat conduction coefficient. Finally, the bonded film can be removed, if desired so, simply by cutting.

Table 1 summarizes the general properties of the film.

Because of these unique properties, the authors expect future use of this material in both interior and exterior bonded point fixing for glazing as well as in direct glass-to-glass bonding applications, such as in structural glass fixing of facades, balustrades, or glass stairs as well as of glass furniture (replacement of mechanical fixing bolts in point supports, structural bonding along the glass edges in structural glazing, bonded glass corners). The film may also find further application in the production of structural laminated glass. Early trial installations have been completed at Ginza Matsuya Dept. Store and Okinawa History Memorial Hall in Japan.



FIG. 3—Stainless steel button attached to glass with TSSA (seen from side and rear face).

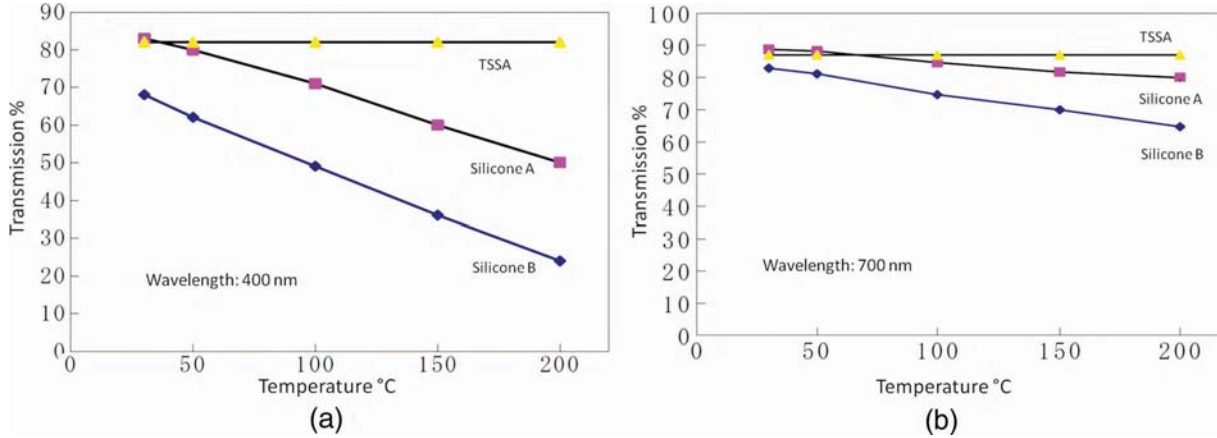


FIG. 4—Dependency of optical transmission (1 mm thick film) on temperature for TSSA and other silicone adhesives at wavelengths of 400 and 700 nm.

TABLE 1—General properties of structural silicone film adhesive.

Property	Test Method	Characteristics/Value
Application		Simple application, multiple layers possible
Removal		Simple cutting procedure
Transparency, color	JIS K 7105 [17], JIS Z 8729 [18] (HITACHI UV-Vis U-1650 spectrophotometer)	Crystal clear, no visible tint (2 mm thick film)
Adhesion	Single lap joint peel after exposure to hot water, elevated heat/humidity, or elevated heat, humidity and UV light [15]	Strong adhesion, typically without primer
Durability	Film adhesive exposed to heat, hot water and accelerated weathering (heat, moisture, UV); stainless steel button point-fixing on glass exposed to natural outdoor and artificial accelerated weathering with and without simultaneously applied loads [15]	Excellent UV, water, and heat resistance
Refractive index (1 mm thick film at 589.3 nm)	JIS K 7105 [17] (Abbe refractometer)	1.41
Thermal conductivity [W/(m K)]	JIS A1412 [19]	0.2
Linear thermal expansion coefficient (10 ⁻⁶ 1/K)	JIS K7197 [20]	281
Volatile loss during cure for 30 min at 130°C (%)	Gravimetric evaluation, similar to ASTM D2369 [21]	0.26

Mechanical Properties

The bulk material properties, reported in Table 2, were obtained on the 2.2 ± 0.2 mm thick film adhesive after curing it between two sheets of PTFE release liners in an autoclave for 30 min at a temperature of 130°C and a pressure of 0.8 MPa, except for indentation hardness, as noted below. Tensile tests were conducted according to JIS K 6251 standard [22] on adhesive dumbbells with a procedure similar to the one set out in ISO 527 Parts 1 and 2 [23,24]. Indentation hardness (durometer) was measured in accordance with JIS K 6253 [25] by stacking three layers of the cured film adhesive on top of each other to achieve a specimen thickness of approximately 6.6 mm. Tear strength was measured according to JIS K6252 [26].

Furthermore, as has been reported earlier, the physical properties of the silicone film adhesive show a low dependency on temperature [15].

Figure 5 shows the tensile stress-strain curve of the cured silicone film adhesive at room temperature as averaged over a separate set of 50 uniaxial tensile extension measurements [obtained with a strain rate of 500 mm/min on ASTM D 412 [27] type (dumbbell) specimens], as well as the corresponding graphs for secant modulus (stress-strain ratio) and tangent modulus (slope of the stress-strain curve). The graphs for the tangent and secant moduli of elasticity converge towards a Young's modulus of about 9.3 MPa. For this set of data, an ultimate tensile strength of 8.6 MPa is reached at 250 % (95 % fractile $R_{u5} = 7.85$ MPa). Additionally, the form of the graph indicates that the material data can be characterized by an incompressible neo-Hookean material model with a shear modulus of 2.5 MPa [28].

Durability of Bonded Stainless Steel Button Point Fixing on Glass

In an earlier paper, some data on the durability of the cured structural silicone film adhesive itself as well as of single-lap-joint shear specimens and stainless steel button point fixing on glass made with the film were reported [15]. As can be seen from the data presented in this paper, the structural silicone film adhesive combines high transparency, strong adhesion performance, thermal stability, and excellent weatherability with high tensile and shear strengths, unmatched by RTV (condensation curing) structural silicones. For illustration, Fig. 6 summarizes the data from the previous paper obtained on stainless steel

TABLE 2—*Typical properties of cured silicone film adhesive.*

Property	Test Method	Typical Value	Unit
Indentation hardness	JIS K 6253 [25] Durometer	70	JIS A
100% modulus	JIS K 6251 [22] (dumbbell 3)	4.0	MPa
Young's modulus	ISO 527 Parts 1 and 2 [23,24]	9.3	MPa
Max. tensile strength	JIS K 6251 (dumbbell 3)	9.0	MPa
Elongation at break	JIS K 6251 (dumbbell 3)	250	%
Tear strength	JIS K6252 [26] (crescent specimen)	35	N/mm

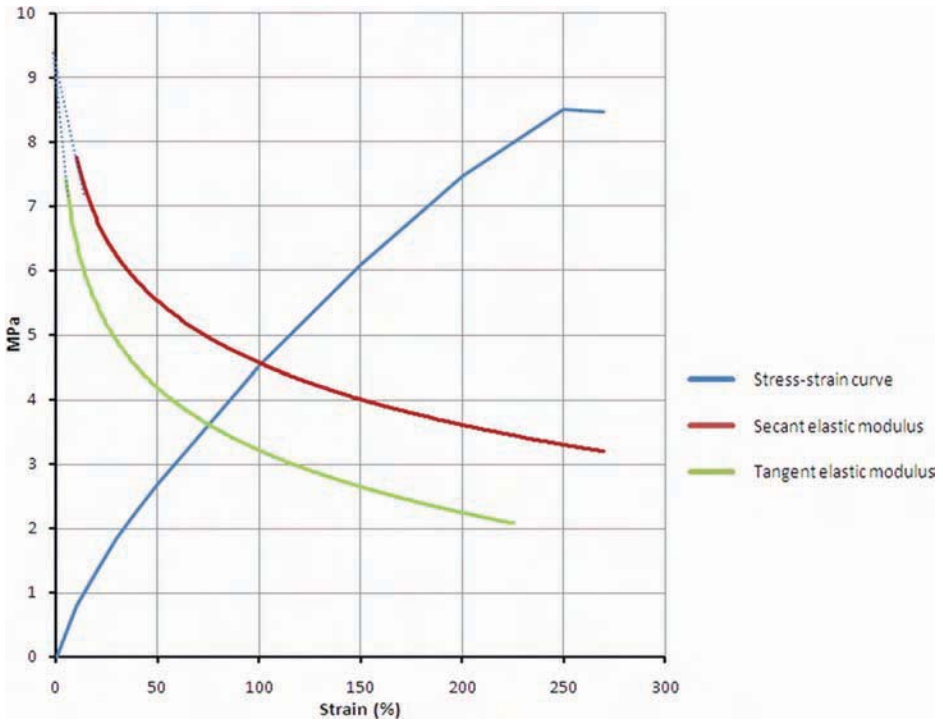


FIG. 5—Tensile stress-strain curve and corresponding graphs for secant modulus (stress-strain ratio) and tangent modulus (slope of the stress-strain curve) of the cured silicone film adhesive at room temperature (dotted lines show extrapolation of data to Young's modulus).

button point-fixing specimens on glass combined with some new data on the short-term resistance to constant load exposure.

Specimens for testing the durability of point fixing on glass were prepared by bonding a 20 mm diameter stainless steel “button” with a threaded socket head (see Fig. 3) to a glass plate (cross section of adhesive interface: 314 mm²). The structural silicone film adhesive (1 mm initial and 0.8 mm final thickness) was cured between the button and the glass by placing the complete assembly into an industrial autoclave operated at a pressure of 1.275 MPa and a temperature of 130°C for a total of 25 min. Separate test specimens were exposed to hot water immersion, to accelerated weathering, and to outdoor weathering, allowed to recondition for 1 day, then fixed to a tensile test machine, and pulled vertically to the glass surface at a rate of 50 mm/min. The hot water immersion was carried out at 50°C for a period of up to 8 weeks. Accelerated weathering occurred for up to 12,000 h in a machine with a fluorescent light source [ATLAS UVCON UC-1 Ultraviolet Condensation Weathering Device with UV-A 340 (340 nm) fluorescent bulbs]. The specimen was positioned in the tester such that the glass surface was exposed to the irradiation (accelerated weathering of

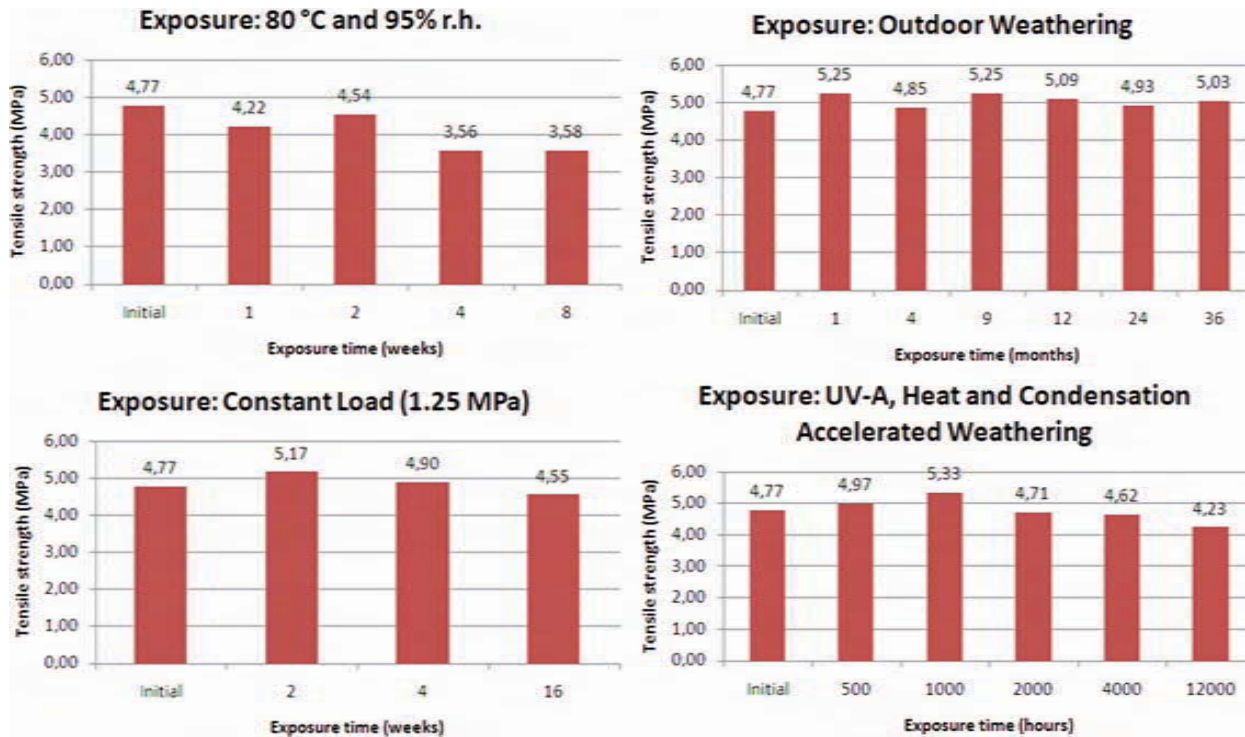


FIG. 6—Tensile strength of silicone-bonded stainless steel button point-fixing specimens on glass after different exposures.

the silicone through the glass) and the machine was operated according to ASTM G154-06 [29] with a cycle of 4 h UV at 60°C and 4 h of dark (no UV) and condensation occurring at 40°C. Outdoor weathering was carried out for up to 36 months in Chiba, Japan, in a weathering rack oriented towards the southeast with an inclination angle of 33° and the solar irradiation of the silicone occurring through the glass surface. Exposure to a constant load of 1.25 MPa occurred for a period of up to 16 weeks, after which the test specimens were tested to destruction in the tensile tester using a pull rate of 50 mm/min.

As can be seen from Fig. 6, after 16 weeks of loading the test specimen with a constant stress at 1.25 MPa, a reduction in the ultimate failure strength to 4.55 MPa from an original value of 4.77 MPa was noted. However, this decline may very well be within the error of the test when comparing all of the data shown in Fig. 6.

Preliminary Evaluation of the TSSA Film Adhesive With the Aim of Developing Static and Dynamic Design Stress Values

Performance specifications for structural glazing, such as ASTM C1184-05 Standard Specification for Structural Silicone Sealants [30], ETAG 002 Guideline for European Technical Approval for Structural Sealant Glazing Systems [11], or EN 15434:2006+ A1:2010 Glass in building-Product standard for structural and/or ultraviolet resistant sealant (for use with structural sealant glazing and/or insulating glass units with exposed seals) [31], were developed for linear bonded bearings and with cold and liquid applied, chemically curing elastomeric structural silicone sealants in mind. While applications of the structural silicone film adhesive are not directly covered by these standards, based on their internal evaluations, the authors expect the structural silicone film adhesive to pass the durability aspects of these standards without problems, as similar exposures have been carried out internally.

Adhesives used in structural bonding in buildings are required to carry certain design loads in their resistance to fracture and meet certain serviceability limit states which define functional performance and behavior under loads. Since the design strengths of the individual building components contribute to the overall strength limit state of the building, which is important to the safety of the structure, building codes and requirement standards traditionally focus on this aspect. While there are well-accepted dynamic and static design strengths for standard structural silicone sealants arrived at by industry consensus based on past performance of structural glazing façades, currently no widely accepted procedure or framework exists for the derivation of long-term design strengths of novel structural adhesives.

Therefore, this paper attempts to contribute towards such procedure by investigating the specific performance and durability characteristics of the novel structural silicone film adhesive. These results could provide insights into the robustness of the structural silicone tape adhesive for glazing applications and lead to an improved understanding for the design process.

Long-term static load resistance (creep rupture) studies have been used in the past in establishing both the short-term dynamic and the long-term static

maximum design strengths of adhesive systems [32]. While such studies are useful in establishing long-term performance, they do not reflect the wide range of loading rates as experienced by the adhesive in the field when subjected to wind loading and; therefore, are less suitable for establishing short-term dynamic design loads. Furthermore, creep rupture failure tests take the specimens to destruction and the time to failure is affected by micro- or macroscopic defects, such as cracks and voids, in the adhesive layer. A major disadvantage with this approach is the large variation associated with time-to-failure measurements. Therefore, creep rupture tests, especially those carried out to determine short-term design strength, require a large number of specimens and the use of suitable statistics, such as the use of Weibull distributions [33], in order to obtain meaningful information from the scatter of failure times using probabilistic modeling. Using nondestructive tests with a load limit criterion that correlates with the ultimate strength of the joint, as described below; therefore may be a more desirable approach in deriving the dynamic design strength value.

Tensile and Shear Creep Rupture Tests and Static Design Load

Under high steady stresses, materials may undergo time-dependent deformation resulting in failure called creep rupture which limits their lifetime. Structural silicones were first subjected to this type of testing by Sandberg and Rintala [34]. The original testing was done using tensile/adhesion joints (H-piece specimens) that used a block of structural silicone sealant cast between parallel plates that measured 12.5 mm × 12.5 mm × 50.8 mm. These dimensions were in accordance with the dimensions stated in ASTM C1135-00 (2011) Standard Test Method for Determining Tensile Adhesion Properties of Structural Sealants [35]. In the current study, a similar test protocol was used to study the dead load resistance of structural silicone film adhesive bonded between stainless steel buttons and glass substrate.

Specimens for testing the creep resistance of point fixing on glass were prepared by bonding a 20 mm diameter stainless steel “button” with a threaded socket head (see Fig. 3) to a glass plate (cross section of adhesive interface: 314 mm²). The structural silicone film adhesive (1 mm initial and 0.8 mm final thickness) was cured between the button and the glass by placing the complete assembly into an industrial autoclave operated at a pressure of 1.275 MPa and a temperature of 130°C for a total of 25 min.

Creep rupture testing was performed at ambient laboratory climate conditions (23 ± 2°C, 50 ± 5% relative humidity) by loading the stainless steel button fixations in tensile with weights of 20 and 40 kg, corresponding to dead loads of 1.25 and 0.63 MPa, respectively. The specimens exposed to 1.25 MPa load failed, on average, after 7 years, while no failures were observed for the specimens loaded with 0.63 MPa after now more than 11 years (as the time of this writing). Figure 7 shows the tensile loading creep rupture experiments conducted in the laboratory.

A separate experiment was set up to evaluate the behavior of the bonded steel button/glass specimens described above in shear loading by monitoring the time to failure. Again, testing was carried out at ambient laboratory climate.

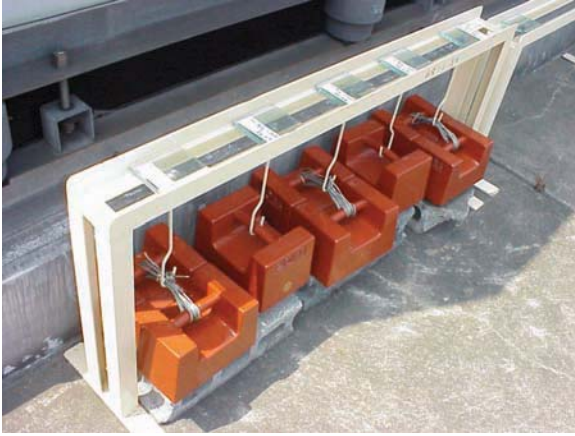


FIG. 7—Tensile loading creep rupture experiments conducted in the laboratory. (Note weights on the left are 20 kg and 40 kg loading a 20 mm diameter steel button in tension, with an adhesive bond area of 314 mm².)

Figure 8 shows the experimental setup and the specimen orientation chosen in order to place the load in perfect shear mode.

When pulled in an extensometer at a rate of 6 mm/min, the five specimens failed cohesively within the TSSA layer at an average maximum shear stress of 4.25 MPa. When loaded with a constant shear load of 3.40 MPa, all five specimens failed within a few seconds. The average time to failure was estimated to be around 1.4 s (future tests will utilize an electric mechanism in order to record the time to failure more exactly). When loaded with a constant shear stress of 2.55 MPa, the five replicates failed between 5 and 6 h, with an estimated average time to failure of about 5.5 h. At a constant shear stress of 1.95 MPa, the five specimens failed within 4 to 24 h, with an estimated average time to failure of about 14 h. The five replicates subjected to a shear load of 1.70 MPa failed after



(a)



(b)

FIG. 8—Experimental setup and specimen configuration for testing time to failure in shear mode.

34, 49, 49, 113, and 126 days. All specimens that failed during the experiment thus far failed in cohesive failure mode within the TSSA layer. As of the time of this writing (190 days after starting the test procedure), no failures have been observed under loads of 1.42, 1.13, 0.85, and 0.57 MPa. Figure 9 shows the average time to failure values obtained at different shear stress levels on a set of five replicate test specimens.

As can be seen from Fig. 9 with the data plotted on a log/log scale, the logarithm of the time-to-failure periods shows an apparent linear relationship to the logarithm of the constant shear stress levels applied in the creep rupture experiment. The linear appearance on a log-log plot corresponds to a power relation of the form

$$\sigma_{\text{creep}} = A \cdot t_{\text{fail}}^B \tag{1}$$

For polymeric materials it has been shown that double logarithmic plots of stress versus failure time often yield straight lines [36]. This allows the use of the power law shown in Eq 1 to fit the data with a least-squares regression line, which minimizes log creep stress errors. Using the average time to failure data, the best fit is obtained with the $A = 2.1611$ and $B = -0.064$, with shear stress expressed in MPa units and time in days. This least square fit is associated with a coefficient of determination R^2 of 0.9269. Using the shortest times to failure experienced at all loads yields a power law fit with $A = 2.0844$ and $B = -0.067$ and a R^2 of 0.8737. Using the longest time to failure seen at all loads thus far into the experiment yields a fit with $A = 2.2059$ and $B = -0.061$ and a R^2 of 0.955. At the failure load observed in the extensometer testing (4.25 MPa), these power laws give time to failure periods between 1.85 and 2.22 s.

Obviously these power laws can also be used to extrapolate future failure events. Given the current, limited amount of data and the uncertainty in the

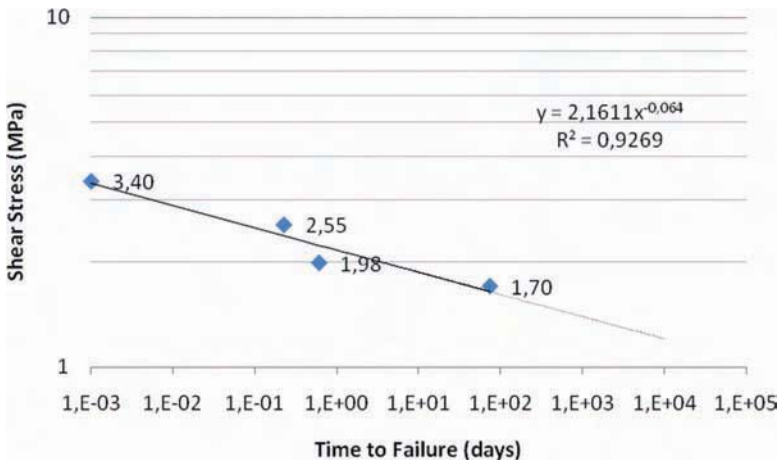


FIG. 9—Average time to failure obtained at different constant shear stress levels on a set of five replicate test specimens.

accuracy of the short time failure periods, such extrapolations are speculative in nature. However, it is still useful to predict the time to failure periods for the next lowest shear load levels that are applied within the current range-finding experiment. Use of the above power law trend curves yields time to failure predictions for the 1.42 MPa shear load of 732 days (average), 318 days (shortest), and 1420 days (longest). If these “ball park” figures are only approximately correct, then a new series of experiments with higher shear loads needs to be designed, as the least square fit to the shortest failure times observed thus far does not yield any failure within a 30 years time period for loads of 1.118 MPa or less. Obviously, such extrapolation of short-term creep rupture data assumes that no change in the creep or degradation mechanism occurs over the predicted service, an assumption that is less likely to hold true the more one tries to extrapolate into the future (for example, the power law extrapolations used above still give a residual strength 10 times greater than the currently accepted dead load design strength value for structural silicone glazing sealants after $>10^{10}$ years exposure duration). However, the concept is still valid; testing at higher sustained loads (approaching the bond's ultimate strength as determined in the extensometer testing) necessarily results in failure after short periods of time, while lower levels of load provide corresponding longer time periods prior to failure. As shown in Fig. 10, such a curve would show, at some level of sustained load, an asymptotic “run-out” behavior, whereby failure does not occur for any reasonably anticipated time duration.

The tensile rupture tests discussed previously provide further corroboration that the above extrapolations may hold true within reasonable timeframes. The failure for the specimens loaded with 1.25 MPa in tensile that actually occurred, on average, after 7 years, is predicted to occur, based on the shear creep rupture test data extrapolations, to occur between 5.7 (minimum) and 30.3 (maximum) years, with an average time to failure predicted of 14.2 years.

As can be seen from Fig. 10, at some point in time, the safety margin between the sustained load curve and the permissible design load becomes constant. This approach is outlined in ASTM D 4680 Test Methods for Establishing Allowable Mechanical Properties of Wood-Bonding Adhesives for Design of Structural Joints [38] and its merits discussed in a review of durability test methods and standards [39]. However, significantly more work will be required (and is planned) to demonstrate such behavior under different accelerated weathering regimes for the TSSA film adhesive.

A further consideration in deriving the dead load design strength of the TSSA material is what happens if the point supported glass pane fails. When glass is supported by point connections, typically no more than two points are required to support the dead weight. Figure 11 shows a drawing of a glass pane with six attachment points noting the top two points are required to support the dead load. Additional connection points will be used to support the live load only. This is due to the reality of construction tolerances. Therefore the weight of a piece of glazing supported by two attachment points will have to be part of the design, and furthermore a single attachment point must support the dead weight of the entire glass panel in the event of a mechanical failure of the hardware or glass defects. Whatever the permissible load is determined to be, it

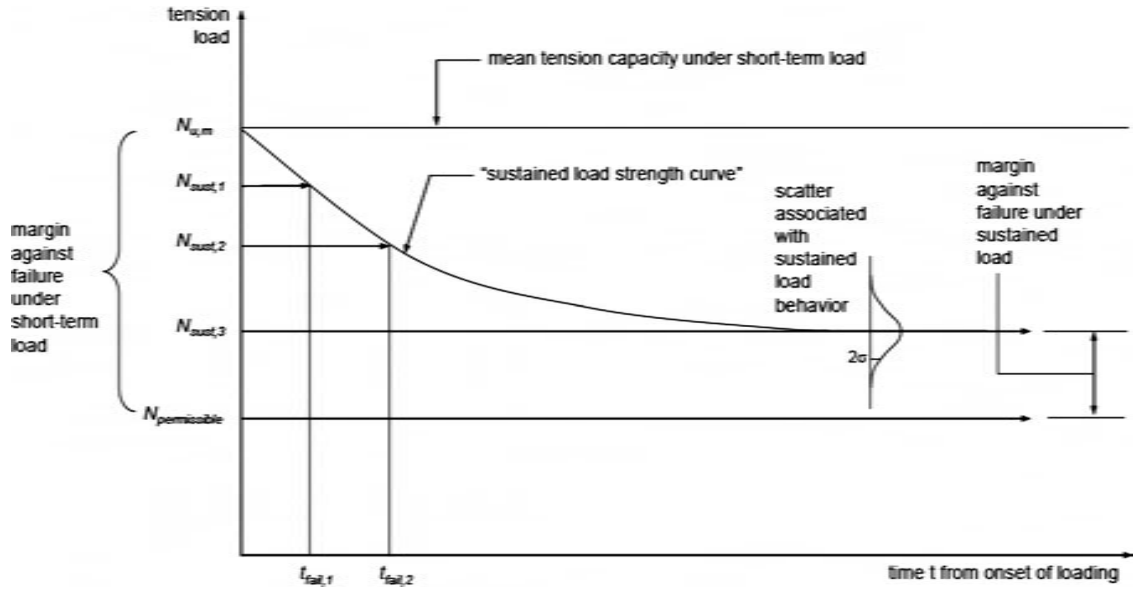


FIG. 10—Concept of sustained load strength curve (reprinted with permission from [36]).

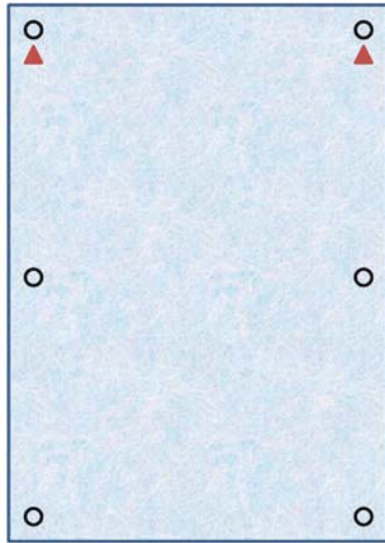


FIG. 11—Schematic of a glass pane with six attachment points noting the top two also take the dead load of the glass.

must provide sufficient short term duration at double its value to allow for the repair and replacement glazing.

For example, if the permissible load is determined to be 0.6 MPa for constant stress, then the adhesive must have integrity at 1.2 MPa to allow for fix and repair. Noting Fig. 6 above, 16 weeks of constant loading in tension at 1.25 MPa demonstrated only a minor change in ultimate strength when pulled to destruction in tension. Shear loading at 1.42 MPa has resulted in no loss of bond after 180 days. Such data applied to the reality of the application give assurance to the determination of the design load. For example, a value of 0.6 MPa can very well be a reasonable dead load design stress for TSSA when the endurance limit is confirmed. On the other hand, if the constant permissible dead load design stress is determined to be 1.0 MPa based on endurance limit validation, the fact that dead load shear at 1.95 MPa resulted in material failure in one day, provides an uncomfortable situation if the adhesive is required to sustain a constant load in the event one attachment point is damaged during the service life. The derivation of the static design strength must consider and reflect the reality of field repair and serviceability.

Furthermore, one must also consider the fact that while a point support is subjected to a constant shear load due to the dead weight of the glazing, a live load due to wind events will subject the adhesive to tension loads normal to the plane of the glazing (out-of-plane loads). The combination of tension and shear loading on specific attachment points needs careful evaluation. Sandberg and Ahlborn [40] confirmed through testing of structural silicone materials that the interaction between nominal tensile and shear forces is elliptical based on the following equation

$$\frac{f_s^2}{F_s^2} + \frac{f_t^2}{F_t^2} = 1 \tag{2}$$

where F_s and F_t are the ultimate strengths in shear and tension, respectively, f_s and f_t are the actual stresses under test. The data that was taken on the structural silicones showed that the ultimate shear stress was roughly equal to the tension stress. This is also the case with the TSSA material presented in this paper.

When combining shear design stress and tension design stress for TSSA, the following equation should apply

$$\frac{f_s^2}{F_{s\ des}^2} + \frac{f_t^2}{F_{t\ des}^2} \leq 1 \tag{3}$$

where f_s and f_t are the actual stresses in dead load shear and live load tension and $F_{s\ des}$ and $F_{t\ des}$ are the permissible design loads in dead load shear and live load tension, respectively. This will ensure that there is enough strength in each attachment point to support both the long term dead weight and live loading without exceeding the permissible stresses on the point.

Cantilever Pull-Off Test and Static Design Load

Cantilever pull-off tests were conducted at ambient ($23 \pm 2^\circ\text{C}$) and at elevated ($82 \pm 2^\circ\text{C}$) temperatures in the laboratory as well as under exposure to outdoor climate using dead loads attached to cantilever beams with the displacement force acting on metal buttons of two different diameters (20 and 50 mm) attached to float glass plates with the TSSA film adhesive (see Fig. 12 for a schematic of the test equipment configuration).

Test specimens were prepared by bonding stainless steel buttons of different diameters with the TSSA (1 mm film thickness prior to compression) to standard (uncoated) float glass coupons in a typical autoclave process used for the production of laminated glass at BGT Bischoff Glastechnik Bretten (Germany). The following procedure was used for the manufacture of the point-fixing specimens:

1. Clean glass and steel surface using dow corning r40 cleaner.
2. Apply Dow Corning® 92-023 primer on both glass and steel surfaces.
3. Remove polyester film cover on one side of the structural silicone film adhesive and place the steel button on the film adhesive.

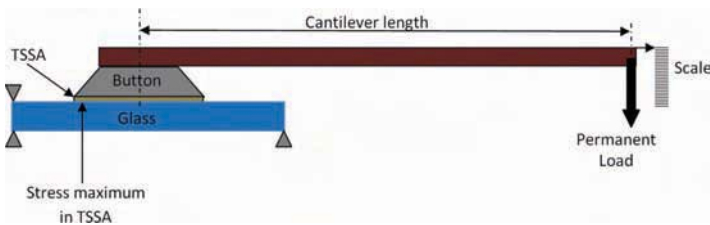


FIG. 12—Schematic of cantilever pull-off test equipment (not to scale).

4. Cut the excess of film adhesive around the button.
5. Remove second polyester cover from the adhesive and place button with the film adhesive face on glass.
6. Using manual load equipment, place pressure of approximately 0.7 MPa on the button for a short period of time (10 s).
7. Place glass vertically with attached buttons in standard autoclave process for laminated glass, run at 13 bar and 140°C for 4 h.
8. Cut glass by water jet to generate individual test specimens.

The above process conditions were chosen primarily based on their suitability to fit into a standard glass lamination process.

In the laboratory, cantilever pull-off tests were conducted at ambient climate ($23 \pm 2^\circ\text{C}$, $50 \pm 5\%$ relative humidity) and at elevated temperature climate ($82 \pm 2^\circ\text{C}$, relative humidity not controlled); in the latter case by placing the whole test apparatus into a forced-convection oven. Test specimens with 50 mm diameter buttons were exposed to two dead loads by placing weights of 55 N for 56 days and 81.3 N for 59 days, respectively, at the free end of a cantilever of 320 mm length. It is estimated that these loads correspond to a maximum stress of 1.17 and 1.68 MPa, respectively, in the structural silicone film adhesive (see calculation method provided in the Appendix). No failure occurred during the test and only reversible, elastic elongation of the film adhesive was observed with a displacement of about 2 mm registered on the ruler scale (having 1 mm graduation which allows readings within 0.5 mm). No differences were observed between tests run at ambient and elevated temperatures.

Test specimens with 20 mm diameter buttons were exposed to two dead loads by placing weights of 3.5 N for 56 days and 5.1 N for 59 days, respectively, at the free end of a cantilever of 222 mm length. It is estimated that these loads correspond to a maximum stress of 0.65 and 1.02 MPa, respectively, in the structural silicone film adhesive. No failure occurred during the test and only reversible, elastic elongation of the film adhesive was observed with a displacement of about 1 mm registered on the ruler scale (having 1 mm graduation which allows readings within 0.5 mm). No differences were observed between tests run at ambient and elevated temperatures.

Only test specimens with 50 mm diameter buttons were exposed simultaneously to outdoor weathering and to a dead load by placing a weight of 80 N at the end of a cantilever of 370 mm length. The test apparatus was installed in southern Germany facing south at an inclination angle of 24° (see Fig. 13). It is estimated that the force of 80 N corresponds to a maximum stress of 1.87 MPa in the structural silicone film adhesive.

The outdoor exposure test was started on 3 Jan. 2011 and no failure has been observed until now (150 days of exposure). Furthermore, no creep has been observed over this period of time beyond the initial elastic response of the specimen (resulting in a displacement of about 1 mm on the gauge).

Stress Whitening and Dynamic Design Load

During the characterization of the TSSA film adhesive it was noted that the material started to whiten when exposed to a certain stress which was significantly



FIG. 13—Cantilever pull-off test equipment used in outdoor exposure in southern Germany.

lower than the ultimate tensile stress. Stress whitening is a well understood phenomenon in thermoplastic materials (see, for instance, literature [41,42]); however, its occurrence in elastomeric materials is rather seldom. In plastic materials stress whitening is generally attributed to a microcracking (crazing). Stress whitening has also been described in elastomer-modified (rubber-toughened) plastics [43,44] where the cause of the whitening has been considered to be cavitation (microvoid formation) between the polymeric network and the elastomeric particles induced by the dilatational deformation. Cavitation and crazing are related: when the density of microvoids increases to a critical value, they expand rapidly together to form craze [45]. The stress whitening observed then results from the grouping of quite tiny but highly concentrated crazes. However, cavitation itself may also cause stress whitening by inducing changes in the refractive index of the material. Information on stress whitening occurring in elastomers is rather limited. Some layered silicate (clay) filled elastomers were shown to display stress whitening when undergoing deformation [46,47]. In these cases, stress whitening was attributed to microvoid formation at the polymer/filler interface. Furthermore, tensile stresses at the interface of poorly aligned tactoids (stacks of parallel clay platelets at about 1 nm separation) were believed to contribute to void formation that was evidenced via stress whitening [46]. Except for the special cases of platelet-filled elastomers, there appears to be a paucity of information on stress whitening of elastomers.

In order to demonstrate the phenomenon and its reproducibility in the structural silicone film adhesive, some of the information obtained on stainless steel button point fixings on glass exposed to various stresses will be discussed below. However, the phenomenon can be observed in any test specimen (tensile dumbbell, single lap shear, bonded buttons, etc.) and independent of the loading state (uniaxial, biaxial, torque, etc.).

Test specimens were prepared by bonding stainless steel buttons of different diameters with the structural silicone film adhesive (1 mm film thickness) to standard (uncoated) float glass coupons in a typical autoclave process used for the production of laminated glass at BGT Bischoff Glastechnik Bretten

(Germany) using the same procedure as described in section Cantilever Pull-Off Test and Static Design Load.

The test specimens (using 20 and 50 mm buttons) were then stored at laboratory room conditions (approximately 23°C and 50% relative humidity) for 2 weeks prior to testing them to destruction at a rate of 6 mm/min in a tensile-test machine using suitable attachments for tensile and shear loadings (see Fig. 14). Some of the test specimens were stored at 90°C for additional 6 h prior to the testing, placed as quickly as possible into the tensile tester, and then tested to destruction without temperature control. Based on separate measurement of cooling rates it is assumed that the average temperature of these specimens during the test was about 80°C.

Figure 15 shows the findings in tensile and in shear loading for the buttons with 50 mm diameter. Note that the zero load displacements are probably due to initial specimen slippage in the extensometer or flexibility (lack of stiffness) within the test specimens. The onset of whitening was visually observed and manually recorded. As can be seen, the onset of whitening occurred, quite reproducibly, at a stress of around 2.0 to 2.5 MPa, regardless whether the specimens were subjected to tensile or shear forces and irrespectively of the test temperature. Excluding the tests where failure of the glass substrate occurred, failure always occurred cohesively within the structural silicone film adhesive at stress levels of >4 MPa.

Figure 16 shows test specimens undergoing tensile testing at the onset of stress whitening and with the whitening fully developed.

The preliminary testing indicates that the stress whitening effect in the structural silicone film adhesive is a response to a consistent stress level, regardless whether the dilation of the specimen was carried out in tensile, shear, or in torque. The whitening was observed to be reversible; under cyclic loads the whitening disappeared when the specimen was unloaded and reappeared when reloaded. Furthermore, the whitening did not appear to propagate until the material was loaded to a higher load state.

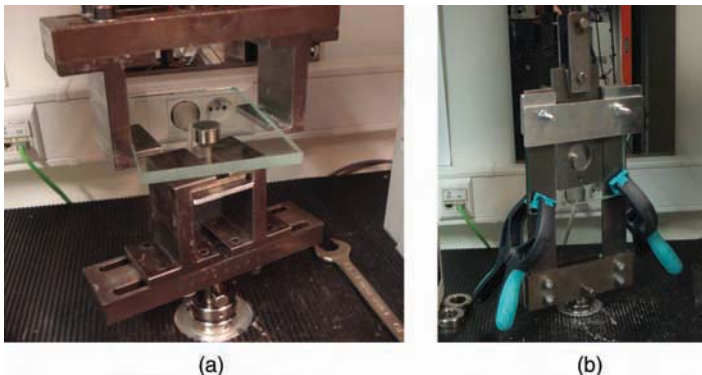


FIG. 14—Test specimens inserted in tensile tester with suitable attachments for tensile and shear loading.

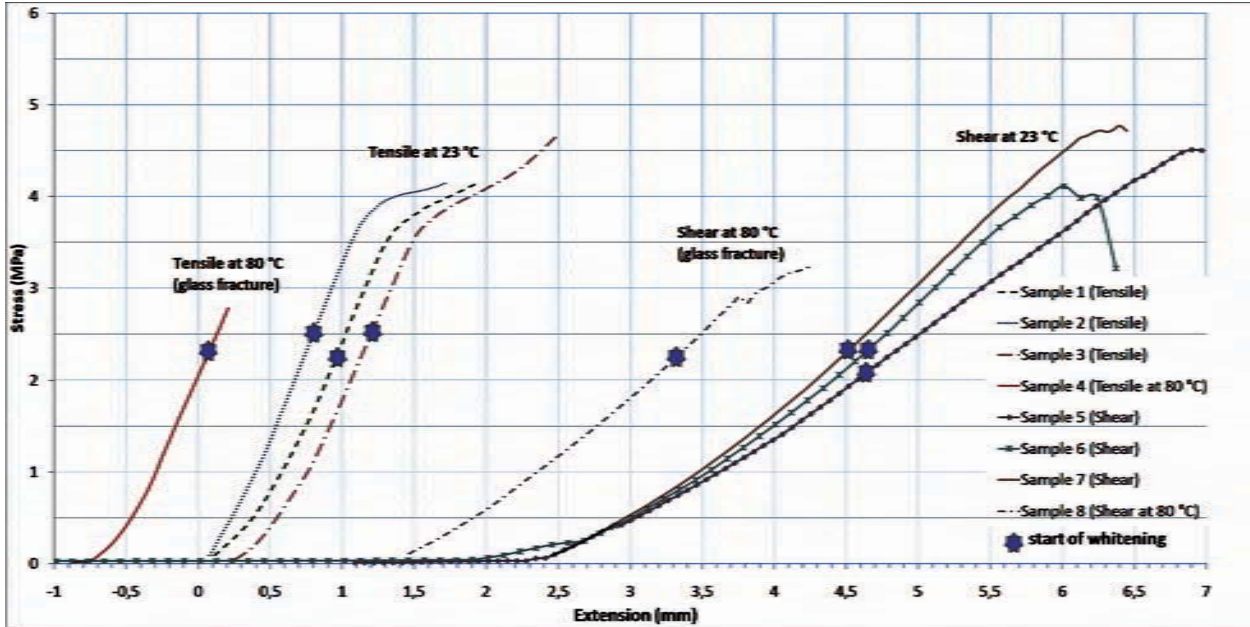


FIG. 15—Stress versus displacement curves in tensile and in shear for bonded steel fixings with 50 mm diameter buttons and 1 mm thick structural silicone film adhesive (extension rate: 6 mm/min).

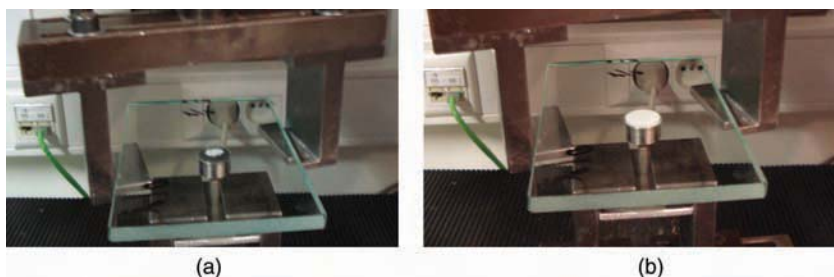


FIG. 16—Development of stress whitening during tensile extension test.

Stress whitening is generally considered to be a proven sign of a material's plastic deformation as it occurs in plastics at the outset of yielding [45]. However, this is certainly not the case for the structural silicone film adhesive, as stress whitening was observed at a much lower value than the maximum stress point. It is hypothesized that the stress whitening in the TSSA is due to cavitation at the polymer/filler interface which is fully reversible. Further studies are currently underway with the intent of characterizing the reversibility of the whitening in more detail (hysteresis). Once the whitening phenomenon and the associated stress level is more fully understood, the authors expect that a safety factor of two can be confidently applied to the stress whitening limit state in order to determine the design load (estimated to be around 1.0–1.3 MPa) for conditions where the material must only resist transient loads, such as wind loads.

Hyperelastic Modeling

The unique capability offered by TSSA to support glass under dynamic and static loads via adhesive anchorage offers clear advantages for the design and aesthetics of the system, but more over it offers a technical advantage by eliminating concentrated stresses at drilled connections. Furthermore drilled connections within an insulating glass unit provide an additional potential path for moisture intrusion affecting the visual and thermal performance of the IG unit. Placements of adhesive anchors at closer intervals reducing the span between supports can allow thinner glass to be used which in turn may affect the dimensioning of the support structure installed behind the glazing. These are the types of scenarios that come about using this new anchorage system that lend themselves to be validated with computer models to aid in optimizing designs. Software to analyze and predict behavior of hyperelastic materials is readily available that allows designers and engineers to understand the behavior of this silicone film adhesive when used in construction systems (see, for instance, [48]). For a comparative discussion of different material models used in the prediction of hyperelastic properties of silicone rubbers, such as Mooney–Rivlin, Yeoh, neo-Hookean, Arruda–Boyce, polynomial, and Ogden laws, see, for instance, various recently published reviews [49–52].

Due to the increased strength and modulus of the TSSA material compared to classic structural silicones, additional applications are readily identified. The engineering community that uses finite element analysis to validate safety of structures prior to mockup testing has great interest in validating the behavior of systems anchored with TSSA.

Evaluation of the mechanical properties by uniaxial tension, planar tension (pure shear), and equal biaxial tension experiments are often used in the characterization of hyperelastic properties of silicone materials (see, for instance, [53–55]). Testing on TSSA was done in accordance with these test protocols to ascertain the material properties under slow cyclical loading with the intent of developing a data set that would satisfy the input requirements of mathematical materials models that are used in existing software for nonlinear finite element analysis once hysteresis effects are removed [54]. TSSA was characterized by these three tests using 1 mm thick film that was cured in an autoclave run in a regular production environment for curing PVB interlayers. The conditions in the autoclave ramped up to 12.4 bar (180 psi) and 135°C (275°F) over a period of 3.5 h. The 1 mm thick TSSA material was cured between polyester films. The testing was specified to pull the specimens five times each at a loading rate of 0.01 strain/s (0.01 mm/mm/s) to an extension of 25, 50, 75, and 100%, respectively, before pulling the test specimen to destruction. The results of these cyclical tests in uniaxial tension, planar tension (pure shear), and equibiaxial tension are shown in Figs. 17–19.

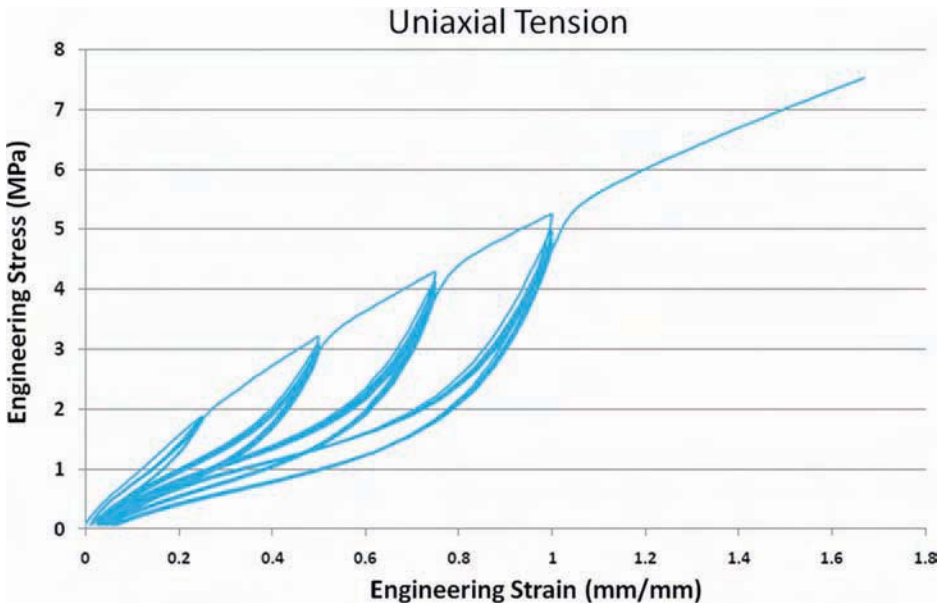


FIG. 17—Results of cyclical uniaxial extension tests (engineering stress versus engineering strain).

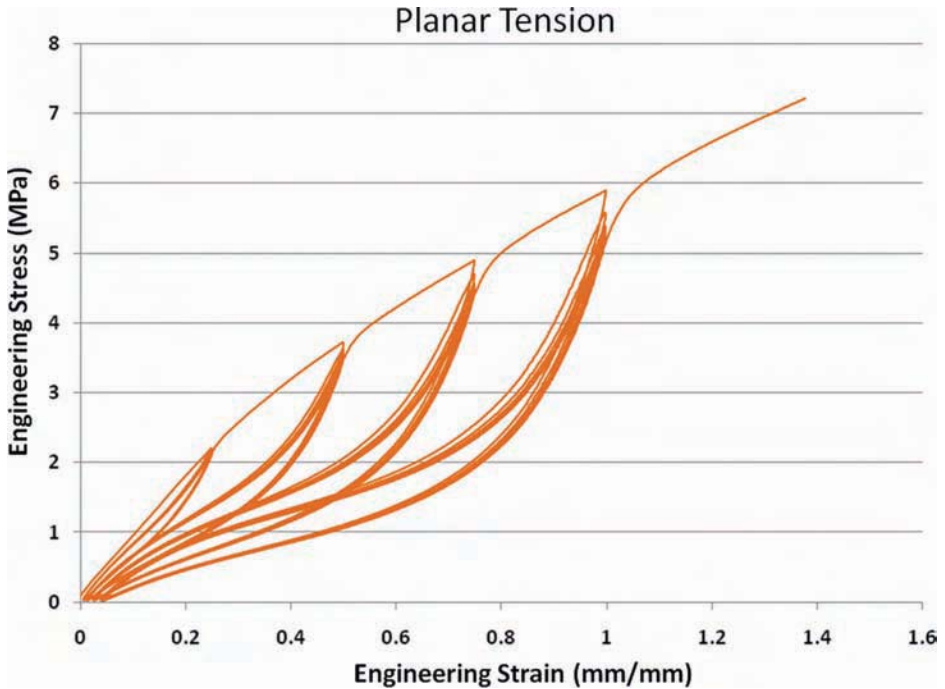


FIG. 18—Results of cyclical planar tension (pure shear) tests (engineering stress versus engineering strain).

The results of the cyclical tests indicate that, as the load is cycled, the shape of the stress-strain curve changes from concave-down to an S-shaped curve. In both cases, the engineering stress-strain curve increases monotonically. The peak stress for each cycle does not change, but the stress at each strain falls until it equalizes at 4–5 cycles. Furthermore, the cyclical tests indicate a failure point in the range of 7.5 MPa. The discrepancy between the failure load observed in the D412-type tests (see Fig. 5) and the failure load observed in the cyclical tests appears to be connected to the rate of loading; the cyclical tests were conducted at a rate of 0.01 strain/s, while the D412-type tests were conducted at a rate of 500 mm/min.

The findings of these three types of tests are further summarized in Fig. 20.

The experimental data were entered into a finite element model based on finite strain theory. Finite strain theory deals with situations where the undeformed and deformed configurations of the continuum are significantly different and a clear distinction has to be made between them. This is commonly the case with elastomers. Elastomers that exhibit high strains in a uniaxial tension test have larger true stresses associated with the finite elements due to the fact that the test specimen cross section is changing with strain.

Therefore, it was acknowledged that the tensile engineering stress (force/original unit area) and strain data would need to be converted to true stress

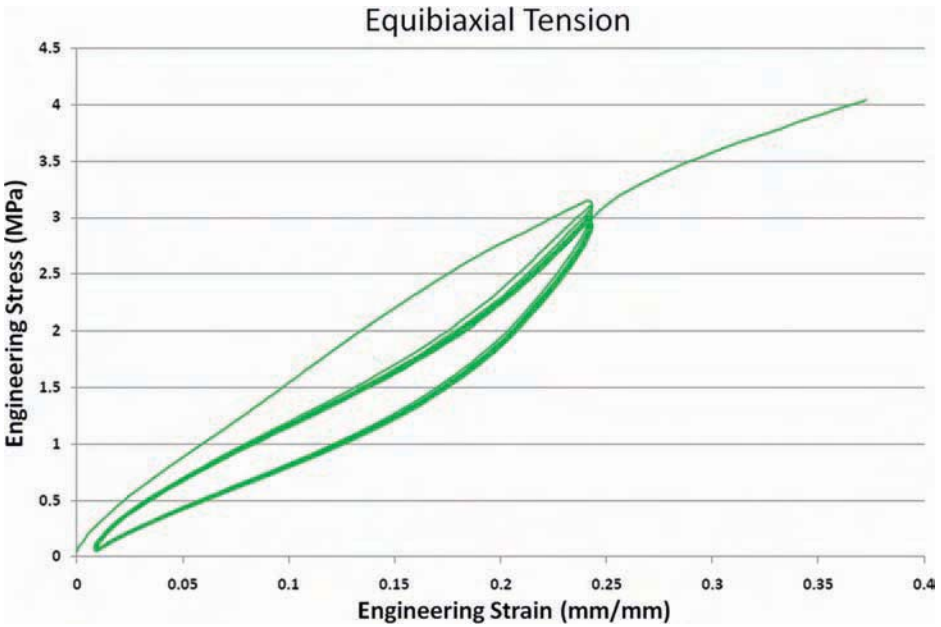


FIG. 19—Results of cyclical equibiaxial tension tests (engineering stress versus engineering strain).

(force/actual unit area) and strain to provide a good comparison between generalized material testing and the results obtained in full-scale mockup of the bonded point fixing system. Without plastic flow occurring (i.e., strain being uniform along the specimen length), the engineering stress and strain can be converted to true stress and strain based on the following equations (assuming incompressibility of the material, i.e., a Poisson ratio of 0.5, which is an excellent approximation for silicone rubbers)

$$\sigma_t = \sigma_e(1 + \epsilon_e) = \sigma_e \lambda \tag{4}$$

$$\epsilon_t = \ln(1 + \epsilon_e) = \ln \lambda \tag{5}$$

with σ_t as true stress, ϵ_t as true strain, σ_e as engineering stress, ϵ_e as engineering strain, and λ as L/L_0 the extension ratio.

Clift et al. [28] converted the data taken for TSSA in uniaxial tension to true stress versus strain by accounting for the changing in element sizes. Figure 21 shows an overlay of the engineering stress versus strain and true stress versus strain graphs as obtained from uniaxial tension testing.

Figure 22 shows the true stress distribution calculated based on finite strain theory in a model of the ASTM D412 type (dumbbell) specimen tested at 8.5 MPa engineering stress. As can be seen, significantly higher maximum true stress values occur in the thin section of the dumbbell than the 8.5 MPa measured, with a maximum true stress of 31.9 MPa calculated.

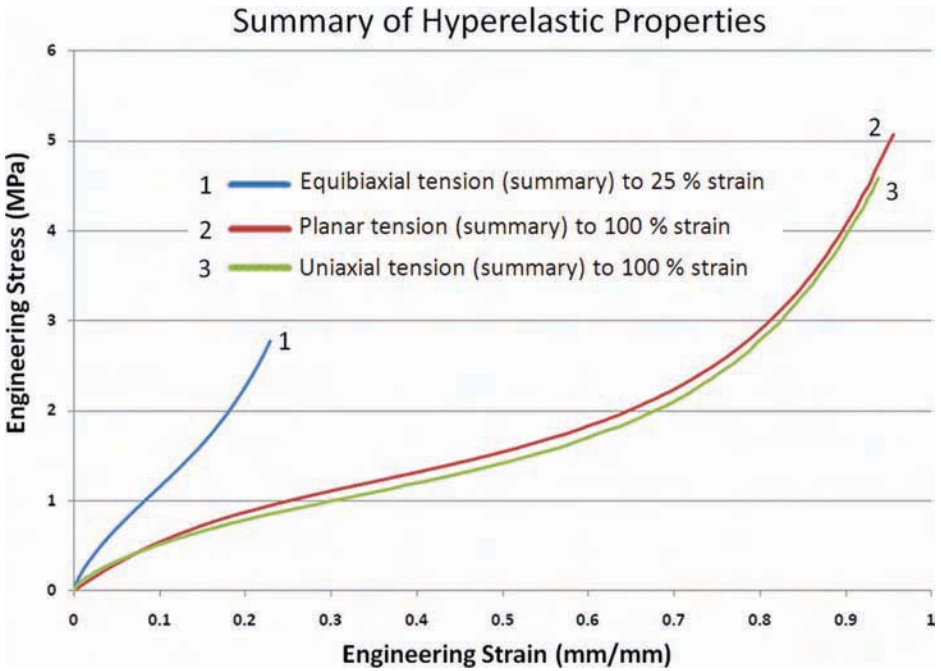


FIG. 20—Summary of equibiaxial, planar tension, and uniaxial tension in hyperelastic material testing (engineering stress versus engineering strain).

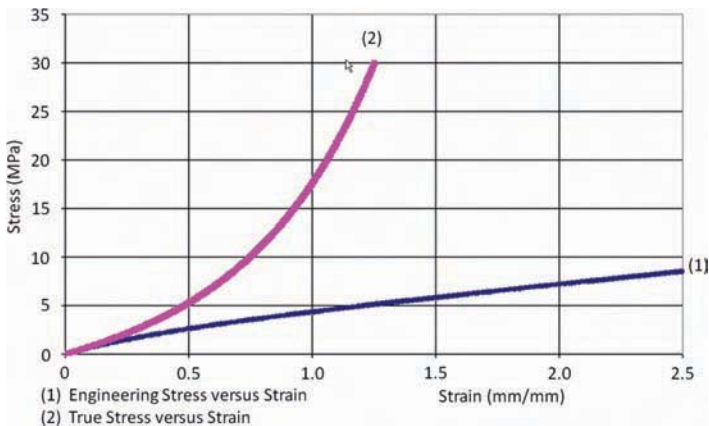


FIG. 21—Overlay of engineering stress versus strain and true stress versus strain graphs as obtained from uniaxial tension testing.

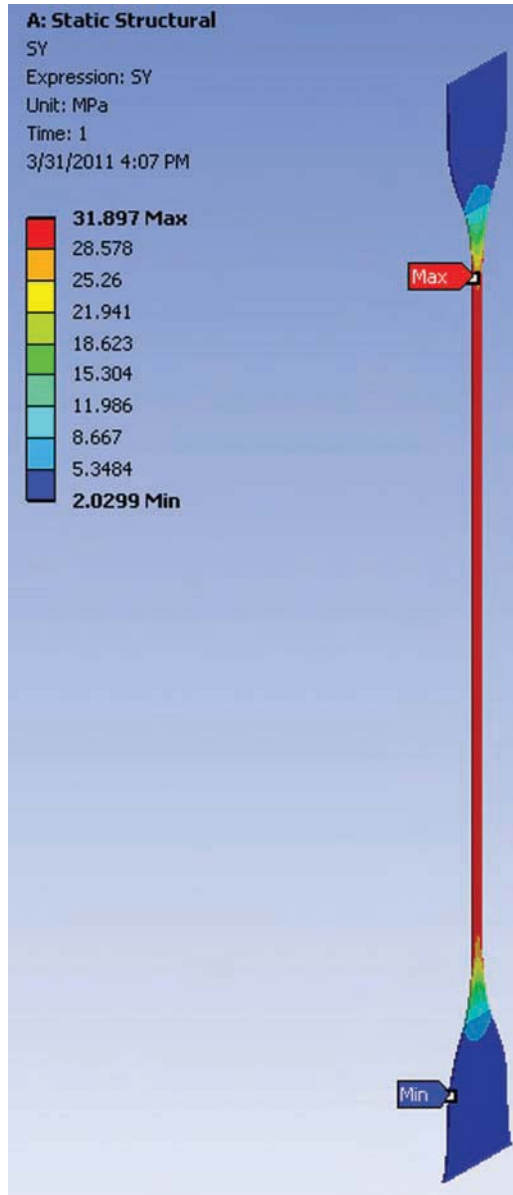


FIG. 22—True stress distribution calculated based on finite strain theory in a model of the ASTM D412 type (dumbbell) specimen tested at 8.5 MPa engineering stress.

Visual observations in a full scale mockup testing of a glass pane held with TSSA bonded point circular supports showed a “crescent moon” shaped stress whitening in the TSSA at certain loads. The whitening was also visible in specimens subjected to destructive pull or to creep rupture tests. Since the stress

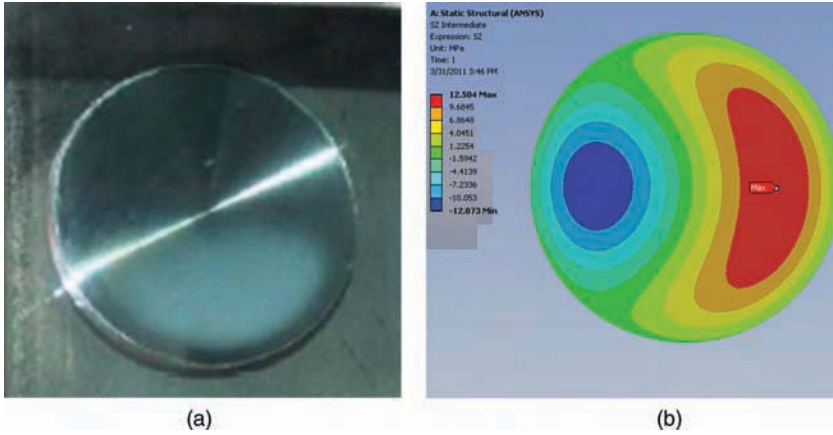


FIG. 23—Stress whitening in actual mockup testing (left) and corresponding calculated stress distribution in TSSA material at whitening load state (note: rotated axis).

whitening appears to be a consistent response to a particular stress state, efforts were made to validate the stress whitening observed in the mockup scenario by using finite element modeling. Figure 23 shows the stress whitening observed in the actual mockup testing as well as the calculated stress distribution in the TSSA material at the whitening load state.

When the mockup was taken to destruction, cohesive failure of the TSSA was observed with a similar crescent moon shaped pattern as observed in the stress whitened bonded point support. Figure 24 shows the cohesive failure pattern in the TSSA at the point support as well as the calculated stress distribution in the TSSA material at failure load state.

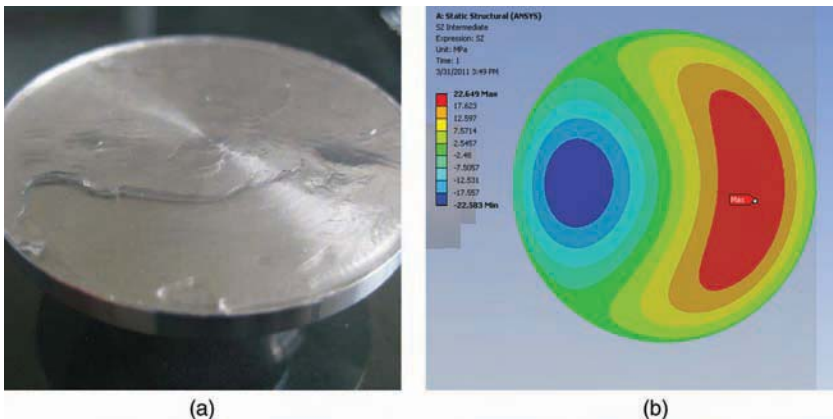


FIG. 24—Cohesive failure pattern and calculated stress distribution in TSSA material at failure load state (note: rotated axis).

Conclusions

The paper reports on the preliminary evaluation of a transparent structural silicone adhesive (TSSA), developed for point fixing in glazing.

The transparent film adhesive is a heat curing one-part material that shows strong bonding to glass, metals, ceramics, and even plastics typically without primer. While this evaluation is preliminary in nature and more detailed and comprehensive evaluations are planned or already underway, the following conclusions can be drawn from the present work:

- The transparent structural silicone (film) adhesive (TSSA) combines high transparency, strong adhesion performance, thermal stability, and excellent weatherability.
- The TSSA has dynamic and static failure strengths substantially beyond what is observed for commercially available structural silicone materials today.
- Current work provides guidance in establishing a more detailed and comprehensive work program aimed at establishing the dynamic and static design strength of TSSA material.
- The stress whitening of the TSSA appears to be a consistent response to a particular stress state and is considered a positive feature, as it may allow derivation of dynamic design strength based on nondestructive testing as well as serve as an indicator of bonding strength in quality assurance testing.
- Hyperelastic modeling of TSSA bonded point supports is suitable for the analysis of the design and the explanation of performance.

Acknowledgment

The writers would like to thank their Japanese colleague, Kazuo Hirai, Dow Corning Toray Company, Ltd., for his contributions in the initial evaluation and the tensile creep rupture tests of the TSSA material.

APPENDIX: STRUCTURAL CIRCULAR POINT CALCULATION

Assuming a structurally bonded point fixing as a flat circular plate bonded with a sealant interlayer of constant thickness to a substrate. Forces might act in a point of the center line with a certain distance to the bonding interface. An additional torsion momentum can be considered around the center axis (as shown in Fig. 25). The sealant is considered to be an ideal elastomer, i.e., to be fully incompressible corresponding to a Poisson ratio of 0.5.

The following nomenclature and units are used for the parameters in the formulas below:

D (mm): diameter of the structural point fixing plate

d (mm): distance of bonding interface from the point, where forces are attacking

E (MPa): elastic modulus (Young's modulus) of the sealant

e (mm): origin thickness of structural sealant layer

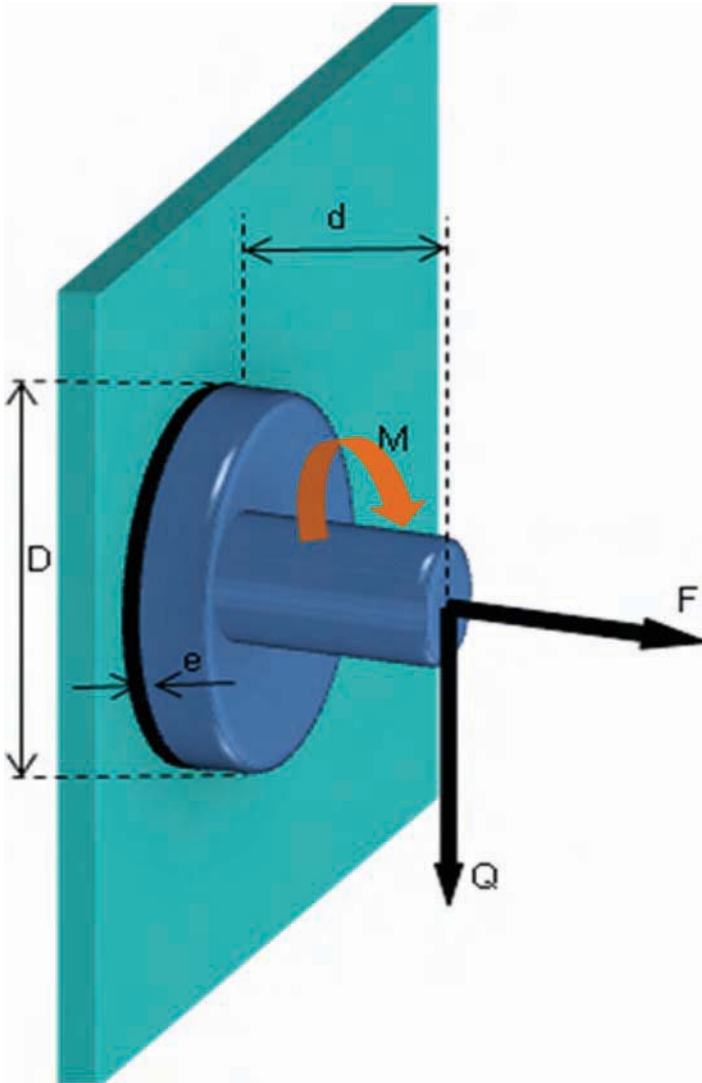


FIG. 25—Forces acting on a bonded circular point fixation.

F (N): tension force acting in normal direction along center axis

G (MPa): shear modulus of the sealant

Q (N): tangential force acting parallel to the bonding interface

M (Nm): torsion momentum around the center axis

r (mm): radius of the structural point fixing plate ($r = D/2$)

t (mm): distance of rotation point form edge

β (rad or deg): angle of inclination

λ (mm/mm): engineering strain ($\lambda = 1 + \Delta e/e$)

Calculation of Sealant Tension Stress and Elongation Caused by Normal Load F Acting on Its Own

The force F acting along the center axis creates a tension stress (engineering stress) in the sealant, which, assuming a homogenous stress distribution, can be expressed as follows:

$$\sigma = \frac{F}{\pi \cdot r^2} \quad (\text{A1})$$

This tension stress results in an elongation of the sealant (increase in sealant thickness), which for the case of the linear stress model can be expressed as follows:

$$\Delta e = \frac{F \cdot e}{E \cdot \pi \cdot r^2} \quad (\text{A2})$$

Calculation of Sealant Shear Stress and Displacement Caused by Tangential Load Q

The force Q acting on a point along the center axis causes shear stress in the sealant, which, assuming a homogenous distribution, can be expressed as follows:

$$\tau = \frac{Q}{\pi \cdot r^2} \quad (\text{A3})$$

The resulting displacement of the structural point in the direction of Q then is given by Eq A4

$$\Delta y = \frac{Q \cdot e}{G \cdot \pi \cdot r^2} \quad (\text{A4})$$

Calculation of Sealant Tension Stress and Elongation Caused by Loads Q and F

Assuming a force Q acting on a point along the center axis with distance d from the bonding interface, the force then causes an inclination of the structural point. The resulting tension stress in the sealant shows a certain stress distribution with a stress and elongation maximum located at one side of the structural point. The following derivation follows assumptions for both linear and nonlinear stress distributions (see Fig. 26).

Achieving a basic momentum balance around the bottom edge of the structural point ($y = 0$) yields the following formula for small inclination angles β

$$M_p = Q \cdot d + F \cdot D/2 = \int_0^D \sigma(y) \cdot b(y) \cdot y \cdot dy \quad (\text{A5})$$

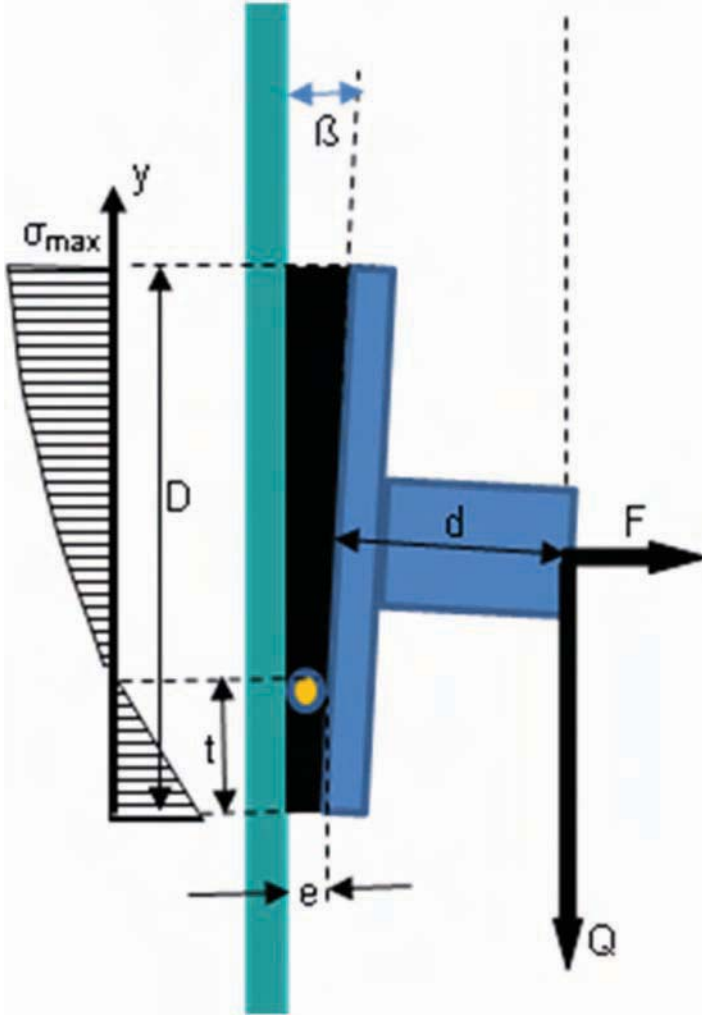


FIG. 26—Nonlinear stress distribution in adhesive layer.

Achieving a basic force balance horizontally provides the following formula

$$F_{\text{tot}} = F = \int_0^D \sigma(y) \cdot b(y) \cdot dy \quad (\text{A6})$$

The local width b of the bonding layer can be calculated based on the circle relation

$$b(y) = 2 \cdot \sqrt{D \cdot y - y^2} \quad (\text{A7})$$

Assuming a linear function for the sealant extension over y provides

$$\lambda(y) = 1 + \Delta e(y)/e = (\lambda_{\max} - \lambda_0) \cdot y/D + \lambda_0 \tag{A8}$$

with λ_0 and λ_{\max} as extension maxima at the lower and upper edge of the structural point.

This also provides a function for the inclination angle β

$$\tan \beta = (\lambda_{\max} - \lambda_0) \cdot e/D \tag{A9}$$

For the following derivation a *linear* distribution for tension stress in the sealant may be used as shown in Eq A10

$$\sigma(y) = E \cdot \frac{\Delta e(y)}{e} = E \cdot (\lambda - 1) \tag{A10}$$

Alternatively, a *nonlinear* stress function (see lit [56].) may be used, as shown in Eq A11

$$\sigma(y) = G \cdot \left(\lambda - \frac{1}{\lambda^2} \right) \tag{A11}$$

Basic momentum and force equations (Eqs A5 and A6) combined with the relationships defined in Eqs A7 and A8 can be solved by numerical integration and iteration and yield λ_0 and λ_{\max} .

The maximum tension stress values are obtained for λ_0 and λ_{\max} by using the linear or nonlinear stress functions (Eqs A10 or A11) above.

The maximum sealant strain in tension and inclination of the structural point are calculated as shown in Eqs A12 and A13

$$\Delta e_{\max} = e \cdot (\lambda_{\max} - 1) \tag{A12}$$

$$\tan \beta = (\lambda_{\max} - \lambda_0) \cdot e/D \tag{A13}$$

The location of the rotational axis is given by Eq A14

$$t/D = \frac{1 - \lambda_0}{\lambda_{\max} - \lambda_0} \quad (\text{for } \lambda_{\max} \neq \lambda_0) \tag{A14}$$

For the simple case of linear stress function and assuming no normal force ($F = 0$) acting on the fixing point, Eq A15 can be derived

$$Q \cdot d = 2 \cdot \sigma_{\max} \cdot \int_0^r y/r \cdot b(y) \cdot y \cdot dy = 4\sigma_{\max} \cdot \int_0^r y^2/r \cdot \sqrt{r^2 - y^2} \cdot dy = 0.7854 \cdot r^3 \cdot \sigma_{\max} \tag{A15}$$

Equation A15 allows a simple approximation of the maximum tension stress as shown in Eq A16

$$\sigma_{\max} = 10.185 \cdot Q \cdot d/D^3 \quad (\text{A16})$$

Calculation of Sealant Shear Stress and Rotation Caused by Torsion Momentum M

Assuming a torsion momentum M acting around the center axis, this causes a shear stress in the sealant and a rotation of the structural point, as shown in Fig. 27.

The nature of the circular geometry and the momentum balance around the center results in the following relationships.

Shear stress as a function of the radius

$$\tau(r) = \frac{r \cdot \alpha \cdot G}{e} \quad (\text{A17})$$

Maximum displacement at the edge

$$dx_{\max} = \frac{D \cdot \alpha}{2} = \frac{\tau_{\max} \cdot e}{G} \quad (\text{A18})$$

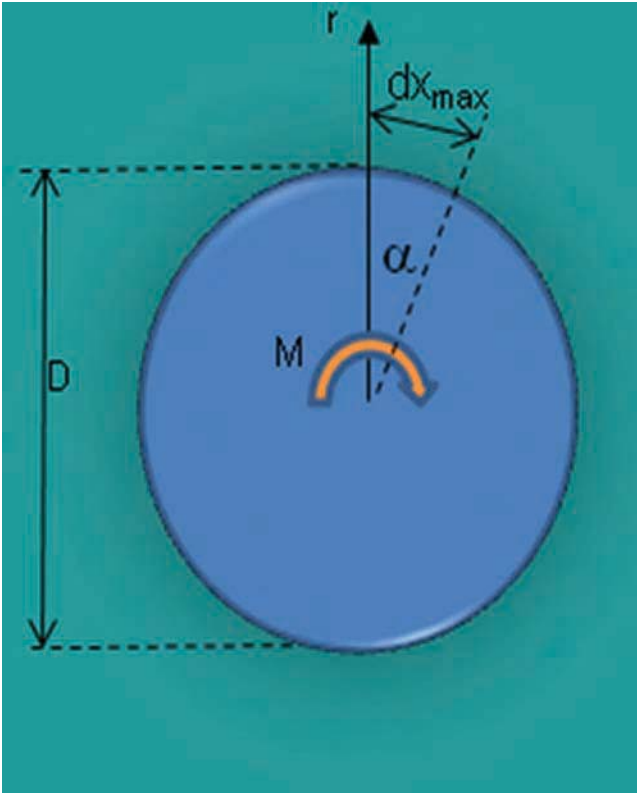


FIG. 27—Torsion momentum acting on point fixing support.

Momentum balance

$$M = \int_0^{D/2} \tau(r) \cdot 2\pi r \cdot r \cdot dr = \int_0^{D/2} 2\pi r^3 \frac{\alpha \cdot G}{e} \cdot dr \quad (\text{A19})$$

Solving the above equations (Eqs A17–A19) results in
Angle of rotation

$$\alpha = \frac{32 \cdot e \cdot M}{\pi \cdot G \cdot D^4} \quad (\text{A20})$$

Maximum shear stress

$$\tau_{\max} = \frac{D \cdot \alpha \cdot G}{2e} = \frac{16 \cdot M}{\pi \cdot D^3} \quad (\text{A21})$$

References

- [1] Siebert, B., "Safety Aspects of Point-Fixed Glass Constructions," *Glass Performance Days*, J. Vitkala, Ed., Glaston Finland Oy, Tampere, Finland, 2007, pp. 432–436.
- [2] Hagl, A., "Punktueller Kleben mit Silikonem," *Stahlbau*, Vol. 77, No. 11, 2008, pp. 791–801.
- [3] ASTM Standard C1048, 2004, "Standard Specification for Heat-Treated Flat Glass—Kind HS, Kind FT Coated and Uncoated Glass," *Annual Book of ASTM Standards*, ASTM International, West Conshohocken, PA.
- [4] Tasche, S., 2007, "Strahlungshärtende Acrylate im Konstruktiven Glasbau, Ph.D. Thesis, Technische Universität," Dresden, Germany.
- [5] Weller, B. and Tasche, S., "Experimental Evaluation of Ultraviolet and Visible Light Curing Acrylates for Use in Glass Structures," *Durability of Building and Construction Sealants and Adhesives, 3rd Volume*, A. T. Wolf, Ed., ASTM International, West Conshohocken, PA, 2010, pp. 135–156.
- [6] Hagl, A., "Bonded Point-Supports: Understanding Today—Optimizing for the Future," *Challenging Glass 2, Conference on Architectural and Structural Applications of Glass*, F. Bos and C. Louter, Eds., Univ. of Technology, Faculty of Architecture, Delft, The Netherlands, 2010.
- [7] Hagl, A., "Silicone Bonded Point Supports—Behaviour Under Cyclic Loading," *Engineered Transparency—International Conference at Glasstec*, Düsseldorf, Germany, J. Schneider and B. Weller, Eds., Technical Univ. of Dresden, Dresden, Germany, 2010, pp. 139–148.
- [8] Anonymous, *VHB Structural Glazing Tape G23F/B23F Technical Datasheet*, 3M Deutschland GmbH, Neuss, Germany, 2007.
- [9] Parise, C. J., *Science and Technology of Glazing Systems, STP1054*, ASTM International, West Conshohocken, PA, 1989.
- [10] ASTM Standard C1401-09a, 2009, "Standard Guide for Structural Sealant Glazing," *Annual Book of ASTM Standards*, ASTM International, West Conshohocken, PA.
- [11] EOTA Recommendation, *ETAG 002 Structural Sealant Glazing Systems, Part 1: Supported and Unsupported Systems*, 1999; *Part 2: Coated Aluminium Systems*, 2002; *Part 3: Thermal Breaks*, 2003, European Organization for Technical Approvals (EOTA), Brussels, Belgium.

- [12] ISO Standard 8339, 2005, *Building Construction - Sealants - Determination of Tensile Properties (Extension to Break)*, International Standardization Organization (ISO), Geneva.
- [13] Wolf, A. T., "Durability of Silicone Sealants," *Durability of Building Sealants - State-of-the-Art Report of RILEM TC 139-DBS*, A. T. Wolf, Ed., RILEM Publications, Bagneux, France, 1999.
- [14] ISO Standard 6502, 1999, *Rubber — Guide to the Use of Curemeters*, International Standardization Organization (ISO), Geneva.
- [15] Wolf, A.T. and Hirai, K., "Evaluation of Transparent Structural Silicone Film Adhesive for Bonded Point-Fixed Glazing," *Engineered Transparency – International Conference at Glasstec, Düsseldorf, Germany*, J. Schneider and B. Weller, Eds., Technical Univ. of Dresden, Dresden, Germany, 2010, pp. 167–177.
- [16] Meloan, C. E., James, R. E., and Saferstein, R., "Refractive Index (RI) of Glass Fragments," *Criminalistics: An Introduction to Forensic Science, Lab Manual*, 6th ed., Prentice-Hall, Upper Saddle River, NJ, 1998, pp. 29–35.
- [17] JIS Standard K 7105, 1981, *Testing Methods for Optical Properties of Plastics*, Japanese Standards Association, Akasaka Minato-ku, Tokyo, Japan.
- [18] JIS Standard Z 8729, 1980, *Specification of Colour of Materials According to the CIE 1976 (L*A*B) Space and the CIE 1976 (L*U*V) Space*, Japanese Standards Association, Akasaka Minato-ku, Tokyo, Japan.
- [19] JIS Standard A 1412-1, 1999, *Test Method For Thermal Resistance And Related Properties Of Thermal Insulations - Guarded Hot Plate Apparatus*, Japanese Standards Association, Akasaka Minato-ku, Tokyo, Japan.
- [20] JIS Standard K 7197, 1991, *Testing Method for Linear Thermal Expansion Coefficient of Plastics by Thermomechanical Analysis*, Japanese Standards Association, Akasaka Minato-ku, Tokyo, Japan.
- [21] ASTM Standard D2369, 2010, "Standard Test Method for Volatile Content of Coatings," *Annual Book of ASTM Standards*, ASTM International, West Conshohocken, PA.
- [22] JIS Standard K 6251, 2004, *Rubber, Vulcanized or Thermoplastic - Determination of Tensile Stress-Strain Properties*, Japanese Standards Association, Akasaka Minato-ku, Tokyo, Japan.
- [23] ISO Standard 527-1, 1993, *Plastics – Determination of Tensile Properties – Part 1: General Principles*, International Standardization Organization (ISO), Geneva.
- [24] ISO Standard 527-2, 1993, *Plastics – Determination of Tensile Properties – Part 2: Test Conditions for Moulding and Extrusion Plastics*, International Standardization Organization (ISO), Geneva.
- [25] JIS Standard K 6253, 2006, *Rubber, Vulcanized or Thermoplastic - Determination of Hardness*, Japanese Standards Association, Akasaka Minato-ku, Tokyo, Japan.
- [26] JIS Standard K 6252, 2007, *Rubber, Vulcanized or Thermoplastic - Determination of Tear Strength*, Japanese Standards Association, Akasaka Minato-ku, Tokyo, Japan.
- [27] ASTM Standard D412-06ae2, 2006, "Standard Test Methods for Vulcanized Rubber and Thermoplastic Elastomers—Tension," *Annual Book of ASTM Standards*, ASTM International, West Conshohocken, PA.
- [28] Clift, C., Hutley, P., and Carbary, L. D., "Transparent Structural Silicone Adhesive," *Glass Performance Days*, J. Vitkala, Ed., Glaston Finland Oy, Tampere, Finland, 2011.
- [29] ASTM Standard G154-06, 2006, "Standard Practice for Operating Fluorescent Light Apparatus for UV Exposure of Nonmetallic Materials," *Annual Book of ASTM Standards*, ASTM International, West Conshohocken, PA.
- [30] ASTM Standard C1184-05, 2005, "Standard Specification for Structural Silicone Sealants," *Annual Book of ASTM Standards*, ASTM International, West Conshohocken, PA.

- [31] EN Standard 15434:2006+A1, 2010, *Glass in Building – Product Standard for Structural and/or Ultra-violet Resistant Sealant (for Use With Structural Sealant Glazing and/or Insulating Glass Units With Exposed Seals)*, European Committee for Standardization (CEN), Brussels, Belgium.
- [32] Townsend, B. W., 2008, "Characterization and Lifetime Performance Modeling of Acrylic Foam Tape for Structural Glazing Applications," M. Sc. Thesis, Virginia Polytechnic Institute and State Univ., Blacksburg, Virginia.
- [33] Little, R. E. and Ekvall, J. C. (Eds.), *Statistical Analysis of Fatigue Data: A Symposium*, ASTM International, West Conshohocken, PA, 1981.
- [34] Sandberg, L. B. and Rintala, A. E., "Resistance of Structural Silicones to Creep Rupture and Fatigue," *Building Sealants: Materials, Properties, and Performance*, ASTM STP 1069, T. F. O'Connor, Ed., ASTM International, West Conshohocken, PA, 1990, pp. 7–21.
- [35] ASTM Standard C1135-00, 2011, "Standard Test Method for Determining Tensile Adhesion Properties of Structural Sealants," *Annual Book of ASTM Standards*, ASTM International, West Conshohocken, PA.
- [36] Lampman, S., *Characterization and Failure Analysis of Plastics*, ASM International, Materials Park, OH, 2003.
- [37] Eligehausen, R. and Silva, J., "The Assessment and Design of Adhesive Anchors in Concrete for Sustained Loading," White Paper, Hilti North America, <http://www.us.hilti.com/data/techlib/docs/technical%20publications/anchoring/hiltiadhesivesustainedloading.pdf>, Jan 2008, viewed May 28, 2011.
- [38] ASTM Standard D5574-94, 2005, "Standard Test Methods for Establishing Allowable Mechanical Properties of Wood-Bonding Adhesives for Design of Structural Joints," *Annual Book of ASTM Standards*, ASTM International, West Conshohocken, PA.
- [39] Broughton, W. R. and Mera, R. D., "Review of Durability Test Methods and Standards for Assessing Long Term Performance of Adhesive Joints," National Physical Laboratory, Teddington, Middlesex, United Kingdom, May 1997, available at: [http://www.adhesivestoolkit.com/Docu-Data/NPLDocuments/P%20A%20J/PAJ%20Reports/PAJ3%20Reports/PAJ3%20Report%201%20CMMT\(A\)61.pdf](http://www.adhesivestoolkit.com/Docu-Data/NPLDocuments/P%20A%20J/PAJ%20Reports/PAJ3%20Reports/PAJ3%20Report%201%20CMMT(A)61.pdf), viewed May 28, 2011.
- [40] Sandberg, L. B. and Ahlborn, T. M., "Combined Stress Behavior of Structural Glazing Joints," *J. Struct. Eng.*, Vol. 15, No. 5, 1989, pp. 1212–1224.
- [41] Bucknall, C. B. and Smith, R. R., "Stress-Whitening in High Impact Polystyrenes," *Polymer*, Vol. 5, 1965, pp. 437–446.
- [42] Kambour, R. P., "A Review of Craze and Fracture in Thermoplastics." *J. Polymer Sci., Macromol. Rev.*, Vol. 7, 1973, pp. 1–154.
- [43] Bucknall, C. B., "The Kinetics of Craze and Shear Yielding in Rubber-Toughened Plastics," *Rubber Chem. Technol.*, Vol. 60, 1987, pp. 35 (<http://dx.doi.org/10.5254/1.3536120>), viewed May 28, 2011.
- [44] Thomas, R., Ding, Y., He, Y., Yang, L., Moldenaers, P., Yang, W., Czigan, T. and Thomas, S., "Miscibility, Morphology, Thermal, and Mechanical Properties of a DGEBA Based Epoxy Resin Toughened with a Liquid Rubber," *Polymer*, Vol. 49, No. 1, 2008, pp. 278–294.
- [45] Kinloch, A. J. and Young, R. J., *Fracture Behavior of Polymers*, Applied Science Publishers, London and New York, 1983.
- [46] Nathani, H., Dasari, A. and Misra, R. D. K., "On the Reduced Susceptibility to Stress Whitening Behavior of Melt Intercalated Polybutene–Clay Nanocomposites During Tensile Straining," *Acta Mater.*, Vol. 52, 2004, pp. 3217–3227.
- [47] Finnigan, B., Casey, P., Cookson, D., Halley, P., Jack, K., Truss, R., and Martin, D., "Impact of Controlled Particle Size Nanofillers on the Mechanical Properties of

- Segmented Polyurethane Nanocomposites,” *Int. J. Nanotechnol.*, Vol. 4, No. 5, 2007, pp. 496–515.
- [48] Anonymous, “Hyperelasticity,” Release 11.0 Documentation for ANSYS, http://www.kxcad.net/ansys/ANSYS/ansyshelp/thy_mat5.html.
- [49] Dorfmann, A. and Muhr, A. (Eds.), *Constitutive Models for Rubber: Proceedings of the First European Conference, Vienna, Austria, 9–10 Sept 1999*, Taylor & Francis, London, United Kingdom, 1999; Besdo, D., Schuster, R. H., and Ihlemann, J. (Eds.), *Constitutive Models for Rubber II: Proceedings of the Second European Conference ECCMR 2001, Hanover, Germany, 10–12 Sept 2001*, Taylor & Francis, London, United Kingdom, 2001; Busfield, J. and Muhr, A. (Eds.), *Constitutive Models for Rubber III: Proceedings of the Third European Conference on Constitutive Models for Rubber, London, UK, 15–17 Sept 2003*, Taylor & Francis, London, United Kingdom, 2002; Austrell, P.-E., and Kari, L. (Eds.), *Constitutive Models for Rubber IV: Proceedings of the Fourth European Conference on Constitutive Models for Rubber, ECCMR 2005, Stockholm, Sweden, 27–29 June 2005*, Taylor & Francis, London, United Kingdom, 2005; Boukamel, A., Laiarinandrasana, L., Méo, S., and Verron, E. (Eds.), *Constitutive Models for Rubber V: Proceedings of the 5th European Conference, Paris, France, 4–7 Sept 2007*, Taylor & Francis, London, United Kingdom, 2007.
- [50] Aidy, A., Hosseini, M., and Sahari, B. B., “A Review of Constitutive Models for Rubber-Like Materials,” *Am. J. Eng. Appl. Sci.*, Vol. 3, No. 1, 2010, pp. 232–239.
- [51] Martins, P. A. L. S., Jorge, R. M. N., and Ferreira, A. J. M., “A Comparative Study of Several Material Models for Prediction of Hyperelastic Properties: Application to Silicone-Rubber and Soft Tissues,” *Strain*, Vol. 42, No. 3, 2006, pp. 135–147.
- [52] Duncan, B. C., Crocker, L. E., and Urquhart, J. M., *Evaluation of Hyperelastic Finite Element Models for Flexible Adhesive Joints*, National Physical Laboratory, Teddington, Middlesex, United Kingdom, 2000, available online at: [http://www.adhesives-toolkit.com/Docu-Data/NPLDocuments/P%20A%20J/PAJex%20Reports/PAJex2/PAJex2%20Report%202%20CMMT\(A\)285.pdf](http://www.adhesives-toolkit.com/Docu-Data/NPLDocuments/P%20A%20J/PAJex%20Reports/PAJex2/PAJex2%20Report%202%20CMMT(A)285.pdf), viewed May 28, 2011.
- [53] Miller, K., *Experimental Loading Conditions Used to Implement Hyperelastic and Plastic Material Models*, Axel Products, Inc., Ann Arbor, MI, USA, available online at: <http://www.mssoftware.com/support/library/conf/auto00/p04500.pdf>, viewed May 28, 2011.
- [54] Miller, K., *Testing Elastomers for Hyperelastic Material Models in Finite Element Analysis*, Axel Products, Inc., Ann Arbor, MI, USA, available online at: <http://www.axelproducts.com/downloads/TestingForHyperelastic.pdf>, viewed May 28, 2011.
- [55] Johlitz, M. and Diebels, S., “Characterisation of a Polymer Using Biaxial Tension Tests. Part I: Hyperelasticity,” *Archive of Applied Mechanics*, published online: DOI: 10.1007/s00419-010-0480-1, available online at: <http://www.springerlink.com/content/e163804m21472606/>, viewed May 28, 2011.
- [56] Treloar, L. R. G., *The Physics of Rubber Elasticity*, 3rd ed. (Reissue), Oxford Univ. Press, Oxford, 2005.

Bernhard Weller¹ and Iris Vogt²

Adhesive Joints in Glass and Solar Engineering

ABSTRACT: The architecture of the past 100 years is characterized by a desire for ever greater transparency. Inevitably, that goes hand in hand with a constantly growing proportion of glass in the building envelope. But owing to the brittle nature of glass, there are only limited options for transferring tried-and-tested methods of jointing—derived from structural steelwork and other engineering disciplines—to this material. However, adhesive joints are much more suited to creating a material bond between glass components. Structural adhesive joints for load bearing glass components have been the subject of research and development work all over Europe in recent years. This article looks at some of that work. The research has led to the development of practical adhesive joints for glass-glass and glass-metal connections. The work includes the study of surface pretreatments and aging scenarios so that types of application for the tensile and shear loads encountered in practice can be specified. Material specimens tested at various load application rates and temperatures enable the material parameters to be determined. A torsion specimen with a glued butt joint is being used to improve the in situ testing of glass-metal connections. There are plenty of potential applications for adhesive joints in structural glazing and solar technology, including the following: Point adhesive joints for overhead glazing and for oversize photovoltaic modules subjected to high environmental loads, linear adhesive joints for hybrid steel-glass composite beams with good ductility and for glass fins with a reduced cross-section in minimized steel-and-glass facades, or full-bond adhesive joints for photovoltaic facades suspended in front of a ventilation cavity and for fully transparent load bearing adhesive joints to an all-glass pavilion (first approved application in Germany).

Manuscript received May 31, 2011; accepted for publication March 6, 2012; published online May 2012.

¹Professor, Dr.-Ing., Institute of Building Construction, Technische Universität Dresden, 01062 Dresden, Germany, e-mail: bernhard.weller@tu-dresden.de

²Senior Researcher, Dr.-Ing., Institute of Building Construction, Technische Universität Dresden, 01062 Dresden, Germany, e-mail: iris.vogt@tu-dresden.de

Cite as: Weller, B. and Vogt, I., "Adhesive Joints in Glass and Solar Engineering," *J. ASTM Intl.*, Vol. 9, No. 5. doi:10.1520/JAI104076.

Copyright © 2012 by ASTM International, 100 Barr Harbor Drive, PO Box C700, West Conshohocken, PA 19428-2959.

KEYWORDS: glass, adhesive, acrylate, hybrid beam, photovoltaic facade, glass fin, glass frame

Gluing—A Method of Jointing Ideal for Glass

Jointing Method According to Physical Principles

When building any structure, various elements and components, often made from different materials, have to be joined together. Jointing or connecting is the designation given to assembling the parts of a structure to form a whole. Safety at the ultimate and serviceability limit states, system requirements, and environmental conditions influence the configuration of joints and connections, and the applicability of the known methods of jointing. A distinction is made between positive connection, nonpositive connection, and material bond depending on the physical principles (Fig. 1).

When at least two components at a joint mate in such a way that their geometry prevents mutual displacement, we speak of a positive or interlocking connection. The forces are transferred perpendicular to the contact face. In many cases a third component, usually a pin or bolt, is necessary to create an interlocking connection between two components. A bolt bearing on the side of its drilled hole is one of the typical types of positive connection used in glass assemblies.

Nonpositive connections are created by applying an additional force generated by a suitable prestress and acting perpendicular to the contact face between the components. The adhesive force thus generated prevents mutual displacement of the components at the joint. A friction joint is an example of a nonpositive connection. It is frequently the case that more than one principle applies at a joint. For example, individual clamp fixings for glazing transfer forces in the direction of the plane of the glass through friction, i.e., a nonpositive connection. But for forces acting perpendicular to the plane of the glass, the clamp fixing encloses the edge of the glass and, hence, forms a positive connection.

A material bond is generated by atomic or molecular forces that hold the components together at the joint. Normally, such connections are not detachable and the parts can only be separated by destroying the joint. Welding, for instance, is a material bond between two identical materials. However, not every material can be joined in this way. High process temperatures may damage, even destroy, the material. Adhesive joints; on the other hand, are more universal because they can connect both identical and disparate materials.

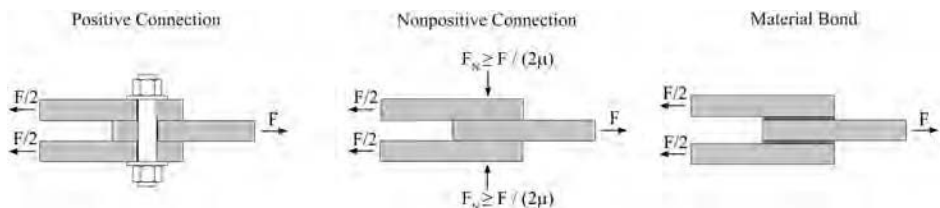


FIG. 1—Classification of jointing methods according to the physical principle for transferring the forces.

Connections for Glass Components

Apart from adhesives [1], there are two other methods of jointing that are suitable for glass: friction connections and bolts in bearing. A pin or bolt bearing on the side of a drilled hole has established itself as a form of connection for glass as well as steel and timber because the final assembly on the building site is very simple [2]. Furthermore, such connections can be detached again at any time. Nevertheless, in glass, concentrations of stress occur in the vicinity of the drilled hole, caused by a local, limited load transfer and the weakening of the cross-section (Fig. 2, left). As in a brittle material, such as glass, stress concentrations cannot be redistributed or dissipated locally through plastic deformation, the origin of the failure of a pane of glass due to an overload can often be found in the region of drilled holes [3].

Friction connections—in the form of a nonpositive jointing method for glass—have been used in unique projects, e.g., in the Glasgow Wolfson Medical Building, where the viscoplastic interlayer of casting resin is replaced by plates made from soft aluminum alloys at the point of application of the load [4]. Generally, such connections have little relevance in practice because their usage is essentially restricted to toughened safety glass owing to the creep of the polyvinyl butyral (PVB) film used in laminated safety glass [5]. Adhesive joints; on the other hand, enable the creation of a planar joint and, hence, a uniform stress transfer between the components. Local stress peaks can be minimized through the thickness of the layer of adhesive and its elasticity (Fig. 2, right). The components at the joint are not weakened by drilled holes or cut-outs.

State of the Art

Adhesives have long since been used successfully for load bearing connections in steel, timber, polymer, and railroad track construction. In structural glazing, adhesive joints have been considered for certain projects. Early applications using transparent adhesives are described in [6–8] for example. The glass beams with their glued corner joints at Broadfield House Glass Museum in Kingswinford (UK) can be regarded as a milestone in load bearing adhesive design [9];

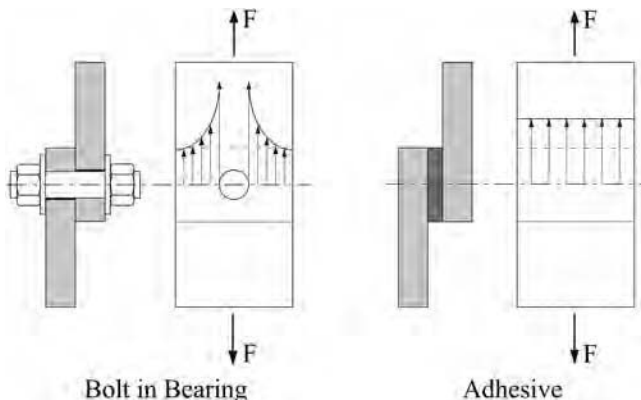


FIG. 2—Stress distribution principles at bolted and glued connections in single shear.

15 years after being erected, the adhesive joints of this structure are still showing no signs of any deterioration [10]. Another example of the successful use of adhesives in structural glazing is the Glass Cube in Harlem (Netherlands) [11]. Samples exposed to the weather for many years were used by Blandini [12] to investigate the use of adhesives in frameless glass shells. An ionomer interlayer that has become established in recent years has positive material properties that have resulted in numerous innovations in structural glazing [13,14].

If we are to improve durability, then special attention must be paid to the cleaning and pretreatment of the surfaces of the components to be joined together. The results of numerous studies of these aspects show that removing organic contamination with atmospheric plasma can increase the surface energy and therefore achieve permanent adhesive forces [15,16].

Numerous tests have been carried out on small-scale specimens and sample components in order to increase the popularity of adhesives for glass-glass and glass-metal connections. Besides looking for suitable geometries and adhesives [17], the selected connections are subjected to aging scenarios and different loads. For example, the buckling behavior of panes of glass glued to a substructure is investigated [18]. One promising area of application for the future is to be found in so-called hybrid beams [19–21]. In such beams, the brittleness of the glass is compensated for by combining the glass with a ductile material.

Structural Sealant Glazing

The state of the art for glued glass applications in Germany is currently structural sealant glazing (SSG) [22]. In such systems, the glazing is connected to metal load bearing frames or adapter sections via linear adhesive joints. Stainless steel or anodized or coated aluminum can be used as the material for the supporting members. Such glued glazing arrangements are classified as supported or unsupported systems, depending on the way in which the load of the glass itself is carried. Supported SSG systems include setting blocks that ensure that the self-weight of the glazing is transferred directly to the supporting frame and from there to the load bearing structure. All other loads, which are generally of only brief duration, e.g., wind, are carried by the adhesive joints. In contrast to this, in an unsupported SSG system, all permanent loads are carried by the adhesive.

SSG systems can be further classified according to any retaining systems that may be necessary, which in the event of failure of the adhesive joints prevent the glass from slipping out of its frame. Metal brackets or clamps, undercut anchors, and wire retainers are examples of suitable retaining systems. This classification results in four types, the usage of which may be restricted depending on national stipulations (Fig. 3). Building legislation restrictions in Germany mean that apart from a few exceptions, the only systems possible are those in which no permanent loads are carried via the adhesive joints (type I and II) and those above a mounting height of 8 m that include mechanical retainers as a backup, should the adhesive fail (type I).

European guideline ETAG 002 [23–25] describes the principles of the construction, the materials to be used, and the experimental testing required if

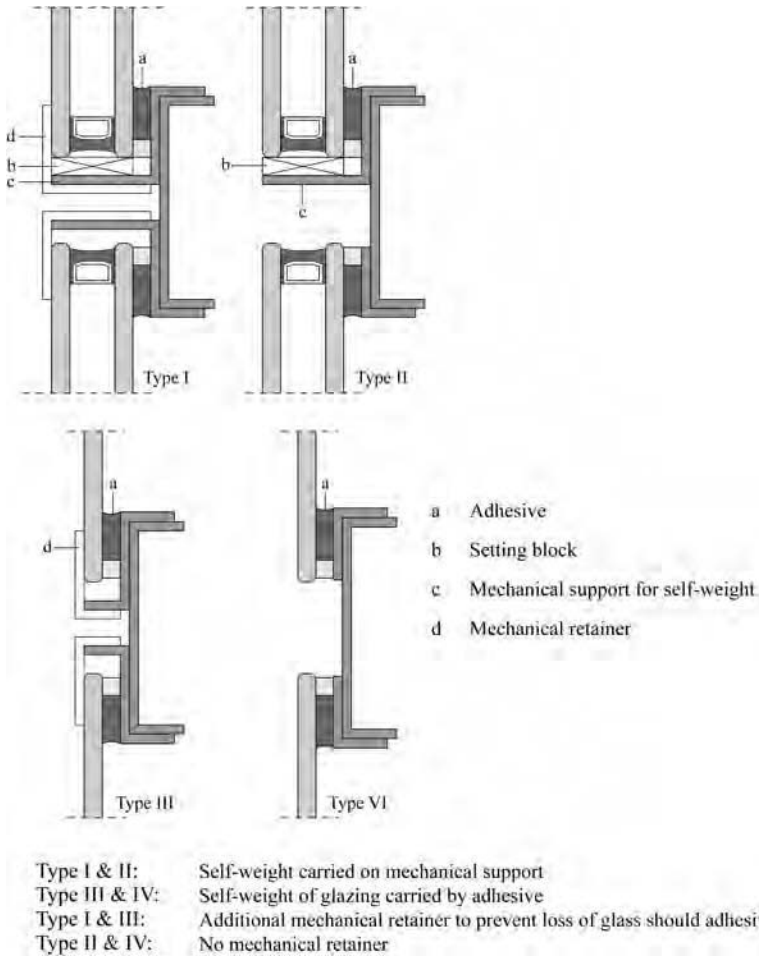


FIG. 3—Classification of structural sealant glazing systems according to ETAG 002.

approval for a glued facade design is to be applied for. According to the guideline, the choice of adhesives is restricted to silicones—adhesives for which test results and long-term experience are available and accepted by the building authorities. Silicone adhesives exhibit excellent adhesion on glass surfaces and are highly resistant to environmental influences. However, their low stiffness, low strength, and black coloring are regarded as disadvantages. Adhesive joints for SSG systems are normally produced under controlled ambient conditions during the further treatment of the glass or at the facade fabricator’s plant. In certain cases silicones are also used for in situ adhesive joints produced on site. However, the method then no longer complies with the stipulations of ETAG 002, which means that the work must be approved by the building authority responsible. Very careful workmanship and comprehensive quality control measures are essential for in situ adhesive joints produced on the building site.

Innovations Through Adhesives

It is primarily innovative projects and visionary design studies and prototypes that extend the range of construction beyond those described so far and those forms regulated by legislation in Germany. In particular, transparent or high-modulus adhesives open up new types of applications for glued glass joints. One example of a further development is the glass hybrid component (Fig. 4). Linear joints between glass and ductile materials increase the load bearing and residual load bearing behavior of glass. Potential combinations with steel, aluminum, timber, and glass fiber-reinforced plastics (GFRP), even reinforced concrete, have already been investigated in a number of research projects [26–29]. Glass-metal [28] and glass-timber composite cross-sections represent interesting approaches and the first transfer projects, based on research and leading to practical applications [28,29]. Linear adhesive joints have already been used for connecting panes of glass to delicate aluminum frames for transparent partition systems for interior use.

Likewise, adhesive point fixings have already been used in facades in a few isolated cases. Penetrating or clamping the glass is therefore avoided and the glass surface takes on a very homogeneous appearance. Another advantage of adhesive point fixings is that stress peaks can be reduced. As a rule, these systems require additional components for carrying the self-weight of the glass and for retaining the glazing should an adhesive joint fail. One special development for a bonded glass retention system is therefore based on a combination of countersunk drilled holes, which do not penetrate the glass, and point fixings fitted into these [30].

In addition, several glass elements can be joined together to form more complex load bearing structures. In order to be able to omit all metal connectors and fixings in such a situation, transparent adhesives can be used for planar adhesive joints (Fig. 5). Such a design—an all-glass pavilion supported by



FIG. 4—Design studies at *glasstec 2010* in Düsseldorf, Germany: Sample facade made from a hybrid glass-steel assembly.



FIG. 5—Design studies at *glasstec 2010* in Düsseldorf, Germany: transparent bonded glass frame corners.

bonded glass frames—was erected for the first time in Germany in 2009 within the scope of an Individual Approval [31].³

Adhesives for Structural Applications

Fundamental Material Properties

Most of the adhesives belong to the group of organic polymer compounds. The polymerization, polycondensation, and polyaddition produce molecular structures that through their configuration have a major impact on the properties of a layer of adhesive. The most important factors that influence the final properties are the chemical structure of the monomers, the reactions that take place in order to create the polymers, and the resulting structure of the adhesive. Adhesives are very similar to plastics in terms of their chemical structures and material properties. Consequently, they frequently exhibit a material behavior dependent on duration and temperature. Their heat resistance and durability are generally inferior to those of metals. Environmental influences can damage the adhesive and the boundary layers between the components, and thus can reduce the strength of a joint.

Of all those adhesive systems conceivable and commercially available, a few systems have proved to be particularly suitable for glass applications in buildings owing to their chemical, physical and mechanical properties. These include UV- and light-curing adhesives, epoxy resin, and polyurethane adhesives, as well as silicones. The material behavior of these adhesives varies considerably, ranging from high-strength adhesives with low elongation at failure to highly deformable elastic adhesives that have only a low tensile shear strength (Fig. 6).

³Projects with bonded glass frames have been erected before by Tim McFarlane [6] [9]. Nevertheless, this concept was not pursued.

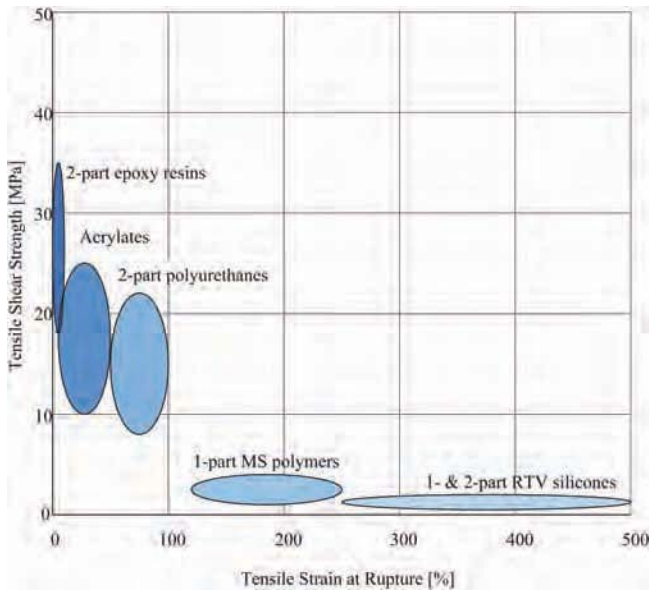


FIG. 6—A comparison of the mechanical properties of various adhesives used for glass applications in building.

According to their material properties, epoxy resin adhesives are thermosets. These products exhibit high strengths but at the same time only very low elongation at failure [32]. Especially important among the UV- and/or light-curing adhesives are various acrylates and methacrylates. Most of them are classed as thermoplastics and are characterized by their high strengths and comparatively low elongation at failure [33]. Adhesives based on polyurethane include a wide range of materials. Reactive two-part polyurethanes represent the type most often used for glass in building. This group of adhesives includes both thermosets and elastomers. Their strengths are similar to those of acrylates, although much greater elongations are possible [33]. Chemically, MS polymers are very similar to polyurethanes. On the other hand, their curing behavior is similar to the silicones. And in terms of strength and elongation at failure, they fill the gap between polyurethanes and silicones [34,35].

Owing to their chemical structure, silicones are fundamentally different from the other organic, polymer adhesives. In contrast to these systems formed by chains of carbon atoms, in the silicones it is silicon-oxygen compounds that form the elements linking the molecules. The cross-linking at room temperature to form a high-molecular polymer (room temperature vulcanizing, RTV) for the adhesive and sealing systems used for glass in building applications takes place either through the action of the moisture in the air (1-part) or through the addition of a hardener (2-part). The adhesives obtained in this way are classed as elastomers and exhibit very low strengths with extremely high elongation at failure [33].

Specification

The selection criteria for an adhesive should take into account the special characteristics of the materials to be joined, the properties of the surfaces at the joint, the strength requirements, the environmental influences to be expected, the weather and temperature fluctuations, the presence of chemicals, the constructional design of the adhesive joint, and the types of loads. In addition, the process of forming the adhesive joint should also be considered at this early stage. Important criteria here are the working time and the way the adhesive is measured out and applied.

The mechanical and thermal properties adequate for the respective application must be clearly defined. Furthermore, an evaluation of the adhesives with respect to their tendency to creep and their relaxation behavior under permanent loading is necessary so that their suitability for systems carrying self-weight can be determined. Beside these important, measurable factors, there are also other aspects to be considered, e.g., appearance and aesthetics. The main assessment criteria for adhesive joints for structural glass and facades include:

- Adequate strength
- Durability (UV, salt-laden and acidic atmospheres, moisture, cleaning agents)
- High stiffness for point fixings
- High elasticity for linear or planar joints between materials with different coefficients of thermal expansion
- Reduced tendency to creep
- Service temperatures from -20°C to $+80^{\circ}\text{C}$
- Transparency in the case of visible joints

Owing to the large range of adhesives, it is almost always possible to find a suitable adhesive system for the respective application. The quality of the material, the properties, and the internal strength of an adhesive normally vary only minimally across different batches and can be well controlled by the manufacturer. This makes it all the more important to provide a good, reproducible surface quality that enables adequate, good adhesion between adhesive and substrate.

Determining the Parameters of Adhesives

Methods for Determining the Parameters

Describing an adhesive material by way of comprehensive parameters is the foundation for realistic results in the calculation of glued forms of construction. The scope of the determination of the parameters depends on the material to be described and the mechanical modeling. Two experimental options for determining parameters have proved worthwhile for the phenomenological description of the material: studies of material specimens and in situ specimens. The material specimens consist merely of pure adhesive material. Parameters specific to the material, e.g., elastic modulus and Poisson's ratio, can be determined with the help of such specimens. The in situ specimens consist of the components that are joined together by the adhesive [36–38].

Uniaxial Tensile Test

ISO 527-1 [39] describes the procedure for determining the tensile properties of plastics by means of material specimens (Fig. 7). These are stretched along their longest principal axis at a constant rate until failure occurs or until the stress or strain has reached a predetermined value. Load and deformation are recorded during the test. So-called dumbbell specimens are preferred for this test: the wider ends of these specimens ensure that they are properly clamped in the testing machine, and the transition between the wide and narrow parts of the specimen ensures that the force introduced is concentrated in the narrow central section; thus generating a uniform stress distribution. Different types of dumbbell specimens are recommended depending on the material to be investigated and the manufacturing process. The standard form is type 1 according to ISO 527-2 [40].

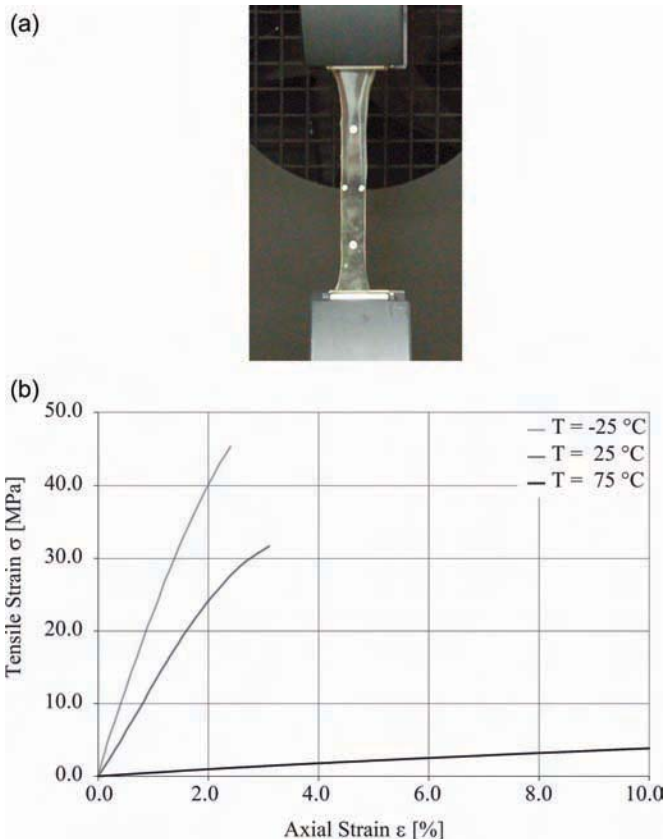


FIG. 7—Dumbbell specimen in the testing machine (left). Stress-strain diagram for a 2-part epoxy resin adhesive at different testing temperatures (right).

Torsion Test

In order to achieve a state of stress that is as uniform as possible, in situ specimens are prepared according to DIN EN 14869-1 [41] from butt-bonded hollow cylinders with a complete ring of adhesive (Fig. 8). Two cylinders made from the relevant material are connected with the adhesive to be investigated and subsequently subjected to torsion or tension. This means the details of the tensile stress-strain relationship and the shear stress-shear strain relationship are possible with a single specimen geometry. Combinations of loading are also possible. This type of specimen was further developed for glass-metal joints within the scope of the work by Vogt [37].

Test Method with Butt-Jointed Specimens

In the course of research work concerning glass-metal joints, Tasche [42] developed specimens that allow the tensile and shear strengths of thin adhesive joints

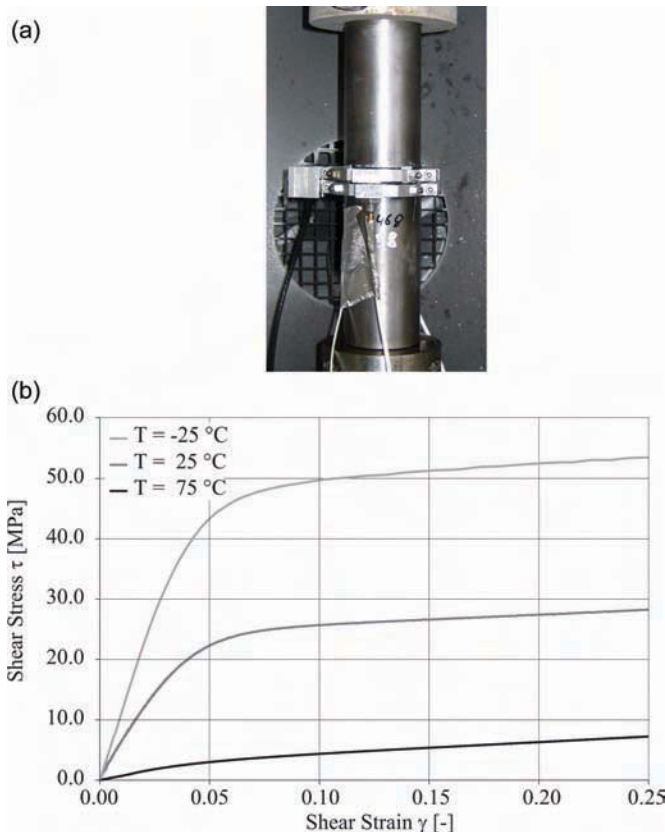


FIG. 8—Butt-bonded hollow cylinder in the testing machine (left). Shear stress-shear strain diagram for a 2-part epoxy resin adhesive at different testing temperatures (right).

to be determined using small-scale in situ specimens. These specimens allow an adhesive joint with the brittle material glass to be loaded in tension or shear. They enable the adhesive layer within the composite construction to be investigated and therefore take into account the influences of the materials being connected. Furthermore, tests on these specimens allow statements to be made regarding the mechanical behavior of the joint. For instance, in order to evaluate the adhesive behavior of various adhesives for bonded fittings, tensile tests were carried out on these specimens. The determination of the adhesive behavior was carried out at different temperatures. As the temperature rises, so the strength of the adhesive joint decreases for all the adhesives investigated (Fig. 9). Embrittlement is frequently apparent at low temperatures.

In many cases the adhesion depends on the surface of the annealed glass to which the adhesive is applied. Owing to the production process, the surface characteristics of the tin and air sides are different. The influences of both sides of the annealed glass on the adhesive behavior were therefore investigated. However, it is not possible to derive a generally applicable statement for all the adhesives investigated.

Glass in Building

Structural Adhesive Joints with UV- and Light-Curing Acrylates

Adhesive joints can be designed with different forms: point, linear or planar. In structural glass designs, load bearing adhesive joints have so far been mainly

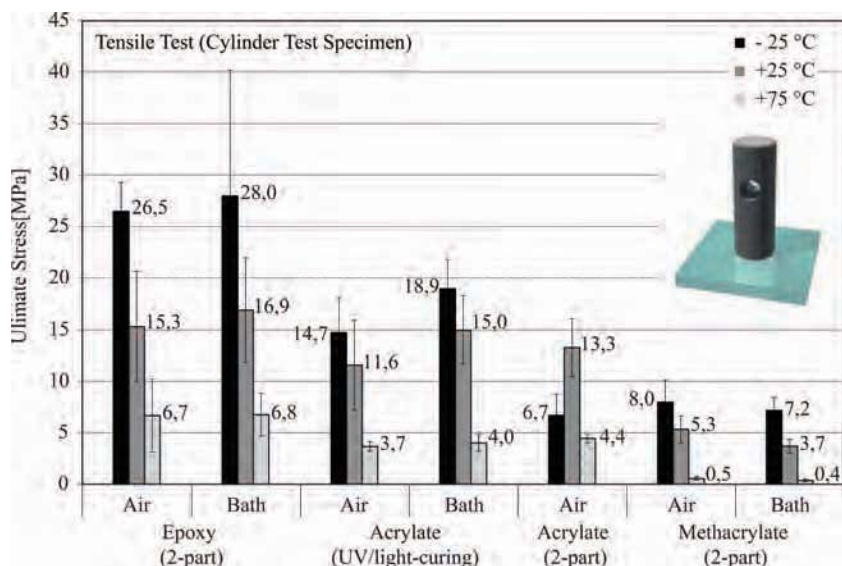


FIG. 9—Adhesive strengths (cylinder tensile test) for various adhesives and different testing temperatures.

planar or linear [43]. The planar joints include the laminating of panes of glass to form laminated or laminated safety glass. The linear joints, beside the edge seals around insulating glass units, include structural sealant glazing (SSG) systems according to ETAG 002-1 [23].

Load bearing point adhesive joints with transparent adhesives are being investigated in order to increase the benefits of using glass in buildings. The UV- and light-curing acrylates are particularly interesting because in contrast to silicone adhesives they exhibit much higher initial strengths although applied in much thinner layers. The adhesives investigated are completely transparent and hardly visible to the naked eye. Curing is carried out with a special lamp, preferably using ultraviolet radiation. The adhesive is fully cured after exposure to the radiation for a length of time ranging from a few seconds to a few minutes, and the joint can be loaded immediately. The aging resistance of acrylate adhesives has been investigated and described in detail in Ref. [44].

Verification of load bearing and residual load bearing capacities has also been carried out on bonded component models, also punctually bonded glass panes in the form of a canopy system stored outdoors in order to be able to assess durability under natural weathering conditions [37,42]. The panes of glass were stored either suspended from above or supported from below depending on the options presented by the system (Fig. 10). Visual inspections of the adhesive joints were carried out at regular intervals to see if any changes had taken place. After a period of three years outdoors, various changes are visible: the volume of small air bubbles, caused by the manual method of producing the joint, increased at some points. In the case of the overhead glazing supported from below, restraint stresses were detected in the adhesive joint due to the extremely stiff construction of the components, and this had led to delamination. On the basis of this experience, a structural determinate system is recommended which supports without restraint in the plane of the glass pane.



FIG. 10—Outdoor overhead glazing test: in the foreground the suspended pane, in the background the supported pane.

Hybrid Facade

Conventional post-and-rail designs for facades are generally carried out with the opaque materials steel or aluminum. However, such systems do not fit in well enough with the trend in modern architecture toward more transparency in the facade, even with generous areas of glazing.⁴ Therefore, glass these days is used not only as an infill material, with an enclosing function, but increasingly as a load bearing and bracing material, e.g., in the form of glass fins. So far, facades with load bearing glass fins and beams have been exclusively custom designs because currently there are no technical building regulations covering the design and construction of such elements. The brittleness of glass frequently leads to uneconomical design for such applications because beside the ultimate and serviceability limit states, the issue of residual load bearing capacity must also be considered. Scientific studies [45–47] show that the residual load bearing capacities of glass beams made from laminated safety glass loaded in bending are not adequately guaranteed, irrespective of the type of glass used.

Hybrid glass beams with a linear adhesive joint between the glass and the steel have therefore been developed in order to pave the way for new facade designs [48]. In this case the joint is a load bearing connection between a minimized steel facade section and a vertical glass fin, which together carry the wind loads. Upgrading the brittle glass with ductile (plastically deformable) steel also makes a significant contribution to improving the residual load bearing capacity and the necessary redundancy in the design. In addition, the steel elements enable conventional jointing methods to be used for connecting the hybrid components to each other or to other parts of the structure.

In the future architects could therefore make use of a modular system that still permits individual designs. Up until now, similar forms of construction have been built using silicone joints. The normally used silicone adhesives need larger contact faces and because of its black color complete transparency is not ensured. (New developments show a structural silicone film adhesive, developed for point-fixed interior and exterior glazing, which combines a high transparency with high tensile and shear strength, strong adhesion performance, thermal stability, and excellent weatherability [49].) Bonding with transparent light-curing acrylates therefore offers new opportunities for architects. In a similar way to reinforced concrete, we can speak of reinforced glass beams: the transparent glass is reinforced by the ductile steel. And like reinforced concrete, which although a technical breakthrough, in the end led to a whole new architectural vocabulary, the hybrid beams embody great potential for a new style of architecture.

The hybrid glass beams consist of laminated safety glass with additional stainless steel elements that are connected by way of linear adhesive joints with

⁴Energy regulations pay special attention to the summer overheating protection. If necessary, measures—for example, controlled ventilation, sun protection glazing, or external solar shading—are to be taken to ensure the verification of the summer overheating protection.

a transparent adhesive. The linear joints enable a continuous load transfer between the steel and the glass, and therefore avoid local stress concentrations. The essential requirements to be fulfilled by the adhesive are therefore high strength to carry the loads and at the same time adequate elasticity to compensate for thermal expansion and contraction. As the mechanical properties of the adhesives depend on the temperature, the given ambient conditions and the magnitude and duration of the load, the research project initially focused on vertical facade systems for interior use. One focal point of the study was the development of suitable cross-sectional geometries for hybrid glass beams that would guarantee the permanent mechanical function of the adhesive joint between the steel and the glass and permit adequate exposure to the light to ensure proper curing during production [50].

Three different cross-sections, which permit an adapter connection at a later date, were investigated (Fig. 11). In variant S1 a steel plate measuring 20 mm × 2 mm was attached to the edges of the glass. Cross-section S2 has steel side plates measuring 13 mm × 2 mm. In cross-section S2 the central pane of glass in the laminated safety glass is set back by 12 mm so that a T-section (web: 12 mm × 3 mm; flange: 20 mm × 1.5 mm) can be inserted into the ensuing groove. The nominal thickness of the layer of adhesive in all cross-sections is 2 mm. In addition, a laminated safety glass element without any steel (S0) served as a reference.

The test setup was modified for the four-point bending test according to DIN EN 1288-3 [51] in order to carry out the experimental investigations into the load bearing and residual load bearing behavior of the specimens developed, which for facade applications are primarily loaded in bending about the major axis. The hybrid glass beams investigated consisted of laminated safety glass made from three plies of 6 mm annealed glass with ground edges and inter-layers of polyvinyl butyral with a nominal thickness of 0.76 mm. The steel elements were made from stainless steel grade 1.4401. The first load was applied

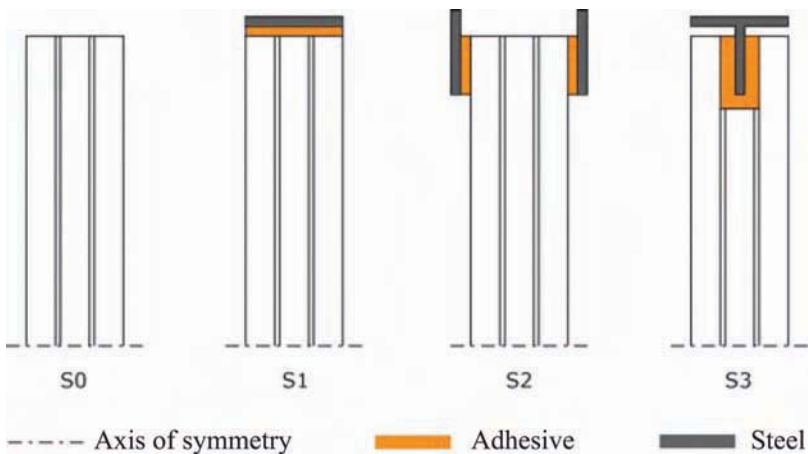


FIG. 11—Sections through the beams investigated (been symmetrical about centerline).

until one pane of the laminated safety glass fractured. The load was then relieved and subsequently re-applied until all three panes of the laminated safety glass had developed at least one crack (Fig. 12). Once all three panes of glass had fractured, further load was applied in order to assess the residual load bearing behavior.

The bending stiffness of the specimen was calculated from the force and deformation depending on the structural system. An intact glass beam with steel elements of course has a higher bending stiffness than a glass beam without steel elements. After the failure of all three panes of glass, the glass beam without any steel elements lost almost its entire load-carrying capacity. Compared with the hybrid cross-sections, its residual load bearing behavior was very low. But unlike the glass beam without steel elements, the hybrid beams did not collapse and continued to carry the loads, albeit with greater deformations. Cross-section S1 exhibited the highest bending stiffness prior to the first crack, but the highest bending stiffness for the residual load bearing capacity was shown by hybrid cross-section S3 [50]. The results clearly show the improved load bearing and residual load bearing capacities of hybrid glass beams under short-term loading. Further long-term loading tests to determine the creep and relaxation behavior are currently in progress. Investigating the effects of thermal stresses, caused by the different coefficients of thermal expansion of the materials used, was not such a priority here because in the applications considered hitherto, the adhesive joints are on the inside of the facade and the temperature fluctuations are minimal.

On the basis of the results obtained from this research project, a sample facade was developed (Fig. 4) for the “glass technology live” exhibition at the glasstec 2010 trade fair in order to illustrate the general design principle and the appearance of hybrid glass beams in use. The current energy requirements with which facades must comply—a decisive criteria when selecting products—can

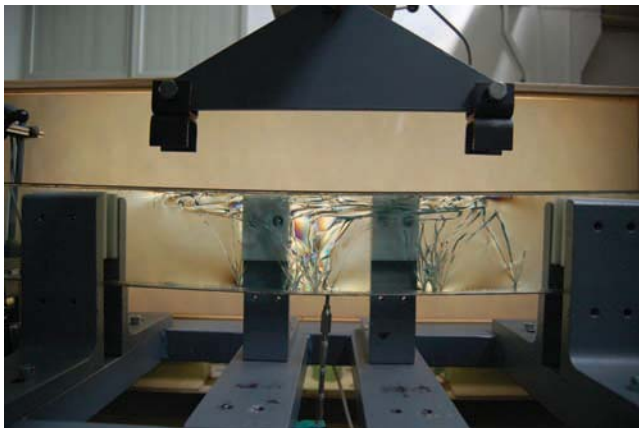


FIG. 12—Hybrid glass-steel beam in the test rig for investigating the load bearing and residual load bearing behavior.

be satisfied by using insulating glass units with three panes of glass (triple glazing). Thermal transmittance values as low as $0.78 \text{ W/m}^2\text{K}$ can be achieved. The total energy transmittance of the glazing lies between 24 % and 55 % depending on the coating.

The hybrid facade design consists of four glass posts at a spacing of 1.75 m. The glass posts 3.50 m high and 0.2 m deep consisted of laminated safety glass made from three plies of 8 mm toughened safety glass. Consequently, attractive story-high glazing is possible. Cross-section S1 with the best adhesive joint geometry was selected for this facade. Stainless steel plates were attached to both edges of the glass post via linear adhesive joints using a UV- and light-curing, transparent acrylate adhesive (Fig. 13). The stainless steel plate on the inside edge measured $27 \text{ mm} \times 3 \text{ mm}$, the stainless steel plate ($50 \text{ mm} \times 4 \text{ mm}$) on the edge adjacent to the insulating glass was attached as an adapter. The connection between the adapter and the facade section was achieved with countersunk-head screws. This mechanical connection guarantees uncomplicated replacement of the post should the glass break. The facade section 50 mm wide \times 25 mm deep is a conventional steel section for facade systems. The linear support to the glazing was guaranteed on the outside by a very flat glazing bar 50 mm wide \times 5 mm thick.

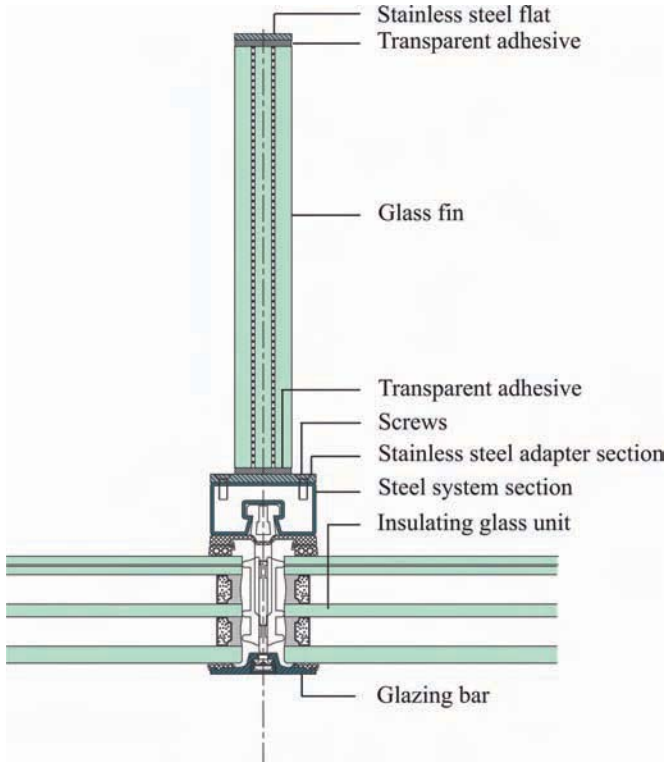


FIG. 13—Section through sample facade with hybrid steel-glass beams.

Frame Corners

Bonded frame corners are classed as planar adhesive joints (Fig. 5). Special attention must be given to the choice of adhesive for transparent, all-glass frame corners if load bearing but also fully transparent and totally bubble-free joints are to be achieved [52]. Preliminary studies of numerous material specimens form the starting point for determining the material parameters. Small-scale specimens are tested under various boundary conditions (temperature, moisture, UV radiation, aging) in order to establish the strengths of a number of suitable adhesives.

Specimen components (Fig. 14) are loaded in a testing machine in order to study the structural effect of these glued glass frame corners. The results enable digital prototypes to be designed and calibrated for numerical simulation. The verified and validated computer model should then be used to assess the distribution of stresses in the adhesive joint and in the glass. Numerical calculations and experimental investigations are carried out in parallel in order to optimize the geometry, load-carrying capacity, long-term reliability, and durability of the glued all-glass frame corners. The findings are incorporated in the design of the adhesive joint and help in the development and testing of an optimum form of connection with the aim of achieving a practical solution suitable for carrying loads permanently. The structural system of the all-glass enclosure was designed with redundancies so that the failure of or damage to individual elements would not lead to the complete collapse of the structure. In addition to the system as planned, the failure of adhesive joints (hinges form at the corners of the frame) and the failure of the roof and rail elements (the fixed-end frame legs and the vertical enclosing elements are responsible for the stability) were analyzed numerically.

Finally, the principles for gaining approval for what was up until now a nonregulated form of construction are prepared. The goal is a fully transparent



FIG. 14—Applying a transparent adhesive to a sample component with the help of a special injector.

glass corner—a goal that has inspired architecture since the dawn of the Modern Movement.

Glass in Solar Technology

Photovoltaic Modules Mounted with Adhesive Point Fixings

Solar technology, like glass in building, is making use of ever larger glass formats [53]. Correspondingly higher component weights call for improvements to the fixings. The comparison between positive connection, nonpositive connection, and material bond frequently results in a decision in favor of adhesives because of the many advantages. New developments for point, linear, and planar adhesive joints in solar technology are presented below.

Essentially influenced by the progress in coating technology, very large photovoltaic (PV) modules are now being produced which can no longer be secured with conventional clamp fixings.

An adhesive point fixing for fitting on the back of thin-film PV modules has been developed within the scope of a research project [54]. This fixing (Fig. 15) can be adapted to suit the supporting frameworks of various manufacturers available on the market. The adhesive used can carry the structural and dynamic loads acting on the joints for the duration of the anticipated service life of a PV module.

Selected adhesives are characterized in the laboratory. Following initial tests on fixings with preliminary dimensions, the suitability of the optimized fixing is tested according to DIN EN 61646 [55]. The pneumatic testing apparatus (Fig. 16) enables the evaluation of the mechanical load-carrying capacity of PV modules, also when subjected to rapidly changing loading cycles. The fatigue behavior of the adhesive joint and the fixing is estimated with the help of



FIG. 15—Prototype of an adhesive point fixing.

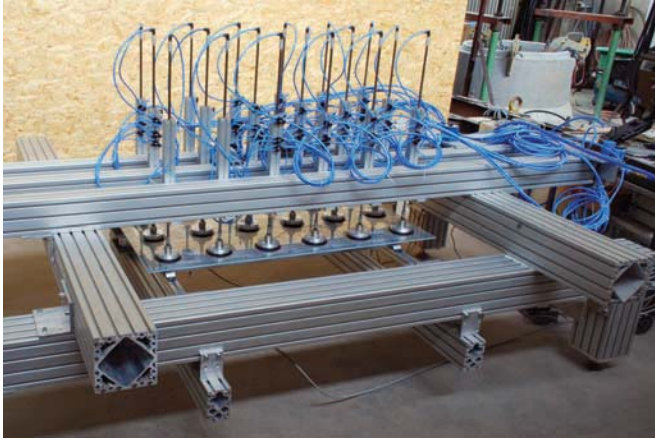


FIG. 16—*Pneumatic testing apparatus.*

dynamic tests. The material parameters determined in the laboratory and the experience gained with small-scale specimens is incorporated in the optimization. The tests, including accelerated aging methods and in conjunction with the fixing material selected, back up the permanent properties of the adhesives. Furthermore, studies are carried out to optimize the adhesive parameters, e.g., surface preparation, application, and curing.

Photovoltaic Modules Fixed with a Linear Adhesive Joint

Individual laminate clamp fixings are frequently adequate for fixing frameless PV modules. This means that in contrast to conventional module frames with a linear support to the glass laminate on all sides, and hence a “gentle” form of mechanical fixing, stress peaks cannot always be avoided. With large-format modules in particular, the interplay between the geometry of the fixing elements and their position on the module offers considerable potential for optimization with respect to a mounting solution that is safe and also efficient in terms of materials. In the light of this, innovative roof- and ground-mounted arrays are increasingly being based on adhesive fixings [56]. Using adhesive for joints involving glass is a method very much suited to this material. It also offers the chance of stiffening a thin module on the back and for leaving the front flat and unobstructed, which is advantageous for photovoltaics as it assists the self-cleaning function, helps to ensure that snow slides off, and avoids microshadows (Fig. 17). However, fundamental research into this innovative type of fixing, for various applications and loads, still has to be carried out. The linear load bearing rails are usually made from galvanized steel, stainless steel or anodized aluminum, and are connected to the back of the PV module with liquid or paste adhesives, e.g., 2-part silicone, or with double-sided adhesive tape, e.g., acrylate foam tape.

In accordance with the existing German testing regulations [23], the Institute of Building Construction has carried out tests using the example of an



FIG. 17—PV module with mounting rails fixed to the back of the module with adhesive.

acrylate adhesive tape for attaching the back rail in order to analyze its suitability and significance for this application. Beside thermal analysis methods and tensile tests on dumbbell specimens punched out of the material, in situ specimens were also tested in tension and shear (see, for example, the tensile test specimen in Fig. 18).

Bonded Photovoltaic System Facade

In cooperation with partners from research and industry, the Institute of Building Construction has developed new PV composite panels as integral components for a facade suspended in front of a ventilation cavity [57]. The 1.20 m × 0.60 m CIS (copper, indium, selenium) thin-film solar modules, some with a colored cover glass, are bonded to a backing plate made from foamed recycled glass over their full area. So they can be adjustable suspended from a load bearing framework at the rear (Fig. 19). Individual insulation thicknesses on the external wall behind the facade guarantee the thermal performance required and electric cables are routed through the ventilation cavity.

The homogeneous surface—available in six different colors and with printing—and the frameless design represent great potential for applications in architecture, including the refurbishment of existing buildings. Output compared to the standard black version is reduced by 10%–25%, depending on the color of or the printing coverage on the cover glass. This suspended PV facade has already been used in a practical application on a new company building in Reutlingen in south-west Germany (Fig. 20).

Outlook

It is primarily the innovative projects and prototypes—which do not fall within the remit of approved types of application in Germany—that are expanding the design spectrum. Transparent and high-modulus adhesives, in particular, are

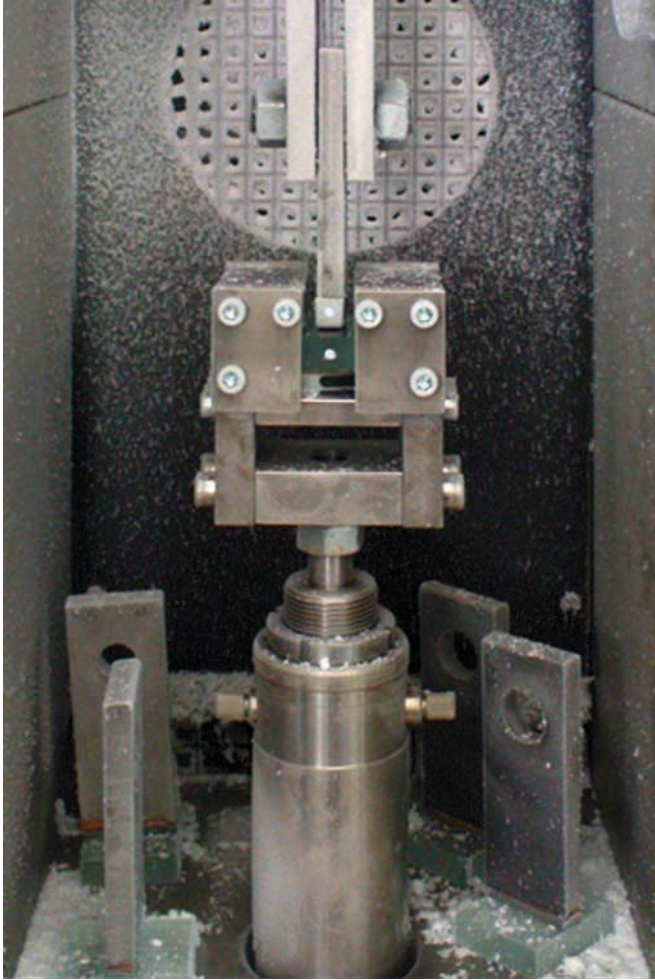


FIG. 18—Tensile test specimen in the testing machine at -25°C .

opening up new fields of application for load bearing adhesive joints in glass structures, with point, linear, or planar adhesive joint geometries. Other adhesive systems such as epoxy resins, polyurethanes, or acrylates represent alternatives to the silicones traditionally used. Investigating the options for gluing glass to other materials and assessing the durability of such joints can lead to new types of structure and a wealth of opportunities in the medium-term.

Beside the use of adhesives for glass in building applications, options for developing the use of adhesives in solar technology and intensifying the use of that technology are being investigated more and more. These include current topics such as integrating PV elements into facades as part of the “Spitzencluster Solarvalley” project (www.solarvalley.org). Together with facade fabricators,



FIG. 19—Construction of a facade for generating electricity.

solutions with a high aesthetic quality are drawn up based on various construction principles, the planning process is optimized, and attention-grabbing demonstration projects devised. As part of this, both opaque and semi-transparent PV elements for facades with and without a ventilation cavity plus new fixing systems should be developed.

The range of designs permits a fundamental analysis of the additional loads due to PV elements which result from new applications in various types of facade. Specifications drawn up based on this ease the development of the technology. Beside the respective requirements placed on the modules, e.g., dimensions, weight, stability, and yield; architectural aspects and electrical safety issues are taken into account in the development of suitable jointing



FIG. 20—Bonded Photovoltaic system facade, Manz Automation, Reutlingen, Germany (Hank und Hirth Freie Architekten; photo: Oliver Starke).

methods, e.g., adhesives, standardized mounting methods, and optimized cabling variants.

In this joint project, the Institute of Building Construction is responsible for the overall management of the scientific side and assists in the facade development by the industrial partners. One primary objective is the further development of adhesives for facade construction. Experimental proof obtained from small-scale specimens right up to full-size prototypes supports the validation. Rules for applications in accordance with building legislation are developed on the basis of the results of tests and practical experience gained with systems already in place.

Acknowledgments

The writers are grateful to all project partners and supporters who enable the diverse tests within the scope of the various research projects.

References

- [1] Weller, B., Kothe, M., Nicklisch, F., Schadow, T., Tasche, S., Vogt, I., and Wunsch, J., "Kleben im konstruktiven Glasbau [Bonding for Structural Glass Applications]," *Stahlbau Kalender 2011*, Ulrike Kuhlmann, Ed., Ernst & Sohn, Berlin, Germany, pp. 585–646, 2011 (in German).
- [2] Schadow, T., 2006, "Beanspruchungsgerechtes Konstruieren von Klebverbindungen in Glastragwerken [Designing Adhesively Bonded Joints to Meet Structural

- Requirements],” Ph.D. thesis, Technische Universität Dresden, Dresden, Germany (in German).
- [3] Baitinger, M., “Zur Bemessung von SL-belasteten Anschlüssen im konstruktiven Glasbau [Contribution to the Design of Lapped Glass Joints with Bolts in Bearing],” *Schriftenreihe des Lehrstuhls für Stahlbau und Leichtmetallbau der RWTH Aachen [Scientific Series of the Institute of Stelle Structures]*, Heft 71, Shaker, Aachen, Germany, 2010 (in German).
- [4] Wurm, J., 2007, *Glas als Tragwerk [Glass Structures]*. Birkhäuser, Basel, Switzerland.
- [5] Techen, H., 1997, “Fügetechnik für den konstruktiven Glasbau [Joining Technology for Structural Glass Applications],” Ph.D. thesis, Technische Universität Darmstadt, Darmstadt, Germany (in German).
- [6] MacFarlane, T., “Glass—The New Structural Engineering Material,” *Glass in Buildings*, Bath, England, 1999, pp. 45–52.
- [7] Wilson, P. and Vasilchenko-Malishev, G., “The Design and Construction of All Glass Structures,” *International Association for Shell and Spacial Structures, Madrid, Spain, Asia-Pacific Conference on Shell and Spatial Structures, Seoul, Korea, Beijing, China, October 16–19, 2006*.
- [8] Pye, A. and Ledbetter, S., “Realising Composite Glass-Adhesive Beams in Practice,” *Glass in Buildings*, Bath, England, 1999, pp. 185–190.
- [9] Richards, B., *New Glass Architecture*, Yale University Press, New Haven, CT, 2006.
- [10] Schittich, C., “Taking a Second Look: Glass Pavilion at Broadfield House in Kingswinford,” *Detail—Rev. Archit.*, Vol. 51, No. 1/2, 2011, pp. 6–9.
- [11] Nijse, R., “Design and Construction of an All Glass Cube for Raaks Project in Haarlem (NL),” *Challenging Glass 2*, F. Bos, C. Louter, and F. Veer, Eds., TU Delft, Delft, Netherlands, 2010, pp. 161–168.
- [12] Blandini, L., “Structural Use of Adhesives for the Construction of Frameless Glass Shells,” *Int. J. Adhes. Adhes.*, Vol. 27, No. 6, 2007, pp. 499–504.
- [13] Stelzer, I., “High Performance Laminated Glass,” *Challenging Glass 2*, F. Bos, C. Louter, and F. Veer, Eds., TU Delft, Delft, Netherlands, 2010, pp. 467–474.
- [14] O’Callaghan, J., “Innovations in Glass Design and Fabrication,” *Engineered Transparency*, J. Schneider and B. Weller, Eds., Technische Universität Darmstadt, Technische Universität Dresden, Düsseldorf, Germany, 2010, pp. 13–21.
- [15] Geiß, P. L., Luhn, R., Sändig, S., and Wagner, A., “Verbesserung der Langzeitbeständigkeit von Glasklebung durch prozessintegrierte umweltverträgliche Oberflächenbehandlungsverfahren [Improvement of the Long-Term Durability of Glass Bonds by Process-Integrated Sustainable Surface Treatment Processes],” *8. Kolloquium: Gemeinsame Forschung in der Klebtechnik*, DECHEMA - Gesellschaft für Chemische Technik und Biotechnologie e.V./Fachsektion Klebtechnik, Frankfurt, Germany, February, 26–27, 2008, pp. 20–22 (in German).
- [16] Luhn, R., Sändig, S., Geiß, P., and Wagner, A., “Influence of Surface Treatment on the Adhesion Qualities of Glasses,” Organised by IOM Communications Ltd on behalf of The Society for Adhesion and Adhesives, The Institute of Materials, Minerals and Mining, London, UK. The Society for Adhesion and Adhesives, The Institute of Materials, Minerals and Mining, London, UK, *Euradh 2008—Adhesion ’08*, Oxford, Great Britain, September 3–5 2008, pp. 305–308.
- [17] Overend, M., Jin, Q., and Watson, J.: “The Selection and Performance of Adhesives for a Steel-Glass Connection,” *Int. J. Adhes. Adhes.*, Vol. 31, No. 7, 2011, pp. 587–597.
- [18] Mocobob, D., “Glass Panel under Shear Loading—Use of Glass,” Ph.D. thesis, École Polytechnique Fédérale de Lausanne, France, 2008.

- [19] Abeln, B. and Preckwinkel, E., "Entwicklung hybrider Stahl-Glas-Träger [Development of Hybrid Glass-Steel-Beams]," *Stahlbau*, Vol. 80, No. 4, 2011, pp. 218–225 (in German).
- [20] Louter, C., Belis, J., Veer, F., and Lebet, J.-P., "Durability of SG-Laminated Reinforced Glass Beams: Effects of Temperature, Thermal Cycling, Humidity and Load-Duration," *Constr. Build. Mater.*, Vol. 27, No. 1, 2012, pp. 280–292.
- [21] Weller, B. and Weimar, T., "Development of a New Facade System with Hybrid Glass-Steel Elements," *Glass Performance Days 2011*, Glass Performance Days, Tampere, Finland, pp. 522–524.
- [22] Hagl, A., "Kleben im Glasbau," *Stahlbau-Kalender 2005*, Ulrike Kuhlmann, Ed., Ernst & Sohn, Berlin, Germany, 2005, pp. 819–862.
- [23] ETAG 002, 1999, *Guideline for European Technical Approval for Structural Sealant Glazing Systems (SSGS), Part 1: Supported and Unsupported Systems*, EOTA, Brussels, Belgium.
- [24] ETAG 002, 2002, *Guideline for European Technical Approval for Structural Sealant Glazing Systems (SSGS), Part 2: Coated Aluminium Systems*, EOTA, Brussels, Belgium.
- [25] ETAG 002, 2002, *Guideline for European Technical Approval for Structural Sealant Glazing Systems (SSGS), Part 3: Systems Incorporating Profiles with a Thermal Barrier*, EOTA, Brussels, Belgium.
- [26] Peters, S., "Kleben von GFK und Glas für baukonstruktive Anwendungen [Bonding of Glass Fiber Reinforced Plastics (GFRP) and Glass for Applications in the Area of Structural Design]," Ph.D thesis. Universität Stuttgart, Germany, 2006 (in German).
- [27] Geiss, P. L., Kessler, C., Kurz, W., and Turcinkas, S., "Evaluation of Adhesive Bonding Between Steel and Concrete," *Composite Construction in Steel and Concrete Conference VI*, Engineering Conference International and The Structural Engineering Institute of American Society of Civil Engineers, Reston, VA, July 20-24, 2008, Tabernash, CO, ASCE.
- [28] Weller, B. and Weimar, T., "Stahlglasträger in der Fassade—Entwicklung einer hybriden Fassadenkonstruktion aus Glas und Stahl [Steel-Glass-Beams in the Facade - Development of a Hybrid Construction of Glass and Steel]," *Dtsch. Bauzeitschrift (DBZ)*, Vol. 58, No. 11, 2010, pp. 62–64 (in German).
- [29] Kreher, K., Natterer, J., and Natterer, J., "Timber-Glass Composite for a Hotel in Switzerland," *Struct. Eng. Int.* (IABSE, Zurich, Switzerland), Vol. 14, 2004, pp. 149–151.
- [30] Knaack, U., Führer, W., and Wurm, J., *Konstruktiver Glasbau 2—Neue Möglichkeiten und Techniken [Glass Structures 2 - New Options and Technologies]*, Müller, Köln, Germany, 2000 (in German).
- [31] Weller, B., Döbel, F., Nicklisch, F., Prautzsch, V., and Rucker, S., "Geklebte Ganzglaskonstruktion für das Leibniz-Institut für Festkörper- und Werkstoffforschung in Dresden [All Glass Enclosure for the Leibniz Institute for Solid State and Material Research in Dresden]," *Stahlbau Spezial 2010—Konstruktiver Glasbau*, B. Weller and S. Tasche, Eds., 2010, pp. 34–40 (in German).
- [32] DELO Industrie Klebstoffe, *BOND it – Nachschlagewerk zur Klebtechnik [Reference Work for Bonding Technology]*, Windach, Germany, 2007 (in German).
- [33] Domininghaus, H., *Die Kunststoffe und ihre Eigenschaften*, Springer, Berlin, Germany, 2005 (in German). Plastics and their characteristics.
- [34] Brockmann, W., Geiß, P. L., Klingen, J., and Schröder, B., *Klebtechnik: Klebstoffe, Anwendungen und Verfahren [Bonding Technology: Adhesives, Applications and Techniques]*, Wiley-VCH, Weinheim, Germany, 2005 (in German).

- [35] Lechner, M. D., Gehrke, K., and Nordmeier, E. H., *Makromolekulare Chemie [Macromolecular Chemistry]*, Birkhäuser, Basel, 2003 (in German).
- [36] Grellmann, W. and Seidler, S., *Kunststoffprüfung [Testing of Plastics]*, Hanser, München, 2005 (in German).
- [37] Vogt, I., 2009, "Strukturelle Klebungen mit UV- und lichthärtenden Acrylaten [Structural Bonded Joints with UV and Light Curing Acrylates]," Ph.D. Thesis, Technische Universität Dresden, Dresden, Germany (in German).
- [38] Schlimmer, M., Bornemann, J., "Berechnung und Auslegung von Klebverbindungen," part 2: *Adhäsion* 48 (2004), Vol. 6, pp. 40–42 (in German).
- [39] DIN EN ISO 527-1, 1996, Plastics—Determination of Tensile Properties—Part 1: General Principles, Beuth, Berlin, Germany.
- [40] DIN EN ISO 527-2, 1996, Plastics—Determination of tensile properties—Part 2: Test Conditions for Moulding and Extrusion Plastics, Beuth, Berlin, Germany.
- [41] DIN EN 14869-1, 2004, Structural Adhesives—Determination of Shear Behaviour of Structural Bonds—Part 1: Torsion Test Method Using Butt-Bonded Hollow Cylinders (ISO 11003-1:2001, Modified), Beuth, Berlin, Germany.
- [42] Tasche, S., 2007, "Strahlungshärtende Acrylate im Konstruktiven Glasbau [Light curing acrylates in glass structures]," *Ph.D. Thesis*, Technische Universität Dresden, Dresden, Germany (in German).
- [43] Weller, B., Härth, K., Tasche, S., and Unnewehr, S., *Glass in Building—Bases, Applications, Projects*, Institut für Internationale Architektur-Dokumentation, Munich, Germany, 2009.
- [44] Weller, B. and Tasche, S., 2009, "Experimental Evaluation of Ultraviolet and Visible Light Curing Acrylates for Use in Glass Structures," *J. ASTM Int.*, Vol. 6, No. 9, pp. 135–156.
- [45] Hess, R., "Glasträger [Glass Beams]," *HBT Bericht Nr. 20*, Institut für Hochbautechnik, ETH Zürich, Zurich, Switzerland, 2000 (in German).
- [46] Louter, P.C., "Adhesively Bonded Reinforced Glass Beams," *Heron*, Vol. 52, No. 1/2, 2007, pp. 31–58.
- [47] Weller, B., Härth, K., Werner, F., and Hildebrand, J., "Hybridbauteile im Konstruktiven Glasbau [Hybrid Structural Elements for Glass Constructions]," *Stahlbau Spezial 2009—Konstruktiver Glasbau*, B. Weller and S. Tasche, Eds., 2009, pp. 29–35 (in German).
- [48] Weller, B., Weimar, T., and Meier, A., "Hybrid Façade System Made of Glass and Steel," *Engineered Transparency*, J. Schneider and B. Weller, Technische Universität Darmstadt, Technische Universität, Dresden, Germany, 2010, pp. 149–158.
- [49] Sitte, S., Brasseur, M. J., Carbary, L. D., and Wolf, A. T., "Preliminary Evaluation of the Mechanical Properties and Durability of Transparent Structural Silicone Adhesive (TSSA) for Point Fixing in Glazing," *J. ASTM Int.*, Vol. 8, No. 10, pp. 1–27.
- [50] Weller, B., Meier, A., Weimar, T., Menkenhagen, J., and Koschecknick, K., "Hybride Glasträger als Fassadenelement [Glass Beams as Structural Members in Facades]," *Stahlbau Spezial 2010—Konstruktiver Glasbau*, B. Weller and S. Tasche, Eds., 2010, pp. 41–45 (in German).
- [51] DIN EN 1288-3, 2000, Glass in Building—Determination of the Bending Strength of Glass—Part 3: Test with Specimen Supported at Two Points (Four Point Bending), Beuth, Berlin, Germany.
- [52] Weller, B., Döbbel, F., Nicklisch, F., Prautzsch, V., and Rucker, S., "All Glass Enclosure with Transparently Bonded Glass Frames," *Challenging Glass 2*, Delft, Netherlands, 2010, pp. 207–216.
- [53] Weller, B., Hemmerle, C., Jakubetz, S., and Unnewehr, S., *DETAIL Practice Photovoltaics. Technology, Architecture, Installation*, Birkhäuser, Basel, Switzerland, 2010.

- [54] Weller, B., Jakubetz, S., and Tautenhahn, L., "Adhesive Fixing of Large-Sized Thin-Film Photovoltaic Modules," *Engineered Transparency*, Beuth, Berlin, Germany, 2010, pp. 575–582.
- [55] DIN EN 61646, 2009, "Thin-Film Terrestrial Photovoltaic (PV) Modules—Design Qualification and Type Approval."
- [56] Weller, B., Hemmerle, C., Tautenhahn, L., and Jarzembowski, A., "Innovative Befestigungen für rahmenlose PV-Module: Mechanische und baurechtliche Herausforderungen [Innovative Fixings for Frameless PV Modules]," 25. *Symposium Photovoltaische Solarenergie, March 3-5, Bad Staffelstein, Germany, Ostbayerisches Technologie-Transfer-Institut e.V. (OTTI)*, Regensburg, Germany 2010, pp. 382–387 (in German).
- [57] Weller, B. and Hemmerle, C., "Innovative BIPV Products Based on Adhesive Technology," *24th European Photovoltaic Solar Energy Conference and Exhibition*, Hamburg, Germany, September 21-25, 2009, WIP, Munich, Germany, pp. 4272–4275.

Bernhard Weller,¹ Felix Nicklisch,² Volker Prautzsch,³
and Iris Vogt⁴

Outline of Testing and Evaluation Program Used in Selection of Adhesives for Transparent Adhesive Joints in All-Glass Load-Bearing Structures

ABSTRACT: Architects are increasingly demanding all-glass load-bearing structures with fully transparent adhesive joints. Usually, such structures are classed as nonregulated forms of construction. The Institute of Building Construction at Dresden's Technische Universität has now obtained the first individual approvals in Germany for all-glass structures with transparent adhesive joints for two buildings in Dresden and Grimma. In these cases, the loads are carried via load-bearing glued frames that rely on a material bond between the individual parts without any metal fixings. This solution is based on the results of many years of development. Currently, various frame corners covering a wide range of parameters are being studied in a follow-up project. The aim is to optimize the adhesive joints and the bonding technology. The requirements placed on the joint are being identified and corresponding adhesive systems researched. Preliminary studies of numerous material specimens form the starting point for determining the material parameters. Small-scale specimens are being tested under various boundary

Manuscript received June 1, 2011; accepted for publication December 19, 2011; published online April 2012.

¹Professor, Dr.-Ing., Institute of Building Construction, Technische Universität Dresden, 01062 Dresden, Germany, e-mail: bernhard.weller@tu-dresden.de

²Research Assistant, Dipl.-Ing., Institute of Building Construction, Technische Universität Dresden, 01062 Dresden, Germany, e-mail: felix.nicklisch@tu-dresden.de

³Research Assistant, Dipl.-Ing., Institute of Building Construction, Technische Universität Dresden, 01062 Dresden, Germany, e-mail: volker.prautzsch@tu-dresden.de

⁴Senior Researcher, Dr.-Ing., Institute of Building Construction, Technische Universität Dresden, 01062 Dresden, Germany, e-mail: iris.vogt@tu-dresden.de

Cite as: Weller, B., Nicklisch, F., Prautzsch, V. and Vogt, I., "Outline of Testing and Evaluation Program Used in Selection of Adhesives for Transparent Adhesive Joints in All-Glass Load-Bearing Structures," *J. ASTM Intl.*, Vol. 9, No. 4. doi:10.1520/JAI104088.

Copyright © 2012 by ASTM International, 100 Barr Harbor Drive, PO Box C700, West Conshohocken, PA 19428-2959.

conditions and aging scenarios to establish the strengths of a number of suitable adhesives. These results will enable prototypes to be designed for numerical simulation. Numerical calculations and experimental investigations are being carried out in parallel to optimize the geometry, load-carrying capacity, long-term reliability, and durability of the glued all-glass frame corners. Specimen components are loaded in a testing machine to study the structural effect of these glued glass frame corners. The findings will be incorporated in the design of the adhesive joint and in the development of a numerical simulation for the glued connection. Data for executing an adhesive joint, specific to each adhesive and crucial for the quality of the transparency, conclude the project.

Introduction

Striving for complete transparency obviously also calls for load-bearing structures to be made from transparent materials, such as glass. Glass is a brittle material, which means that tried-and-tested methods of jointing, derived from structural steelwork and other engineering disciplines, cannot simply be transferred to this material. Glued connections enable a homogeneous flow of forces via the material bond between the components being joined and at the same time reduce local stress peaks in the glass. So, besides the customary mechanical connections, load-bearing adhesives are becoming very important as a form of connection, ideally suited to glass. For example, individual linear load-bearing elements made from glass can be glued together to form transparent load-bearing frames, which are addressed in this paper.

Appropriate adhesives for joining glass are entirely or partially based on polymeric compounds. Thus, their chemical structure and their material properties resemble plastics to a high degree. The aging behavior and durability of relevant types of adhesives have been examined in recent research projects focusing on glass–glass and glass–metal bonds. Usually, the experimental investigations comprise comprehensive testing on small-scale samples. Typically, those samples run through severe artificial aging scenarios, like climatic or thermal cycling, exposure to UV-light, high-humidity, corrosive media, or immersion in water or in a solution of a cleaning agent.

In general, thorough cleaning and surface pretreatments enhance the long-term stability and overall quality of the bond [1,2]. As an example, treating the glass surface with atmospheric plasma can increase the surface energy and remove specific organic impurities. The selection of a suitable adhesive is another crucial parameter for the design of bonded connections. Overend et al. [3] propose an approach toward the characterization of the adhesive and the derivation of essential data for analytical and numerical models. Another substantial study [4] focuses on the ageing resistance of several UV- and light-curing acrylates, which were used for glass–metal bonds. As a consequence, those adhesives could prove their suitability for load-bearing connections in glass applications under the condition that long-lasting exposure to moisture is avoided and temperature-dependent material behavior is taken into account for

design calculations. Their tendency to significant creep deformations under permanent long-term loading [5] requires further improvement and careful consideration in the structural design.

Although durability testing has also been done on larger bonded elements, the dimensions of the weathering equipment generally limit the size and quantity of specimen components to be tested. Some research activities focus, for example, on the combination of glass with ductile materials to improve the structural performance after failure and expand the scope of applications beyond the initial limits. The so-called “reinforced glass beams” or “hybrid glass beams” are examined in Refs [6–8].

Nevertheless, the correlation of simulated conditions in the laboratory and outdoor exposure is still one of the main challenges of scientific research on adhesive bonding. Hence, testing on life-size glazing elements exposed to long-term outdoor conditions is often required to verify the assumptions made by scaling up the findings from small specimens. Experimental studies were done, for example, on a frameless glass shell [9], as well as on glued point fixings for glass canopies [10] or bonded glass lamellas [4].

Another significant step toward a more regular application of structurally bonded glass can be done transferring the knowledge achieved into innovative pilot projects. This paper presents experimental and numerical investigations that lead to the realization of a currently built glass corridor. The glass components are connected without using additional metal fasteners.

Bonded Glass Frames

Construction Principle

The entrance foyer to Broadfield House Glass Museum in Kingswinford, England, was one of the first structures to be built almost entirely of glass [11]. The structure, which was completed in 1994, served as a prototype for numerous subsequent all-glass designs, including the form of construction discussed in this article. The glass pavilion is supported by glass frames with glued corners. The statements of users and designers confirm the suitability of the structural solution chosen. So far, after 15 years in use, no negative changes to the adhesive joints have become evident in this glued glass structure [12]. Another all-glass structure, a conservatory in Leiden in the Netherlands, which was obviously inspired by the entrance foyer in Kingswinford, is also in good condition [13].

Usually, each glued glass frame consists of three- or four-ply laminated safety glass elements, depending on the required factor of safety against failure. The corner detail is similar to the mortise and tenon joint used in carpentry; at the corners the outer plies of the posts overlap the inner plies of the beams to form what woodworkers might call a “corner bridle joint” (Fig. 1). The overlapping plies of glass are glued together with a transparent adhesive over their full area. The width of the gap for the adhesive is dictated by the thickness of the polyvinyl butyral (PVB) interlayer.

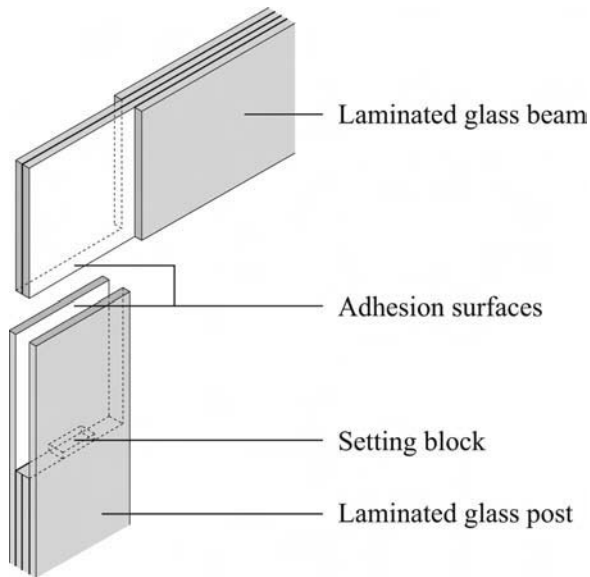


FIG. 1—Principle of the bonded frame corner.

Previous Work

The research and development work at the Institute of Building Construction focuses on the development of structural adhesive joints, as well as on the associated theoretical and experimental studies. The first tests on glued frame corners supplied promising results; the adhesive joints remained intact, whereas the glass failed [14]. Based on further investigations, the first research results were transformed into a building project that up until then was unique in Germany.

A highly modern helium liquefaction unit was set up at the Leibniz Institute for Solid State and Materials Research (IFW) in Dresden in 2009. The project included an all-glass enclosure for the historical helium pressure vessels (which are, however; still in use) in front of the institute building (Fig. 2(a)). Load-bearing adhesive joints are used exclusively to connect the individual glass elements. Without any opaque components or visible forms of connection, this housing represents a complete departure in Germany in terms of both building legislation and building technology. The primary structure of this glass pavilion consists of four glass frames of the type described above. These support the infill panes of glass and constitute the lateral bracing for the structure. A transparent, UV- and/or light-curing acrylate adhesive was used for connecting the individual frame elements. Linear structural sealant glazing (SSG) silicone joints connect frames and infill panes [15].

This project demonstrated the efficiency of such adhesive joints. In addition, specific application options could be presented to a wider circle of industry professionals with the help of design studies (Fig. 2(b)). Beside gaining valuable



FIG. 2—Transparently bonded glass frames: (a) all-glass enclosure at the IFW in Dresden, and (b) prototypes at glasstec 2010 in Düsseldorf.

insights into the structural and material behavior, the numerous tests also provided a wealth of experience on the production of such joints.

Nevertheless, a number of questions remained unanswered, which had to be addressed in further research. For example, so far it had been necessary to heat the glue cartridges and the glass to reduce the viscosity of the adhesive during application. Owing to the shrinkage in the volume of the adhesive, the preparations for the adhesive joint and also its intermittent curing were both very time consuming [15]. Therefore, a series of tests was carried out to assess the suitability of other promising adhesives. Studies involving the numerical simulation of glued frame corners, and aimed at optimizing the method of producing the joint, were also carried out. And a new construction project enabled further research results to be applied in practice and, hence, increase the acceptance of gluing in the building industry.

Glass Corridor for Law Courts

Major refurbishment work is currently being carried out at the palace in Grimma in Saxony, so that it can house law courts in the future. The new function requires the construction of a number of extensions to the historic building. To ensure that the historical spatial relationships of this ensemble, now protected by a conservation order, remain tangible, the new extensions are to be built in glass and as transparent as possible (Fig. 3(a)). One of these, a 25-m-long corridor, has been conceived as an almost completely glued construction.

A total of 17 half-frames made from laminated safety glass form the load-bearing structure to this glazed corridor (Fig. 3(b)). To achieve maximum transparency, the frames are not bolted at the corners, but instead joined with a transparent, high-strength adhesive. Each frame is let into the existing stone



FIG. 3—New glass structures for the historic courtyard: (a) visualization (Bauconcept Planungsgesellschaft mbH), and (b) Vertical section through new glass corridor (GSK – Glas Statik Konstruktion GmbH).

wall at the upper support and fixed to a new reinforced concrete ramp at the base. The glazed envelope is glued to its supporting structure via structural sealant glazing (SSG) adhesive joints.

Experimental proof is often required within the scope of the approval procedures for nonregulated construction products and forms of construction, which applies to glued glass structures in particular. There are no building-industry regulations covering the assessment of adhesive joints for structural glass in Germany, apart from those for SSG systems. Therefore, for this project, it was first necessary to carry out extensive preliminary studies to enable a suitable adhesive to be selected. Material parameters and adhesive properties were determined experimentally. The building authorities also required the load-bearing capacity to be verified by way of loading tests on sample components in addition to the static analysis.

Preliminary Study to Select Adhesive

Specification

There are more than 250000 industrial adhesives available worldwide, which suit different types of applications and fulfill diverse requirement criteria [16]. Taking into account the specific application profiles for the use of glass as a structural material, it is possible to reduce the wealth of different adhesives to just a few candidates. The material of glass is characterized by the hydrophilic surface. The moisture of the surface cannot be removed permanently as it is build up constantly by the humidity. Concerning the bonding of glass, that surface acts as a barrier. The adhesive must be able to break through (for example, by adding promoters or primers) and to build up stable adhesion forces. Furthermore, the specifications for the applications are diverse, which means that adhesives for structural glass include types with medium modulus, e.g., silicones, as well as adhesives with high and ultra-high modulus, e.g., epoxy resin and polyurethane adhesives. Bearing in mind the specific needs of this project, drawing up a shortlist requires a differentiated analysis and the compilation of the requirements with which the adhesives must comply:

- suitability for glass–glass joints,
- full-bond joints ($300 \times 300 \text{ mm}^2$),
- minimum joint thickness of 1.5 mm (compensation of tolerances, pouring),
- highly transparent and clear for a joint thickness up to 2 mm,
- curing possible in joints up to 2 mm thick,
- viscosity of 15000 to 50000 mPas,
- low shrinkage in volume,
- few air bubbles in the joint,
- resistant to moisture and UV radiation, and
- load-bearing over a temperature range from -25 to $+75^\circ\text{C}$.

As an example, the joint thickness was influenced by conflictive factors: the tolerances of the laminated glass elements, the curing behavior of the adhesive, the filling process, the structural behavior of the flexible corner joint, and,

finally, the visual appearance. Flat glass panels with high aspect ratios as for glass beams tend to warp during the tempering process. Hence, a minimum gap of 1.5 mm was necessary to avoid contact between the individual glass panes of the post, as well as to provide sufficient space for a nozzle to fill in the adhesive. In contrast, a thick bond line may reduce the stiffness and the transparency of the joint and impair the curing of the adhesive.

Adhesives

Owing to the requirements, 14 adhesives from various manufacturers made it onto the shortlist, including acrylate, epoxy resin, and polyurethane adhesives, see Table 1. The acrylates are 1-part products. Curing is carried out with a special lamp, preferably using UV radiation. The adhesive can cure within just a few minutes, depending on the intensity of the radiation. The epoxy resins are 2-part products consisting of resin and hardener, which are mixed together in the ratio specified by the manufacturer. The curing starts to take place at room temperature immediately after mixing. Increasing the strength by curing at a higher temperature was not used because this would be very difficult to accomplish for the intended application. The polyurethanes are also 2-part products that cure at room temperature. Owing to the planar geometry of the adhesive joints, 1-part adhesives that cure using the moisture in the air cannot be considered. In larger planar joints, moisture could not migrate sufficiently into the inner part of the joint. Hence, the curing of the adhesive processes slowly and may not be fully completed. Silicone adhesives, which cure by polycondensation, are also not suitable for this joint geometry. The gaseous condensates cannot escape from the inner parts of the joints and this may lead to impairments and weak curing.

Tensile Tests on the Materials

Type-1A material specimens to DIN EN ISO 527-2 [17] were used to analyze the material behavior at various temperatures and determine the material parameters under tensile loads. The specimens were loaded according to DIN EN ISO 527-1 [18] with displacement control at a rate of 1 mm/min. Between five and ten specimens per adhesive were tested at temperatures of -25 , $+25$, and $+75^{\circ}\text{C}$. Each specimen was preconditioned at the respective temperature for 24 h prior to the test. A video extensometer was used to ensure noncontact measurement of the deformation. The stress–strain diagrams (stress and strain in these diagrams are technical data referring to the original section) show just how much the behavior of each adhesive depends on the temperature. By way of example, only the two most interesting adhesives of each type are described here.

The epoxy resins (Fig. 4) exhibit a very stiff material behavior at low temperatures with brittle material failure, and a very resilient behavior at high temperatures. The stiffness of EP4 only drops after room temperature has been exceeded, but then very distinctly. The polyurethanes (Fig. 5), too, were found to be very resilient at high temperatures. At low temperatures they are almost as stiff as the epoxy resins, but exhibit a plastic behavior after reaching the

TABLE 1—Adhesives investigated.

Adhesive	Adhesive basis	1-part/2-part	Curing	Producer	Adhesive name
AC1	Acrylate	1-part	UV	First Glas ^a	FG1033-II ^g
AC2	Acrylate	1-part	UV	First Glas ^a	FG965-2 ^g
AC3	Acrylate	1-part	VIS/UV	Delo ^b	Delo-Photobond [®] GB VE 56903 ^g
AC4	Acrylate	1-part	VIS/UV	Delo ^b	Delo-Photobond [®] GB VE 512247 ^g
AC5	Acrylate	1-part	VIS/UV	Delo ^b	Delo-Photobond [®] 4468
AC6	Acrylate	1-part	VIS/UV	Delo ^b	Delo-Photobond [®] 437
AC7	Acrylate	1-part	VIS/UV	Panacol ^c	Vitralit UV 7516
EP1	Epoxy resin	2-part	RT	First Glas ^a	FG Flex1 ^g
EP2	Epoxy resin	2-part	RT	First Glas ^a	FG210 ^g
EP3	Epoxy resin	2-part	RT	First Glas ^a	FG210R6 ^g
EP4	Epoxy resin	2-part	RT	Huntsman ^d	Araldite [®] 2020
EP5	Epoxy resin	2-part	RT	Henkel ^e	Hysol [®] 9483 TM
PUR1	Polyurethane	2-part	RT	Huntsman ^d	Araldite [®] 2028
PUR2	Polyurethane	2-part	RT	3M ^f	Scotch-Weld [®] DP 610

^aFirst Glas, Rhinstraße 132, 12681 Berlin, Germany.

^bDELO Industrie Klebstoffe, Delo-Allee 1, 86949 Windach, Germany.

^cPanacol-Elosol, Daimlerstraße 8, 61449 Steinbach, Germany.

^dHuntsman Advanced Materials, Klybeckstraße 200, 4057 Basel, Switzerland.

^eHenkel AG & Co. KGaA, Henkelstraße 67, 40191 Düsseldorf, Germany.

^f3M Deutschland, Carl-Schurz-Straße 1, 41453 Neuss, Germany.

^gPrototype.

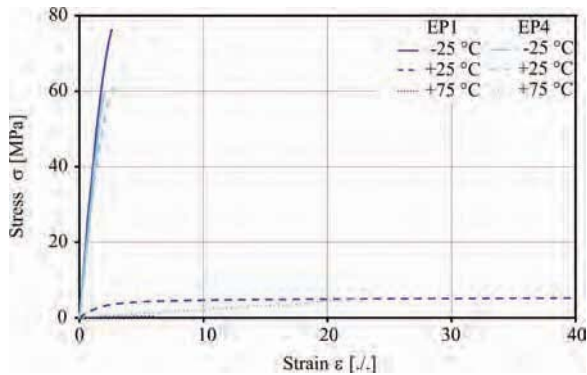


FIG. 4—Stress–strain diagram for epoxy resins EP1 and EP4 at various temperatures.

maximum stress. The acrylate adhesives (Fig. 6) also exhibit a temperature-dependent behavior, which is typical of this group of adhesives [10]. However, this behavior is not as pronounced as it is with the epoxy resins. The rise in the stiffness as the temperature drops is less pronounced. The material behavior at low temperatures has proved to be particularly advantageous for the acrylic adhesives investigated; the adhesives exhibit good flexibility at low temperatures and only fail after a distinct yield range.

Dynamic Mechanical Analysis

The adhesives were also subjected to a thermal analysis. The viscoelastic material properties of the adhesives were determined by means of a dynamic mechanical analysis (DMA). The test involves subjecting the specimen to a sine-wave-type loading over a given temperature range. The specimen likewise exhibits a sine-wave-type response with the same period and a deformation.

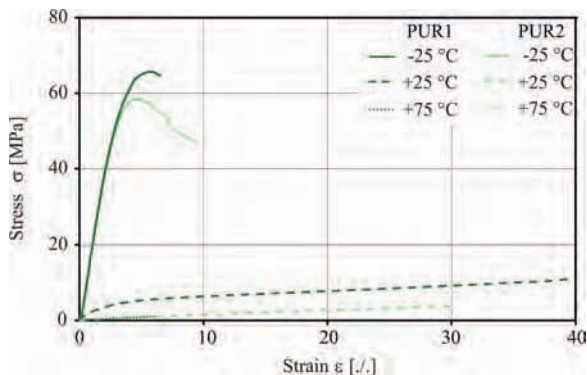


FIG. 5—Stress–strain diagram for polyurethanes PUR1 and PUR2 at various temperatures.

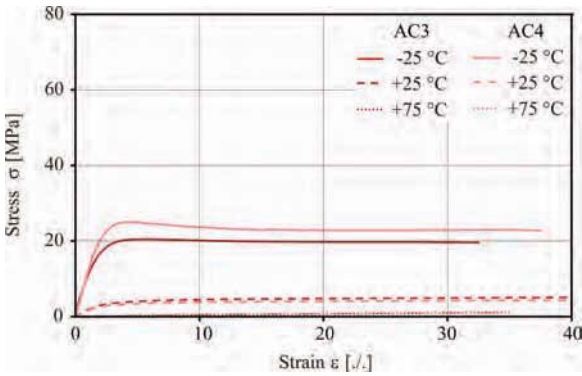


FIG. 6—Stress–strain diagram for acrylates AC3 and AC4 at various temperatures.

The amplitudes of the force and the deformation, as well as the phase shift between force and deformation, are recorded during the test.

These tests involved subjecting each specimen to tensile load (maximum load 7 N) with an excitation frequency of 1 Hz, using a DMA 242 C (Netzsch, Germany) in tension mode. Rectangular bar specimens were used for the study. The material specimens were heated from -60 to $+120^{\circ}\text{C}$ at a rate of 3 K/min; the evaluation took place in the range between -25 and $+100^{\circ}\text{C}$. This involved ascertaining the viscoelastic properties of the material by way of the storage modulus (E'), the loss modulus (E''), and the dissipation factor ($\tan\delta$). The relationship between these properties is given by $\delta = E''/E'$. The larger the storage modulus (E'), the greater is the amount of induced mechanical energy that can be recovered from the specimen. The energy irreversibly converted into heat is known as the loss modulus (E'').

The results of the DMA for the adhesives shortlisted are shown in Figs. 7–9. In these diagrams, the storage modulus (E') is shown as a solid line, the

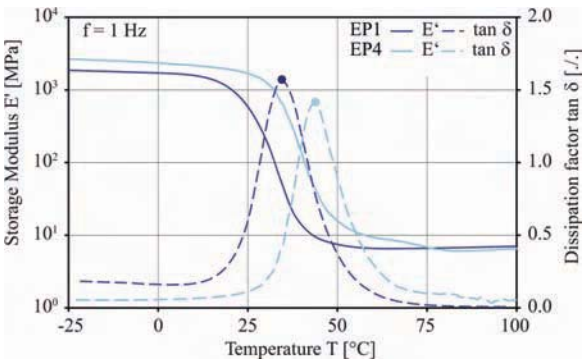


FIG. 7—DMA graph for epoxy resins EP1 and EP 4 (glass transition temperature T_g is marked).

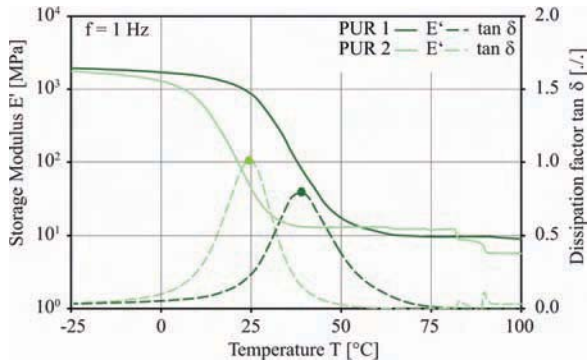


FIG. 8—DMA graph for acrylates PUR1 and PUR2 (glass transition temperature T_g is marked).

dissipation factor ($\tan\delta$) as a dotted line. Every adhesive was tested by means of at least two specimens.

The epoxy resins tested (EP1 and EP4) exhibit high storage moduli at low temperatures. In the service temperature range, e.g., room temperature, the adhesives exhibit a very definite glass transition temperature zone in which the storage modulus drops to a very low value within a narrow temperature range. Afterward, the storage modulus remains approximately constant at a low level. Polyurethanes PUR1 and PUR 2 are quite similar in their behavior. In contrast, the Acrylates AC3 and AC4 also have a high storage modulus at a low temperature, but it decreases continuously as the temperature continues to rise. The graph of the dissipation factor forms a plateau with an extended range of the glass transition temperature. The peak is not very distinctive. Furthermore, in the temperature range above $+40^\circ\text{C}$ these adhesives have a higher storage modulus than the epoxy resins and polyurethans tested.

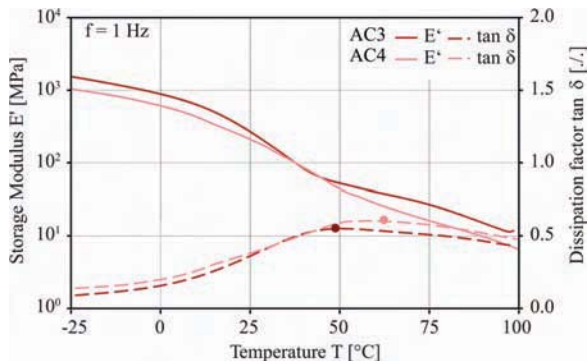


FIG. 9—DMA graph for acrylates AC3 and AC4 (glass transition temperature T_g is marked).

The results with respect to the glass transition temperature of each adhesive obtained from the DMA are summarized in Table 2. The glass transition temperature (T_g), as the mean value of the softening range, is evaluated according to ASTM D 4065 [19] for the peak of the dissipation factor ($\tan\delta$). This reveals that the glass transition temperatures for the acrylates tested have higher values than the epoxy resins and the polyurethanes and are more suitable for the intended application.

Results and Selection of Adhesive

On the basis of the behavior of individual adhesives established over the temperature range considered, acrylic adhesive AC4 was selected for the intended adhesive joints at the glass frame corners. In contrast to the epoxy resins and the polyurethanes, this adhesive exhibits a less pronounced temperature-dependent behavior and a higher glass transition temperature. Compared with acrylate adhesive AC3, acrylate AC4 is characterized by better strength at low temperatures and the ease with which it can be injected into the gap.

Experiments to Establish Adhesive Strength and Load-Bearing Capacity

Series of Tests

Numerous parameters have an influence on the load-bearing capacity and serviceability of an adhesive joint. First of all, the adhesive itself with its material properties and their complex dependence on external factors, such as temperature, and the materials to be joined together, as well as the geometry and thickness of the layer of adhesive, and the loads on it. Verifying the durability is also important, which must take into account the degradation of the adhesive and the adhesive bond as a result of various environmental effects or adjacent materials.

Therefore, once the material parameters of the UV- and light-curing acrylate adhesive AC4 selected had been determined with material specimens, further tests on small-scale in situ specimens and sample components were necessary. Load-carrying tests on specimen components enable a realistic assessment of the load-bearing behavior and serve to back up a static analysis. The test setup and the results of the component tests, which were called for

TABLE 2—Glass transition temperatures according to ASTM D 4065.

Adhesive	Glass transition temperature (°C)
AC3	48
AC4	67
EP1	36
EP4	44
PUR1	24
PUR2	39

within the scope of the approval procedure for the glass corridor, are summarized below.

In addition, shear strength values had to be obtained from small-scale specimens (glass–glass adhesive joints in single shear). Compression shear tests were carried out at various temperatures between -25 and $+75^{\circ}\text{C}$, as well as following accelerated aging.

Methods and Test Setup

Block Shear Test—The shear strengths were determined using glass–glass adhesive joints in single shear at temperatures of -25 , 0 , $+25$, $+50$, and $+75^{\circ}\text{C}$ in a block shear test (Fig. 10), according to the works standard of the adhesive manufacturer DELO-Norm 5 [20,21]. Besides taking into account different temperatures, some of the test specimens were subjected to accelerated aging and subsequently tested at room temperature following conditioning for 24 h. The parts joined by the adhesive were made from annealed glass, but chemically toughened glass for the tests at -25 , 0 , and $+25^{\circ}\text{C}$. Toughened glass became essential to avoid glass failure during the tests at lower temperatures. A preliminary study has proven that the bonding strength was not affected by using the two different glass types. The glass components measured 20×20 mm and were 5 mm thick. The adhesive joint was set to a thickness of 1.5 mm, with a 5-mm overlap between the two parts. Loading in a universal testing machine was carried out with displacement control at a rate of 10 mm/min until failure of the specimen. The load at failure was recorded. Ten specimens were tested per parameter.

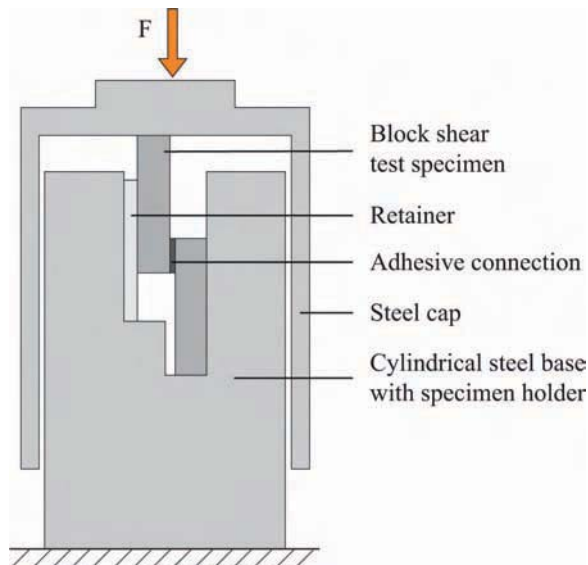


FIG. 10—Block shear test setup (schematic).

Climatic cycle tests plus immersion in water and cleaning agent (commercial dish liquid W5 Power Blue, basic) have proved to be relevant aging scenarios for acrylate adhesive joints [22]. The specimens were, thereafter, stored for 21 days in a climate chamber with cyclic variation of humidity and temperature. The conditions at the start of the test were +40°C and 95 % relative humidity. After maintaining these conditions for 15 h, the temperature was lowered to -20°C and kept constant at this level for 2 h. Afterward, the climatic conditions were changed to +80°C and 50 % relative humidity. A weathering cycle lasted a total of 24 h, including the ramp up/down times, which means that within the period of the test, the cycle was repeated 21 times. Other test specimens were stored for 21 days at +45°C in a 0.1 % detergent solution or in pure water.

Loading Test—Both the dimensions and the glazing of the specimens—frame corners with short legs 0.75 m long—corresponded with those of the original component. The laminated safety glass of the elements consists of four plies of fully tempered glass each 10 mm thick. The two outer layers of PVB are 1.90 mm thick, the inner layer 1.52 mm. The depth of the cross section was 300 mm throughout. A total of ten non-aged sample components were tested at room temperature. Five tests were carried out with a transparent plastic setting block, but the setting block was omitted from the other five to study the influence of the use and positioning of the setting block in more detail. The transparent plastic setting block carries the vertical load in the event of failure of the adhesive to meet the requirements of a fail-safe concept. Additionally, the block prevents creeping of the bonded joint under long-term loading, which otherwise may lead to large deformations and unwanted glass-glass contact.

Each sample component was clamped in a test rig and loaded by a hydraulic cylinder at the outermost end of the cantilever (Fig. 11(a)). The base of the sample components was cast into the frame using an injection mortar to reduce slip to a minimum. The load was applied incrementally up until failure or until a maximum load, governed by the test setup, of about 95 kN was reached (Fig. 11(b)). The load increment was 10 kN up to a total load of 40 kN, thereafter, the

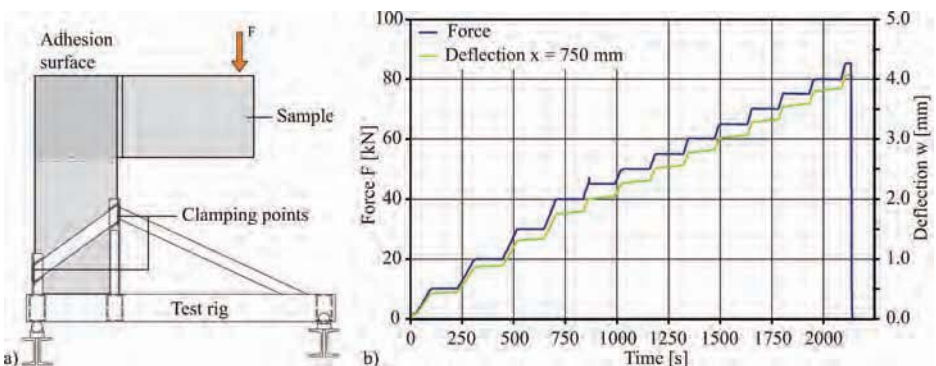


FIG. 11—(a) Loading test setup (schematic), and (b) load and deflection in component testing, frame SC7.

increments were reduced to 5 kN. Every loading increment was held for 2 min. A numerical simulation to check the loading level in the test revealed that the characteristic strengths of toughened safety glass were far exceeded at maximum load. If the joint does not fail, then the glass, therefore, becomes relevant to the design.

The deflection at the end of the cantilever essentially depends on the rotation at the adhesive joint. The deformation of the glass itself; on the other hand, is small. The vertical displacement of the frame beam was, therefore, measured by transducers at two points along its top edge. The vertical deflection at the end of the cantilever was obtained from the two measurements by linear extrapolation. A specific fixture was developed to support the displacement transducers. The device was clamped onto the specimen directly above the restraint. The transducers measured only the relative deformation between the post and the cantilever beam. Hence, potential slip at the fixing of the specimen component did not impair the results. The stresses in the glass were recorded with strain gauges (Fig. 12). The critical points for this were determined in a numerical model. A photoelastic analysis was carried out during the tests on the components to obtain a qualitative statement regarding the change in the stress distribution within the corner zone.

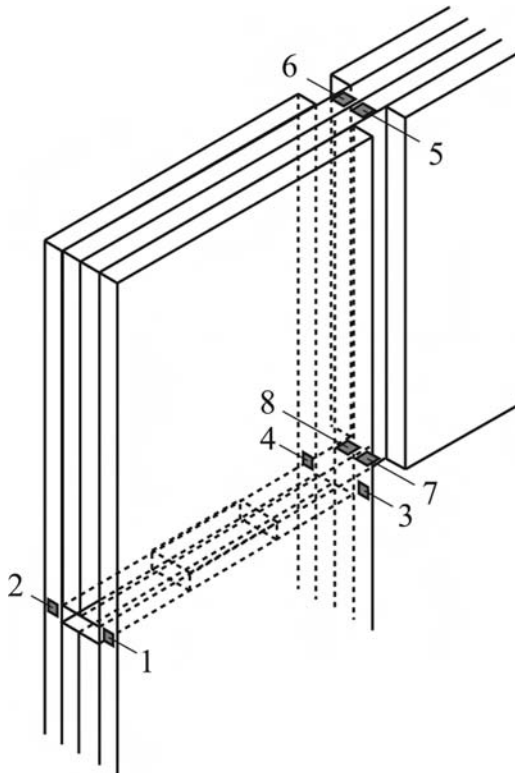


FIG. 12—Strain gauge positions.

Specimen Preparation

Block Shear Test Specimens—The small-scale components to be joined were produced under laboratory conditions. Following thorough cleaning of the surfaces, the adhesive was applied exclusively to the air side of the glass, because scientific studies [4] have proved that the adhesion of acrylate adhesives is lower on the bath side. The radiation for curing the adhesive is transmitted from both sides for a period of 60 s with an intensity of about 60 mW/cm² UV-A, measured at the position of the component to be joined.

Specimen Components—The adhesive joints at the frame corners were produced at room temperature in the testing shed of the Institute for Building Construction. The areas to which adhesive was to be applied on both components—frame support and cantilever—were thoroughly cleaned with a mixture of acetone and isopropanol. Final, careful cleaning shortly before fitting the parts together was carried out with a solvent-based cleaner supplied by the adhesive manufacturer.

The two individual parts of the sample component were aligned in a jig and fixed in position. The bottom and sides of the joint were sealed to prevent uncontrolled loss of the adhesive during application. The bottom seal, a transparent adhesive tape made from acrylate, remains in place, whereas the side seals are removed once the adhesive has cured.

The two adhesive joints at the frame corner were filled with adhesive one after the other. A flat nozzle with an oval cross section enables the viscous adhesive (viscosity approximately 17500 mPas) to be injected into the ~1.9-mm-wide gap provided for the adhesive. A housing shields the working area against the ingress of unwanted daylight. Once the adhesive had been injected, intermittent exposure to low-energy radiation from UV fluorescent lamps on both sides followed (intensity at a distance of 7 cm: UV 1.8 mW/cm², blue 3.5 mW/cm²; intensity at 12 cm: UV 1.3 mW/cm², blue 2.9 mW/cm²). Three lamps positioned at a slight angle were placed on both sides. This meant that curing in the bottom part of the adhesive joint proceeded faster than in the top part of the joint, and that meant that the loss of adhesive, the volume of which decreases during curing, could be compensated for by the reserves of adhesive at the sides and top of the joint. Finally, brief exposure to radiation from a focused beam lamp with a high output (intensity at a distance of 60 cm: UV 12.7 mW/cm², blue 67.9 mW/cm²) ensured that the final strength and stiffness were achieved. This production method was developed for the all-glass enclosure described in Ref [15] (see also “Previous Work” above). Comprehensive technology testing for this project revealed that the combination of low-intensity curing in the first stage and high-intensity curing in the second stage lead to a high bearing capacity, as well as to an excellent optical quality of the joint.

Results

Shear Strength—In the majority of specimens, the adhesive joint failed in the compression shear test. Owing to the use of chemically toughened glass for the tests below room temperature, failure of the glass was rare. The results of

the tests are given in Table 3. The block shear figures represent the 5 % fractile for a 95 % confidence level on the basis of a logarithmic normal distribution.

For the acrylic adhesive tested, the shear strength is dependent on the temperature. However, the degree of this influence is not the same as that for the tests on the pure material specimens. The mean shear strength values are quite similar between -25 and $+50^{\circ}\text{C}$. Only at a temperature of $+75^{\circ}\text{C}$ does the mean shear strength decrease significantly. The results of the test show considerable scatter at a temperature of -25°C , which indicates embrittlement of the material. The 5 % fractiles for similar mean values are, therefore, far below the values obtained in tests at 0°C , room temperature, and $+50^{\circ}\text{C}$. Therefore, limit value considerations, taking into account the different stiffnesses and strengths, are recommended for the structural calculations.

The shear strength of the joint was seriously reduced by storing the specimens in water or detergent. One prime reason for this could be the small size of the specimen's adhesive joint (5×20 mm). The surface area is very large when compared with the area of the adhesive joint, which considerably increases the influence of external media. As this ratio is much more favorable with a typical bonded frame corner, an improvement is to be expected here. Tests on aged full-size specimens were, however, regarded as too involved, meaning that for the applications shown above, direct weathering and the direct ingress of cleaning agents were ruled out by the detailing at the joint. No negative influence can be deduced from the results following climatic cycle tests. Indeed, the mean shear strength values rise. However, greater scatter of the results leads to the 5 % fractiles lying on a similar level as the values for room temperature.

Load-Bearing Capacity—The adhesive joints remained intact in all ten tests. In most cases the outer plies of glass in the posts failed (Fig. 13(a)). In some tests the specimens did not fail at all, which meant that these tests had to be stopped after reaching the upper load limit of the testing machine. The maximum stress was in all cases detected in the tension zone of the frame post at the transition from four to two plies of glass (strain gauges 1 and 2). Consequently, there is a direct relationship between the failure load of the frame corner and

TABLE 3—Results of block shear tests.

Test conditions	Average value (MPa)	Variation coefficient (%)	5 % fractile (MPa)
$T = -25^{\circ}\text{C}$, no aging	12.6	27.3	5.5
$T = 0^{\circ}\text{C}$, no aging	14.8	9.0	11.2
$T = +25^{\circ}\text{C}$, no aging	13.2	9.9	9.9
$T = +50^{\circ}\text{C}$, no aging	13.4	10.2	10.0
$T = +75^{\circ}\text{C}$, no aging	7.3	8.1	5.6
$T = +25^{\circ}\text{C}$, cleaning agent	5.1	37.9	1.5
$T = +25^{\circ}\text{C}$, water immersion	4.6	53.8	1.0
$T = +25^{\circ}\text{C}$, climatic cycle	19.6	17.0	11.7

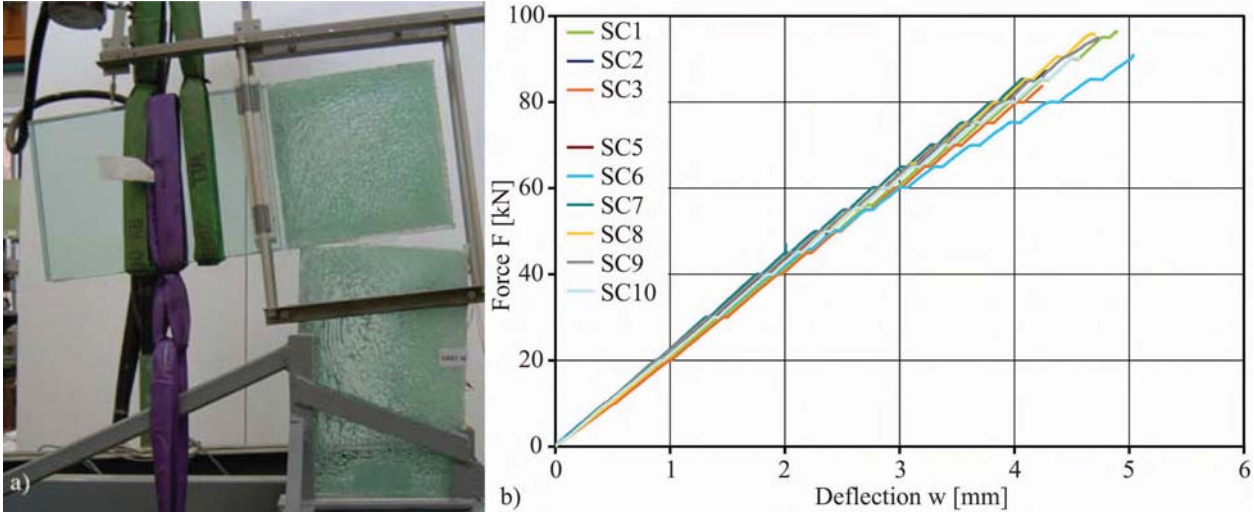


FIG. 13—Component testing: (a) glass failure, and (b) load-bearing behavior of specimen components.

TABLE 4—Results of component testing.

Specimen component	Setting block	Maximum load F_{max} (kN)	Glass stress $\sigma_{g,max}$ (MPa)	Strain gauge no.	Failure/stop criterion
SC 1	Yes	96.4	165.3	2	Limit of testing machine
SC 2	Yes	87.2	148.0	1	Breakage of glass post
SC 3	Yes	83.7	147.5	2	Breakage of glass post
SC 4	Yes	93.5	158.3	2	Breakage of glass post
SC 5	Yes	80.0	137.4	1	Breakage of glass post
SC 6	No	90.9	157.1	1	Breakage of glass post
SC 7	No	85.4	151.1	2	Breakage of glass post
SC 8	No	95.9	165.5	2	Limit of testing machine
SC 9	No	94.9	167.0	1	Limit of testing machine
SC 10	No	90.3	165.6	2	Breakage of glass post
Mean value		89.8	Coefficient of variation $\nu = 0.0622$		
5 % fractile		73.8			

the maximum achievable tensile bending strength of the glass. Table 4 shows the results of the tests.

The tests were evaluated statistically. For this, in the case of sample components that remained intact, the maximum load was defined as the failure load. As the measurements exhibit only a small scatter, a normal distribution can be assumed. A logarithmic normal distribution should only be used with coefficients of variation >0.10 [23]. The 5 % fractile (95 % confidence level) of the failure force is 73.8 kN.

The force-deflection curves (Fig. 13(b)), based on the load-bearing tests, reveal a homogeneous picture and are almost linear. All frame corners—with or without setting block—exhibit an equivalent deformation behavior both qualitatively and quantitatively. These results indicate that a setting block does not exert any significant influence on the load-bearing behavior of an intact frame corner at room temperature. Only the measurements obtained from test No. 4 (SC4) are incorrect because of a measuring error. The deformation measurement was distorted by contact between the displacement transducer mounting and the test rig. These values are, therefore, not shown in the diagram.

Numerical Simulation

The geometry and the loads on the specimen used in the component tests were modeled with the ANSYS FEM software⁵ in a numerical simulation. In this simulation, the glass and the adhesive joint were modeled with volume elements

⁵ANSYS release 12.1: ANSYS, Inc., Southpointe 275 Technology Dr., Canonsburg, PA 15317.

TABLE 5—Material constants.

Material	E (MPa)	μ (-)
Glass	70,000	0.23
Adhesive	234	0.42

(SOLID 186, 3D 20-node structural solid). The plastic setting block was omitted from the model. For reasons of symmetry, calculation of half the glass structure was adequate. The material constants used in the numerical analysis are shown in Table 5. It was assumed that strains remain small and lie below the yield point of the adhesive, so a linear-elastic material behavior could be assumed. The Young's modulus of the adhesive was determined according to Ref [18] using the average values of the stress–strain relation (Fig. 6) at room temperature. The model was first applied for planning the component tests to determine the positions of maximum tensile stress in the glass. It was at these positions that strain gauges for monitoring the tensile stresses were attached for the tests. In a second step, the results of the numerical simulation (Figs. 14–16) were compared with the values measured during the component tests.

The maximum tensile stresses were found to occur in each case at the transition from the frame beam or frame post to the adhesive. This is where only two glass plies are involved in transferring the load. Table 6 shows the calculated and measured stress and deformation values at the critical points for a

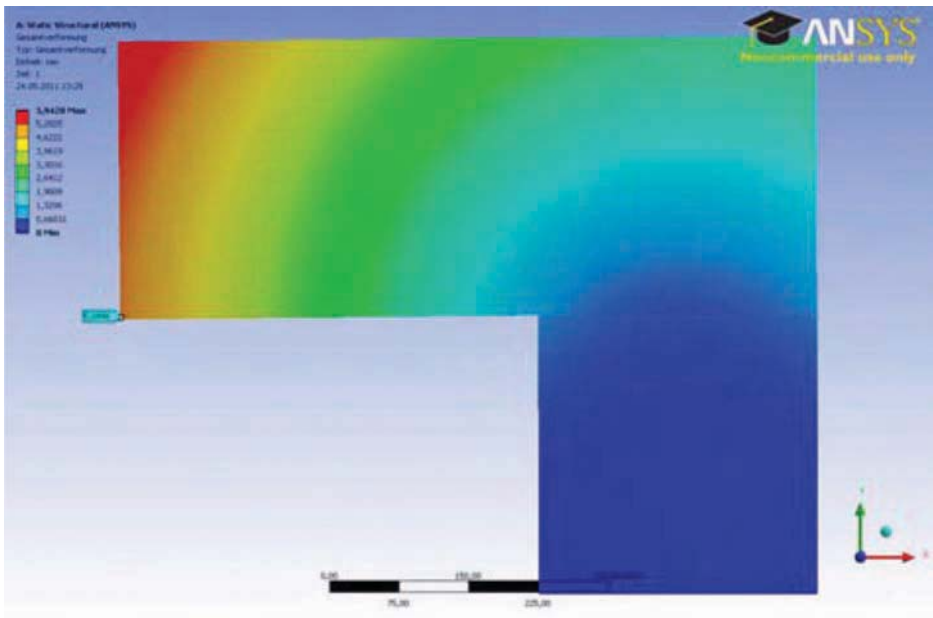


FIG. 14—Results of the numerical analysis with a load of 80 kN – overall deformations.

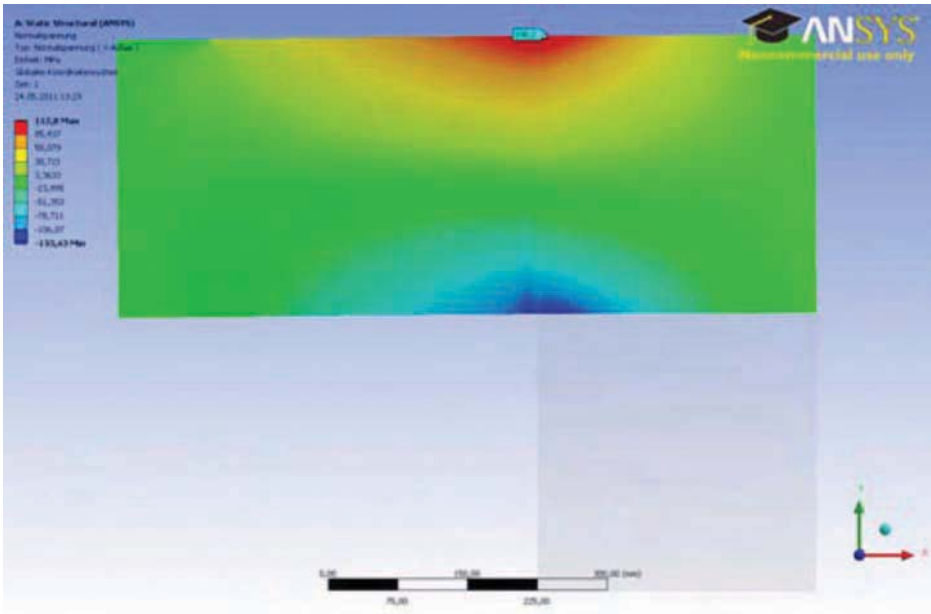


FIG. 15—Results of the numerical analysis with a load of 80 kN – stresses in x direction in glass cantilever.

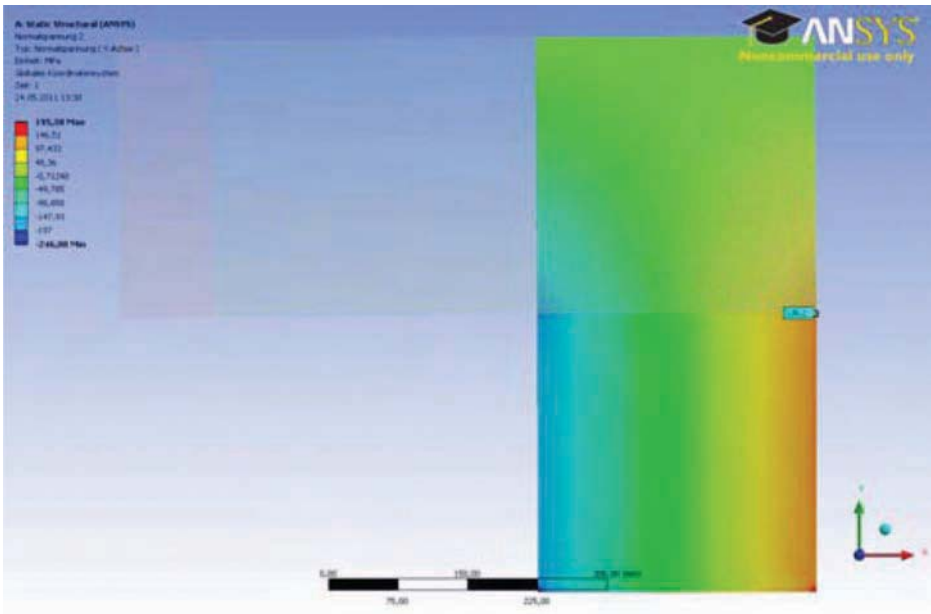


FIG. 16—Results of the numerical analysis with a load of 80 kN – stresses in y direction in glass post.

TABLE 6—Comparison of calculated and measured values at a load of 80 kN.

Strain gauge position	1	2	5	6		
Specimen component		Glass	Glass	Glass	Glass	Deflection at
	Load	stress	stress	stress	stress	end of cantilever
	(kN)	σ_g (MPa)	σ_g (MPa)	σ_g (MPa)	σ_g (MPa)	f_y (mm)
SC 1	80.0	138.9	139.4	110.9	108.9	4.0
SC 2	80.0	136.5	—	108.7	109.7	3.9
SC 3	80.0	136.4	141.8	108.7	113.8	4.1
SC 5	80.0	137.4	136.9	—	—	3.9
SC 6	80.0	141.0	128.4	113.3	104.8	4.3
SC 7	80.0	130.3	142.8	104.8	116.1	3.8
SC 8	80.0	136.1	140.0	112.3	96.8	3.8
SC 9	80.0	144.0	132.9	—	—	3.9
SC 10	80.0	124.5	148.5	—	—	3.9
Measured value (mean)		136.1	138.8	109.8	108.3	4.0
FE calculated		135.2	135.2	108.2	108.2	5.1
Deviation		-0.7 %	-2.6 %	-1.5 %	-0.1 %	+29.0 %

load of 80 kN. There was good agreement between the calculated values and the mean values obtained from experimental studies. The model predicts the stresses in the glass with very good accuracy. The deformations are slightly overestimated by the numerical calculations but are, therefore, on the safe side. This may result from the identification of the material properties on the bulk material. Assuming a linear-elastic material behavior for modeling the adhesive is, therefore, suitable for the numerical analysis of the global load-bearing system. As a next step, the numerical model may be utilized for a sensitivity analysis focusing on the structural behavior at different temperature levels.

Conclusions

Adhesives enable individual glass elements to be combined to form transparent load-bearing structures. Previous research work and a construction project that has already been realized enabled the derivation of key requirement criteria that must be met by an adhesive suitable for a glued frame corner. Preliminary studies enabled an adhesive to be determined that exhibits improved working properties compared with the composition used in the past and at the same time still satisfies the structural requirements. The load-carrying capacity of the glued connection at room temperature was confirmed by tests on components. A setting block provided for the failure case of the adhesive joint was shown to have no effect on the global load-bearing behavior of the frame corner.

Acknowledgments

The authors would like to thank the German Federal Ministry of Economics and Technology for supporting this research project. Our thanks are also

extended to the research project partners GSK—Glas Statik Konstruktion, First Glas, and Bayer Glasbau in Germany, as well as 3M, DELO Industrial Adhesives, and Henkel, Huntsman, and Panacol for supplying the adhesives.

References

- [1] Geiß, P. L., Luhn, R., Sändig, S., and Wagner, A., "Improvement of the Long-term Durability of Glass Bonds by Process-integrated Sustainable Surface Treatment Processes," *8. Kolloquium: Gemeinsame Forschung in der Klebtechnik*, Dechema, Frankfurt, Germany, 2008, pp. 20–22.
- [2] Luhn, R., Sändig, S., Geiß, P., and Wagner, A., "Influence of Surface Treatment on the Adhesion Qualities of Glasses," *Euradh 2008—Adhesion '08*, Oxford, Great Britain, 2008, pp. 305–308.
- [3] Overend, M., Jin, Q., and Watson, J., "The Selection and Performance of Adhesives for a Steel-Glass Connection," *Int. J. Adhes. Adhes.*, Vol. 31, No. 7, 2011, pp. 587–597.
- [4] Weller, B. and Tasche, S., "Experimental Evaluation of Ultraviolet and Visible Light Curing Acrylates for Use in Glass Structures," *J. ASTM Int.*, Vol. 6, No. 9, 2009, pp. 135–156.
- [5] Watson, J., Overend, M., Jin, Q., and Lai, W., "Premature Failure in UV-Cured Adhesive Joints," *ISAAG 2010*, Munich, Germany, 2010.
- [6] Louter, C., Belis, J., Veer, F., and Lebet, J.-P., "Durability of SG-Laminated Reinforced Glass Beams: Effects of Temperature, Thermal Cycling, Humidity and Load-Duration," *Constr. Build. Mater.*, Vol. 27, No. 1, 2011, pp. 280–292.
- [7] Abeln, B. and Preckwinkel, E., "Development of Hybrid Glass-Steel-Beams," *Stahlbau*, Vol. 80, No. 4, 2011, pp. 218–225.
- [8] Weller, B. and Weimar, T., "Development of a new facade system with hybrid glass-steel elements," *Glass Performance Days*, Tampere, Finland, 2011, pp. 522–524.
- [9] Blandini, L., "Structural Use of Adhesives for the Construction of Frameless Glass Shells," *Int. J. Adhes. Adhes.*, Vol. 27, No. 6, 2007, pp. 499–504.
- [10] Vogt, I., *Strukturelle Klebungen mit UV- und lichterhärtenden Acrylaten [Structural bonded joints with UV and light curing acrylates]*, Dissertation, Technische Universität Dresden, 2009.
- [11] Richards, B., *New Glass Architecture*, Laurence King Publishing Ltd., London, 2006.
- [12] Schittich, C., "Taking a Second Look: Glass Pavilion at Broadfield House in Kingswinford," *Detail – Review of Architecture*, Vol. 51, Nos. 1/2, 2011, pp. 6–9.
- [13] Nijisse, R., "Design and Construction of an All Glass Cube for the Raaks Project in Haarlem (NL)," *Challenging Glass 2*, Delft, The Netherlands, 2010, pp. 161–168.
- [14] Schadow, T., *Beanspruchungsgerechtes Konstruieren von Klebverbindungen in Glas-tragwerken [Designing adhesively bonded joints to meet structural requirements]*, Dissertation, Technische Universität, Dresden, 2006.
- [15] Weller, B., Döbbel, F., Nicklisch, F., Prautzsch, V., and Rucker, S., "All Glass Enclosure at the Leibniz Institute for Solid State and Materials Research in Dresden, Germany," *Stahlbau Spezial 2010 – Konstruktiver Glasbau*, March 2010, pp. 34–40.
- [16] Weller, B., Kothe, M., Nicklisch, F., Schadow, T., Tasche, S., Vogt, I., and Wunsch, J., "Bonding for Structural Glass Applications," *Stahlbau Kalender 2011*, Ernst & Sohn, Berlin, 2011, pp. 587–646.
- [17] DIN EN ISO 527-2 (1996-07), *Plastics – Determination of Tensile Properties – Part 2: Test Conditions for Moulding and Extrusion Plastics*, Beuth, Berlin, 1996.
- [18] DIN EN ISO 527-1 (1996-04), *Plastics – Determination of Tensile Properties – Part 1: General Principles*, Beuth, Berlin, 1996.

- [19] ASTM D4065, 2006, "Standard Practice for Plastics: Dynamic Mechanical Properties: Determination and Report of Procedures," *Annual Book of ASTM Standards*, Vol. 08.02, ASTM International, West Conshohocken, PA, 2006.
- [20] DELO Norm 5 (2010-03), *Determination of the Block Shear Strength*, DELO, Windach, 2010.
- [21] DELO Industrial Adhesives, *Bond It: Reference Book on Bonding Technology*, DELO, Windach, 2007.
- [22] Tasche, S., *Strahlungshärtende Acrylate im Konstruktiven Ingenieurbau [Light curing acrylates in glass structures]*, Dissertation, Technische Universität, Dresden, 2007.
- [23] Deutsches Institut Für Bautechnik, *Basics for the Evaluation of Building Materials, Components and Building Types in the Mark and Registration Procedure*, Berlin, 1986.

Christopher C. White,¹ Donald L. Hunston,² Kar Tean Tan,²
James J. Filliben,³ Adam L. Pintar,³ and Greg Schueneman⁴

A Systematic Approach to the Study of Accelerated Weathering of Building Joint Sealants

ABSTRACT: An accurate service life prediction model is needed for building joint sealants in order to greatly reduce the time to market of a new product and reduce the risk of introducing a poorly performing product into the marketplace. A stepping stone to the success of this effort is the precise control of environmental variables in a laboratory accelerated test apparatus in order to produce reliable weathering data that can be used to generate a predictive model. This contribution reports a systematic study, using a novel laboratory test apparatus, investigating the individual and synergistic impacts of four environmental factors (cyclic movement, temperature, relative humidity, and ultraviolet radiation) on the durability of a sealant system. The apparatus used is unique because it not only allows the precise control of environmental factors but also permits in situ characterization tests so that the specimens

Manuscript received June 7, 2011; accepted for publication February 29, 2012; published online May 2012.

¹National Institute of Standards and Technology, Engineering Laboratory, Materials and Structural Systems Division, 100 Bureau Dr., Stop 8615, Gaithersburg, MD 20899-8615 (Corresponding author), e-mail: christopher.white@nist.gov

²National Institute of Standards and Technology, Engineering Laboratory, Materials and Structural Systems Division, 100 Bureau Dr., Stop 8615, Gaithersburg, MD 20899-8615.

³National Institute of Standards and Technology, Information Technology Laboratory, Statistical Engineering Division, 100 Bureau Dr., Stop 0001, Gaithersburg, MD 20899-0001.

⁴Forest Products Laboratory, 1 Gifford Pinchot Dr., Madison, WI 53726.

Certain commercial products or equipment are described in this paper in order to specify adequately the experimental procedure. In no case does such identification imply a recommendation or endorsement by the National Institute of Standards and Technology (NIST), nor does it imply that the mentioned item is necessarily the best available for the purpose.

Cite as: White, C. C., Hunston, D. L., Tan, K. T., Filliben, J. J., Pintar, A. L. and Schueneman, G., "A Systematic Approach to the Study of Accelerated Weathering of Building Joint Sealants," *J. ASTM Intl.*, Vol. 9, No. 5. doi:10.1520/JAI104091.

Copyright © 2012 by ASTM International, 100 Barr Harbor Drive, PO Box C700, West Conshohocken, PA 19428-2959.

need not be removed from the apparatus chamber. Graphical and quantitative statistical approaches have been used to analyze the data. The study shows that the critical role of each individual factor, as well as synergism among the different factors, can be readily quantified, and modes of degradation possibly can be identified.

KEYWORDS: Sealant, Service Life Prediction, model, construction, modulus, SPHERE, Statistics

Introduction

The accurate prediction of in-service performance in less time than is required for field tests and tests on structures has remained a modern unresolved scientific issue. Reliable performance data still require long-term field exposure. Such tests are needed in order to decrease the risk of introducing a poorly performing product into the marketplace. However, the cost of developing new products is directly related to the product development time and the time to market. The more time a product spends in the pipeline, the greater investment required and the smaller the eventual profit. Furthermore, long test times clearly hamper product innovations. Therefore, extensive efforts have been made to design short-term tests that provide an accurate indication of how well a sealant will perform in actual use. Although modern commercial sealants typically are designed to last for 20 years or more, studies in the construction industry have found a 50 % failure rate in less than 10 years and a 95 % failure rate within 20 years after installation [1–3]. These findings clearly show the inadequacy of current accelerated test methods and the need for the development of a reliable service life prediction methodology based on improved accelerated test methods.

The difficulties that hinder efforts to relate field and laboratory results include (a) unresolved differences between, and a poor understanding of, the failure modes in the two environments [4–6] and (b) a lack of methods with which to accurately quantify the effects of the environmental degradation factors in laboratory and field tests [4,5]. In particular, visual evaluation of physical performance, including crack and chip size, chalking behavior, and color change, is one of the main tests for the effects of weathering [7–9]. Although such a methodology might relate to a customer-perceived failure mode, it is qualitative and time consuming and provides little insight into the mechanisms leading to these macroscopic changes. In this paper and in previous reports [10–19], many of these issues have been resolved. Previous studies examined the impact of temperature [10–17], humidity [13,16–18], applied static and dynamic strain [18], and outdoor field exposure [10,14,15,17,19] on the durability of sealants, and they also reported the design of novel laboratory and field testing devices [14,15,19,20]. The success of this endeavor depends upon the use of a reliability-based methodology to make rapid, precise, and accurate environmental performance predictions. In this paper, we consider only the problem of identifying and ranking important degradation factors.

The research reported here represents a continuing effort in predicting the service life of building joint sealants. Although temperature, relative humidity, ultraviolet (UV) radiation, and cyclic movement have been identified as

prevalent aging factors for sealants [21], there is no study thus far that systematically and quantitatively shows the impact of these environmental factors when they are acting either independently or synergistically on sealant properties. The objective of this study, therefore, is to design a systematic accelerated protocol that can provide a quantitative platform for investigating the individual and synergistic impacts of environmental factors. The study employs a custom-made laboratory apparatus with the capability to control these four environmental factors to high levels of accuracy, precision, and reproducibility [20]. Moreover, because the deformation can be controlled, in situ mechanical characterization tests can be performed without removing specimens from the chamber. Thus, this method permits comparison of the dose of laboratory degrading factors in a quantitative manner. It is demonstrated that the individual and synergistic effects of factors on the durability of sealants can be revealed using this reliability-based approach. The wealth of data generated from the study is expected to facilitate the prediction of potential failure modes and the generation of a service life prediction model for sealant materials.

Experiment

Materials and Specimen Preparation

A commercial sealant, provided by a member of a National Institute of Standards and Technology/industry consortium [5], was fabricated into sealant joints conforming to ASTM C719 [22] (Fig. 1). The chemistry of the sealant tested was unknown, but physical examination and testing revealed an elastomeric behavior typical of sealants, and the specimen had a white, opaque appearance.

Exposure Conditions and Characterization

The four custom-built sealant testing chambers employed in this study have the ability to independently control temperature ($\pm 0.2^\circ\text{C}$), relative humidity (RH) ($\pm 0.5\%$), UV radiation, and cyclic movement. Because the deformation can be controlled, mechanical characterization tests can be performed without removing the specimens from the chamber. A full description of the chamber design is documented elsewhere [20]. The temperature was controlled with a precision temperature regulator, humidity control was accomplished via proportional mixing of dry and saturated air, and a highly uniform flux of UV radiation was attained by attaching the chambers to an integrating sphere-based radiation source (simulated photodegradation via high energy radiant exposure

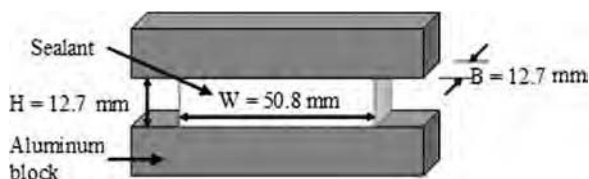


FIG. 1—Schematic illustration of the test specimen geometry used (not to scale).

[SPHERE] [23]). The SPHERE is equipped with a microwave-powered lamp system consisting of six VPS/I600-60 lamp modules. Partially enclosing each light source is a dichroic mirror that removes almost all of the thermal radiant energy (i.e., visible and infrared radiation) from the beam while reflecting the spectra UV emissions into the SPHERE. Thus, without external heating, the temperature in the chamber is about $27^{\circ}\text{C} \pm 2^{\circ}\text{C}$. A cut-off filter is positioned between the light source assemblage and the SPHERE that prevents almost all of the radiation below 290 nm from entering the SPHERE. It should be noted that no attempt was made in this study to simulate the full spectrum of terrestrial solar radiation or the spectra power distribution of the UV portion of such. Thus, the sealants were exposed to an output in the spectral region between 290 nm and 450 nm and an irradiance of approximately 500 W/m^2 . A comparison of the spectral power distribution of the SPHERE radiation source with the reference solar UV spectral distribution from ASTM G173-03 [24] is shown in Fig. 2. Hereinafter, the radiation is referred to as UV for simplicity.

The sealant specimen was attached between a fixed and a movable grip with a computer-controlled stepper motor and a transmission system providing precise movement control. Each chamber had two motors, with four specimen holders on each motor, for a total of eight specimen holders. Each specimen holder was attached to a hermetically sealed load cell with a capacity of $\pm 113.4 \text{ kg}$. Two linear variable differential transformers (LVDTs), one for each motor, with a deflection range of $\pm 6.35 \text{ mm}$ were used to measure sealant movement. Data from load cells

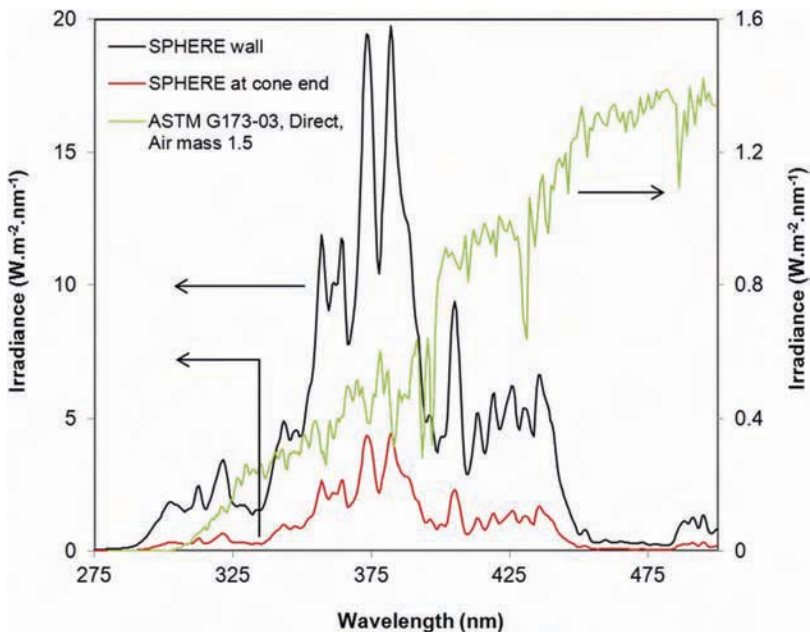


FIG. 2—Comparison of the irradiance of SPHERE and the ASTM G173-03 solar spectrum.

and LVDTs were fed directly into a Keithley 2701 ethernet-based data acquisition system. A custom LabVIEW program was written to collect the voltage measurements from the Keithley system every 15 s. The data were averaged once per minute and appended to a tab-delimited database on a remote server.

Data

There were four exposure variables: temperature, RH, cyclic movement, and UV radiation. In all cases, the exposure time was fixed at 1 month. The air temperature was held at 30°C, 40°C, or 50°C. The RH was maintained at 0 %, 25 %, 50 %, or 75 %. Note that exposure to higher levels of RH, liquid water (which allows the possibility for the abstraction of components in the sealants), and freezing conditions is an important area that is not covered in the current study. The deformation involved cyclic movement in a triangular wave varying from 0 % strain to a prescribed maximum strain level at a rate of 38 min/cycle. The maximum strain level was 0 %, 8 %, 15 %, or 25 %. The UV radiation was either on or off. Of 96 possible conditions in the full factorial experimental design, 54 were investigated. These conditions generated a total of 312 data points, which were subsequently trimmed down to 293 after data cleaning to remove out-of-range or suspicious values resulting from faulty collection.

Prior to and after the exposure tests, the specimens were allowed to recover and the mechanical properties of each were characterized at room temperature. The specimens first were subjected to two loading-unloading-recovery cycles at a maximum strain of 26 %. This was followed by a stress relaxation measurement at a strain of 18 %. The strain history used is shown schematically in Fig. 3. The loading-unloading tests utilized a crosshead speed of 2.64 mm/min, so the total time under load was 150 s. To allow for viscoelastic recovery, the specimen was held at 0 % strain for 1500 s before the next step. The purpose of the two loading-unloading cycles was to quantify the Mullins effect and eliminate its influence in the subsequent characterization test. In stress relaxation measurements, the crosshead speed was 70 mm/min, which meant that the specimen reached the hold strain in just under 2 s. In order to allow for non-instantaneous loading, data points during the first 15 s were ignored.

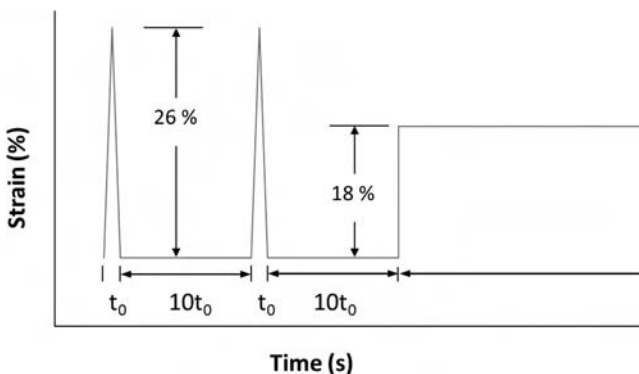


FIG. 3—Strain history used for Mullins cycles and stress relaxation tests.

From the stress relaxation data, an apparent modulus E_a was calculated using a relationship based on the statistical theory of rubberlike elasticity [25–27].

$$E_a(t, \lambda) = \frac{3L(t)}{WB(\lambda - \lambda^{-2})} \quad (1)$$

where:

W and B = width and breadth of the sealant (Fig. 1), respectively,

L = load,

t = time, and

λ = extension ratio, which is given by

$$\lambda = 1 + \frac{\Delta}{H} \quad (2)$$

where:

Δ = crosshead displacement, and

H = undeformed height of the sealant.

From this information, an apparent modulus versus time curve is generated. The magnitude and time dependence of this apparent modulus are related to the molecular structure of the sealant. If the changes in this modulus with exposure time are monitored in a degradation experiment, changes in the molecular structure of the sealant can be estimated. Changes in the modulus over time also provide crucial information about how a sealant responds to the stresses imposed by the expansion and contraction of a structure over the diurnal cycle. A modulus ratio F was used to characterize the effect of the environment on E_a .

$$F = \frac{E_a(t)}{E_{a,0}(t)} \quad (3)$$

in which $E_a(t)$ and $E_{a,0}(t)$ are the apparent moduli before and after exposures, respectively.

The relative effects of the various environmental factors can also depend on the type of evaluation used as the criterion of failure. We believe that changes in the modulus are a clear indication that there are chemical and mechanical changes occurring in the sealant. Initially, these changes might be either detrimental or beneficial to sealant performance, but eventually, if the changes become large enough, the performance will likely deteriorate. For the particular material tested here, we have found that a decrease in the modulus is a precursor to cracking and debonding, which would allow moisture penetration (the usual definition of failure).

Results and Discussion

Mullins Effect

As mentioned, the characterization tests involved two load-unload-recovery cycles so as to examine the Mullins effect. Typical results for the stress-strain curves generated with a fresh sample are shown in Fig. 4. Like other rubberlike

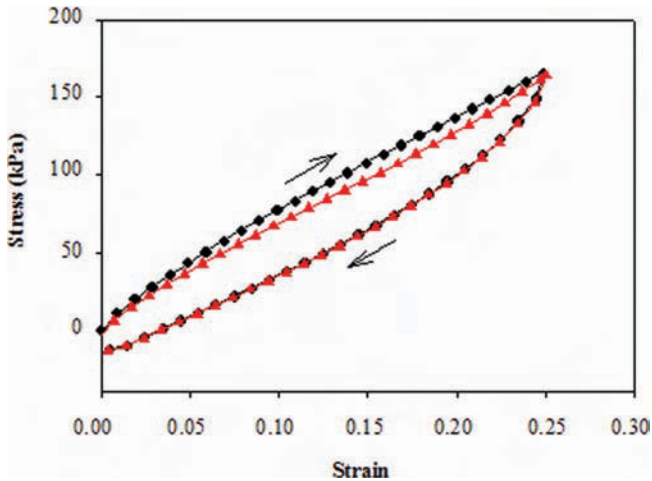


FIG. 4—Loading-unloading tests on a fresh specimen at a crosshead speed of 2.64 mm/min to a max strain of 25 %. Circles and triangles represent the first and second loading cycles, respectively. Arrows indicate the loading-unloading directions.

materials, these sealants exhibit a strong Mullins effect in that there is a significant reduction in the stress at a given strain level during the second loading, as compared to the stress level on the first loading. The unloading curves, however, are identical.

Stress Relaxation Behavior

Apparent moduli versus relaxation time curves for specimens before and after exposure to motion at 25 % maximum strain, 75 % RH, and 30°C and with UV radiation are shown in Fig. 5(a). The curves represent the average of up to four replicates, and the vertical bars indicate one standard deviation. The difference seen in Fig. 5(a) between the two curves is significant. Note that there is no change in the curve shape, implying that the time dependence of the apparent modulus is very similar before and after exposures. However, the magnitude of the apparent modulus decreased by a small amount after exposure. In order to facilitate comparison between different exposure conditions, stress relaxation data are presented as a modulus ratio (F) as a function of the relaxation time [Eq 3, Fig. 5(b)]. In such a graph, no change would be represented by a horizontal straight line at $F = 1$. A horizontal line above or below $F = 1$ indicates that exposure caused a vertical shift in the stress relaxation curve but no change in shape; i.e., the time dependence did not change. Something other than a horizontal straight line indicates a change in the time dependence. The experimental uncertainty can be shown as a hashed region on either side of $F = 1$, so if the points for a given curve fall within this region, there are no changes outside the experimental uncertainty.

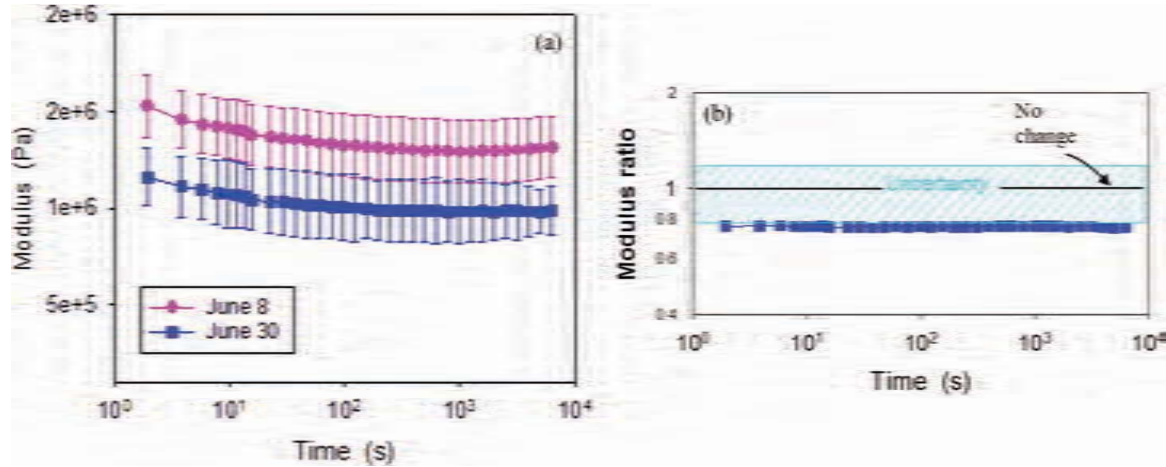


FIG. 5—(a) Variation of apparent modulus as a function of relaxation time for the sealant under conditions of 25 % max strain/30°C/75 % RH before and after exposures. The error bars represent one standard deviation from mean values. (b) Variation of modulus ratio as a function of relaxation time for the sealant under the same conditions as in (a) before and after exposures. The hashed region represents the combined experimental error from the data before and after exposures. If the points for a given curve fall within this region, there is no change in the experimental uncertainty.

Data Analysis

One approach to examining the results is the use of 3D graphs such as that shown in Fig. 6, which plots the apparent modulus ratio against the temperature and the maximum strain in the cyclic movement during 1 month of exposure at 75 % RH with UV radiation. The graph shows that both motion and temperature produce a significant reduction in the modulus for the range of conditions tested. Moreover, the effects are synergistic in that the combination of motion and temperature produced a larger reduction in modulus than that seen for either variable alone.

This approach is useful for illustrating general trends and highlighting the nature of the response surface. However, as the goal of this paper is to identify and rank environmental factors that are important to sealant degradation, we take a different approach to the data analysis. More specifically, design of experiments (dex) scatter plots, dex mean plots, analysis of variance (ANOVA), and block plots [28] are used. Of all of these statistical techniques, the block plot bears the most weight.

dex Plots

Figure 7(a) shows the dex scatter plot of the data. The vertical axis is the modulus ratio in, and the horizontal axis depicts the four exposure variables, i.e., three-level temperature, four-level cyclic movement, four-level RH, and two-level UV exposure. It can be seen that there is no apparent relationship between

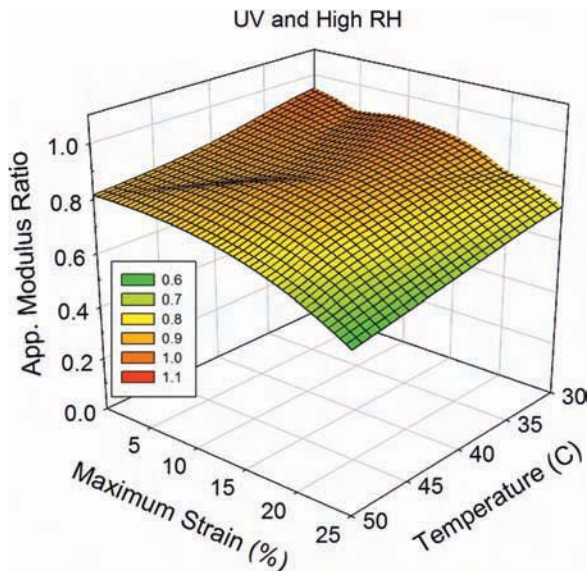


FIG. 6—Dependence of modulus ratio on max strain and temperature for specimens exposed to UV radiation and high RH (75 %).

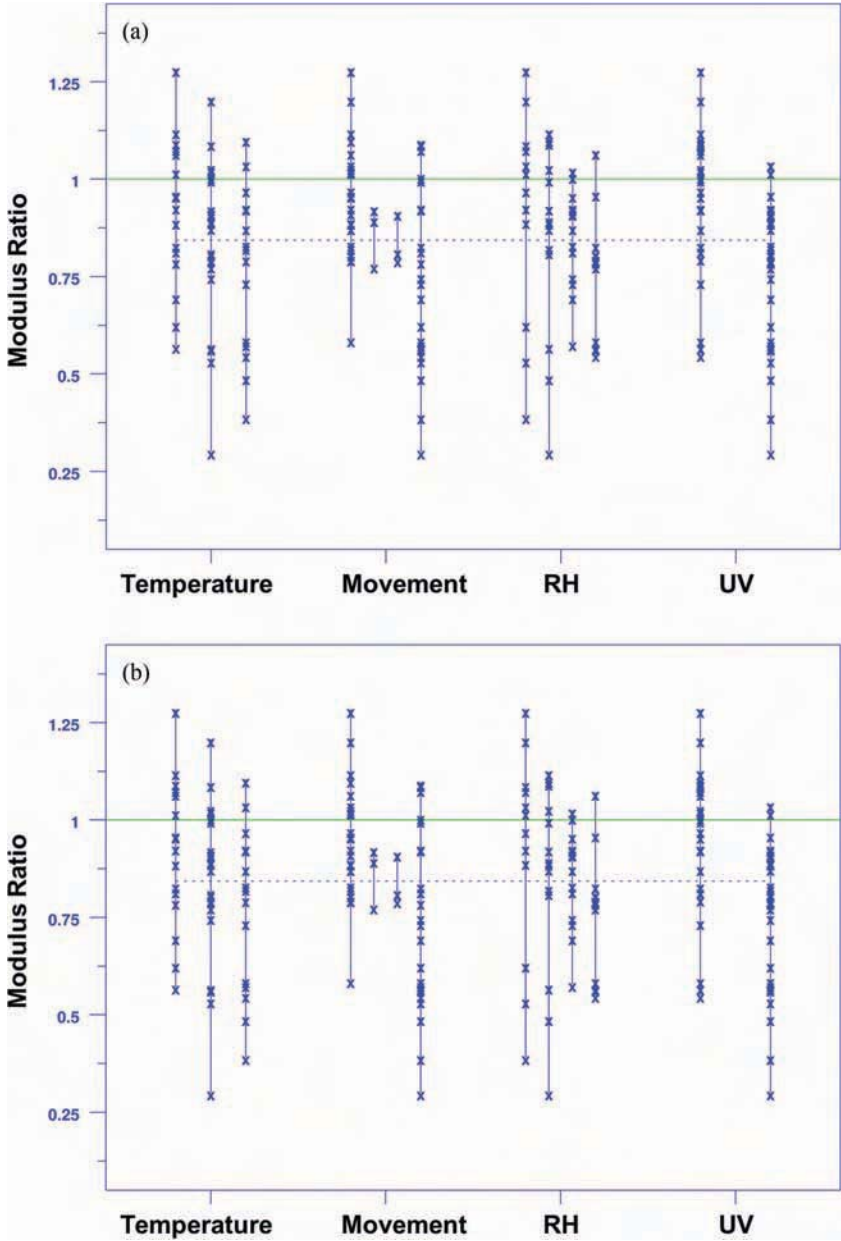


FIG. 7—(a) dex scatter plot and (b) mean plot of data for various exposure conditions. Although no obvious relationship between the modulus ratio and exposure variables is present in the dex scatter plot, the mean plot reveals that all exposure variables seem important for modulus decrease.

the modulus ratio and the four exposure variables due to large differences in the modulus ratio for a given setting of exposure variable.

In contrast, the dex mean plot [Fig. 7(b)], which shows the mean values of the modulus ratio for various levels of each exposure variable, reveals that all exposure variables have an effect on modulus decrease. A relation between the change in modulus ratio and exposure to the various environmental variables is evident, suggesting that the presence of UV radiation, an increase in temperature, a larger cyclic movement, or increased RH leads to a decrease in the modulus ratio for the particular sealant tested here. The effects of all of the exposure variables on the modulus decrease are evident, with cyclic movement and UV being the most important factors.

ANOVA

ANOVA, with main effects only, was used to compare the effects of temperature, cyclic movement, RH, and UV on the modulus ratio. Statistical significance was set at the conventional 5 % level. Table 1 summarizes the results of ANOVA. *F*-tests show a significant effect of UV, cyclic movement, and RH on the modulus decrease; however, ANOVA fails to reveal a significant impact of temperature on the modulus decrease at the 5 % level. We find this result unbelievable after looking at the dex plots, and it might be due to at least one of the following assumptions' being faulty: normality, homogeneity of variance, independence, or no interactions.

With the above ANOVA caveats in mind, we may form, based on the significance levels, the following ranked list of factors: (1) cyclic movement, (2) UV, (3) RH, and (4) temperature. Because of the caveats, we use the second statistical method (block plots) to assess factor significance and form a ranked list of importance.

Block Plots

A sensitivity analysis based on block plots was performed [28–30]. Block plots assess whether the factor of interest (known as the target factor) has a statistically significant effect on the decreasing mean modulus ratio, and whether that conclusion about the target factor is valid robustly or unconditionally over all other non-target factors (known as robustness factors) in the experiment. The

TABLE 1—ANOVA results.

Exposure Variable	Degrees of Freedom	Sum of Squares	Mean Squares	<i>F</i> Value	Pr (<i>F</i>)
Temperature	4	0.69060	0.172651	1.466906	0.2131036
Relative humidity	3	1.31257	0.4375124	3.717369	0.0122131
Cyclic movement	3	1.92587	0.641956	5.454293	0.0012248
UV	1	1.10464	1.104640	9.385429	0.0024503
Residuals	228	26.83499	0.117697		

block plot is essentially a character plot with the boxes superimposed for each setting in order to force attention on the within-box target values, as opposed to the between-box differences. It is an excellent graphics tool for robustly assessing the importance of each individual factor.

Effect of Temperature

Figure 8(a) displays the block plot targeting temperature (i.e., 30°C, 40°C, and 50°C) over 22 distinct combinations of RH, cyclic movement, and UV radiation. In this plot, temperature is the target factor (as denoted by the plot character), and UV radiation, cyclic movement, and RH are all robustness factors. The vertical axis shows the magnitude of modulus ratio, and the horizontal axis comprises various combinations of the three robustness factors. In order to facilitate comparison among different exposure conditions, the mean modulus ratio is determined by averaging the modulus ratio at the same temperature within each bar and is displayed in Fig. 8(b). For example, the first bar shows the effect of temperature on the modulus for the 0 % RH/no cyclic movement/no UV condition. Note that a temperature of 30°C yields a modulus ratio of ≈ 1.25 and thus an increase of 25 %, whereas 50°C yields a 13 % decrease. For the second bar (i.e., the combination of 0 % RH and UV radiation without cyclic movement), the sealants exhibit modulus increases, but the magnitude of increase is comparatively less than those in the first bar. However, a lower decrease in the modulus of 25 % is observed for exposures at 50°C.

Scanning across the various robustness factor settings (horizontally), it can be seen that 40°C or 50°C is almost always located at the bottom of each bar, and that the corresponding modulus ratios are almost always below unity. Indeed, 14 of the 16 robustness factor settings show that elevated temperature exposures of either 40°C or 50°C result in a greater modulus reduction than those at 30°C. In order to quantify whether temperature is statistically significant over all robustness factor settings, the chance for 14 of the 16 robustness factor settings showing the importance of the temperature effect involving randomness is calculated using a binomial model.

$$P(x, n, p) = \binom{n}{x} p^x (1 - p)^{n-x} \quad (4)$$

where:

x = number of successes in n trials, and

p = probability of success in a single trial.

The probability of obtaining at least 14 of the 16 robustness factor settings under the null hypothesis of $p = 0.5$ is ~ 0.2 %. Such a low probability event is rejected as unrealistic, allowing the conclusion that elevated temperature is statistically significant in decreasing modulus irrespective of the robustness factor settings. The importance of the temperature effect is supported further by Fig. 9(a), which shows the values of the modulus ratio for different temperatures arranged in order of increasing magnitude for 54 combinations of exposure conditions. It is evident that modulus data for 40°C or 50°C are always

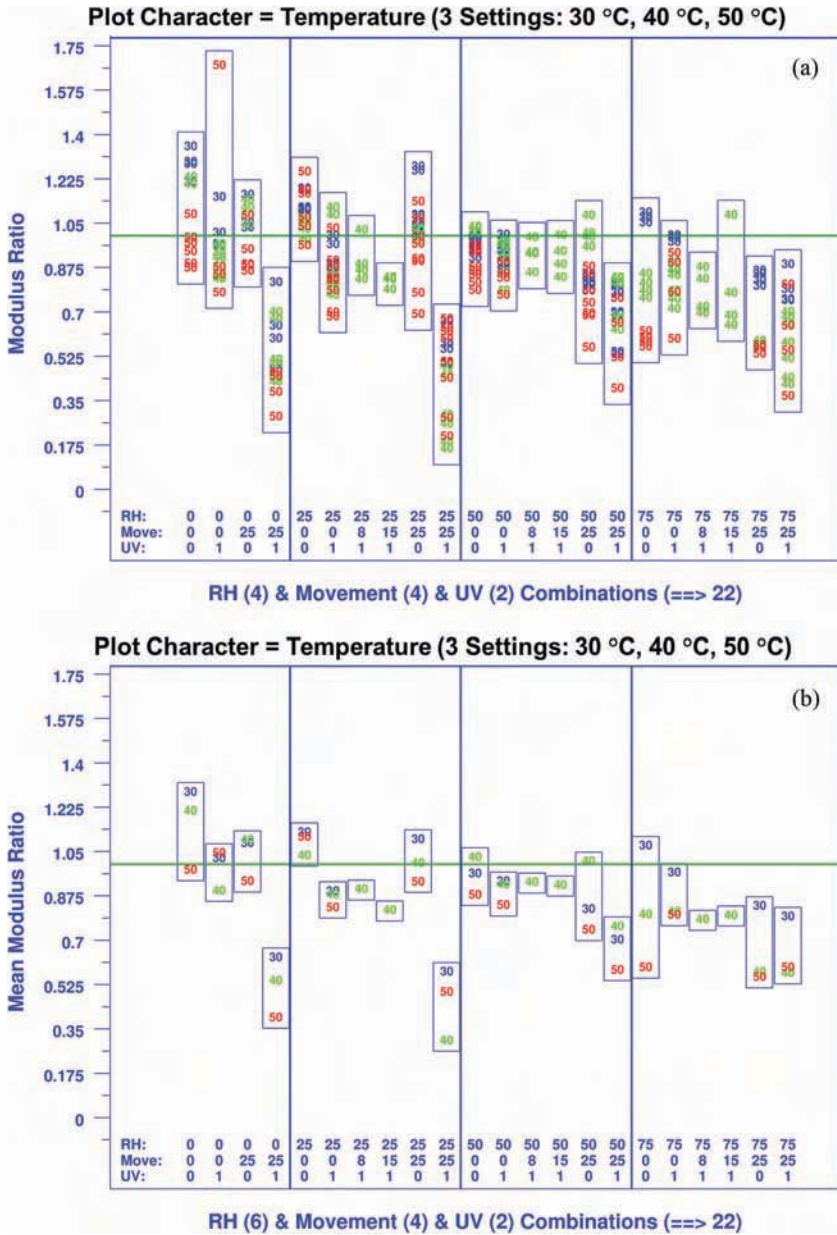


FIG. 8—Block plot of (a) modulus ratio and (b) mean modulus ratio targeting temperature across 22 distinct combinations of RH, cyclic movement, and UV. Consistencies in terms of the local arrangement of 40°C or 50°C movement within each bar and large block heights over all settings of robustness factors show the deleterious effect of elevated temperatures on modulus reduction.

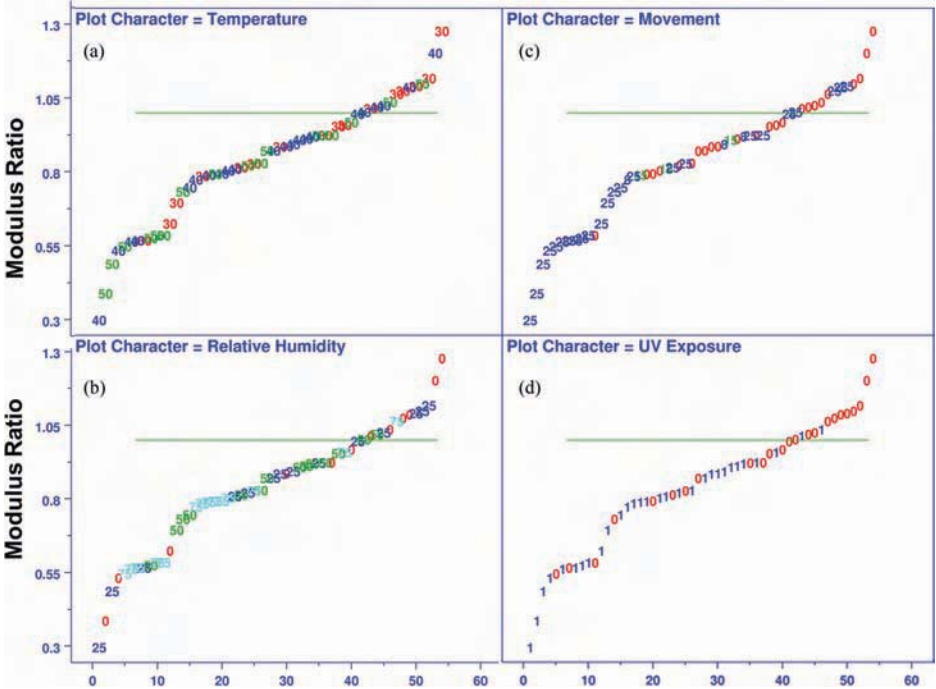


FIG. 9—Plots of modulus ratio targeting (a) temperature, (b) RH, (c) cyclic movement, and (d) UV arranged in order of increasing magnitude for 54 distinct conditions. The deleterious effects of temperature, cyclic movement at 25 % strain, and UV can be seen from the consistent location of these variable extremes in the bottom left corner of the plots. The inconsistency of RH arrangements suggests that RH is less important.

located at the bottom left corner of the plot, which indicates a lower modulus. Moreover, there is a large “local” (i.e., for that particular combination of robustness factors) temperature effect on modulus reduction, which is manifested in the large within-block difference (i.e., tall blocks). The existence of (a) consistently large block heights and (b) consistent temperature arrangement within blocks demonstrates that the temperature effect on modulus reduction is important. Note that less important factors will have only one of these two properties, and unimportant factors will have neither.

The decrease in sealant modulus as a function of exposure temperature suggests that chain scission is more likely than cross-linking as the dominant degradation mode. Thermally enhanced chain scission may be attributed to an increase in the average kinetic energy of polymeric chains and other reactants with increasing temperature, thereby leading to faster sealant degradation. In addition, temperature contributes directly to degradation by increasing the diffusion rates of oxygen and radicals, further enhancing the accessibility of oxygen and radicals for the degradation process.

Effect of Moisture

The block plots of raw and averaged data targeting RH levels (i.e., 0 %, 25 %, 50 %, and 75 %) over 14 different combinations of robustness factors are shown in Figs. 10(a) and 10(b). Although the bar heights for some robustness factor settings are considerably large, the local arrangement of RH levels within each bar depends on the settings of robustness factors on the horizontal axis. Unlike temperature, RH exhibits fairly consistently large block heights but inconsistent local RH level arrangements over all settings of robustness factors. This implies that RH is a less important factor. From Fig. 10(b), RH levels of 50 % and 75 % resulted in the greatest modulus reduction in 7 of the 14 settings of robustness factors. Based on binomial considerations, the probability of this happening by chance is ~60 %. The usual cutoff of 5 % has not been achieved here. Therefore, this observation, coupled with the inconsistency of the effect of RH over all of the robustness factor settings, suggests that RH is statistically less important. This observation is supported further by Fig. 9(b), which shows that many, but not a majority, of the data points associated with 50 % and 75 % RH are located at the bottom left corner of the plot. Although the RH effect on modulus decrease is not robust or universal over various robustness factor settings, the role of RH in modulus decrease cannot be dismissed for specific exposure conditions, i.e., RH might interact with other environmental factors. The inconsistency in the local RH arrangement in each bar across all of the robustness factor settings [Figs. 10(a) and 10(b)] lends support for such a hypothesis; this is discussed in more detail shortly.

Effect of Cyclic Movement

Turning now to the effect of cyclic movement (0 %, 8 %, 15 %, and 25 % strain) on modulus change, the block plots of raw data and averaged data focusing on the movement effects of over 24 distinct robustness factor settings are shown in Figs. 11(a) and 11(b). It is evident that all of the 20 robustness factor settings show that 25 % cyclic movement results in the greatest decrease in modulus. The probability of this happening randomly according to the binomial distribution is virtually zero ($<1 \times 10^{-4}$ %). Thus, the overall pattern of modulus decrease due to 25 % movement is unlikely to stem from random occurrence. Indeed, as shown in Fig. 9(c), the data for 25 % movement are always located to the bottom left of the plots. Further, the height of each block in Figs. 11(a) and 11(b) is large, signifying the prevalence of local effects of movement on modulus decrease. Such consistencies in terms of the local arrangement of 25 % movement within each bar and the large block heights over all settings of robustness factors show the deleterious effect of cyclic movement on modulus reduction. Interestingly, cyclic movements at 8 % strain and 15 % strain do not seem to affect the modulus. In fact, the modulus ratios at these values are similar to those in the tests without cyclic movement. This observation suggests that there might be a threshold value of cyclic strain below which the modulus is not affected.

To date, the incorporation of cyclic movement during exposure has not been widely used in routine outdoor testing of sealants, despite the fact that a

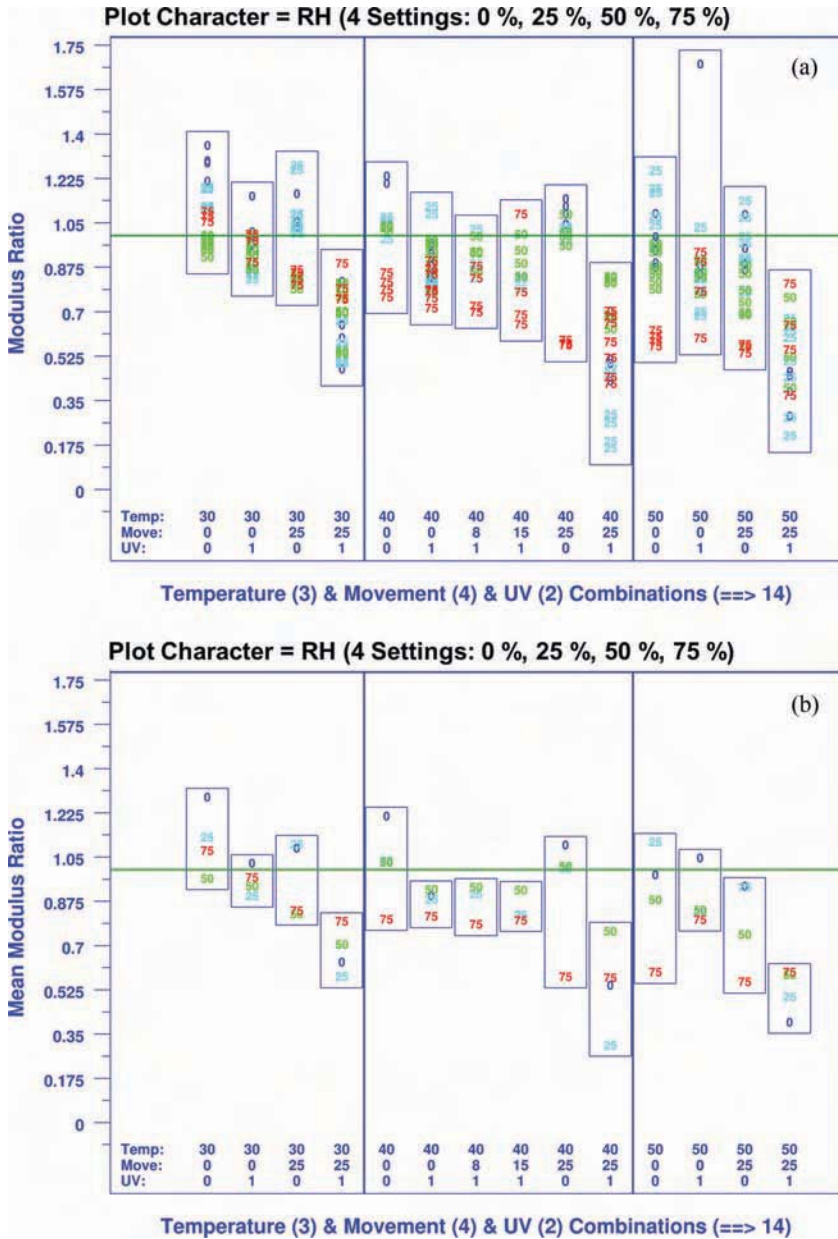


FIG. 10—Block plot of (a) modulus ratio and (b) mean modulus ratio targeting RH across 14 distinct combinations of temperature, cyclic movement, and UV. Fairly consistently large block heights and inconsistent local RH level arrangements over all settings of robustness factors suggest that RH is a less important factor.

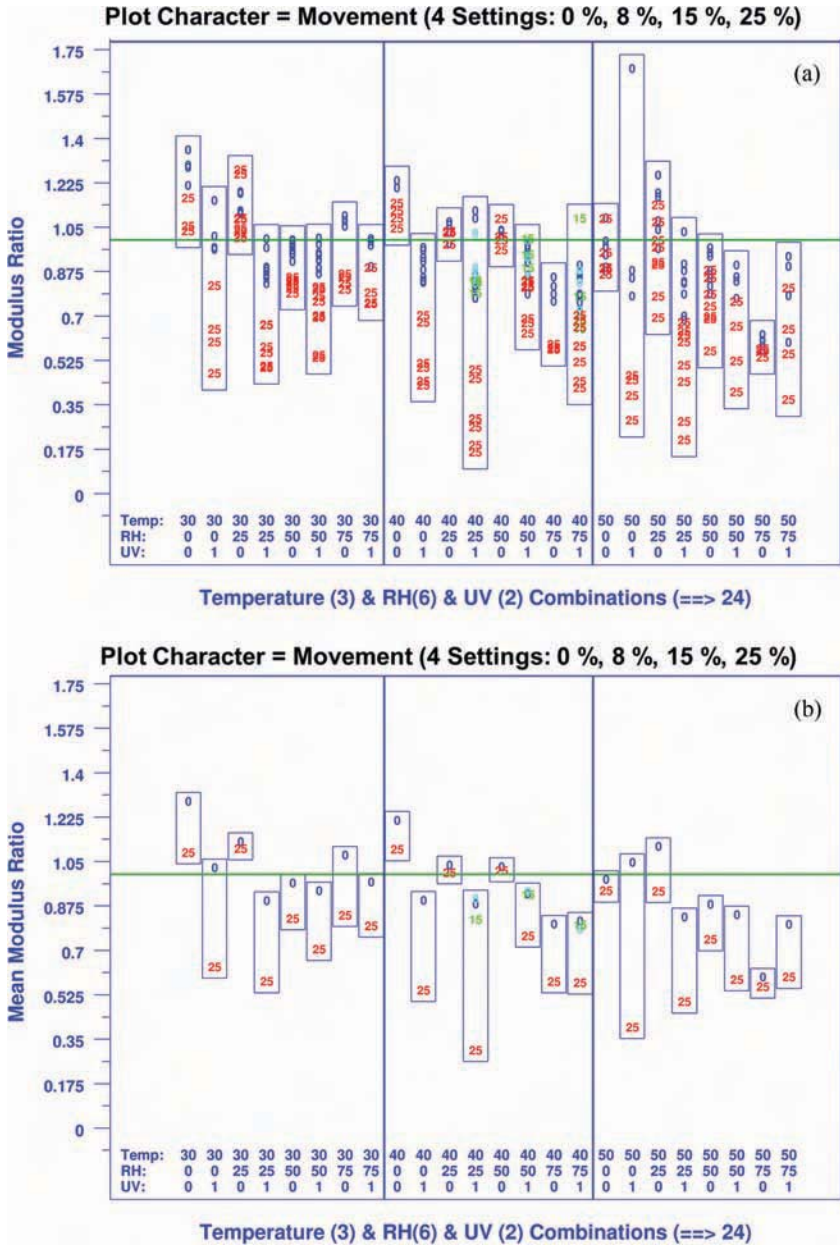


FIG. 11—Block plot of (a) modulus ratio and (b) mean modulus ratio targeting cyclic movement across 24 distinct combinations of RH, cyclic movement, and UV.

number of studies [31–35] have shown that accelerated aging under cyclic movement simulates the effects of in-service environments more closely. For the sealants studied here, the incorporation of cyclic movement in the durability tests not only will enable the use of an appropriate combination of environmental factors that closely simulates in-service conditions, but also yields an even greater acceleration factor to reduce test times for commercial sealants with a usual target service life of 20 years. It should be noted, however, that in some types of sealants the effect of cyclic movement does not greatly accelerate degradation, or it even has a negligible effect. For example, in a study by Enomoto et al. [36], mechanical cycling during outdoor exposure had no effect on the rate of degradation of two-part polyurethane and two-part silicone modified polyether (general purpose) sealants, and only a small effect on one-part polyurethane sealants.

Effect of UV

A block plot of the modulus ratio targeting UV is shown in Fig. 12(a). An examination of the arrangement of UV (“1”) and no UV (“0”) within each block shows that UV radiation is always located at the bottom of each bar, with the modulus ratios below unity. The block plot of the mean modulus ratio [Fig. 12(b)] indicates that 27 of 30 different robustness factor settings show that UV is an important factor in the modulus reduction. Based on binomial considerations, the probability of getting at least 27 of the 30 total settings by chance is $4 \times 10^{-4} \%$, showing that the role of UV in modulus decrease is statistically significant. In addition, the importance of UV in modulus reduction is further attested to by the consistently large block heights across the various combinations of robustness factors [Figs. 9(d), 12(a), and 12(b)] in that most modulus data for UV exposure are below unity and located at the bottom left corner of the plot. Thus, it is concluded that UV is statistically important across the various robustness factor settings.

The effect of UV in decreasing modulus may be understood based on the fact that UV photons have sufficient energy to rupture the polymeric bonds present in the sealant. Because the sealant chemistry is unknown, it is impossible to propose the exact mode of chain scission. However, it is believed that UV photons are absorbed by chromophores, which are introduced into the polymer backbone during manufacturing in aliphatic type and aromatic type polymers. The chemical structures of the latter contain chromophores capable of absorbing the UV photons, which split the covalent bonds to produce free radicals. The excited chromophores then dissipate the photon energy via chain scission, leading to the rupturing of molecular bonds. The low molecular weight fragments produced by scission reactions directly correlate with the decrease in modulus.

The Worst Factor for Modulus Decrease

We have identified temperature, cyclic movement, and UV radiation as statistically significant factors for modulus decrease over all robustness factor settings, but determining which factor is the most important among these three is also of

interest. This determination is done by deciding which plot has the consistently largest block heights, along with consistent arrangement within blocks showing the target factor located at the bottom of each bar. An examination of all block plots leads to the identification of cyclic movement as the most important factor for modulus decrease, followed by UV and temperature; RH is the least important factor. This ranking is consistent with that obtained from the dex plots. In a study of various latex and solvent-borne acrylic sealant products, Karparti [37] also discovered that cyclic movement was the major aging factor during outdoor exposure, and that outdoor weathering without cyclic movement alone had a negligible effect. This systematic laboratory approach clearly reveals the importance of cyclic movement in the degradation of sealants in a quantitative manner.

Although the results here suggest that cyclic movement is the most important factor in degrading the sealants, followed by UV, this should not be misinterpreted as meaning that cyclic movement causes the degradation of sealants in the absence of UV. This is not true for the sealant in this study, based on the information in the next section, and it would not be true for most sealants currently in use. For most polymeric materials, UV is required in order to initiate degradation because it has sufficient energy to break many types of polymeric chemical bonds, which leads to secondary reactions promoted by other environmental factors. For applications of building sealants in which movement has a significant effect on deterioration, the addition of cyclic movement to the exposure test is essential in order to promote the type of failure produced during in-service application of the sealant as a secondary reaction following initiation by radiation.

Interaction of Environmental Variables

Thus far, the effect of individual target factors on the decrease of the modulus has been examined over various robustness factor combinations. In investigating the interaction of robustness factors, a comparison among external block-to-block differences is performed. From the plot of average modulus ratios targeting RH [Fig. 10(b)], the effect of RH in decreasing the modulus ratio is seen for exposures without UV, and vice versa. For instance, high RH levels always reside at the bottom of each bar for 50°C/25 % movement/UV, whereas low RH levels are located at the bottom of each bar for 50°C/25 % movement/no UV. Furthermore, a close examination of the results for 50°C over all levels of cyclic movement and RH reveals that with UV exposure, the modulus decrease depends on the level of cyclic movement, but the humidity effect is small. Without UV, humidity has a greater effect than cyclic movement. Indeed, high RH levels are found at the bottom of each bar in all six settings involving combinations of temperature and movement without UV. Ignoring the bars showing a small local RH level effect, low RH levels with the presence of UV are located at the bottom of each bar in five of six different settings involving different temperatures and movement with UV. These results suggest that the interaction between UV and RH is significant in that UV seems to overwhelm the effect of moisture.

The negligible effect of humidity on modulus decrease for specimens exposed to UV prompts an examination of the interactions between temperature and motion. The block plots in Figs. 8 and 11 reinforce the two conclusions drawn from Fig. 6. First, the individual effect of temperature or cyclic movement is significant, as shown by the progressive decrease in modulus with increasing magnitudes of cyclic movement or temperature. Second, the combination of temperature and cyclic movement produces even greater effects. In particular, a modulus decrease of $>75\%$ is observed for $50^\circ\text{C}/25\%$ movement. This also can be seen in Table 2, which is simply a rearrangement of the data that groups temperature and cyclic movement on the vertical axis and RH level and UV on the horizontal axis. The combinations of elevated temperatures and 25% movement always are located at the top left corner of the table, showing the deleterious effect of combining UV radiation, cyclic movement, and elevated temperature. Indeed, this combination of environmental variables is the worst setting for modulus decrease. This is consistent with a prior study on two sealants with different formulations, which showed that sealant joints were able to resist the individual influence of cyclic movement, high temperature, or RH but degraded substantially when exposed to a combination of cyclic movement and high temperature or RH, or a combination of these three factors [1].

The simultaneous application of UV and cyclic movement has a pronounced effect on crack formation in sealants. As shown in Fig. 13, small, deep cracks are visible on the surface of specimens exposed to $50^\circ\text{C}/75\%$ RH/UV/ 25% cyclic movement, but fewer shallow cracks are observed in the specimens under the same conditions but without cyclic movement. These observations imply that exposure without cyclic movement results in only surface degradation, and that simultaneous cyclic movement during weathering accelerates the bulk deterioration of sealants. Notably, specimens under similar conditions without UV did not exhibit any cracking. This indicates the significant deleterious impact of UV exposure and cyclic movement on the aging of this particular

TABLE 2—Data rearrangement grouping temperature and cyclic movement on the vertical axis and RH level and UV on the horizontal axis.

Temperature (3) and Movement (4)	Relative Humidity (4) and UV (2)								
	25,1	75,0	0,1	75,1	50,1	50,0	25,0	0,0	Mean
50,25	0.49	0.55	0.39	0.59	0.58	0.74	0.93	0.93	0.65
40,25	0.30	0.57	0.54	0.57	0.75	1.01	1.00	1.09	0.73
30,25	0.57	0.83	0.63	0.79	0.70	0.82	1.10	1.08	0.82
40,15	0.82			0.79	0.91				0.84
40,8	0.90			0.78	0.93				0.87
50,0	0.83	0.59	1.04	0.80	0.84	0.88	1.10	0.97	0.88
40,0	0.88	0.80	0.89	0.81	0.92	1.02	1.03	1.21	0.94
30,0	0.89	1.07	1.02	0.96	0.93	0.96	1.12	1.28	1.03
Mean	0.71	0.74	0.75	0.76	0.82	0.90	1.05	1.09	0.84

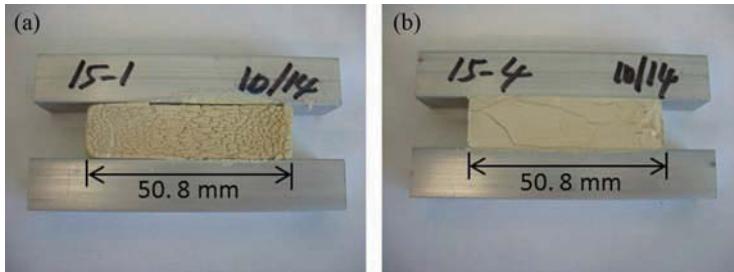


FIG. 13—Appearance of representative test specimens exposed to the combination of 50°C, 75 % RH, and UV radiation (a) with 25 % cyclic movement and (b) without cyclic movement. Exposure without cyclic movement results in only surface degradation, whereas simultaneous cyclic movement during weathering accelerates the bulk deterioration of sealants.

sealant. Cyclic tensile stress might promote the penetration of UV into the sealants and enable microcrack initiation in the degraded polymer surface layer to propagate into the bulk sealants. In contrast, cyclic compressive loads might lead to the alignment of molecular segments and the packing of molecules such that the ease of UV penetration into the sealant is reduced and sealant degradation is minimized. This is a subject for further study.

It is recognized that the relative effects of the various environmental factors on the properties of the sealant can differ with the type of base polymer in the sealant, other components included in the formulation, and impurities and reaction products. Each ingredient reacts to the various environmental factors in different ways, so the relative effects of stresses will vary from one sealant formulation to another. The present study presents findings based on tests with a single sealant; however, the experimental protocol could be applicable to broad classes of materials.

Conclusions

The accurate prediction of in-service performance in less time than is required for field tests and tests on structures has been hindered by a poor understanding of the failure modes in the two environments, a lack of methods for accurately quantifying the effects of environmental degradation factors, and crude techniques for monitoring sealant degradation. In this study, a reliability-based approach was implemented in order to systematically assess the individual and synergistic impacts of four major environmental factors (temperature, cyclic movement, UV exposure, and RH) on a sealant system. This methodology utilized laboratory exposure devices that allowed accurate control and monitoring of these environmental factors, as well as a quantitative measurement procedure for characterizing sealant degradation. Changes in the modulus were used as an indicator of the effects of environmental factors because a decrease in the modulus was found to be a precursor to cracking and debonding in our sealant system, which allow moisture penetration (the usual definition of failure).

Because each material responds differently to environmental factors, the modulus should not be viewed as a universal performance indicator for all sealants. The main conclusions are summarized as follows:

1. Elevated temperature is statistically significant for decreasing modulus irrespective of the robustness factor settings (i.e., cyclic movement, RH, and UV radiation).
2. Cyclic movement at 25 % strain is statistically significant for decreasing modulus irrespective of the robustness factor settings (i.e., temperature, RH, and UV radiation). However, unlike with 25 % strain, cyclic movement at 8 % and 15 % strain does not have any impact on the modulus. This observation suggests that there might be a threshold value of cyclic strain below which the effect of strain is negligible.
3. UV is statistically significant for decreasing modulus irrespective of the robustness factor settings (i.e., cyclic movement, RH, and temperature).
4. RH seems less important for decreasing modulus irrespective of the robustness factor settings (i.e., cyclic movement, temperature, and UV radiation).
5. UV radiation suppresses the effect of RH on modulus decrease. In the absence of UV, RH has a greater effect than cyclic movement.
6. Among various environmental factors, cyclic movement at 25 % strain is the most important factor for modulus decrease, followed by UV radiation, temperature, and RH.
7. The combination of cyclic movement and temperature produces a synergistic effect leading to a larger reduction in modulus than that seen with either variable alone.

Acknowledgments

The support from a NIST/industry consortium on Service Life Prediction of Sealant Materials is greatly appreciated. Participating companies include DAP, Degussa, Dow Corning, Kaneka Texas, SIKA, Solvay, Tremco, and Wacker Silicones.

References

- [1] Woolman, R. and Hutchinson, A., *Resealing of Buildings: A Guide to Good Practice*, Butterworth-Heinemann, Oxford, UK, 1994.
- [2] Grunau, E., "Service Life of Sealants in Building Construction" (in German), Research Report, Federal Ministry for Regional Planning, Building and Urban Planning, Bonn, Germany, 1976.
- [3] Chiba, R., Wakimoto, H., Kadono, F., Koji, H., Karimori, M., Hirano, E., Amaya, T., Sasatani, D., and Hosokawa, K., *Improvement System of Waterproofing by Sealants in Japan*, Japan Sealant Industry Association, Tokyo, Japan, 1992, pp. 175–199.
- [4] *Durability of Building and Construction Sealants and Adhesives*, STP 1453, A. T. Wolf, Ed., ASTM International, West Conshohocken, PA, 2004, pp. 385–398.
- [5] Martin, J. W., Nguyen, T., and Wood, K. A., *Service Life Prediction—Challenging the Status Quo*, J. W. Martin, R. A. Ryntz, and R. A. Dickie, Eds., Federation of Societies for Coatings Technology, Blue Bell, PA, 2005, p. 13.

- [6] Fischer, R. M., Ketola, W. D., and Murray, W. P., *Prog. Org. Coat.*, Vol. 19, 1991, p. 165.
- [7] ASTM C1519-10, "Standard Test Method for Evaluating Durability of Building Construction Sealants by Laboratory Weathering Procedures," *Annual Book of ASTM Standards*, ASTM International, West Conshohocken, PA.
- [8] ISO 11431:2002, "Building Construction—Jointing Products—Determination of Adhesion/Cohesion of Sealants after Exposure to Heat, Water and Artificial Light through Glass."
- [9] ISO 11600:2002, "Building Construction—Jointing Products—Classification and Requirements for Sealants."
- [10] White, C. C., Tan, K. T., Hunston, D. L., and Williams, R. S., *Service Life Prediction of Polymeric Materials: Global Perspective*, J. W. Martin, R. A. Ryntz, J. Chin, and R. Dickie, Eds., Springer, New York, 2008, pp. 115–128.
- [11] Tan, K. T., White, C. C., Benatti, D. J., and Hunston, D. L., *Service Life Prediction for Sealants Industry/Government Consortium Technical Report: Precision Exposure Chambers and Screening Experiments*, C. C. White, Ed., 2007, pp. 127–155.
- [12] Tan, K. T., White, C. C., Benatti, D. J., Stanley, D., and Hunston, D. L., *Handbook of Sealant Technology*, K. L. Mittal and A. Pizzi, Eds., CRC Press, Boca Raton, FL, 2009, pp. 75–92.
- [13] White, C. C., Hunston, D. L., and Tan, K. T., *J. ASTM Int.*, Vol. 6(2), 2009.
- [14] Lacher, S., Williams, R. S., Halpin, C., and White, C. C., *Service Life Prediction—Challenging the Status Quo*, J. W. Martin, R. A. Ryntz, and R. A. Dickie, Eds., Federation of Societies for Coatings Technology, Blue Bell, PA, 2005, pp. 207–216.
- [15] Williams, R. S., Lacher, S., Halpin, C., and White, C. C., *Service Life Prediction—Challenging the Status Quo*, J. W. Martin, R. A. Ryntz, and R. A. Dickie, Eds., Federation of Societies for Coatings Technology, Blue Bell, PA, 2005, pp. 171–185.
- [16] Tan, K. T., White, C. C., Benatti, D. J., and Hunston, D. L., *Polym. Degrad. Stab.*, Vol. 93, 2008, pp. 648–656.
- [17] Tan, K. T., White, C. C., Benatti, D. J., and Hunston, D. L., *Polym. Degrad. Stab.*, Vol. 95, 2010, pp. 1551–1556.
- [18] White, C. C., Tan, K. T., Hunston, D. L., Benatti, D. J., Nguyen, T., Stanley, D., and Chin, J. W., *Polym. Degrad. Stab.*, Vol. 96, 2011, pp. 1104–1110.
- [19] White, C. C., Tan, K. T., O'Brien, E. P., Hunston, D. L., Chin, J. W., and Williams, R. S., *Rev. Sci. Instrum.*, Vol. 82, 2011, 025112.
- [20] White, C. C., Hunston, D. L., Tan, K. T., Hettner, J., and Garver, D. J., "An Accelerated Exposure and Testing Apparatus for Building Joint Sealants," *Rev. Sci. Instrum.* (submitted)
- [21] Wolf, A. T., *Proceedings of the Sealant Technology Conference*, Oxford Brookes University, School of Technology, Oct. 13, 2004.
- [22] ASTM C719.
- [23] Chin, J. W., Byrd, E., Embree, N., Garver, J., Dickens, B., Finn, T., and Martin, J., *Rev. Sci. Instrum.*, Vol. 75, 2004, p. 4951.
- [24] ASTM G173-03.
- [25] Taylor, C. R., Greco, R., Kramer, O., and Ferry, J. D., *J. Rheol.*, Vol. 20, 1976, pp. 141–152.
- [26] Ferry, J. D., *Viscoelastic Properties of Polymers*, 3rd ed., John Wiley & Sons, Inc., New York, 1980.
- [27] Ketcham, S. A., Niemiec, J. M., and McKenna, G. B., *J. Eng. Mech.*, Vol. 122, 1996, pp. 669–677.
- [28] National Institute of Standards and Technology, 2003, *NIST/SEMATECH e-Handbook of Statistical Methods*, NIST Handbook 151, <http://www.itl.nist.gov/div898/handbook/>

- [29] Filliben, J. J., *Proceedings of the Indo-U.S.-Japan Conference: Quality through Engineering Design*, W. Kuo, Ed., Elsevier, Amsterdam, 1993, pp. 199–223.
- [30] Filliben, J. J., “Dataplot—Introduction and Overview,” *NBS Special Publication 667*, National Bureau of Standards, Washington, D.C., 1984.
- [31] Searle, N. D., *Handbook of Sealant Technology*, K. L. Mittal and A. Pizzi, Eds., CRC Press, Boca Raton, FL, 2009, pp. 93–142.
- [32] Wolf, A. T., *Handbook of Sealant Technology*, K. L. Mittal and A. Pizzi, Eds., CRC Press, Boca Raton, FL, 2009, pp. 143–189.
- [33] Beech, J. C., *Mater. Struct.*, Vol. 18, 1985, pp. 473–482.
- [34] Jones, T. G. B. and Lacasse, M. A., “Durability of Building Sealants,” *RILEM Report 21*, A. T. Wolf, Ed., RILEM Publications, Paris, 1999, pp. 73–105.
- [35] Wolf, A. T., “Durability of Building Sealants,” *RILEM Report 21*, A. T. Wolf, Ed., RILEM Publications, Paris, 1999, pp. 365–380.
- [36] Enomoto, N., Ito, A., Shimizu, I., Matsumura, T., Takane, Y., and Tanaka, K., *J. ASTM Int.*, Vol. 4, (2), 2007.
- [37] Karpati, K. K., *Adhesive Age*, Vol. 23(1), 1980, pp. 41–47.

FACTORS INFLUENCING THE DURABILITY OF SEALED JOINTS AND ADHESIVE FIXATIONS

Keith Besserud,¹ Matt Bergers,² Andrew J. Black,³
Lawrence Donald Carbary,⁴ Arkadiusz Mazurek,⁵
Donald Misson,⁶ and Kenneth Rubis⁷

Durability of Cold-Bent Insulating-Glass Units

ABSTRACT: Architectural influences upon the commercial building industry have resulted in the design and development of high-performing complex curtain walls that may include bent or warped glass. Glass on modern day curtain-wall projects is mostly insulating glass (IG). When an IG is bent out of plane, a shearing action occurs to both the primary and secondary seals. The testing described in this paper was done to determine the effect on the durability of the IG as measured by argon retention, frost point change, and visual changes after aging in a displaced condition. Full-size IG units, $5 \times 10 \text{ ft}^2 \times 1 \text{ in.}$ ($1.52 \times 3.05 \text{ m}^2 \times 25.4 \text{ mm}$), were fabricated, bent out of plane at 2–12 in. (50–300 mm) in 2-in. (50-mm) increments, and placed under a 100-psf (4788-Pa) wind load. One unit was displaced 15 in. (380 mm) where breakage occurred. An assessment was made based on the data as to what would be a reasonable amount of bending to avoid excessive glass stress and to avoid breakage. This full-size unit was then modeled and measured to predict and validate the stresses and strains on the primary and secondary seals. Upon completion of the bending tests and the review of modeling, small IG units $14 \times 20 \text{ in.}^2$ ($350 \times 500 \text{ mm}^2$)

Manuscript received June 9, 2011; accepted for publication November 9, 2011; published online March 2012.

¹Associate Studio Head, SOM, Chicago, IL 60604.

²R&D Manager, Viracon Inc., Owatonna, MN 55060.

³Sr. Mechanical Engineer, Permasteelisa NA, Mendota Heights, MN 55120.

⁴Industry Scientist, Dow Corning Corporation, Midland, MI 48686-0994 (Corresponding author), e-mail: l.carbary@dowcorning.com

⁵Structural Engineer, SOM, Chicago, IL 60604.

⁶Structural Engineer, Permasteelisa NA, Mendota Heights, MN 55120.

⁷Technical Service Specialist, Dow Corning Corporation, Midland MI 48686-0994.

Fourth International Symposium on Durability of Building and Construction Sealants and Adhesives on 16 June 2011 in Anaheim, CA.

Cite as: Besserud, K., Bergers, M., Black, A. J., Donald Carbary, L., Mazurek, A., Misson, D. and Rubis, K., "Durability of Cold-Bent Insulating-Glass Units," *J. ASTM Intl.*, Vol. 9, No. 3. doi:10.1520/JAI104120.

Copyright © 2012 by ASTM International, 100 Barr Harbor Drive, PO Box C700, West Conshohocken, PA 19428-2959.

were tested according to the protocol specified in ASTM E2188-10 and E2190-10 with an equivalent amount of edge-seal displacement in X, Y, and Z directions. Argon-retention and frost-point measurements were taken before and after the durability testing and results reported. During the durability testing, the glass of several of the units broke in thermal cycling because of high local stresses in the glass. However, the units that did survive the aging protocol passed both frost-point and argon-retention tests, while maintaining their appearance. Additionally, the methodology developed in this research provides a strong foundation for future testing in the area of cold-bent glass durability.

KEYWORDS: insulating-glass durability, ASTM E2190, ASTM E2188, bent glass, cold-bent glass, structural silicone, architectural design feature, PIB durability, argon retention, warped glass, doubly curved glass

Introduction

History and Reasons for Research

Over the past decade, the practice of architecture has witnessed the widespread introduction and adoption of new modeling software programs that facilitate the rapid conceptualization of highly complex, curvilinear building geometries. Based on non-uniform rational B-spline geometry that was developed in the automotive, nautical, and aerospace industries, these types of programs have become very popular among designers. Often resulting in surfaces that are doubly curved, these building designs inevitably proceed through some process of “post-rationalization” in which the architect’s aesthetic design intent must be reconciled with the realities of construction limitations (budgets), material behavioral properties, and laws of physics.

One approach often considered in this process of post-rationalization is known as “cold-bending.” Cold-bending refers to a practice of fabricating unitized curtain-wall panels in a standard process (without any curvature induced) and then bending the panels into a cold-bent condition as they are installed on the face of the building. The theoretical appeal of this approach is primarily twofold: (1) aesthetically, it has the potential to allow designers to realize a continuously smooth, industrial-design-quality reflective surface (as opposed to a faceted surface); and (2) it can prove to be a cost-effective strategy for cladding a building surface of double curvature (relative to the other options available).

Currently, however, architects are often hesitant to pursue this approach. Naturally, there are limits to the amount of bending that can be induced in the panels, but unfortunately there is currently little information available that clarifies these limitations. Manufacturers, fabricators, installers, and designers (and their insurers) are all left to establish their own comfort levels with respect to cold-bending practices in an *ad hoc* and extremely conservative manner because so little is known about the structural and other performance-related qualities of the glass, the sealants, and the other components of the panels when exposed to long- and short-term bending forces, in combination with the complications of weathering.

Therefore, the goal of this research is to begin to establish some empirical data with respect to cold-bending. Because this study is necessarily constrained to a single specific set of conditions (particular panel size and aspect ratio, particular panel components by particular manufacturers, etc.) and because the study was primarily focused on the behavior of the polyisobutylene (PIB) primary seal, much more research will be required to develop a more comprehensive understanding of the behavior of cold-bent curtain-wall panels. Nevertheless, this research has yielded some valuable insights.

Past Experience

The behavior of the glass and frame system under cold-bending has been previously studied on several projects. One of the first appearances of cold-bent glass in the architectural façade industry was in insulating-glass strip windows at the City Hall building of Alphen aan den Rijn in the Netherlands in 2002 [1]. Another Netherlands project constructed in 2002, the Floriade Pavilion in Haarlemmermeer, used point-supported laminated glass panels cold formed on site to glaze three large openings in the pavilion. The cold-bent panels created a curved-glass surface matching the free-form exterior of the Pavilion [1]. In addition to building façades, the smooth curved transitions between cold-bent laminated panels gave designers the freedom to create an undulating-point-supported glass roof for the Tramstation at Zuidpoort in Delft, Netherlands [2]. More recently this innovation was employed in the renovation of the Victoria and Albert Museum in London where the glass panels were cold worked on site to create a 4000-ft² (370-m²) twisting roof over a previously unused courtyard space [2].

However, despite its growing presence in the international construction scene, this technology has been used sparingly in the United States. Concerns regarding long-term stresses and deformations induced on the glass and silicone by the cold-bending process as noted in prior research [1,3] may be one of the reasons for its sparse use. Nevertheless, the engineers and designers of these successful cold-bent projects and others were able to use various methods of finite-element modeling and physical experimentations to determine the structural resiliency, code compliance, and warrantability of the curved glass [3–5]. From these analyses and testing, glass manufacturers developed enough confidence to warrant their glass products for use in cold-bending applications. However, the amount of cold-bending utilized in previous projects was relatively small compared to the bending performed during this research. This research seeks to gain a more complete understanding of the limits of the durability of a cold-bent insulating-glass unit (IGU) under cold deformation by exceeding the amount of deflection previously used, and to assess the durability of such a deflected IGU.

Scope of Research

The scope of this research was to determine the durability of the primary weather seal of an insulating-glazing unit under cold-bending deformation. The research team hypothesized that the primary cause of IGU failure (moisture

infiltration) would be caused by a strain in the edge seal. The standard test for determining durability is specified in American Society of Testing and Materials (ASTM) E2188-10 [6] and E2190-10 [7] and these standards specify an IGU of a certain size and make-up. Because of scaling problems, these standard IGUs cannot be deformed in the same way as a full-scale curtain-wall panel to obtain the same edge-seal strains. Therefore, the team devised a test procedure that had the following steps: (1) model a full-sized curtain-wall panel with *Finite Element* software, (2) perform a full-scale test on a curtain-wall panel for model verification, (3) deform the edge seal of a small IGU specimen equal to the deformation in the finite-element model and full-scale test, and (4) perform ASTM durability testing on the small specimen to determine the relative performance of a cold-bent IGU as compared to a “flat” IGU.

This testing and evaluation was all done within the scope of inch pound units. SI units are provided in parenthesis throughout this document.

Full-Scale Testing

The full-scale test units consisted of a 10-ft-high by 5-ft-wide ($3.05 \times 1.52 \text{ m}^2$) IGU framed by vertical and horizontal extruded aluminum profiles. Three identical test units were fabricated and each one was anchored at all four corners to its own wood test frame. Each individual wood frame was rigidly connected and sealed to a strong wall integrated with an air compressor capable of producing both negative and positive pressures. During testing the anchor at the same top corner of each test frame was removed to apply the out-of-plane displacement.

A preliminary finite-element model of a full-scale test unit was created to determine the limit of out-of-plane deflections that can be applied in actual construction practice. In the model beam, elements represented the framing members and plate elements simulated a single glass layer. Two adjacent edges of the glass were restrained in the out-of-plane direction, whereas the other two edges were allowed to freely translate. An incremental displacement was applied to the free corner of the model to determine at what displacement the maximum long-term stress in the glass (factored to account for the stiffness two layers of glass in the actual unit) would exceed limits specified in ASTM E1300-07 [8] and *Glass Association of North America (GANA) Glazing Manual* [9]. The finite-element analysis indicated that 12 in. (300 mm) was the maximum amount one corner of the full-size unit could be pulled out of plane before exceeding the long-term allowable stresses in the glass. A more-refined model was developed later in the project to accurately predict edge-seal strains.

The three test assemblies (a test assembly is the full-scale test unit, wood frame, and associated measurement devices) were each subjected to unique test procedures and data-acquisition methods to evaluate the various behaviors of the IGU under applied cold-bending, and also to validate computer finite element models. The first test assembly was set up as a baseline test to evaluate the structural capacity of the test unit in cold-bending. Measurements were taken at incremental out-of-plane displacement up to the maximum of 12 in. (300 mm). The second test assembly provided information about the edge-seal deformations between the outer and inner glass layers at the same increments used in

the first test assembly. The third test assembly was designed to validate the results of the first and second test assembly through comparisons between their strain data, and also to determine if the unit under maximum bending was capable of withstanding repeated applications of static pressure.

All three test assemblies were also designed with measurement devices to correlate their cold-bending and compare strains at specific locations on the glass. However, only test assemblies one and three were subjected to a baseline test performed in accordance with ASTM E330-02 [10] Procedure A. Test assembly 2 required access to the displaced corner for measurements and thus could not be sealed to the test wall for pressurization. During the pressure test, the air compressor applied a pressure of 100 lbf/ft² (4788 Pa) to the glass surface through the sealed pressure chamber. Engineering judgment and prior job experience were used to identify 100 lbf/ft² as a typical maximum wind pressure that a high-rise building might experience in a 50-year-return period. The structural silicone used as the secondary seal for the IGU and also to attach the insulating glass to the metal frames was sized and designed around the above-mentioned wind load so that the structural silicone would maintain its industry standard 20 psi (138 kPa) design stress. Because of the limited sample size and inherent imperfections in glass, this test provided a necessary baseline performance criterion that units had to pass to be accepted as fit for cold-bending. This test also provided additional information about the deformation states of the cold-bent surfaces under pressure.

Curtain-Wall Frame

The curtain-wall panel frame was pin-anchored in three corners by steel angles to restrain in-plane and out-of-plane displacement and allow for the rotation at the corners. The fourth corner was pulled out of plane using a hook-and-slide mechanism that is typical to a curtain-wall anchoring system. The anchoring and pulling mechanism was designed to allow for a full 12 in. (300 mm) of deflection in one direction.

The framing profiles used were designed for a previous flat-glazed project and no prior considerations for cold-bending the frame were developed into the frame design. The framing members were open-channel vertical shapes and closed tubular horizontal shapes. The horizontal members were attached to the vertical members with three to four fasteners, which were attached through clear holes in the vertical framing members and threaded into screw races in the horizontal member. See Fig. 1 for framing member profiles and section properties.

The IGUs were structurally glazed in shop into the frame using structural silicone sealant with a bite of 0.75 in. (19 mm) and a depth of 0.25 in. (6.4 mm), so that the 20-psi (138-kPa) industry-standard structural silicone design strength would be maintained at the 100 lbf/ft² (4788 Pa) wind load.

Glass Make-up

The IGUs for the full-scale test were fabricated using two 0.25 in. (6.4 mm) pieces of fully tempered clear glass. A 13.2-mm mill-finish aluminum spacer

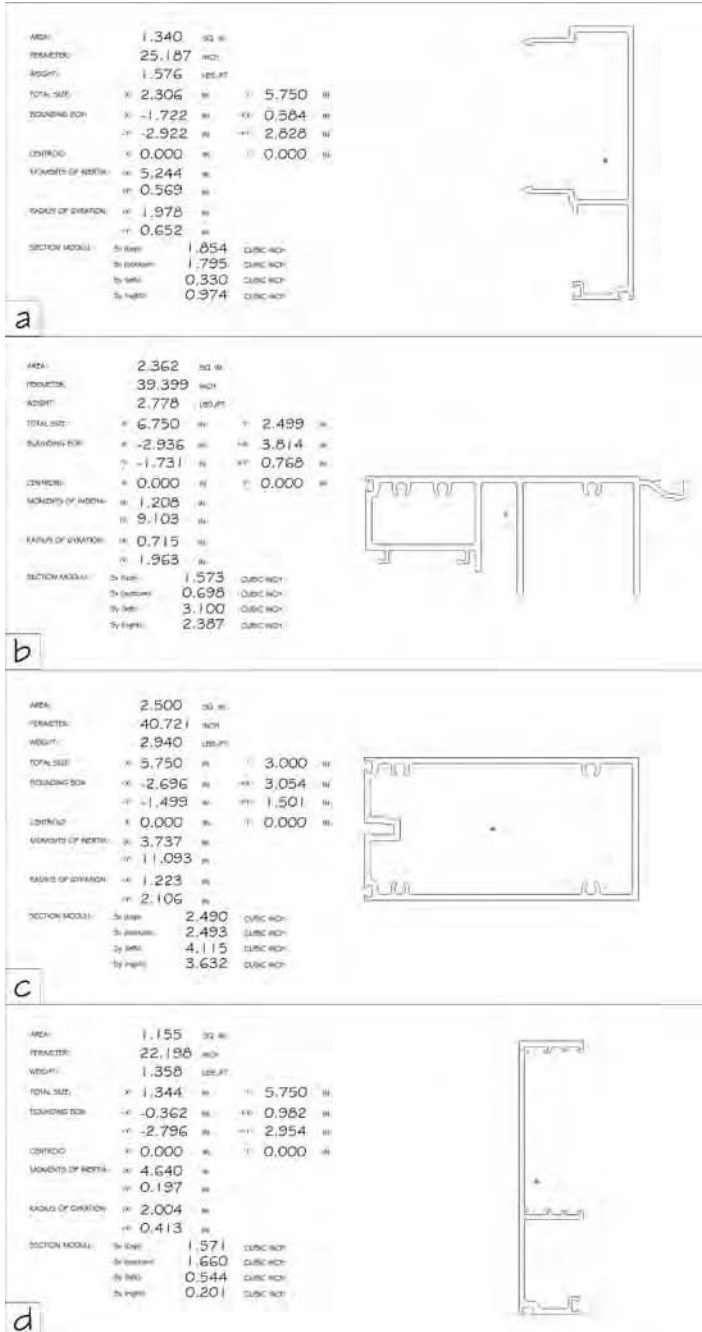


FIG. 1—Aluminum framing profiles and section properties: (a) male vertical mullion, (b) lower sill transom, (c) upper head transom, and (d) female vertical mullion.

established a 0.520-in. (13.2-mm) air space. On both sides of the spacer, an average of 0.015 in. (0.4 mm) of pressed PIB provided a primary seal between the spacer and the glass. The IGU was glazed with 3/8 in. (9.5 mm) of structural silicone insulating-glass sealant.

Silicone

The structural silicone that was used as the secondary seal for this study was also the silicone used to attach the IGU to the aluminum frame. This two-part structural silicone conforms to both ASTM C1184 [11] and ASTM C1369 [12]. This particular silicone is described as Sealant "D" previously by Wolf and Cleland-Host [13], as shown in Fig. 2. Data gathered on the tensile strength of the IGU edge-seal assembly per the ASTM C1265 [14] configuration is presented in Table 1. This data includes ultimate tensile strength, as well as stress data at 2.5 %, 5 %, and 10 % strain.

Full-Scale Test Procedure

Test assembly 1 consisted of a curtain-wall frame anchored to a wood test frame at each corner (see Fig. 3). The wood frame was rigidly anchored and sealed to the test wall with the exterior lite of glazing facing the test wall. All gaps between the curtain-wall unit and wood test frame were also sealed. It was subjected to initial pressurization of four positive and four negative cycles of 10 s each at 100 lbf/ft² (4788 Pa) in general accordance with ASTM E330-02 [10] to ensure that the glass could attain design pressures prior to cold-bending. The upper-right anchor was removed and the top corner of the unit was pulled 2 in. (50 mm) out of plane away from the test wall. The anchor was reinstalled, and one 10-s cycle was run for the positive and the negative pressures. This procedure of displacement followed by pressurization was repeated in 2-in. (50-mm)

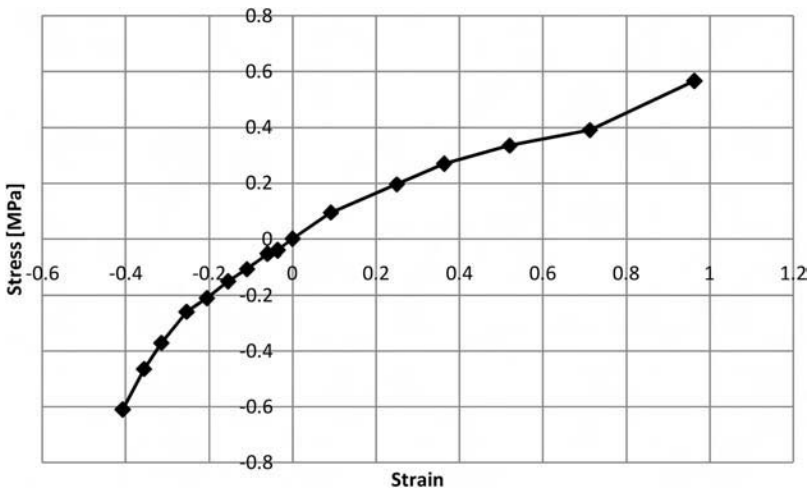


FIG. 2—Stress-strain relationship of silicone at 22°C.

TABLE 1—*Sealant data based on ASTM C1265-94(2005)e1 [14].*

Specimen #	Length (in.)	Thickness (in.)	Peak stress (psi)	Peak stress (MPa)	Strain at peak (%)	Stress at 2.5 % strain (psi)	Stress at 2.5 % strain (MPa)	Stress at 5 % strain (psi)	Stress at 5 % strain (MPa)	Stress at 10 % strain (psi)	Stress at 10 % strain (MPa)
1	2	0.375	205.4	1.42	65.842	2.3	0.02	42.1	0.29	79.1	0.55
2	2	0.375	216.4	1.49	66.557	8.9	0.06	13.3	0.09	66.2	0.46
3	2	0.375	216.1	1.49	63.818	14.1	0.10	53.2	0.37	82.9	0.57
4	2	0.375	221.7	1.53	91.867	34.7	0.24	71.6	0.49	84.8	0.58
5	2	0.375	218.8	1.51	63.277	37.8	0.26	61.9	0.43	94.6	0.65
Mean			215.7	1.49	70.272	19.6	0.14	48.4	0.33	81.5	0.56
SD			6.2	0.04	12.149	15.8	0.11	22.4	0.15	10.3	0.07

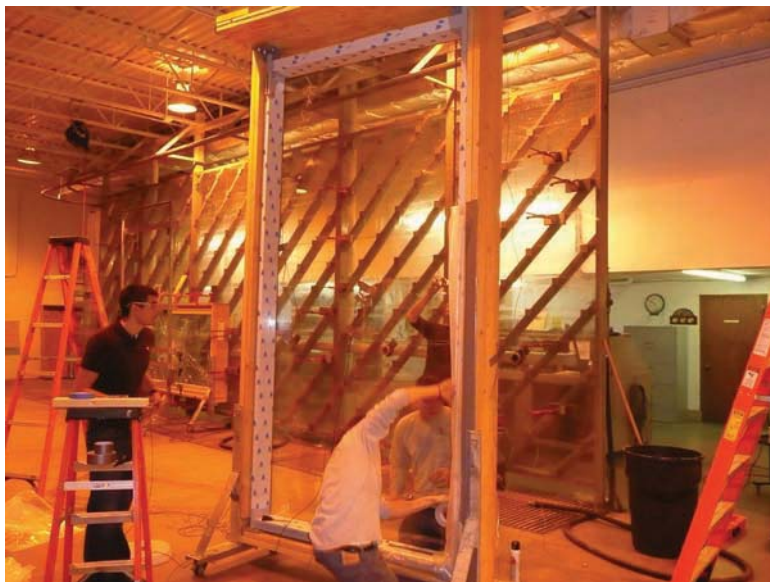


FIG. 3— $120 \times 60 \times 1 \text{ in}^3$. ($1.5 \times 3.0 \text{ m}^2 \times 25 \text{ mm}$). Full-scale test assembly 1.

increments until a total displacement of 12 in. (300 mm) was reached. After pressurization at a displacement of 12 in. (300 mm), the unit was displaced till breakage at 15 in. (380 mm). Linear and rosette strain gauges provided strain information at key locations, and linear variable displacement transducers (LVDTs) were attached to the glass in the corners to provide accurate displacement data. Data from these gauges was recorded for each displacement increment and during all load cycles. Figure 4 shows the locations of these gauges on assembly 1.

Assembly 2 was installed in a partial-wood test frame and anchored at three locations, leaving the top right corner free (Fig. 5). The partial frame allowed access to the side of the glazing where six dial indicators were mounted to the outer pane of glass (Fig. 6) to monitor the edge-seal strains as the unit was displaced. Consequently, the frame was unable to be sealed and no pressure was applied to assembly 2. The free corner was displaced in 2-in. (50-mm) increments until a total displacement of 12 in. (300 mm) was achieved. Dial indicator and linear strain (Fig. 7) readings were recorded at each 2-in. (50-mm) increment and LVDTs were again used to measure glass bending.

Assembly 3 followed the same installation as assembly 1. For this assembly, the top right corner was displaced to 10 in. (250 mm) and secured. Eight 10-s, 100 lbf/ft² (4788 Pa) test loads were applied in accordance to ASTM E330-02 [10], alternating between positive and negative directions. Linear and rosette strain gauges and LVDTs were applied to this assembly as shown in Fig. 8. During the time of testing, the authors decided that design cold bend would be 8 in. (200 mm) and the 10 in. (250 mm) displacement would correspond to 125 % of the design displacement of assembly 1. This was done to determine if repeated loading beyond the 100 % cold-bend design would result in glass breakage of this single assembly.

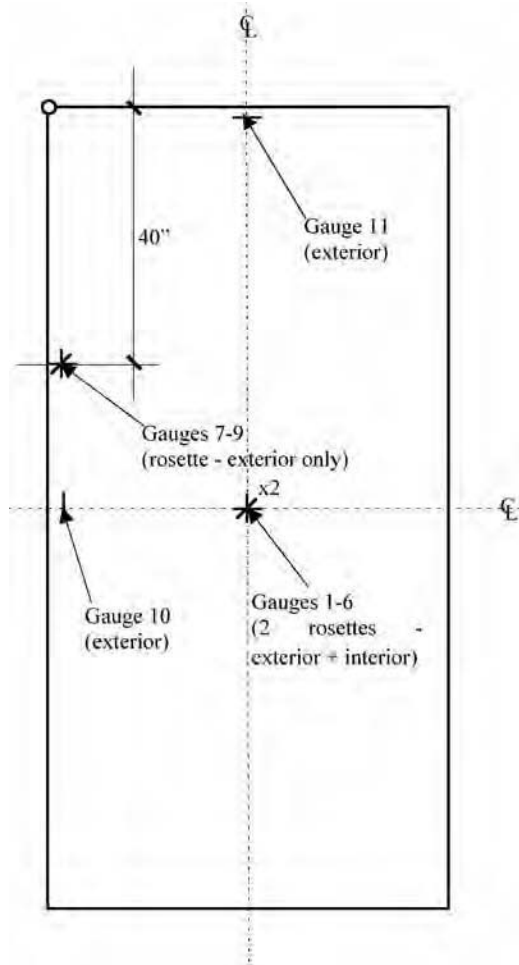


FIG. 4—Full-scale test assembly 1 gauge location schematic.

Small-Unit Durability Testing

The purpose of the small-unit test was to determine the durability of a cold-bent IGU using the industry-standard testing protocol as specified in ASTM E2188-10 [6]. The edge-seal conditions of a full-scale, cold-bent curtain-wall panel cannot be simply converted into an equivalent degree of bending in a small test specimen. Because of the specific requirements of this testing protocol, the glass stiffness, the IGU spacer size, and PIB size could not be scaled and still maintain comparable results to a “standard” ASTM E2188-10 test. Therefore, the edge seal was strained an amount equal to that observed in the full-scale testing and validated by the finite-element model. Following this method a similar edge-seal condition was recreated between the full-scale and small-scale tests.



FIG. 5— $120 \times 60 \times 1$ in³. (1.5×3.0 m² \times 25 mm). Full-scale test assembly 2 in partial test frame.

The small-scale test was broken into four sets of identically constructed specimens with varying amounts of edge-seal strain. The first set was a control and was tested without any additional edge-seal deformation. The second set had edge-seal deformations that corresponded to a “100 %” allowable amount of bend. The 100 % allowable amount of bend was determined through a combination of engineering judgment and the results of full-scale testing. The third and fourth set contained edge-seal deformations that corresponded to “50 %” and “150 %” of the allowable amount of bend. It is important to note that 50 % and 150 % are not indicative of the amount of edge-seal strain, but relate to the amount of displacement in the full-scale test. The amount of edge-seal strain in these cases was determined through a combination of the full-scale test and finite-element model.

Design of Test Apparatus

The testing procedure for the small scale durability test (as specified in ASTM E2190-10 [7]) required a compact and portable displacement mechanism to impart movements on the two lites of glass that would replicate the edge-seal



FIG. 6—Dial gauge used to measure relative displacement between glass panes in full-scale test assembly 2.

strains in the full-scale test unit. The final design consisted of a four-sided frame made from a bent and welded steel 1/4-in. (6.4-mm) plate. The 14 × 20 in.² (350 × 500 mm²) IGU was placed into the frame and the lower lite was secured to the frame on all four sides using epoxy resin. The frame was designed to surround the four edges of the IGU to adequately apply load to displace the pane of glass; however, there was a nominal clearance of 3/8 in. (9.5 mm) between the steel and IGU edge seal. This allowed for adequate clearance around the edge seal as specified in ASTM E2188-10 [6]. Fasteners and bearing plates were used to displace the upper pane of glass in-plane relative to the lower. In-plane displacements are defined as X and Y directions. Another set of fasteners attached to plates adhered by epoxy to the surface of the glass was used to pull the upper pane of glass away from the lower. This out-of-plane displacement is defined as the Z direction. See Fig. 9 for a photograph of the small test frame. In this photograph, there are steel plates and fasteners bonded to the glass at the mid-span of the long 20-in. (500-mm) dimension. The screws shown at these locations were used to lift the outer lite away from the inner lite in the Z direction.

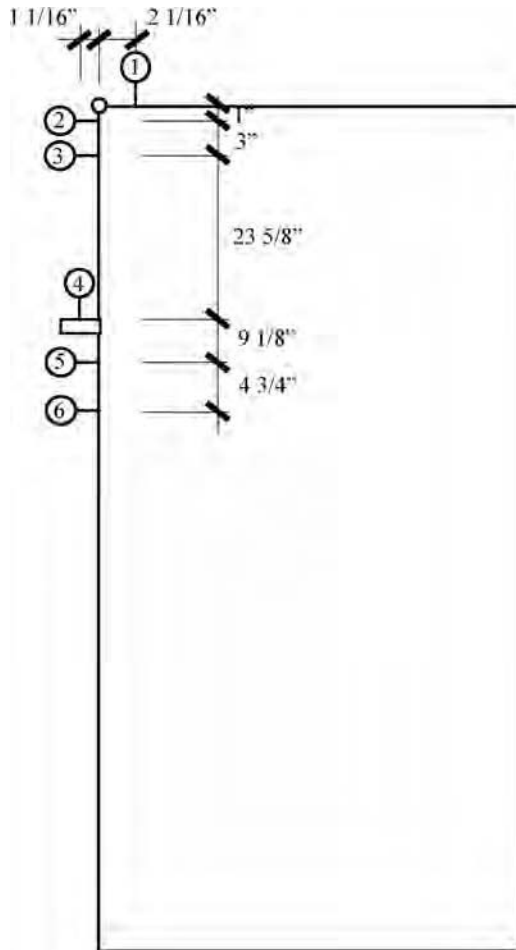


FIG. 7—Full-scale test assembly 2 gauge location schematic.

To apply the desired displacement between the two panes of glass, two #6-40 socket-head machine screws were used in each in-plane direction. The data in Table 1 was used to estimate the forces required to strain the outboard lite of the small test units and to determine the size of the screws used to produce the strains. Steel shims and silicone bearing plates were used to distribute load and protect the glass edge (Fig. 10) when moving the plates in the X and Y directions. The applied displacement was measured between the steel frame and displaced glass pane using a dial caliper. The out-of-plane displacement was applied using two #6-40 flat-head machine screws that were adhered to the upper unfixed pane of glass with an epoxy resin. This displacement was measured between the steel frame and glass pane using an outside micrometer. Additionally, measurements were taken between the lower fixed pane of glass and

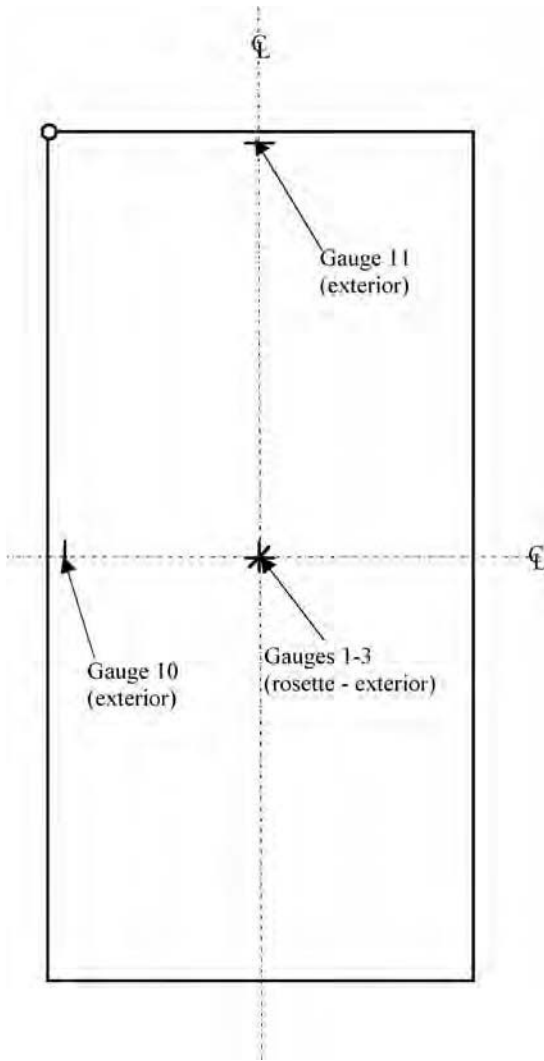


FIG. 8—Full-scale test assembly 3 gauge location schematic.

the steel frame to ensure that the entire IGU did not move relative to the steel frame. All of these measurements were recorded at the time of application and subsequently measured throughout testing. See Table 2 for recorded measurements and Fig. 11 for the locations of displacements.

A slight modification was made to the original test frame design because of the high loads required to displace the glass out of plane in the Z direction for the 150 % design test specimens. The outer pane of glass broke in two glass specimens during the application of displacements and these were discarded. Also, two of the tension mechanisms that were secured to the glass with epoxy



FIG. 9— $14 \times 20 \text{ in.}^2$ ($350 \times 500 \text{ mm}^2$) small test frame with IGU installed.

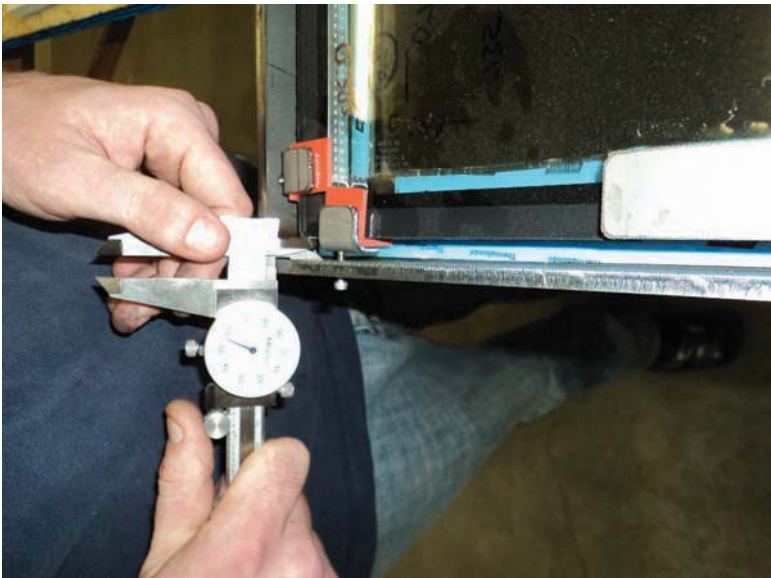


FIG. 10—Application of small-specimen edge-seal displacements.

TABLE 2—Edge-seal measurements.

Frame number	Design value	Front lite x2 ^a Δ	x3 ^a Δ	y3 ^a Δ	y4 ^a Δ	Z_t ^a Δ	Z_b ^a Δ	Date completed
25	50 %	0.014	0.015	0.018	0.019	0.010	0.010	1/24/2011
16	50 %	0.014	0.015	0.022	0.015	0.009	0.011	1/24/2011
18	50 %	0.014	0.015	0.017	0.018	0.010	0.011	1/25/2011
26	50 %	0.013	0.015	0.018	0.016	0.014	0.009	1/25/2011
12	50 %	0.015	0.016	0.021	0.020	0.011	0.009	1/27/2011
24	50 %	0.013	0.014	0.017	0.019	0.011	0.010	1/24/2011
29	100 %	0.022	0.022	0.033	0.034	0.018	0.013	1/25/2011
28	100 %	0.023	0.022	0.031	0.034	0.013	0.015	1/25/2011
33	100 %	0.023	0.020	0.033	0.031	0.016	0.016	1/25/2011
36	100 %	0.021	0.021	0.031	0.033	0.014	0.015	1/25/2011
27	100 %	0.021	0.020	0.031	0.033	0.016	0.014	1/25/2011
3	100 %	0.021	0.022	0.032	0.033	0.016	0.015	1/27/2011
13	150 %	0.045	0.039	0.058	0.057	0.035	0.035	3/8/2011
15	150 %	0.043	0.041	0.057	0.058	0.033	0.036	3/8/2011
37	150 %	0.042	0.043	0.059	0.058	0.036	0.037	3/8/2011
38	150 %	0.041	0.043	0.059	0.1	0.036	0.038	3/8/2011
40	150 %	0.036	0.042	0.063	0.058	0.037	0.033	3/8/2011
42	150 %	0.042	0.044	0.061	0.061	0.035	–	3/8/2011

^aSee Fig. 11 for displacement locations.

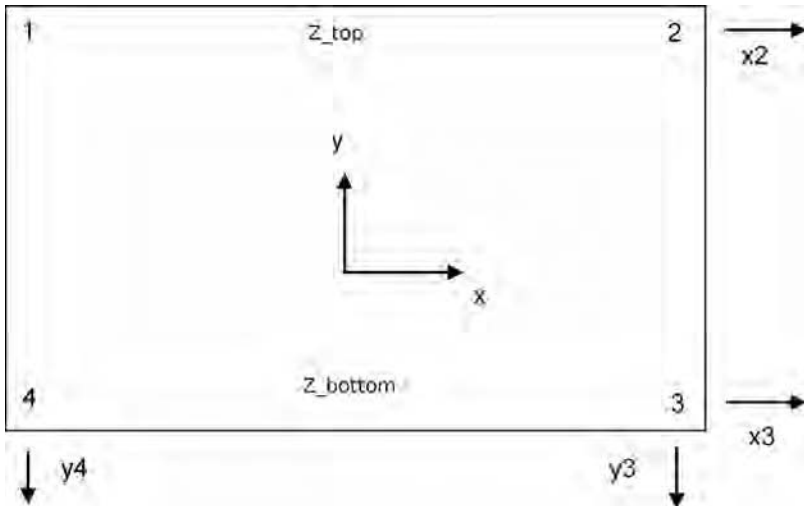


FIG. 11—Edge-seal displacement table locations.

broke free and had to be reinstalled. To avoid stress concentrations for the 150 % tests, a revised tensioning mechanism was designed and installed for these specimens. This mechanism consisted of a longer steel plate adhered to the glass to more effectively distribute load and thereby reduce stress. The new tension mechanism allowed the glass to be deflected in tension to the required degree without additional glass breakage.

Insulating-Glass Make-up

Twenty-four units of IGU for the durability testing were manufactured using standard 14 × 20 in. (350 × 500 mm) configurations as prescribed by ASTM E2190-10 [7]. The units were fabricated using tempered glass with a thickness of 0.185 in. (4.7 mm) for each lite. The outer lite has a Low-E coating on the #2 surface that is deleted to the PIB interface. The air space was established using a 13.2-mm, mill-finish aluminum spacer. The PIB thicknesses ranged between 0.010 in. (0.25 mm) and 0.030 in. (0.76 mm) and an average PIB thickness of 0.015 in. (0.38 mm) was attained. Two legs of the spacer were filled with a 3A molecular sieve desiccant. The units were filled with argon to greater than 90 % fill level and then sealed with 3/8 in. (9.5 mm) of silicone insulating glass sealant.

Weathering Test Procedure

The durability of the test specimens was evaluated by industry established and accepted methods of exposing the units to high humidity environment, alternating temperatures and periods of ultraviolet (UV) exposure and water spray. The method chosen is described in detail in ASTM E2188-10 [6]. The procedure and the cyclical phase are shown in Fig. 12. Evaluation of argon retention was conducted per ASTM E2649 [15].

The test began by establishing an initial frost point per ASTM E546 [16]. The ASTM E546 test method placed a cold plate on the surface of the glass.

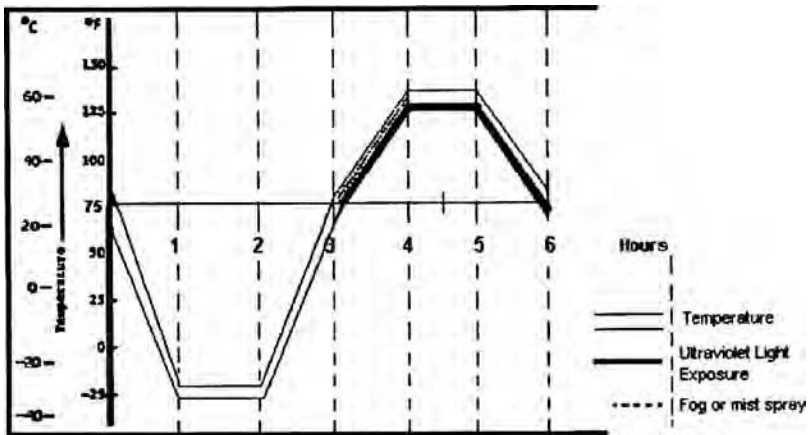


FIG. 12—ASTM E2188-10 [6] test cycle.

Condensation in the form of frost or, at higher temperatures, dew would be observed if there was sufficient moisture in the IG unit. Factory-made units are expected to demonstrate low-temperature frost points at the start of the test, because the desiccant is new and not subjected to any extreme environmental influences. Typically, the initial-frost-point results are expected to be lower than -90°F (-68°C).

Additionally, testing for Argon in the units was conducted per ASTM E2649 [15]. All units began the test with greater than 90 % argon concentration.

After these initial tests, the units were placed in a high humidity chamber for a period of 2 weeks. The chamber was maintained at 140°F (60°C) and 95 % relative humidity for the entire two weeks.

Once this phase was completed, the units were removed and allowed to equilibrate to standard temperatures and conditions for a period of 24 h. The units were then measured again for frost point and argon retention and the values were recorded.

At the completion of the data collection, the units were placed in a weather-cycling phase. During this phase, the units experienced cold temperatures to -20°F (-29°C). After a hold period, they were allowed to return to standard temperatures at which point they are exposed to ultraviolet light and mist spray while their temperatures were raised to 140°F (60°C). The spray was turned off and after a hold at high temperature and while the ultraviolet light is still on, the units were allowed to return to standard temperatures where the cycle begins again. This 6-h cycle was repeated for 9 weeks.

At the completion of the weather cycling phase, the units were once again removed, allowed to equilibrate for 24 h and the frost-point and argon values were measured and recorded.

Finally, the units were placed back in the humidity chamber (as described above) for an additional 4 weeks. At the completion of the 4 weeks, they were removed, allowed to equilibrate for 24 h and the final frost-point and argon values were taken and recorded.

Argon-Testing Procedure

Testing for argon gas content was performed on all of the small testing units at four specific time frames, (initial, after 2 weeks in high-humidity exposure, after 9 weeks of weather cycling, and then again after 4 more weeks of high-humidity exposure). Units were tested by non-destructive spark emission spectrography in accordance with ASTM E2649 [15]. For an IGU to be listed as complying with gas content certification, the unit must demonstrate an average argon containment of greater than 90 % before weathering, and the average argon levels of the entire sample group must be greater than 80 % after weathering.

ASTM E2188-10 Test Procedure: Expectations

Test-unit failure caused by workmanship issues related to the initial fabrication of the 14×20 in.² (350×500 mm²) units is normally expected to be seen very early in the testing process, typically in the first couple of weeks of high humidity [6]. Once

past this point, test units of the configuration in this study can be expected to complete the entire cycle without evidence of increased frost temperatures or argon loss caused by workmanship of the construction. If there was a sign which indicated that a unit was either demonstrating higher frost temperatures (therefore gaining moisture from the outside atmosphere) or losing argon, which could be interpreted as the induced effects of edge-seal strains at the PIB-to-glass or PIB-to-spacer interface.

Finite-Element Modeling and Validation

Full-Scale Unit Modeling

The glass has been modeled using 0.5-in.- (12.7-mm-) square shell elements. The structural effect of the PIB layer is negligible and was not considered in the model. The silicone has been modeled using 0.5×0.25 -in.²- (12.7×6.35 -mm²-) rectangular shell elements. Because of the one- and two-dimensional nature of the beam and shell elements, rigid links were used to hold the actual three-dimensional locations of the elements in space. Rigid links are linear elements that connect two nodes rigidly in space. The silicone was modeled as nonlinear material with shell elements configured perpendicular to the surface of the glass. The stress-strain curve of the material has been obtained from physical tests at room temperature (22°C) and is presented in Fig. 2 [13]. The corner portion of the finite-element (FE) model is presented in Fig. 13.

The aluminum framing members are typical of a four-sided, structurally glazed, unitized curtain-wall system. Each framing member profile was unique and the properties of the sections have been calculated and are presented in Fig. 1. The volume of the air cavity has been maintained with fluid elements with bulk stiffness of 100 kPa. The four corners of the frame have been modeled with pinned anchors where one corner had non-zero out-of-plane restraint. The end of the horizontal beam elements were moment released at the shared node of the vertical beams to represent a pinned connection between the horizontal and vertical framing members.

There are certain elements of the physical specimen that have not been modeled numerically. These parameters include negligible effects, such as the stiffness of PIB, the effect of gravity, and local distortions of framing profiles. Other parameters that were not modeled and may have significant effects include the flexibility/plasticity of the frame corner connections and thin-walled beam behavior of the frame members. The torsional behavior of the thin-walled frame members differs from the as-modeled solid members. The influence of warping of the thin-walled section changes the torsional shape of deformation of the frame members and may have significant impact on the overall results. A difference in torsional deformation to the one observed in the physical test has been obtained in the numerical model.

Analysis of the Full-Scale Unit Model

There are several possible failure scenarios during the cold-bending of a curtain-wall unit. Some of the major ones are: structural failure of the frame,

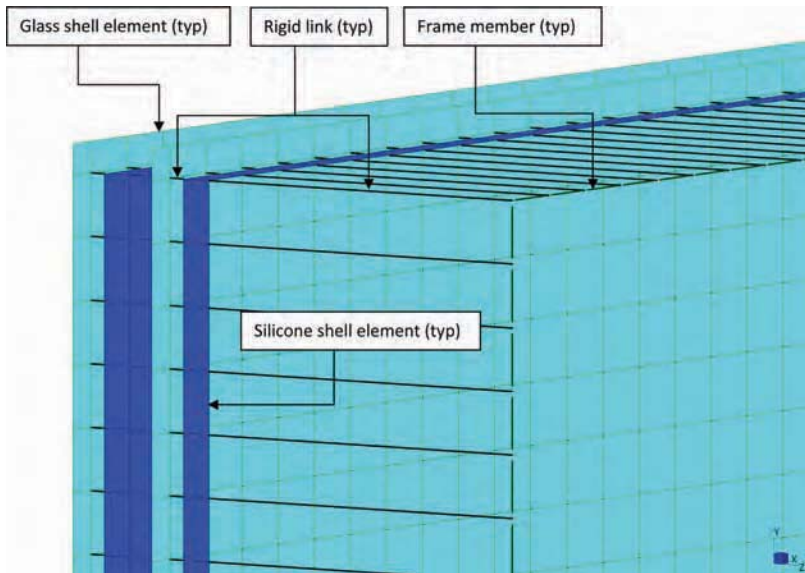


FIG. 13—Corner of FE model of full-size test.

breakage of glass, structural silicone failure, or PIB seal separation in the IGU. Structural failure of the frame can be safely predicted through the typical structural analysis involved in curtain-wall design. Glass can be designed to perform with the sustained stresses induced through cold-bending. Structural silicone is considered to be a strong component in the system and not a critical link. On the other hand, it is suspected that the PIB seal is the governing element during cold-bending of IGUs. Long-term performance of such a seal under sustained strains is unknown. However, the seal is known to fail under a regime of ASTM testing procedures even without applied strains.

Based on the results of the FE model, the locations of maximum edge-seal strains in the PIB were predicted. Preliminary FE analysis of the full-scale unit revealed that the maximum edge-seal deformations were located on the long side of the panel about 40 in. (1016 mm) away from the loaded corner. Intuition and engineering judgment, however, led to the conclusion that strains at the corner of the unit may also be significant. Therefore, these two locations were selected for the measurements of the edge-seal strains on assembly 2. The strain state at each of the locations was measured using three displacement dial gauges attached to the external ply of the glass to measure the relative in-plane edge displacements of the internal ply of the glass. Figure 7 shows locations of all six of these gauges. From these measurements the edge-seal strains in the PIB were calculated and presented in Table 3.

In addition to measuring the in-plane movements of the glass, several strain gauges were attached to the glass to understand its true bending behavior. These gauges were used to validate the results obtained between the three full-scale test assemblies and FE model. The locations of strain gauges in the

TABLE 3—Theoretical and applied PIB strains.

Direction of PIB displacement	Idealized bending	True bending as measured by LVDTs	Loaded corner	10 in. below loaded corner	20 in. below the loaded corner	30 in. below the loaded corner	10 in. to the right from the loaded corner	20 in. to the right from the loaded corner	30 in. to the right from the loaded corner	Gauges 1–3	Gauges 4–6	Used in small specimens
X	4	3.69	−0.008	−0.007	−0.004	−0.001	−0.009	−0.009	−0.009	−0.007	−0.006	0.014
	8	7.34	−0.019	−0.015	−0.002	0.010	−0.017	−0.017	−0.019	−0.022	−0.026	0.022
	12	10.92	−0.029	−0.019	0.007	0.028	−0.028	−0.029	−0.034	−0.040	−0.055	0.042
Y	4	3.69	−0.011	−0.021	−0.021	−0.021	−0.006	−0.002	0.005	−0.017	−0.022	0.018
	8	7.34	−0.016	−0.037	−0.039	−0.040	−0.001	0.007	0.023	−0.037	−0.041	0.032
	12	10.92	−0.026	−0.050	−0.054	−0.056	0.008	0.023	0.045	−0.057	−0.060	0.059
Z	4	3.69	−0.001	0.004	−0.001	0.000	−0.001	−0.001	−0.001	−	−	0.010
	8	7.34	0.010	0.027	0.002	−0.005	−0.001	−0.003	−0.007	−	−	0.015
	12	10.92	0.052	0.059	0.007	−0.015	−0.004	−0.013	−0.017	−	−	0.036

full-size test specimen of tests one and three are shown in Figs. 4 and 8, respectively. Two rosette strain gauges (numbered 1 through 6) were placed at the center of the glass on the inner and outer pane. Rosette gauges 7 through 9 are placed at the location of maximum stress in the glass as predicted by FE model. These gauges helped in understanding the shape of deformation of the glass during its bending. Unidirectional strain gauges were placed on all three test assemblies on the outer glass layer at the midpoints of the free edges. Readings of gauges 10 and 11 are affected mainly by the stiffness of the frame members.

The amount of applied out-of-plane deformation of the IGU in the physical testing was measured using four LVDTs attached near the corners of the glass (Fig. 14). The out-of-plane displacement in the numerical model however, was applied using forced displacement values of the node at the loaded corner with the other corners of the frames restrained. Because these measurements were taken at different locations, a correlation between the out-of-plane deformation in the physical and numerical models needed to be developed. Therefore, the displacements obtained directly from LVDT readings in the physical test were



FIG. 14—One of four LVDTs measuring bending in the full-scale test specimen.

compared to the corresponding nodal displacement results of the glass in the FE model. This comparison between physical and FE model out-of-plane displacements (bending) is presented in Fig. 15. Data presented in this paper corresponds to displacements as measured in the physical test.

Validation of Models

To correctly create a structural model we need to understand the behavior of glass bending, its expected displacements and other factors that have an effect on the glass deformation. To understand the cold glass bending, it is useful to study simplified models of deformation. The shape of the cold-bent glass is more complex than the following two theoretical models, but they are the major contributors to the overall state of deformation.

For a cold-bent plate, the first idealized deformation shape is one where straight lines parallel to the edges remain straight after the plane is deformed. The deformed shape that follows the straight lines rule is presented in Fig. 16.

Such deformation will create a state of stress in the glass such that:

$$\sigma_{xx}(z) = \sigma_{yy}(z) = \tau_{xz}(z) = \tau_{yz}(z) = 0 \tag{1}$$

and

$$\tau_{xy}(t/2) = -\tau_{xy}(-t/2) \neq 0 \tag{2}$$

where t = thickness of the plate.

This state of stress represents two-directional bending along $x'-y'$ directions, where $x'-y'$ are axes rotated 45° away from $x-y$ (Fig. 16).

The second idealized state of deformation is unidirectional bending. There are two statically equivalent states of deformation with unidirectional bending

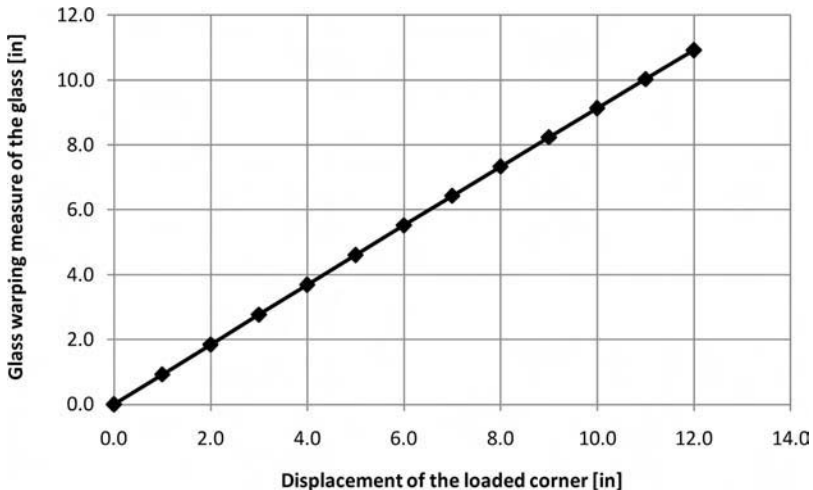


FIG. 15—Relation between physical and numerical out-of-plane displacements.

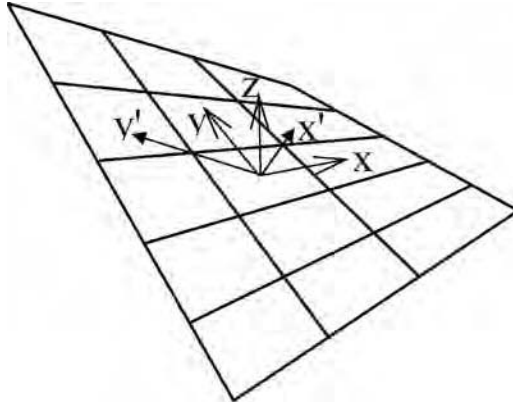


FIG. 16—*Idealization of purely cold-bent rectangular plate.*

where the bending could occur about either of the two diagonals. Both of these states are presented in Fig. 17. Depending on the initial deformation, a structure can arrive at either state of equilibrium. The diagonal about which the glass bends can be selected by forcing the bend during the initial deformation. This effect is very difficult to obtain numerically. Depending on the initial deformation state, nonlinear FE analysis will return various outcomes. However, simple tests, such as bending a credit card by hand will reveal that unidirectional bending requires the least amount of energy to force four corners of a rectangular plate out of plane. Applying external pressure to the surface of such bent glass can cause an effect known in the literature as “snap through buckling” [17].

The major differences between the two cold-bent shapes described above are:

- In the bidirectional bending example, the edges of the rectangular glass remained straight (Fig. 16).
- In the pure unidirectional bending example, the edges of the glass deform freely (Fig. 17). One of the diagonal lines remains undeformed. The direction of bending is perpendicular to the undeformed diagonal.

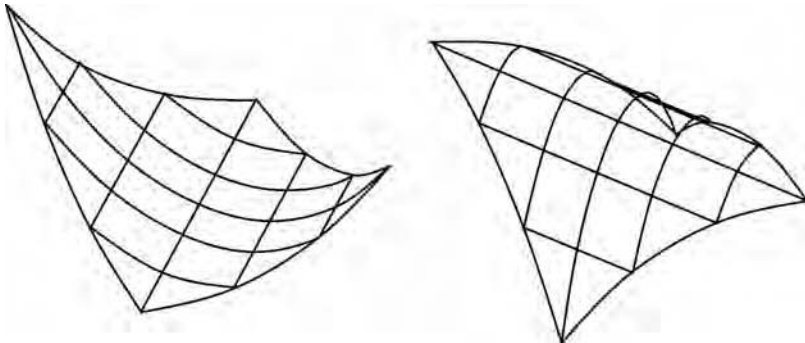


FIG. 17—*Two states of unidirectional bending.*

- In both pure unidirectional and bidirectional conditions, if the glass edge is framed the framing members are subject to torsion.
- The energy required to obtain unidirectional deformation is much smaller from the energy required in the bidirectional bending condition. Therefore the deformation state of bidirectional bending is possible but unstable.

The above states of deformation were observed with experimental testing [4], where the two-directional bending is observed with small deformations and the unidirectional bending is a post-buckling form.

The duality of the large deformation state was observed during the full-scale testing presented earlier in the paper. The application of pressure to the IGU in the cold-bent condition forced the deformed glass from one state of minimum energy to another. This is referred to as “snap through buckling” in the literature. This was quite a visual surprise during the full-scale testing applying the wind load to deformed unit.

An intuitive understanding of the principles laid out above would lead us to the following conclusions: a cold-bent plane with infinitely stiff edges would deform purely in a bidirectional manner, and a cold-bent plane with no frame at all would result in a simple unidirectional bend (about one of the diagonals). In our test, there are frame members that stiffen the sides of the rectangular IGU and the outcome was somewhere in between these two idealized cases.

Considering the above concepts, the deformation of the glass during the cold-bending process depends on the proportions between the flexural stiffness of the stiffening frame members and the glass panel itself. It should be noted here that the torsional deformation of the frame is a result in both of the idealized cases. Therefore, to allow for this deformation without high torsional forces in the frame, some members should be torsionally weak (i.e., thin-walled, open-section frames). The two vertical frame members in the full-size specimen are significantly weaker in torsion than the two horizontal members. A combination of framing members with different bending and torsional stiffness creates a complex system where the state of bending deformation may not be intuitive.

The physical tests of cold-bending of glass were intended to proceed to failure and large deformations were a part of the testing protocol. Whereas the behavior of many of the materials (such as glass or aluminum) had a linear physical behavior, the silicone connecting these parts had nonlinear physical behavior. Therefore, a model considering material nonlinearity and large deformation needed to be built.

Sources of Error and Modeling Inaccuracies

As previously discussed, the modeling of the full-scale test unit required consideration of the many different variables and how they interacted with one another. Given these possible variables and interactions, sources of error and modeling inaccuracies are inevitable. The research team sought to mitigate as many of these factors as possible through the testing regime and through

identifying potential areas of inaccuracy. The warped shape of the glass and modeling of the framing connections are two such areas of possible error.

The dual deformation modes of the glass proved to be one main area of uncertainty in the results. Because of the complex deformation of the glass, the readings of the rosette strain gauges did not show a close correlation to the strains in the numerical model. Buckling of the glass can cause a dramatic change in stress values which could not be obtained in the FE model. However, the linear strain gauges showed a much closer correlation to the tested unit (see Figs. 16 and 17), so it was reasonable to consider the model a good representation of the behavior of the full-scale test unit.

As previously stated, the connections between the framing members in the full-scale testing consisted of several machine screws fastening the horizontal members to the vertical members. In the FE model, these connections are modeled as pins (not restraining any moment) or fixed (restraining relative rotation). However, the actual connections are able to transfer some amount of moment before there is enough rotation to consider the connection pinned. This difference between the actual connection and the modeled connection can impact the correlation between recorded and modeled strains. The stiffness of the connections is unknown and it is difficult to predict without additional tests. It has been decided that the assumption of a pinned connection is the closest prediction of a real behavior because it ultimately led to a closer correlation in data.

To illustrate the effect of the stiffness of the connections on the behavior of the model, two graphs are presented (Figs. 18 and 19). These graphs show unidirectional strain gauges #10 and #11 (see Figs. 4 and 8) readings for pinned and fixed conditions of the connections respectively. Graphs noted as FE are

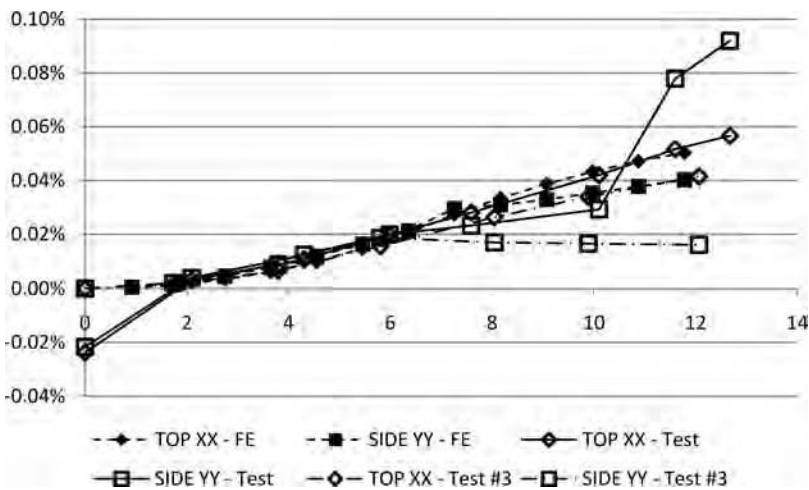


FIG. 18—Comparison of strains at unidirectional strain gauge locations for pinned frame connections. TOP XX are strains in the location and direction of strain gauge #11 and SIDE YY of strain gauge #10.

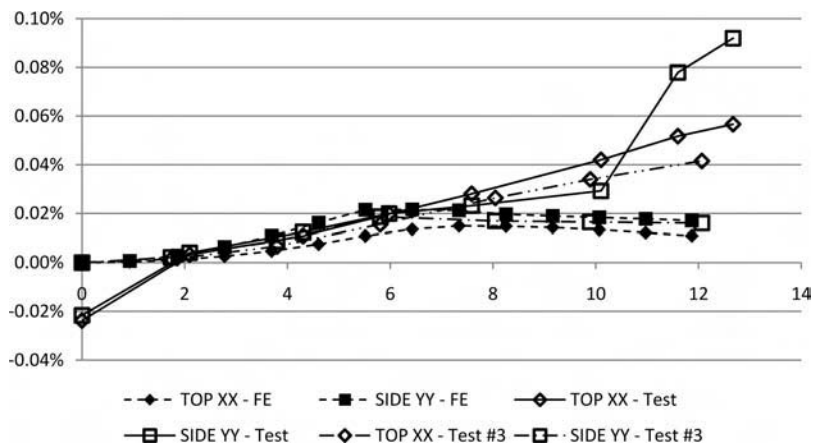


FIG. 19—Comparison of strains at unidirectional strain gauges locations for fixed frame connections. TOP XX are strains in the location and direction of strain gauge #11 and SIDE YY of strain gauge #10.

numerical results, and tests 1 and 3 are physical results of the two tests. Note that the fixed model captures an event at 6 in. (150 mm) of applied bending. This is possibly a location where the system deforms in one of two possible states. Also, the outcome of two very similar tests being different past this point reveals a potential instability of the system. Note, that non-zero initial strains in test 1 are residual strains after the specimen had been loaded to 4-in. (100-mm) displacement for the first time. A reset in the test procedure was required to correct the loading mechanism. The graph shows strains after this process.

Determination of Small Unit Displacements

The four specimen sets that were tested in the weatherization chamber have been subjected to edge-seal deformations that correlate to maximum strains in the full-size specimen at four values of out-of-plane displacement. These groups represented 0%, 50%, 100%, and 150% of the maximum design displacement. The maximum design displacement was determined with an engineering judgment. In practical applications, this would depend on the wind pressures, the size or shape of the panels, the makeup of the IGU and many more parameters. The engineering judgment has been made considering the maximum glass stress from the FE model. Numerical tests performed on the model revealed that 8 in. (200 mm) of displacement produces maximum stresses of 4.7 ksi (32 MPa). This is still well below the long-term limit stress of the fully tempered glass but considering additional possible stresses from positive and negative wind pressures, climatic loads and other safety factors, 8 in. (200 mm) of bending has been determined to be a reasonable limit of engineering design. Therefore the maximum applied edge-seal deformations during cold-bending of the full-size unit have been recorded for 4, 8, and 12 in. (100, 200, and 300 mm) of corner displacement. The location of where the PIB is strained the most varies

depending on the stiffness of the framing elements, connections between them and many other factors. From preliminary numerical modeling it has been determined that the location is about 40 in. (1.016 m) below the loaded corner. After the physical tests were performed, the numerical model needed to be revised. These revisions included applying the proper glass offsets, modeling the air pressure in the cavity, considering the pin behavior for the framing members and modeling an accurate location of the applied load. The outcome of the analysis was very sensitive to these minor model modifications but after the above modifications have been applied, the location of the maximum shear displacements of the PIB did not change significantly from the initial model and the modeled system correlated much more accurately to the test data.

To obtain edge-seal strain between the two panes of glass, three dial gauges per location of concern have been used in phase two of the full-scale test. The three dial gauges have been configured to obtain the differential movement along the short edge, the differential movement along the long edge and in-plane rotation of the panes with respect to each other at each of the edge locations (Fig. 7). The recorded differential displacements between panes have been converted to the displacement at single points of interest and they have been compared with the numerical results. Because of the sensitivity of the model and some modeling inaccuracies (described above) the results of the model match very well only for selected displacement values. Readings of all six dial gauges compared with numerical results are presented in Fig. 20. Refer to Fig. 7 for dial gauges numbering. Values of edge-seal strains from various locations of the numerical model have been put side by side with the physical results in Table 3. It should be noted here that the edge-seal deformations are applied to the small test specimens on all four edges simultaneously; therefore a displacement that is perpendicular to the long edge of the small specimen will be at the same time parallel to the shorter edge. The strains applied to the small specimens are shown in the right-most column of Table 3 and are summarized in Figs. 21 and 22, 23 and 24 which graphically depict the deformations for the control, 50 % design, 100 % design, and 150 % design specimens, respectively.

Results

Table 4 summarizes the test results of the ASTM E2188-10 [6] weathering protocol of the small IG units. During the test protocol the small IG units have the frost point and argon percentage measured initially, after 2 weeks of high temperature and humidity, after nine weeks of accelerated weathering (hot, cold, UV, and water spray) and after 4 weeks of high temperature and humidity. Each argon-percentage test point for a specific specimen is an average of five readings according to ASTM E2649 [15]. These averages are further averaged and plotted in Fig. 25.

All six of the control specimens qualified per ASTM E2190-10 [7], meaning that the frost points of the specimens remained below -90°F (-68°C) and the average argon retention of all the specimens was greater than 80 %. On the other hand, the 50 %, 100 %, and 150 % samples did not meet the testing criteria. Six

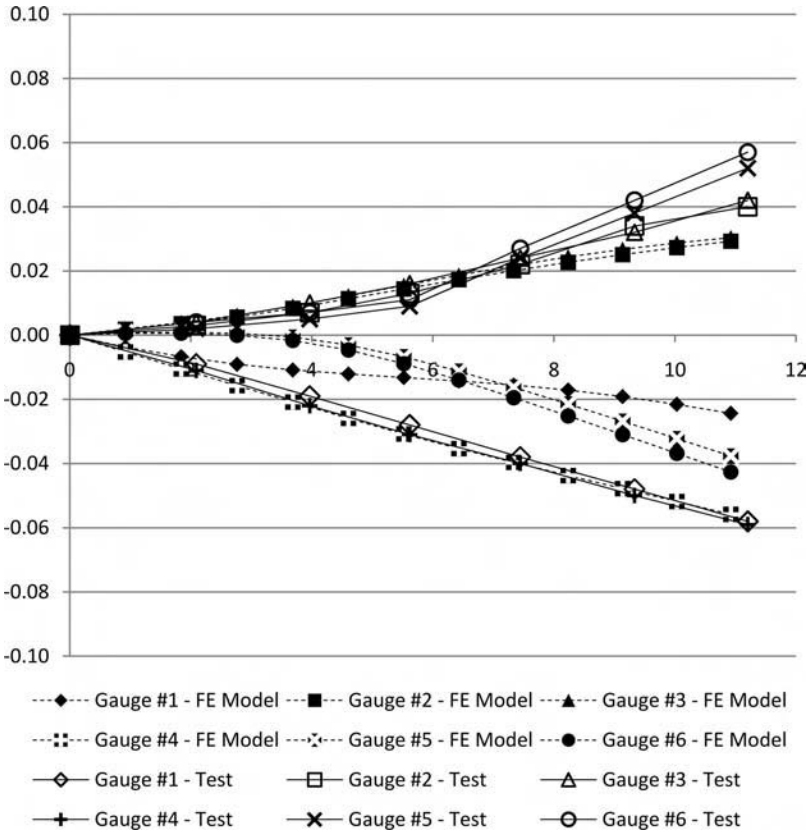


FIG. 20—Overlay of PIB in-plane displacements as measured in test 2 and obtained from numerical model.

specimens must meet the requirements described in Sec. 4 of ASTM E2190-10 but, because there were no available replacement specimens when a specimen broke during testing, the entire sample group could not be qualified. The reason for the limited number of specimens was because the research team did not strictly follow the requirements of the ASTM E2188 standard [6] and procure twelve total samples as put forth in Sec. 5.7. Had this been done, the broken specimens could have been replaced with a new one from the remaining specimens. Any lites that broke are noted in the table as “breakage” or “thermal break.” The “breakage” label refers to breaks that occurred during the initial displacement of the specimens before the testing began. “Thermal Break” refers to lite failure that occurred during testing.

All of the 50 %, 100 %, and 150 % units that did not experience breakage showed frost points below -90°F (-68°C). Additionally, the average argon retention of these specimens was greater than 80 %

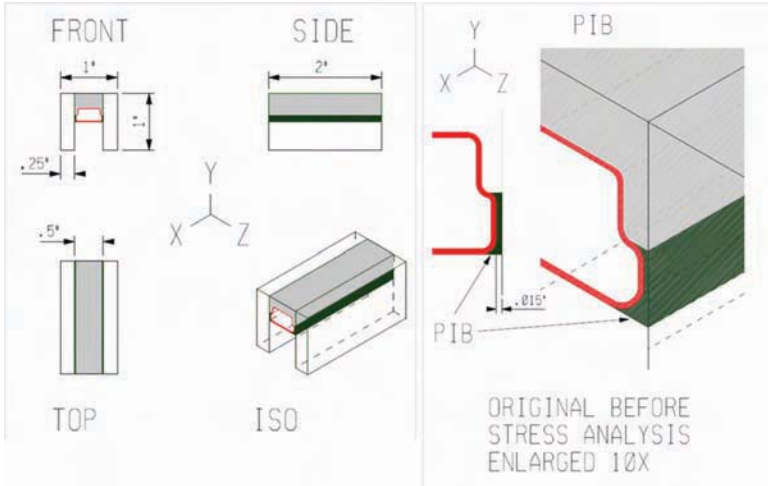


FIG. 21—Dimensions of primary (PIB) and secondary (silicone) at control no bending.

An unforeseen result from the durability testing was the failure of the epoxy adhesive in tension. The test units used an epoxy adhesive in several locations. The epoxy was used to keep the small IG units attached into the steel frame. This epoxy held fast in all of the tests, however, the epoxy adhesive used to induce displacement in the Z direction during the humidity and accelerated weathering cycles. Because the epoxy failed in all of the tests where tension was applied, this testing represented stressing the PIB in the Z direction for only a portion and not the entire test.

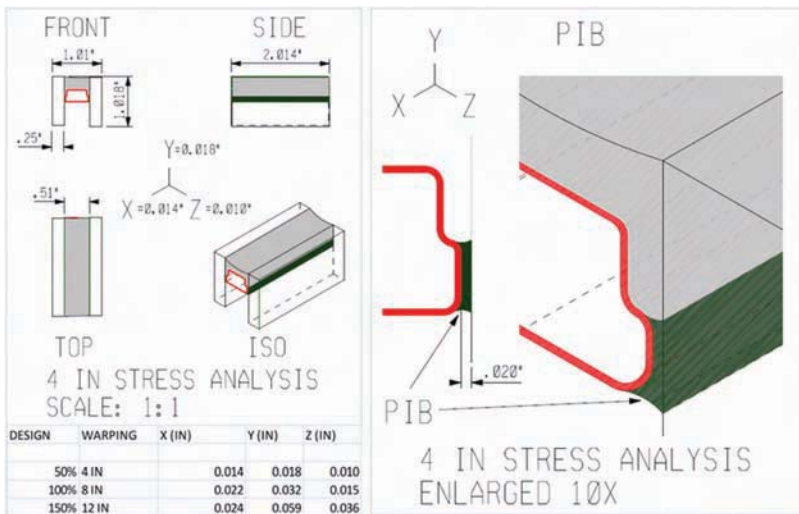


FIG. 22—Deformations of PIB and silicone at 50 % or 4 in. (100 mm) of bending.

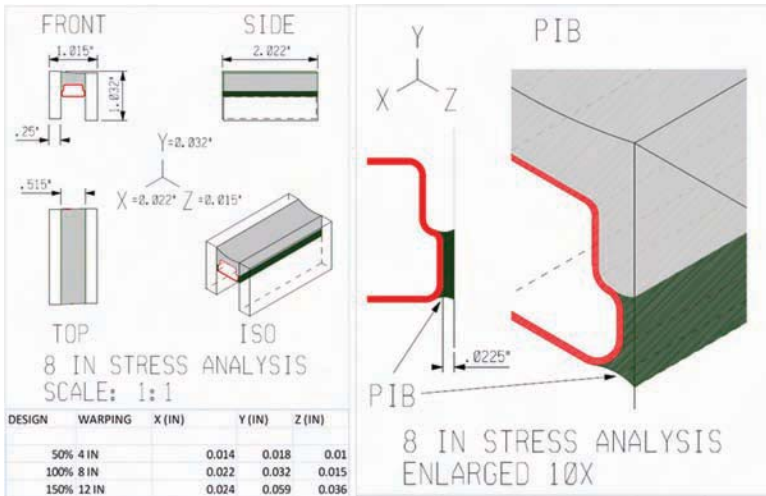


FIG. 23—Deformations of PIB and silicone at 100 % or 8 in. (200 mm) of bending.

The measurements that were taken to document the edge-seal displacement were monitored after the first high-humidity phase to ensure that the edge-seal strain was maintained. The measurements between the steel frame and the pane of glass that was adhered to it were maintained and no relative movement occurred between these two elements. The measured distance between the steel frame and the displaced piece of glass, however, increased by approximately 0.005 in. (0.13 mm) from its initial value. All other measurements, including the

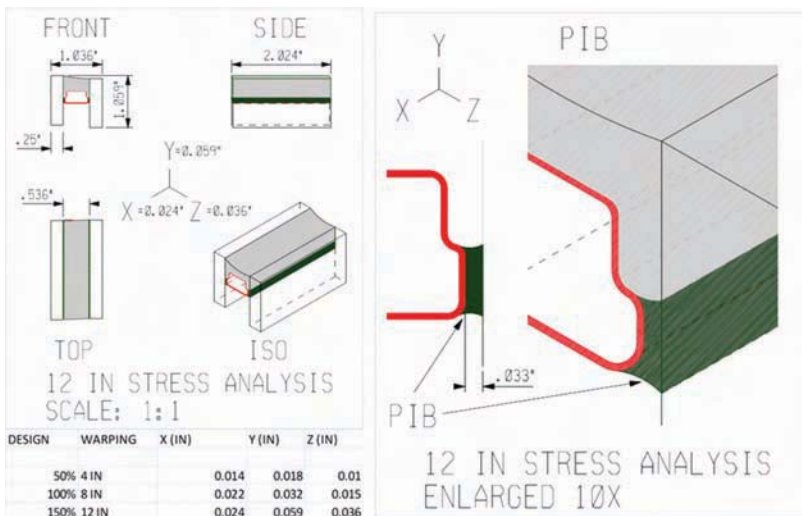


FIG. 24—Deformations of PIB and silicone at 150 % or 12 in. (300 mm) of bending.

TABLE 4.

Sample ID	Initial data		2 weeks high humidity 140°F 95 % RH		9 weeks accelerated weathering cycling: Heat, UV, and water		4 weeks high humidity 140°F 95 % RH	
	Frost point °F	% Argon	Frost point °F	% Argon	Frost point °F	% Argon	Frost point °F	% Argon
Set 1—No deflection (control) representing no bending								
5	<−90	88.3	<−90	86.0	<−90	80.9	<−90	77.7
7	<−90	94.8	<−90	92.6	<−90	85.5	<−90	78.9
9	<−90	92.6	<−90	91.0	<−90	87.9	<−90	85.5
20	<−90	92.4	<−90	90.4	<−90	84.9	<−90	80.7
21	<−90	94.1	<−90	92.3	<−90	87.4	<−90	85.1
44	<−90	92.7	<−90	90.1	<−90	85.4	<−90	81.2
Average	<−90	92.5	<−90	90.4	<−90	85.3	<−90	81.5
Set 2—50 % deflection representing 4-in. bending								
16	<−90	94.1	<−90	93.3	<−90	91.9	<−90	88.9
18	<−90	94.4	<−90	93.4	<−90	92.4	<−90	89.7
23	<−90	93.9	Breakage	N/A	—	—	—	—
12	<−90	87.3	<−90	85.3	<−90	84.0	<−90	82.6
24	<−90	94.7	<−90	93.4	<−90	92.7	<−90	89.8
25	<−90	93.1	<−90	92.2	<−90	90.0	<−90	85.5
26	<−90	91.3	<−90	89.8	Thermal break	—	—	—
Average	<−90	92.7	<−90	91.2	<−90	90.2	<−90	86.9

TABLE 4—Continued

Sample ID	Initial data		2 weeks high humidity 140°F 95 % RH		9 weeks accelerated weathering cycling: Heat, UV, and water		4 weeks high humidity 140°F 95 % RH	
	Frost point °F	% Argon	Frost point °F	% Argon	Frost point °F	% Argon	Frost point °F	% Argon
Set 3—100 % deflection representing 8-in. bending								
27	<−90	91.7	<−90	90.6	<−90	89.1	<−90	86.0
28	<−90	95.3	<−90	94.2	Thermal break	−	−	−
29	<−90	93.2	<−90	91.9	<−90	90.1	<−90	86.3
33	<−90	95.1	<−90	94.5	<−90	92.3	<−90	89.1
36	<−90	94.9	<−90	94.2	<−90	93.6	<−90	92.2
41	<−90	93.0	Breakage	N/A	−	−	−	−
3	<−90	84.3	<−90	83.3	<−90	80.3	<−90	78.0
Average	<−90	92.5	<−90	91.5	<−90	89.1	<−90	86.3
Set 4—150 % deflection representing 12-in. bending								
13	<−90	87.1	<−90	84.0	Thermal break	−	−	−
15	<−90	93.8	<−90	91.9	Thermal break	−	−	−
37	<−90	94.1	<−90	93.1	Thermal break	−	−	−
38	<−90	92.6	<−90	91.8	<−90	89.8	<−90	87.5
40	<−90	94.9	<−90	93.1	Thermal break	−	−	−
42	<−90	92.3	<−90	90.4	<−90	80.0	>−90 <−80	74.0
Average	<−90	92.5	<−90	90.7	<−90	84.9	−87.0	80.8

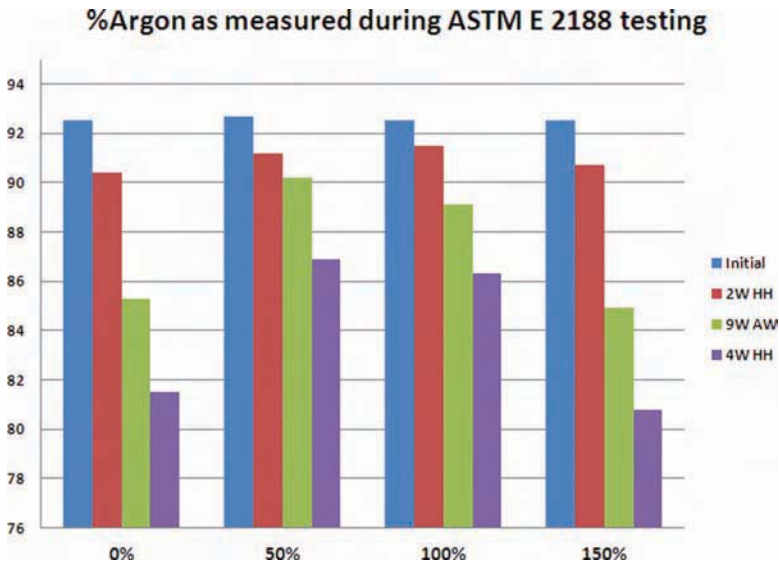


FIG. 25—% Argon within the test units as measured during the ASTM E2188-10 [6] testing protocol.

“z” displacements were maintained after the first high-humidity phase. It was during the weathering phase of testing that epoxy adhesive failure caused the tensioning mechanism to fail and release strain on the edge seal in the “z” direction.

Conclusions

The full-scale units that were subjected to wind load of $\pm 100 \text{ lb/ft}^2$ (4.8 kPa), while under a cold-bend did not break. The initial modeling suggesting at 8 in. (200 mm) of bending as the limitation of our design was a good engineering judgment. The successful completion of testing on assembly 3 shows that the curtain-wall system was able to survive a pressure, which was greater than what the profiles were designed for on a previous project. In fact, the immediate failure of the glass during the over-deflection of 15 in. (38.1 cm) suggests that the initial calculation of long-term glass stress at 12 in. (30.48 cm.) was indeed a good estimation of allowable bending from a glass-stress standpoint.

There were no thermal failures in the control set of small IGUs tested to the ASTM E2188-10 [6] protocol. Additionally, all of the control specimens qualified under ASTM E2190-10 [7] by maintaining a low frost point and high argon retention. This is evidence of the quality of workmanship in the specimens as they were all procured at the same time using the same methodology. Therefore, the workmanship of the other specimens is not in question and the weathering data collected bears this conclusion out.

The argon was retained in each of the small units that represented deflected large-scale units to the same degree or better than the control group. This is a very positive signal. In no case were the frost points reduced below -90°F (-68°C). Therefore the surviving units must have had the insulating-glass primary and secondary seals remaining intact. Further testing would require an appropriate number of specimens for each specimen set.

The epoxy that was used in this testing was not adequate to be placed under load in the accelerated weathering environments. The adhesive loss of the epoxy was a significant disappointment because the epoxy was thought to be a very-high-performing product. When the epoxy was performing, keeping the glass strained in the Z direction, the glass failed.

The deformations in the X and Y direction of the IGUs did not affect the frost point and argon retention of the surviving units. In fact, because of the creep of the structural silicone secondary seal and the relative stiffness of the silicone protection pad, the X and Y direction displacements increased throughout the high humidity testing. This means that the displacements induced were conservative because they increased throughout the high-humidity phase of testing. This also is a very positive signal. It is very likely that a revision in the method to deflect small insulating-glass units subjected to the ASTM E2188-10 [6] protocol can be done and a full compliance with the ASTM E2190-10 [7] specification can be obtained.

This study was not intended to test the strength of the glass during the weathering cycles, but to test the effect of strains on the primary and secondary seals. The thermal breakage that occurred during the weathering cycling does not constitute a failure in the spirit of this testing, but it is a result of an underestimation of the physical strength of the tempered glass. The measurements that were taken while the glass was intact suggest that a strained edge seal is quite resilient to moisture infiltration. Further testing may provide evidence in favor of these preliminary conclusions.

Limitations

This work was done on clear, tempered $60 \times 120 \times 1$ in.³ (1.52×3.05 m² \times 25.4 mm) insulating-glazing units to determine the durability of the secondary and primary seals through the ASTM E2190-10 [7] and ASTM E2188-10 [6] testing protocol. The data generated targeted a specific sized unit, a specific spacer system design, and a specific aspect ratio. It is unknown if this data applies to every case of IG size, glass make-up, and spacer system, and it is unlikely that it does. Before a project is undertaken mimicking this type of cold-bending, this testing should be repeated using actual sizes and anticipated bending dimensions. This is the first data generated on this topic of durability with cold-bending, and is likely just the beginning of many research projects on this topic. Cold-bending of IGUs is easiest when the units are attached to the glazing frame using structural silicone. It may be specified that cold-bent IGUs are to be used in a mechanically attached curtain-wall system, but the structural silicone used to attach an IGU to a frame is a combination adhesive and sealant, retarding air and water infiltration. Mechanically held cold-bent IGUs may put undue

stresses on gasket systems that result in unwanted air and water infiltration. Because of the likeliness of structural silicone attachment of cold-bent glass the durability testing was done to the ASTM E2190-10 protocol, which uses a UV cycle in the test. This protocol is not the same as the EN1279 Glass In Building – Insulating Glass Units [18] protocol used in Europe. It is unknown if the two protocols produce similar results.

Future Work

The breakage of the small insulating-glass units in the thermal cycling is most likely caused by the way the assemblies containing the test specimens were fabricated. This was the first attempt and the epoxy-anchorage method appeared to have the best chance for success. Additional testing of small IG units to the protocol in a deflected position is the most challenging, yet the protocol is the basis for specifications of pass or fail. In hindsight, the glass in the small test units should have been increased to a 3/8-in. (9-mm) thickness in lieu of the thinner glass suggested by the specification. There was also a consideration regarding the thickness of the assembly to be able to fit into the test chamber. Finally, the epoxy that was used to displace the glass in the Z direction should have been replaced with an extremely-high-strength silicone adhesive, such as the one also presented in this symposium [19].

Additionally, future work needs to be done to more strongly correlate the amount of bending in a full-size panel to the exact amount of edge-seal strain in an IGU. The sample size of the full-scale test was too small (one panel; assembly 2) to properly conclude that the induced edge-seal strains are exactly equal to those used in the small-scale durability test. Also, this research has not correlated other factors to edge-seal strain, such as: glass aspect ratio, framing member section properties, glass thickness or makeup, spacer design, etc.

Future research would refine the testing methods as laid out in this project by reexamining the design of the small unit displacement apparatus to lower the induced stress on the glass and reduce the risk of thermal breakage, to procure glass with a higher resistance to thermal fracture (thicker glass or higher edge strength), to improve the method of application of “z” displacement so that it survives the weathering process, and to anticipate thermal breakage and procure more specimens to complete the testing.

Future projects that consider cold-bend IGUs should indeed have a level of understanding whether or not the bent glass will indeed hold up to the durability standards. This knowledge must come from a study of the particular variables present in such a project. As mentioned above, the effects of glass make-up, frame behavior, spacer design, silicone size, or unit typology and geometry could drastically affect durability, as well as other factors that were not examined in this study, such as glass stress, silicone stress, or aesthetic appeal.

Acknowledgments

The writers would like to specifically thank the personnel at Architectural Testing Inc. in St. Paul Minnesota for the willingness to customize the testing to

support this project. Specifically, Dan Johnson, Eric Schoenthaler, Brian Goetzke, Mark Lewke, Michael Resech, and Zane Wybest at ATI made this work possible. The writers have collaborated with each other in the spirit of advancing the understanding the physical attributes and science behind cold-bent glass. The collaboration was necessary, as each party brought their own industry experience to the project. It is not likely that a single industry entity could produce this type of work. For this the authors wish to thank their employers for the time and expense that this work has required, all for the spirit of industry advancement. This publication is for informational purposes only. None of the parties involved in this research make any representations that this data is appropriate for use in other applications. Any party electing to use any of the data contained herein assumes all risks related to such use. To the extent permitted by applicable law, no liability whatsoever is accepted by any of the parties participating in this research for any direct or consequential loss, damage, costs or prejudices whatsoever arising from the use of this publication or its contents.

References

- [1] Eekhout, M., Lockfeer, W., and Staaks, D., 2007, "Application of Cold Twisted Tempered Glass Panels in Double Curved Architectural Designs," *Glass Perform. Days*, Vol. 2007, pp. 213–220.
- [2] Eekhout, M. and Niderehe, S., 2009, "The New, Cold Bent Glass Roof of the Victoria & Albert Museum, London," *Glass Perform. Days*, Vol. 2009, pp. 408–412.
- [3] Dodd, G. and Thieme, S. 2007, "Comparison of Curved Glass and Cold Bent Panels," *Glass Perform. Days*, Vol. 2007, pp. 83–86.
- [4] van Herwijnen, F., Staaks, D., and Eekhout, M., 2004, "Cold Bent Glass Sheets in Façade Structures," *SEI*, Vol. 14, No. 2, pp. 98–101.
- [5] Belis, J., Inghelbrecht, B., Van Impe, R., and Callewaert, D., 2007, "Experimental Assessment of Cold-Bent Glass Panels," *Glass Perform. Days*, Vol. 2007, pp. 115–117.
- [6] ASTM Standard E2188-10, 2010, "Standard Test Method for Insulating Glass Unit Performance," *Annual Book of ASTM Standards*, ASTM International, West Conshohocken, PA.
- [7] ASTM Standard E2190-10, 2010, "Standard Specification for Insulating Glass Unit Performance and Evaluation," *Annual Book of ASTM Standards*, ASTM International, West Conshohocken, PA, 2010.
- [8] ASTM Standard E1300-09a, 2009, "Standard Practice for Determining Load Resistance of Glass in Buildings," *Annual Book of ASTM Standards*, ASTM International, West Conshohocken, PA.
- [9] GANA *Glazing Manual—50th Anniversary Edition*, Glass Association of North America, Topeka, 2010, pp. 55–60.
- [10] ASTM Standard E330-02, 2002, "Standard Test Method for Structural Performance of Exterior Windows, Doors, Skylights and Curtain Walls by Uniform Static Air Pressure Difference," *Annual Book of ASTM Standards*, ASTM International, West Conshohocken, PA.
- [11] ASTM Standard C1184-05, 2005, "Standard Specification for Structural Silicone Sealants," *Annual Book of ASTM Standards*, ASTM International, West Conshohocken, PA.

- [12] ASTM Standard C1369-07, 2007, "Standard Specification for Secondary Edge Sealants for Structurally Glazed Insulating Glass Units," *Annual Book of ASTM Standards*, ASTM International, West Conshohocken, PA.
- [13] Wolf, A. T. and Cleland-Host, H. L., "Material Properties for Use in FEA Modeling: Sealant Behavior with Ambient Laboratory Climate Aging," *Durability of Building and Construction Sealants and Adhesives*, Vol. ASTM STP 1453, A. T. Wolf, Ed., ASTM International, West Conshohocken, PA, 2004.
- [14] ASTM Standard C1265-94(2005)e1, 2005, "Standard Test Method for Determining the Tensile Properties of an Insulating Glass Edge Seal for Structural Glazing Applications," *Annual Book of ASTM Standards*, ASTM International, West Conshohocken, PA.
- [15] ASTM Standard E2649-09, 2009, "Standard Test Method for Determining Argon Concentration in Sealed Insulating Glass Units Using Spark Emission Spectroscopy," *Annual Book of ASTM Standards*, ASTM International, West Conshohocken, PA.
- [16] ASTM Standard E546-08, 2008, "Standard Test Method for Frost/Dew Point of Sealed Insulating Glass Units," *Annual Book of ASTM Standards*, ASTM International, West Conshohocken, PA.
- [17] Wempner, G. and D. Talaslidis, D., *Mechanics of Solids and Shells: Theories and Approximations*, CRC Press, Boca Raton, 2003.
- [18] EN 1279, 2002, "Glass in Building—Insulating Glass Units: Part 2 Long Term Test Method and Requirements for Moisture Penetration. Part 3: Long Term Test Method and Requirements for Gas Leakage Rate and for Gas Concentration Tolerances," European Committee for Standardization, Brussels.
- [19] Wolf, A. T., Sitte, S., Brasseur, M. J., and Carbary L. D., 2011, "Preliminary Evaluation of the Mechanical Properties and Durability of Transparent Structural Silicone Adhesive (TSSA) for Point-Fixing in Glazing," *J. ASTM Int.*, Vol. 8, No. 10, 104084.

W. (Voytek) S. Gutowski,¹ Gary Toikka,² and Sheng Li³

The Mechanism of Adhesion Improvement of Elastomeric Silicone Sealants to Difficult-to-Bond Polymeric Substrates through Reactive or Interpenetrating Molecular Brushes

ABSTRACT: High-quality and durable adhesion of elastomeric adhesives to metallic, ceramic, and organic substrates is essential to a broad range of industries, e.g., building and construction, automotive, electronic, aerospace, biomedical, and others. The principles of engineering substrate surfaces through grafted connector molecules are discussed in this paper. In particular, two important modes of interaction for surface-grafted “molecular brushes” are investigated and experimentally verified. It is demonstrated that the inclusion of silicone- and/or amine-terminated graft molecules, such as silanes or polyethyleneimines, at polymer interfaces, results in the formation of strong molecular bridges between a range of organic substrates and elastomeric sealants leading to significantly improved bonding. The technology has been successfully adopted by global automotive industry for improving adhesion of a variety of adhesives and coatings to polyolefinic substrates.

Manuscript received August 23, 2011; accepted for publication February 8, 2012; published online May 2012.

¹Associate Professor, Dr.-Ing., CSIRO Materials Science and Engineering, Interphase Engineering and Intelligent Materials Surfaces Group, P.O. Box 56, Melbourne-Highett, Victoria 3190, Australia (Corresponding author), e-mail: voytek.gutowski@csiro.au

²CSIRO Materials Science and Engineering, Interphase Engineering and Intelligent Materials Surfaces Group, P.O. Box 56, Melbourne-Highett, Victoria 3190, Australia, e-mail: gary.toikka@csiro.au

³CSIRO Materials Science and Engineering, Interphase Engineering and Intelligent Materials Surfaces Group, P.O. Box 56, Melbourne-Highett, Victoria 3190, Australia, e-mail: sheng.li@csiro.au

Cite as: Gutowski, W. S., Toikka, G. and Li, S., “The Mechanism of Adhesion Improvement of Elastomeric Silicone Sealants to Difficult-to-Bond Polymeric Substrates through Reactive or Interpenetrating Molecular Brushes,” *J. ASTM Intl.*, Vol. 9, No. 5. doi:10.1520/JAI104275.

Copyright © 2012 by ASTM International, 100 Barr Harbor Drive, PO Box C700, West Conshohocken, PA 19428-2959.

KEYWORDS: adhesion, surface engineering, durability, silicone adhesion, organic substrate, metallic substrate, molecular brushes, silicones, polyethyleneimines

Introduction

Elastomeric silicone sealants are an important class of structural adhesives commonly used by the building, automotive, aerospace, electronic, and other industries.

Specifically formulated silicone adhesives are presently the only materials that possess all the necessary properties for meeting the demanding needs of these industries: reliable adhesion to a variety of substrates, elastomeric properties that allow accommodation of both thermal and structural movements of the bonded components, and, finally, adhesive and cohesive properties that are little affected by ultraviolet (UV) radiation and other environmental factors.

Whereas the outstanding bonding capacity of structural silicone adhesives to glass and metallic surfaces is well documented, the mechanism of adhesion to other types of substrates is not yet fully understood. For instance, various decorative or functional finishes, such as wet paints, powder coatings, or self-cleaning coatings applied to building façade components, exhibit a broad range of decorative and functional attributes but frequently may have surface properties that adversely affect the adhesion of sealants.

One particular example of these are fluorinated powder coatings, which exhibit outstanding long-term durability guaranteed for up to 25–30 years and, yet, require careful assessment of adhesion performance and frequently need priming to ascertain long-term sealant adhesion and façade integrity.

It is well known throughout the industry that a great number of paint finishes and metallic or polymeric substrates create various degrees of difficulty in attaining satisfactory long-term adhesion.

In many cases, the improvement of adhesion requires the use of a primer. It is applied to the substrate as a “tie layer” acting as a sealant/substrate compatibilizer, which promotes improved adhesion. In some cases, however, this approach is unsuccessful, resulting in a need to change the substrate or the type of surface finish. Sometimes, despite good initial results, the adhesion problems become apparent during the service life of a structure.

This is caused by the lack of durable, chemical bonds between either the silicone adhesive and substrate, or across the interfaces between the primer and the substrate, or that between the primer and silicone adhesive.

In this paper, we demonstrate and examine an effective process that provides the potential for improved adhesion of silicone adhesives to selected types of difficult-to-bond polymers, such as polypropylene (PP)-ethylene-vinyl acetate (EVA) blend, and polyacetal, through the use of surface-grafted, chemically reactive connector molecules based on organo-functional silanes. These results are then compared with those from other types of surface-grafted macromolecules.

The new surface-engineering process enables simple on-line surface engineering of a broad range of architectural substrates, e.g., paint finishes or powder coating, anodized aluminum, rigid plastics, polymeric films, etc. The chemical

composition and the nano-scale topography of the substrate surface are controlled to optimize the durability of the adhesive/substrate interface.

This new process opens up new opportunities to the end-users of silicone-based and other generic types of adhesives. The following are regarded as the main potential advantages for any commercial application of this technology:

- Longer warranties for applications involving the adhesion of silicones to a wider range of substrates,
- Improved potential for exploiting problematic substrates, such as polyolefins, poly(vinylidene fluoride) (PVDF), siliconized coatings, organically-anodized aluminum, stainless steel, etc.,
- Greatly reduced need for solvent-based primers,
- Simplification of the design techniques for structural silicone adhesives, as the sealant cohesive strength itself becomes the main design parameter because of the improved adhesion, and
- Simplification of the adhesive chemistry.

The technology discussed in this paper has been successfully adopted by the global automotive industry for improving adhesion of a variety of adhesives and coatings to polypropylene-based substrates (body-trim panels, instrument panel, and door-trim panels).

Elastomeric Silicone Adhesives

The majority of silicone adhesives and sealants use polydimethylsiloxane (PDMS) as the base polymer, which affords these adhesives their special properties, such as excellent ultraviolet (UV) light and ozone resistance, low-temperature resistance, flexibility at temperatures down to -40°C , high-temperature resistance (retention of elasticity up to 100°C), and long-term durability under adverse service conditions.

In most cases, the hydroxy-terminated PDMS (see Fig. 1) is used as polymer base in most silicone adhesives and sealants. Table 1 provides a typical formulation for an elastomeric silicone adhesive.

Condensation cure one-part and two-part room-temperature vulcanizing (RTV) systems are typically formulated from hydroxy-terminated polymers with molecular weights ranging from 15,000 to 150,000. One-part systems are the most widely used in practical applications. These systems are cross-linked with moisture-sensitive multi-functional silanes in a two-stage reaction. In the first stage, after compounding with fillers, the silanol is reacted with an excess of multi-functional silane [1]. The silanol is in essence displaced by the silane. This is depicted in Fig. 2 for an acetoxy-cross-linked system.

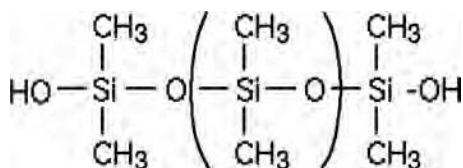


FIG. 1—Hydroxy-terminated polydimethyl siloxane (PDMS) polymer [1].

TABLE 1—A typical formulation (wt. %) for an elastomeric silicone adhesive [2,3].

Component	(%)
Hydroxy-terminated silanol polymer (PDMS): MW 15,000 to 150,000	60–85
Plasticizer: trimethylsilyl-terminated PDMS	10–20
Fumed silica (treated and/or untreated)	5–10
Cross-linker	5–7
Tin catalyst (e.g., dibutyl tin dilaurate)	0.05–0.1
Adhesion promoter (e.g., aminopropyltriethoxy silane (γ -APS))	0.25–2

As seen from Fig. 2, after the first-stage reaction, the silicone has two groups at each end that are susceptible to hydrolysis. The silicone adhesive in the form presented in Fig. 2 is stored and protected from moisture until ready for use. The second stage of the reaction takes place immediately after installation, as the end groups are exposed to moisture and a rapid cross-linking reaction occurs.

The cross-linker system is typically a combination of a reactive tri- or tetra-functional silane and a condensation catalyst. Examples of typical functional groups in cross-linkers are shown in Table 2.

The schematics of the cross-linking reactions of the most commonly used cross-linkers in 1-component moisture-curing silicone adhesives are outlined in Fig. 3 [1].

The cross-linking reaction is catalyzed by titanates, frequently in combination with tin compounds and other organo-metallic compounds. One-part acetoxy-cross-linked systems usually rely solely on tin catalysts, e.g., dibutyltin diacetate, dibutyltin dioctanoate, or dibutyltin dilaurate. The tin contents in one-part RTV systems is above 50 ppm with a ratio of 2500:1 for Si-OR to Sn. Typical formulations, however, have up to ten times the above minimum [1].

The moisture-curing one-part silicone systems gradually polymerize as atmospheric humidity diffuses into the adhesive. In this process, water reacts with the prepolymer molecules, forming cross-linked macro-molecules [2–4].

Improved Adhesion of Elastomeric Silicone Adhesives through Surface-Grafted Connector Molecules

Surface-Grafted Connector Molecules Interpenetrating into the Adjacent Adhesive

The theoretical principles of adhesion enhancement through surface-grafted connector molecules, interpenetrating the cross-linked network of an adjacent

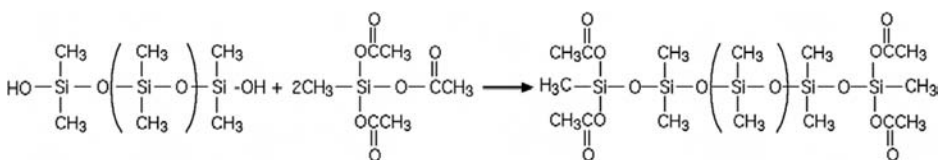


FIG. 2—First-stage reaction of hydroxy-terminated PDMS with the acetoxy cross-linker [1].

TABLE 2—Typical functional groups of cross-linkers used in silicone adhesives [3].

Order of commercial usage	Substituent	Formula with functional group
1	Acetate ⁴	
2	Amines ⁴	R—NH-
3	Benzamide ⁴	
4	Oximes ⁴	
5	Alkoxides ⁴	R—O-
6	Octoate ⁴	

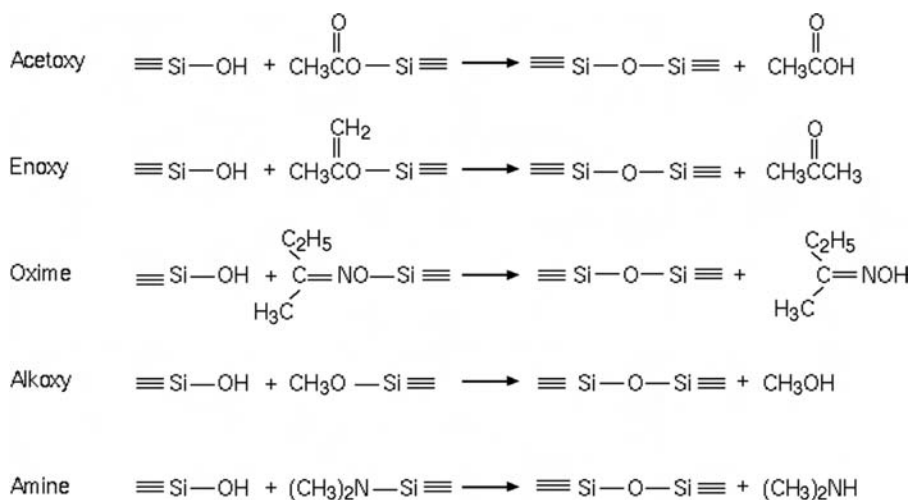


FIG. 3—Schematic representation of the reaction of typical cross-linkers in one-component moisture curing silicone adhesives [1].

adhesive, were developed by de Gennes [5–7] and his co-workers [8–12] (see Fig. 4 for schematic illustration of the mechanism of interactions between surface-grafted macromolecular chains and an elastomeric silicone adhesive).

According to de Gennes' theory, in the simplest case of interface reinforcement involving chain pull-out in the presence of van der Waals interactions in the macromolecular chain/elastomer system (where connector chains and adhesive polymer are identical), the fracture energy associated with deformation and extraction of the connector chains is

$$G = 2\gamma(1 + \sigma N) \quad (1)$$

where γ is the surface energy of the polymer and that of connector chains and σ is the surface density of connector chains.

It has been subsequently demonstrated that the normalized increase in the fracture energy of the interface between a solid substrate "tethered" with surface-grafted connector molecules and the PDMS elastomeric adhesive is as follows [9]:

$$G - W \cong \gamma N \sigma (1 - \sigma^{2/3} N_c^{1/3}) \quad (2)$$

where G is the fracture energy of the interface reinforced with surface-grafted connector molecules, W is the energy of adhesion ($W = 2\gamma$) between the chemically identical PDMS adhesive and PDMS connector molecules, N is the degree

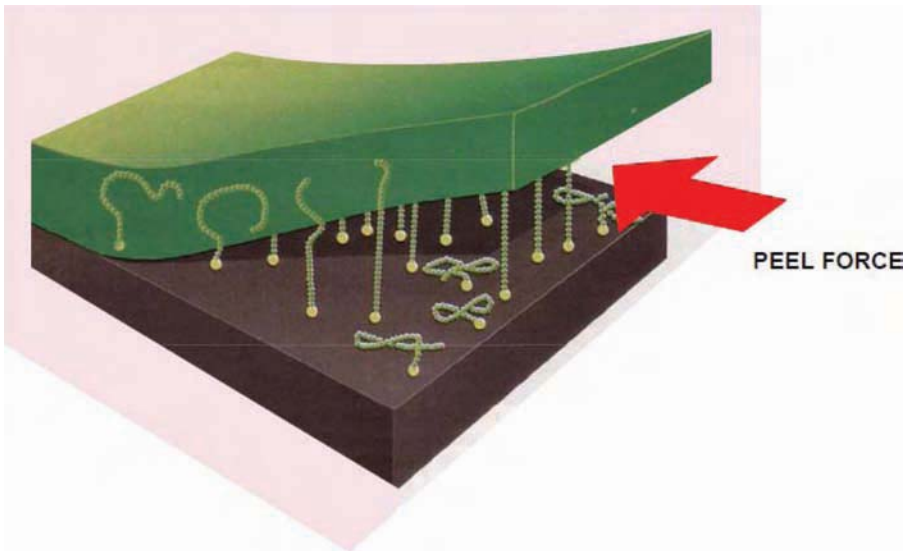


FIG. 4—Schematics of the mechanism of interactions between the "tethered substrate surface" (a substrate with surface-grafted macromolecular chains) and an elastomeric silicone adhesive (adopted with changes from [7]).

of polymerization ($N = MW/m$) of connector chain molecules, N_c is the degree of polymerization of cross-links of the PDMS adhesive.

The following can be seen from Eq 2:

- For $\sigma > N_c^{-1/2}$, the connector molecules completely separate from the PDMS network and G reduces to W .
- The optimum adhesion occurs for:

$$\sigma_{\text{OPT}} \cong 0.465 N_c^{-1/2} \quad (3)$$

- The corresponding value of the optimum fracture energy, G_{OPT} , is:

$$G_{\text{OPT}} - W = 0.186\gamma \frac{N}{N_c^{1/2}} \quad (4)$$

Figure 5(a) illustrates the results for Eq 2 solved numerically for $N = 2300$ and $N_c = 230$, and $\gamma = 21.6 \text{ mJ/m}^2$ at 25°C [11]. These results indicate that there is a distinct optimum (σ_{OPT}) in the surface density (σ) of the connector molecules which has to be achieved to maximize the adhesion between a surface-modified substrate and the adhering polymeric material, i.e., adhesive.

The theoretical model described by Eq 2 has been verified experimentally.

An example of this is illustrated in Fig. 5(b) [10]. It shows the normalized fracture energy $(G - W)/W$ for the interphase comprising molecular brushes interacting with the elastomeric silicone adhesive through van der Waals forces as a function of surface density of molecular chains, σ , for a cross-linked PDMS elastomer ($N_c = 230$) in contact with a silicon wafer grafted with PDMS connector chains exhibiting $N = 2300$. W is the thermodynamic work of adhesion and $W = 2\gamma$, where γ is the surface energy of PDMS ($\gamma = 21.6 \text{ mJ/m}^2$ at 25°C).

Surface-Grafted Connector Molecules Chemically Bonded to an Adjacent Adhesive

The theoretical principles of interfacial reinforcement by surface-grafted connector molecules capable of chemically bonding with an adjacent adhesive were developed and discussed by Brochard-Wyart and de Gennes [12]. Their theory predicts that the adhesion enhancement provided by surface-grafted and chemically bonded macromolecular chains can be expressed as:

$$G_b = W_a + W_b N \sigma \quad (5)$$

where N is the degree of polymerization of connector molecules, W_a is a reversible energy of adhesion between the bare (ungrafted substrate) and the adjacent polymer (because of van der Waals forces only), and W_b describes the energy required to disrupt a dense array of chemical bonds as given by the following:

$$W_b = \frac{U_b}{a^2} \quad (6)$$

where U_b is the energy of a bond occupying an areas of a^2 .

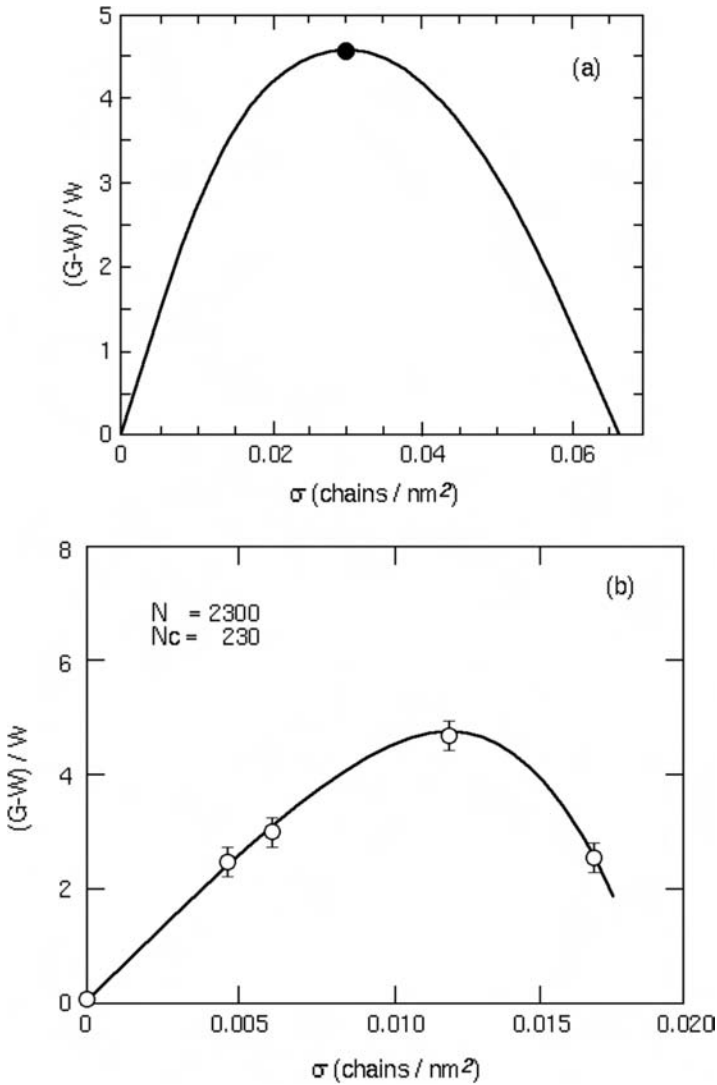


FIG. 5—(a) Numerical solution to Eq (2) for a change in adhesion measured by the increase in the normalized fracture energy $(G-W)/W$, for connector molecules characterized by $N = 2300$ interacting with cross-linked PDMS elastomer with $N_c = 230$ [7]. (b) Experimentally determined normalized fracture energy, $(G-W)/W$ as a function of the surface density $[\sigma]$ of molecular chains for the molecular brush/elastomeric adhesive interphase interacting through van der Waals forces with a cross-linked PDMS elastomer ($N_c = 230$) in contact with silicon wafer grafted with irreversibly adsorbed chains ($N = 2300$). W is the thermodynamic work of adhesion, $W = 2\gamma$, with γ the surface energy of PDMS $\gamma = 21.6 \text{ mJ/m}^2$ at 25°C [10].

Figure 6 illustrates the following findings of Brochard-Wyart and de Gennes [12] in relation to interfaces reinforced by macromolecular connector chains grafted onto the substrate surface and chemically bonded to the adhesive:

- An increase in graft density from zero to a certain cut-off value (σ_{CRIT}), as described by Eq 7, results in a linear increase of interfacial fracture energy

$$\sigma_{CRIT} = \frac{N_c^{1/2}}{N} \quad (7)$$

- For higher graft densities ($\sigma \geq \sigma_{CRIT}$), no further increase in joint fracture energy should be expected.

Enhancement of Adhesion of Silicone Adhesives through Surface-Grafted Molecular Brushes

Untreated polymeric materials in the form of rigid plastic, flexible polymeric film or a decorative coating (e.g., wet paint or powder coating) are frequently not adequately receptive to reactive species available in elastomeric sealants, adhesives, or decorative coatings in terms of reactivity through hydrogen or covalent bonding because of a lack of reactive chemical functionalities at the substrate surface.

The above drawback can be partially overcome by surface activation of polymer surface by commodity “oxidative” processes, such as corona discharge

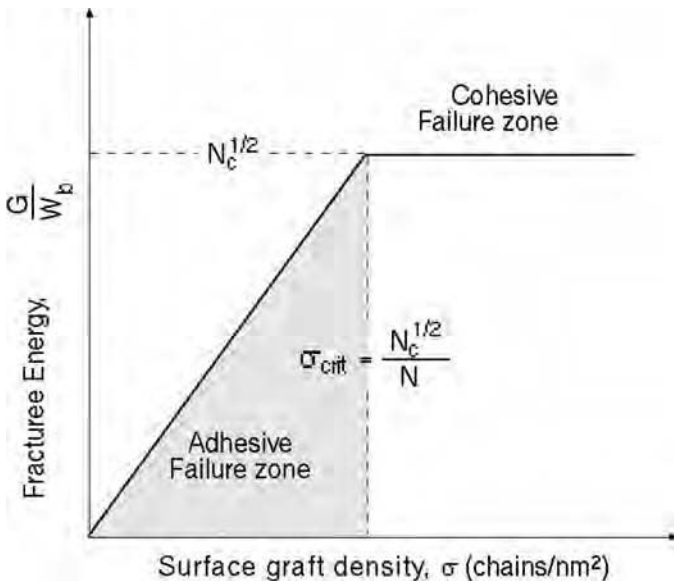


FIG. 6—Interfacial fracture energy versus surface graft density, σ , of surface-grafted and chemically bonding (with adhesive) macromolecular connector chains [12].

or flame treatment, which create surface-functional sites, such as OH, C=O, and COOH groups, through which the polymer surface energy and, hence, its wettability by adhesives and coatings is improved.

The key drawbacks of such oxidative treatments are: (i) fast decay of surface effects owing to restructuring of the surface because of rotation of functional groups and, hence, short operating time for completing adhesive bonding, joint sealing, or coating, and (ii) a lack of control of substrate surface chemistry and, hence, its reactivity with specific sealants or adhesives.

In this work, we discuss our novel polymer surface-engineering process, which utilizes specific receptor sites created by corona discharge, flame, or oxygen plasma treatments, e.g., OH, C=O, and COOH groups, which are, in turn, capable of chemically reacting with designated functional groups available at the ends or branches of specific connector molecules.

The process [13–15] commonly known as SICOR (originally derived from the combination of silane and corona) for fabrication of polymer surfaces “tethered” by designated types and surface architecture of molecular brushes, comprises the following:

- surface oxidation, e.g., by flame, corona discharge, ozone, or UV treatment, which are the precursor activation processes for subsequent grafting of specific molecular chains, and
- application of silanes, organo-metallic [16–22], or other polyfunctional chemicals [16,17] containing atomic species or molecules capable of creating ionic or covalent bonds with the receptor groups on the oxidized polymer surface. These are applied to modify the properties of polymer surfaces such as surface chemistry and surface architecture in a desired manner.

As outlined in the section on “Surface-Grafted Connector Molecules” above, a certain surface density of macromolecular chains needs to be grafted onto the surface for maximizing the performance of the interphase. To facilitate this, the polymer surface first needs to be oxidized at a required energy input, E , determined by the following expression

$$E = Ptn \quad (8)$$

where P = power output (W) of the energy source, e.g., corona discharge or flame burner, t = time of exposure, per unit length, under the electrode or flame cone of width, d (mm) [$t = d/V$, where V = the treatment velocity of the substrate (mm/s)] and n = number of substrate passes through the energy source.

The energy output, E_u (mJ/mm²), per unit area of substrate is given by

$$E_u = \frac{Pn}{LV} \quad (9)$$

where L is the length (mm) of the treating electrode, flame burner, or other energy source.

Figure 7 provides a schematic illustration of the SICOR process (silane-on-corona discharge treated polymer). In the first step of this process, surface hydroxyl or carboxyl groups are introduced to the substrate surface by

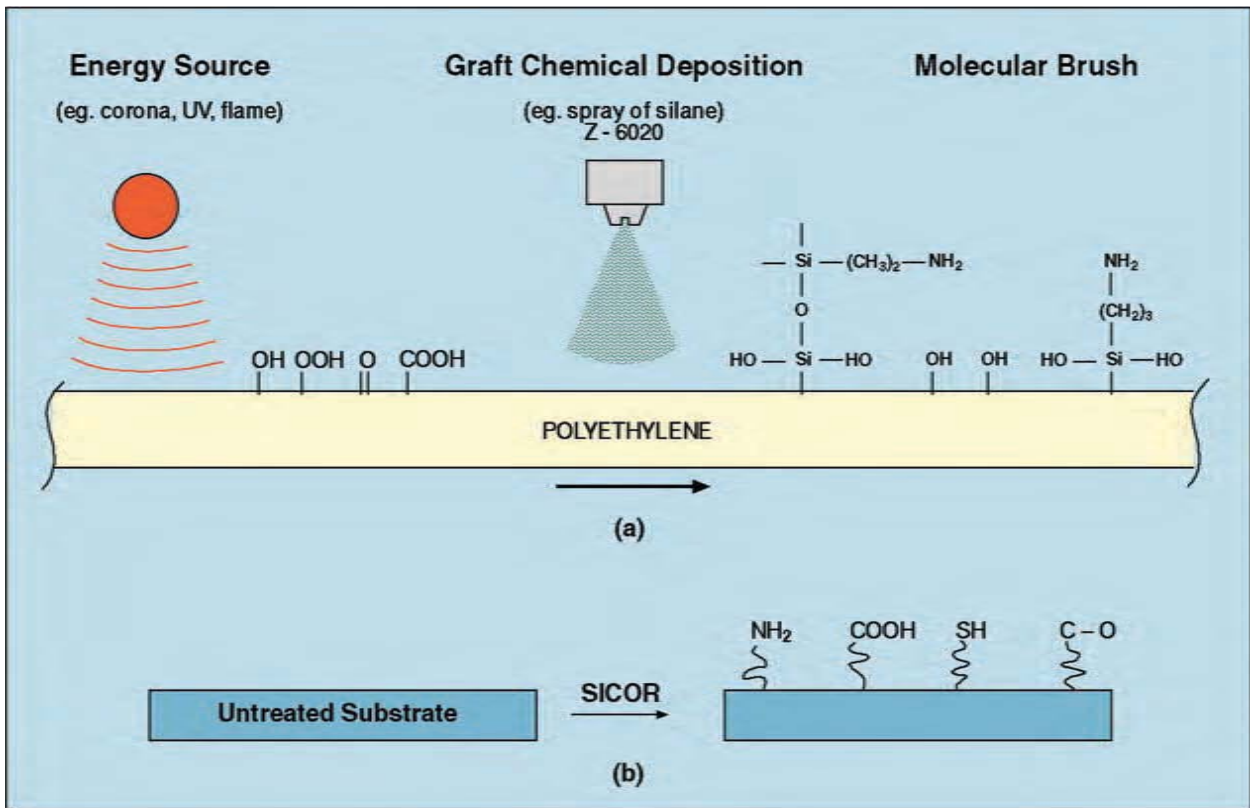


FIG. 7—Schematic representation of the SICOR process.

oxidation. These subsequently provide attachment sites for organo-functional compounds such as silanes, titanates, and zirconates.

The functionality of these compounds, as illustrated in Fig. 7 [6], is chosen to provide a surface reactivity that is compatible with the adhesive, or any other material brought into contact with the surface-modified polymer.

The process allows for the continuous and inexpensive incorporation of a wide range of surface-functional groups onto the surface of a polymeric substrate. This provides the possibility of tailoring the surface chemistry of a polymer, without altering its bulk properties, to optimize the adhesion between the surface-engineered substrate and adhesive, or other materials.

Full details of theoretical and practical aspects of adhesion enhancement of a variety of adhesives to representative types of difficult-to-bond polymers such as polyolefines, e.g., low-density polyethylene (LDPE) or polypropylene, and to other engineering polymers through commodity surface-treatment processes such as corona discharge and flame treatment as well as our novel surface-tethering technology, the latter comprising surface activation by corona discharge or flame oxidation followed by surface grafting of an amino-functional silane or polyethylene imines as polymeric pre-cursors of molecular brushes, are presented in [16-21] and [32]. A rigorous discussion on surface chemistry of polyolefinic substrates subjected to these alternative types of treatment is also provided in Refs 19, 21, and 32, and hence, the authors of this paper refer the reader to these specific publications for details not covered in this paper.

Experimental

Substrate Preparation and Treatment Methods

Substrate Surface Cleaning—Prior to any further processing such as surface analyses or surface treatment, all substrates were cleaned with lint-free tissues soaked with isopropyl or ethyl alcohol and subsequently stored at ambient laboratory conditions, i.e.,: $20 \pm 2^\circ\text{C}$ and $50 \pm 5\%$ relative humidity.

Substrate Activation—Surface activation of polymeric substrates was carried out by the use of corona discharge treatment. It was performed with a Tantec EST unit, model HV 2010 (maximum power output of 1 kW and an output frequency range of 13–30 kHz)⁴

The system comprises the following key modules:

- High-frequency generator HV 2010 240 V/50–60 Hz,
- High-voltage transformer HT 10–28 kV output,
- Conveyor: controlled treatment speed 0.1–70 m/min.

In this work, the distance between the substrate surface and electrode was maintained at a constant 2.5 mm, whereas the treatment speed and energy output were controlled to achieve energy outputs, E_w , from 76 to 755 mJ/mm^2 (Eq 8).

⁴Tantec A/S, Indusrivej 6 6640 Lunderskov, Denmark.

Alternative means for surface activation are the UV irradiation or flame treatment. The latter is carried out using an Aerogen⁵ or Arcotec⁶ flame-treatment units fuelled with natural gas. The stoichiometry of flame is controlled by tuning the excess content of oxygen in the “after-burn” flame at the level of 0.4 to 1.5 %, while the intensity of flame activation is controlled by adjusting the flow rate of air (220-360 L/min).

The flame-activation conditions used in this work are as follows:

- Treatment speed: 60 m/min,
- Oxygen excess content: 1.4 %,
- Substrate surface-burner distance: 20 mm.

Materials

Nominated Difficult-to-Bond Polymeric Substrates—

- Ethylene vinylacetate/polypropylene (EVA/PP) blend,
- Polyoxymethylene (Acetal).

Silicone Adhesives—

- DC 983 (Dow Corning): two-component, neutral alkoxy system,
- RP-4 (Rhone Poulenc): acetoxo-curing system,
- GE 100 (General Electric): acetoxo-curing system.

Organo-Functional Silanes—

- N-(2-aminoethyl)-3-aminopropyltrimethoxy silane (2-AE-3-APTMS): Z-6020 (Dow Corning),
- 3-Glycidoxo-propyltrimethoxy silane: Z-6040 (Dow Corning).

Polyfunctional Amines—

- Polyethylene imines (PEI) from BASF: $MW = 800; 2000; 25,000; 750,000$.

*Graft Chemical Preparation and Application—*Two following types of graft chemicals, as listed in the sections above on “Organo-Functional Silanes” and “Polyfunctional Amines,” were used for surface modification of nominated polymers targeting enhancement of adhesion:

1. Organo-functional silanes, and
2. Polyethyleneimines.

Silanes were first hydrolyzed with distilled water at a 1:3 silane/water mole ratio for 24 h and were then diluted with isopropanol to obtain solutions of graft chemical in the range of 0.05 to 1 %. Non-silane graft chemicals (polyethylene imines [PEI’s]; see the section below on “Adhesion Improvement by Surface-Grafted Connector Molecules Interpenetrating into Silicone Adhesives” for more details) were diluted in deionized water to an appropriate concentration.

⁵The Aerogen Company Ltd., Unit 3, Alton Business Centre, Omega Park, Alton, Hampshire GU34 2YU, UK.

⁶Arcotec GmbH, Rotweg 24, 71297 Mönsheim, Germany.

Aqueous solutions of graft chemicals were sprayed onto the sample surface using commodity industrial spray equipment. Throughout this work, this task is performed on a conveyor line (Fig. 8(c)), or using a robotized spray system at the speed controlled within the range of 2 to 10 m/min. The sample-to-nozzle distance is kept constant at 150 mm and the atomizing air pressure maintained at 1.5 bar.

The deposition rate of spray-applied graft chemical is adjusted to maintain a constant level of the “normalized deposition rate” [ml/m] expressed as the ratio of the fluid flow rate through the nozzle (ml/min) divided by conveyor speed in m/min]. After spraying, the samples surface is dried using either the conveyer-controlled exposure to infrared lamps or by allowing an ambient air flash-off (approximately 2 min) under the standard laboratory conditions (20°C/50 % RH).

The standardized parameters of an on-line application of graft chemicals are as follows:

- i Spray pressure: 1.5 bar,
- ii Chemical deposition rate (at 1.5 bar): ~3.5 ml/min per 1 m/min of conveyor speed,
- iii Conveyor speed: calculated as per (ii),
- iv Spray nozzle distance: 150 mm,
- v Specimens location on conveyor belt: 120 mm out from conveyor edge,
- vi No. of spray passes: 1,
- vii Surface drying: RT air. If fast flash-off needed: one-pass-IR lamps.

Test Methods

Shear Strength—The shear strength of adhesive bonds was determined using single lap-shear specimens, 25-mm wide, with an overlap of 10 mm. All substrates were cleaned with isopropyl or ethyl alcohol prior to any further treatment. The bonded specimens were tested in an Instron mechanical tester at a rate of 10 mm/min. Five specimens were tested per experimental point.

Peel Strength—The peel strength was determined using 180° peel specimens, which were prepared in accordance with ASTM C794 [23] but modified by CSIRO [24,25], by reducing the sealant thickness from the recommended 1.6 mm to 0.2 mm to provide greater stress concentration at the substrate/sealant interface. When inherent adhesion problems are present, this modified procedure favors adhesive delamination rather than cohesive failure within the relatively weak silicone sealants. The specimens were tested in an Instron mechanical tester at the rate of 10 mm/min. Two peel specimens were tested per experimental point.

XPS Analysis—XPS analyses were performed on a VG Escalab MkII spectrometer⁷ equipped with an AlK_α source, non-monochromatized, at a power of 150 W. Samples were exposed to irradiation for less than 30 min to avoid

⁷VG Scientific Factory, East Grinstead, West Sussex RH19 1UB, UK.



(a)



(b)



(c)

FIG. 8—(a) robotized flame treater, (b) substrate activation by corona discharge on a conveyer, and (c) graft chemical application on conveyer.

substantial decomposition of the polymer surfaces in the analysis beam. Spectra were recorded at the normal emission of the photoelectron relative to the surface plane of the samples (0°). The spectrometer did not provide for charge neutralization. Elements present were identified from survey spectra, and the atomic concentrations were estimated from integrated peak intensities and published sensitivity factors [26]. Components of the C1s signal were estimated by curve fitting using Gaussian–Lorentzian line shapes and a nonlinear background substraction. The binding energy scale was calibrated using a value of 285.0 eV for the CH₂ component as an internal reference. The random error in the quantitative analysis of elemental compositions is between 5 % and 10 % in the present cases.

Results and Discussion

Spacial Orientation of Surface-Grafted Amino-Functional Silane Molecules

Amino-functional silanes such as (gamma)-aminopropyltrimethoxysilane (γ -APTMS), (gamma)-aminopropyltriethoxysilane (γ -APTES), (2-aminoethyl)-3-aminopropyltrimethoxy silane (2-AE-3-APTMS) are traditionally used as coupling agents for improving the strength and long-term durability of adhesively bonded metals or glass fiber-reinforced composites. In these applications, the primary mode of bonding the amino-functional silane to the hydroxyl-rich metallic or silicate-based substrate is through the silanol end of the molecule, as illustrated in Fig. 9(a). The secondary mode of bonding is through hydrogen bonding between the silane's amino groups and either the silanol groups or hydroxyl groups present on the oxidized surface of glass or metal [27-31]. This mechanism is schematically illustrated in Figs. 9(b) and 9(c).

It has been shown [27] that the extent of amino-silane protonation can be correlated to the isoelectric point (IEP) of the respective oxides. The lowest degree of amino-functional silane protonation, e.g., γ -APTMS, has been thus observed for magnesium (IEP = 12.0) and the largest on silicon, aluminum, and titanium (IEP = 4.0, 6.0, and 7.0, respectively).

The degree of amine protonation near the substrate surface, in γ -APTMS adsorbed onto silicon metal substrate (see Fig. 10(a)) is approximately 28 % [22,27].

Figure 10(b), in turn, illustrates the XPS spectrum of the N1s peak of 2-AE-3-APTMS silanized low-density polyethylene (LDPE). Two components of the N1s peak were observed near 399.3 and 400.4 eV, which were attributed to free and protonated amino groups, respectively. Based on the relative intensities of the two components, it turned out that about 55 % of the amino-silane was protonated and 45 % contained free amine.

The above observation indicates that both types of amino groups are present in the interphase:

- Protonated amine groups ($-\text{NH}_3^+$): hydrogen-bonded to the oxidized polymer surface,
- Free amino groups ($-\text{NH}_2$): species available for further reaction with the sealant.

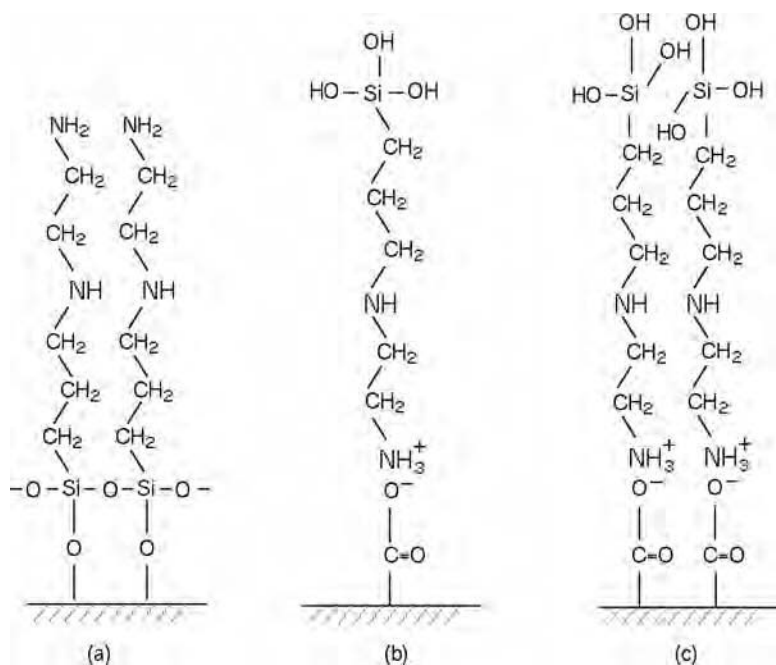


FIG. 9—Schematic representation of the molecular attachment mechanism and orientation for the *N*-(2-aminoethyl)-3-aminopropyltrimethoxy silane: (a) condensation attachment mechanism with "amine end up," (b) and (c) attachment of molecules through protonation of amine with surface hydroxyl groups, "amine end down" orientation.

Based on the above information, it appears that a molecular brush of *N*-APTMS silane grafted onto the surface of a polyolefin, comprises approximately an equal number of molecules orientated with the "amine group up" (see Fig. 9(a)) and "amine group down" (see Figs. 9(b) and 9(c)). The "amine group up" molecules are available for further reaction with adhesives or sealants.

Adhesion Improvement by Surface-Grafted Connector Molecules Interpenetrating into Silicone Adhesives—The influence of surface-grafted molecular brushes on adhesion of polymeric substrates bonded with silicone adhesives was investigated using the following materials:

- substrate: EVA/PP blend,
- silicone adhesive: RP-4/Rhone Poulenc,
- molecular brush system:
 - (ii) interpenetrating system: polyethylene imines (PEIs) $MW = 800$ ($N = 19$), $MW = 2000$ ($N = 46$), $MW = 25,000$ ($N = 581$), $MW = 750,000$ ($N = 17,442$).
 - (iii) chemically bonding system: amino-functional silane: Z-6020.

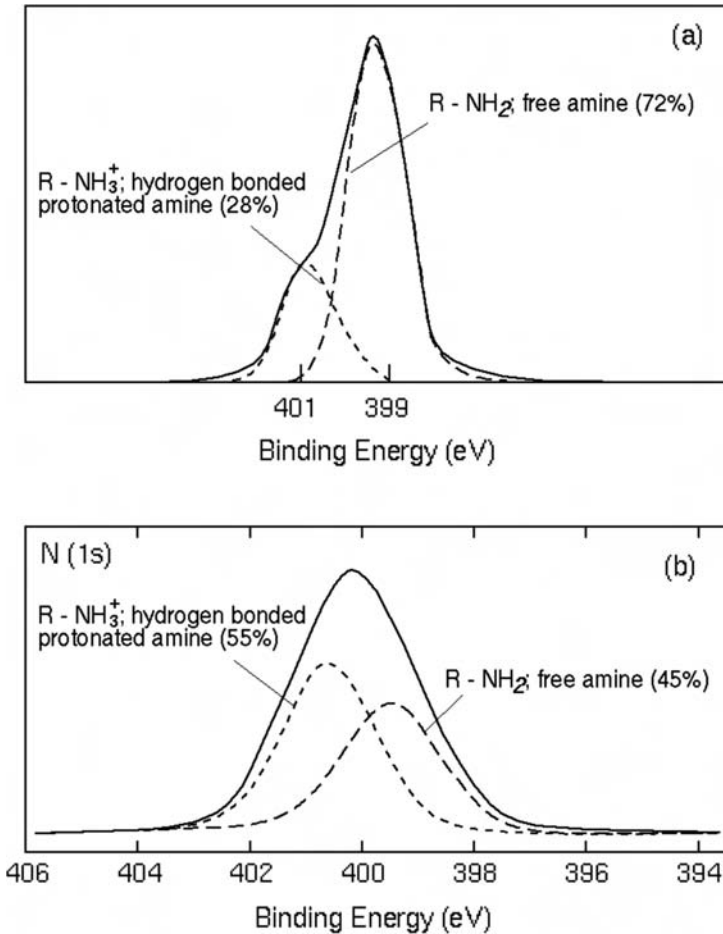


FIG. 10—XPS spectrum of the N1s peak for: (a) γ -APTMS silane (0.1 %) grafted onto silicone surface, and (b) 2-AE-3-APTMS (0.1 %) grafted onto oxidized LDPE surface [19].

The adhesion quality was assessed by lap-shear tests involving SICOR-treated substrates. These were first surface-activated by corona discharge and subsequently surface grafted using PEIs and Z-6020 silane at the concentration of 0.1 %. The PEIs with $MW = 25,000$ and $MW = 750,000$ were also used at concentrations of 0.5 and 1.0 %.

Lap-shear specimens were prepared as described in the above section on "Shear Strength" with an overlap of 10 mm. They were allowed to cure at room temperature for 3 days prior to testing.

The specimens were tested in a dry condition and after 7 days immersion in water at 40°C.

The graphs in Fig. 11 [32] demonstrate the difference in effectiveness of interfacial reinforcement using either interpenetrating or chemical bonding mechanisms of interactions. They also illustrate the influence of the type and concentration of interpenetrating graft molecules on the strength of assemblies bonded with silicone adhesive.

The results indicate that the bond strength of specimens modified with interpenetrating molecular brushes using PEI connector molecules is always greater than that after oxidative treatment only (in this work: corona discharge treatment).

An interesting trend is observed in Fig. 11 regarding the influence of the length of “connector molecules” on the strength of adhesion. The “bare” interface of an oxidized polymer produces a bond strength of 180 kPa in dry condition. After 7 days immersion in 40°C water, the bonds between the substrate and silicone adhesive are cleaved resulting in complete loss of strength associated with 100 % delamination of the adhesive at the interface.

For surfaces grafted with interpenetrating only (non-reactive) connector molecules of PEI, it appears that increasing the length of graft chemical molecules results in a corresponding increase in the bond strength, up to approximately

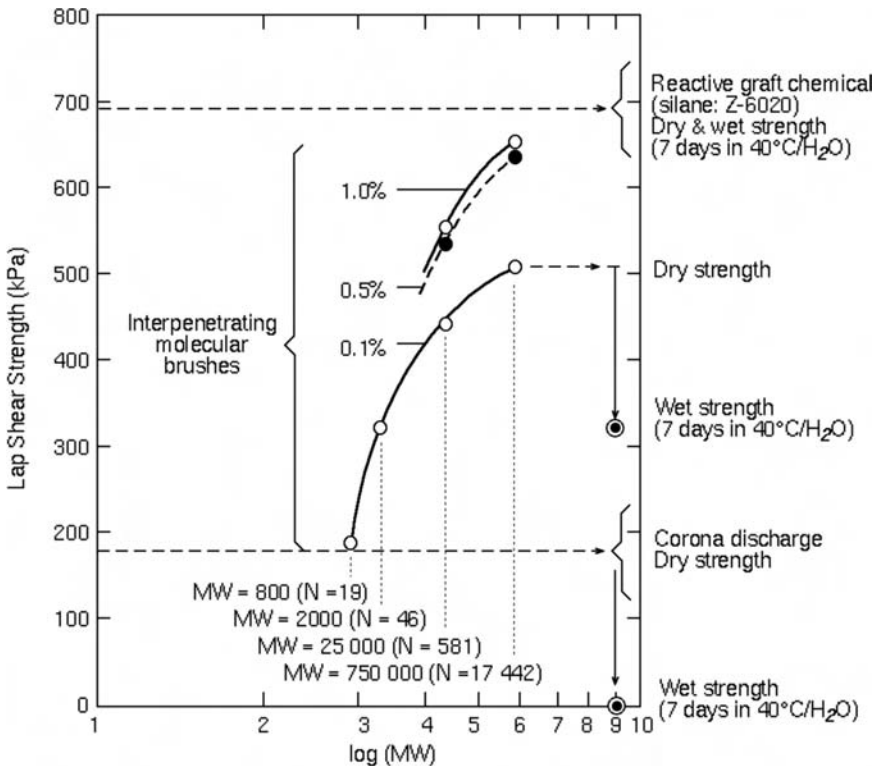


FIG. 11—The influence of PEI molecular weight and chain length ($L \propto N$) and amino-silane Z-6020 on the strength of assemblies involving surface-grafted substrates and RP-4 silicone adhesive [32].

500 kPa for a polymerization index of $N = 17,442$ and concentration of 0.1 %. The exposure of this type of interface to a 7-day immersion in water at 40°C results in a 35 % loss of strength. An increase in the surface density of the chains, achieved by using higher concentrations of the graft chemicals (0.5 % and 1 %) also appears to increase bond strengths in the case of the PEIs characterized by higher molecular weights (2,000 to 750,000). However, despite the increase in the bond strength, the failure mode is interfacial delamination because of the pull-out of interdigitated molecular chains from the matrix of the silicone elastomer.

When surface-grafted “connector molecules” are chemically reactive with the silicone adhesive, as in the case of the amino-functional silane (Z-6020), the highest degree of interphase reinforcement (690 kPa) is achieved. This particular type of the interface/interphase system (i.e., involving chemically bonded “connector molecules”) retains its original bond strength of 690 kPa even after 7 days of immersion in 40°C water.

Another example of the effectiveness of surface-grafted molecular brushes, capable of improving adhesion through interpenetration or through chemical bonding with the adhesive, involves substrates that are difficult to bond such as Acetal (polyoxymethylene). The effect of molecular brushes on the adhesion of Acetal to elastomeric silicone adhesives was examined by comparing the peel strength of untreated, corona-treated, and SICOR-treated substrates. The latter involved corona oxidation followed by the application of amino- and epoxy-functional silane.

Two types of silicone adhesives were evaluated, i.e., Dow Corning 983 and GE 100. The first of these is chemically reactive with both amino-terminated and epoxy-terminated molecular brushes. Whereas GE 100 does not exhibit chemical reactivity with either type of connector molecule, it is able to interact with the molecular brush structure through the interpenetration of macromolecular chains into the matrix of the elastomeric adhesive.

The results listed in Table 3 [32] show that the bond strength of Acetal without treatment is very poor, and surface oxidation through corona discharge alone is not sufficient to provide a significant improvement in adhesion. On the other hand, surface-grafted molecular brush provided through the SICOR process leads to a significant increase in the peel strength.

TABLE 3—Peel force (N) of Acetal/silicone adhesive bonds following various surface treatments on the substrates [32].

Acetal surface treatment	Silicone adhesive			
	Dow Corning 983		GE 100	
	Strength	Failure mode	Strength	Failure mode
None	0.0	100 % AF	3.65	100 % AF
Corona discharge	3.25	100 % AF	7.5	100 % AF
SICOR (amine grafting)	17.5	80 % CF	19.0	100 % AF
SICOR (epoxy grafting)	24.0	100 % CF	20.0	100 % AF

Note: AF, delamination at the substrate/sealant interface; CF, cohesive failure within sealant.

As would be expected, relatively short and interpenetrating (but non-reactive) molecules of graft chemicals (amino- and epoxy-terminated silanes) increase the bond strength of specimens prepared with GE100 elastomer through interdigitation, but are not able to reinforce the interphase to the level required for achieving cohesive failure of the elastomeric adhesive. On the other hand, an appropriate choice of adhesive such as DC 983, which is capable of cross-linking with functional ends of the amino- and epoxy-functional graft molecules, results in high levels of cohesive failure within the adhesive.

Conclusions

- (a) The adhesion and fracture performance of interfaces between polymers can be effectively improved and controlled by surface-grafted macromolecular “connector molecules.”
- (b) “Connector molecules” grafted onto solid polymer surfaces interact with adjacent materials such as adhesives or sealants through either one or a combination of the following mechanisms:
 - (i) Interpenetration into the adjacent adhesive, and (ii) chemical reaction/cross-linking with the adjacent adhesive.
- (c) The effectiveness of the interface reinforcement by surface-grafted connector molecules depends on the following factors: (i) The surface density of grafted molecules, (ii) the length of the individual chains of the grafted molecules, and (iii) the optimum surface concentration/surface density in relation to the length of connector molecules.
- (d) At the interfaces reinforced with interpenetrating connector chains, a distinct maximum/optimum (σ_{OPT}) is recorded for joint fracture energy versus graft density, as expressed by Eq 3. An increase of σ above σ_{OPT} results in a decrease of fracture energy enhancement because of a decrease in the efficiency of the interdigitated macromolecular chains.
- (e) It has been effectively demonstrated that surface-engineered difficult-to-bond polymeric substrates such as polyolefines or polyacetal, “surface tethered” by chemically surface-grafted molecular brushes, the latter provided by a process comprising surface oxidation (e.g., by flame or corona discharge treatment) and application of polyfunctional connector molecules exhibit significantly improved adhesion to elastomeric silicone sealants and adhesives.
- (f) It has been conclusively demonstrated in this paper that adhesion of elastomeric silicone adhesives to polymers surface engineered through designated types of surface-grafted molecular brushes provided by SICOR process is drastically better than that of the same polymers modified by commodity surface-treatment processes such as corona discharge or flame treatment.

References

- [1] Arkles, B. *Silicone, Germanium, Tin and Lead Compounds, Metal Alkoxides, Diketonates and Carboxylates, A Survey of Properties and Chemistry*. 2nd ed., B. Arkles, Ed., Gelest, 1998, pp. 434–508.

- [2] Flackett, D., "One Part Silicone Sealants," *Silicone, Germanium, Tin and Lead Compounds, Metal Alkoxides, Diketonates and Carboxylates, A Survey of Properties and Chemistry*, 2nd ed., B. Arkles, Ed., Gelest, 1998, pp. 473–479.
- [3] Knop, B., "Chemie der Fugendichtungsmassen," *Kunststoffe German Plastics*, Vol. 76(9), 1986, pp. 783–785.
- [4] Klosowski, J. M., *Sealants in Construction*, Marcel Dekker, New York, 1998.
- [5] de Gennes, P. G., "Weak Adhesive Junctions," *J. Phys.*, Vol. 50, 1989, pp. 2551–2562.
- [6] de Gennes, P. G., "Fracture of a Bulk (Glassy) Polymer," *CR Acad. Sci.*, Vol. 309, 1989, pp. 939–943.
- [7] Raphael, E. and de Gennes, P. G., "Rubber Adhesion with Connector Molecules," *J. Phys. Chem.*, Vol. 96, 1992, pp. 4002–4007.
- [8] Leger, L., and Raphaël, E., *Short and Long Chains at Interfaces*, J. Dailant, P. Marques, and P. Muller, Eds., T. Van, Trans., Editions Frontiers, Gif-sur-Yvette, 1995.
- [9] Léger, L., Raphaël E., and Hervet H., "Surface-Anchored Polymer Chains: Their Role in Adhesion and Friction," *Adv. Polymer Sci.*, Vol. 138, 1999, pp. 186–225.
- [10] Léger, L., Hervet, H., and Tardivat, C., "Molecular Mechanisms of Elastomer-Solid Adhesion through Connector Molecules," *Proceedings of the 5th European Adhesion Conference, Lyon, 18-21 Sept. 2000*, SFV, Paris, 2000, pp. 118–122.
- [11] Brochard-Wyart, F., de Gennes, P. G., Léger, L., and Marciano, Y., "Adhesion Promoters," *J. Phys. Chem.*, Vol. 98, 1994, pp. 9405–9410.
- [12] and Brochard-Wyart, F. and de Gennes, P. G., "Adhesion Between Rubbers and Grafted Solids," *J. Adhesion*, Vol. 57, 1996, pp. 21–30.
- [13] Gutowski, W., "Silanization of Polymers," *CSIRO DBCE, MM/RR*, Vol. 3, Confidential CSIRO Report, June 1989, p. 232.
- [14] Gutowski, W., "Silanization of Polymers," *CSIRO DBCE, MM/RR*, Vol. 4, Confidential CSIRO Report, July 1989, p. 3.
- [15] W., Gutowski, "A Method of Surface Treatment of Polymeric Materials and Fibres, Including Carbon and Graphite Fibres," Provisional patent application (December 15, 1989).
- [16] W. Gutowski, D. Y. Wu, and S. Li, "Surface Treatment of Polymers," U.S. Patent No. 5,879,757 (1999).
- [17] W. Gutowski, D. Y. Wu, and S. Li, "Surface Treatment of Polymers," Australian Patent No. 680716.
- [18] Gutowski, W. and Pankevicius, E. R., "A Novel Surface Treatment for Enhanced Adhesion of Ultra-High Modulus Polyethylene Fibres to Epoxy Resin," *Comp. Interfaces*, Vol. 1, 1993, pp. 141–151.
- [19] Gutowski, W., Wu, D. Y., and Li, S., "Surface Silanization of Polyethylene for Enhanced Adhesion," *J. Adhes.*, Vol. 43, 1993, pp. 139–155.
- [20] D. Y., Wu, S., Li, and W. S., Gutowski, "Surface Treatment of Polymers," U.S. Patent No 5,922,161 (1999).
- [21] Gutowski, W. S., Wu, D.Y., and Li, S., "Process Improvements for Treatment of TPOs for Enhanced Adhesion of Paints and Adhesives," *Proceedings of SPE Automotive TPO Global Conference '99*, SPE/USA, Troy/Michigan, 1999, pp. 365–378.
- [22] Plueddemann, E. P., *Silane Coupling Agents*, 2nd ed., Plenum, New York, 1991.
- [23] ASTM C794-80, 1980, "Standard Test Method for Adhesion-in-Peel of Elastomeric Joint Sealants," *Annual Book of ASTM Standards*, ASTM International, West Conshohocken, PA.
- [24] Cerra, A. P., "Development of a New Accelerated Adhesion Test for Silicone Sealants," *J. Testing Eval.*, Vol. 23-5, 1995, pp. 370–376.
- [25] Gutowski, V. S., Russell, L., and Cerra, A., "New Tests for Adhesion of Silicone Sealants," *Science and Technology of Building Seals, Sealants, Glazing, and*

Waterproofing, Vol. 2, J. M. Klosowski, Ed., ASTM International, West Conshohocken, PA, 1992, p. 87.

- [26] Scofield, J. H., "Hartree-Slater Subshell Photoionization Cross-Sections at 1254 and 1487eV," *Electron Spectrosc. Relat. Phenom.*, Vol. 8, 1976, pp. 129–137.
- [27] Horner, M. R. Boerio, F. J., and Clearfield, H. M., "An XPS Investigation of the Adsorption of Aminosilanes onto Metal Substrates," *J. Adhes.Sci. Technol.*, Vol. 6-1, 1992, pp. 1–22.
- [28] Hook, D. J., Vargo, T. G., Gardella, J. A., Litwiler, K. S., and Bright, F. V., "Silanization of Radio-Frequency Glow-Discharge Modified Expanded Poly(Tetrafluoroethylene) Using (Aminopropyl)Triethoxysilane," *Langmuir*, Vol. 7, 1991, pp. 142–151.
- [29] Fowkes, F. W., Dwight, D. W., Cole, D. A., and Huang, T. C., "Acid-Base Properties of Glass Surfaces," *J. Non-Cryst. Solids*, Vol. 120, 1990, pp. 47–60.
- [30] Dillingham, R. G. and Boerio, F. J., "Interphase Composition in Aluminum Epoxy Adhesive Joints," *J. Adhesion*, Vol. 24, 1987, pp. 315–335.
- [31] Elridge, B. N., Buchwalter, L. P., Chess, C. A., Golderberg, M. J., Goldblatt, R. D., and Novak, F. P., "A Time-of-Flight Static Secondary Ion Mass Spectrometry and X-Ray Photoelectron Spectroscopy Study of 3-Aminopropyltrihydroxysilane on Water Plasma Treated Chromium and Silicon Surfaces," *J. Adhes. Sci. Technol.*, Vol. 6-1, 1992, pp. 109–125.
- [32] Gutowski, W. S., Li, S., Filippou, C., Hoobin, P., and Petinakis, S., "Interface-Interphase Engineering for Adhesion Enhancement. Part II: Theoretical and Technological Aspects of Surface-Engineered Interphase-Interface Systems for Adhesion Enhancement," *J. Adhesion*, Vol. 79, 2003, pp. 483–519.

Anneliese Hagl¹

Mechanical Characteristics of Degraded Silicone Bonded Point Supports

ABSTRACT: Tensile loading of bonded point supports is considered as the critical load case for adhesive material, e.g., silicone applied to such kinds of fixtures. From a durability point of view, the following defects of two-component adhesives are expected to have a significant impact on the response to this loading regime: the wrong mixing ratios of the adhesive components, inhomogeneous mixing due to insufficient or poor mechanical mixing procedures, load degradation of the adhesive bonding material, local degradations of the bonding, e.g., bubbles or poor adhesion. In order to investigate these aspects, different experimental approaches have been pursued. Regarding the mixing ratio aspect, material tests were performed with systematically varied mixing ratios for the analysis of the elastic and strength properties while for the other topics, tensile tests of bonded point supports were evaluated in detail. Cyclic tests of point supports in the tensile load regime were set up, differing in amplitudes and maximum peaks of the cycles, in order to analyze the impact of load histories on the mechanical characteristics of the specimens. For point supports subjected to monotonically increasing loads the qualitative assessment of the fracture surfaces revealed the existence and the potential impact of disturbances inside the bonding, such as bubbles or locally lacking adhesion, on the damage behavior and on related inferior mechanical performance. The main motivation for this kind of research is to improve confidence in the durability of bonded designs. Thus, our activities were focused on aspects which might affect durability from an application point of view, not from a purely academic one. Especially in Germany, the confidence of the authorities in this joining technique has to be strengthened by demonstrating a high degree of robustness in the application, and in view of the risk associated with potential in-field problems.

Manuscript received June 3, 2011; accepted for publication September 27, 2011; published online October 2011.

¹Managing Director, A. Hagl Ingenieurgesellschaft mbH, Munich, Bodenseestr. 217, D-81243 Munich, Germany, e-mail: mail@a-hagl-ingenieure.de

Cite as: Hagl, A., "Mechanical Characteristics of Degraded Silicone Bonded Point Supports," *J. ASTM Intl.*, Vol. 9, No. 2. doi:10.1520/JAI104061.

Copyright © 2012 by ASTM International, 100 Barr Harbor Drive, PO Box C700, West Conshohocken, PA 19428-2959.

KEYWORDS: Structural glazing, silicone adhesive, bonding design, cyclic loading, degradation, mixing ratio

Nomenclature

ETAG = European Technical Approval Guideline

Introduction

Structural sealant glazing based on silicone adhesives is a well-known and powerful design concept with respect to line-type bonding geometries of rectangular cross sections. On the one hand, over 40 years of experience exists for such kinds of applications, especially in the United States. On the other hand, gaining a systematic and profound knowledge of the mechanical properties of the adhesive material for varying operating conditions during its service life and from a fatigue and durability point of view is still a challenging task today. A comprehensive knowledge of the mechanical properties of the bonding adhesive for different loads is the key point in order to assess the structural integrity of glass facades. This is also important from a durability point of view. This paper intends to provide insight into selected issues linked to the mechanical properties of the silicone material.

Up to the present, the use of advanced bonded design solutions beyond the applications covered by ETAG 002 [1] is significantly limited by the lack of full acceptance of the approving authorities. Even in the case of ETAG 002, only a sub-set of potential applications is approved in Germany, i.e., Type 1 and Type 2 designs. The main reason behind this attitude is the missing confidence in the durability aspects of bonded designs. Authorities claim a lack of knowledge with respect to durability, especially in the case of novel designs and assume in-field problems that are not reproduced by the range of standard laboratory conditions. Thus, this paper compiles the initial results of various aspects which might impact the durability of bonded point supports in order to identify topics which need more attention in future research.

In principle, the paper is organized in two sections: in the first part, focus is given to mixing issues of the two components of the adhesive, while in the second part, the behavior under tensile loading for structural applications is addressed. In order to study the effects of the mixing quality, conventional material tests are considered, such as tensile tests of dog-bone specimens and shear tests of H-type specimens similar in adhesive geometry as described in ETAG 002 [1]. In addition, the behavior under cyclic load schemes was investigated for circular point supports. Furthermore, an attempt is made to link the quality of the bonding to the mechanical characteristics for the investigated specimens as a first step, based on monotonically increasing loads. Mixing aspects discussed in this paper focus, on the one hand, on the variation of the mixing ratios and, on the other hand, on incomplete mixing procedures; both aspects are investigated with respect to their impact on basic material characteristics. Regarding the cyclic loading schemes, the mechanical behavior during the load

cycles and the post-cycle failure characteristics are of special interest in order to gain insight into the mechanical performance of the adhesive.

Varying Mixing Ratios

Compared to one-component adhesives, two-component adhesives provide additional complexity in their application, which is also expected to have an impact on durability. Although the mixing ratio is clearly defined by the adhesive manufacturers as one key parameter in application, the robustness of the adhesive with respect to the mixing ratio deviations is of interest for confidence in, and reliability of, bonded structures. In this section, experimental results are presented with a focus on pre-defined mixing ratio variations of a two-component silicone adhesive which has been widely used for structural sealant glazing for decades. The nominal mixing ratio by volume is defined as 10:1 [2] while the intended variation of this ratio spans from 7:1 up to 11:1, as shown in Table 1.

In order to judge the fitness of the adhesive in a first step, tensile tests and shear tests were performed and post-processed with respect to strength and stiffness properties. All tests were performed at room temperature and at displacement rates of 50 mm/min for the tensile tests and 5 mm/min for the shear tests; Fig. 1 shows the load curves obtained by tensile tests of all tested dog-bone type specimens. The nominal size of the specimens was a 25 mm gauge length and a 6 mm × 4 mm cross section area. In order to provide more insight, Fig. 2 is reduced to averaged curves for each mixing ratio. Slight differences in stiffness are visible with the mixing ratio of 7:1 featuring the highest stiffness, and with the mixing ratio of 11:1 featuring the lowest stiffness. A similar trend is also visible for shear tests performed by quadruple ETAG H-type specimens; see Figs. 3 and 4. The nominal dimensions of the adhesive applied in the test specimens are 50 mm in length, 12 mm in height, and 12 mm in thickness (double twinned

TABLE 1—*Strength properties for varying mixing ratios.*

Mixing Ratio by Volume	7:1	8.5:1	10:1	11:1
Tensile strength ^a	45.0 N 1.88 MPa	44.2 N 1.84 MPa	42.3 N 1.76 MPa	43.7 N 1.72 MPa
Tensile deviation ^b	1.9 N 0.08 MPa	1.9 N 0.08 MPa	3.5 N 0.15 MPa	2.4 N 0.10 MPa
Shear strength ^c	440.1 N 0.88 MPa	431.7 N 0.86 MPa	491.8 N 0.98 MPa	462.7 N 0.93 MPa
Shear deviation ^d	16.7 N 0.03 MPa	37.8 N 0.08 MPa	23.0 N 0.05 MPa	28.2 N 0.06 MPa

^aDog-bone specimen: 25 mm nominal gauge length, 6 mm × 4 mm nominal cross section.

^bStatistics based on ten specimens.

^cH-type specimen: Strength related to one test specimen with adhesive dimensions of 50 mm in length, 12 mm in height and 12 mm in width.

^dStatistics based on four specimens.

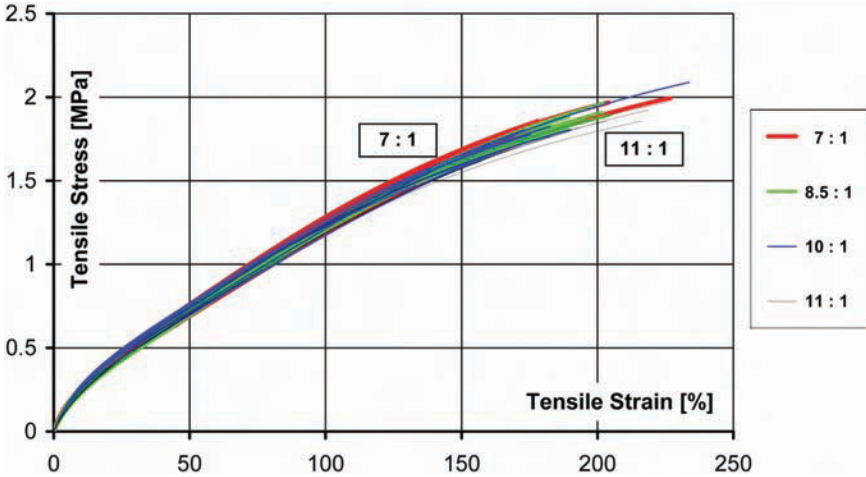


FIG. 1—Tensile test results for varying mixing ratios.

specimens which are loaded in parallel). The conclusion of our findings is that the mixing ratio cannot be considered a primary parameter in terms of its influence on the elastic behavior of the two-component silicone adhesive.

Regarding strength characteristics, Fig. 5 presents the maximum loads for the tensile tests, while Fig. 6 displays the load levels for the shear tests. Interestingly, the shear test results show a superior mechanical behavior for the nominal mixing ratio, while the tensile tests do not. In general, the variations of the strength levels is quite small demonstrating a high robustness of the silicone adhesive with respect to mixing ratio errors from a mechanical property point of view for the investigated test conditions. Nevertheless, for the final conclusions, the database of ten tensile tests and four shear test specimens is considered to be quite small.

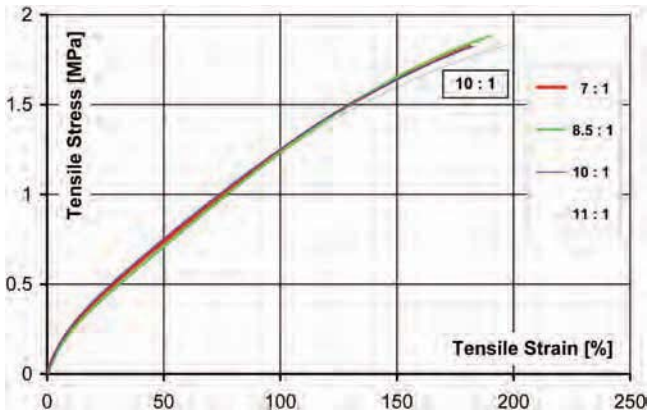


FIG. 2—Averaged tensile test results for varying mixing ratios.

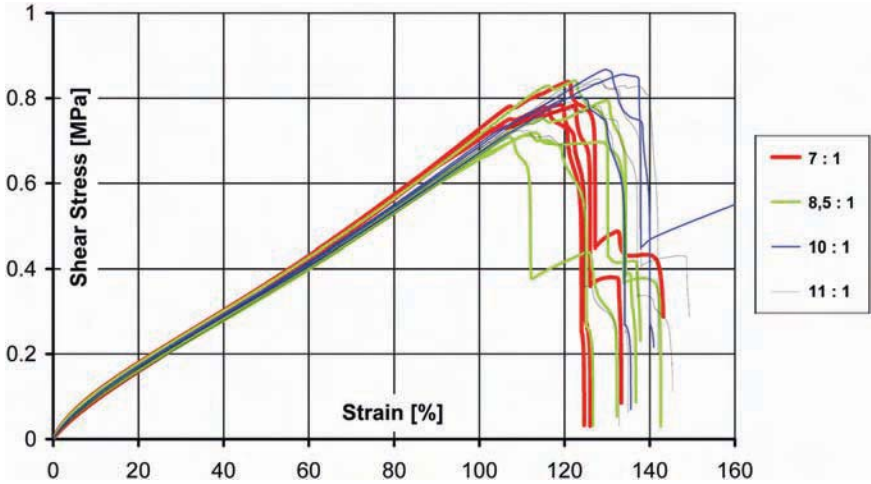


FIG. 3—Shear test results for varying mixing ratios.

These results might be interpreted as an indication that the durability of the investigated two-component silicone adhesive is probably quite insensitive to small variations in the mixing ratio in view of its mechanical properties. Please note that this statement is related to mechanical aspects only; the change of chemical characteristics due to varying mixing ratios are not considered within these investigations.

Incomplete Mixing Procedures

In addition to the varying mixing ratios, an adequate physical mixing procedure itself was also of concern in view of the mechanical fitness of the adhesive and

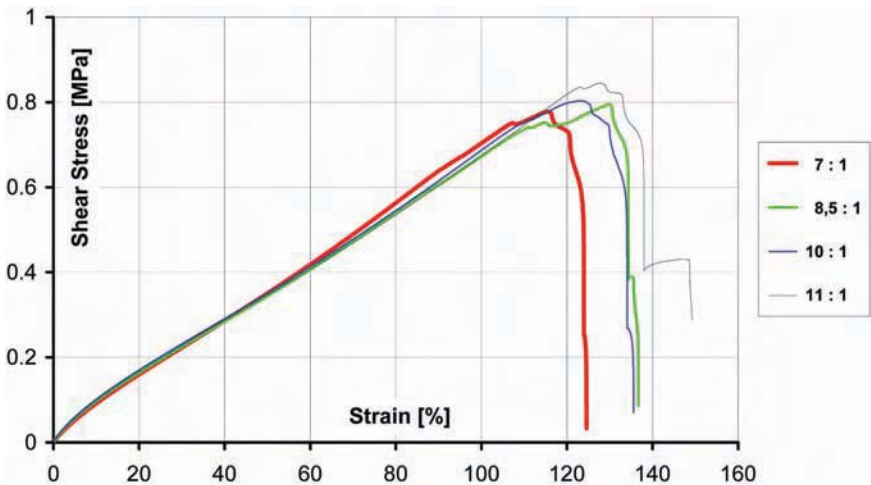


FIG. 4—Averaged shear test results for varying mixing ratios.

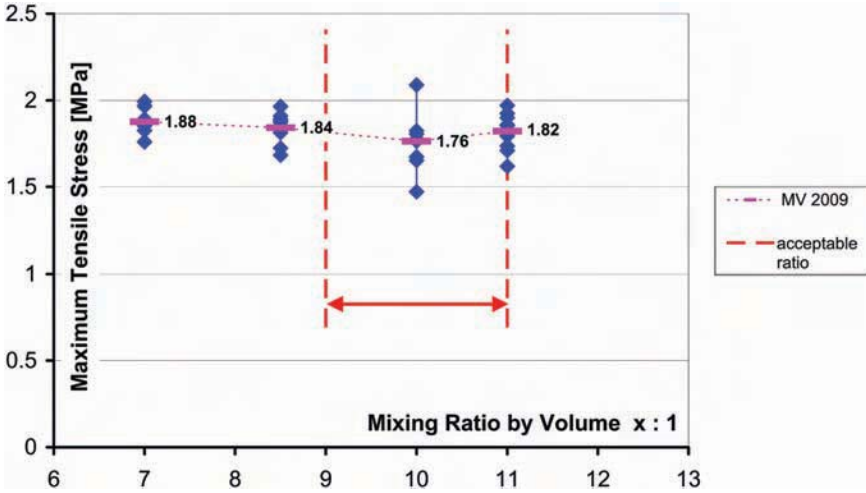


FIG. 5—Tensile tests strength for varying mixing ratios.

its impact on durability. The test sequence presented in the section titled “Varying Mixing Ratios” was also performed for specimens with low mixing quality, which are described in this section and are shown in Table 2. Again, all tests were performed at room temperature and at displacement rates of 50 mm/min for the tensile tests and 5 mm/min for the shear tests. Please note that a quantification of the mixing quality is quite difficult and the assessment of the low mixing quality for the test campaign presented in this section is based on an

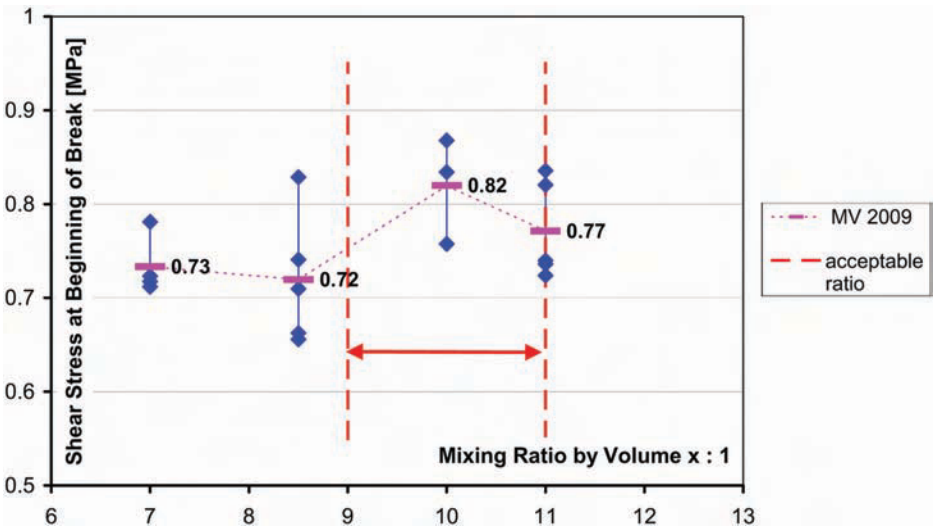


FIG. 6—Shear test strength for varying mixing ratios.

TABLE 2—Strength properties for varying mixing ratios—incomplete mixing.

Incomplete Mixing: Ratio by volume	8:1	9:1	10:1	11:1	12:1
Tensile strength ^a	39.5 N 1.65 MPa	39.0 N 1.63 MPa	44.2 N 1.84 MPa	33.2 N 1.38 MPa	45.4 N 1.89 MPa
Tensile deviation ^b	7.1 N 0.30 MPa	4.2 N 0.18 MPa	5.1 N 0.21 MPa	9.3 N 0.39 MPa	2.2 N 0.09 MPa
Shear strength ^c	369.2 N 0.62 MPa	389.4 N 0.66 MPa	394.4 N 0.66 MPa	441.7 N 0.74 MPa	404.2 N 0.67 MPa
Shear deviation ^d	12.4 N 0.02 MPa	10.1 N 0.02 MPa	26.3 N 0.04 MPa	26.6 N 0.04 MPa	16.6 N 0.03 MPa

^aDog-bone specimen: 25 mm nominal gauge length, 6 mm × 4 mm nominal cross section.

^bStatistics based on eight to eleven specimens.

^cStrength related to one test specimen with adhesive dimensions of 50 mm in length, 12 mm in height and 12 mm in width.

^dStatistics based on five samples.

optical assessment of the specimens showing inhomogeneity, i.e., white or whitish streaks within the otherwise black (properly mixed) material; see Fig. 7. Figure 8 presents the loads versus the deflection curve for tensile tests on the inhomogeneously mixed test specimens comparable to Fig. 1. It is obvious that the scatter of the individual specimens is significantly higher for Fig. 8 than for Fig. 1, which is expected to some extent, due to the irregularities introduced by the incomplete mixing conditions in the adhesive material. An average of these curves is shown in Fig. 9. Compared to Fig. 2, trends are noted towards lower stiffness for incomplete mixing and towards larger differences in the mechanical properties between different mixing ratios. In addition, the sequence of stiffness versus mixing ratio differs when compared to the homogenous test



FIG. 7—Specimens featuring incomplete mixing.

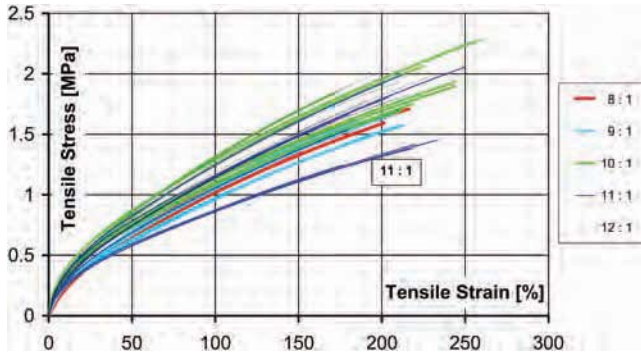


FIG. 8—Tensile test results for incomplete mixing cases.

specimen described in the section titled “Varying Mixing Ratios.” Nevertheless, the drawing of final conclusions is difficult due to the absence of metrics for incomplete mixing.

The increased scatter in the mechanical characteristics of the specimens is also visible in the strength values obtained in tensile and shear tests. Compared to Figs. 5 and 6, it is obvious that in Fig. 10 and Fig. 11, the span between maximum and minimum values for tensile and shear values is, in general, larger. Furthermore, the mean values are in general lower with the exception for the nominal mixing ratio test specimens subjected to tensile loading.

We assume that the exception is an outline due to the low number of specimens. In case of more specimens we would expect that the behavior is in line.

Cyclic Tensile Loading of Point Supports

The following experimental results for cyclic tensile loading of point supports were already presented in detail in an earlier paper [3]. A brief discussion is given here, additionally covering the durability aspects. Regarding the

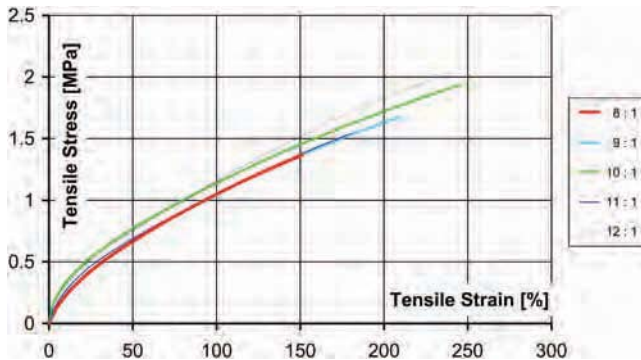


FIG. 9—Averaged tensile test results for incomplete mixing cases.

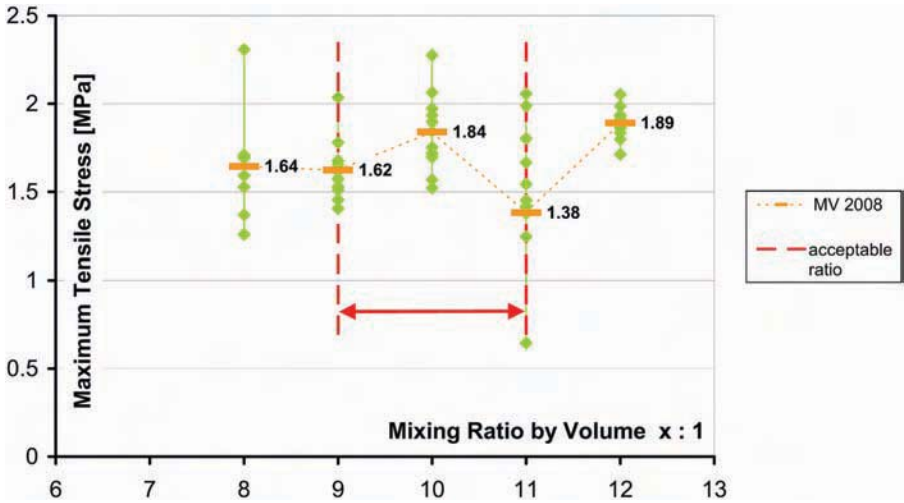


FIG. 10—Tensile tests strength for incomplete mixing cases.

performance of the silicone adhesive under cyclic load regimes, a representative application was selected in the form of a planar bonded circular point support [3]; see Fig. 12. If the silicone material is free to deform, a significant lateral contraction of the material appears under tensile loads, such as is observed in case of a dog-bone test specimen used in the section titled “Incomplete Mixing Procedures” during the study of varying mixing ratios. If the silicone adhesive is bonded to a significantly stiffer material as in the case of the point supports, the lateral contraction of the almost incompressible silicone [4] is suppressed at the

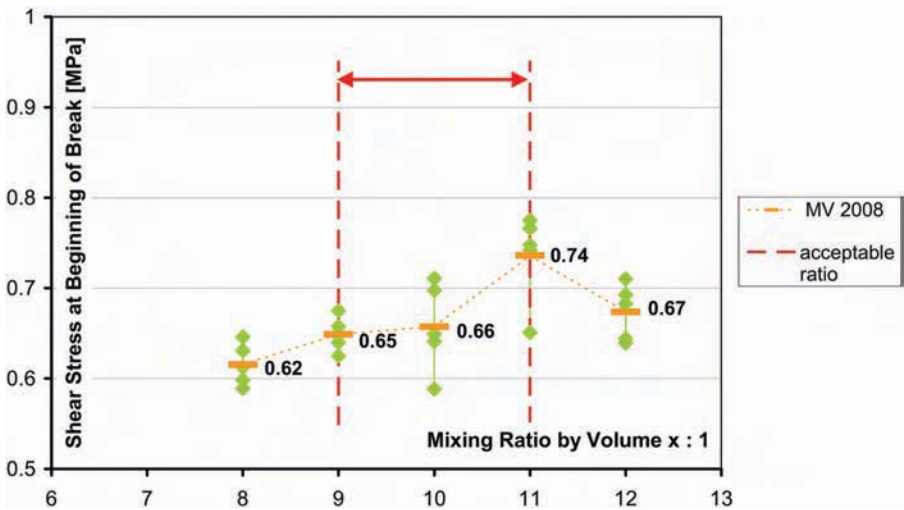


FIG. 11—Shear test strength for incomplete mixing cases.

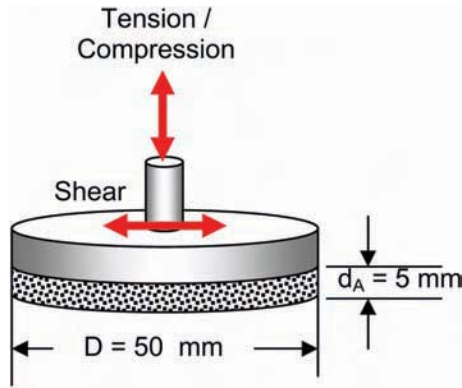


FIG. 12—Point support geometry.

interface leading to complex 3D stress states and an increased effective stiffness of the bonding under tensile loads [5].

This specific behavior is also observed with respect to the failure of the silicone material. Under simple one-dimensional loading schemes such as tension or shear, the silicone adhesive suddenly fails, as shown in Fig. 1 and Fig. 2 for dog-bone tests and in Fig. 3 and Fig. 4 for ETAG 002 shear tests. On the contrary, it is well-known that the failure of point supports under tensile loads shows a more complex pattern [6]. In Fig. 13 the test setup is shown using a special point support specimen which is made from stainless steel for improved bonding geometry accuracy. Cross-checks with conventional point support specimens bonded to glass samples have demonstrated similar mechanical characteristics. Figure 14 shows the load curve obtained for a 5 mm thick silicone adhesive bonded to a 50 mm diameter button, measured at room temperature and a 1 mm/min displacement rate. The load curve features three distinct areas of behavior similar to those previously observed for U-type bonding

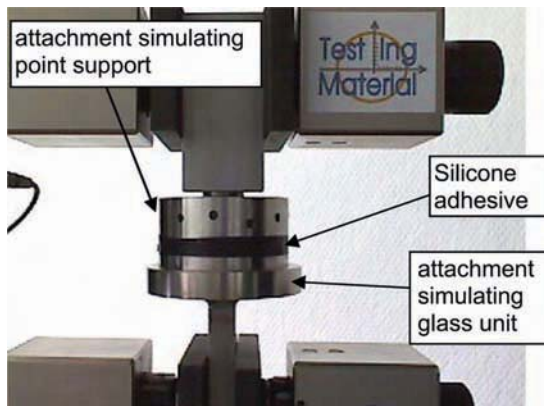


FIG. 13—Test setup for bonded point supports.

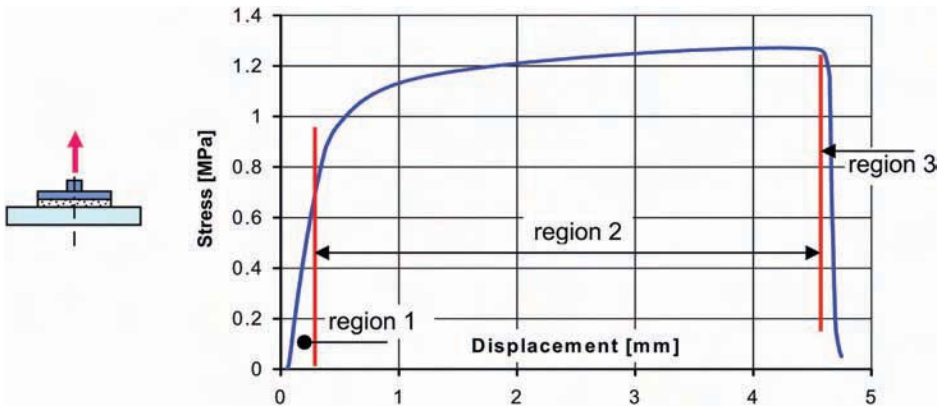


FIG. 14—Load curve for bonded point supports under tensile loads.

geometries [7]. The first area is characterized by a high stiffness, visible by the large positive slope at the beginning of the diagram, which indicates a fully functional adhesive material. The second area differs by a significantly reduced slope of the curve which is obviously related to damage mechanisms in the adhesive material. Finally, the bonded point support fails due to the propagation of cracks in the adhesive until total separation occurs.

Cyclic loading has been applied to bonded point supports for various load levels in order to check mechanical integrity. In order to avoid problems of a backlash nature evoked by load direction changes, the lower reversal point of the cycles was set to a minimum tensile load of 100 N. Taking the non-linearity of the material behavior into account, the upper reversal point was determined by displacement levels, not by load levels. The upper boundaries (reversal points) were varied between 0.25 mm for the smallest amplitude and 1.5 mm for the largest amplitude leading to cyclic loads between 0.4 MPa and 1 MPa, which are higher than the usual design strength level of 0.14 MPa. Therefore, these tests can also be seen as exploratory tests for the potential future modifications of design stress limits and safety factors. Regarding the load history, 100 cycles were selected as a compromise between the test duration on the one hand, and a sufficiently high number of loadings in order to introduce some fatigue on the other hand. After the last cycle, the specimen was loaded until complete failure.

Two aspects are of great interest with respect to the cyclic loading of point supports: the behavior during cyclic loading and the behavior after cycling. The degradation of the material during the cycles was assessed by the displacements for the lower reversal point and the maximum loads at the upper reversal point. Since only one load rate was investigated during the campaign, it is not possible to differentiate between visco-plastic and visco-elastic effects of the adhesive material in the analysis. The failure behavior of the specimens after the cyclic loading is of special interest with respect to the remaining load bearing capabilities after the cyclic loading scheme.

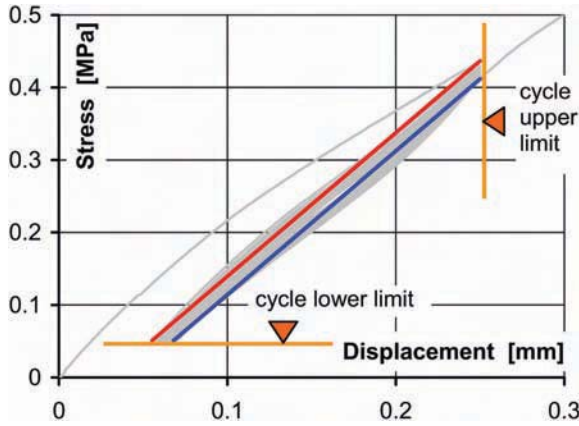


FIG. 15—Cycles slope range for low amplitude [3].

Figure 15 shows the cyclic loading scheme related to the low amplitude test case of the 0.25 mm upper limit (reversal point) for a bonding geometry of 50 mm in diameter and 7 mm in the adhesive thickness. For a quantitative comparison of the different load levels, the slopes of the various cycles obtained by secants through the upper and lower reversal points were added to the figure. For low amplitude cycles the slopes do not significantly change for an increasing number of cycles, which obviously implies that there is no significant loss of material integrity during small load cycles. In Fig. 16, the stress versus displacement cycles for the high amplitude test case are plotted. In contrast to the low amplitude case, the slopes significantly decrease for an increasing number of cycles, probably evoked by material damages. In order to allow a quantitative assessment, the relative change of loads is plotted for the various test cases in Fig. 17. As expected, the amplitudes are linked to the load reductions. Furthermore, the low and medium amplitudes show an asymptotic behavior, while for the large

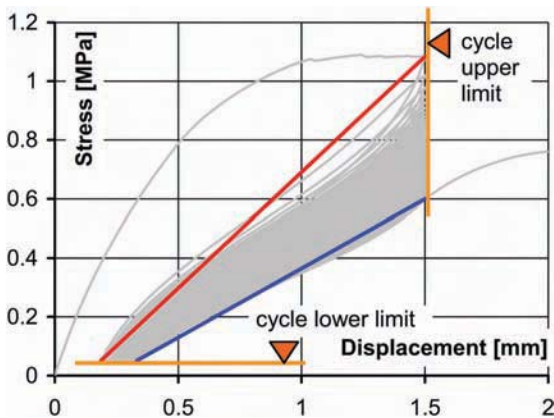


FIG. 16—Cycles slope range for high amplitude [3].

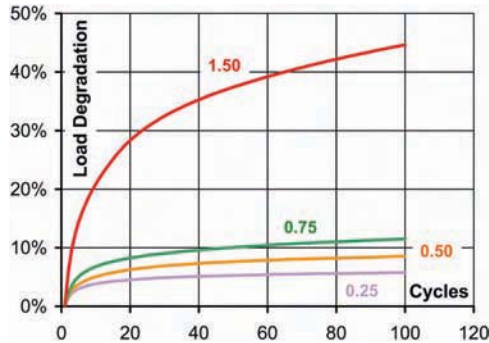


FIG. 17—Relative load degradation for various cycle amplitudes.

amplitude test case it is not obvious whether an asymptotic value is obtained for a very high number of cycles.

In order to allow an assessment of the remaining load bearing capability after cyclic loading, Fig. 18 shows the loads experienced during the final test step until failure. In this figure, the cyclic load history is deleted from the curves by connecting the load history before cyclic loading directly to the load history after the cyclic loading. In this figure, it is quite obvious that the maximum load bearing capability after the loading cycles is significantly reduced for the largest amplitude, which is not the case for the lower amplitudes. The step decrease observed for the largest amplitude is related to the reduction of loads during the cyclic load scheme, which is eliminated from this figure. Since there is apparently no recovery of the bonding for the high amplitude case, the high load cycles lead to significant material damage beyond the Mullins effect. The Mullins effect only refers to a softening of the material below the experienced maximum load but does not affect the material behavior beyond the experienced maximum loading.

This test campaign demonstrated that the impact of cyclic loading might have an impact on the ultimate load bearing capability of the adhesive, depending on the dynamic load levels. The test results are in agreement with the

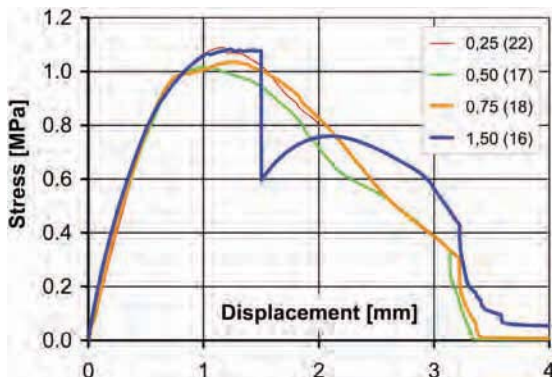


FIG. 18—Overall load curve for various amplitudes (cycles suppressed) [3].

current strength design limit used in actual field applications (0.14 MPa) since no obvious degradation effects have been observed for low stress levels. The effect of dynamic loading on structural integrity is covered today by the existing, quite conservative, and thus quite high, safety factors with respect to design stress values derived from quasi-static tests. The current test results demonstrate that a more precise determination of design limits aimed at higher design stresses, and thus lower safety factors, should also consider the impact of dynamic loading on the performance of the adhesive.

Adhesive Imperfections and Fracture Behavior

Figure 14 presents an obviously perfect behavior of point supports under tensile loading for a monotonic load history. Despite the special test fittings allowing an almost perfect bonding geometry and despite careful application of the adhesive to the specimens, the mechanical characteristics of the tested point supports show a significant scattering, as can be seen in Fig. 19.

The ultimate failure of the specimens occurs at different strain and load levels. Furthermore, samples 5 and 3 show a degradation of the mechanical characteristics significantly before the final failure. This poses the question of why the investigated specimens differ in their mechanical characteristics although manufacturing was carefully done under laboratory conditions. In order to identify indications for the different failure behavior, the fracture surfaces of the circular bonding specimens were investigated. Figure 20 displays photographs of the fracture surfaces of the specimens corresponding to the load curves shown in Fig. 19.

The following statements can be drawn by studying these fracture surfaces in detail:

- Only two specimens do not show any flaws and can thus be considered perfect; these are specimen 1 and specimen 8. The test of specimen 8 was stopped before total break. Afterwards the specimen was cut up in two pieces for analysis of the core material.

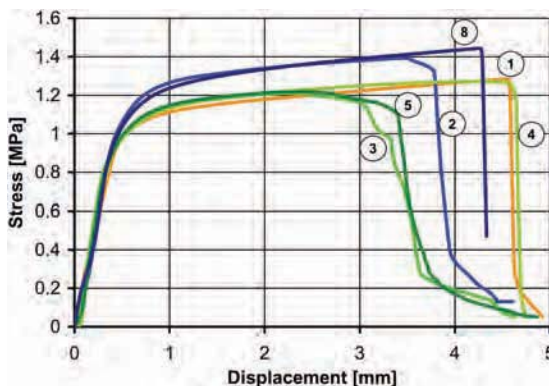


FIG. 19—Load curves for point supports with and without adhesive defects.



FIG. 20—Characteristic fracture surfaces of specimens.

- Specimen 4 shows a flaw near the center of the circular bonding, i.e., within an inner circle of 30% of the total test specimen radius.
- Specimens 2, 3, and 5 show flaws in offset positions with respect to the centre, i.e., in an annulus ranging from about 30 to 60% of the total test specimen radius.
- Specimen 1 and 8 present a fracture surface of high regularity, i.e., a “rose” pattern almost perfectly centered in the circular bonding.
- This rose pattern is disturbed in the other specimens by the flaws. The severity of the disturbance of this pattern is as follows: specimen 4 > specimen 2 > specimen 5 > specimen 3.

As a next step, the establishment of a relationship between the fracture surface pattern and the mechanical fracture behavior was considered. According to Fig. 19, specimens 1, 4, and 8 show a high performance in terms of successfully resisting high loads and/or high strains. This high performance can obviously be attributed to the total absence of flaws or to flaws located near the center of the bonded specimen. On the contrary, the performance of specimens 2, 5, and 3 is obviously deteriorated by the flaws in the annulus extending from ~ 30 to 60% of the total radius. Furthermore, it seems that from a qualitative point of view the generation of the rose pattern in the fracture surface is directly linked to ultimately high mechanical performance. Concluding these findings, flaws in a circle with less than 30% radius are obviously less critical for the mechanical characteristics while flaws in an annulus between 30 and 60% strongly affect the overall mechanical performance of the bonding.

These results support the hypothesis that the failure of the circular bonding under tensile loading initiates within an annulus between 30 and 60% of the total specimen radius. Synchronization of the testing machine recordings with video sequences indicates that the initial rupture indeed starts inside the bonded test specimen since no cracks on the surfaces of the adhesive are visible when the load starts declining. On the contrary, when one interrupts the tensile test prior to the onset of failure, it can be shown that an inner core exists (see specimen 8 shown in Fig. 21) which is still functional. This observation led to the hypothesis of the initial break occurring in the annulus region as previously defined. One potential explanation for such behavior from a chemical point of view is the fact that diffusion of cure by-products from the adhesive to the exterior environment, as well as the reactive formulation components towards the curing region results in gradients in the elastomeric network density which reflect the circular symmetry of the overall test specimen. For one-component silicone adhesives such effects have been described in the literature [9] and for these materials diffusion processes are triggered by the diffusion of moisture into the adhesive bulk material; however, one may hypothesize that the occurrence of (smaller) gradients in crosslink density even in two-component silicone adhesives are due to the diffusion of crosslink by-products from the bulk to the environment.

Furthermore, local stress loads in the bonded point specimen probably also peak upon tensile loading within the annulus previously described, irrespectively of the changes in crosslink density within the adhesive material. This hypothesis is supported by the fact that a similar annulus is observed in a

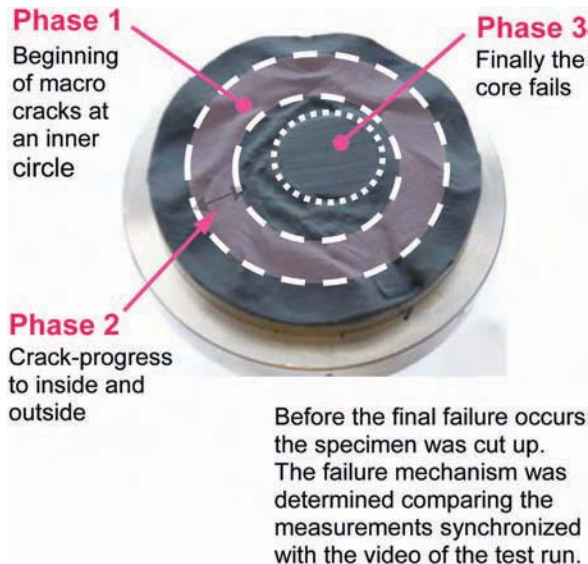


FIG. 21—Hypothesis of fracture surface propagation [3].

stress-whitening, transparent silicone structural adhesive applied in bonded point supports and subjected to tensile loads at high strains [9].

In the section titled “Cyclic Tensile Loading of Point Supports” the focus was placed on cyclic testing and related mechanical performance. Figure 22 compares the mechanical characteristics of specimen 1 subjected to simple tensile testing (without flaws in the adhesive) with those of specimen 9, which was loaded in a cyclic manner up to 1400 N corresponding to approximately 0.7 MPa stress.

The related fracture surfaces are displayed in Fig. 23. While specimen 1 shows the regular rose pattern, specimen 9 reveals totally different surface characteristics. Obviously, the rather flat unstructured fracture surface of specimen 9 is linked to the poorer mechanical characteristics as plotted in Fig. 22. A potential explanation for the differences in the mechanical performance of these specimens may be the smaller surface area created by the fracture of specimen 9 when compared to the rose pattern observed for specimen 1. Since the creation of the free surface is linked to energy consumption, the larger the fracture surface, the larger the mechanical work required to generate the fracture, which is represented by the area under the load versus deflection curve. At the current stage it is unknown whether these statements hold true for other bonding diameters and thickness values.

In addition to the need for exploring other point support geometries in a similar manner, activities are underway for establishing a procedure dedicated to a reproducible and reliable provision of defects within the adhesive for improved quantitative control of defects in future test campaigns of point supports.

Summary and Conclusions

Tensile and shear tests were performed for varying mixing ratios and the mixing quality of the investigated representative two-component silicone adhesive

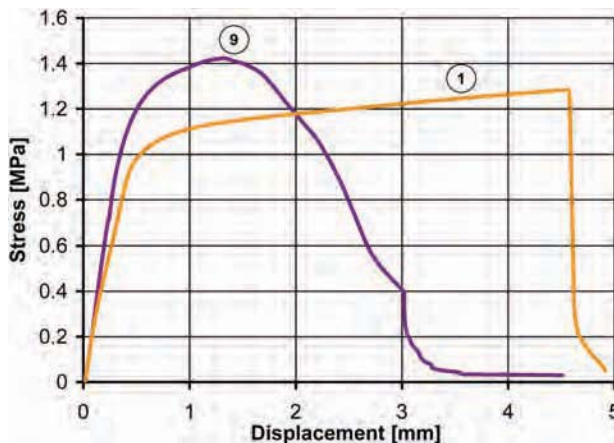


FIG. 22—Load curves for cyclic and non-cyclic tensile tests.

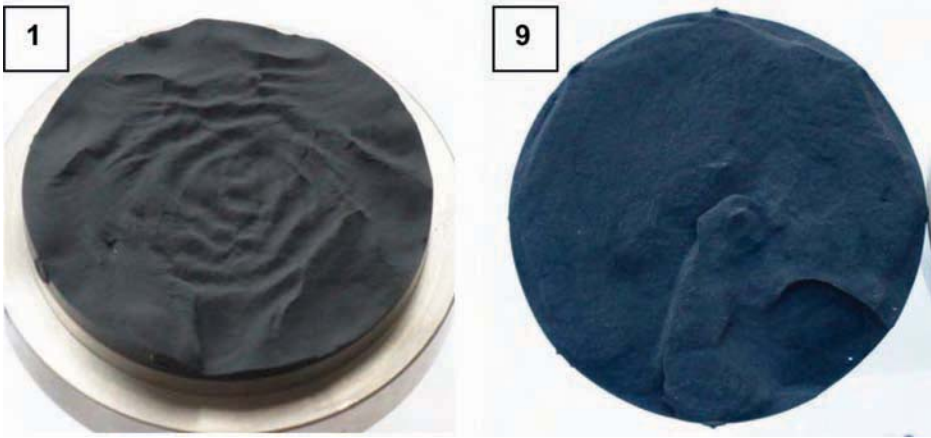


FIG. 23—Fracture surfaces for cyclic and non-cyclic tests.

widely used in structural glazing. Concerning the material properties such as stiffness and strength, the adhesive shows a quite robust behavior with respect to variations in mixing ratios within the investigated mixing range. In view of the tensile and shear test campaigns, the variation of the properties with the mixing ratio is assessed to be relatively small. Furthermore, incomplete mixing, although not quantitatively judged, leads to an increased scatter of the investigated mechanical properties. Furthermore, the mechanical characteristics in terms of stiffness and strength are degraded due to incomplete mixing. It is assumed that the outcome of these tests can also be mapped in a first attempt on durability issues related to the mechanical properties of the two-component silicone adhesive.

In order to understand the mechanical behavior of bonded point supports under varying load schemes, cyclic test campaigns have been performed for circular specimens 50 mm in diameter and 7 mm in bonding thickness. The cyclic part of the test profile consisting of 100 cycles was defined by a lower tensile force of 100 N and by upper displacements ranging from 0.25 to 1.5 mm in order to avoid backlash on the one hand, and in order to take into account the significant non-linearity of the adhesive material on the other hand. Analyses have been performed for both the cyclic part of the test curves and the post-cyclic part up to failure.

As expected, the degradation of the material depends on the amplitudes of the cycles. Two major aspects have been identified: first, the change of behavior during the cycles and second, the post-cycle characteristics with respect to the remaining load bearing capabilities. Regarding the cyclic part, the slopes decrease depending on the cycle amplitudes. For small amplitudes an asymptotic behavior is obtained, while for large amplitudes additional tests with significantly higher number of cycles are recommended in order to be able to draw final conclusions. The investigation of the load bearing capabilities after cycling showed that high amplitude cycles significantly reduce the remaining material performance.

For point support specimens of the same geometry, a relationship between failure as observed in the load curve and the break in surface texture was hypothesized by analyzing the tested specimens of 5 mm bonding thickness subjected to tensile loading. Although special care was undertaken during the manufacturing of the test specimens aiming at perfect bonding application, flaws were identified in different instances, such as bubbles in the bulk material (which later showed up on the fracture surfaces). Obviously, defects located in a radial interval of 30 to 60% of the total specimen radius have a high impact on the failure behavior of the specimens while flaws located near the center of the specimen have less of an impact on the physical properties. It is unknown whether similar conclusions can be drawn for other bonding geometries, e.g., varying diameters and bonding thicknesses.

In terms of the impact on the mechanical performance of the test specimens, the impact of the investigated parameters on the durability of the bonded point supports is assessed as follows:

- Cyclic load exposure and defects of the adhesive are primary candidates in view of durability issues.
- Poor mixing quality of the investigated two-component adhesive is a secondary candidate in view of durability aspects. However, low mixing quality is difficult to quantify, so this requires the development of specific metrics.
- Varying the mixing ratios of the investigated two-component adhesive within the range studied has a low impact.

Thus, it is recommended focusing future studies on the durability issues on cyclic load schemes and on representative specimens with controlled defects; first, cyclic loading schemes and controlled defects should be studied in separate campaigns and afterwards they should be applied in parallel in order to analyse potential interactions. A technical challenge that still needs to be solved in this context is the controlled seeding of the adhesive material with defects in a reproducible and reliable manner.

Acknowledgments

The writer would like to thank Dow Corning GmbH and especially Mr. Sigurd Sitte for supporting the experimental test campaigns. Furthermore, the author would like to thank the Test-Ing Material Company [3] for the successful performance of the test campaigns.

References

- [1] ETAG 002 Guideline for European Technical Approval for Structural Sealant Glazing System (SSGS)—Part 1: Supported and Unsupported Systems, www.eota.be/pdf/ssgs-fin-am3.pdf (Last accessed October 2001).
- [2] Dow Corning, "Product Information," *Dow Corning DC993*.
- [3] Hagl, A., "Silicone Bonded Point Supports – Behaviour under Cyclic Loading," *Engineered Transparency: International Conference*, Glasstec, Duesseldorf, Germany, Sept 29–30, 2010, Glasstec, Duesseldorf, Germany.

- [4] Wolf, A. T. and Descamps, P., "Determination of Poisson's Ratio of Silicone Sealants from Ultrasonic and Tensile Measurements," *Performance of Exterior Building Walls*, ASTM Spec. Tech. Publ. 1422, P. G. Johnson, Ed., American Society for Testing and Materials, West Conshohocken, PA, 2002.
- [5] Hagl, A., "Beyond ETAG 002: U-Type Bonding Geometries for Structural Glazing," *Modern Steel Constr.*, Vol. 1, No. 1, 2009, pp. 50–57.
- [6] Hagl, A., "Bonded Point-Supports: Understanding Today – Optimizing for the Future," *Challenging Glass 2*, Delft, The Netherlands, May 20–21, 2010, Technical University Delft.
- [7] Hagl, A., "Punktuelles Kleben mit Silikon," *Stahlbau*, Vol. 77, No. 11, (2008), pp. 791–801.
- [8] Wolf, A. T., "Preliminary Evaluation of the Mechanical Properties and Durability of Transparent Structural Silicone Adhesive (TSSA) for Point-Fixing in Glazing," *J. ASTM Int.*, (in press).
- [9] Comyn, J., de Buyl, F., Shephard, N. E., and Subramaniam, C., "Kinetics of Cure, Cross-linking Density and Adhesion of Water-REactive Alkoxy silicone Sealants," *Int. J. Adhes. Adhes.*, Vol. 22, (2002), pp. 385–393.

Anneliese Hagl¹ and Oliver Dieterich²

Glass Unit Corner Loading—Key Parameter in Durability

ABSTRACT: Bent glass has garnered increased interest on the part of architects for the realization of curved glass façades. As one method of bending of glass façade units, cold bending is an economically efficient procedure for manufacturing; however, it introduces permanent stresses in the glazing structure, especially in the corner zones of the glass units for warped designs. In a similar manner, high stresses in the corner zones are also generated in general by constant surface loads acting on the panes of the glass unit, which can be explained by thin plate theory. Thus it can be expected that these unsteady loads, e.g., evoked by wind and/or snow loads, unfavorably interfere with the permanent stresses in the adhesives of both the structural glazing sealant and the insulating glass sealant from a durability point of view. The existence of these corner loads is not adequately accounted for by the ETAG 002 guideline for structural glazing applications, which postulates a trapezoidal load distribution in the bonding with diminishing stresses in the corner zones. This paper presents numerical results of a parametric study of pressure-loaded glass units, with a focus on corner loads and stresses. The results show that the stress levels in the corner zones might be significantly higher than the design stress values used for sizing the bonding.

KEYWORDS: cold bent glass, corner load, silicone adhesive, structural glazing, warped glass

Manuscript received July 28, 2011; accepted for publication January 6, 2012; published online April 2012.

¹Managing Director, A. Hagl Ingenieurgesellschaft mbH, Munich, Bodenseestr. 217, D-81243 Munich, Germany, e-mail: mail@a-hagl-ingenieure.de

²A. Hagl Ingenieurgesellschaft mbH, Munich, Bodenseestr. 217, D-81243 Munich, Germany, e-mail: mail@a-hagl-ingenieure.de

Fourth Symposium on Durability of Building and Construction Sealants and Adhesives on 16 June 2011 in Anaheim, CA.

Cite as: Hagl, A. and Dieterich, O., "Glass Unit Corner Loading—Key Parameter in Durability," *J. ASTM Intl.*, Vol. 9, No. 4. doi:10.1520/JAI104229.

Copyright © 2012 by ASTM International, 100 Barr Harbor Drive, PO Box C700, West Conshohocken, PA 19428-2959.

NOMENCLATURE

ETAG = European Technical Approval Guideline

ETA = European Technical Approval

FEA = finite element analysis

SSG = structural sealant glazing

Introduction

In order to open the design space for curved glass façades and meet increased architectural demand, hot and cold bending techniques have become available for manufacturing bent glass façade units. Hot bending refers to the bending of glass under high temperature, leading to mainly plastic deformation of the glass panes, and cold bending is related to the elastic bending of the glass units while they are being bonded to the curved façade structure. The cold bending manufacturing procedure leads to an inherent permanent stress state of the glass façade, with the elastic bending of the glass panes counteracted by tension and compression loading of the bonding adhesive. Thus the adhesive transfers the glass pane bending moments to the supporting structure of the glass façade. One attempt to classify the related bending patterns from a kinematic point of view might involve sorting into warped, conical, or cylindrical displacement fields (see Fig. 1). Due to the enforced elastic deformation of the glass panes within the cold bending process, maximum adhesive loading in tensile and compressive directions is expected in the corner zones of the glass units subjected to warping. Cylindrical and conical bending patterns are considered less critical from a stress and durability point of view, as the maximum adhesive loading is

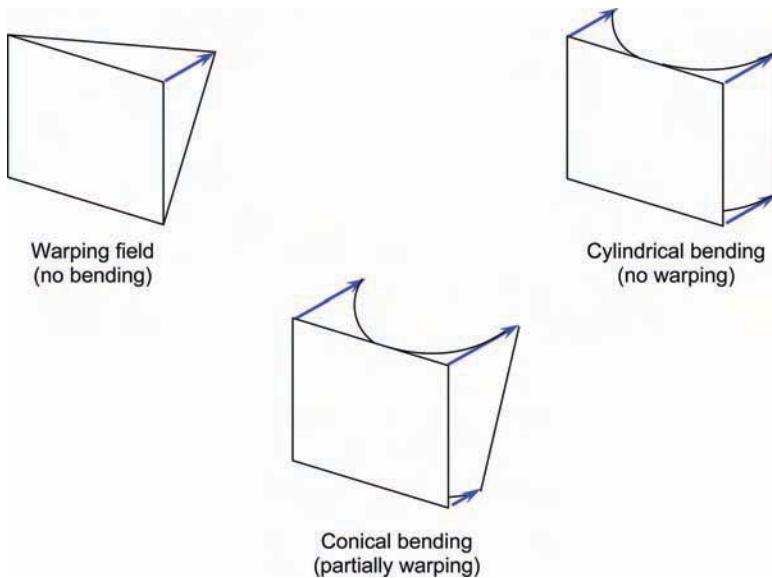


FIG. 1—*Bending patterns of potential architectural interest.*

mainly distributed along the non-curved edges. This paper focuses on the consideration of the mechanically challenging case of warping. Figure 2 presents as a numerical example the case of a laminated glass pane (Young’s modulus = 70 000 MPa, Poisson’s ratio = 0.23) 1.5 m in length, 1.25 m in width, and 6 mm in thickness, with each pane subjected to a warping of 0.1 m. The warping in the model is applied by a bi-linear warping field established via linear displacements of the edges linked to a dedicated corner that is offset by 0.1 m in the perpendicular direction (see Fig. 3). The bonding was specified to a width of 20 mm and a height of 9 mm. The material properties of the adhesive are based on a hyperelastic material law for a

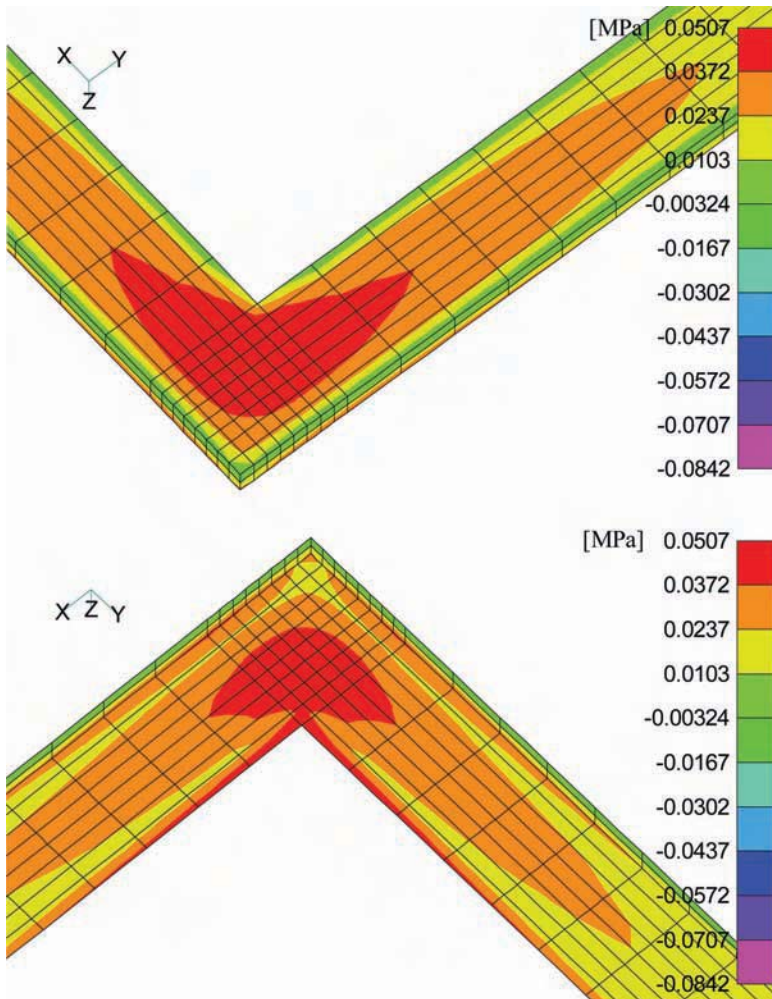


FIG. 2—Permanent tensile stress distributions in the corner zones due to warping: bi-linear warping of 10 mm (glass unit: 1.5 m in length, 1.25 m in width, 2 mm × 6 mm glass thickness; bonding: width = 20 mm, thickness = 9 mm).

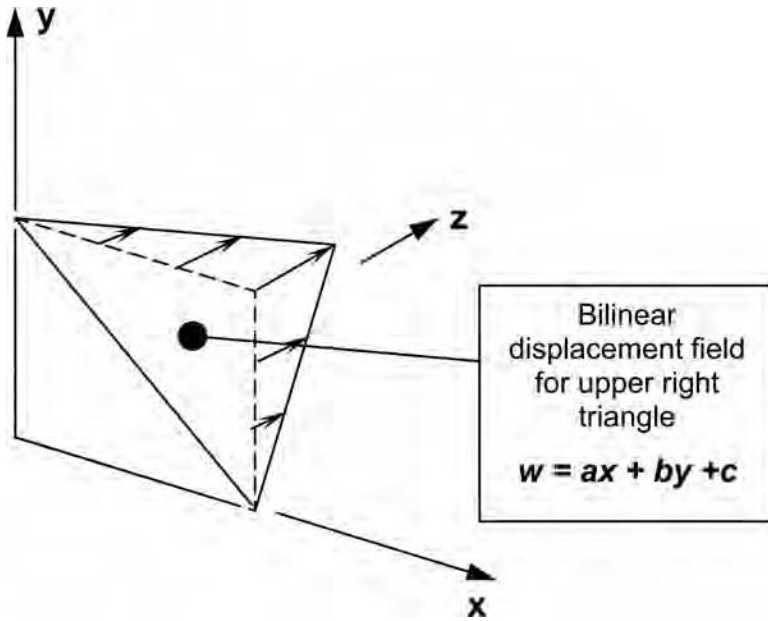


FIG. 3—Approximation of warping field as a boundary condition for the support definition.

two-component silicone adhesive typically applied for structural sealant glazing (SSG) (initial Young's modulus ≈ 1.5 MPa). As this load regime is of the permanent type, creep of the adhesive in the corner zones is a major topic for cold bending technologies. Thus cold bending applications favor highly flexible glass panes and bond geometries of large widths in order to reduce the permanent stress levels (a more detailed discussion of the results is given later in the context of Fig. 16).

Regarding the operating loads of the warped glass unit, typical load cases consist in distributed ("pressure type") loads acting on the surface of the glass panes, e.g., wind loads. Constant surface loads as approximations for sizing might be due to wind loads either in suction or in compression, snow weight, or glass dead loads in the case of almost horizontal glazing. Due to the complex stress and strain characteristics of structural glazing applications, design rules such as the European guideline for structural glazing ETAG 002 [1] use simplifying assumptions for the load and stress distributions for sizing. In the case of ETAG 002, a trapezoidal load distribution is assumed, ignoring any corner loads. Thus, ETAG 002 does not give any indication of the potential interference of the cold bending permanent stresses for short- to mid-term constant pressure load cases. This paper focuses on a review of the bond load assumptions for constant surface loads and the mechanical impact these have on cold bending warped glass façade designs from a durability point of view. The paper starts with a short review of plate theory for rectangular plates under constant pressure loads. After that, the outcome of plate theory is compared with parametric finite element analysis (FEA) studies.

Simply Supported Rectangular Glass Units

It is well known in civil engineering that for simply supported rectangular plates, concentrated corner loads will be generated in the case of constant surface loads. In addition, these concentrated corner loads are oriented in the direction opposite that of the surface loads, i.e., pressure loads evoke tensile corner forces, whereas suction loads lead to compressive corner forces. In the case of SSG applications, the significant impact of the corner forces on bond loading was highlighted in the 1990s, for instance, by Vallabhan [2] and Krueger [3]. Please note that in order to ensure the overall equilibrium condition in the plate for deformations in the out-of-plane direction (i.e., the sum of the surface loads must equal the support loads in magnitude), the concentrated corner loads lead to increased distributed loads along the plate edges. The following partial differential equation links the vertical plate displacements w of the rectangular plate in the xy -plane to the surface loads p , assigning D as the plate bending stiffness, as discussed, for instance, in detail by Blaauwendraad [4].

$$D \left(\frac{\partial^4}{\partial x^4} + 2 \frac{\partial^4}{\partial x^2 \partial y^2} + \frac{\partial^4}{\partial y^4} \right) w = p \quad (1)$$

For a complete description, boundary conditions have to be added in order to obtain a solution for the displacement w in the z -direction. In order to get a rough impression for the case of structural glass façades featuring rectangular units, the vertical displacement w is set to zero along the plate edges in the x - and y -directions. Furthermore, it is assumed that the bending moments along the edges can be neglected, leading to the following boundary conditions for the second derivatives of w along the edges in the x -direction (Eq 2),

$$\frac{\partial^2 w}{\partial y^2} = 0 \quad (2)$$

and in the y -direction (Eq 3),

$$\frac{\partial^2 w}{\partial x^2} = 0 \quad (3)$$

Please note that the mixed partial derivative $\partial^2 w / (\partial x \partial y)$ along the plate edges is still existent as the slopes $\partial w / \partial y$ along the edges in the x -direction and $\partial w / \partial x$ in the y -direction vary, approaching zero in the corners. The mixed partial derivative is linked to twisting moments m_{xy} according to Eq 4, with ν as Poisson's ratio.

$$m_{xy} = -D(1 - \nu) \frac{\partial^2 w}{\partial x \partial y} \quad (4)$$

This twisting moment is the key element for understanding the existence of the concentrated corner loads. Due to the mechanical equilibrium conditions for infinitesimal corner segments—as shown in Fig. 4—the twisting moments are

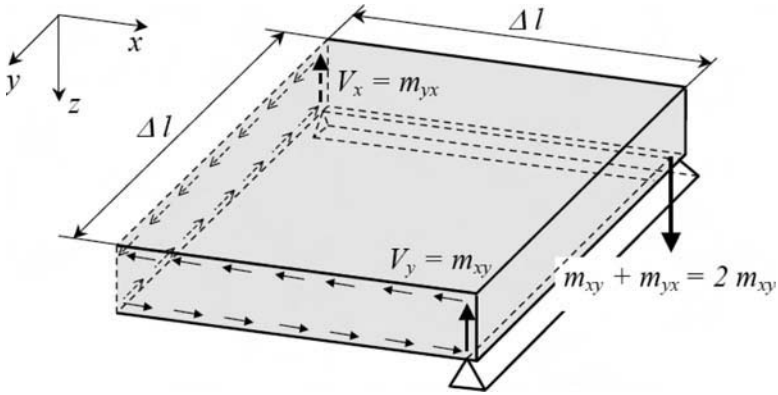


FIG. 4—Concentrated corner force for simple support.

related to vertical forces in the corners. Figure 5 underlines this behavior by illustrating a torsion panel relating dedicated corner loads to a constant twisting moment within the panel. In the case of isotropic plates ($m_{xy} = m_{yx}$), the related concentrated corner reaction force $F = m_{xy} + m_{yx} = 2m_{xy}$.

For the quantification of the corner loads, tables are usually applied for civil engineering problems (see, for instance, those published by Czerny [5] or Stiglat and Wippel [6]). Two major cases are typically treated: one-directional support and bi-directional support. In the case of one-directional support, e.g., when only compressive loads are transferred, the plate edges lift off, leading to a re-distribution of the support loads as shown for a plate aspect ratio of 1.2 in Fig. 6. It is obvious that for this case, no corner forces will be generated.

Closely representing the situation of SSG is the case of bi-directional support established by the bonding adhesive. As already noted, the corner forces quantified in Fig. 7 are acting in opposite directions. In addition to the pressure load magnitude and the size of the plate unit, the magnitude of the corner forces

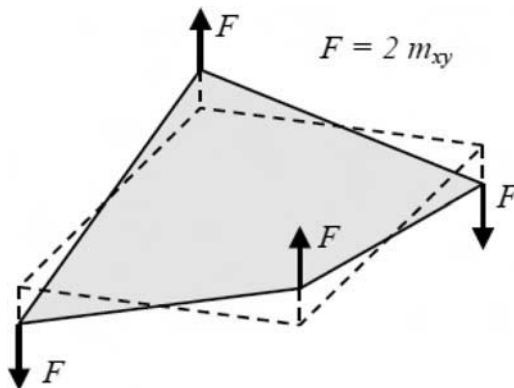


FIG. 5—Torsion panel featuring constant twisting moment.

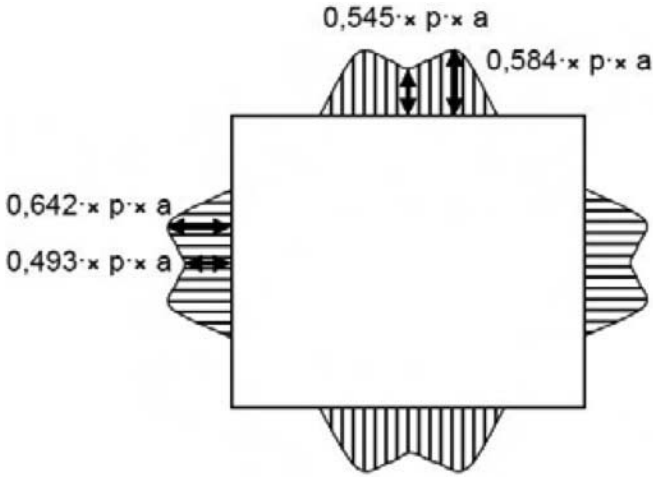


FIG. 6—One-directional plate support.

is also affected by the aspect ratio of the plate unit, as shown in Fig. 8. Consequently, the aspect ratio of glass units is one of the key parameters investigated in this paper.

Simplified Treatment of Bond Loading: Case Study ETAG 002

SSG typically involves complex mechanical characteristics of its components and the interplay among them. One of the key issues for performance assessment consists in the adequate treatment of the mechanical behavior of the adhesive material, which typically belongs to the class of elastomers. Elastomers

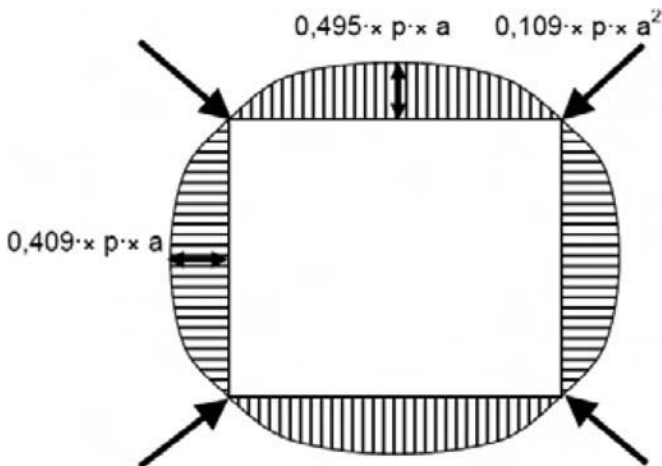


FIG. 7—Bi-directional plate support.

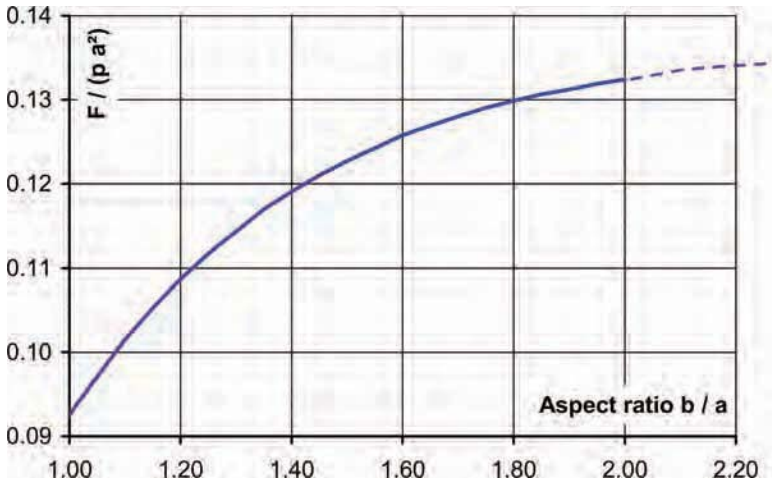


FIG. 8—Concentrated corner force as a function of aspect ratio.

differ significantly from metal alloys and glass in terms of their behavior at room temperature; special topics to be addressed are incompressibility and large strain, the Mullins effect, visco-elasticity, and creep. It is obvious that design rules are needed to simplify the material properties of the adhesive for practical applications. Thus, ETAG 002 is based on an assumed load distribution that does not require detailed knowledge of the adhesive properties. However, the price to be paid for this simplification is significant restriction of the applicability of ETAG 002, for instance, in terms of bond geometries.

Figure 9 and Fig. 10 show the underlying geometric and load assumptions of ETAG 002 with the bond cross-section being of a rectangular shape. Please note that in this assumption the corner loads are vanishing, which is contradictory to thin plate theory as presented in the preceding section. The bond load assumption of Fig. 10 directly leads to a stress equation that can be exploited for sizing. The maximum stress value along the edge, σ_{center} , is related to the

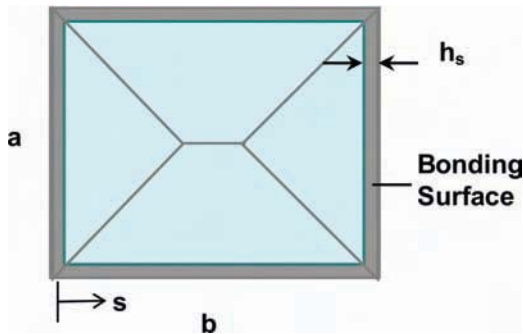


FIG. 9—Four-sided bonded geometry as assumed for ETAG 002.

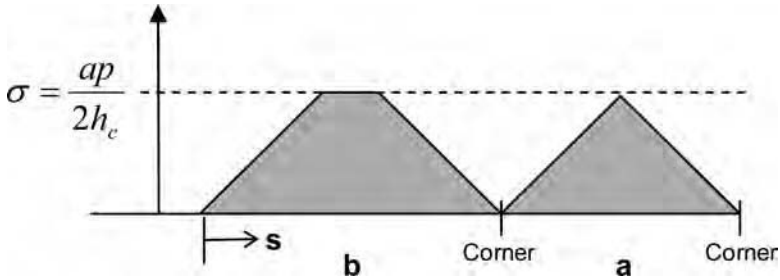


FIG. 10—Simplified bond load assumption for ETAG 002.

length of the smaller side a , the constant surface load p , and the bond bite h_c by Eq 5.

$$\sigma_{\text{center}} = \frac{ap}{2h_c} \tag{5}$$

Complementary to the design rules, design stress limits are defined for approved silicone adhesives in related documents, called European Technical Approval (ETA) documents. Table 1 shows two representative and widely used two-component silicone adhesives approved by the European Organisation for Technical Approvals for structural sealant glazing in the frame of ETAG 002.

Using the design stresses in Table 1, the minimum width h_c of the bonding geometry can be calculated by the re-arranged formula shown in Eq 6.

$$h_c \geq \left| \frac{ap}{2\sigma_{\text{design}}} \right| \tag{6}$$

Given the limited numbers of input parameters for this quite simple design rule, it is obvious that this formula has to neglect a variety of phenomena. The most important approximations are related to the following issues (see also a previous publication by one of the authors of this work [7]):

- The non-linear distribution of loading along the edges as supposed by plate theory (including sign changes in the corner area) is neglected (see the preceding section).
- Stress variations in the bond width direction that are evoked by edge bending moments caused by the deformation of the attached glass panes are not taken into account.

TABLE 1—European Technical Approvals for representative two-component silicone adhesives.

Two-component silicone adhesive	European Technical Approval	Tension design	Shear design	Shear design
		stress, MPa σ_{design}	stress, MPa τ_{design}	stress (creep), MPa τ_{∞}
DC 993	ETA-01/0005	0.14	0.11	0.011
SG 500	ETA-03/0038	0.14	0.105	0.0105

- The impact of façade design element stiffness/flexibilities, such as of the supporting frame and spacers, on the bonding interface with the frame or in the insulating glass seal is neglected.
- The geometry and bending properties of the glass panes leading to deformations of the bonding interface with the glass are not taken into account.
- The effective mechanical properties of the adhesive in addition to the limit stress values for a more accurate determination of load paths in view of hyperstatic analysis are not exploited for sizing.

A sketch illustrating the complexity of SSG behavior is shown in Fig. 11.

Numerical Finite Element Models for the SSG Parameter Study

Based on a glass pane 1.25 m by 1.5 m in size, different configurations of monolithic and laminated glass units have been studied that exactly fulfill the design requirements of ETAG 002 with regard to bond sizing [8]. Regarding laminated glass, both fully functional and totally degraded shear layer conditions are considered in this study as extreme cases. The fully functional shear layer assumes no shear strains of the interlayer (Kirchhoff plate theory, shear stiffness infinity), whereas the total degradation model allows relative slipping of the glass panes without shear stresses (panes decoupled in shear, shear stiffness zero). The first model is representative for low temperatures of the interlayer, and the second model is a limiting case for high temperatures. It is assumed that the behavior of insulating glass units in shear also is covered by these two extreme configurations of laminated glass, as the shear stiffness of the insulating sealant is between zero and infinity. Within the parametric studies, the glass thickness for laminated glass was varied from 6 mm to 8 mm to 10 mm, and for laminated glass two panes of 6 mm thickness are modeled, taking into account a shear layer with a thickness of 1.52 mm. For the load case of interest, a compressive constant surface load p was chosen in such a way that the sizing rule of ETAG 002 (Eq 6) was exactly fulfilled, leading to surface loads of 4.48×10^{-3} MPa for a bond width of 20 mm and 2.24×10^{-3} MPa for a bond width of 10 mm. Warping

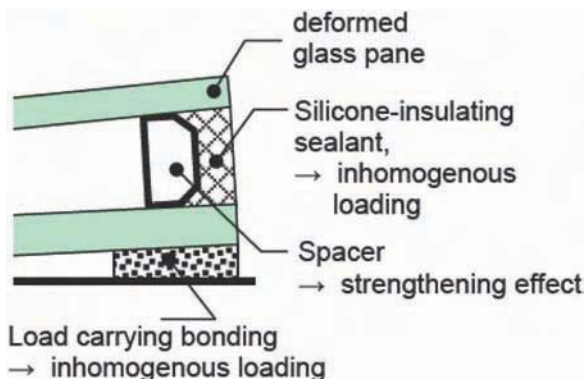


FIG. 11—*Imperfections not covered by ETAG 002 assumptions.*

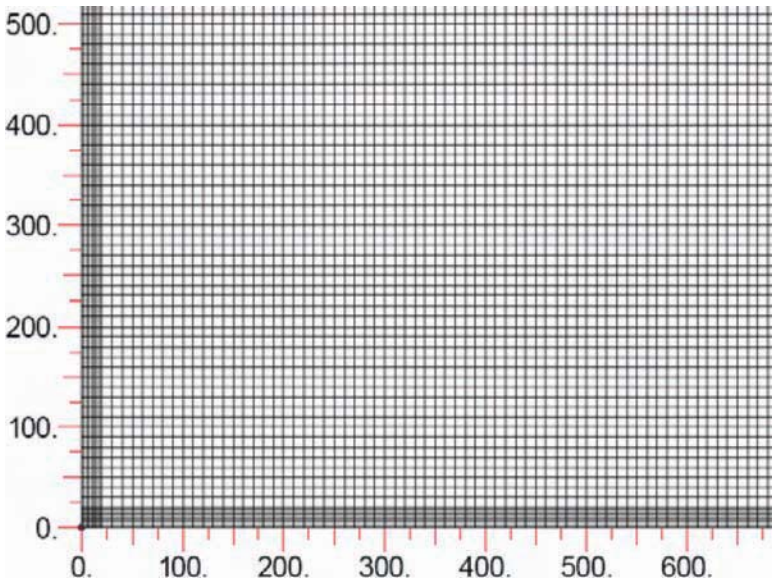


FIG. 12—Top view of a quarter of the SSG finite element mesh.

was not applied, with the assumption that for low amplitudes linear superposition can be applied for the warping and unsteady loads, and thus the investigation of these phenomena is treated separately.

The numerical model is based on FEA (i.e., plate elements featuring linear elasticity for the glass units and solid elements featuring hyperelasticity for the adhesive, with both element types using quadratic shape functions). The supporting frame is assumed to be rigid, thus being considered as a boundary condition for the flexible structure. The assumption of total rigidity is a conservative approach typically leading to higher adhesive loads. A representation of the finite element model is given in Fig. 12 and Fig. 13. The meshing is

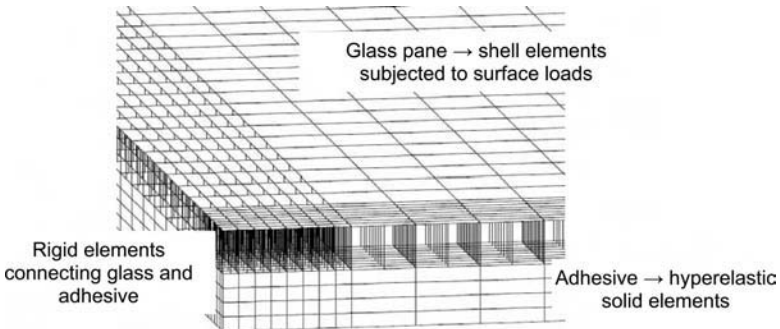


FIG. 13—Composition of the finite element model.

considered quite coarse, as the focus is put on mean or integral values within the adhesive bond.

For comparison with ETAG 002 and for a detailed assessment of the numerical results, the reaction loads of the adhesive are summed up element-wise in the bond width directions in order to get average values across the adhesive cross section for the distributed loads along the edges. In the corners, the reaction loads are related to the corner cross section as a natural extension of this approach. Afterward, the averaged stresses are plotted along the boundary edges, starting with the long side. Because of the symmetry conditions, it is sufficient to plot the stress values along one long edge and the adjacent short edge. The post-processing procedure for the stress values is sketched in Fig. 14.

Figure 15 presents results for both compressive and suction loads for a monolithic glass pane of 6 mm thickness and a bonding geometry of 20 mm bite and 9 mm thickness. This figure reveals two major issues; First, sign changes of the bonding stresses are observed in the corner areas, which is expected from plate theory. Second, the peak stress levels in the corner areas exceed the stress levels along the edges. Thus the assumption of trapezoidal stress distributions with vanishing strains in the corner zones, as incorporated in ETAG 002, is in complete contradiction to this numerical analysis. The remaining open issue is now the dependence of the averaged corner stresses with respect to various design variables.

For comparison purposes, Fig. 16 presents a typical stress distribution for a warped glass unit, assuming linear warping of the edges as shown in Fig. 3. For a consistent numerical approach taking into account large displacements, second order effects such as displacements in the x - and y -directions due to rotation along one of the diagonals are considered as well, in addition to the vertical displacement field and in-plane rotations. In addition to the stress distribution, Fig. 16 presents the stress distribution of ETAG 002 and a postulated tensile design stress limit of 0.014 MPa for permanent loads extrapolated from Table 1.

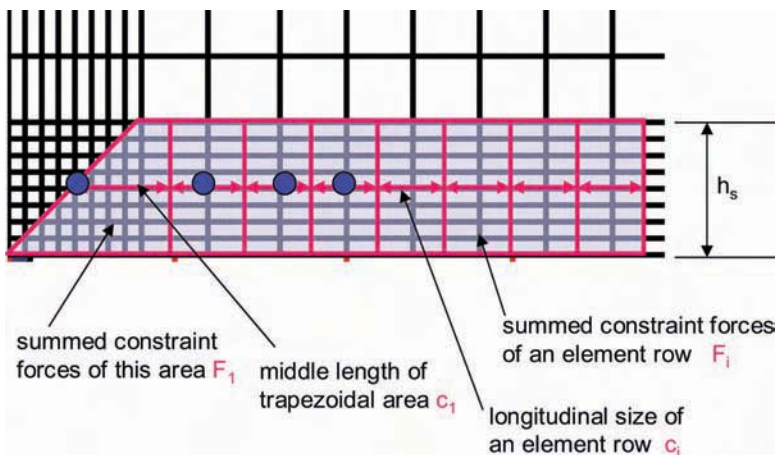


FIG. 14—Sampling of averaged stresses.

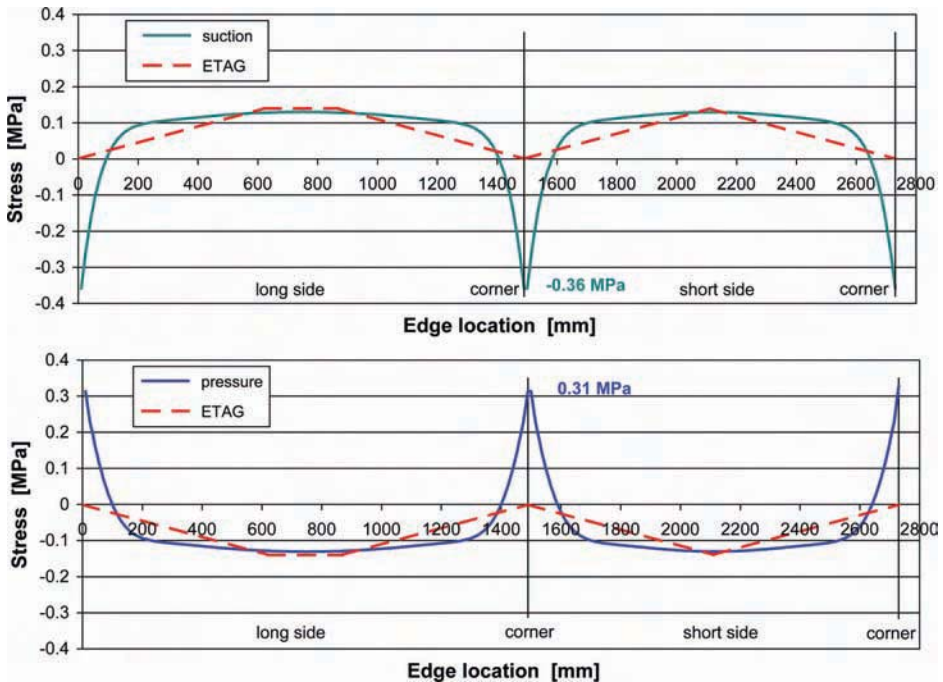


FIG. 15—Baseline results for compressive and suction loads; surface load of 4.48×10^{-3} MPa (glass unit: 1.5 m in length, 1.25 m in width, 6 mm in thickness; bonding: width = 20 mm, thickness = 9 mm).

The comparison with ETAG 002 shows that whereas the guideline predicts low stress levels in the corner region, warping leads to high stress levels in the corner area, leading to a wrong impression that interference between unsteady operational loads and warping loads might be low due to the missing corner peak loads in ETAG 002. The comparison with the extrapolated stress design limits demonstrates that even moderate warping amplitudes lead to obviously unacceptable stresses due to the assumed low stress limits. This issue underlines the need for improved silicone material knowledge with respect to creep and creep combined with operational loads in order to allow for higher design stress levels for cold bending techniques. In conclusion, the stress distribution field shows the following features:

- Peaks of the warping stress in the corner zones are obtained in Fig. 16 as expected due to the warping field.
- The warping stress field shows an almost vanishing interference with the ETAG 002 simplified (“trapezoidal”) stress field, i.e., no or low coincidence of the warping stresses and the ETAG stresses.
- A significant interference of the warping stress field with the calculated stress field of Fig. 15 is obtained, as both stress fields show high levels in the corner zones.

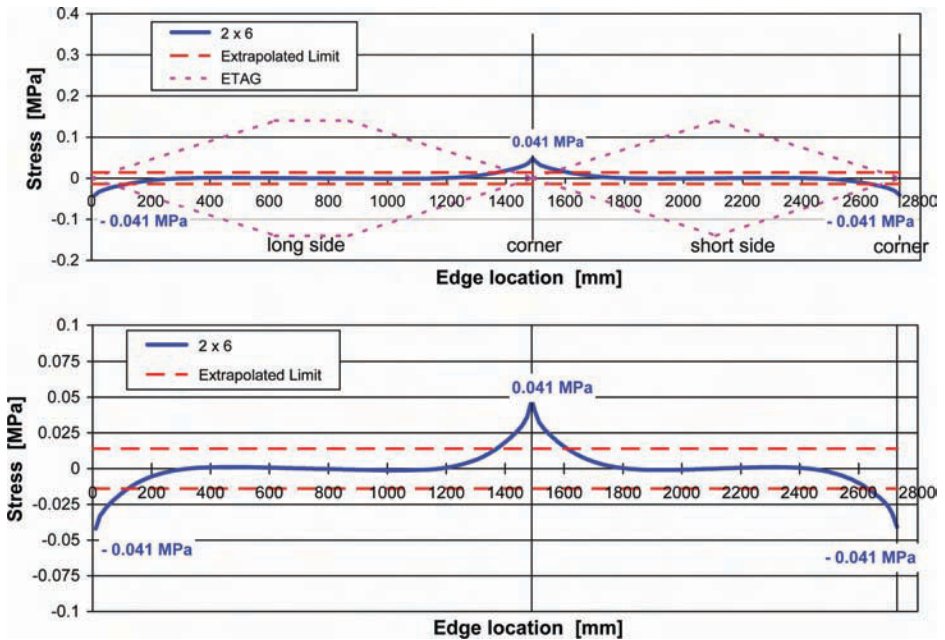


FIG. 16—Bond loading due to linear warping; bi-linear warping of 10 mm (glass unit: 1.5 m in length, 1.25 m in width, 2 mm \times 6 mm in thickness; bonding: width = 20 mm, thickness = 9 mm).

- Warping stress levels are lower for the selected warping amplitude than the calculated wind load stress fields but are of a permanent nature.

Structural Sealant Glazing Parameter Studies with a Focus on Glass Components

The first step in the parametric study consists of variation of the glass pane thickness. Figure 17 presents the evolution of the corner stresses with glass thickness. The lower the effective thickness, and thus the lower the resulting bending stiffness, the higher the peak loads in the corner zones. Obviously, low bending stiffness of the glass units favors the existence of peak corner stresses, as for the limiting case of totally rigid panes, a uniform adhesive loading will result due to the homogenous “rigid body” kinematics of the glass pane.

The impact of the glass thickness directly guides us to the issue of shear load transfer of the interlayer in the case of laminated glass units. For laminated glass, the combination of two panes of 6 mm thickness is analyzed in detail in Fig. 18 for the two extreme conditions of fully operational (default) and fully degraded (no shear stiffness) shear transfer by the interlayer. The outcome of the thickness parameter variation as shown in Fig. 15 confirms the tendency for low effective bending thickness to favor corner peak stresses; in Fig. 18 the fully active shear layer—resulting in high effective bending stiffness—leads to low

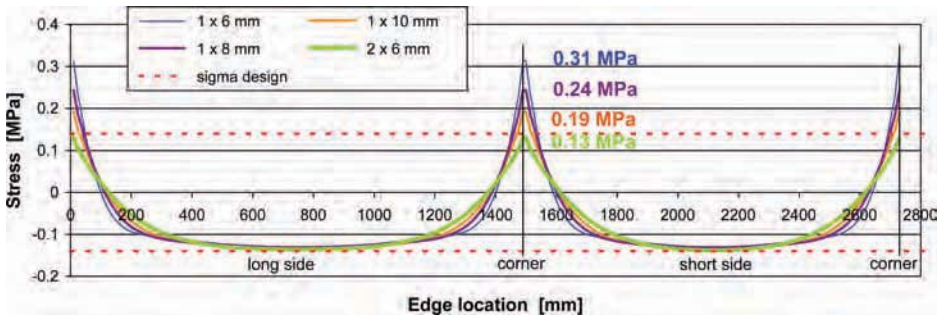


FIG. 17—Stress distribution for different glass units; surface load of 4.48×10^{-3} MPa (glass unit: 1.5 m in length, 1.25 m in width, varying thickness; bonding: width = 20 mm, thickness = 9 mm).

corner stresses, whereas in the case of a degraded interlayer (no shear stress), linked to low effective bending stiffness, the peak stresses are doubled for the investigated configuration.

In order to link these results to the corner loads obtained via thin plate theory, the relationship between corner load magnitude and glass unit aspect ratio is mirrored to the stress distributions shown in Fig. 19 for the three different aspect ratios 1, 1.2, and 2, representing panel sizes of 1250 mm × 1250 mm, 1500 mm × 1250 mm, and 2500 mm × 1250 mm. The trend of increasing corner stresses with increasing aspect ratio is in line with the characteristics of the shape function shown in Fig. 8, thus confirming the origin of the numerical corner stresses as an outcome of the special equilibrium conditions in the corners. Interestingly, also for the compressive stresses, the rule “the higher the aspect ratio, the higher the magnitude of the stresses” obviously applies as well. This result is directly linked to the concentrated corner forces, which have to

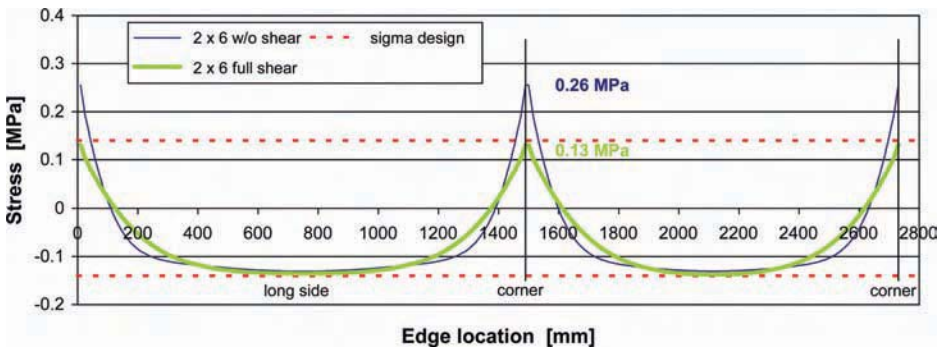


FIG. 18—Stress distribution for laminated glass units differing in interlayer functionality; surface load of 4.48×10^{-3} MPa (glass unit: 1.5 m in length, 1.25 m in width, 2 × 6 mm in thickness; bonding: width = 20 mm, thickness = 9 mm).

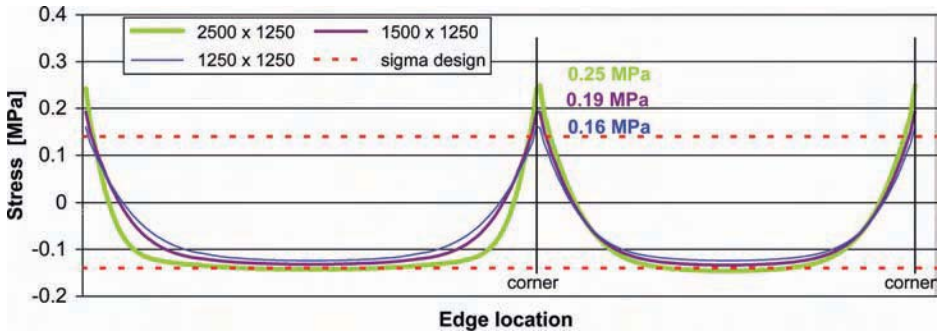


FIG. 19—Stress distribution for varying glass unit sizes; surface load of 4.48×10^{-3} MPa (glass unit: varying length, 1.25 m in width, 10 mm in thickness; bonding: width = 20 mm, thickness = 9 mm).

compensate for equilibrium conditions by means of additional compressive loads of the adhesive along the edges.

Structural Sealant Glazing Parameter Studies with a Focus on the Structural Sealant Bond

Nevertheless, the thickness of the glass units is typically related to stress levels experienced by the glass panes and thus is independent of the corner loading of the adhesive. Consequently, the glass thickness has to be considered as a boundary condition for bond sizing. Design parameters that are directly linked to the adhesive are the bite (or width) of the bond geometry and the height (thickness). Starting with the variation of the height of the adhesive, three different bond configurations were analyzed featuring heights of 6.7 mm, 9 mm, and 20 mm. Thus the investigated configurations with respect to the bond geometry limits of ETAG 002 ask for height-to-width ratios between 1:3 and 1:1 for the selected width of 20 mm. Typically, the bond height is determined by thermal loads in order to limit related thermal shear strains to acceptable values.

Figure 20 shows stress distributions for the investigated configurations based on a monolithic glass pane of 6 mm thickness. According to the results presented in this figure, the greater the bond height, the lower the corner peak stress values. This behavior can be explained by the relationship of bond flexibility and bond height (glue thickness), as the joint has a lower modulus when the aspect ratio is closer to 1:1 than to a 1:3 ratio of bond height to bite. An absolute displacement due to glass deformation results in less stress in the joint with greater bond height (glue thickness). If the bond is more flexible, the glass bending due to the twisting moments in the corner region has a lower impact, as the bond deformations are generally higher, and thus the uneven deformation pattern of the glass panes in the corners is of less importance. Please note that the effective tensile or compressive stiffness of the bond geometry is not exactly linear with respect to the reciprocal value of the bond height as expected by a simple 1D stiffness formula. The suppression of lateral contraction of the almost

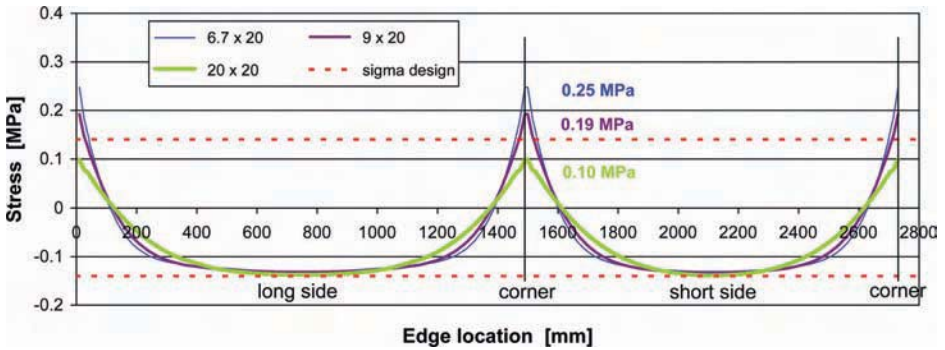


FIG. 20—Stress distribution for varying adhesive height; surface load of 4.48×10^{-3} MPa (glass unit: 1.5 m in length, 1.25 m in width, 10 mm in thickness; bonding: width = 20 mm, varying thickness).

incompressible adhesive leads to inhomogeneous deformation patterns inside the bond, thus resulting in non-reciprocal characteristics for increasing height.

The second major parameter for the bond geometry is the bond width or bite. Please note that this parameter is determined based on the wind (and other surface) loads. Thus, in order to compare different bites, the load case has to be adapted in accordance with the ETAG 002 sizing rule. Two different configurations were selected: in addition to the baseline bond geometry of 9 mm × 20 mm, the bite has been reduced from 20 mm to 10 mm, which leads to a similar reduction of the surface load p according to the sizing rule (see Eq 6). The reduction of the bite leads to a more flexible bond. Figure 21 presents a reduction of the peak corner loading for this configuration. This result is in line with the statements made before for the case of varying height. Similarly, the relationship between bond width and tensile/compressive bond stiffness is non-linear in bite due to inhomogeneous loading of the adhesive.

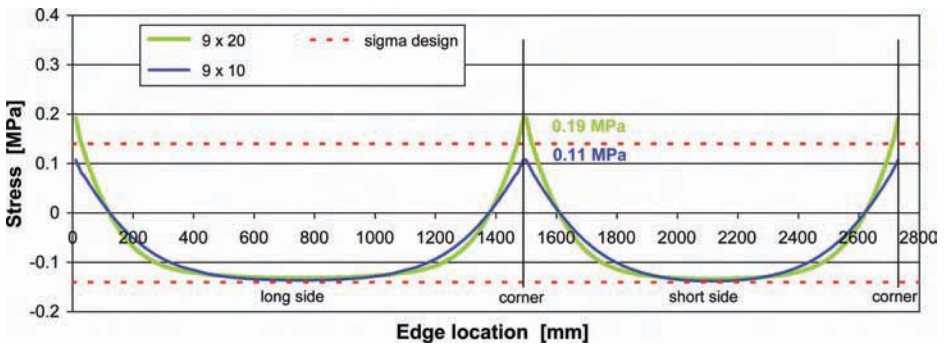


FIG. 21—Stress distribution for varying adhesive width; surface load of 2.24×10^{-3} MPa for a 10 mm bond width and 4.48×10^{-3} MPa for a 20 mm bond width (glass unit: 1.5 m in length, 1.25 m in width, 10 mm in thickness; bonding: varying width, 9 mm in thickness).

Stress Distributions in the Adhesive within the Corner Zone

Because the stress levels shown in Figs. 15–21 are averaged across the bond geometry for the purpose of the visualization of basic principles, these values do not directly represent the peak loadings within the adhesive, as the stress distribution of the adhesive, especially in the corner zone, is of a more complex 3D nature. Figure 22 gives an impression of the inhomogeneous characteristics of

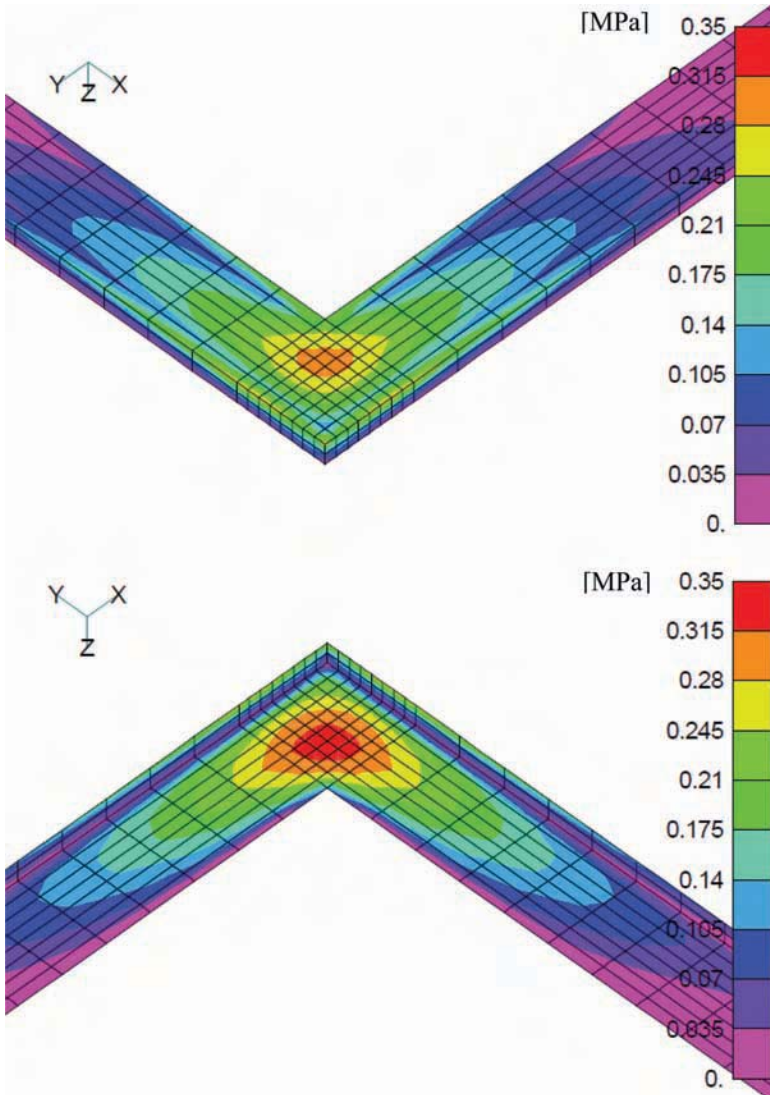


FIG. 22—Normal corner stress distribution for laminated glass with degraded interlayer (left: top view; right: middle plane); surface load of 4.48×10^{-3} MPa (glass unit: 1.5 m in length, 1.25 m in width, 2×6 mm in thickness; bonding: width = 20 mm, thickness = 9 mm).

stress in the corner zone for the case of a bond geometry of 9 mm × 20 mm for the investigated laminated glass with a degraded interlayer (no shear stresses). The “hot spot” in the corner zone, which can be understood as a continuous representation of the concentrated corner force, is clearly evident for the normal stress distribution presented here.

Whereas the averaged corner stress level of the configuration discussed amounts to 0.26 MPa, the local stresses rise up to 0.35 MPa and higher, according to the FEA shown in Fig. 22. This finding of significantly higher local stresses is underlined by data in Table 2, presenting the differences with respect to peak stresses for selected configurations for a bonding geometry of 6.7 mm × 20 mm and glass panes 1.5 m in length and 1.25 m in width.

The ETAG 002 and the related ETA documents refer to a design stress of 0.14 MPa based on tensile test data of H-type specimens of the adhesive by applying a safety factor of six. However, it is well known that the H-type specimens favor stress concentrations along the edges and in the corners due to the interfacing of the adhesive with significantly stiffer materials such as steel, aluminum, and glass, as has been discussed previously by one of the authors of this work [7]. Thus, the “real” performance of the adhesive material for other geometries is not measured by experiments on H-type specimens, as the failure load is triggered by local stress concentrations. However, testing with H-type specimens results in an “averaging” equivalent to using engineering stress and strain definitions, thus relating the local failure to global parameters.

Summary and Conclusions

Numerical parameter studies based on FEA have been performed for structural bonding designs exposed to constant surface loads that are adjusted to the bond design stresses of ETAG 002. Special focus was placed on concentrated corner loads as predicted by thin plate theory. The FEAs confirmed the theoretical result for the case of SSG models that the effect of corner loads significantly influences the stress distribution in the corners. This effect leads to averaged stresses in the corner area that can be higher than nominal design values according to ETAG 002. Thus, the stress levels induced by the corner loads cannot be neglected in the assessment of the overall mechanical performance of SSG.

TABLE 2—Averaged stress levels versus peak stress levels for selected configurations; surface load of 4.48×10^{-3} MPa (glass unit: 1.5 m in length, 1.25 m in width, varying thickness; bonding: width = 20 mm, thickness = 6.7 mm).

Glass unit configuration	Averaged corner stress, MPa	FEA corner stress, MPa
8 mm	0.31	0.52
10 mm	0.25	0.42
2 × 6 mm without shear	0.32	0.55
2 × 6 mm without shear	0.18	0.29

These averaged corner stresses increase for the following:

- increasing aspect ratios of the glass panes,
- increasing glass bending flexibility, and
- increasing bonding stiffness.

Nevertheless, successful real world installations for more than two decades proved the applicability of the ETAG 002 recommendations for SSG designs within the limited scope of ETAG 002. Removing structural silicone from the corners or reducing its cross-section at the concerns in order to let the corners flex during wind events (recall also Fig. 6 in this context) might seem to be a theoretical solution, but it is not applicable in the real world because of air and water infiltration issues.

Unfortunately, several design parameters of the bond geometry suitable for reducing corner loads directly counteract favorable design solutions for the improved durability of cold bending warped designs. In general, cold bending techniques favor a small glass bending stiffness and large bites in order to keep the permanent cold bending stresses low. Due to low design stress limits for permanent loads, cold bending designs are highly sensitive to changes in the various key performance parameters. Therefore, the often-made request to select for low glass stiffness (if possible) and large bites is evident. However, this combination is detrimental for the occurrence of corner loading. As the aspect ratio is given by design considerations, one key parameter remains open for specification: the height of the bond. For low corner loads induced by pressure loading, a large height is favorable. However, the warping requirement—or, more generally, the cold bending requirement—itsself might pose an upper limit for the flexibility of the SSG from architectural point of view. Due to these contradictory requirements, bond geometry tailoring (e.g., dedicated bond height or width distributions along the edges) will probably be only partially effective, if at all.

A potential geometric parameter for improved stress distribution and thus durability might be the warping field itself. In the analysis, a bi-linear warping field is assumed for simplicity. In reality, warping of the glass units might be achieved by built-in shapes (warping established by design), elastic bending (warping by elastic bending), or inelastic bending (warping based on plastic hinges) of the supporting frames. This paper does not answer the question of to what extent the stress distribution evoked by warping depends on the different warping fields for a given corner offset. The related optimization problem necessitates a warping design that improves the stress distribution in the corners due to warping and still fulfills architectural and cost efficiency requirements.

Alternative approaches might involve the investigation of non-rectangular glass units with respect to their suitability for cold bending or cylindrical or conical bending patterns. These proposals significantly impact the architectural design space.

ETAG 002 gives the impression of vanishing corner loads in the case of surface loads such as wind, etc. Thus, the reader might suspect that the problem of mastering the wind loads is almost independent of the consideration of the cold bending permanent loads. As has been shown in this paper, the related stress peaks associated with surface loads and cold bending loads are highly coherent in space. Thus, the interference between these load cases is obvious and should

be quantified in more detail for the durability assessment of façades featuring cold bending assembly techniques. Please note that within the framework of ETAG 002, permanent shear design stresses are 1 order of magnitude lower than the shear design limits for unsteady loads. For tensile design stresses, no values are specified for permanent loads, but a reasonable extrapolation from shear to tensile loading involves a similar reduction of the stress limits by 1 order of magnitude.

From a mechanical point of view, the true performance of SSG adhesives under the related operating conditions—either creeping under permanent loads or creeping plus unsteady loads—and thus the technological limits of SSG, are not really known. The development of an improved knowledge of the material performance attributes of the adhesive that might result in reduced safety margins might improve the applicability of cold bending techniques significantly. In this context, it has to be kept in mind that cold bending failures might be attributed to different issues such as air and water infiltration and aesthetic deficiencies (or glass breakage). Thus, different requirements are related to the mechanical performance of the bond and the adhesive, and these need to be covered by adequate technological know-how and design procedures.

From an approval point of view, a simple and straightforward extrapolation of ETAG 002 does not seem possible due to the simplifying assumptions regarding the stress distribution of the bond. One way of extending the applicability of ETAG 002 is to parameterize corner stresses and warping stresses in a similar fashion. Nevertheless, in order to be conservative, the simpler the assumptions and the procedures, the higher the required safety margins (and/or the more limited the scope), with adverse impact on the available design space for cold bending. It is highly likely that dedicated FEA is better suited for such kinds of applications, allowing one to achieve optimum design solutions with respect to today's knowledge and the technological limits. Parametric finite element studies accompanied by dedicated tests for fundamental baseline cases might be used to compile the results for standard configurations into graphs or tables that could be used for pre-design purposes.

References

- [1] European Organization for Technical Approvals (EOTA), 1999, "Guideline for European Technical Approval for Structural Sealant Glazing System (SSGS)—Part 1 Supported and Unsupported Systems," *EOTA Recommendation ETAG 002*, Brussels, Belgium.
- [2] Vallabhan, C. V. G. and Chou, G. D., "Sealant Stresses in Structural Glazing: A Mathematical Model," *Building Sealants: Material Properties and Performance*, ASTM STP 1069, T. F. O'Connor, Ed., ASTM International, West Conshohocken, PA, pp. 22–41.
- [3] Krueger, G., Voelkel, G. E., and Wohlfahrt, R., "Loading Investigation in the Adhesive Joint of a Structural-Glazing-Element," *Research Report T 2492*, IRB Verlag, FMPA Stuttgart, Germany, 1992.
- [4] Blaauwendraad, J., "Plates and FEM—Surprises and Pitfalls," *Solid Mechanics and its Applications*, Vol. 171, Springer, Dordrecht, Germany, 2010.

- [5] Czerny, F., "Tables for Rectangular Plates," *Betonkalender*, Ernst & Sohn, 1987, pp. 311–373.
- [6] Stiglat, K. and Wippel, H., "Massive Plates, Selected Chapter for Internal Force Determination and Sizing," *Betonkalender*, Ernst & Sohn, Berlin, Germany, 1992, pp. 287–366.
- [7] Hagl, A., "Bonding in Glass Construction," *Stahlbaukalender*, U. Kuhlmann, Ed., Ernst & Sohn, Berlin, Germany, 2005, pp. 819–861.
- [8] Hagl, A., "Review of ETAG 002 Guideline with Focus on Glass Unit Corner Loading," *Proceedings of the 4th International Symposium on the Application of Architectural Glass*, Munich, October 4–5, 2010, University of the Armed Forces, Neubiberg, Germany, pp. 45–54.

*Biruk W. Hailesilassie*¹ and *Manfred N. Partl*²

Mechanisms of Asphalt Blistering on Concrete Bridges

ABSTRACT: Blistering is a major problem in asphalt-covered concrete structures, such as multi-storage parking buildings, built-up roofs, tunnels, pedestrian areas, or concrete bridge decks. In this particular research, a linear viscoelastic finite-element model is developed to simulate time-dependent blister growth in an asphalt layer under uniformly applied pressure with and without temperature and pressure fluctuation. Indirect tensile tests on mastic asphalt (MA) are performed at three different temperatures to characterize and determine the material properties for the model. A three-dimensional thick-plate axisymmetric finite-element model is developed using *ABAQUS* with linear viscoelastic properties and validated with closed-form solution from first-order shear-deformation theory for thick plates. Elastic–viscoelastic analogy is used to find an analytic solution for the time-dependent deflection of the blister. In addition, the blister test is conducted on different samples of MA in the laboratory and digital image correlation measurement technique is used to capture the three-dimensional vertical deflection of the MA with time. Finally, the results from image correlation are compared with the finite-element simulation and thick-plate theory analytic solution. The finite-element model simulation shows that the daily temperature variations may have a

Manuscript received June 12, 2011; accepted for publication November 29, 2011; published online March 2012.

¹Infrastructure Engineering, Division of Highway and Railway Engineering, School of Architecture and the Built Environment, Royal Institute of Technology (KTH), SE-100 44 Stockholm, Sweden (Corresponding author), e-mail: biruk.hailesilassie@abe.kth.se

²Associate Professor, Royal Institute of Technology (KTH), SE-100 44 Stockholm, Sweden; Adjunct Research Professor, Department of Civil and Environmental Engineering, Carleton University, 1125 Colonel By Drive, Ottawa K1S 5B6, Canada; and Director, Road Engineering/Sealing Components, EMPA, Swiss Federal Laboratories for Material Science and Technology, CH-8600 Dübendorf, Ueberlandstrasse 129, Switzerland, e-mail: manfred.partl@empa.ch

Fourth Symposium on Durability of Building and Construction on 16 and 17 June 2011 in Anaheim, CA.

Cite as: Hailesilassie, B. W. and Partl, M. N., “Mechanisms of Asphalt Blistering on Concrete Bridges,” *J. ASTM Intl.*, Vol. 9, No. 3. doi:10.1520/JAI104135.

Copyright © 2012 by ASTM International, 100 Barr Harbor Drive, PO Box C700, West Conshohocken, PA 19428-2959.

significant influence on blister growth in asphalt pavements. It is found that the blister can grow continuously under repeated loading conditions over subsequent days. The study concludes that temperature fluctuation in the blister has more influence on blister growth than fluctuation of the pressure inside the blister.

KEYWORDS: blister growth, indirect tensile test, finite-element method, master curve, *ABAQUS*TM, Prony series, sigmoidal function, creep, relaxation, closed-form solution

Introduction

Elements of a Bridge-Deck System

The primary aim of waterproofing layers under a bridge-deck pavement is to protect the structural concrete from penetrating water and de-icing chemicals. As shown in Fig. 1, such a waterproofing system often consists of a polymer-modified bitumen membrane (PBM) that is glued to the concrete surface by an adhesive-bonding agent or by welding with a torch. Generally, the bridge-deck pavement consists of two layers of mastic asphalt (MA), composed of aggregate with a maximum aggregate size of 8 mm, 11 mm, or 16 mm and a 6.5% by weight binder of 20/30 penetration grade to survive extreme traffic conditions [1]. In addition to this, epoxy sealing, acrylate, or polyurethane is used as a waterproofing layer on concrete bridge decks. MA has virtually no air voids. Therefore, it contributes to the waterproofing properties of the system. In general, bituminous waterproofing membranes on bridges have a thickness of 5 mm. They are typically made of styrene-butadiene-styrene polymer-modified bitumen that is carried by glass fiber and polyester fabrics in the center of the sheet. Usually, the upper surface is treated with talcum, sand, and granules for ultraviolet radiation protection. High-quality waterproofing membranes have good thermal stability, flexibility at low temperature, and good adhesion to the concrete surface.

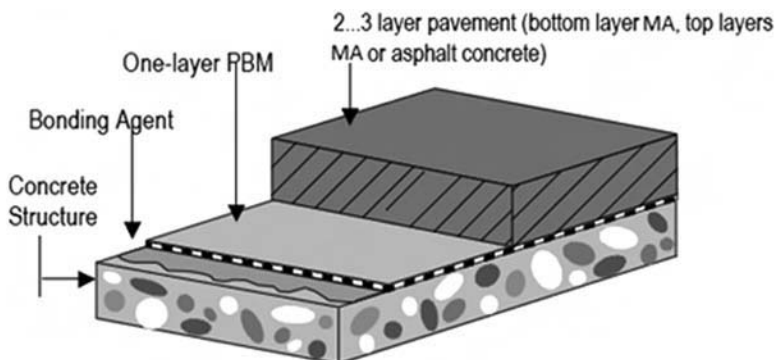


FIG. 1—Scheme of a concrete bridge-deck waterproofing system [2].

Failure of the adhesive bond between a concrete surface and a waterproofing membrane PBM can occur because of the lack of strength of the concrete or insufficient adhesion and cohesion of the bituminous membrane layer. In addition to this, the welding process can affect the strength of the concrete. Heating can lead to tension in the upper surface followed by cracking or detachment. Various techniques can be used to improve the adhesion, such as sandblasting and water jetting, etc. Possible use of low-viscosity epoxy resin as bonding agent and seal against humidity may be helpful [3].

Reasons for Blister Formation

Mechanical properties, dimensional change with temperature, permeability, the ability to vent gas, etc., are major issues concerning blistering of waterproofing membranes. The main reason for blister formation is attributed to pressure produced by air and water vapor under the pavement [4]. Blisters can be caused by the expansion of hot, humid air in the concrete after torching of the membrane with an open gas flame.

Short-term blisters occur when placing hot MA and result from humid air trapped in the asphalt mixture. These blisters are often removed in practice by punching a steel stick into the blister of the mixture to release pressure. This bad practice indicates a quality problem either in the material or construction process. Because it is practically impossible to release all pressure by punching through the blisters, some of the smaller blisters may get “frozen” during the cooling process and the trapped air may be the trigger for the formation of long-term blisters that may gradually grow under service condition. Reference 5 suggests that blisters on concrete with asphalt overlay are caused by thermal buckling of the pavement slab.

Waterproofing sheets on roofs may also show blister formation. In a broad analysis of blister phenomena [6], the authors indicate that blisters can only develop in initial voids or unbound areas because of poor membrane application during construction. After such blister initiation, gas expansion inside the blister can cause blisters to grow. When the temperature rises, obviously, the pressure increases. However, from actual pressure measurements within blisters, it was found that the pressure is much lower than calculated for totally entrapped gases [6]. Because of temperature fluctuation in the surrounding environment, air is forced out during daytime and sucked in at night. It is supposed that temperature variation leads to breathing or pumping action, which changes the blister volume.

Objectives

The primary objective of this study is to develop a finite-element model, which simulates blister growth with focus on long-term blistering. This includes investigation of blister growth in the laboratory with finite-element simulation focusing on blistering of MA and first-order shear-deformation thick-plate theory. It includes also investigating the influence of temperature and pressure fluctuations on blister growth (viscoelastic thick plate) for linearly varying temperature

and pressure. In addition to this, a simplified model is established which can simulate blister growth for constant blister radius, considering the viscoelastic properties of the MA, as a basis for future research.

Thick-Plate Theory

Generally, shell elements are used in models, where the thickness is significantly smaller than other dimensions. Shells with a thickness of more than about 1/15 of the span of the shell are considered as thick shells; otherwise as thin shells [7]. In this report, the exact bending solution from the classical plate theory [8] and the Mindlin plate theories [9] are used. These theories are applied to calculate the out-of-plane displacement–pressure relationship of thin and thick solid isotropic plates, respectively.

In case of thick plates, where the shear deformation is significant, shear-deformation plate theories can be applied. There are numerous shear-deformation plate theories available, the simplest of which is the first-order shear-deformation plate theory (FSDT) also known as the Mindlin plate theory. The deflection equation of the FSDT can be expressed in terms of the corresponding quantities of the classical plate theory for axisymmetric bending of isotropic circular plates as shown in Eq 1 [9]. A similar equation was used by Fini et al. [10] to calculate the out-of-plane displacement for a thick circular plate (see Fig. 2) under axisymmetric uniform pressure with built-in edge constraint

$$w_o = \frac{p_o}{64D}(R^2 - r^2)^2 + \frac{p_o R^2}{4SGh} \left(1 - \left(\frac{r}{R}\right)^2\right)^2 \tag{1}$$

where p_o = pressure, r = distance from the center of the thick circular plate, R = radius of the thick circular plate, h = thickness of the thick circular plate, w_o = displacement at a distance r from the center of thick circular plate, S = shear correction factor (5/6 for the thick circular plate), D = flexural rigidity of the plate, $D = Eh^3/[12(1 - \nu^2)]$, G = shear modulus of the plate, $G = E/[2(1 + \nu)]$, E = modulus of elasticity, and ν = Poisson’s ratio.

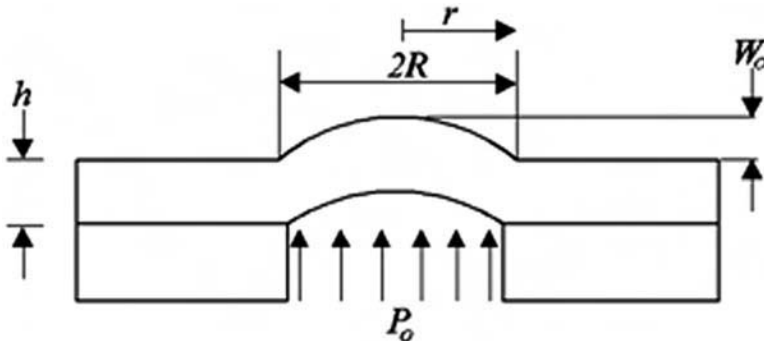


FIG. 2—Scheme of a pressurized blister plate.

Finite-Element Model: Geometry and Loading

The bending properties of different meshing elements have been studied with linear elastic analysis and then the dimensions and boundary condition of the viscoelastic model were defined. The continuum three-dimensional twenty-node-reduced (C3D20R) element was selected for its good agreement with the linear elastic analytic solution for the vertical deflection of a thick plate. This model had 56 elements and all elements were arranged in a single layer. The linear elastic model for blister formation in a thick plate was used as reference for the viscoelastic finite-element simulation in this chapter.

In this particular case, a three-dimensional (3D) half-circular model was considered. As long as the symmetry conditions hold at the edges, the radial symmetry in the pressurized circular plate allows any size of pie slices or segments to be used in the model. A 3D finite-element model was developed using *ABAQUS* version 6.8 (SIMULIA Scandinavia Abaqus Scandinavia AB SE-72210 Västerås SWEDEN).

Modeling blister growth in MA has been done by Michalski [11] and blister formation in thermo-viscous material was studied by Rogosch [12]. In this paper, a 3D model is established to simulate the time-dependent vertical blister deflection of a thick plate for different types of loading amplitudes.

The geometric finite-element model setup of the 3D plate is shown in Fig. 6(b), where the entire contact area between the plate and supporting substrate is constrained in all df ($u_x = u_y = u_z = 0$, where u_x , u_y , and u_z are displacement in x , y , and z axis, respectively, and $u_{RX} = u_{RY} = u_{RZ} = 0$, where u_{RX} , u_{RY} , and u_{RZ} are rotational displacements in x , y , and z axis, respectively). This condition of support represents full adhesion to a rigid substrate beyond the area of the interface. Symmetry plane x - z has a degree of freedom $u_y = 0$. A uniform pressure load of 0.03 MPa is applied over the entire region (blister radius) of the circular half-plate. The pressure load applied in this model is the same as the pressure used in the laboratory test, which is described below. A constant average temperature of 59 °C is used in the finite-element simulation model. This temperature is measured during the experiment as mentioned in the next section.

Test Development

Digital image correlation experiment technique gives the possibility to measure displacement and deformation fields at the surface of objects under any kind of loading condition. The post processing software uses the images taken at different loading times to construct the impression of the distribution of vertical deflection in the measured object. This system can be used in bubble inflation tests to measure the strains on the surface of the bubble [13]. In this case, the blister growth is measured with a 3D digital image correlation system (Limes Vic3D-4Mp) where two cameras were used to measure the out-of-plane deflection of the MA see Fig. 3(b). MA thickness of 25 mm at temperature of 250 °C was applied to a concrete plate 500 × 500 mm². Because it was intended to study the blister growth caused by bending and stretching of MA, it was important to avoid interfacial fracture between the layer of MA and concrete by keeping the

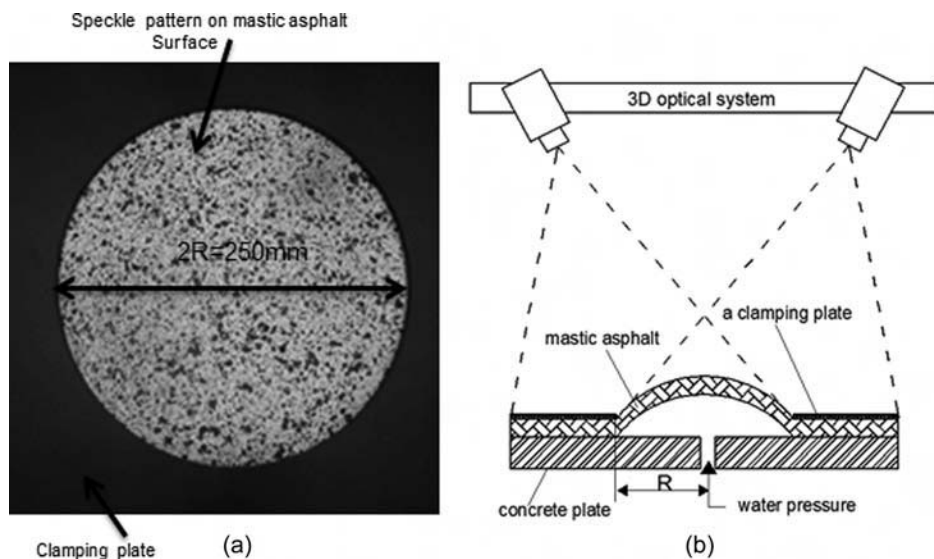


FIG. 3—(a) Top view of the MA sample after spraying paint to produce speckle image (b) the blister test devise (Vic3D-4Mp).

blister radius constant. Therefore, an aluminum clamping plate having a hole with a diameter of 250 mm was used at the top of the MA, and ordinary white and black paint spray was used to produce a speckle pattern on the surface of the MA, as shown in Fig. 3(a). Water pressure was injected through the concrete plate to produce a pressure for blister growth. The pressure was controlled with a manometer and the pressure was kept constant at 0.03 MPa during the testing period. The temperature inside the blister was recorded using a thermo-element and the average temperature inside the MA was found to be 59°C. The measured vertical deflection data are presented in Fig. 9.

Viscoelastic Material Characterization

Figure 4 describes the steps followed to determine the Prony series parameters as input for the finite-element model. After performing the creep-compliance test with the indirect tensile test (IDT), the master curve is constructed using a sigmoidal function; then the master curve (experimental data) is fitted to a power-law function. Using this power-law function and Laplace transform, the relaxation modulus in power-law representation is determined and approximated by a four-parameter Prony series as input for the finite-element calculation. Details of the work are shown below.

Creep-Compliance Test

To predict the blister response accurately, proper characterization of the MA is needed. The viscoelastic properties of MA are measured using either simple

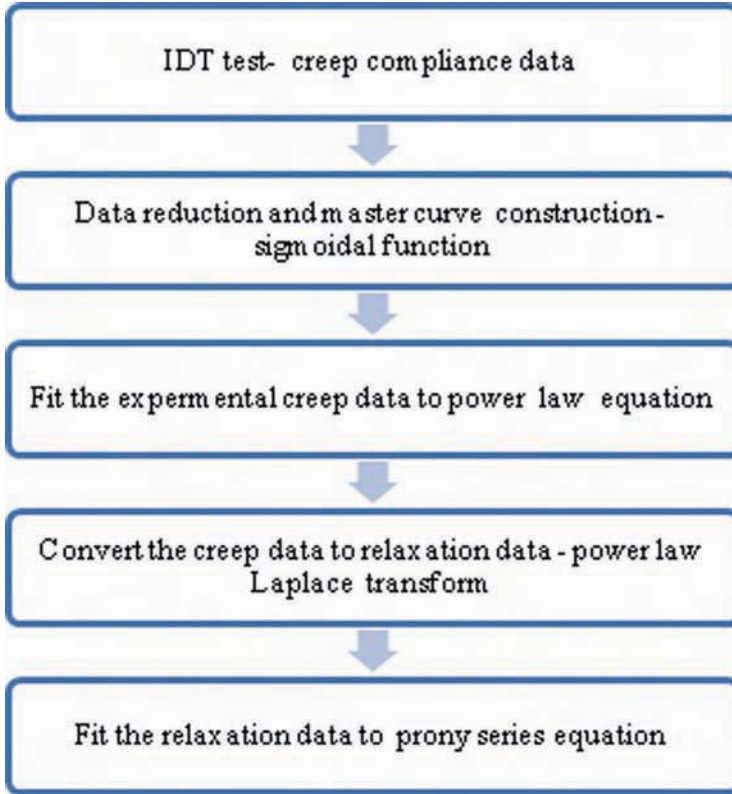


FIG. 4—Scheme of a material characterization for the finite-element model.

creep tests (time domain) or complex modulus tests (frequency domain). In this study, time domain IDT results are used to describe the viscoelastic properties of the material in *ABAQUS*. In case of IDTs, a static constant load was applied along the vertical diametrical axis of a temperature-controlled cylindrical specimen for a specified period of time (100 or 1000 s), while measuring the horizontal deformation. The load was controlled such that the upper linear-elastic limit of the specimen, typically 100–500 μstr , was not exceeded (see Ref 14).

In this report, the dimensions of the indirect tensile specimens were 100 mm in diameter and 49.8 mm in height. These specimens were cored from MA slabs. Each specimen was tested at 5 °C, 15 °C, and 25 °C temperatures. A load was applied to cause a horizontal strain in the order of 100 μstr , so that the electric noise during data acquisition process became insignificant. During the loading period, horizontal deformations were measured on both sides of the specimens using four extensometers.

Different theoretical assumptions are commonly used for evaluating IDT results: homogeneity, isotropy, Poisson's ratio, coefficient of thermal contraction, and the estimation of relaxation modulus from the creep compliance are important issues in the IDT analysis [15].

Huang [16] suggested that the Poisson's ratio for most asphalt-mixture ranges between 0.3 and 0.4. It is stated that it can be appropriate to assume the Poisson's ratio value rather than determining it from actual tests because the effect of Poisson's ratio is not significant. Hence, for simplicity, Poisson's ratio is often assumed to be time independent in spite of the fact that this is not the case in reality [17].

Data Reduction

In this research, creep compliance is calculated as a function of horizontal deformations. A detailed review of the measurement and analysis system is presented in Ref 18. All correction factors are considered to depend on Poisson's ratio. With this adjustment, the creep compliance was obtained as follows:

$$D(t) = \frac{\frac{H_{\text{TRIM}}(t)}{L_G} \cdot 1.071 \cdot C_{\text{BX}}}{\frac{2P}{\pi W d} (C_{\text{SX}} + 3\nu \cdot C_{\text{SY}})} \quad (2)$$

where $D(t)$ = creep compliance, 1/GPa; ν = Poisson's ratio; P = creep load, N; C_{BX} = horizontal bulging correction factor; C_{SX} = horizontal stress correction factor; C_{SY} = vertical stress correction factor; D = diameter of the specimen, mm; L_G = length between gauge point centers, mm; W = thickness of the specimen, mm; and $H_{\text{TRIM}}(t)$ = trimmed average horizontal deformation, mm.

The trimmed average horizontal deformation is calculated by ranking each of the horizontal arrays according to their deflection values in considering a window around the middle of the test (46–50 s). After ranking, the horizontal deflection with the highest and the lowest measurement values are removed from the data analysis and four of these results are used out of the six measurements to determine the creep compliance; for details see Ref 18. Creep compliance is calculated with Eq 2. from the row data of IDT for three different temperatures (5 °C, 15 °C, and 25 °C) as indicated in Table 1.

Master Curve Representation

As shown in Eq 3, the sigmoidal function in combination with the Williams-Landel-Ferry (WLF) equation may be used to construct master curves. Shifting to an arbitrary temperature (in case of this investigation 5 °C) is done by solving for the shifting factors with the parameters of the sigmoidal function by least-squares method.

The different parameters of Eq 3, as determined from non-linear representation analysis with the curve-fitting toolbox of Matlab (MathWorks Knarrarnäsgratan 7, Kista Entré, Box SE-16421Kista, SWEDEN), are indicated in Table 2. R -square is the square of the correlation between the response values and the predicted response values. The master curve constructed from Eq 3 is shown in Fig. 5(a) and will be used in ABAQUS to define the thermorheologically simple behavior of the MA

TABLE 1—Creep compliance from IDT.

Time, s	Measured creep compliance, 1/GPa		
	log (D) at 5, °C	log (D) at 15, °C	log (D) at 25, °C
1	$3.70 \cdot 10^{-02}$	$8.14 \cdot 10^{-01}$	$6.92 \cdot 10^0$
2	$1.34 \cdot 10^{-01}$	$7.13 \cdot 10^{-01}$	$1.53 \cdot 10^{01}$
5	$2.59 \cdot 10^{-01}$	$1.57 \cdot 10^0$	$2.35 \cdot 10^{01}$
10	$4.26 \cdot 10^{-01}$	$2.19 \cdot 10^0$	$3.73 \cdot 10^{01}$
20	$7.72 \cdot 10^{-01}$	$3.79 \cdot 10^0$	$6.07 \cdot 10^{01}$
50	$1.33 \cdot 10^0$	$6.17 \cdot 10^0$	$8.46 \cdot 10^{01}$
100	$2.01 \cdot 10^0$	$1.97 \cdot 10^{01}$	$9.79 \cdot 10^{01}$
200	$2.91 \cdot 10^0$	$3.22 \cdot 10^{01}$	$1.21 \cdot 10^{02}$
500	$4.68 \cdot 10^0$	$5.78 \cdot 10^{01}$	$1.85 \cdot 10^{02}$
1000	$6.50 \cdot 10^0$	$8.60 \cdot 10^{01}$	$2.58 \cdot 10^{02}$

$$\log(D) = b_1 + \frac{b_2}{1 + e^{\left[a_1 + a_2 \left(\log(t) + \frac{c_1(T - T_{ref})}{c_2 + (T - T_{ref})} \right) \right]}} \tag{3}$$

where D = creep compliance, 1/GPa; T = time of loading, s; T_{ref} = reference temperature, K; T = temperature, K; b_1 = minimum value of D ; b_2 = span between maximum and minimum value of D ; a_1 and a_2 = parameters describing the shape of the sigmoidal function; c_1 and c_2 = WLF constants.

Power-Law Analytical Form of Interconversion

The power-law analytic form of interconversion is used to predict the relaxation modulus from measured creep-compliance data and as input for characterizing asphalt mixtures in ABAQUS. It is evident that creep and stress relaxation phenomena are caused by the same linear viscoelastic properties. For linear viscoelastic material, this interconversion can be done by applying Laplace transform

$$\varepsilon(s) = sD(s)\sigma(s) \tag{4}$$

where s is the Laplace transform variable, ε and σ are strain and stress, respectively

$$\sigma(s) = sE(s)\varepsilon(s) \tag{5}$$

TABLE 2—Sigmoidal parameters and the WLF constants.

b_1 , MPa	b_2 , MPa	a_1	a_2	c_1	c_2	R-square
$3.70 \cdot 10^{-02}$	$6.98 \cdot 10^{03}$	2.097	-0.908	1520	11750	0.976

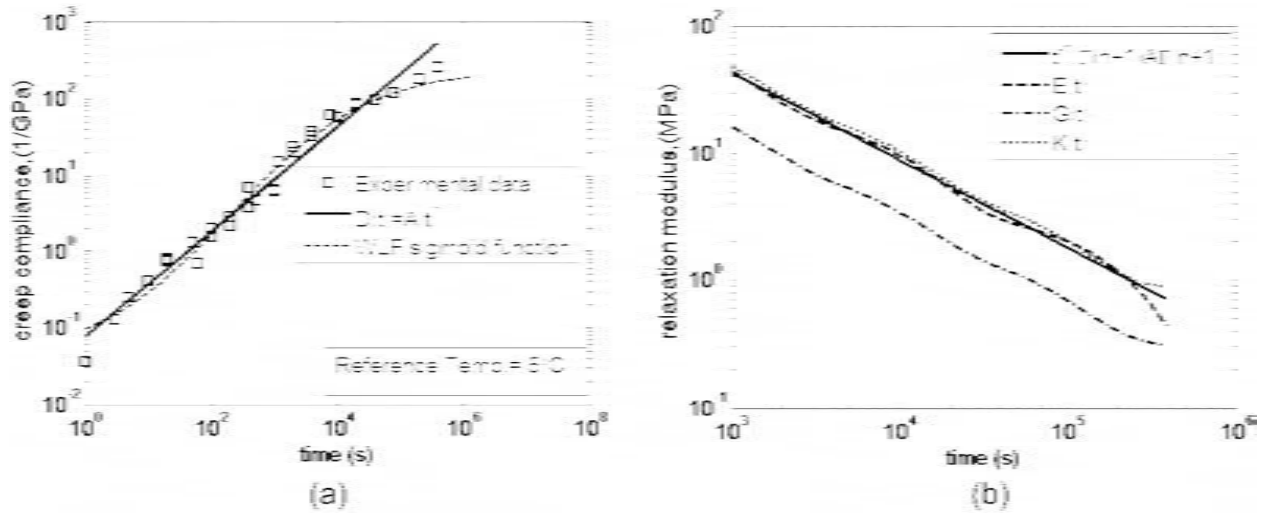


FIG. 5—(a) Approximation of the creep behavior of MA with a power function, Prony series and master curves for MA at reference temperature 5 °C (WLF, sigmoid function); (b) shear and bulk relaxation modulus variation with time at 5 °C.

where E is the relaxation modulus. Hence

$$E(s) = \frac{1}{s^2 D(s)} \tag{6}$$

According to Eq 6, the relaxation modulus can be calculated from the creep compliance. Hence, it is easier to express the creep compliance by the power-law function

$$D(t) = At^n \tag{7}$$

where t is time and $D(t)$ is creep compliance (1/GPa).

In this report, the experimental creep data are limited to the linear part of the sigmoidal function with maximum slope. Hence, instead of using a sigmoidal function, the data is approximated by a power function for easier interconversion of the creep data to the relaxation modulus. The power-law equation fitted to the creep-compliance data for an arbitrary reference temperature of 5°C is expressed by Eq 7 as shown in Fig. 5(a) with, $A = 7.71 \cdot 10^{-02}$ 1/GPa and $n = 6.88 \cdot 10^{-01}$. Transforming Eq 7 into the Laplace domain and substituting into Eq 6 leads to the following Eq 8 after back-transforming the equation into the time domain. The result is shown in Fig. 5(b)

$$E(t) = t^{-n} \frac{1}{\Gamma(n + 1)A\Gamma(n + 1)} \tag{8}$$

where A and n are constants and $\Gamma(n + 1)$ is the gamma function.

Relaxation Modulus Determination

For numerical analysis in ABAQUS, the power-law representation of the relaxation modulus was fitted and replaced by a four-element Prony series according to Eq 9, as shown in Fig. 5(b). The fit with Prony series for a reference

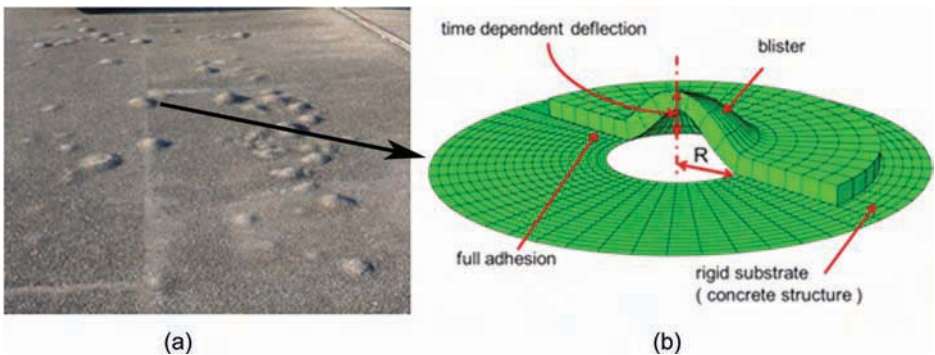


FIG. 6—(a) Observed blisters, (b) schematic 3D model setup for blister growth simulation.

temperature of 5 °C is shown in Fig. 5(b). The fit is not exactly identical to the power-law representation because, for simplicity, only four elements were used. However, for this investigation, four Maxwell elements are considered to be sufficient. The relaxation times of the four Maxwell elements and the Prony series parameters are presented in Table 3

$$E(t) = \sum_{i=1}^{N+1} E_i e^{-\frac{t}{t_{ri}}} \tag{9}$$

where $E(t)$ is the relaxation modulus, E_i are Prony series spring-constant parameters for the relaxation modulus master curve (spring constants or moduli), and t_{ri} are the relaxation times for each Maxwell element.

For 3D multi-axial stress state, it is convenient to describe the stress state with deviatoric and dilatational components. A detailed description is given in Ref 19, a generalized solid Maxwell model is used in *ABAQUS* to characterize these two stress-state components. The bulk relaxation modulus follows from Eq 10 and the shear relaxation modulus from Eq 11

$$K(t) = K_0 \left(1 - \sum_{i=1}^n K_i (1 - e^{-\frac{t}{t_{ri}}}) \right) \tag{10}$$

$$G(t) = G_0 \left(1 - \sum_{i=1}^n G_i (1 - e^{-\frac{t}{t_{ri}}}) \right) \tag{11}$$

where G is shear modulus, K is bulk modulus, t is actual time, t_{ri} are relaxation times, G_0 and K_0 are instantaneous shear and bulk elastic moduli, respectively, and G_i and K_i are Prony series parameters.

Assuming constant Poisson’s ratio in the analysis simplifies the problem. This assumption was made in spite of the fact that Poisson’s ratio in viscoelastic materials is generally time dependent. The time-dependent Poisson’s ratio of viscoelastic materials can increase or decrease depending on the bulk and shear relaxation with time [17]. However, because the modeling of blister in this study was assumed to remain in the small strain regime, this simplification was considered acceptable. A time-independent Poisson’s ratio of 0.35 was assumed for MA, and introduced in Eqs 12 and 13 to relate time-dependent relaxation modulus to the time-dependent bulk and shear relaxation modulus

TABLE 3—Prony series parameters at reference temperature 5 °C.

Prony series relaxation time, s				Prony series spring constants, MPa			
tr_1	tr_2	tr_3	tr_4	E_1	E_2	E_3	E_4
747.384	$186.358 \cdot 10^{03}$	$9.183 \cdot 10^{03}$	29.146	90.89	3.457	18.84	32.69

$$K(t) = \frac{E(t)}{3(1 - 2\nu)} \tag{12}$$

$$G(t) = \frac{E(t)}{2(1 + \nu)} \tag{13}$$

As shown in Fig. 5(b), the power function of the relaxation modules was used for determining the parameters of the Prony series for the generalized Maxwell model by curve fitting. Because the master curve is constructed for the reference temperature of 5 °C, the Prony series parameters represent the time-dependent shear and volumetric behavior of the material at this particular temperature. The Prony series parameters for 25 °C are determined by shifting the creep compliance data to the reference temperature of 25 °C and by applying a similar procedure as mentioned above. Table 4 lists the Prony series parameters at 5 °C.

Closed-Form Solution for Viscoelastic Creep

In any solid body subjected to external loading or displacement, the resulting stress and strain must simultaneously satisfy three basic equations: the equilibrium equations, the kinematic equations, and the constitutive equations. Viscoelastic stress analysis problems are more difficult to solve than elasticity problems because time dependency requires the solution of the differential equations of the constitutive law. If the boundary conditions and the temperature remain invariable, the time variable in the equations can be removed by transforming the equation into the Laplace transform domain as shown earlier.

In this section, the elastic solution shown in Eq 1 is used to determine the deflection of the thick plate. As shown below, for constant Poisson’s ratio, Eq 1 is transformed to the equivalent elastic solution with the Laplace domain variable *s*

$$w_0(s) = \frac{3(1 - \nu^2)}{16sE(s)h^3} p(s)(R^2 - r^2)^2 + \frac{p(s)R^2(1 + \nu)}{2sE(s)Sh} \left(1 - \left(\frac{r}{R}\right)^2\right) \tag{14}$$

Rearranging the above expression with Eq 6 results in the following relation

$$w_0(s) = \left(\frac{3(1 - \nu^2)}{16h^3}(R^2 - r^2)^2 + \frac{R^2(1 + \nu)}{2Sh} \left(1 - \left(\frac{r}{R}\right)^2\right)\right) p(s)sD(s) \tag{15}$$

TABLE 4—Shear and bulk relaxation modulus Prony series parameters at 5 °C used for modeling.

Instantaneous modulus, MPa	<i>N</i>	<i>G_i</i> , MPa	<i>K_i</i> , MPa	<i>t_{ri}</i> , s
79.81	1	1.605	4.757	10
	2	42.09	39.92	44.62
	3	29.21	82.91	200.60
	4	6.598	20.54	26874.5

To make the conversion back from the Laplace domain to the time domain, Maple software (Maplesoft, Adept Scientific Nordic, DK-2600 Glostrup, Produktionsvej 26, Sweden) is used. The shear relaxation modulus, the corresponding relaxation times and the Poisson's ratio are used and converted into the creep equation, Eq 16. The parameters of Eq 16 are shown in Table 5. The vertical deflection of the thick plate is calculated based on the analytic Eq 17

$$D(t) = D_o + \sum_{i=1}^N D_i(1 - e^{-\frac{t}{t_{ri}}}) \quad (16)$$

$$w_o(t) = \left(\frac{(3(1 - \nu^2))}{16h^3} (R^2 - r^2)^2 + \frac{R^2(1 + \nu)}{2Sh} \left(1 - \left(\frac{r}{R} \right)^2 \right) \right) p_o D(t) \quad (17)$$

where w_o is vertical deflection of the thick plate (mm).

Temperature and Pressure Influence in Blister Growth

The thermal environmental conditions have significant impact on stability and long-term performance of a pavement during its life span. Daily temperature variations influence the deformation of asphalt pavement significantly. A linear viscoelastic 3D finite-element model is more realistic than a linear elastic model because it considers time-dependent behavior of the MA and temperature effects on material property. The 3D finite-element simulation will therefore be used to study blister growth (vertical deflection) of a MA pavement plate subjected to diurnal heating and cooling temperature fluctuation. During daytime of sunny days, heat energy transfer by interaction between pavement and its surroundings exists. This interaction consists of the radiation balance and exchange by convection which comprises solar radiation, thermal radiation heat flux and convection heat flux at the pavement surfaces or at the bottom of the bridge deck [20].

The 3D finite-element model in this study was developed based on the following assumption. The bridge deck pavement lies directly on the bridge deck, i.e., no PBM sheet is applied, the radius of the blister will remain constant, which prohibits horizontal blister growth, i.e., the adhesion between the MA and concrete (rigid substrate) has sufficient strength to prevent debonding. The pavement is idealized as thick plate. The MA is considered to be homogenous, isotropic and linear viscoelastic. The asphalt pavement's temperature

TABLE 5—Prony series parameters at reference temperature 5 °C.

D_o , MPa	N	D_i , MPa	t_{ri} , s
0.02729318695	1	$5.68528967271 \cdot 10^{-03}$	317.5685434
	2	$29.35788435 \cdot 10^{-03}$	10.52481012
	3	$0.1712212104 \cdot 10^{-03}$	19.48316577
	4	$29.592292201577 \cdot 10^{-03}$	1.935661701

fluctuation is the same in the whole cross section of the pavement. The pressure build up inside the blister is only caused by gas pressure; vapor pressure and off-gassing pressures are not considered. The blister cavity is assumed to be closed; therefore, there is no exchange of gas between inside and outside of the blister. The analysis assumes constant Poisson's ratio.

C3D20R Elements were used and one single layer was used to model the blister. Linear quasi-static analysis was used to model time-dependent material response, such as creep and recovery. *ABAQUS* allows controlling time incrementation automatically or directly by specifying the time. As long as the output results of the simulation are compared with closed form solution, the fixed-time incrementation of 0.8 s was applied in the analysis. The pressure load applied in this model was estimated from ideal gas law equation, Eq 18

$$\frac{p_1 V_1}{T_1} = \frac{p_2 V_2}{T_2} \quad (18)$$

Where p_1 and p_2 are initial pressure (0.1 MPa at 273.15 K) and the required pressure, respectively, V_1 and V_2 are initial volume and final volume of the blister, respectively, and T_1 and T_2 are initial temperature (273.15 K) and final temperature, respectively.

It was assumed that the initial volume is equal to 268.083 mm³ (which corresponds to radius of 800 mm and blister height $1 \cdot 10^{-04}$ mm) and the final volume is $4.02 \cdot 10^{06}$ mm³ (for radius of 800 mm and blister height 1.5 mm). The pressures at 5 °C and 25 °C are calculated based on the input variables described in Eq 18.

The thick-plate modeling consisted of 80-mm-thick asphalt layer with a constant blister radius of 800 mm. Hence, the ratio of the width to height was 1/10, identical to that of the laboratory-produced blister.

To assess blister growth for 12 h (1/2 day) under uniformly applied pressure, an initial temperature of 15 °C was selected at start of the analysis and the temperature of the MA was assumed to increase linearly up to 25 °C at different rates, as shown in Fig. 7(a). In addition, it was assumed that the temperature inside the blister was rising simultaneously as in the asphalt layer. In this way, gas pressure in the blister corresponded directly to the temperature history as shown in Fig. 7(b).

Moreover, actual temperature measurements on and within the blister, as reported in Ref 21, are shown in Fig. 8(a). The temperature inside the blister was measured by putting a temperature probe in the MA, whereas the temperature on the surface was measured by fixing the temperature probe using a transparent tape. Because the surface temperature was exposed to air convection it appeared that, the highest temperature was measured inside the blister. These temperature measurements were considered as basis to assess the significance of the daily temperature and pressure variations on the blister growth for one week, a history with repeated temperature and pressure cycles was investigated. For simplicity it was assumed that one cycle consisted of a linear increase within 12 h and a linear decrease within the following 12 h, as shown in Fig. 8(b). As indicated in the Data Reduction section above, the IDT test is conducted and a master curve for the temperature range between 5 °C to 25 °C is determined. Because the MA property is determined for the above specified

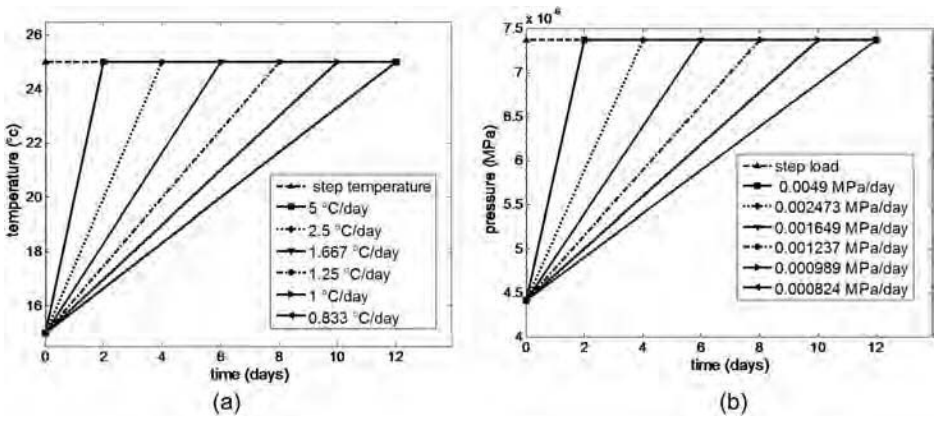


FIG. 7—(a) Temperature history, and (b) pressure history for different rate (1/2 day).

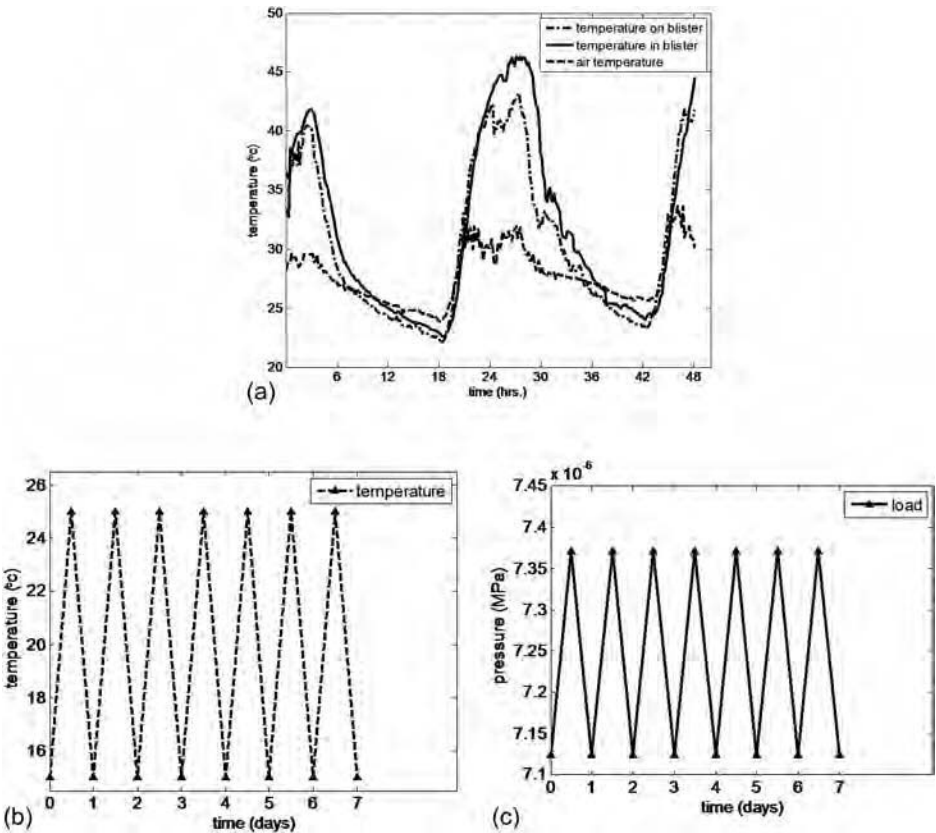


FIG. 8—(a) Temperature measurement in a blister on a bridge deck [21] as compared to idealized (b) temperature, and (c) pressure history (one week) assumed for this study.

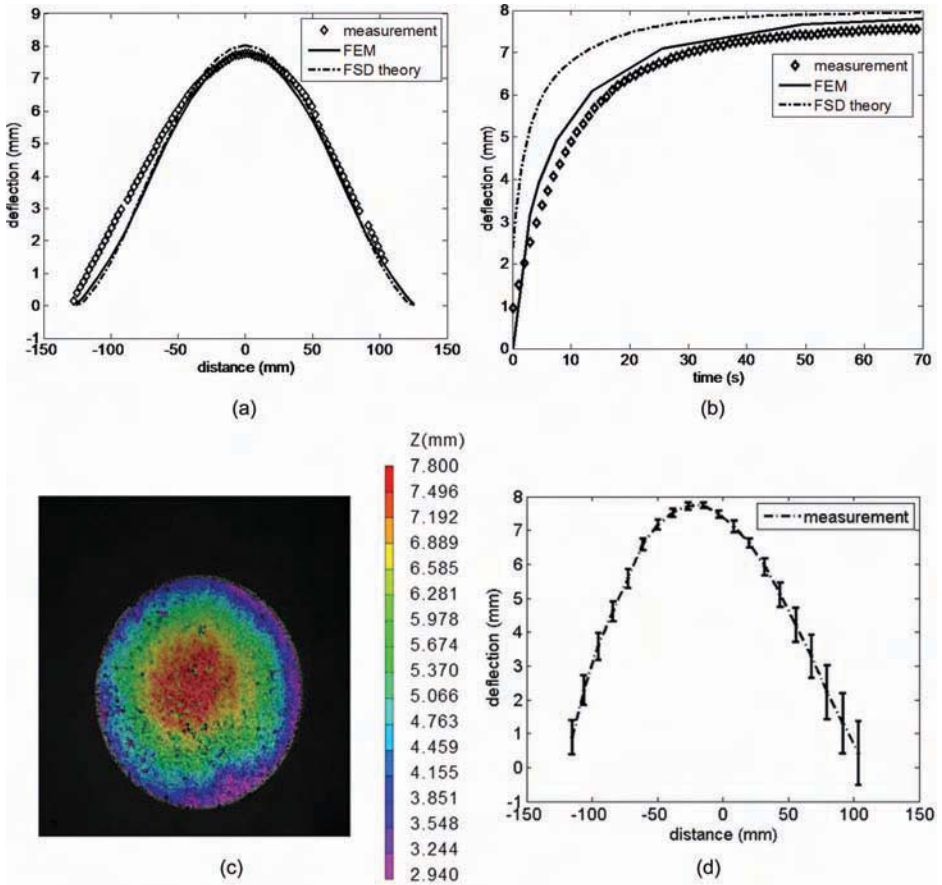


FIG. 9—Comparison of MA plates with finite element method (FEM) simulation, first-order shear deformation (FSD) plate theory and measurement from image correlation; (a) vertical deflection profile, (b) max vertical deflection as a function of time, (c) image correlation 2D plot of vertical deflection after 70 s of measurement, and (d) vertical deflection with standard deviation.

temperature, the temperature in the finite-element simulation was assumed to vary moderately between 15 °C and 25 °C. The corresponding pressure history was defined using Eq 18, in a similar way varying from $7.12 \cdot 10^{-06}$ MPa to $7.37 \cdot 10^{-06}$ MPa within one day. This frequency of temperature variation was chosen based on earlier experience [21] in a different case as shown in Fig. 8(b).

Results and Discussion

Three samples of MA were tested as described in the Test Development section above and the average deflection found from the 3D digital image correlation software profile measurement was compared with the finite-element simulation and the

analytic solution as shown in Figs. 9(a) and 9(b). The standard deviation in Fig. 9(d) was calculated from the image correlation measurement by taking different sections on two-dimensional (2D) vertical deflection contour plot shown in Fig. 9(c).

The blister growth estimated with the viscoelastic model produced different deflections depending on the pressure and temperature rate. The pressure and temperature histories from Fig. 7 resulted in vertical deflections shown in Fig. 10(a). The step-function temperature and pressure produced higher vertical deflection (1.7332 mm) compared to other types of temperature and pressure histories. The minimum vertical deflection was 1.0304 mm.

To assess only the effect of temperature increase in the MA, the temperature histories shown in Fig. 7(a) were applied while keeping the pressure ($7.37 \cdot 10^{-06}$ MPa) in the blister constant for 12 h. The result in Fig. 10(b) indicates that temperature increasing rate has significant effect on the deflection of the plate. The entire deflection in the MA was almost completely caused by change in temperature. The deflections found from temperature variation were similar to those from simultaneous temperature and pressure variation as shown in Fig. 10(b). The maximum deflection was 1.7332 mm for temperature and pressure step function and the minimum deflection of 1.0380 mm was produced by the slowest temperature and pressure rate.

Moreover, the results shown in Fig. 11(a) is found when the temperature was constant throughout the thickness (25 °C) and a linearly varying load history shown in Fig. 7(b) was applied. This result shows that the rate at which the pressure increases has no significant influence on the vertical deflection of the MA. The deflection found from pressure variation is clearly different to the deflection from simultaneous variation of temperature and pressure as shown in Fig. 11(b). The maximum vertical deflection obtained was 1.7332 mm and the minimum vertical deflection was 1.7148 mm.

In Fig. 12 the vertical deflection from pressure and temperature fluctuation in one week is presented. The highest deflection of 1.2877 mm was found for repeated simultaneously varied temperature and pressure. In case of fluctuating temperature and constant pressure ($7.124 \cdot 10^{-06}$ MPa corresponding to a temperature of 15 °C), a vertical deflection of 1.2228 mm was found. Pressure fluctuation had no significant influence, as shown previously, and results in the lowest deflection of 0.02521 mm. Moreover, Fig. 12 clearly shows that, repeated temperature and pressure cycles may well produce continuous blister growth. The blister growth tends to slow down when more cycles are applied. This corresponds to observations in practice as shown Fig. 6(a).

Conclusion

The time-dependent vertical deflection in MA blisters depends on three factors: material characterization of the model, temperature of the MA at the time of loading, and the rate at which the load is applied to the material. It was found that vertical deflection of MA is much more depending on the rate of the applied temperature than on the applied pressure. The 12-h simulation showed that, slower applied uniformly distributed pressure and temperature produces smaller vertical deflection.

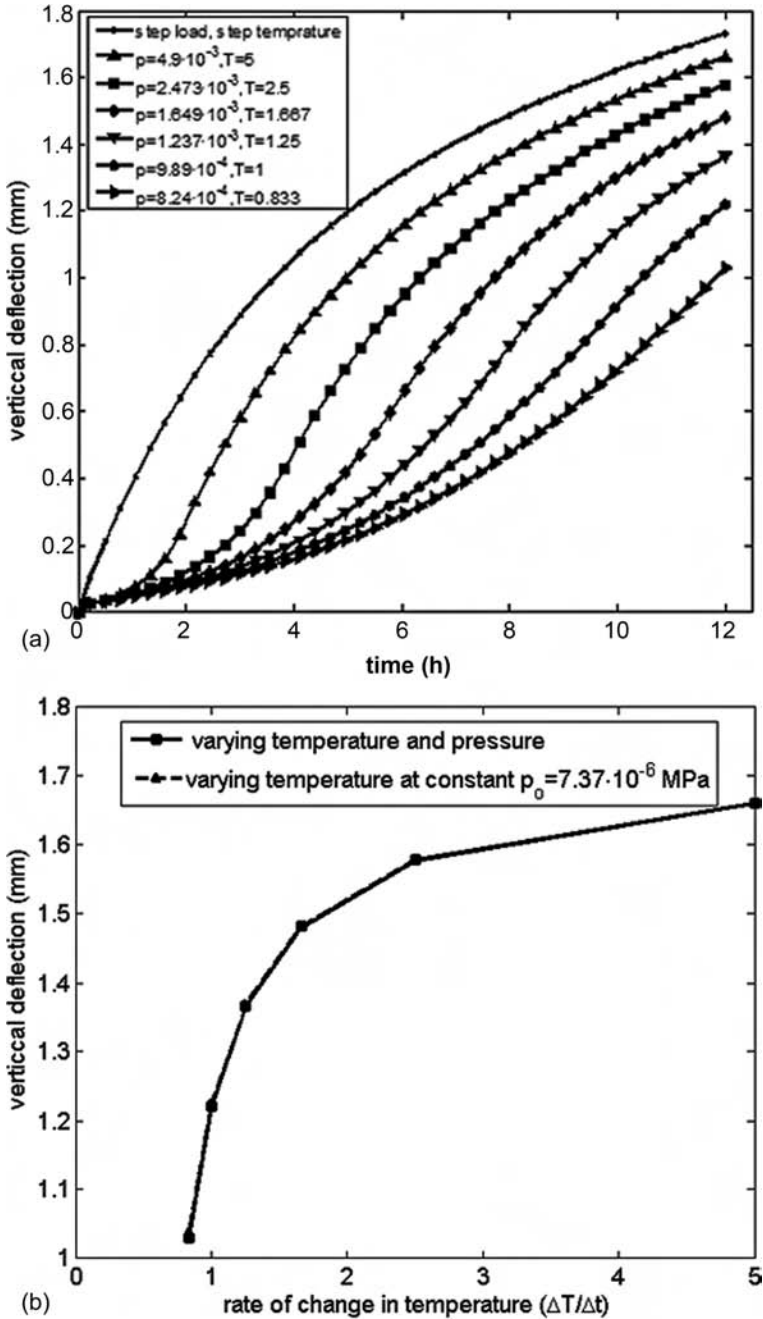


FIG. 10—(a) Vertical deflection at the center of the plate when both temperature (T , °C/day) and pressure (P , MPa/day) rate are involved (12h), and (b) rate of change in temperature versus vertical deflections at the center of the plate.

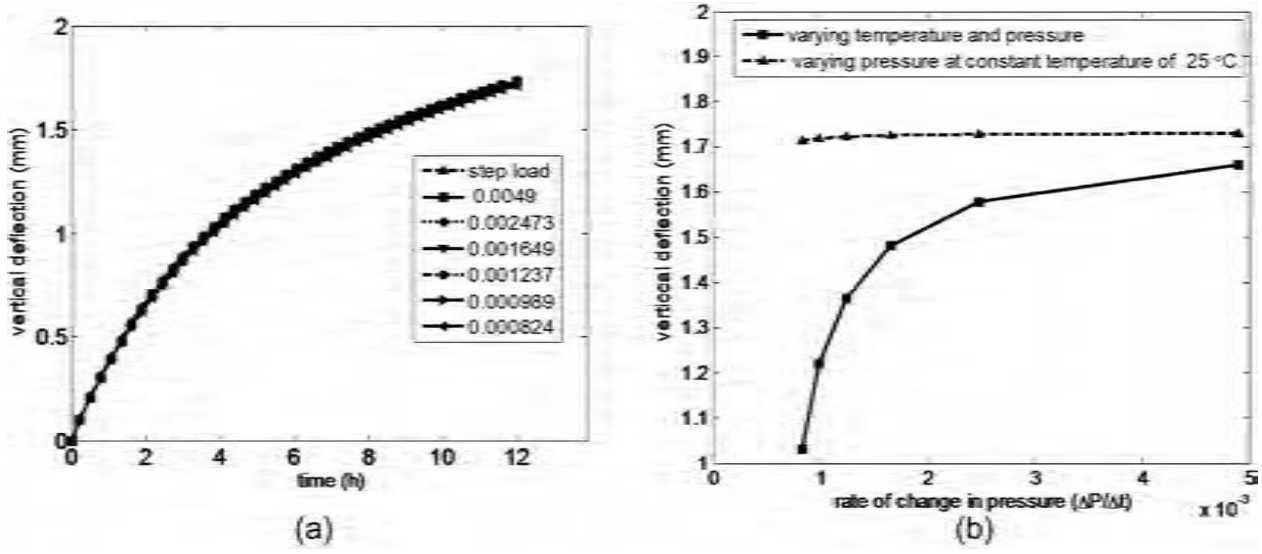


FIG. 11—(a) Vertical deflection at the center of the plate for different pressure rates (MPa/day) at constant temperature of 25 °C (12 h), and (b) rate of change in pressure versus vertical deflections at the center of the plate.

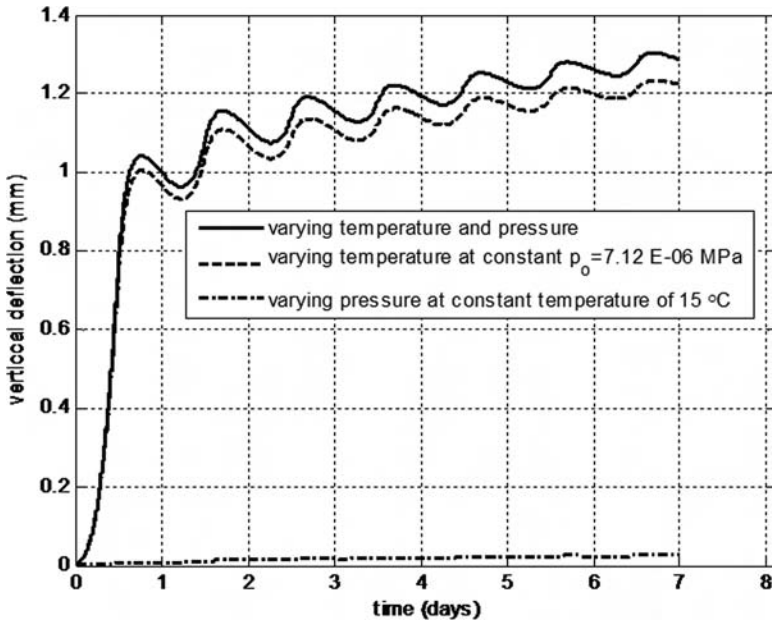


FIG. 12—Vertical deflection at the center of the plate for repeated temperature and pressure cycles for 7 days (cycles of linear increment with 12 h and a linear decrement within the following 12 h).

For constant pressure ($p_0 = 7.12 \cdot 10^{-06}$ MPa) and fluctuating temperature, the temperature dependency of the material had a great influence on the vertical deflection of the blister. This indicates that constant gas pressure inside the blister can produce significant amount of blister growth with increasing temperature.

On the other hand, for constant temperature ($T = 25^\circ\text{C}$) and fluctuating pressure, as shown in Fig. 11(b), the blister growth is much less than in the previous case. This is because of the fact that the MA has enough stiffness to resist pressure changes. In fact, deflection would even be less if the weight of the MA was incorporated in the simulation.

Finally, from simulation of the consecutive cycles of heating and cooling, it was noticed that the daily temperature variations have a significant influence on asphalt-pavement deflection. During the unloading process, i.e., when pressure and temperature decrease, the blister still grows at a slower rate. The simulation indicates that the blister can grow continuously under repeated loading conditions over subsequent days.

References

- [1] EN 13108-6, 2008, "Bitumenious Mixtures-Material Specification- Part 6: Mastic Asphalt," *European Standard*, VSS, Zurich.

- [2] Partl, M. N. and Hean, S., "Practical Aspects of Interaction Between Mastic Asphalt and Waterproofing System in Bridge and Tunnel Construction," *Proceedings of the Fourth European Symposium on Performance of Bituminous and Hydraulic Materials in Pavements*, Nottingham, United Kingdom, 11 and 12 April, 2002, Balkema, Lisse, The Netherlands, 2002, pp. 58–61.
- [3] Partl, M. N., *Deterioration Mechanisms in Polymer-Modified Bitumen's Water Proofing Membranes Sheets During Torching*, Swiss Federal Laboratories for Material Science and Technology, Duebendorf, Switzerland, 2004, pp. 12–16.
- [4] Rosenberg, J., 2000, "Thin Pavements with Synthetic Binder Used in Denmark," Asphalt De Danish Road Institute, pp. 5–9.
- [5] Croll, J. G. A., *Thermal Buckling of Pavement Slabs*, The Institution of Civil Engineers, London, 2005, Vol. 158, pp. 115–126.
- [6] Alison, M., Robert, B., and Ralph, P., "Blistering in Build-up Roofs: A Review," *The Fourth International Symposium on Roofing Technology*, Gaithersburg, MD, Sept. 17–19, 1999, National Roofing Contractors Association, Rosemont, IL, 1999.
- [7] *Abaqus 6.9 User Documentation Collection, version 6.9.1*, Dessault Systems, 2009.
- [8] Timoshenko, S. and Woinowsky-Krieger, S., *Theory of Plates and Shells*, second ed., McGraw-Hill, New York, 1959, pp. 51–78.
- [9] Reddy, J. N., *Shear Deformable Beams and Plates*, first ed, Elsevier, New York, 2000, pp. 11–37.
- [10] Fini, E. H., Al-Qadi, I. L., Masson, J. F., and McGhee, K. K., 2001, "Interfacial Fracture Energy: An Indicator of the Adhesion of Bituminous Material Adhesion," *Electron. J. Assoc. Asph. Paving Technol.*, Vol. 77, pp. 827–850.
- [11] Michalski, C., "Modellvorstellung Zur Deutung Des Blasewachstums Im Gussasphalt Und Anderen Thermoviskosen Stoffen Fur Den Strassenbau," *Mitteilungen aus dem Fachgebiet Konstruktiver Strassenbau im Institut für Verkehrswirtschaft, Straßenwesen und Städtebau der Universität Hannover*, Alexander, G., Ed., Institut für Verkehrswirtschaft Straßenwesen und Städtebau der Universität Hannover, Appelstr. 9A, D-3000 Hannover, 1992.
- [12] Rogosch, N., "Zur Blasenbildung in Thermoviskosen Stoffen Unter Berücksichtigung Rheologischer Materialkennwerte Und Geometrischer Randbedingungen," *Mitteilungen aus dem Fachgebiet Konstruktiver Strassenbau im Institut für Verkehrswirtschaft, Straßenwesen und Städtebau der Universität Hannover*, Alexander, G., Ed., Institut für Verkehrswirtschaft Straßenwesen und Städtebau der Universität Hannover, Appelstr. 9A, D-3000 Hannover, 1994.
- [13] Galliot, C. and Luchsinger, R. H., 2011, "Uniaxial and Biaxial Mechanical Properties of ETFE Foils," *Polym. Test.*, Vol. 30, pp. 356–365.
- [14] Di Benedetto, H. D., Partl, M. N., Franken, L., and De La Roche, C., 2001, "Stiffness Testing for Bituminous Mixtures," *RILEM TC 182-PEB Performance Testing and Evaluation of Bituminous Materials*, 2001, pp. 66–70.
- [15] Christensen, D. W. and Bonaquist, R. F., 2004, "Evaluation of Indirect Tensile Test Procedures for Low-Temperature Performance of Hot Mix Asphalt," *National Cooperative Highway Research Program*, Report No. 530, Eileen, P. D. and Eileen, M. C., Eds., Transportation Research Board of the National Academies, Washington, D.C, 2004, pp. 11–15.
- [16] Huang, Y. H., *Pavement Analysis and Design*, second ed, Pearson Education, Upper Saddle River, NJ, 1993, pp. 328–329.
- [17] Tschoegl, N. W., Wolfgang, G. K., and Igor, E., "Poisson's Ratio in Linear Viscoelasticity: A Critical Review," *Mechanics of Time-Dependent Materials*, Kluwer Academic, New York, 2002, Vol. 6, pp. 3–51.
- [18] Witczak, M. W., "Modification and Re-Calibration Superpave Thermal Cracking Model," *Final Document to Transportation Research Board*, Reynaldo, R., Dennis,

- R. H., and William, G. B., Eds., Arizona State University, Mesa, AZ, 2000, pp. 80–97.
- [19] Findlay, W. N., James, S. L., and Onaran, K., *Creep and Relaxation of Nonlinear Viscoelastic Materials*, second ed, Dover, Mineola, NY, 1976, pp. 50–130.
- [20] Shaopeng, W., Hong, W., and Mingyu, C., 2009, “Analysis of High Temperature Fluctuations on Asphalt Pavement of Cement Concrete Bridge,” *J. Test. Eval.*, Vol. 37, pp. 1–4.
- [21] Partl, M. N., Remy, G., and Hean, S., “Belagsschäden Infolge Blasenbildung Auf Einer Neuen Hängebrücke in Hongkong,” *Nachhaltige Material-und Systemtechnik*, Walter, M. and Kurt, S., eds., Swiss Federal Laboratories for Material Science and Technology, Dubendorf und St. Gallen, Switzerland, 2001.

*P. Vandereecken*¹ and *I. Maton*¹

Ways of Improving the Interfacial Durability of Silicone Adhesives in Building Applications

ABSTRACT: Beyond their application as sealants, silicone formulations are used as adhesives in insulated glass and structural glazing applications. The adhesion durability of such assemblies is a function of both the adhesion at the glass-interface surfaces and the internal cohesion of the adhesive. Failure in the bulk of the adhesive will occur if external stresses exceed the ultimate strength of the adhesive or when the movement capability of the adhesive is lower than required by the application. The most often observed reasons for failure are, however, substrate-adhesive interface ruptures. If similar silicone adhesives are used in different building projects, the substrates can vary widely, leading to many different interfaces. Interface adhesion can be improved by modifying the substrate surface, modifying the adhesive formulation, or using a primer. In this work, improved adhesion durability on different substrates will be shown with an improved version of a two-part silicone adhesive used for insulated glass and structural glazing applications, which was introduced in Europe in 2010. Results without primer and with the use of either a wet primer or a dry SiO_x (Pyrosil[®]) flame treatment will be shown. Adhesion durability after water immersion, UV irradiation, and high humidity will be reported for new low E insulated glass coatings, powder coated aluminum, stainless steel, and some other standard building substrates.

KEYWORDS: adhesion, durability, primers, silicones

Manuscript received May 18, 2011; accepted for publication June 22, 2011; published online July 2011.

¹Dow Corning Europe sa, 7180 Seneffe, Belgium.

Fourth Symposium on Durability of Building and Construction Sealants and Adhesives on 16 June 2011 in Anaheim, CA.

Cite as: Vandereecken, P. and Maton, I., "Ways of Improving the Interfacial Durability of Silicone Adhesives in Building Applications," *J. ASTM Intl.*, Vol. 8, No. 8. doi:10.1520/JAI103960.

Copyright © 2011 by ASTM International, 100 Barr Harbor Drive, PO Box C700, West Conshohocken, PA 19428-2959.

Introduction

In the last two decades, mankind became increasingly aware of the scarcity of earth resources and the necessity to reduce their carbon footprint. Amongst the different sectors, the building sector is one of the most important carbon emitters and most of the energy is used to satisfy the heating demands of those buildings. To reduce building energy consumption by more than 80 %, architects have improved insulation of walls and windows, reduced air leakage, and eliminate thermal bridges. Sealants and foams are widely used to improve the building air tightness, whereas silicone adhesives used for structural glazing can be used to prevent thermal bridges due to their low thermal conductivity [1].

It has been demonstrated that very low-energy consumption buildings can be fabricated (sometimes also called passive houses), however, people need to ensure that excellent air tightness and insulation is maintained during the lifetime of the building, which is currently expected to be at least 50 years, but often up to 100 years.

In the building industry, silicones are used as sealants to air-tighten buildings and as adhesives to structurally bond glass to facades (Fig. 1) or maintain the insulated glass integrity (Fig. 2). Those sealants or adhesives are subject to numerous different environmental stresses. When bonding two substrates with different coefficients of thermal expansions, thermal elongations are induced by temperature changes between day and night or summer and winter. Constant



FIG. 1—Skyscraper – structural glazing with insulating glass.

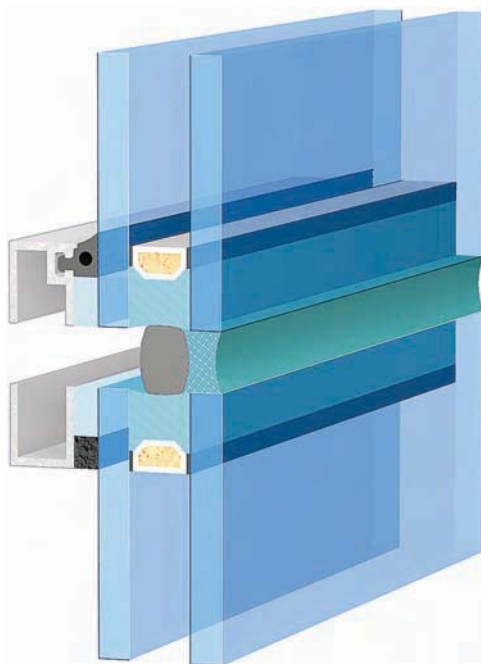


FIG. 2—Structural glazing application.

deformation in a sealant can also occur due to earth movements or building settlement. Furthermore, when the sealant is applied outdoors, those stresses are combined with exposure to rain, ozone, and sunlight. Due to their high Si-O energy bond, silicone sealants are especially suited for outdoor applications (Fig. 3). The durability of a sealant/adhesive is a function of both the adhesion at the sealant-substrate interfaces and the internal cohesion of the sealant. Failure in the bulk of the sealant will occur if external stresses exceed the ultimate strength of the adhesive or when movement capability of the adhesive is lower than required by the application. It has already been shown [2] that, due to their excellent elastic recovery, silicone sealants outperform organic sealants when subject to combined cyclic movements and exposure to UV/humidity.

The most often observed reasons for failure are, however, substrate-sealant interface ruptures. If similar silicone sealants or adhesives are used in different building projects, the substrates can vary widely, leading to many different interfaces. When adhesion does not occur on certain substrates the adhesive/sealant formulation needs to be improved, the substrate surface needs to be modified (using plasma treatment, for instance), or primers can be used.

In this work, adhesion durability on different substrates used in glazing applications is evaluated, comparing 2K silicone adhesives used for insulated glass (DC 3362) and structural glazing applications (DC 993) with a formulation which was optimized (DC opt) for adhesion build-up. The effect of the application of a wet primer (1200 OS Primer Clear, Dow Corning [3]) or a dry primer



FIG. 3—Silicone versus organic sealant after 5000 h QUV exposure.

(Pyrosil[®], Bohle AG [4]) was also evaluated. This study concentrated on adhesion on low E glasses (soft coatings on face 2) which is a key contributor for improved glass energy efficiency. Different substrates used for the structural bonding of glass in glass facades or in solar thermal panel applications were also evaluated.

The wet primer was applied with a brush as a thin film. The dry primer (Pyrosil[®]) was applied from a small hand burner (Fig. 4), which applies a thin



FIG. 4—Application of Pyrosil[®].

SiO_x layer on the surface, which is obtained by atmospheric pressure combustion chemical vapor deposition of a silane/gas mixture [5].

Adhesion Buildup

Fast adhesion buildup is an important property, since this will define the ability of the adhesive to be rapidly functional after application. For insulated glasses, for instance, manipulation of the insulated glass takes place directly after application and transportation often occurs within the first 24 h. Internal stresses due to temperature increase when stored in uncontrolled environments or during transportation within the first 24 h can also lead to pre-mature failure or weaknesses in interface adhesion which will affect the adhesion durability.

Tables 1 and 2 compare 180° peel adhesion (ASTM C974-2010 “Standard Test Method for Adhesion-in-Peel of Elastomeric Joint Sealants”) [6] on different substrates used in glass assemblies; the peel strength was not measured but only the percentage of cohesive failure (% CF). When the result is denoted as CF, the failure is more than 90 % CF; when it is denoted as AF, the failure is more than 90 % AF. Mixed failures would be denoted as CF/AF. Such tests can easily be used on-site for a rapid qualitative evaluation of adhesion build-up. The substrates used are: float glass (Float), coated glass (Low E), anodized aluminum (AA), aluminum mill finish (AMF), powder coated anodized aluminum (PCAA), stainless steel (SS) and galvanized steel (GS). It is well-known that the surface nature of the different substrates can vary depending on their origin but the aim of this work was to evaluate the effect of the adhesive and primer on standard substrates used in the building industry and therefore cohesive failure

TABLE 1—Peel adhesion tests on substrates used in the building industry.

Condition	Product/Surface Treatment	Float	Low E	AA	AMF	PCAA	SS	GS
1 day cure	DC 993	CF	AF	CF	AF	AF	CF	AF
	DC opt	CF	CF	CF	CF	CF	CF	CF
	DC 993 + 1200 OS	CF	CF	CF	CF	CF	CF	CF
	DC 993 + Pyrosil	CF	CF	CF	CF	CF	CF	CF
1 day cure + 1 h WI	DC 993	CF	AF	CF	AF	AF	AF	AF
	DC opt	CF	CF	CF	CF	CF	CF	CF
	DC 993 + 1200 OS	CF	CF	CF	CF	CF	CF	CF
	DC 993 + Pyrosil	CF	CF	CF	CF	CF	CF	CF
3 day cure + 1 week WI	DC 993	CF	CF	CF	CF	CF	CF	CF
	DC opt	CF	CF	CF	CF	CF	CF	CF
	DC 993 + 1200 OS	CF	CF	CF	CF	CF	CF	CF
	DC 993 + Pyrosil	CF	CF	CF	CF	CF	CF	CF

TABLE 2—Peel adhesion tests on substrates for solar thermal applications.

Substrate	Treatment	1 Day Cure	1 Day + 1 Week WI (23 °C)	1 Day + 1 Week WI (55 °C)
AMF	None	AF	AF	AF
	1200 OS	CF	CF	CF
	Pyrosil	CF	CF	CF
AA	None	CF	CF	CF
	1200 OS	CF	CF	CF
	Pyrosil	CF	CF	CF
PCAA	None	CF	AF	AF
	1200 OS	CF	CF	CF
	Pyrosil	CF	CF	CF

on anodized aluminum, for instance, does not guarantee cohesive failure for all anodized aluminums on the market.

For Table 1, peel adhesions are given after a 1 day cure, a 1 day cure followed by 1 h 23°C water immersion, and a 3 day cure at room temperature followed by 1 week immersion in 55°C water. For all tests under water immersion (WI), peeling is performed directly after water immersion. For Table 2, peel adhesions are measured after a 1 day cure followed by one week water immersion, either at 23°C or 55°C. In Table 2, substrates used in the solar thermal industry were tested: those are similar substrates to the ones used in the building industry (AMF, AA, PCAA) but their manufacturing origin differs.

Both Tables 1 and 2 show that adhesion buildup can be improved either by the use of a primer (dry or wet) or by modifying the product formulation. This adhesion survives 1 week of water immersion.

Table 3 evaluates the capability of the sealant/adhesive to maintain a glass-to-glass assembly (H-bar) under a 0.45 MPa constant stress applied for 10 min with the lower glass immersed in water. The adhesive thickness is 12 mm and the adhesive surface is 12 mm × 20 mm. This test is sometimes used in the insulated glass industry since those assemblies can be submitted to high stresses rapidly after production due to pressure buildup in the assembly with an increase in temperature. In the case of “soft” low E coatings, edge deletion is

TABLE 3—Adhesion on low E coated glass.

Coating	Sealant	Priming	Time to Failure (min)
Standard	DC 3362	None	<2
	DC 3362	1200 OS	>10
	DC 3362	Pyrosil	>10
	DC opt	None	2–10
New	DC opt	None	>10

usually required before sealant application to avoid glass corrosion to take place in the long term [7]. Glass corrosion is due to the sensitivity of the low E coating towards hydrolysis. However, edge deletion often does not lead to the complete removal of the coating and adhesion is often also required on the coated layer. DC 3362 is a two component sealant used for insulated glass. Two low E coatings were evaluated: a standard low E (Standard) coating and a newly developed coating (New) with a lower sensitivity towards hydrolysis. With the standard coating, the optimized formulation did not pass this severe test, however, fast and strong adhesion buildup was obtained when using both the wet or the dry primers. The optimized formulation did, however, lead to good results with the new low E coating.

Adhesion Durability

In this section, adhesion durability is evaluated using accelerated ageing conditions under static load conditions; in other words, no stress is applied during the ageing, but only while testing at the end of the ageing period. It is, however, known that in the real world, ageing usually occurs under stress and tests have been performed which are evidence of the higher severity of tests using alternate cycles of stresses and ageing [8].

Adhesion on Low E Coated Glass

Table 4 reports tensile strengths measured after different ageing cycles for 12 mm × 12 mm × 50 mm glass/glass H-bars. The glass is a low E coated glass (with low sensitivity to hydrolysis), as such or edge deleted. Two primers were also evaluated: 1200 OS Primer Clear (wet primer) and Pyrosil[®] (dry primer).

All results showed 100 % cohesive failure with little impact on the tensile strength, which indicates excellent adhesion durability. Usually, 6 weeks of water immersion at 45°C are required in the European technical agreement for sealants used in structural glazing [9], however, up to 7 weeks of water immersion in 55°C water were successfully tested in this study, however, with some softening of the sealant (lower modulus and hardness). The use of primers and/or edge deletion did not affect the results.

Adhesion on Substrates Used in the Building Industry

In this section, adhesion durability under severe conditions (immersion in 80°C water) of two-component tin catalyzed sealants (DC 993 and DC opt) and a one-part titanate catalyzed sealant (DC 895) are compared. Pyrosil[®] treatment was used as a dry primer.

The peel adhesion tests are shown in Table 5.

Despite the improvement in the adhesion build up by the use of a primer (Pyrosil[®]) or by the use of the adhesive formulation optimized for adhesion build up (DC opt), this improvement is not confirmed after immersion in hot

TABLE 4—Tensile strength after accelerated ageing with low E coated glass (*: glass breakage).

Tensile Strength	Coated No Primer (MPa)	Edge Del. No Primer (MPa)	Coated 1200 OS (MPa)	Coated Pyrosil (MPa)	Edge Del. Pyrosil (MPa)
1 week RT	0.94	>0.70*	0.87	1.00	1.02
3 week WI (55°C)	>0.65*	0.75	>0.67*	0.84	...
7 week WI (55°C)	0.58	0.60	0.60	0.68	0.56
6 week WI (45°C)	0.77	0.89	0.84	0.89	0.84
1000 h 85°C/85 % RH	0.79	0.85	0.82	0.95	0.94
2000 h 85°C/85 % RH	0.93	0.91	0.90	0.85	0.84
1000 h QUV ^a	0.93	>0.60*	>0.90*	>0.70*	>0.50*
2500 h QUV ^a	0.87	...	0.83
5000 h QUV ^a	0.94	0.89	0.80	0.79	0.98

^aFor the QUV accelerated ageing, a QUV accelerated weathering tester was used with UVA-340nm lamps; the weathering cycle used was 4 hours irradiation at 340nm and 60°C followed by 4 hours condensation.

water, indicating that the benefit of the primer is more for the adhesion buildup than for the durability.

Tensile strengths and percentage of cohesive failure (% CF) for mixed glass-anodized aluminum H-bars (12 mm × 12 mm × 50 mm) are given in Table 6. The results confirm the severity of the test in 80°C water since the results are

TABLE 5—Peel adhesion after immersion in 80°C water.

Condition	Material	Glass	GS	AMF	SS	AA
7 day cure	DC 993	CF	AF	AF	AF	CF
	DC 993 + Pyr	CF	CF	CF	CF	CF
	DC opt	CF	CF	CF	CF	CF
	DC 895	CF	CF	AF	CF	CF
	DC 895 + Pyr	CF	CF	CF	CF	CF
2 week 80°C	DC 993	CF	CF	CF	AF	CF
	DC 993 + Pyr	CF	CF	CF	AF	CF
	DC opt	AF	AF	CF	AF	CF
	DC 895	CF	AF	CF	AF	CF
	DC 895 + Pyr	CF	CF	CF	AF	AF
4 week 80°C	DC 993	AF	CF	CF	AF	CF
	DC 993 + Pyr	AF	CF	CF	AF	CF
	DC opt	AF	AF	AF/CF	AF	AF
	DC 895	CF	AF	AF/CF	AF	AF
	DC 895 + Pyr	CF	CF	CF	AF	AF

TABLE 6—Tensile strengths of H-bars after water immersion.

Condition	Mat	Tensile MPa	%CF ^a Gl	%CF ^a Al
4 week cure RT	DC 895	1.30	95	100
	DC 895 + Pyr	1.32	90	100
	DC 993	1.10	100	100
	DC 993 + Pyr	1.00	100	100
6 week WI 45°C	DC 895	1.20	90	100
	DC 895 + Pyr	1.05	60	100
	DC 993	1.05	100	100
	DC 993 + Pyr	1.02	100	100
1 week WI 80°C	DC 895	0.77	57	95
	DC 895 + Pyr	0.80	30	100
	DC 993	0.75	98	100
	DC 993 + Pyr	0.73	67	100
2 week WI 80°C	DC 895	0.75	48	95
	DC 895+Pyr	0.77	30	100
	DC 993	0.61	0	95
	DC 993 + Pyr	0.57	0	100
3 week WI 80 °C	DC 895	0.68	33	95
	DC 895+Pyr	0.71	20	100
	DC 993	0.40	0	100
	DC 993 + Pyr	0.32	0	100

^aa 30 %CF Gl, for instance, means Glass surface shows 70% adhesive failure.

worse after one week than after 6 weeks in 45°C water. Although the titanate-catalyzed 1K sealant shows faster partial loss of adhesion on glass, some adhesion is maintained longer than observed for 2K systems. Again, no effect of the primer on the adhesion durability could be measured. In hot water immersion, adhesion on anodized aluminum seems to be much better than on glass.

Conclusion

When no adhesion occurred with a specific silicone adhesive on a specific substrate, the use of the 1200 OS Primer Clear or the dry Pyrosil[®] primers was shown to improve the speed of adhesion buildup and therefore contributed to the improvement of the adhesive behavior within the initial days after application. To a lesser extent, the use of a primer also improves adhesion durability, tested after accelerated ageing, on substrates which do not show adhesion in the absence of the primer. Most wet primers have a high volatile organic content compared to the Pyrosil[®] burner which only emits carbon dioxide as a by-product. In our study, adhesion buildup could also be improved by modifying the sealant/adhesive formulation.

However, this study was not able to demonstrate that adhesion durability could be extended by the use of a wet or a dry primer for substrate/formulation combinations which already show good adhesion buildup in the absence of a primer. For those substrate/adhesive combinations, primers show no improvement in the ultimate adhesion properties.

This study also shows that accelerated ageing under water immersion at 80°C is extremely severe when compared to more realistic conditions such as 2000 h at 85°C and 85 % relative humidity (% r.h.) or 5000 h under 340 nm irradiation (QUV).

References

- [1] Carbary, L., and Albert F., "A Thermal Modeling Comparison of Typical Curtain-wall Glazing Systems," *Glass Performance Days*, Tampere, Finland, June 1–5, 2007.
- [2] Longo, D., and Vandereecken P., "Relative Resistance of Silicone and Si-Hybrid Based Sealants to Alternating Periods of Accelerated Weathering and Thermo-Mechanical Movements," *Durability of Building and Construction Sealants and Adhesives, 3rd Volume, J. ASTM Int.*, Vol. 6, No. 2, 2010, pp. 157–164; ASTM STP1514, 2010, A. T. Wolf, ed., *Annual Book of ASTM Standards*, ASTM International, West Conshohocken, PA.
- [3] 1200 OS Primer Clear, *Dow Corning Europe sa, rue Jules Bordet 8, 7180 Seneffe, Belgium*, June 2005.
- [4] Pyrosil, Bohle AG, *Dieselstrasse 10, 42781 Haan, Germany*.
- [5] Tiller, H.-J., Schimanski, A., Grunler, B., Glock-Jager, K., Weidl, R., and Zobel B., "Deposition of SiOx (Pyrosil®) on glass surfaces – An alternative low cost process for various applications," *Glass Performance Days*, Tampere, Finland, 2005.
- [6] ASTM C794, 2010, "Standard Test Method for Adhesion-in-Peel of Elastomeric Joint Sealants," *Annual book of ASTM Standards*, ASTM International, West Conshohocken, PA.
- [7] www.cardinalcorp.com – Bulletin #CG01 05/08.
- [8] Jones, T. G., Hutchinson, A. R., and Wolf A. T., "Experimental Results Obtained With Proposed RILEM Durability Test Method for Curtain Wall Sealants," *Mater. Struct.*, Vol. 34, No. 5, 2001, pp. 332–341.
- [9] ETAG 002, 1999, "Guideline for European Technical Approval for Structural Sealant Glazing systems (SSGS), Part 1: Supported and Unsupported Systems," *EOTA, 40 avenue des Arts, 1040 Brussels, Belgium*.

Daniel N. Huff¹

Development of a Non-Destructive Evaluation Practice of Installed Weatherproofing Sealant Joints Using a Rolling Device—An Introduction to ASTM C 1736

ABSTRACT: This paper provides an overview of the development of standardized methodology to evaluate joint seal continuity, encompassed in the newly published ASTM C 1736-11, “Standard Practice for Non-Destructive Evaluation of Adhesion of Installed Weatherproofing Sealant Joints Using a Rolling Device.” This standard practice was created under the jurisdiction of ASTM Committee C 24 on Building Seals and Sealants and is the direct responsibility of Subcommittee 30 on Adhesion; it was approved July 1, 2011. Fundamental details contributing to the successful usage of this practice are examined by answering the following questions: Where exactly do the stresses produced by this procedure have an effect upon the sealant-to-substrate bond-line? How does joint geometry impact this bond-line stress? What level of stress on a bond-line provides usable information without damaging the seal?

KEYWORDS: ASTM C 1736, continuous sealant evaluation, cured, joint, non-destructive evaluation, rolling device, sealant failure in adhesion

Introduction

The development of a proposed standard practice for the “non-destructive evaluation of adhesion of installed weatherproofing sealant joints using a rolling device” has been ongoing within ASTM Subcommittee C 24.30 for several years

Manuscript received June 28, 2011; accepted for publication January 27, 2012; published online April 2012.

¹Independent Researcher, Salem, OR 97301.

Cite as: Huff, D. N., “Development of a Non-Destructive Evaluation Practice of Installed Weatherproofing Sealant Joints Using a Rolling Device—An Introduction to ASTM C 1736,” *J. ASTM Intl.*, Vol. 9, No. 4. doi:10.1520/JAI104152.

Copyright © 2012 by ASTM International, 100 Barr Harbor Drive, PO Box C700, West Conshohocken, PA 19428-2959.

and has now been published. The intent of this standard is to provide the construction industry with a field practice to facilitate the inspection of sealed joints such that the continuity of the seals can readily be determined.² A practical means with which to assess adequate sealant performance in the field and determine the degree of bonding along the joint substrate following initial installation, as well as for inspections carried out over the life of the jointing, has become of considerable interest in the construction community.

During the development of the standard, several issues emerged related to what actually occurs along the bond-line when a rolling device produces a momentary strain in the sealant; more specifically, the following question were raised:

- How might the results obtained using the proposed method be affected by variations in joint geometry?
- Will applying the “rolling” device to the joint ultimately damage the seal (i.e., are the stresses induced along the bond-line by the device non-destructive, as indicated in the standard’s title)?
- What level of stress should be imposed on the bond-line in order to produce usable information without damaging the seal?

Gaining an understanding of the basic principles that underscore the use of such devices while acquiring information on the degree of adhesion along the sealant bond-line permits the making of informed decisions with respect to use in practice. An attempt is made in this paper to answer some of the questions posed above.

It should be understood, though, that this paper is not about sealant material performance, nor is it the author’s intent to suggest any particular construction design. In this paper, a brief overview is first provided regarding the rationale for the development of this method, including a perspective on a previous standard method for assessing in-field performance, after which we discuss efforts within the ASTM Subcommittee C 24.30 to develop this new standard practice.

Rationale for Joint Seal Continuity Evaluation

It has generally been acknowledged that there is a need for sealants installed in construction jointing to perform as intended over their expected service life. However, building owners perhaps have only recently become aware of the consequences of not ensuring adequate early performance of the joint seals following their installation. As Klosowski said back in 1989, “Sealing is a minor item when the cost of a building is considered ... [Therefore] the importance of sealing and sealants is often overlooked” [1].

²“Seal continuity” as a concept, throughout this paper, refers to fully functioning weatherseals; if the sealant is not fully adhered, the weatherseal is not continuous and fails to perform. Therefore, although ASTM C 1736 is primarily a test for adhesion, as defined by its title, the intended result of the standard practice is seal continuity.

What have been the implications of Klosowski's insight? Historically, not a lot of attention has been given to the preparation of design details and the specifications for construction joint seals. In addition, methods of inspection to ensure a complete joint seal, during or after installation, have not been common in practice. Nevertheless, the fact that sealant products are an important element for ensuring the air- and water-tightness of the building envelope is understood by many expert practitioners. For example, according to Scheffler [2], "Sealants are a primary defense against water penetration and air infiltration [or ex-filtration] in building facades, and their performance is critical to the overall performance of the entire building envelope."

The consequence of failed seals in building joints is likewise understood in instances in which the envelope relies on single-stage joints to ensure watertightness. Lstiburek [3], for example, has consistently asserted that, based on decades of research, joint-sealant-dependent wall designs are dangerously vulnerable to leakage.

Work undertaken by Lacasse et al. [4] helped to confirm in 2008 that substantial amounts of water—i.e., up to several liters per minute—can indeed be transported through very small inter-facial "cracks" along the bond-lines of joints of lengths ranging between 2 mm (0.08 in.) and 16 mm (0.63 in.).

Ruggiero and Myers [5] declared that a 1 % joint seal failure rate in buildings with a single seal can produce significant leakage problems. Significant leakage is, of course, a somewhat vague term that perhaps implies sufficient leakage to cause irritation and discomfort to the people inside the building. However, forensic investigations have determined that hidden leakage can cause serious damage to structural elements, at great cost to repair. Therefore, according to many experts, when it comes to preserving infrastructure, "unseen water [leakage] is the water to worry most about."

ASTM Standard Practice ASTM C 1521 and Its Limitations

The most commonly used industry protocol for checking joint sealant adhesion has been the destructive "pull test." The procedures for properly conducting pull tests are codified in ASTM C 1521-09e [6]. In this method, a 6 in. (150 mm) section of sealant is cut away from the joint, creating a handle that is pulled to two times movement capability or to cohesive failure from both joint substrates in combination (tail procedure) or singly (flap procedure). The average recommended frequency is once every 1000 linear feet (305 m).³ This practice has been used for decades by sealant manufacturers to verify the *adhesive performance* of their product(s) in the field.

³ASTMC 1521-09e: "7.4.1 The frequency of the testing depends upon the reasons for performing the test procedures; 7.4.4 Destructive Procedure—For each area to be inspected, perform procedure every 100 linear ft. in the first 1,000 linear ft. of joint. If no test failure is observed in the first 1,000 ft. of joint, perform procedure every 1,000 linear ft. thereafter or approximately once per floor per elevation."

However, a 6 in. (150 mm) sealant handle pulled every 1000 ft (305 m) is a statistical sampling with a 1:2000 sampling rate if used to evaluate the *continuity of the seal*. Clearly, a new test method has been needed in order to meet the demand for continuous joint seals.⁴

Early Use of Rolling Devices in Continuous Sealed Joint Inspection

As a concept, the idea of pushing on a sealant bead with a blunt object is probably as old as weatherseals. Using a wheeled “rolling probe” is the next logical step if the goal is to obtain larger data samples. Three active long-term members of ASTM C 24 began to use “screen rollers” (Fig. 1) to evaluate joint seals some years ago in their professional practice.⁵ As stated by Klosowski, “With this test, we roll over the entire joint. It is fast, but it is also efficient in that it looks at all of the joint and not just discrete places along the joint. This field test to determine the extent of problems, if any, is not a trivial matter. In fact, it is fundamental and badly needed” [7].

Introduction to ASTM C 1736

ATM C 1736 can be broken down into the following sequence of events: force is introduced to a sealant bead via a rolling probe; this in turn induces a depressive strain in the sealant bead (i.e., creates an elongation of the bead), which in turn stresses the adhesive bond-line of the joint seal at the sealant-to-joint substrate interface.

The primary purpose of the method is to reveal sealant adhesion anomalies not discernible via visual examination of the unstrained seal at the time of the evaluation that might affect the air and/or water infiltration resistance of the sealed joint. Sealant adhesion anomalies might be a pre-existing lack of adhesion or nominal (borderline) adhesion. A pre-existing lack of adhesion might not be detected in an inspection of unstrained sealed joints due to the “elastic recovery” of sealants. Elastic recovery is a desirable sealant quality that incidentally tends to hide adhesive bond loss in cursory inspections, because the bead “recovers” or “snaps back” into its original position at the bond-line, giving the joint a “sealed” appearance.

Borderline sealant adhesion can be exposed when the rolling device procedure induces a non-pre-existing failure. Repairs of identified adhesive failures can restore the seal, which is why progressive applicators have started to use the procedure as an internal quality assurance program. In addition, inappropriate geometry, under which the sealant is too thick and the movement

⁴ASTM C 1521 contains non-destructive procedures; however, the practice is designed to evaluate sealant performance at discrete locations, whereas ASTM C 1736 can be used to facilitate joint seal continuity up to 100 %.

⁵David Nicastro, Engineering Diagnostics, Inc., Austin, TX; Patrick Gorman, Gorman Moisture Protection, El Paso, TX; and Jerome Klosowski, Klosowski Scientific, Bay City, MI.



FIG. 1—Upper portion depicts an uncontrolled “screen roller” type device used in procedural section 7.3, lower portion is the controlled force device per section 7.4.

capability of the joint might be inhibited, can be identified, examined, and, if need be, repaired.

A variety of fixed roller devices can be used to satisfy the requirements of the standard in a “depression inducement procedure,” listed in Section 7.3 of ASTM C 1736, including “window screen insertion devices” (screen rollers), “backer rod insertion devices,” or any other device(s) meeting the criteria. These devices are manually controlled by the user.

The “force control procedure” (Section 7.4 of ASTM C 1736) uses a patented test system [8]. In this system, the roller force load is accurately maintained (using air pressure) on the active test area. Changing the air pressure in the device also changes the force delivered to the bead. The force is monitored with a

gauge and is adjustable. A simple calculation provides the force load delivered to the bead under test.⁶

Case Study Illustrating the Benefits of ASTM C 1736

In 2008, a sealant contractor engaged the author to conduct a 100 % evaluation of newly installed joint seals because a pull test report had placed the seal failure rate at 80 %. The agent conducting the evaluation first used a screen roller to identify locations of questionable adhesion for pull testing; however, only the pull test result from each location was reported. The owner's consultant, referencing the evaluation report, recommended "removal and replacement" of all of the installed sealants. However, 100 % evaluation conducted according to the non-destructive rolling device methodology and reporting according to ASTM C 1736 (under ASTM C 24.30 development at the time) revealed a total seal discontinuity rate of 0.54 % (amounting to 120 unsealed spots in the total joint grid). Thus, the ASTM C 1736 methodology allowed the contractor to implement repairs, save the installation, and deliver a truly sealed joint.

Review of Some of the Questions Examined during Development of ASTM C 1736

Answers to the following three questions provide additional insight into the science behind ASTM C 1736.

Question 1: Where Exactly Do the Stresses Produced by This Method Affect the Sealant-to-Substrate Bond-Line?

Because the joint sealant material is elastic, bond-line stress is created when the sealant is stretched inward from the surface perpendicular to the joint as the roller pushes on the bead. ASTM C 1736 refers to the resulting geometry as a bead "depression." Bond-line stress induced during a roller pass-through-bead "depression moment" is tension concentrated at the uppermost corner of the sealant, where it intersects the substrate. One way to think of this, in comparison, is as a non-destructive in-field peel test (Fig. 2).⁷

As a peel test, the roller width affects the amount of measurable bead depression (and the angle of "peel") per specific amount of force but does not affect the total force at the bond-line stress focus point, provided there is adequate clearance between the wheel and the substrate joint wall.⁸

⁶The force load in the system is equal to the cylinder bore area multiplied by a given air pressure. For example, a cylinder with a bore area of 0.44 in.² (11 mm²) at 20-PSI (0.13 MPa) delivers 8.8 force pounds (39 N).

⁷An "adhesion in peel" test procedure requires force to destruction and a peel angle of 180° (ASTM C794 [9]).

⁸ASTM C 1736 dictates that the wheel is to be at minimum 1/8 in. (3 mm) narrower than the joint under test. If the wheel does not have adequate clearance, the sealant bead might come into shear.

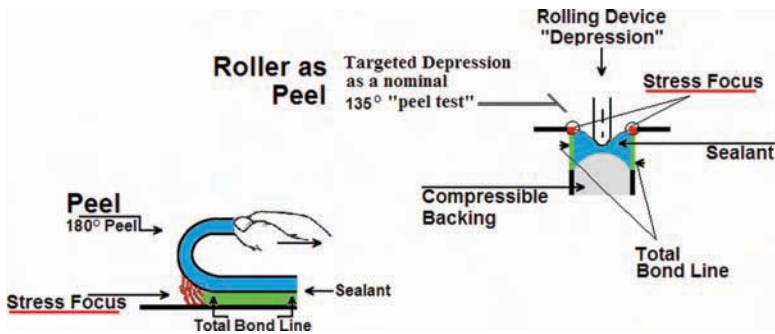


FIG. 2—Depiction of how the method of ASTM C 1736 can be thought of as a field “peel test.”

Question 2: How Does Joint Geometry Impact Bond-Line Stress?

Depth—A thicker sealant bead requires more force in order to be depressed than a thinner one. Therefore, using force control, the depression is reduced when the bead is thick and increased when the bead is thin, per any given maintained force. Studies by the author using controlled force revealed that the force-to-movement/depression relationship is predictable within the movement capability range of high recovery sealants, consistent with their elastomeric design intent. In fact, during early exhaustive data research for calibration of the force-controlled device, it was discovered that the sealant pigmentation affected movement (as indicated by bead depression readings in two out of three sealants in the study) by a very small but measurable amount [10]. If the force had not been accurately controlled, and if the force-to-movement relationship of the sealants were not consistent, this discovery would never have been made.

Changes in the bead depth can be visualized during the procedure via close observation of the roller on the bead from the calibrated starting position when the force is controlled (the roller will ride higher if the bead is thicker and lower if the bead thins), or can be felt when using screen roller “depression inducement.”

Width—Determining an appropriate bond-line stress requires an awareness that sealed joint substrates are subject to thermally induced expansion and contraction [11]. This is why Section 4.3 of ASTM C 1736 mentions the potential influence of temperature during testing, and Section 8.1.4 requires that the temperature and other ambient conditions during evaluation be directly connected to the building elevation, floor line, date, and time of day in a comprehensive report. ASTM C 1736 does not dictate specific temperature parameters for testing, stating only that the temperature during testing must be recognized as important to consider and accurately report.

Question 3: What Level of Stress on the Bond-Line Produces Usable Information Without Damaging the Seal?

Usable information can be obtained from surprisingly small force loads able to depress and elongate the bead. For example, the author's research using force control has determined that on average, approximately 9 to 11 lb (40 to 49 N) is sufficient force when evaluating a sealant of the $\pm 50\%$ movement capability range. Section 3.1.2 of ASTM C 1736 defines "target depression" as "[t]he amount of depression needed to reveal sealant adhesion anomalies, determined either in field or in laboratory, during or prior to a sealant evaluation." Section 6.1 states, "[T]he amount of elongation should be based on joint design and/or joint width, and should produce the elongation within the limits of the joint design."

Section 7.3 ("Depression Inducement Procedure") provides the option of utilizing skill and expertise with devices such as a screen roller in "attempting to control the depression by manually varying the force on the roller."

In Section 7.4.3 ("Force Control Procedure"), force is stipulated to "produce a controlled strain in the sealant and stress on the bond-line sufficient to reveal adhesion anomalies, but less than the amount that could harm the weath-erseal." Section 7.4.3.1, under the heading "Calibration of Force," states, "The amount of force applied to the sealant to create an effective bond-line stress will vary, depending on a given sealant's designed properties in combination with a specific sealant configuration. It is important, when calibrating the device in-laboratory or in-field, to establish a sealant force target(s) for a given evaluation that produces *an appropriate bond-line stress.*"

Information decreases proportionately as the aspect ratio (depth/width) of the sealant bead increases.⁹ However, a lack of information is information in itself in the case of an excessively thick sealant bead; the bead should stretch enough under a reasonable force load that a depression in the bead geometry can be measured. If it will not do so, the bead is unlikely to accommodate all anticipated joint movement during its expected service life, and the long-term durability of the seal can be brought into question. ASTM C 1736 does not dictate a course of action if this occurs. However, as stated earlier, such an occurrence might provide the opportunity to implement repairs to a bead section that might otherwise prematurely fail, as the method will reveal this type of anomaly.

Summary Conclusions for Successful Usage of ASTM C 1736

Bond-line stress using the methodology of ASTM C 1736 is concentrated at the uppermost corner of the sealant where it intersects the substrate in a manner similar to a peel test, without impacting the underlying bond-line. Therefore,

⁹A 2-to-1 width-to-depth ratio is the *industry average* "ideal" joint configuration in standard practice. Specific configuration designs may vary, as should test force calibration to "an appropriate bond line stress."

when the force delivered to the elastic sealant is controlled, the following will hold:

- The test probe wheel width does *not* affect the total stress delivered to the bond-line.
- Geometry, as an aspect ratio of the bead, does not affect the bond-line stress unless the bead thickens significantly relative to the calibrated measure.

A reasonable non-destructive force load producing “appropriate bond-line stress” must be within the limits of the joint design in conjunction with the movement capability of the sealant.¹⁰

References

- [1] Klosowski, J. M., *Sealants in Construction*, Marcel Dekker, New York, 1989.
- [2] Scheffler, M. J. and Connolly, J. D., “Building Sealants,” *Twentieth-Century Building Materials: History and Conservation*, T. C. Jester, Ed., McGraw-Hill, New York, 1995, pp. 272–276.
- [3] Lstiburek, J., “EIFS—Problems and Solutions,” *Building Science Digest 146*, Building Science Press, 2007.
- [4] Lacasse, M. A., Miyauchi, H., and Hiemstra, J., “Water Penetration of Cladding Components—A Comparison of Laboratory Tests on Simulated Sealed Vertical and Horizontal Joints of Wall Cladding,” *Durability of Building and Construction Sealants and Adhesives, 3rd Volume*, ASTM STP 1514, A. T. Wolf, Ed., ASTM International, West Conshohocken, PA, 2010, pp. 359–390.
- [5] Ruggiero, S. S. and Meyers, J. C., “Design and Construction of Watertight Exterior Building Walls,” *Water in Exterior Building Walls—Problems and Solutions*, ASTM STP 1107, T. A. Schwartz, Ed., ASTM International, West Conshohocken, PA, 1991, pp. 11–39.
- [6] ASTM C1521-09e, 2009, “Standard Practice for Evaluating Adhesion of Installed Weatherproofing Sealant Joints,” *Annual Book of ASTM Standards*, Vol. 4.07, ASTM International, West Conshohocken, PA.
- [7] Klosowski, J. M., “Committee on Building Seals and Sealants Developing Field Test Standard for Weatherproofing Sealant,” *ASTM Stand. News*, 2005.
- [8] U.S. Patent No. 6,711,938.
- [9] ASTM C794, *Annual Book of ASTM Standards*, ASTM International, West Conshohocken, PA.
- [10] Huff, D., “Nondestructive Testing of Installed Weatherproofing Sealant Joints,” *Durability of Building and Construction Sealants and Adhesives*, ASTM STP 1453, A. T. Wolf, Ed., ASTM International, West Conshohocken, PA, 2004, pp. 335–345.
- [11] ASTM C1472, “Guide for Calculating Movement and Other Effects When Establishing Sealant Joint Width,” *Annual Book of ASTM Standards*, ASTM International, West Conshohocken, PA.

¹⁰ See ASTM C1736 at Section 6 and note 3.

Jinyoung Jung,¹ Kendo Hahn,² and Hyoungwook Lee³

Weathering Evaluation of Structural Silicone Sealants Used in Korea

ABSTRACT: Super-tall buildings of over 100 stories are coming to Korea. To prove its economic prosperity, which was developed over the last 50 years after the Korean War, Korea is willing to have super-tall buildings as a symbol of its success. Locally, structural silicone glazing has become very common to achieve aesthetically pleasing and high utilization of small land for both residential and commercial building. Because there has been no industry-wide guideline or specification for structural silicone sealants in Korea, it is worthwhile to look at the performance of locally available structural silicone sealants. In this paper, several weathering techniques were adapted from various global industry standards. Artificial weathering using filtered xenon arc radiation was applied to specimens prepared in accordance with ASTM C1135. Comparative evaluations for temperature variations and salt spraying exposure were conducted as well. Silicones in general are known to have excellent resistance to such exposure. However, since the weathering performance of a sealant can be affected by its overall composition (not just the polymer type), some silicone products showed noticeable changes in our testing when compared to their initial properties.

KEYWORDS: structural glazing, silicone, accelerated weathering, adhesive failure, tensile strength, Korea, one part, two part

Introduction

Silicone structural glazing (SSG) is a method utilizing a silicone adhesive to attach glass, metal, or other panel material to the structure of a building. Wind load and other impact loads on the façade are transferred from the glass or

Manuscript received June 2, 2011; accepted for publication November 9, 2011; published online May 2012.

¹Application Development Specialist, Dow Corning Korea, Choongbuk, Korea.

²General Manager, CDC Korea, Seoul, Korea.

³Researcher, Korea Conformity Laboratory, Gyeonggi, Korea.

Cite as: Jung, J., Hahn, K. and Lee, H., "Weathering Evaluation of Structural Silicone Sealants Used in Korea," *J. ASTM Intl.*, Vol. 9, No. 5. doi:10.1520/JAI104101.

Copyright © 2012 by ASTM International, 100 Barr Harbor Drive, PO Box C700, West Conshohocken, PA 19428-2959.

panel through the silicone structural sealant to the systems' framework. Silicone structural glazing systems are currently a very common method of glazing throughout the world. SSG use has become extremely popular, and its principal advantages include the freedom SSG presents to architects by providing infinitely more façade design options, as glass and panels no longer must be secured to the façade with mechanical methods. It also offers economical benefits to the contractors and fabricators by increasing productivity in assembly and installation. For these reasons and performance benefits that SSG provides to the overall glazing system, including waterproofing, acoustic, and thermal benefits, most landmark projects in the world utilize this attractive glazing technology.

SSG in Korea

The history of the structural silicone glazing system in Korea had its beginnings in the mid-1980s. The first two-sided structural silicone project (a glass light or panel mechanically attached to the glazing system on two of its four sides and structurally glazed on the other two) was introduced in Korea in 1986. The project name was City-Bank Korea and the glazing system utilized a one-part silicone structural sealant that was imported from the United States. Korea's first four-sided structural silicone glazing (glazing system utilizing silicone adhesive on all four sides of a panel without any mechanical capturing) was completed in 1992, also utilizing one-part silicone from the US. In the mid-1990s the first unitized glazing system was introduced in Korea using two-part factory installed, fast curing structural silicone sealant.

Although structural silicone glazing has been utilized for approximately 30 years in Korea, the understanding of its technology was low and limited. Consequently, Korean projects experienced many quality issues during assembly and construction, even in very recently finished buildings. Adhesion loss and water infiltration occurred on more than one project, and the time and cost to repair these issues were substantial. More importantly, assessing responsibility for such failures by each participant in the construction process is highly arduous. The causes of such failures are difficult to pinpoint, but one of the culprits would be the lack of availability of an "industry guide" for structural silicone sealant and its application. Knowing the troubles and hurdles associated with SSG, the Cooperative Organization for Standard Development (COSD) and some industry players have been working toward developing a national guide for structural glazing and sealant.

Both ASTM C1401 [1] and ASTM C1369 [2] point out that structural glazing is a high-performance application and not all silicone sealants are suitable for a structural glazing application. They support this further by suggesting that only silicone structural sealants which have been developed and tested specifically for structural glazing applications should be used. The authors of this paper would like to better inform the domestic market about the actual performances of SSG products locally available based on the evaluation following the international industry standard ISO/FDIS 28278-1 [3].

Perhaps as many as 10 super-tall buildings (over 300 m tall) will be erected in Korea in the near future, some of them are already planned and/or under

construction. The erection of such momentous projects locally is a critical point of national pride and prosperity for a country proud to show its growth since the Korean War. Despite the earnest ambition of Korean culture and its workers, there are many aspects regarding the use of SSG that must be reviewed and corrected for construction practices of glazing at the job site and selection of proper building material. Since SSG is one of the chief factors with respect to the performance of a curtain wall system, it is critical that it is selected and installed properly in accordance with industry standards. Currently, the only guideline to classify the kinds of sealant for weather sealant and structural silicone sealant is KS F 4910 [4] which is similar to ISO 11600 [5]. Korean national standards for structural sealant and structural glazing guidelines will be ready soon based on ISO/FDIS 28278-1 and 2 [1,6]. The authors of this paper have contributed to the objective of an adoption of an international standard for SSG in Korea by evaluating locally available structural silicone sealants.

In order to achieve a successful façade system installation there are many factors to be reviewed and confirmed before commencing with the assembly. These factors also affect the total life cycle of the building. If there are any kinds of unexpected water or air leaks occurring in the façade system, the cost of heating and cooling for the building will be increased. As such, the authors would like to share some technical guidance for choosing the proper silicone material by providing the actual evaluation following internationally relevant industry standards. To our knowledge, this is the first publication focused on the evaluation of structural sealants available in Korea.

In this study, 14 different structural silicone products from Korea have been evaluated by ISO/FDIS 28278-1. The Annex B of this standard requires that every structural silicone sealant should have minimum values for tensile strength at rupture for the proposed test conditions. The values are also utilized for calculating the required silicone structural sealant bite for each structural glazing purpose using a certain safety factor during the process. The standard also describes that there should not be much of a tensile property drop after weathering because weathering data can reflect long term safety performance issues of curtain wall glazing throughout the life cycle of the building.

Experiment

It has been well noted that gradual changes in silicone structural sealant properties are affected by exposure to weather and environmental conditions as well as by the composition of sealant materials. Although silicone structural sealants are durable and not significantly affected by long term degradation under harsh conditions, under certain conditions gradual changes can be observed in some properties [7].

As mentioned previously, the principal driving force for the evaluation is to gain support for a Korean national guide for structural silicone sealant and structural glazing. So, evaluating actual performances of locally available structural silicone sealant is critically important to reflect realistic values for the specification. The authors gathered various sealants from as many manufacturers of structural silicone sealants used in the local Korean curtain wall market as possible.

TABLE 1—Products evaluated (for nomenclature refer to text).

Sealant purpose	One-part structural	Two-part structural	Two-part IG secondary	One-part IG secondary
Company A	1	2	3	Not available
Company B	1	2	3	4
Company C	1-a 1-b	2-a 2-b	3-a 3-b 3-c	Not available

Table 1 illustrates the nomenclature for the products used in the evaluation. All products are silicones based on alkoxy cure technology using either one-part or two-part packaging. There are three major companies that supply structural silicone for curtain wall fabrication in Korea (labeled A to C).

In Table 1, “1” stands for one-part structural glazing sealant. “2” for two-part structural silicone sealant. “3” for two-part silicone insulating glass secondary sealant, and “4” for one-part silicone insulating glass secondary sealant (see Fig. 1 for application details). The indices “a,” “b,” and “c” indicate different product names for the same application.

Our study made reference to the following industry standard for the preparation and evaluation of structural silicone test specimens: ASTM C1135 [9] and ISO/FDIS 28278-1 [3]. Of particular note, the intended guide for a future Korea national standard, ISO/FDIS 28278-1 has “Annex B” which describes the requirements for use of structural glazing sealants or insulating glass sealants with exposed applications. Therefore, the testing specimens were prepared according to ASTM C1135 and subjected to weathering tests following the requirements in ISO/FDIS 28278-1. Because the pulling speed of tensile testing

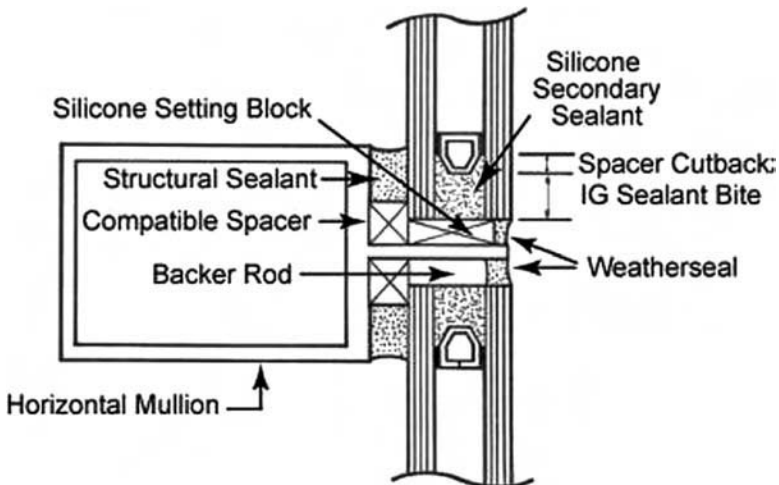


FIG. 1—Section detail of structural silicone glazing [8].

for ISO/FDIS 28278-1 is 5 mm/min compared to 50 mm/min in ASTM C1135, initial properties in tensile testing were evaluated according to both ISO/FDIS 28278-1 and ASTM C1135 in order to detect any difference resulting from the pulling speed. Furthermore, ISO/FDIS 28278-1 suggests that ASTM C1135 can be used as an alternative test method for tensile testing.

Depending on the test method, the dimensions of the test specimen may vary, but the dimensions of the sealant geometry and bead size shall always be 12 mm × 12 mm × 50 mm for both ISO 28278 and ASTM C1135 standards. For this particular evaluation, test specimens were prepared according to ASTM C1135 using anodized aluminum as one support substrate for one side of the test specimen and float glass for the other support substrate (see Fig. 2). The purpose was that the adhesion performance could be evaluated by different weathering conditions simultaneously on two of the most common substrates used (aluminum and glass) along with the mechanical properties of structural silicone sealant.

Before commencing the weathering evaluation, the intrinsic properties of each silicone structural sealant were evaluated. Tensile properties were determined along with the average values based on five test specimens for several temperature conditions (−20, 23, and 80°C) as well as tear strength. Test specimens were conditioned for 4 h at 80 and −20°C. Test specimens were then tested at the same temperature in a conditioned tensile testing machine. Additionally, cohesion/adhesion performances after exposure to artificial light through glass and to water, salt spray, and SO₂ atmosphere were determined. For accelerated weathering, xenon-arc weathering was employed to simulate actinic radiation

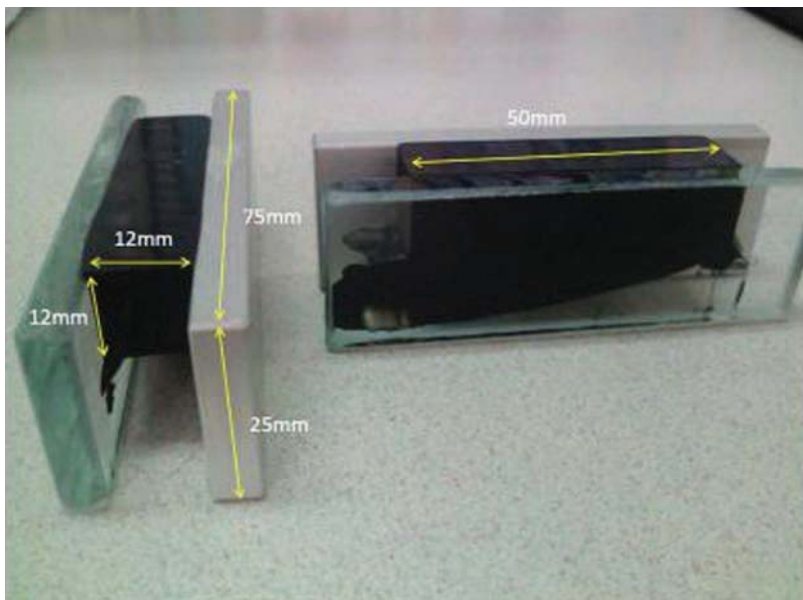


FIG. 2—Tensile adhesion joint used in the evaluation.

[10]. In future work, it is planned to evaluate and compare the effects of both xenon-arc weathering and fluorescent UV light weathering [11].

Results

Tensile Properties at Different Pulling Speeds and Temperature Conditions

Ten test specimens of the ASTM C1135 type were cured for 28 days by conditioning them at $(23 \pm 2)^\circ\text{C}$ and $(50 \pm 5)\%$ relative humidity (RH). They were then pulled in an extensometer at a rate of 5 mm/min (ISO/FDIS 28278-1) and 50 mm/min (ASTM C1135) at 23°C . Figure 3 shows cohesive failure mode of locally compounded one-part structural silicone sealant.

Figure 4 shows for each of the sealants tested some results obtained as an average over three tested specimens.

According to the ISO/FDIS 28278-1 standard, the proposed criteria for successfully passing the tensile testing is a characteristic breaking stress giving 75 % confidence that 95 % of the test results will be higher than this value of 0.5 MPa or larger at 23°C and a rupture pattern that shows equal to or more than 90 % cohesive failure. Additionally, the tensile values after exposure to harsh conditions should be measured, and its delta mean value (ΔX_{mean}) as a ratio of the initial value shall be equal to or larger than 75 %. For definition of ΔX_{mean} and the characteristic value $R_{u,5}$ see Eqs 1 and 2, respectively:

$$\Delta X_{\text{mean}} = X_{\text{mean.c}}/X_{\text{mean.n}} \quad (1)$$

where:

X_{mean} = the average breaking stress, either under tension or shear,

$X_{\text{mean.n}}$ = the average breaking stress, either under tension or shear in the initial state (23°C) and,

$X_{\text{mean.c}}$ = the average breaking stress, either under tension or shear after conditioning or ageing.

$$R_{u,5} = X_{\text{mean}} - \tau_{\alpha\beta} \cdot S \quad (2)$$



FIG. 3—Initial cohesive failure mode of locally compounded one-part structural silicone.

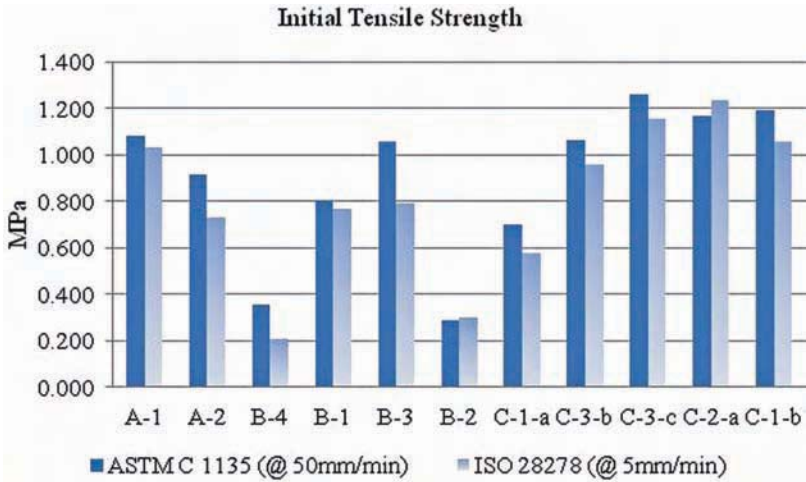


FIG. 4—Initial tensile values prior to exposure to weathering at different pulling speeds.

where *S* is the standard deviation of the series under consideration.

The parameter $\tau_{\alpha\beta}$ is the eccentricity of 5 % with 75 % confidence and this statistical parameter is well elaborated in ISO 3207 [12]. Table 2 shows this parameter as a function of the number of test pieces in a study.

For a country like Korea, which has four distinctive seasons, the class T1 requirements of the ISO/FDIS 28278-1 standard (shown in Table 3) can be applied for tensile strength at different temperatures.

Figure 5 displays the average tensile test results obtained at -20 and 80°C as a percentage of the initial average test result obtained at 23°C (ΔX_{mean} , see Eq 1) for pull rate of 5 mm/min.

As can be seen, some products showed a larger mechanical property difference at 80°C compared to the standard condition at 23°C . These results are linked to poor adhesion (prominent failure mode) of these specimens (Fig. 6). This is the case, for instance, for B-4 which is a one-part IG secondary sealant which displayed adhesive failure and only achieved a tensile strength of 0.2 MPa.

As shown in Fig. 4, with 5 mm/min extension rate called for in ISO/FDIS 28278-1, which has previously been noted as being a slower pulling rate than that of ASTM C1135 (50 mm/min), somewhat lower tensile values were observed than for the faster pulling speed, but the difference was insignificant. Some products, like B-4 and B-2, only showed tensile values around 0.2 and 0.3 MPa, which are far below the minimum requirement of 0.5 MPa defined in ISO/FDIS 28278-1.

TABLE 2—The variable $\tau_{\alpha\beta}$ as a function of the number of test pieces (see ISO 3207).

Number of pieces	5	6	7	8	9	10	15	30	∞
Variable	2.46	2.33	2.25	2.19	2.14	2.10	1.99	1.87	1.64

TABLE 3—Tensile strength requirements as defined in ISO/FDIS 28278-1.

Test temperature, °C	Criteria
80	$\Delta X_{\text{mean}} \geq 75\%$
23	$R_{u,5} \geq 0.5 \text{ MPa}$
-20	$\Delta X_{\text{mean}} \geq 75\%$

Although the initial tensile strength of C-1-a in standard conditions was lower, the property changes at low and high temperatures were reasonable. In case of B-3 and B-4, both sealants showed significant differences when tensile strength were measured at high temperature. There were failure mode changes from 100 % cohesive to some adhesive failure after heat storage conditioning.

Some products such as A-1, A-3, B-4, B-3, B-2, C-1-a, and C-3-b showed adhesive failure mode at 80°C, which means high temperature in a real application has a very critical impact on the long term adhesion durability of these structural silicone sealants. Previous studies have documented that the most detrimental condition for silicone durability is water immersion compared to UV radiation and heat (see, for instance, the paper by Bergstrom [7] and literature cited therein). But it is contrarily noted from this evaluation that for adhesion on float glass and anodized aluminum, high temperature exposure condition could be one of the critical factors to impact negatively on adhesion performance (see Fig. 4). As can be seen, adhesive failures occurred on the glass side as well as the aluminum side.

Load perpendicular to the glass surface, such as wind loads, generate tensile/compression stresses in the structural seal. ISO/FDIS 28278-2 suggests that the maximum tensile stress is considered to develop at the center of the longest side of the pane (trapezoidal loading) and it can be calculated as shown in

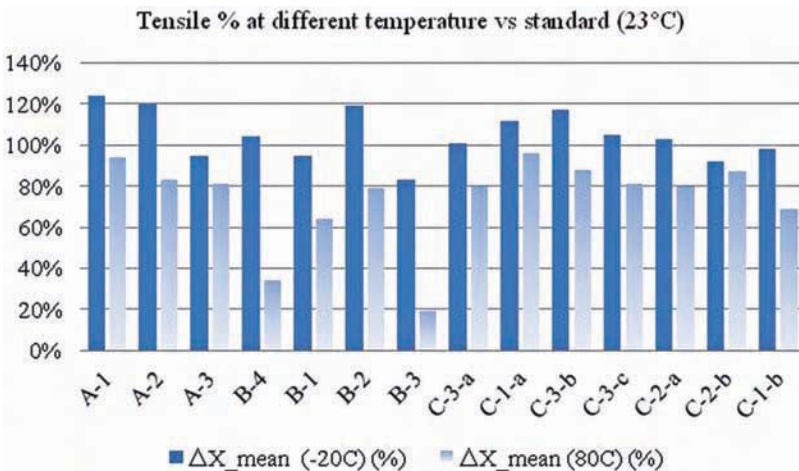


FIG. 5—Average tensile strength at -20 and 80°C.

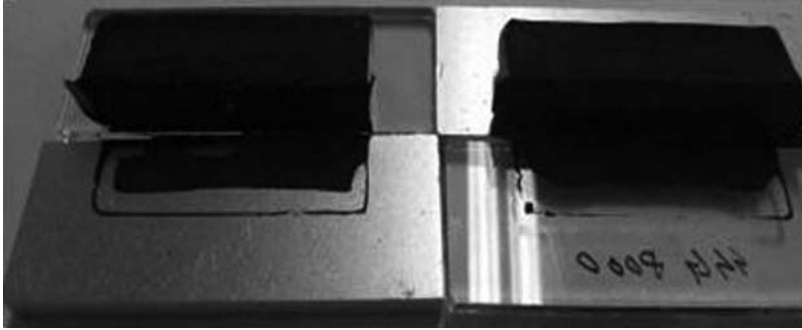


FIG. 6—Adhesive failure mode of locally compounded two-part structural silicone sealant.

$$f_{\text{tensile}} = \frac{aF}{2h} \quad (3)$$

where:

- h = structural sealant bite height,
- a = smallest edge of a rectangular pane, and
- F = wind load.

The selected bite height should ensure that the actual tensile stress acting on the structural sealant stays well below a certain strength, which is determined from the characteristic ultimate limit state value of the structural sealant ($R_{u,5}$ in tensile loading) by applying a certain safety factor, as shown in

$$f_{\text{tensile}} \leq \frac{R_{\text{tensile},u,5}}{\gamma_{\text{tot}}} \quad (4)$$

In Eq 4 γ_{tot} is a safety factor which should be set by national rule. In the case of absence of national value, a γ_{tot} of 6 should be assumed. As ISO/FDIS 28278-2 states in one of its notes, “The use of high value for the partial factor γ_{tot} together with inaccurate calculation model results in structural seal dimensions, which ensure an acceptable safety reliability level as demonstrated by experience during the last twenty years.” Lower γ_{tot} values are acceptable only when accurate calculation models are used together with an appropriate defined safety reliability level.

Therefore, the value of $R_{u,5}$ is an important number required for the calculation of the structural bite for glazing as defined in ISO/FDIS 28278-2 standard using the current global industry consensus of limiting the design tensile strength of a structural sealant to a maximum of 139 kPa (20 psi) [1]. Figure 7 displays the safety factor calculated based on the $R_{u,5}$ values determined for the individual sealants. As can be seen, A-3, B-2, B-3, C-3-a, C-3-c, and C-1-b meet the safety factor of 6 requirement as suggested by the ISO/FDIS 28278-2 standard or have a high possibility of meeting it.

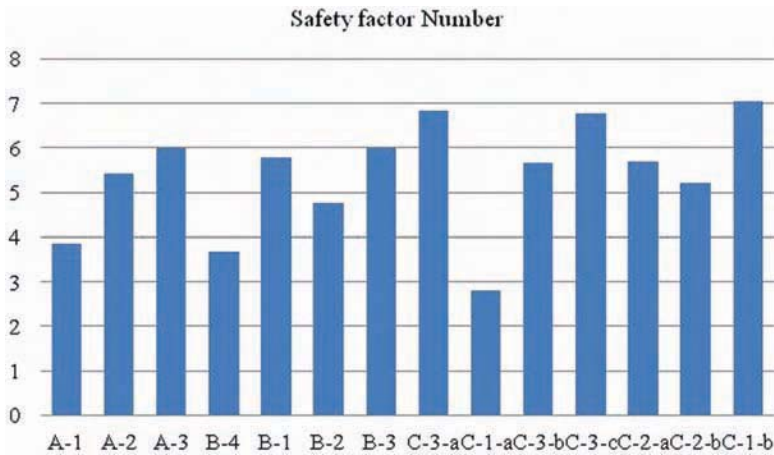


FIG. 7—Calculated safety factor for each sealant based individual on $R_{u,5}$.

When comparing the strain-stress curves of the evaluated products, the different behaviors of the products become apparent. For example, one-part structural sealant from company C showed very high modulus compared with the products from other companies. In general, the products from company C showed only a small difference between the tensile values at the standard condition and those at harsh temperature conditions. It is assumed that the difference in behavior of the various sealant might be caused by differences in their compositions, for instance due to differences in sealant formulations such as different filler loading level, or the quality of the formulation ingredients, such as different polymer chain length or branching.

Accelerated Weathering Test—Cohesion/Adhesion Properties After Exposure to Artificial Light Through Glass and Water

The purpose of this test is to evaluate the sensitivity of the structural sealant to artificial weathering, combining the effect of exposure to UV/visible radiation and water, by measuring the residual mechanical strength of the structural sealant.

As required by ISO/FDIS 28278-2, in this test initial tensile strength values of 10 test specimens are determined after a conditioning period of 28 days at $(23 \pm 2)^\circ\text{C}$ and $(50 \pm 5)\%$ RH. After this conditioning, the tensile test values of an additional 10 test specimens are determined after an immersion in demineralized water at a controlled temperature of $(45 \pm 1)^\circ\text{C}$ with simultaneous exposure to UV light. The test specimens are immersed such that the upper glass surfaces are flush with the water level. During the total time of immersion (1008 h), the test specimens are exposed to the radiation from OSRAM Vitalux lamps. The intensity of the radiation on the upper side of the test specimen shall be $(50 \pm 5) \text{ W/m}^2$ for the wavelength range from 300 to 400 nm. The ISO/FDIS

28278-2 standard suggests that test method and requirements of ASTM C1184 shall be applied to structural sealant evaluation.

For the artificial weathering condition, the authors took a more long term approach along with alternative testing equipments. Xenon-arc radiation, regarded as the artificial source most similar to solar radiation, is often used for its realistic effects in evaluating the long term life cycle of building materials. The xenon-arc exposure cycle consisted of 102 min light only at 0.55 W/(m² nm) at 340 nm followed by 18 min of light plus water spraying. The reason for simultaneous water spraying with radiation is to simulate a harsher accelerated weathering condition in the equipment. Based on the correlation factor provided by one of the technical institute members to join the evaluation, 5000 h of exposure to xenon-arc radiation at 0.55 W/(m² nm) at 340 nm corresponds to an accumulated UV (300–400 nm) exposure of 1108 MJ/m², converted to actual exposure in the field, this is equal to 4 years of outdoor exposure in Seosan, Korea [13].

A xenon artificial weathering machine made by ATLAS laboratory in USA, the model Ci4000, was used for this part of the study. The test was started in April 2009 and finished in February 2010.

The weathering evaluation guidance in ISO/FDIS 28278-1 states that the stress at the breaking point after weathering must be at over 75 % of the initial tensile strength ($\Delta X_{\text{mean}} \geq 0.75$) and the type of failure shall be at least 90 % cohesive (rupture ≥ 90 % cohesive). After weathering, the samples B-3, B-1, B-4, and C-1-a displayed adhesive failure.

As seen in Fig. 8, several products could not meet the value required by ISO/FDIS 28278-1 for the tensile strength specification after weathering compared to their initial value. In the case of ASTM C1184, the requirement is set at ≥ 345 kPa after 5000 h artificial light exposure. Based on the mechanical strength itself, B-4, B-3, and C-1-a had lower tensile values than that required by ISO/FDIS 28278-1

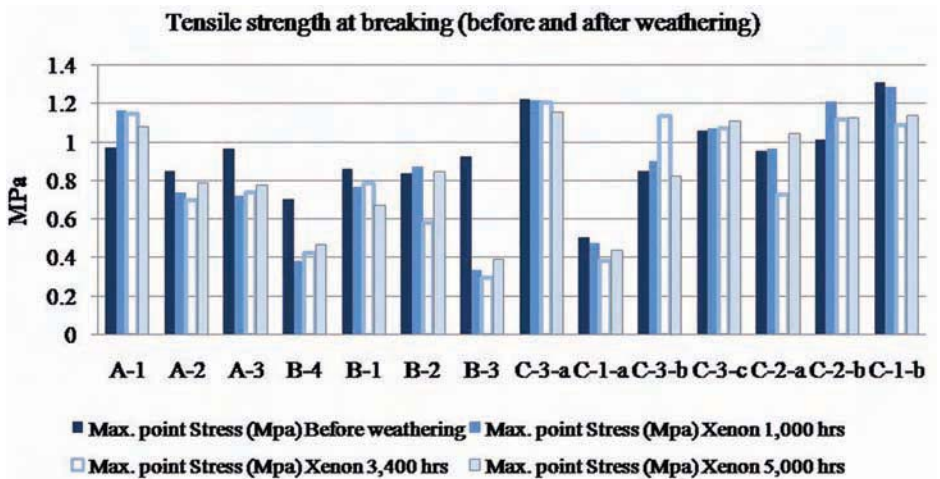


FIG. 8—The tensile strength at breaking point of various sealants before and after various periods of xenon-arc/water spray weathering.

but still they could meet the minimum requirement proposed by ASTM C1184 after weathering. For example, B-3 had the lowest value for tensile strength after 5000 h xenon exposure (397 kPa), but could still fulfill the minimum requirement set by ASTM C1184. Considering the results of the evaluation, it is necessary that the structural performance assessment of structural silicone sealants consider both their adhesion durability as well as mechanical strength. For example, although sealant B-3 showed adhesive failure mode, it had 397 kPa of tensile strength after 5000 h weathering. If there is no adhesion durability on the structural joint, it is impossible to justify the integrity of structural glazing for long term use.

Salt Spray

The testing was conducted in accordance with the test method defined in ISO/FDIS 28278-1. After an initial conditioning period of 28 days at $(23 \pm 2)^\circ\text{C}$ and $(50 \pm 5)\%$ RH, five test specimens were exposed to a salt spray atmosphere which was maintained for 480 h. After salt spray exposure, the test specimens were elongated in tensile to their breaking point and tensile stress, elongation at break, as well as the type of rupture was determined. From the stress/strain curve, also the Young's modulus was determined. As reported in Table 4, essentially all specimens tested exceeded the requirement ($\Delta X_{\text{mean}} \geq 0.75$ and rupture $\geq 90\%$ cohesive) without problems. Only sealants B-3 and B-4 showed adhesive failure.

Discussion

According to our findings, in the accelerated weathering test, cohesion/adhesion properties after exposure to artificial light through glass and to water there is no

TABLE 4—*Salt spray evaluation results.*

	Max. point stress, MPa	Young's modulus, MPa	Break point elongation, mm	Elongation, %	Failure type
A-1	1.096	0.89	30.8	256.8	Cohesive
A-2	0.879	2.361	18.2	151.4	Cohesive
A-3	0.828	1.794	24.4	203.2	Cohesive
B-4	0.486	2.514	2	16.8	Adhesive
B-1	0.724	1.527	14.3	119.3	Cohesive
B-2	0.839	1.998	10.2	85.1	Cohesive
B-3	0.263	2.268	0.7	5.8	Adhesive
C-3-a	1.131	2.255	13.6	113.3	Cohesive
C-1-a	0.526	1.039	16.3	135.8	Cohesive
C-3-b	0.817	2.637	9.4	78.2	Cohesive
C-3-c	1.074	1.499	31.1	258.9	Cohesive
C-2-a	0.948	1.669	23.8	198.3	Cohesive
C-2-b	0.969	1.707	27.7	230.6	Cohesive
C-1-b	1.106	1.371	17.6	147	Cohesive

consistent pattern for the changes in tensile strength as a function of duration of exposure. For example, for some sealants noticeable changes occur already after 1000 to 3400 h of UV exposure, while others show little change over the whole 5000 h period. Furthermore, some sealants showed an increase in tensile strength after exposure, while others had almost no change with exposure.

When one-part structural silicone sealants are compared to each other, the sealant B-4 shows the largest tensile strength change after 1000 h of weathering. In the case of C-1-a, it shows consistently lower tensile strength from initial to 5000 h of weathering. Although C-1-a and C-1-b had different tensile strength values for every measurement point, they had a similar trend for the changes over the total weathering period.

As expected, the effects of combined weathering (water and xenon-arc exposure) are more detrimental to the mechanical properties of the sealant material and its adhesion to the glass surface. From the current evaluation, it was noted that high temperature could be a critical weathering condition important for the assessment of the sealant, and B-4, a one-part structural sealant, had similarly low tensile strength after 80°C exposure and xenon-arc weathering. Test specimens were conditioned for 4 h at 80°C and measured for tensile strength in the same conditioned testing machine. It implies that high temperature exposure for structural glazing sealant can have significant and similar impact on sealant durability as artificial weathering does. However, it is not clearly understood how high temperature exposure could give such material behaviors for structural silicone sealant. More verification of sealant behaviors at different elevated temperature conditions and water immersion could be the focus of the next study.

Conclusions

Structural glazing was introduced to Korea three decades ago, but there is no industry standard available for structural silicone sealant and the structural glazing method. Therefore the establishment of national guideline for silicone structural sealant based on ISO/FDIS 28278-1 and 2 was suggested.

Industry specialists working on local construction projects do not have any durability information for structural silicone sealants used in Korea. Therefore various structural silicone sealants from three major suppliers were gathered and evaluated in accordance to the requirements suggested by international industry standards. Three out of 14 evaluated products could not pass the minimum requirements suggested by ISO/FDIS 28278-1. The data generated will provide a good reference for judging the actual performances of structural silicone sealants used in Korea. Also the evaluation results invoked a urgency for the implementation of a national guideline as soon as possible because of several super-tall buildings are being planned based on the structural glazing method.

Although some products routinely pass the relevant national standard (i.e., ASTM C1184) as this is commonly used in the US and many Asian countries, they do have some difficulty in meeting the adhesion and durability requirements of ISO/FDIS 28278-1. These shortcomings have been noted by the current

evaluation and the products need to be improved for meeting this international guideline and soon to be adapted Korea national standards.

One key finding from the evaluation is that different pulling speed with tensile adhesion joint according to ISO/FDIS 28278-1 and ASTM C1135 did not give significant affect tensile values.

Some products had a significant difference between the values at high temperature (80°C) and low temperature (−20°C). Also, high temperature exposure by itself appears to be enough to have negative impact on the durability of some structural silicone sealants. Similar results for these products could be seen after xenon-arc/water spray weathering. It implies that artificial weathering and high temperature exposure are important tactics for the durability of structural silicone sealants.

A structural silicone sealant is only a small portion of all materials used at the job site when compared to other building materials, thus its durability can be easily overlooked by industry specialists. However, if it fails to meet the durability expectations, there might be a human made disaster such as falling of glasses. Therefore, the industry specialist should be aware of these concerns because the structural glazing system will be exposed to harsh conditions during the life cycle of the building.

References

- [1] ASTM C1401-09a, 2009, "Standard Guide for Structural Sealant Glazing," *Annual Book of ASTM Standards*, ASTM International, West Conshohocken, PA, pp. 18–19.
- [2] ASTM C1369-07, 2007, "Standard Specification for Secondary Edge Sealant for Structurally Glazed Insulating Glass Units," *Annual Book of ASTM Standards*, ASTM International, West Conshohocken, PA, pp. 1–2.
- [3] ISO Standard ISO/FDIS 28278-1, 2011, "Glass in Building—Glass Products for Structural Sealant Glazing—Part 1: Supported and Unsupported Monolithic and Multiple Glazing," International Standard Organization (ISO), Geneva.
- [4] KS Standard KS F 4910-00, 2000, "Sealants for Sealing and Glazing in Buildings," *Annual Book of KS Standards*, Korea Standard Association, Seoul, Korea.
- [5] ISO Standard ISO 11600, 2002, "Building Construction—Jointing Products—Classification and Requirements for Sealants," International Standard Organization (ISO), Geneva.
- [6] ISO Standard ISO 28278-2, 2011, "Glass in Building—Glass Products for Structural Sealant Glazing—Part 2: Assembly Rules, International Standard Organization (ISO), Geneva.
- [7] Bergstrom, D. F. L., Dashner, R. D., and Krahnke, R. H., "Effects of Environmental Exposure Conditions and Sealant Composition on Silicone Sealant Properties, Effects on Mechanical Properties and Apparent Cross-Link Density," in *Durability of Building Sealants, Proceedings 36*, A. T. Wolf, Ed., E & FN SPON (An Imprint of Routledge), London, 1997, pp. 1–21.
- [8] *Insulating Glass Technical Manual*, Dow Corning Americas, Midland, MI, 2007.
- [9] ASTM Standard C1135-00, 2011, "Standard Test Method for Determining Tensile Adhesion Properties of Structural Sealants," *Annual Book of ASTM Standards*, ASTM International, West Conshohocken, PA, pp. 2–3.

- [10] ISO 4892-2, 2006, "Plastics—Methods of Exposure to Laboratory Light Sources—Part 2: Xenon-Arc Lamps," International Standard Organization (ISO), Geneva.
- [11] ISO 4892-3, 2006, "Plastics—Methods of Exposure to Laboratory Light Source—Part 3: Fluorescent UV lamps," International Standard Organization (ISO), Geneva.
- [12] ISO 3207, 1975, "Statistical Interpretation of Data—Determination of a Statistical Tolerance Interval," International Standard Organization (ISO), Geneva.
- [13] Lee, H. W., private communication on UV radiation accumulation data at Seosan Exposure Weathering Center, Korea Institute of Construction Material, 2011.

*Hiroyuki Miyauchi,¹ Michael A. Lacasse,² Shigeki Murata,³
Noriyoshi Enomoto,⁴ and Kyoji Tanaka⁵*

Evaluation of Sealed Joint Performance for the Selection of Sealants Suitable for Use in Autoclaved Lightweight Concrete Panels

ABSTRACT: The strength of autoclaved lightweight concrete (ALC) is evidently lower than that of normal concrete. Therefore, when movement occurs at a sealed joint between ALC panels, the sealant is required to deform and remain intact without damaging the ALC substrate. However, there is currently not sufficient information to permit evaluation of the expected performance of sealants applied to ALC substrates. In this study, static and dynamic tests were carried out in order to obtain an index that could be used to select the modulus of a sealant that can be expected to provide long-term performance when applied to an ALC substrate. To develop this index, an initial study was carried out in order to clarify actual joint movement between ALC panels of buildings; the expansion and contraction at the joint were measured, and shear joint movement was calculated based on the expected story-to-story drift of an external wall due to earthquake loads. Thereafter, in a subsequent stage of the study, five types of two-component polyurethane sealant

Manuscript received June 4, 2011; accepted for publication October 10, 2011; published online November 2011.

¹Assistant Professor, Doctor of Engineering, Dept. of Architectural Engineering, Chungnam National Univ., Daejeon, South Korea (Corresponding author), e-mail: miyauchi@cnu.ac.kr

²Senior Research Officer, Ph.D., P. Eng., National Research Council Canada, Institute for Research in Construction, Ottawa, Canada.

³Scientific committee member, ALC Association, Tokyo, Japan.

⁴Scientific committee member, Doctor of Engineering, Japan Sealant Industry Association, Tokyo, Japan.

⁵Emeritus Professor, Doctor of Engineering, Tokyo Institute of Technology, Kanagawa, Japan.

Cite as: Miyauchi, H., Lacasse, M. A., Murata, S., Enomoto, N. and Tanaka, K., "Evaluation of Sealed Joint Performance for the Selection of Sealants Suitable for Use in Autoclaved Lightweight Concrete Panels," *J. ASTM Intl.*, Vol. 9, No. 1. doi:10.1520/JAI104064.

Copyright © 2012 by ASTM International, 100 Barr Harbor Drive, PO Box C700, West Conshohocken, PA 19428-2959.

products, of different elastic modulus, were subjected to tensile and shear tests from which the relationship between stress and the type of joint fracture was determined. The results from these tests revealed that when the stress is greater than 0.6 to 0.7 N/mm², the ALC substrate is more easily fractured than the sealant. In a final stage of the study, the cyclic fatigue resistance of the same two-component sealants was evaluated using tensile and shear fatigue tests. Results from the fatigue tests indicated that the high modulus sealants lost adhesion from the ALC substrate at an early stage in the test. As well, the fatigue resistance of test specimens with joints having three-sided adhesion was lower than that of specimens having normally configured joints with adhesion on two sides of the sealant. Therefore, on the basis of results derived from all the studies, it was determined that a suitable sealant for use on ALC substrates is a sealant having a low modulus that is applied in the normal fashion as a two-sided joint.

KEYWORDS: sealant, autoclaved lightweight concrete, wall panel, modulus, fracture

Introduction

Autoclaved lightweight aerated concrete (ALC) (also referred to as autoclaved aerated concrete or autoclaved cellular concrete according to the Portland Cement Association) has exceptional qualities with respect to fire resistance, heat resistance, and thermal insulating properties. ALC is commonly used as the primary material for building envelope roof and wall components and is installed in various types of buildings ranging from super high-rise buildings to residential homes. ALC panels are factory-produced materials having lasting quality and adequate durability.

In Japan, ALC panels are typically manufactured according to specifications regarding strength and modulus given in JIS A 5416-2007 [1] (compressive strength > 3 N/mm²; Young's modulus > 1710 MPa). ALC panels manufactured for use as cladding components are, following casting, cured, removed from their bulk casting forms, roughly cut to size as might be required, and thereafter further cured in an autoclave. Hence their surfaces are essentially free of any form-release agents used to ease the removal from casting forms. Following the autoclave process, these panels may then be cut to exact sizes, with edges formed to accommodate the paneling requirements.

When ALC panels are installed as building envelope components, the joints between panels are filled with sealant to ensure the water- and airtightness of the enclosure. Typically a primer is applied to the joint surfaces to ensure a lasting bond should the porous substrate absorb moisture. With respect to the long-term performance (durability) of the air- and watertightness of the envelope, sealed joints are a vulnerable component of the assembly. Consequently, the following issues might be raised when ALC panels are used for exterior wall cladding.

In the first instance it should be recognized that the tensile strength of the ALC panel is relatively low as compared to standard concrete materials. When

there is movement at sealed joints due to dilation of the panel from surface temperature effects, the ALC panels might rupture before the sealant accommodates the expected deformation. It is for this reason that in Japan the Architectural Institute of Japan has provided the "Recommendation for Design of Joints and Jointing for Control of Water and Air Penetration in External Walls" [2], in which it is specified that sealants used should have a reduced modulus of 0.2 N/mm^2 or less at the 50 % tensile stress level (i.e., referring to 50 % modulus). This provision is only for sealants specified for use in ALC panels. However, given that over time the sealant will age, it is possible that the 50 % tensile modulus for an aged deteriorated sealant can eventually exceed 0.2 N/mm^2 . The relationship between the deformation of such aged sealants and ALC panel strength has yet to be thoroughly studied. This is of particular significance with the use of acrylic sealants, as this type of product has been commonly used on ALC panel joints for a long time and is known to be susceptible to hardening and reduced flexibility over time [3]. The importance of considering the effects of the aging and deterioration of sealants on the long-term performance of the joint should not be ignored.

The next issue is the form of sealed joint. A standard exterior wall joint is typically applied as a two-sided adhesion joint system in which the sealant is applied to the surfaces of each adjacent side of the ALC panel and to specified width-to-depth ratios as provided, for example, in Fig. 1. However, in Japan, the use of a three-sided adhesion joint system that bonds joint surfaces at the base of the joint has, for ALC panel cladding, been accepted for a considerable time,

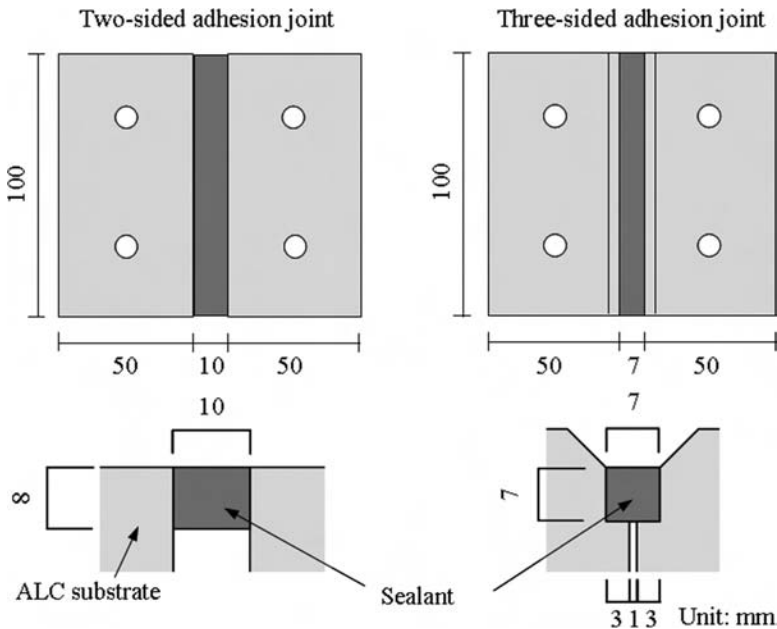


FIG. 1—Test specimens.

and the long-term adhesion of such joints with respect to fatigue resistance remains nonetheless undefined.

Another issue is the degree of movement of a sealed joint and fatigue resistance. The thermal expansion coefficient of ALC panels is small; given such, rather than on the expansion and contraction of panels due to temperature change, the focus should be on the shear movement of joints caused by an earthquake, with the degree of movement being estimated on the basis of the relative story displacement of panels.

Considerable research has been done on the tensile and shear deformation performance, as well as on the fatigue resistance, of sealed joints for metal, concrete, and glass panels. Enomoto et al. [4,5] conducted a quantitative assessment of dynamic fatigue using cyclic movement devices that created continuous movement in expansion and contraction. Takeuchi et al. [6] conducted dynamic loading tests in order to understand the dynamic characteristics of sealant placed between glass panels. In addition, ongoing research has also been done on the adhesive properties of sealant under various conditions of the panel surface. Kenney and Kenney [7] assessed the adhesive properties of sealant, with the moisture condition of the substrate as a variable. Ma et al. [8] studied the adhesive properties of the sealant after solvent cleaning, using various types of glass panels.

It can be observed from these case studies that in every instance the panel substrate was stronger than the sealant; the expectation, then, is that the panel substrate will not fracture. In other words, the focus of existing research on the deformation performance of sealed joints is the tensile strength of the sealant and the adhesive strength between the sealant and the panel substrate. However, in the case of ALC panels with a low tensile strength, the panel itself can fail before the sealant reaches its maximum level of performance in tensile deformation. Consequently, this can yield a significant effect on the performance in the deformation of the sealed joint as a whole.

Given this background information, a research study was developed in which a sealant was formulated to have different values of modulus and was applied to ALC panel joints in order to elucidate the relationship between tensile stress and fracture mode. The variations in the sealant modulus were intended to mimic the effects brought on by the aging and deterioration of the sealant. Panel joint movement was also measured and calculated, and a fatigue test was conducted in order to assess the fatigue resistance of sealed joints against the continuous deformation of ALC panel joints.

Tensile Test and Shear Test

In general, for the type of sealants typically used to seal joints on ALC panels, the modulus of the sealant increases as it ages and deterioration progresses [3]. With an increase in the sealant modulus there is a risk that the surface of an ALC panel onto which the sealant is applied might indeed fracture as the panel contracts and the joints open, if the tensile strength of the concrete is sufficiently low. In order to determine the degree of modulus increase that might bring about surface fracture of the ALC panel and subsequent spalling of the

concrete, the sealant products were formulated with different values of modulus. Thereafter, both tensile and shear tests were conducted for the anticipated deformation of ALC panel joints.

Test Specimen and Test Method

Test Specimens—In this study, the sealant product modulus was varied with the use of a two-component polyurethane sealant that hardened via the reaction between the base material and the curing agent. The formulation ratio of base materials to curing agent was adjusted in order to produce five types of sealant, given in Table 1, with each expected to yield a different modulus.

Figure 1 shows the configuration and relative sizes of the two types of test specimen: a two-sided adhesion joint and a three-sided adhesion joint. The ALC substrate had dimensions of 50 mm in width, 100 mm in length, and 37 mm in depth. The two-sided adhesion joint specimen had a 10 mm joint width and an 8 mm joint depth, whereas the three-sided adhesion specimen had a 7 mm joint width and a 7 mm joint depth; there was a 1 mm space at the base of the three-sided joint. The method for producing the test specimens was as follows: After applying polyurethane resin primer on the surface of the ALC substrate forming the joint (as is typically done to ensure long-term adhesion), sealant was applied to the joint in order to reach the designated joint width and joint depth. In order to comply with JIS A 1439 [9], the specimens were cured in a thermostatic chamber at a temperature of 23°C for two weeks and then further cured in a thermostatic chamber at a temperature of 50°C for another two weeks.

Test Method—Two sets of static tests were conducted: (i) a tensile test to evaluate the degree of material expansion and contraction that can accommodate the expected panel dilation due to temperature changes, and (ii) a shear test to determine the degree to which sealant products can tolerate relative story-to-story displacement brought about by an earthquake event. Figure 2 shows the test setup and test jigs for the tensile and shear tests. Both tensile and shear tests were conducted at a deformation rate of 50 mm/min. The 50 % modulus, maximum stress, and elongation at maximum stress were measured, as well as the elongation at rupture; fracture modes were also examined. For both

TABLE 1—*Sealants and respective formulation ratios.*

Sealant Type	Number	Formulation Ratio: Cure Agent/ Base Material/ Toner	Modulus (Hardness)
Two-component polyurethane sealant	1	100/24/5.1	Soft
	2	100/28/5.1	↓
	3	100/32/5.1	
	4	100/36/5.1	
	5	100/40/5.1	

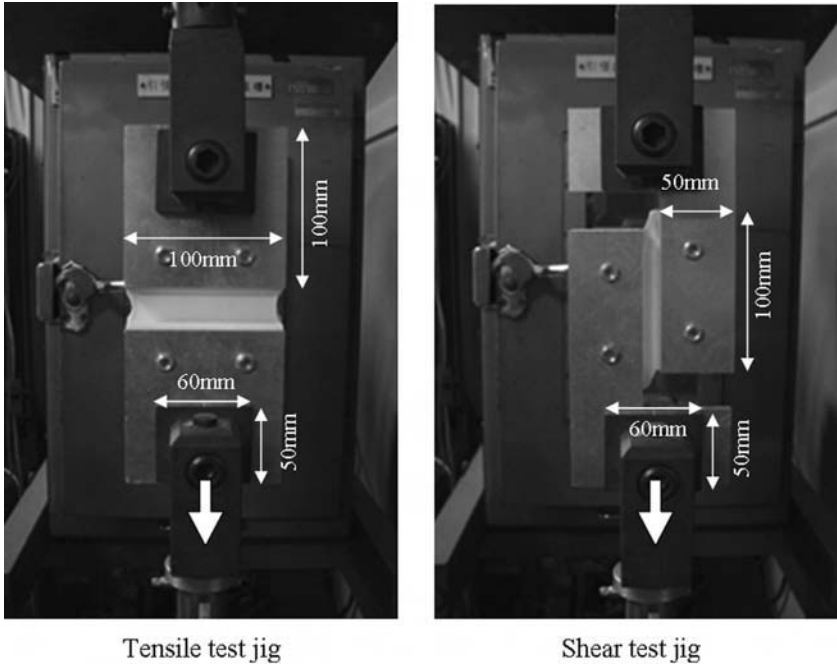


FIG. 2—Static tests.

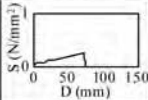
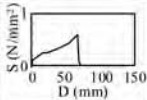
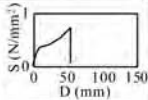
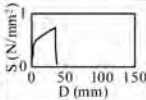
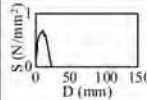

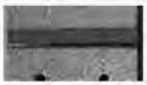

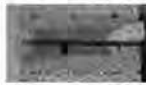
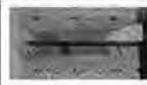
tensile and shear test sets, three test specimens were evaluated for each test condition.

Test Results

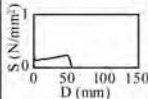
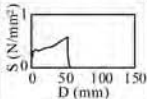
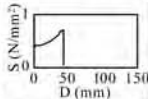
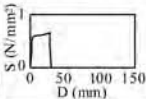
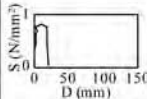
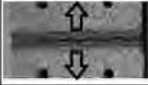
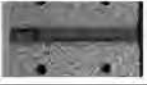
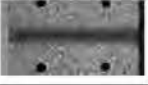
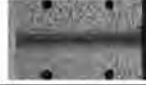
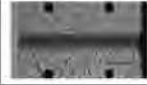
Tensile Test Results—Table 2 shows results of tensile and shear tests that include the relationship between the stress and the amount of displacement for each sealant modulus, as well as the fracture mode for each test specimen. Figure 3 shows the relationship between tensile stress and the modulus of the different types of sealant for both two- and three-sided adhesion joints; for each of these types of joints, the fracture mode of each test set is identified. For the two-sided adhesion joints, sealant products No. 1 and No. 2 showed thin layer cohesion failure (TCF), in which a thin layer of sealant remained on the substrate. In contrast, sealant products Nos. 3 through 5 showed a mixture of cohesion failure (CF) and material failure (AF) of the ALC substrate. Thus the results show a difference in fracture mode between products No. 1 and No. 2 and products No. 3 through No. 5. The maximum tensile stress at which a change in the fracture mode was observed was around 0.7 N/mm^2 . When the maximum tensile stress is less than 0.7 N/mm^2 , the strength of the ALC substrate is greater than that of the sealant and the sealant fractures, given that the tensile stress is dependent on the sealant. In contrast, when the maximum tensile stress is greater than 0.7 N/mm^2 , the sealant has a greater strength than the ALC

TABLE 2—Tensile test results.

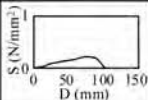
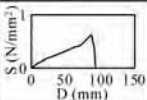
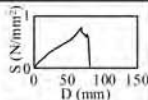
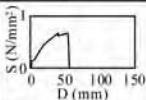
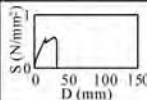
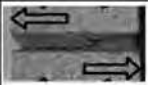
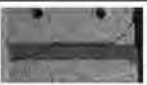
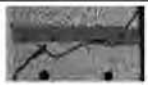

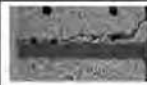
Tensile test results: Two-sided adhesion joint

Specimen No.	No. 1	No. 2	No. 3	No. 4	No. 5
50% modulus	0.05	0.14	0.30	0.47	0.58
Max. stress (N/mm ²)	0.25	0.57	0.76	0.76	0.71
Stress vs. Strain					
Fracture mode					

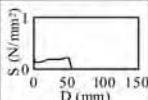
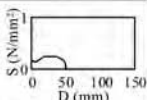
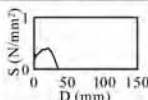
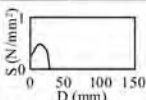
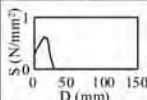
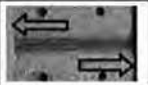
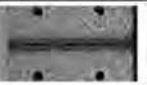
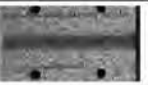
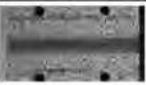

Tensile test results: Three-sided adhesion joint

Specimen No.	No. 1	No. 2	No. 3	No. 4	No. 5
50% modulus	0.15	0.30	0.46	0.63	0.85
Max. stress (N/mm ²)	0.24	0.60	0.66	0.69	0.90
Stress vs. Strain					
Fracture mode					

Shear test results: Two-sided adhesion joint

Specimen No.	No. 1	No. 2	No. 3	No. 4	No. 5
Max. stress (N/mm ²)	0.23	0.64	0.73	0.66	0.62
Stress vs. Strain					
Fracture mode					

Shear test results: Three-sided adhesion joint

Specimen No.	No. 1	No. 2	No. 3	No. 4	No. 5
Max. stress (N/mm ²)	0.14	0.26	0.40	0.49	0.61
Stress vs. Strain					
Fracture mode					

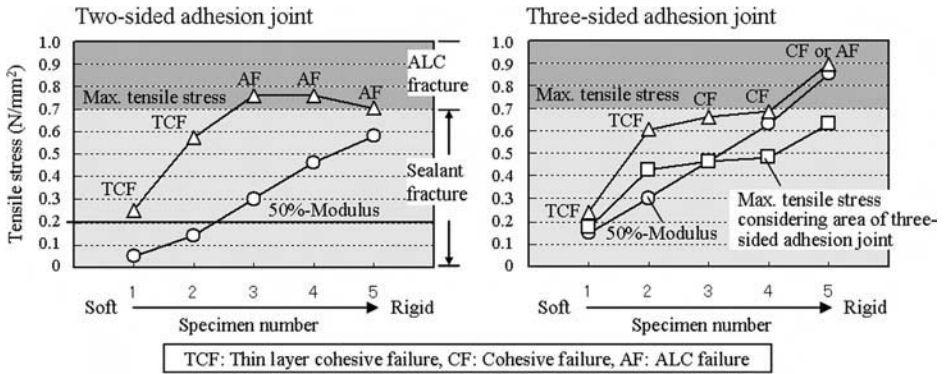


FIG. 3—Fracture mode of sealed joint against tensile deformation.

substrate. At this stress level fracture is initiated in the ALC substrate and the sealant is thereafter damaged as the fracture in the ALC substrate progresses. When the maximum tensile stress exceeds 0.7 N/mm², the tensile strength of the sealed joint is governed by the tensile strength of the ALC substrate. Therefore, the maximum tensile stress that can be attained in tests is that of the tensile strength of ALC substrate, which attains a maximum level of around 0.7 N/mm²; this is irrespective of the value for the sealant modulus.

As for the values for the sealant modulus of products No. 1 and No. 2, the test specimens that had fractures with sealant had 50 % modulus values of 0.2 N/mm² or below, as recommended for exterior wall watertightness design. Specimens for products No. 3 through No. 5 had a 50 % modulus of 0.2 N/mm² or above, and the specimens had fracture modes that corresponded to the recommended value for avoiding causing ALC fracture of 0.2 N/mm² or less for the 50 % modulus of the sealant.

The test specimens having the three-side adhesion configuration had similar results, in which a mixture of sealant CF and ALC AF was shown with a maximum tensile stress of 0.7 N/mm² or above. These test results also showed a trend of tensile stress and fracture similar to that shown for the specimens in two-sided adhesion tests.

The differences between two- and three-sided adhesion joint specimens with respect to the values achieved for tensile stress and percent elongation arise because three-sided adhesion joints bring about greater internal stress in the joint as compared to two-sided joints. In essence, three-sided joints are capable of accommodating less movement than two-sided joints, and for the same degree of movement they give rise to both higher bond and internal stress.

Shear Test Results—Figure 4 shows the relationship between shear stress and the modulus of the different types of sealant for both two- and three-sided adhesion joints; the fracture mode for each sealant product is also given. For two-sided adhesion, specimens of product No. 1 showed TCF at the interface between sealant and substrate, and the sealant remained on the ALC panel

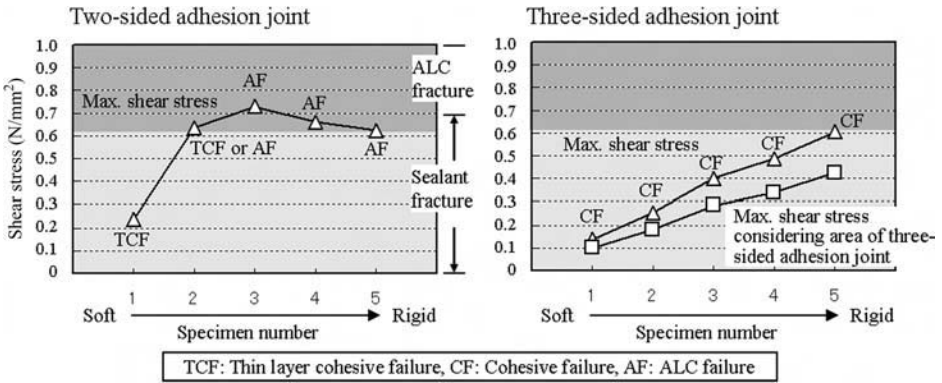


FIG. 4—Fracture mode of sealed joint against shear deformation.

substrate. Sealant product Nos. 2 to 5 had significant fractures that started at the edge of ALC; this led to CF of the sealant or AF of the ALC. The fracture mode was differentiated by sealant fractures and ALC fractures at maximum shear stresses of 0.6 to 0.7 N/mm². For three-sided adhesion, all test specimens showed sealant fractures.

Discussion

The test results given in Figs. 3 and 4 suggest that the maximum tensile stress and maximum shear stress of the ALC panel surface onto which sealant was applied and used in this study was approximately 0.7 N/mm². In order to ensure the long-term durability of sealed joints, the sealant must be designed such that the maximum stress in either tension or shear does not exceed 0.7 N/mm² over its designated service life. In addition, the movement capacity of the joint is an important factor when assessing sealed joint performance. Shear movement capacity is especially important for ALC panels. Figure 5 indicates the average amount of movement achieved at the maximum shear stress for two-sided and three-sided adhesion test specimens of the five different sealant products. The degree of permissible movement (deformation) of sealed joints of two-sided adhesion test specimens tends to be higher than that of three-sided adhesion test specimens. However, product specimens No. 3 through No. 5, each having a "higher" sealant modulus, showed extremely low values for movement accommodation with the two-sided adhesion test specimen, and product specimen No. 5 had a degree of movement capability less than twice that of the value for the corresponding product specimen with three-side adhesion.

ALC Panel Joint Movement

As already mentioned, deformation on the exterior wall of panel joints can be divided into deformation due to expansion and contraction of the joint and that due to shear deformation. In this section, the amount of deformation due to

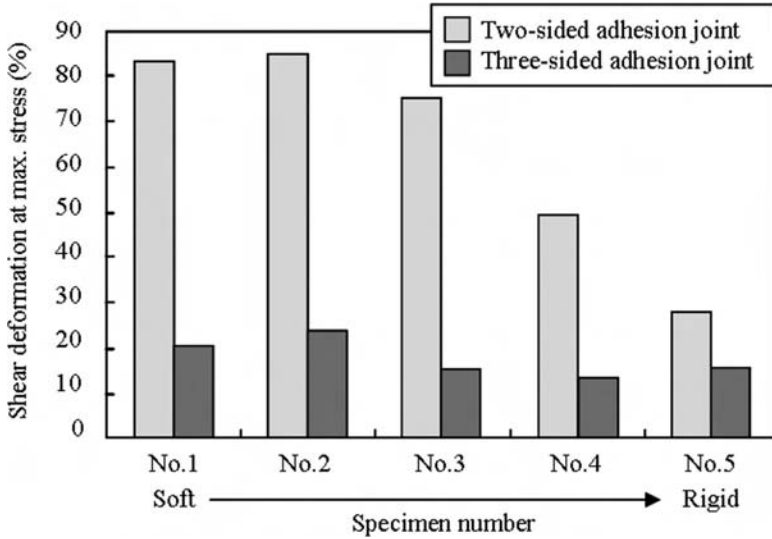


FIG. 5—Comparison of shear displacement at maximum stress.

expansion and contraction of ALC panel joints was measured from actual ALC panel joints used in a building; the amount of deformation in shear was determined via the calculation of joint displacement based on existing knowledge.

Measurement of Expansion and Contraction Movement between ALC Panel Joints—Measurement Method. Tables 3 and 4 provide information on a building having ALC panels of which measurements were made. Figure 6 shows the location on the facade of the actual building at which displacement measurements were recorded. It is a steel-frame building with deep ALC panels that were affixed to the building frame via the “rocking” method. The rocking method is a means of fixing a wall panel to a frame by restraining the rotation (rocking) of the panel when the building frame responds to the effects of and deforms during an earthquake event as depicted in Fig. 7. The joints were sealed using a two-component polyurethane sealant and applied with the two-sided adhesive method. The measurements were taken in both summer and winter and included recording the ambient local temperature at the building location and the ALC surface temperature, as well as the joint displacement. The measurement of the joint displacement was determined on four panel surfaces, each having a different orientation, namely, east, west, south, or north, but limited to

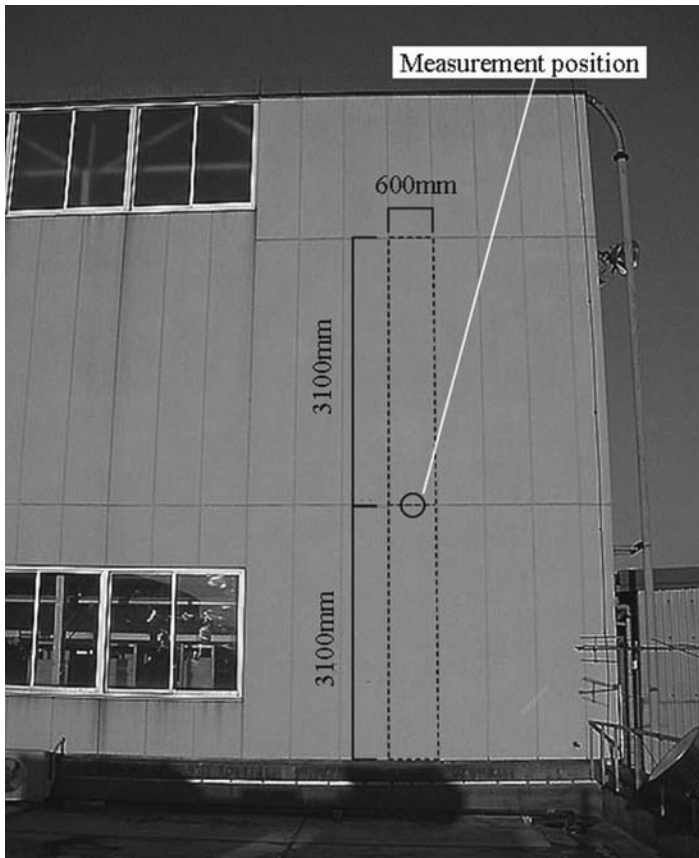
TABLE 3—Summary information for building on which displacement measurements were recorded.

Wall Type	Main Structure	ALC Panel Fixing Method	Joint Type	Joint Width
ALC panel	Steel frame	Rocking type	2 fixed joint	8 mm

TABLE 4—*Information on displacement measurements.*

Direction	Thickness	ALC Width	ALC Length		Measurement Date	Weather
			Upper Floor	Lower Floor		
East-south-west North	100 mm	600 mm	3100 mm 2900 mm	3100 mm 3700 mm	August 23–24, 2001	Good

the shorter joints of selected ALC panels that, in fact, had a greater degree of expansion and contraction. A contact type digital thermometer (resolution of 0.1°C) was used for measurement of the ambient local and ALC panel surface temperatures. Movement at selected panel joints were measured by mounting screws on panels on either side of the joint, as shown in Fig. 8; joint

FIG. 6—*Location of displacement measurements on external wall.*

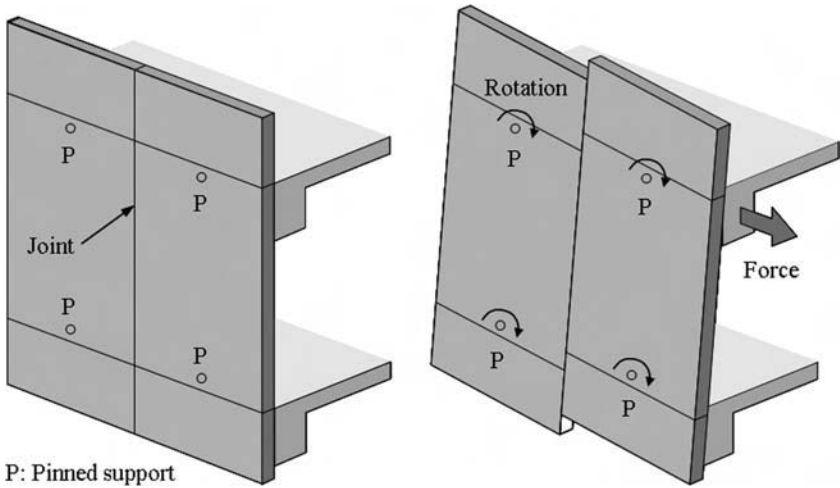


FIG. 7—Rotation (rocking) of the panel.

displacement was determined by measuring the displacement of the screws every two hours using a digital caliper (resolution of 0.01 mm).

Measurement Results. Table 5 shows the results for joint displacement. A large difference in the surface temperature was observed on the west and south sides of the building, and sealed joint movement was largest on the west side of the building. The movement per unit temperature change was also calculated, and the results indicated a thermal expansion coefficient for ALC exterior wall panels of 6 to $7 \times 10^{-6}/^{\circ}\text{C}$, which is close to the standard value for ALC panels of $7 \times 10^{-6}/^{\circ}\text{C}$. On the other hand, when the external wall panel deforms in

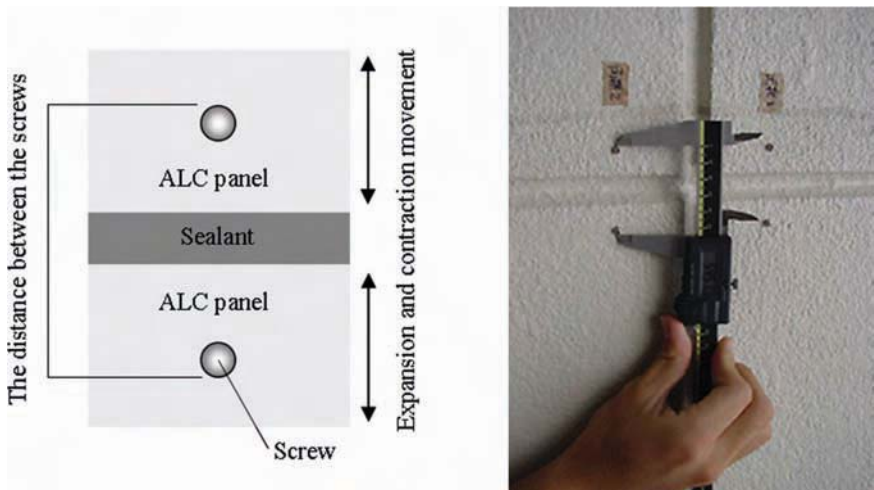


FIG. 8—Example of method for measuring displacement.

TABLE 5—Test results for the surface temperature and joint movement of ALC panels in summer.

Contents	East Side		South Side		West Side		North Side	
Surface temperature high/low, °C	40.0/24.6		42.2/25.0		43.1/24.8		34.0/24.7	
Temperature difference, °C	15.4		17.2		18.3		9.3	
Joint movement, mm	0.31	0.31	0.37	0.37	0.47	0.48	0.2	0.25
mm/m	0.1	0.1	0.12	0.12	0.15	0.15	0.06	0.08
Coefficient of thermal expansion ($\times 10^{-6}$), mm/°C	6.49	6.49	6.94	6.94	8.28	8.46	6.52	8.15

relation to the expected rocking response of the panel, the degree of joint displacement decreases by a fixed ratio [2]. The displacement reduction ratio for the deep ALC panels affixed to the steel frame building could not, however, be confirmed within the measurement range recorded in this study. Figure 9 shows the results for the amount of displacement in the expansion and contraction of sealed joints of a panel located on the exterior of the building of which measurements were taken every two hours, starting at noon, over a 24 h period in the summer (August 6–7, 2001) and in the winter (January 28–29, 2001). Temperature differences between summer and winter on the east side had a maximum of 38.0°C. As for movement, the amount of displacement measured was 0.76 mm on the south side of the building. On the east, west, and north sides of the building, the joint width in the winter was smaller than that in the summer. It is believed that this was caused by certain factors such as the effect of the deformation behavior of the steel building frame and the effect of panel expansion and contraction due to temperature changes on the panel surface. Based on the above measurement results, the movement between ALC panels was small, with measurements of less than 1 mm, and within the measurement range of this study.

Calculation of Shear Movement between ALC Panel Joints—The movement of sealed joints due to shear (i.e., relative story displacement) is mainly caused by the interstory deformation of exterior wall panels due to displacements that occur after earthquake events. Such a shear movement is specified in Ref 2, in which it is stated that “the relative story displacement performance required to ensure water tightness must be considered so that joint design can allow joints to follow relative story displacement at an inter-storey deflection ratio of 1/300 without causing any damage on the joint.” In addition, it must also be considered that the shear deformation of ALC panels is greater along the vertical joint, whereas the amount of deformation is determined by the length of the short side of the joint. The length of the short side of an ALC panel is different from that of other exterior panels and is typically fixed at 600 mm. Therefore, the shear movement can readily be calculated, even without considering the reduction in the ratio with the panel fixation method, as 2 mm, given that the inter-story deflection ratio is 1/300. This is illustrated in Fig. 10.

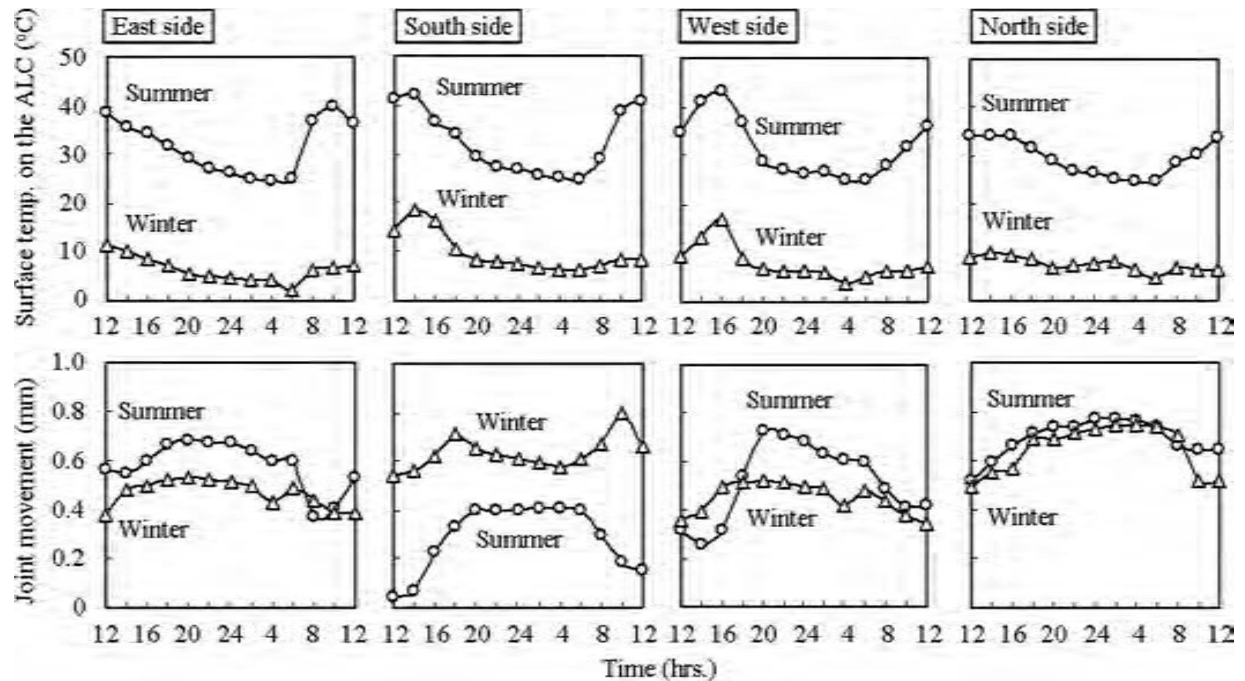


FIG. 9—ALC panel surface temperature and joint movement in summer and winter.

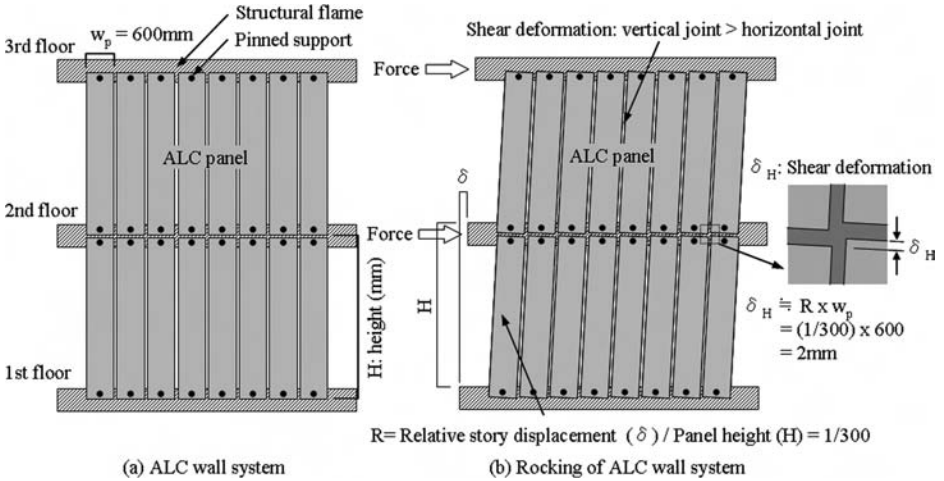


FIG. 10—Calculation of shear deformation at the sealed joint.

Cyclic Fatigue Test of ALC Panel Joints

Summary of Fatigue Test—The fatigue test was conducted to assess the fatigue resistance of joints with sealants having different values of tensile modulus. Both tensile and shear fatigue tests were conducted in order to examine the fatigue resistance against movement of sealed joints. Test specimens similar to those used for the static tensile and shear tests (see the section “Tensile Test and Shear Test”) included two-sided and three-sided adhesion type joints. The sealant used for this test was test specimen No. 5, the sealant product having the highest modulus.

The cyclic fatigue test machine, shown in Fig. 11, was capable of testing several small size test specimens simultaneously. The fatigue test device is placed

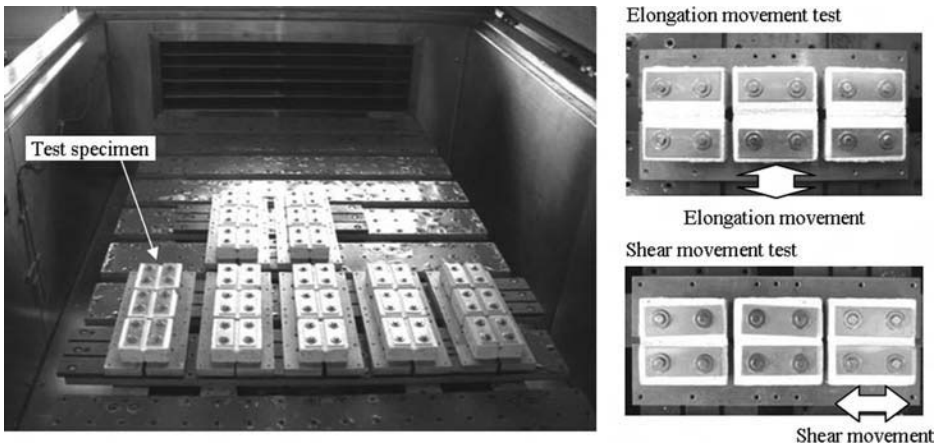


FIG. 11—Fatigue test machine.

inside a chamber in which the temperature can be maintained and tests can be conducted at specified levels. One side of the substrate is fixed, and the other side of the substrate is exposed to a relative movement. A brass fixing plate is placed onto the base to hold the test specimen. Table 6 provides a description of the test specimens and test conditions.

For the tensile fatigue test method, elongation movement was created by applying a tensile force to the specimen. The amount of joint extension on an actual building was considered to behave in a series of five steps, with the entire set forming a fatigue test series; the initial step ranged from 0 mm to +1 mm in tension, and the fifth and final step ranged from 0 mm to +5 mm. The test for shear fatigue was set in relation to a panel's interstory deflection ratio, again with five steps ranging from 0 mm to a shear deformation of ± 1 mm in the initial step (interstory deflection ratio of 1/600) to a final step of 0 mm to a shear deformation of ± 5 mm (interstory deflection ratio of 1/120). The number of cycles for each fatigue test series was a maximum of 5000; this took into consideration both the fatigue due to temperature fluctuations and that due to movement during earthquake events. Three test specimens were used for each test condition; these were also monitored visually every 1000 cycles in order to determine whether there existed the initiation of fatigue cracks.

Fatigue Test Results—Figure 12 shows the test results from the fatigue tests. For both the elongation fatigue test and the shear fatigue test, two-sided adhesion test specimens showed higher fatigue resistance than the three-sided adhesion test specimens. Test specimens subjected to two-sided adhesion passed the elongation fatigue limit of 0 to +2 mm and the shear fatigue limit of 0 to ± 4 mm ($R = 1/150$); for all specimens, the fracture mode for the sealant product was CF. In contrast, some of three-sided adhesion test specimens did not pass the tensile fatigue limit of 0 to +1 mm or the shear fatigue limit of 0 to ± 1 mm ($R = 1/600$). It was also observed that three-sided adhesion test specimens had ALC AF. Such results indicate that test specimens installed with three-sided adhesion are not likely to reach a service life of 10 years.

TABLE 6—*Fatigue test conditions.*

	Items	Contents
Test type	Elongation fatigue test	5 steps: 0 to +1.0 mm → 0 to +2.0 mm → 0 to +3.0 mm → 0 to +4.0 mm → 0 to +5.0 mm
	Shear fatigue test	5 steps: 0 to ± 1.0 mm (1/600) → 0 to ± 2.0 mm (1/300) → 0 to ± 4.0 mm (1/150) → 0 to ± 6.0 mm (1/100) → 0 to ± 12 mm (1/50)
Test condition	Movement cycle	10 s (6 cycle/min)
	Number of cycles	Maximum: 5000 cycles
	Test temperature	20°C
	Number of specimens	Three specimens in each test

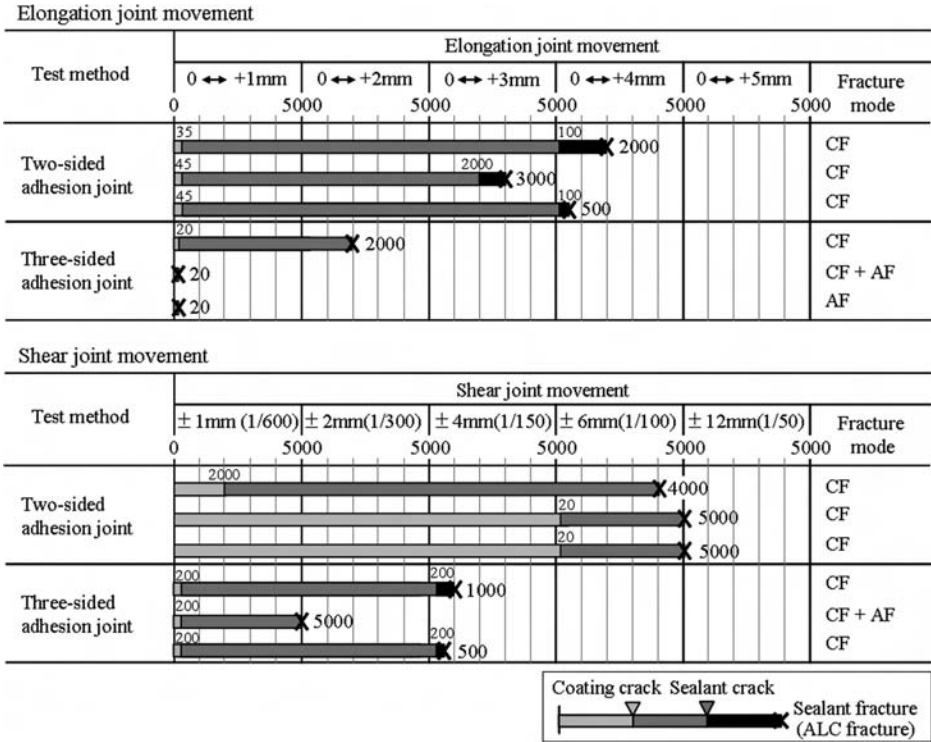


FIG. 12—Fatigue test results.

Conclusions

The results of this research study can be summarized as follows:

- (1) The results of tensile tests and shear tests indicated that the sealed joint fracture location differs with the maximum tensile stress and maximum shear stress of 0.6 to 0.7 N/mm², or 50 % modulus at around approximately 0.2 N/mm². The results of 50 % modulus at 0.2 N/mm² comply with the exterior wall watertightness design to avoid ALC fracture, and anything below that value led to sealant failure, whereas anything above that value caused ALC panel failure. The performance of the sealed joint in accommodating movement was greater for test specimens configured with a two-sided adhesion joint than for specimens having three-sided adhesion. However, a sealant with a two-sided adhesion joint specimen and a high tensile modulus (i.e., given value of modulus) showed a significant reduction in movement capacity.
- (2) The results of actual measurements of expansion and contraction movement on ALC panel joints of an actual building showed that the thermal expansion coefficient of ALC exterior wall panels ranged from 6 to 7 × 10⁻⁶/°C, and the joint movement per year of the ALC panel was very small (less than 1 mm). Shear movement was also calculated based

on Ref 2, and the results indicated that the relative story movement of around 1/300 interstory deflection ratio should be set at 2 mm, given that this is the relative story performance movement requirement in order to ensure watertightness.

- (3) The results of tensile fatigue and shear fatigue tests showed that sufficient fatigue resistance was achieved for test specimens of two-sided adhesion joints. However, some of the three-sided adhesion test specimens did not pass the tensile fatigue limit of 0 to +1 mm or the shear fatigue limit of 0 to ± 1 mm (i.e., $R = 1/600$); in addition, in these instances ALC material failure was also observed. Such results indicate that test specimens configured as three-sided adhesion joints might not fulfill the service life of 10 years.

Therefore, on the basis of the results derived from all the studies, it was determined that a suitable sealant for use on ALC substrates is a sealant having a low modulus that is applied in the normal fashion as a two-sided joint.

Acknowledgments

This work was performed as part of the research activities of the working group for the “Research of Sealants for Sealed ALC panel Joints” conducted by the Tokyo Institute of Technology, Autoclave Lightweight aerated Concrete panels and the Japan Sealant Industry Association. This work was also supported by the Basic Science Research Program of the National Research Foundation of Korea (NRF), funded by the Ministry of Education, Science and Technology, Korea (2009-0069919). Some researchers were funded by the Korean Government and supported by the 2nd Korea Brain (BK21) foundation. The writers are grateful to all these parties for their support.

References

- [1] JIS A 5416, 2007, “Autoclaved Lightweight Aerated Concrete Panels,” Japanese Standards Association, Japan.
- [2] Architectural Institute of Japan, “Recommendation for Design of Joints and Jointing for Control of Water and Air Penetration in External Walls,” Architectural Institute of Japan, Japan, 2008, p. 357.
- [3] Tsukamoto, T., Akita, K., Aono, Y., Miyauchi, H., and Tanaka, K., “Study on Sealed Joint in AutoClaved Lightweight Aerated Concrete Walls—Part 1. Investigation on Sealed Joint Condition of ALC Buildings,” *Summaries of Technical Papers of Annual Meeting*, Architectural Institute of Japan, Japan, 2002, pp. 235–236.
- [4] Enomoto, N., and Tanaka, K., “A Study on the Quantification of the Effect of Dynamic Transformation for the Weatherability of Construction Sealants,” *J. Struct. Constr. Eng.*, Vol. 619, 2007, pp. 27–32.
- [5] Enomoto, N., Ito, A., Takemoto, Y., and Tanaka, K., “New Test Specimen and Method for Evaluation of the Weatherability of Sealants,” *J. Struct. Constr. Eng.*, Vol. 604, 2006, pp. 17–22.
- [6] Takeuchi, T., Tanaka, E., Hisada, T., and Katano, F., “Dynamic Properties of Sealing Material in Glass Walls,” *J. Struct. Constr. Eng.*, Vol. 625, 2008, pp. 481–488.

- [7] Kenney, M. E., and Kenney, R. J., "Moisture Condition of Substrates and Effect of Adhesive Bond of Sealants," *Durability of Building and Construction Sealants and Adhesives, ASTM STP 1453*, ASTM International, West Conshohocken, PA, 2004.
- [8] Ma, J. T., Chen, S. S., Zhou, W., and Wand, S., "Effects on Silicone Sealant Adhesion Buildup on Float Glass," *Durability of Building and Construction Sealants and Adhesives, ASTM STP 1453*, ASTM International, West Conshohocken, PA, 2004.
- [9] JIS A 1439, 2010, "Testing Methods of Sealants for Sealing and Glazing in Buildings," Japanese Standards Association, Japan.

Christoph Recknagel¹

Potential of Dynamic-Mechanical Analysis Toward a Complementary Material and System Testing Approach for Structural Glazing

ABSTRACT: Dynamic-mechanical material analysis as a basis for a general performance exploration complemented by system testing under superimposed climatic and mechanical loading seems to be a promising interdependent test approach addressing the performance behavior of construction sealants under more realistic conditions. With this contribution an attempt is made to adapt dynamic-mechanical material analysis, which has been already successfully validated for different construction types of expansion joint systems in road and bridge engineering, to the field of construction sealants for building façades. Test results from dynamic-mechanical material analysis characterizing the temperature-dependent, deformation-dependent, and frequency-dependent behavior of structural sealant materials are presented and exemplarily discussed for three different sealant products. An attempt is made to address unknown material characteristics in the multi-dimensional loading matrix representing practical use conditions. Furthermore, the applicability of this test approach and its various complex test modes for the exploration of technological performance and especially estimation of fatigue behavior is verified in several examples. Based on this fundamental material exploration, it is planned to complement the dynamic-mechanical assessment methodology by means of system tests on a section of a structural glazing system subjected to a simplified but superimposed loading function. The technical fundamentals and the procedure proposed to develop an adequate system test mode are introduced. The motivation for these investigations is

Manuscript received June 10, 2011; accepted for publication December 19, 2011; published online April 2012.

¹Working Group "Bituminous Materials and Sealing Technology," Federal Institute for Materials Research and Testing (BAM), Unter den Eichen 87, 12205 Berlin, Germany, e-mail: christoph.recknagel@bam.de

Cite as: Recknagel, C., "Potential of Dynamic-Mechanical Analysis Toward a Complementary Material and System Testing Approach for Structural Glazing," *J. ASTM Intl.*, Vol. 9, No. 4. doi:10.1520/JAI104124.

Copyright © 2012 by ASTM International, 100 Barr Harbor Drive, PO Box C700, West Conshohocken, PA 19428-2959.

to identify the actual mechanical system behavior under load combinations and for specimens that both closer resemble reality. The objective is to achieve a consistent and interdependent test program complementary to the existing methodology. Finally, the study is meant to initiate further progress toward a performance-related methodology which considers the design, specification, material, and system selection.

KEYWORDS: sealants, structural glazing, performance assessment, material characterization, dynamic-mechanical testing, system test method, superimposed loading, mechanical characteristics, capability evaluation, durability evaluation

Introduction

Cladding elements made of large-scale glass panes that are installed on metal frames are innovative design elements of modern architecture that nowadays are increasingly dominating the inner urban silhouettes of modern cities. Other than the special aesthetical appearance offered by such façade designs and the potential for complex geometrical solutions, such façades may also provide economical advantages as well as technical benefits in respect to the performance of the building envelope. Enhanced building envelope performance refers to improvements afforded by an in-depth understanding of building physics as applied to, e.g., sealing performance (to control air leakage and water entry), maintaining sustainable energy balances, and noise protection. Such improvements are the special features of the structural silicone glazing (SSG) façade technology. Examples of such building façades are given in Fig. 1.

A substantial advancement for this kind of architecture was achieved over the last few decades by improvements of structural silicone-sealant products. New one- or two-part sealants that were developed provided an increase in the options available to architects and engineers for the design of more sustainable technical solutions of structural façades.

According to their safety-relevant function, local building authorities are mandated to ensure the safe use of new and innovative building systems. As such, they are required to verify the capability of products to sustain loads and assess the durability of structural sealant systems; this is achieved on the basis of the application of generalized technical rules for use of the product or system. In respect to the use of structural sealants in European SSG façades, the harmonized European approval guidelines were introduced in 1998 as ETAG 002 [1]. These guidelines include technical rules for different options of the SSG design with and without additional fixtures, as well as approval requirements and quality-assurance regulations. The technical basis for this guideline was the development of the state-of-the-art in technology of SSG material and systems that occurred in the USA in the late 1980s, as well as the subsequent development of assessment tools. The transfer of these general European regulations (ETAG 002) and related design options to the respective national building codes is within the responsibility of each national approval body for building and construction.



FIG. 1—Inner urban architecture in the administration district of Berlin (www.pixelio.de). (a) Marie-Elisabeth-Lüders-Haus in the German Government district of Berlin. (b) Cupola of the German Reichstag.

Motivation and Methodology for a Complementary Evaluation Approach

With the introduction of the national approval guideline, the German approval body (DIBT) felt impelled to limit possible design options to those systems having additional mechanical fixtures (retaining and supporting devices). According to the requirements of the approval body, the response from the authorities, as well as engineering consultants and the SSG manufacturing industries, a complementary assessment methodology was sought that would overcome deficiencies in the material characterization of structural sealants, as well as characterization of system performance, especially with regard to durability. It was felt that the lack of proper material characterization, hindered, if not precluded, the use of performance-based design, as well as limited the ability to assess the long-term performance of such products and systems and the risks of premature failure.

The current test methodology (ETAG 002) mainly focuses on the specific material behavior in the non-linear visco-elastic region (NLVE-region), i.e., the tensile rupture of sealants (strength at maximum strain). The discontinuous material response to test loads, as well as the actual visco-elastic material behavior is not adequately considered. In addition, there is no physically defined characterization of the linear load-deformation region (linear-visco-elastic (LVE) region) of sealant materials, as illustrated in Fig. 2. Instead, empirical relations are specified with respect to material design stresses using a fixed factor of safety versus the tensile stresses. Primary load dependencies of the materials, as well as dynamic effects or load superposition, are only partially considered (see Fig. 2); this leads to a situation where only single-point loading conditions are verified where, in fact, multidimensional loading conditions exist. This predominantly empirical assessment methodology also affects the general standard of safety represented by the actual test catalogue for initial component testing, factory production control, and third party monitoring. A limited review of the mechanical behavior of the material, generally, also limits the significance of design even if modern technical tools, such as finite-element-method (FEM) analysis, are available. Moreover, an oversimplification of the

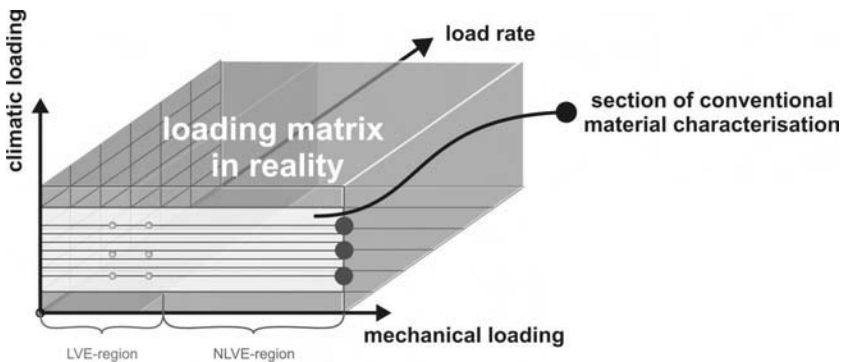


FIG. 2—Classification of material characterization with regard to real loading.

theoretical design model is apparent. Real stress distributions in circumferential adhesion joints (four-sided adhesion bond) and under superimposed loading, as well as effects of geometrical defined points of discontinuities are neglected. Furthermore, load transfer (bearing capacity), considering the planar load bearing capability by the pane-framework-interaction, is not sufficiently taken into account.

Another issue relates to the assessment of the long-term performance of the sealant products and of the complete SSG system. Current assessment methods are predominantly based on decoupled loading tests that involve rupture tests after conditioning (accelerated weathering exposure) of the components. There is no simultaneous superposition of weathering loads (e.g., resulting in quasi-static and/or dynamic mechanical loading) to the primary structural loads. What is also missing is a method suitable for estimating the remaining life (durability) of deteriorated sealant material when conducting a safety assessment of existing buildings. Simultaneously, the design of the common test specimen, which is representative of the structural sealant joint (SSG), is oversimplified. All these issues suggest that a more detailed knowledge of the expected performance of SSG systems is required, especially with regard to its long-term performance (durability) under in-service conditions. Within this context, the fatigue behavior of products and systems should also be explored to ensure their long-term performance and to verify the sustainability of SSG solutions. It must, of course, be considered that SSG solutions, as has been reported, have had good performance over several decades. To explore, in a scientific way, the reasons why is motivation to complement the existing predominantly phenomenological-empirical assessment method by a performance-based method consisting of:

- dynamic-mechanical material analysis (DMA), and
- dynamic-mechanical system analysis.

A schematic of the approach to such a complementary methodology is given in Fig. 3. It is supposed that this methodology would ultimately provide an improved design method, as well as useful durability criteria for SSG materials and systems that, in turn, would also perhaps further improve acceptance of this innovative technology.

This contribution reports about exemplary first material investigations and describes their integration into a complex system test method according to the methodology proposed.

Approach Toward a Performance-Related Material Identification and Deduction of Mechanical Characteristics by DMA Methods

Earlier Development of DMA Methods—Although dynamic-mechanical material analysis is a very common tool in polymer technology (even in the exploration of visco-elastic materials), and in spite of the predominant influence of shear loads on the material performance in this specific field of adhesive application, its adaption in the field of SSG sealant materials for the performance-based identification, quality protection, and further material exploration is still

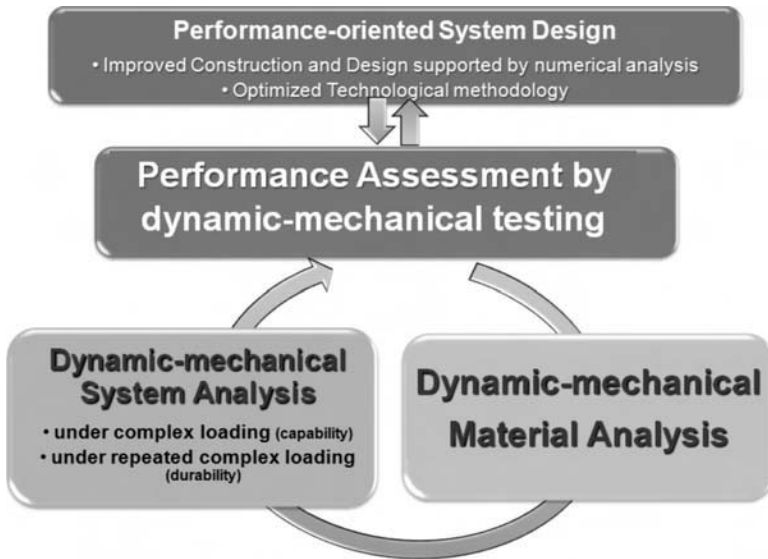


FIG. 3—Schematic of proposed methodology for a complementary approach.

in an early-development stage. In a recent review of silicones in industrial applications [2] the application of DMA to determine the frequency-dependent material characteristic of silicone materials for electronic applications is reported. Temperature regions with fundamental mechanical phase transition are also reported for silicone-based coating materials in electronic technologies [3]. In recent years, the potential of dynamic-mechanical material analysis for sealant characterization is increasingly exploited. Its suitability for a comparative exploration of temperature-dependent visco-elastic properties of epoxy, acrylate, and silicone sealants is reported by Weller and Nicklisch [4] as one of the latest research trends. Gordon et al. [5] extend the use of DMA into the field of fatigue investigations, taking the importance of cycling shear loading into account. Based on our own experiences in the field of joint sealing compounds for pavements [6,7] this contribution builds on these suggestions for an extended dynamic-mechanical material test methodology—not only for material identification—but also for technological as well as durability aspects. These considerations were substantially advanced by the latest improvements in measurement technology.

More Recent Developments—Technical developments in measurement techniques and device development over recent years extended the range of use of DMA not only for the testing of solids but also permitted superimposing both mechanical (even multi-axial) and climate loading (as illustrated in Fig. 4). Examples of these technical developments are:

- rotational motor with speed ranges over nine decimal orders of magnitude and friction-free air bearing with high stiffness (torsional moment up to 300 mNm),

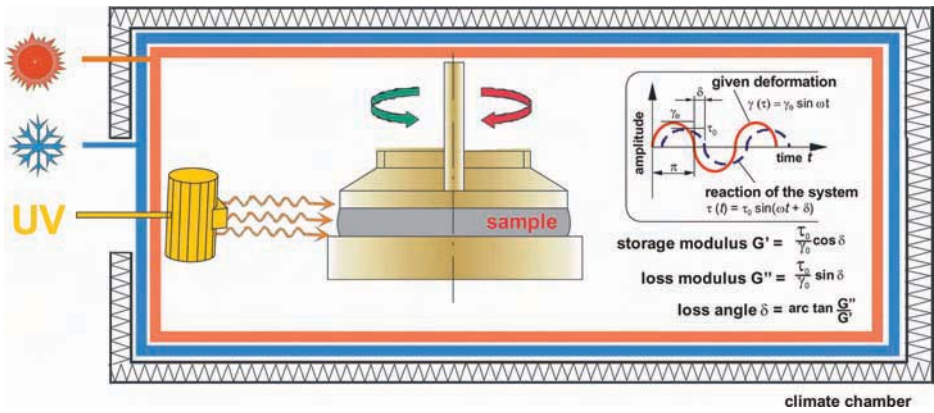


FIG. 4—Schematic illustration of dynamic-mechanical material testing.

- optical encoder for deformation measurement with high resolution ($\sim 0.1 \mu\text{rad}$), and
- additional independent force control for applied normal forces.

Using the advantages of such a measurement technique, a comprehensive material characterization can be obtained for structural sealants in every material phase or phase of working life (e.g., wet, pre-cured, during cure, post-cure, in solid state, under fatigue, artificially aged, etc.). This permits investigations of technical characteristics of sealant materials when wet and soft (prior to being applied), thereafter determining the curing behavior and kinetics of cure, and allows extension to the analysis of the cured sealant at different life-cycle stages as well. Such evaluation may also include an analysis of the material characteristics of already-loaded or damaged material.

Apart from the characterization of the mechanical properties of sealant materials, this approach also permits determining the morphology of the polymeric structure. Encouraged by our previous experiences in the development of a performance-related identification and classification of various polymers used in roadway construction [6–8], it is proposed that the same measurement technique and methodology may be suitable for the development of methods adapted to the characterization of SSG sealant products.

The methodological approach for a characterization of SSG sealant products and—based on the performance-based material exploration—in a second step, the extension to the exploration of system behavior is to be developed within a new research project, sponsored by the German Federal Ministry of Economics and Technology (BMWi) over the next 3 years as a cooperative effort between various industrial partners and the BAM Federal Institute for Materials Research and Testing, Berlin. This paper provides information on preliminary investigations on the use of DMA measurement methods adapted for silicone-sealant materials for SSG systems. In addition, an outlook on the complementary system test methodology is provided to present the comprehensive character of the new approach.

Experimental Studies

Basics—It is common practice in mechanical polymer analysis to describe the complex viscoelastic material behavior as shown in Eqs 1–3:

$$\text{storage modulus: } G' = \frac{\tau_0}{\gamma_0} \cdot \cos \delta \quad [Pa] \quad (1)$$

$$\text{loss modulus: } G'' = \frac{\tau_0}{\gamma_0} \cdot \sin \delta \quad [Pa] \quad (2)$$

$$\text{loss angle: } \delta = \arctan \frac{G''}{G'} \quad [^\circ] \quad (3)$$

$$\text{shear deformation (SRF): } \gamma = \frac{(c_1 \times b \times \varphi_A)}{(c_2 \times L)} \quad [\%] \quad (4)$$

where τ = shear stress and γ = shear deformation (see also Fig. 4; for a more detailed definition of these parameters and their response to stress, deformation, or temperature see Ref [9]). These characteristics subdivide the complex shear modulus G^* into its viscous and elastic components (see Eq 5):

$$|G^*|^2 = G'^2 + G''^2 \quad (5)$$

The methodological tool for exploring these characteristics is the dynamic-mechanical analyzer (DMA) (see also Fig. 4). In addition to the mechanical exploration of materials in various states and exposed to different loading histories as offered by this method, it also provides a direct link to the assessment of the material's inner structure (morphology). A modern dynamic spectrometer, such as the MCR 501 by Anton Paar GmbH² used in this study, completed by special equipped climatic loading devices, is the experimental basis for the material analysis in different test modes (see Fig. 5).

The development of adapted performance-related material characterization using DMA and first investigations to verify this methodological concept on typical SSG materials was done within the following categories:

1. identification of the complex mechanical material behavior,
2. response to technological characteristics such as curing kinetics and processing, and
3. response to fatigue and ageing effects.

Material—To transfer and validate this material test approach, specimens of three types of silicone-sealant products (characteristics are shown in Table 1)

²Anton Paar GmbH, 73760 Ostfildern, Germany, http://www.anton-paar.com/1_corporate_en

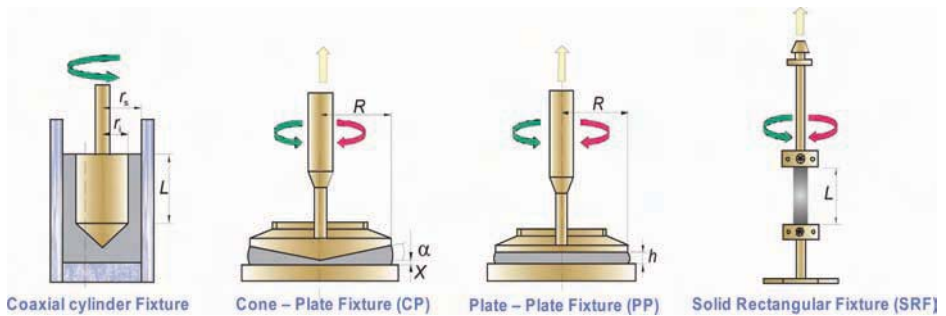


FIG. 5—DMA-test modes in the universal spectrometer *Physica MCR 501* by Anton Paar (for more detailed information, see Ref [9]).

were cast and cured in controlled laboratory conditions (curing time >20 days at +23°C; relative humidity (RH) ~45%). The filler content was determined in accordance with the procedure laid out in the EOTA recommendation [1] with the help of thermogravimetric analysis (heating rate 10 K per minute).

Bar-shaped specimens with dimensions of $25 \times 10 \times 3 \text{ mm}^3$ (length \times width \times thickness of test geometry between the clamps) were cut from laboratory cured sheets of the sealants (3 weeks of cure) for the exploration of the complex dynamic-mechanical behavior in the solid state. For this study, the solid rectangular fixture was used for this DMA test mode. The technological and curing characteristics were investigated within this study by the plate-plate fixture on, respectively, soft and wet samples of the sealants. Analysis and interpretation of the measured parameters are discussed in detail by Mezger in his textbook [9].

Results of Dynamic-Mechanical Material Analysis

Identification of the Complex Mechanical Material Behavior

A precondition to the physically correct identification of the complex mechanical material behavior is the determination of the linear-visco-elastic range of materials properties (LVE region). In this region, a controlled loading causes a proportional material response without any irreversible structural deterioration. In addition, this region also provides some first information about the material's structure.

Figure 6 shows that, even at lowest temperatures down to -60°C , all sealants tested in this study are able to accommodate shear deformations of at least 1%. In detail, the sealants exhibit different responses; however, in general, G' was around ten times larger than G'' , which corresponds to a visco-elastic-solid behavior. The material's stiffness ranking under controlled increasing shear amplitudes at -60°C was as follows: Sealant A > Sealant B \gg Sealant C. The bearable shear deformation γ [%] inside the LVE range for Sealant C is around 9 times higher compared to Sealants A and B. To induce any specimen

TABLE 1—*Sealant materials used in the validation of DMA test approach.*

Material	Material type	Cure classification	Activator	Status
A	1 part Filler content: 33 mol. %	RTV-1 (polycondensation cure)	Air humidity	ETAG approval
B	2 part Filler content: 25 mol. %	RTV-2 (polycondensation cure)	Curing agent (part B)	ETAG approval
C	1 part Filler content: 32 mol. %	HTV (polyaddition cure)	Heat (120–140 °C)	Experimental product

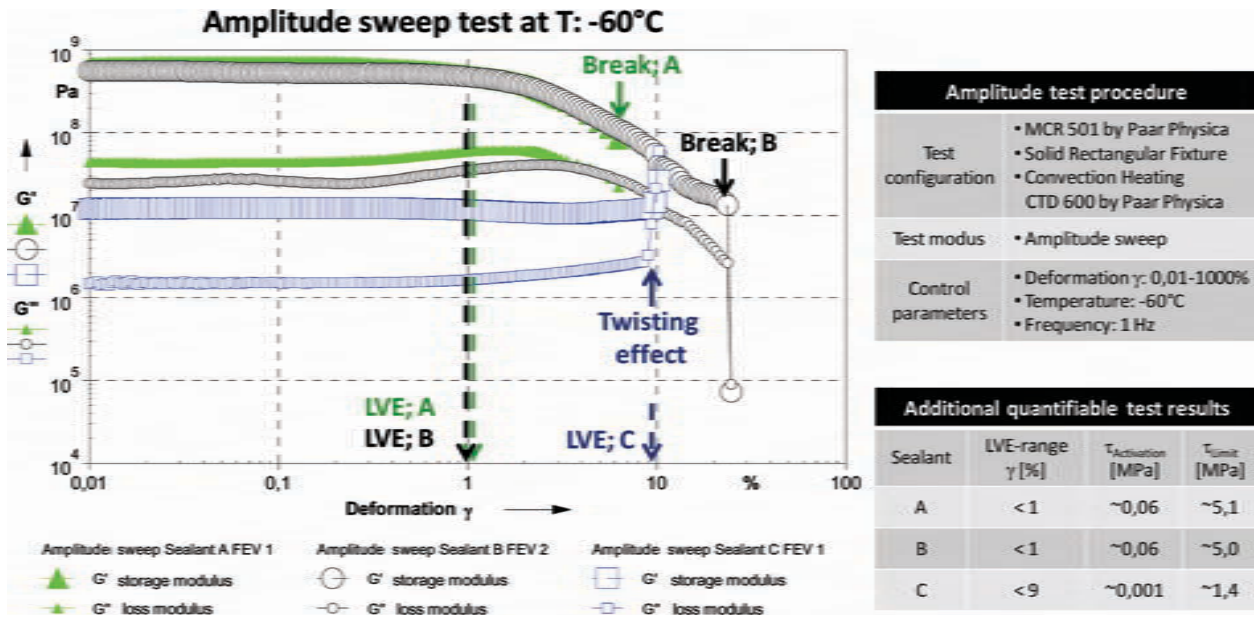


FIG. 6—Storage modulus G' and loss modulus G'' as a function of the deformation amplitude (amplitude-sweep mode at -60°C).

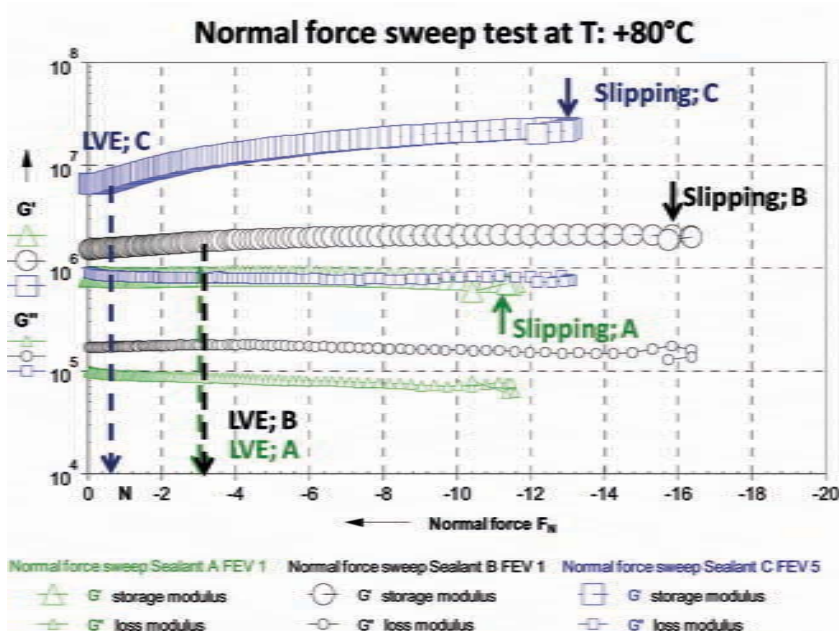
deformation the activating shear stress $\tau_{\text{Activation}}$ for Sealants A and B is much higher. Maximum shear stresses τ_{Limit} above 5.1 and 5.0 MPa, respectively, create irreversible structural deterioration in Sealants A and B specimens, leading to break failure. The maximum test shear stress τ_{Limit} for Sealant C is 1.4 MPa, however, without any specimen deterioration but leaving the use conditions of this test equipment. Another precondition, to make DMA measurements on cured solid sealants with the solid rectangular fixture feasible, was the determination of the maximum tolerable normal force providing physically exact test conditions, without causing structural effects in the sealant specimen.

Interpretation of the results shown in Fig. 7 for the three sealants studied here suggest that at a temperature of $+80^{\circ}\text{C}$ —which seems to be a suitable estimation of the temperature exposure sealants experience during summer [10]—tensile forces of up to 0.7 N do not indicate any structural changes in the sealants. Normal forces above this value indicate leaving of the LVE range for Sealant C. That's why we decided to use this normal force as the control value for all sealant tests with solid rectangular fixture (SRF; see Fig. 5) identifying the complex material behavior. Normal force values above F_{max} . (see Fig. 7) cause slipping effects between the specimen and clamping device, which have to be avoided to ensure reproducible test conditions.

Quite important information about the complex mechanical behavior of the sealants can be deduced from subjecting the specimens to the temperature-sweep mode, where the temperature dependency of the storage and loss moduli (i.e., G' and G'') are quantified. In addition, this sweep mode allows one to obtain detailed polymeric material structural information (morphology) with respect to thermal effects.

According to Fig. 8, over the full range of test temperatures, all sealants show a visco-elastic-solid behavior ($G' > G''$). Sealants A and B are very similar in mechanical behavior but differences in absolute stiffness are evident. Both sealants exhibit changes in temperature-dependent stiffness between $+60^{\circ}\text{C}$ and the end of the rubber-like elasticity range, which is below temperatures ranging between -57°C and -61°C . Entropy-elasticity effects with increasing temperatures were not detected inside the rubber-elasticity range of the sealants, probably attributed to the test configuration chosen. Nearly complete temperature independence of the moduli was evident down to temperatures of -73°C for Sealant C, and this feature characterizes this product as having the broadest field of application. The ranking of the sealant products investigated in terms of stiffness at temperatures ranging from -60°C to $+150^{\circ}\text{C}$ was as follows: Sealant C \gg Sealant B $>$ Sealant A. It is interesting to note that the ranking with respect to the stiffness of the different products was unrelated to the filler content (shown in Table 1 and Fig. 8 as mass% of total formulation); this suggests that either the crosslink density is decisive in influencing the temperature-dependent stiffness or different kinds of fillers were used in these products.

A detailed evaluation of the temperature dependency, e.g., of $\tan\delta$ (ratio G''/G'), yields information on general phase change or transition temperatures. Resulting from the temperature-sweep investigations we found three characteristic effects by T_1 (low transition temperature, indicating lower end of rubber-elasticity region), T_2 (high transition temperature, indicating upper end of



Normal force amplitude test procedure

Test configuration	<ul style="list-style-type: none"> • MCR 501 by Paar Physica • Solid Rectangular Fixture • Convection Heating CTD 600 by Paar Physica
Test modus	<ul style="list-style-type: none"> • Normal force amplitude sweep
Control parameters	<ul style="list-style-type: none"> • Normal force: 0 – (-70 N) • av. force rate: ~ 0,01 N/s • Temperature: +80°C • Deformation γ: 0,1 % • Frequency: 1 Hz

Additional quantifiable test results

Sealant	LVE-range F_N [N]	Max. Tension F_{max} [N]
A	<3	<11
B	<3	<16
C	<0,7	<13

FIG. 7—Storage modulus G' and loss modulus G'' as a function of the variation in normal applied force (normal force-sweep mode).

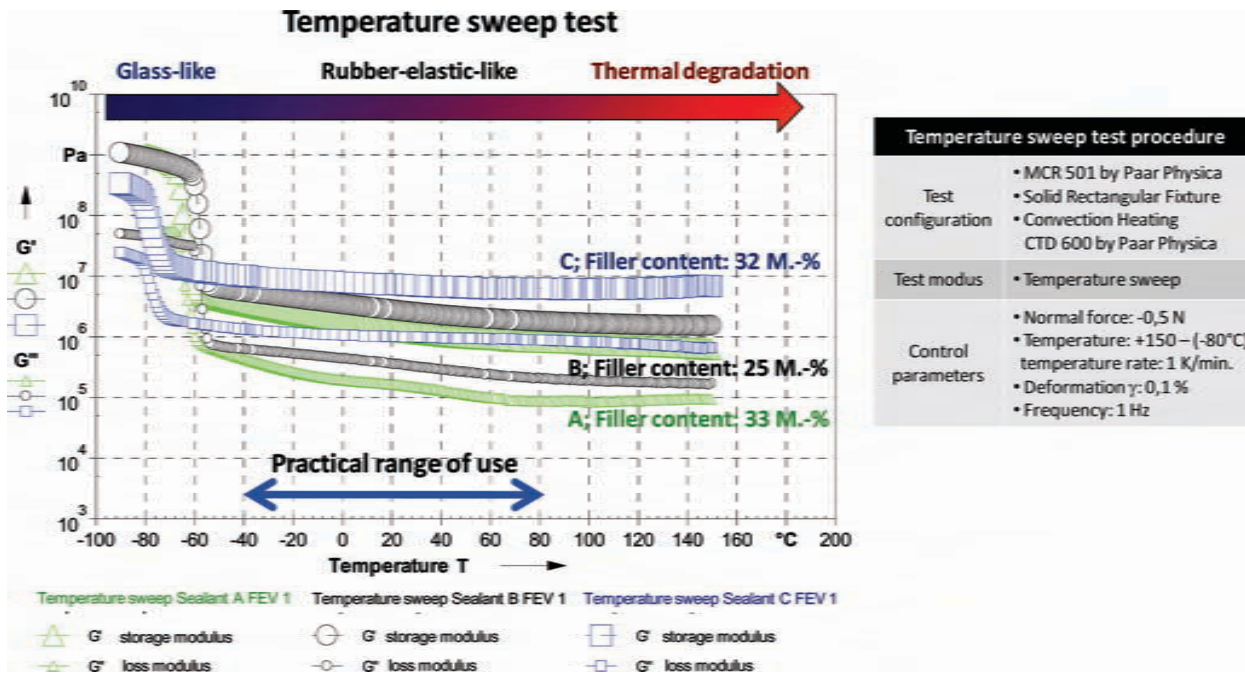


FIG. 8—Storage modulus G' and loss modulus G'' as a function of temperature (temperature-sweep mode).

rubber-elasticity region by melting or, finally, pyrolytic processes), and T_3 (secondary transition temperature, indicating internal structure effects (“areas of relaxation”) without fundamental changes of material performance), which are typical for the formulated product, exploring relevant changes in material performance and which also can be used (as a “fingerprint”) in identifying each product. This kind of assessment underlines the potential of this material test approach also for quality-assurance purposes. Resulting from the temperature-sweep test results for Sealants A, B, and C as shown in Figs. 8 and 9, we found indication for temperature-dependent material effects listed in Table 2.

The determination of the upper phase transition temperature T_2 was supported by additional thermo-gravimetric investigations indicating beginning pyrolytic polymer degradation (not presented here). A traceability of the effects measured to materials composition and their interpretation for more detailed material exploration (differentiation between structural or technological effect), respectively, as well as additional proof of plausibility, e.g., in comparison to other thermo-analytical methods, like DSC, according to variation of loading parameters, will be a task of further investigations. Taking into account possible effects by thermal inertia of specimen geometry (e.g., delayed transition temperatures depending on controlled heating or cooling procedure), a minimized temperature rate was chosen. Nevertheless, it has to be noted that the effects described were strongly connected with controlled cooling test procedures.

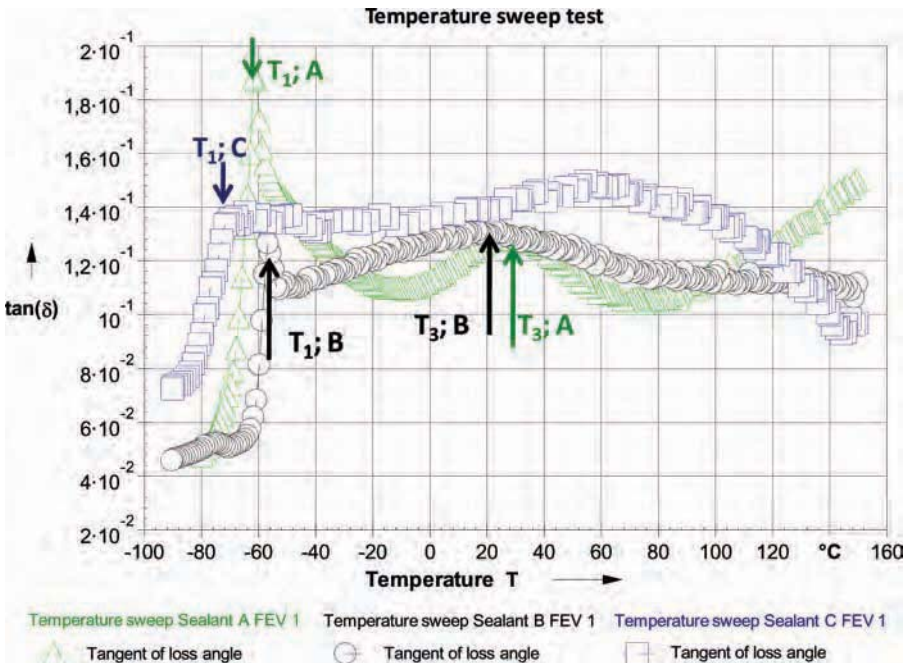


FIG. 9—Tangent of loss angle ($\tan\delta$) as a function of temperature (temperature-sweep mode).

TABLE 2—Material-identifying information by temperature-sweep mode.

Material	Lower transition temperature T_1 (°C)	Upper transition temperature T_2 (°C)	Secondary transition temperature T_3 (°C)
A	-61	+200	+30
B	-57	+200	+20
C	-73	+250	n/a

Taking into account the matrix of decisive loads to which the sealant is subjected in actual service (see Fig. 2), another important aspect is the frequency-dependence of the sealant's mechanical behavior. In frequency-sweep-mode, conducted at +25°C, we obtained moduli graphs typical of cross-linked polymers with steadily low rising slopes between 10^{-2} and 3×10^1 Hz (not shown as figures). As already reported for silicone products (e.g., Ref [2]), simplified repetition of frequency-sweep measurements at various temperatures permits the creation of time-temperature-shift (TTS) master curves using the Williams-Landel-Ferry (WLF) method [11,12] over a substantially extended frequency range for each reference temperature within the service temperature range (see Fig. 10 for an example of a TTS master curve for Sealant A).

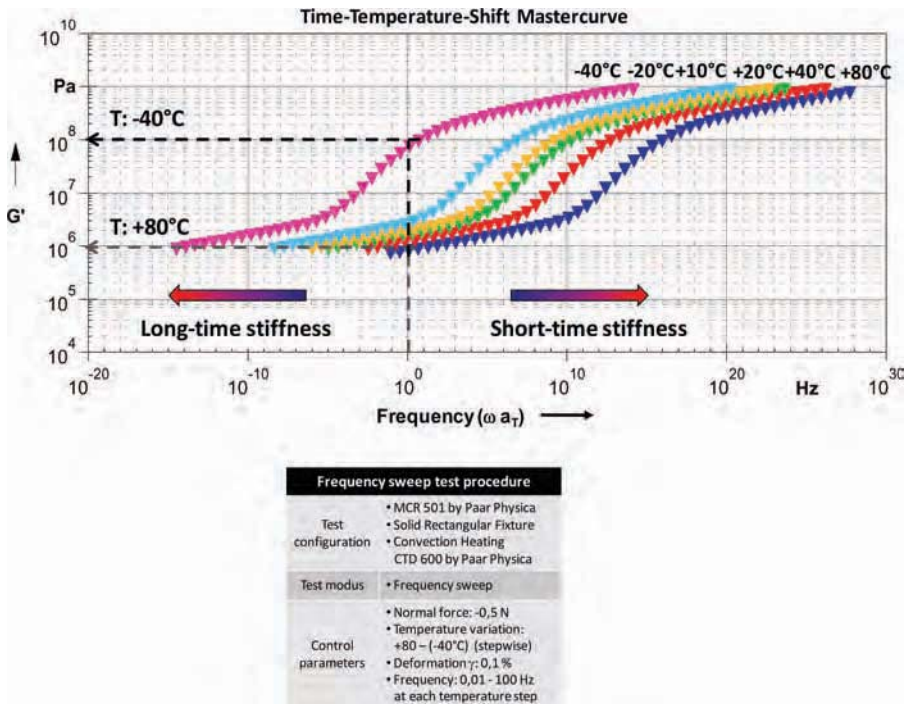


FIG. 10—Time-temperature-shift (TTS) master curves for Sealant A (T : +80, +40, +20, +10, -20, and -40°C).

The theoretical background to the frequency–temperature analogy (i.e., the time–temperature shift) proposed by Williams, Landel, and Ferry can be found in the textbook reference published by Ferry [12]. Use of the WLF method makes mechanical moduli for every temperature or load rate available, which substantially improves the application of modern design tools like FEM during the design process.

Figure 11 compares the time–temperature-shift (TTS) master curves for the three sealants for a given reference temperature of -20°C . The chart also indicates typical frequencies experienced during the service life of SSG sealants, such as static state, wind, seismic, and impact (hurricane debris or explosion blast), and the relevant mechanical behavior of each sealant. Compared to Sealants A and B, the frequency-sweep graph of Sealant C indicates a lower frequency dependency and higher cross-linking degree (see Fig. 11). To validate these first results, as well as to improve the knowledge of temperature–frequency dependencies and their structural effects, further investigations are necessary.

Based on the methods described here for the identification of complex mechanical behavior, the shear moduli for every temperature and loading rate within the LVE region can be determined. If, additionally, the Poisson’s ratio of the material is known, a complete moduli transformation of shear modulus (G) to tensile modulus (E) is possible, permitting new opportunities for modern

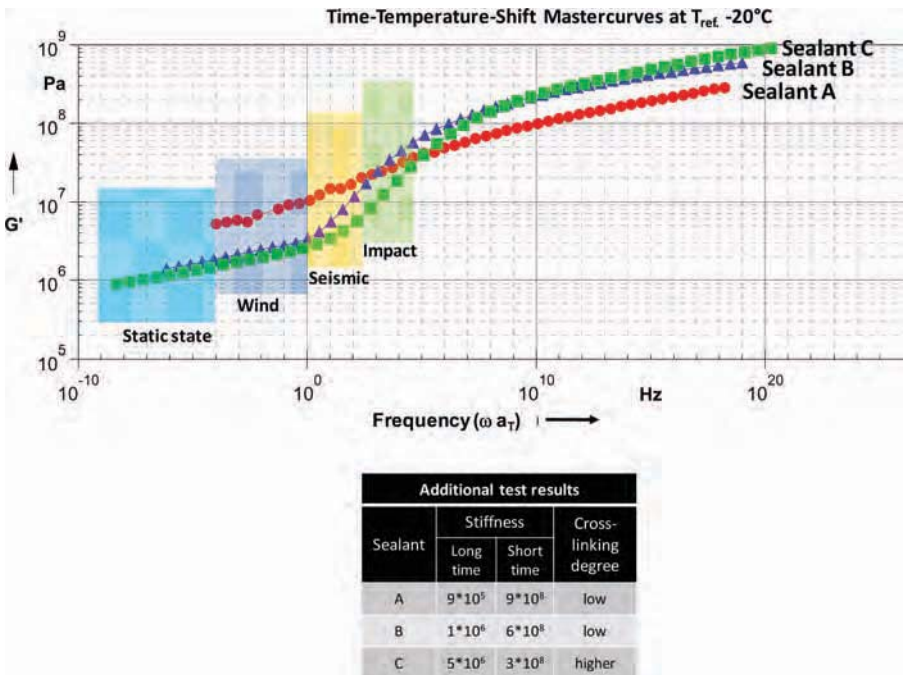


FIG. 11—Comparison of time–temperature-shift (TTS) master curves (for reference temperature $T_{Reference} -20^{\circ}\text{C}$).

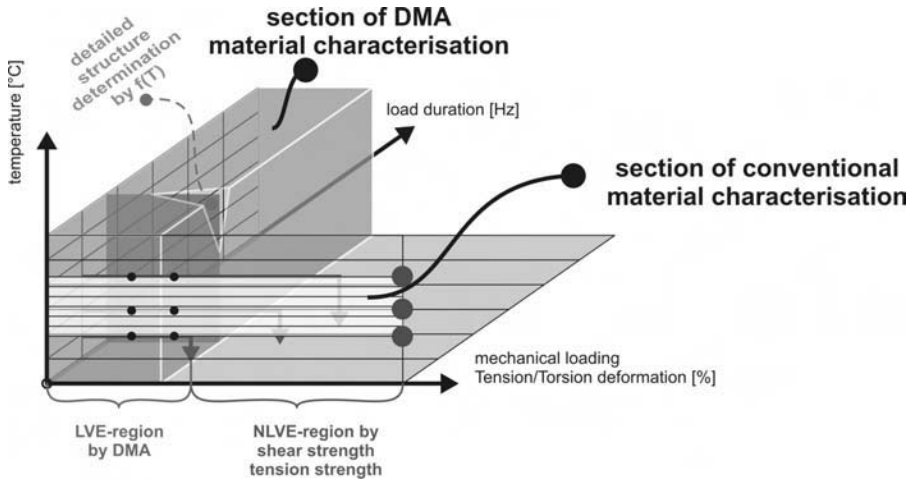


FIG. 12—Identification of the mechanical behavior by dynamic-mechanical analysis (DMA) with respect to material response to loading.

design algorithm (see Fig. 12 for the extended information potential obtained by DMA).

Characterization of Other Technological Properties by DMA

In addition to mechanical material exploration, the DMA technique also can be employed in further performance-related investigations. For instance, an investigation of the rheology of the wet (uncured) sealant can be utilized in characterizing the sealant's behavior during installation or handling processes.

The comparative illustration in Fig. 13 shows a higher zero-shear viscosity for Sealant A (pasty, bitumen-like) compared to Sealant B (syrup-like) indicating an easier handling with lower shear loading for the latter. To achieve flow, a certain yield limit has to be exceeded for Sealant A, which simultaneously can be an indicator for the deformation resistance (stability) during processing. To extrude Sealant A from a conventional cartridge requires a force of at least 62 N. Shear loading above a shear rate of 6×10^0 , corresponding to a rotational speed above 5 rpm for Sealant A, and a shear rate of 4×10^0 corresponding to a rotational speed above 3 rpm for Sealant B, respectively (see Fig. 13), comprises the danger of flow interruption or air infiltration.

An exploration of the technological material characteristics is not complete without an evaluation of the curing processes, especially the exploration of curing under special environmental conditions. Figure 14 highlights the potential to explore such curing behavior by DMA material analysis for Sealants A and B under exploitation of the minimized mechanical loading options by our modern test equipment. At climatic conditions of approximately $+30^\circ\text{C}$ and 40% RH, the reactive Sealant B (two part) attained after 24 h asymptotically an equilibrium stiffness state but exhibited via a secondary stiffness increase a

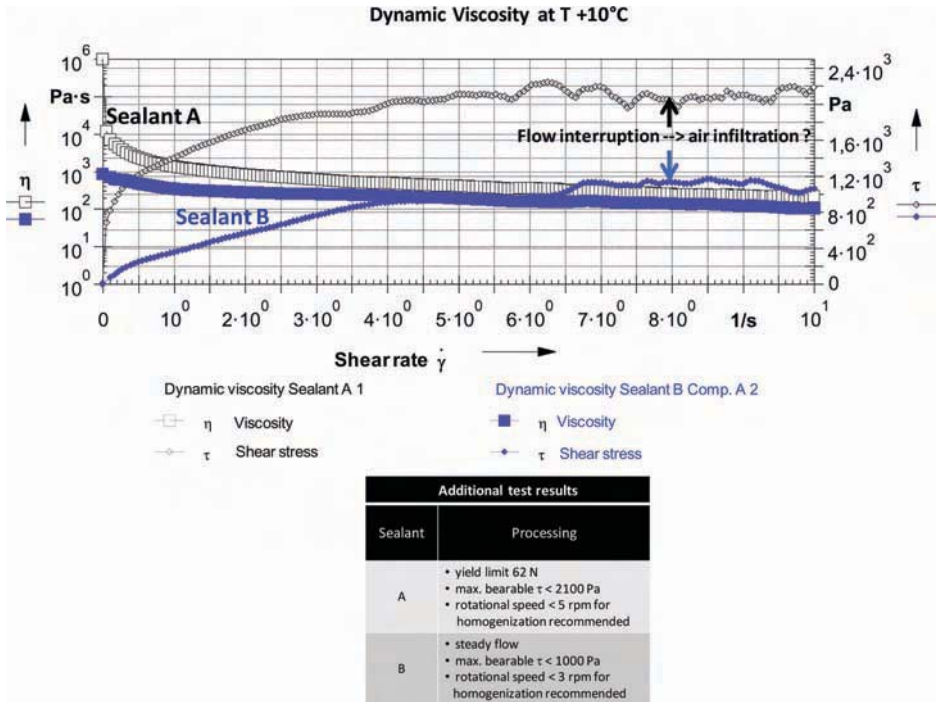


FIG. 13—Rheology of Sealants A and B (after mixing of parts A and B) at critical processing temperature (+10°C).

consecutive reaction (cross-linking), which was even not finished after 48 h at the end of the test. Apart from the outer boundary area of the plate-plate-test geometry, Sealant A (one part) shows, even after more than 14 days, no completion of the cross-linking, although test geometry mirrors the geometrical conditions of a real sealant joint geometry.

According to the DMA tests, also the thermal curing of Sealant C was not completely finished within the recommended curing duration. Considerable secondary stiffness increase indicates consecutive cross-linking (not shown as figure here). In summary, the time-sweep mode used in this part of the investigation could prove its suitability for evaluating curing kinetics of SSG sealants and provide additional opportunities for further investigation, even under superimposed mechanical loading if so desired.

Characterization of Fatigue and Aging Effects

To complete the investigation of the assessment potential of the DMA material testing approach, initial studies to qualify and quantify fatigue and ageing effects were done. A permanent loading of the sealing joint (e.g., one that might result from the permanent (dead) load of the glass pane) under adverse conditions of + 80°C was simulated in the creep-test mode. According to Fig. 15, after

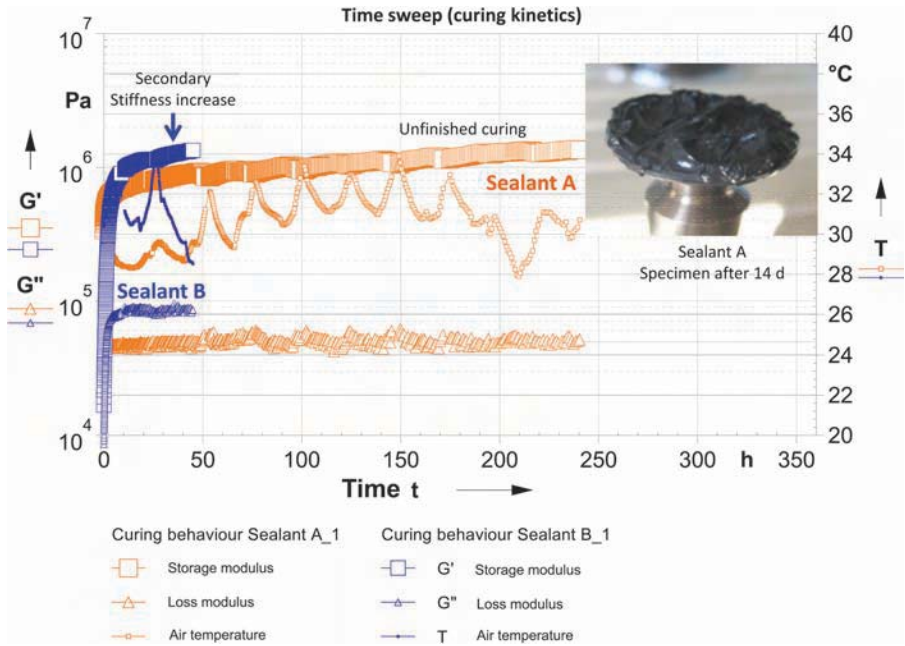


FIG. 14—Curing kinetics for Sealants A and B at +30°C and 40 % RH (time-sweep mode).

20 h of loading, the typical creep deformation, and after an additional release period of 4 h, the material resilience, respectively, permanently viscous deformation could be determined for the three sealants that were exemplarily tested. A time-dependent stability ranking was determined for the sealants as follows: Sealant C \gg Sealant B > Sealant A. Converted to the geometrical conditions of a 12 \times 6 mm² joint (width \times depth), the maximum measured viscous deformation range from 1.6 mm (Sealant A) to 0.6 mm (Sealant B) down to 0.1 mm (Sealant C). Under a permanent load of 0.1 MPa from the time-deformation curve, it was apparent that Sealants A and B had distinctive visco-elastic material characteristics, whereas Sealant C exhibited predominating elastic behavior.

Even for a five times higher permanent load of 0.5 MPa, creep deformation of less than 0.3 mm without any remaining viscous effects after load removal were observed for Sealant C, underlining its special performance (not shown in figure here).

The potential to detect effects of artificial weathering was evaluated by comparative measurements in temperature-sweep mode for Sealants A and B before and after 1300 h of weathering (see Fig. 16). Weathering was carried out according to ASTM C 1442-11 [13]. As can be seen from Fig. 16 for Sealant A, the comparatively lower and steady course of the complex shear modulus G^* after weathering indicates subsequent curing effects (induced by the weathering regime). A secondary transition temperature (T_3) is no longer detected from the

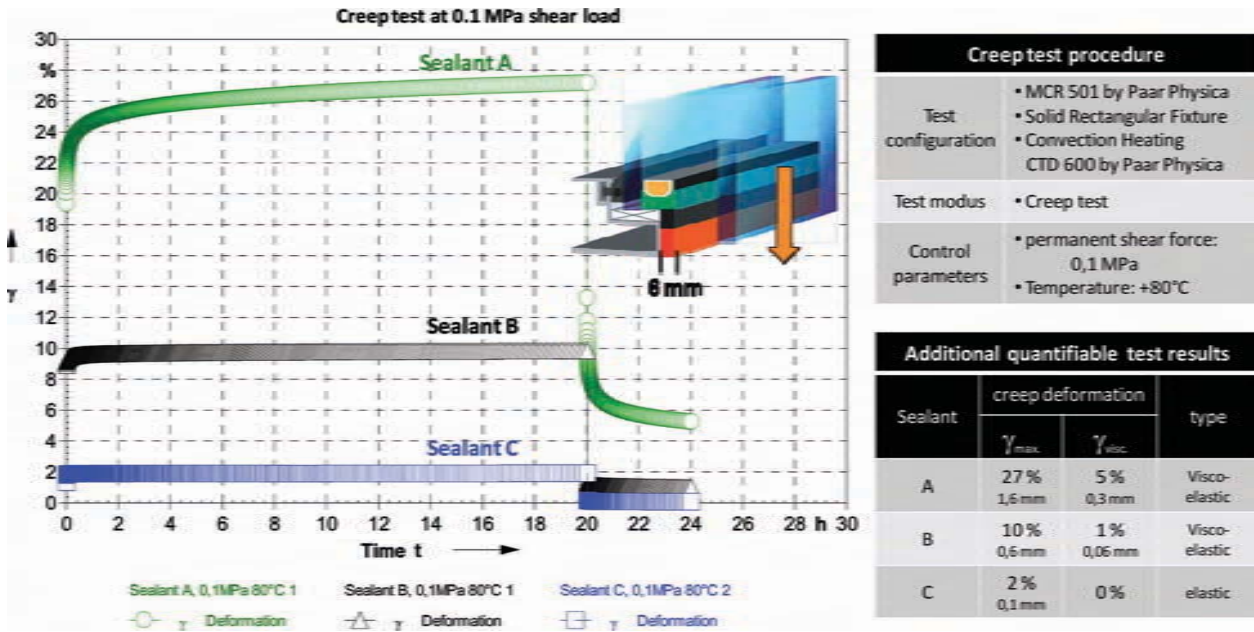


FIG. 15—Creep-test results at +80°C under 0.1-MPa permanent load (creep-test mode).

Creep test procedure	
Test configuration	<ul style="list-style-type: none"> • MCR 501 by Paar Physica • Solid Rectangular Fixture • Convection Heating CTD 600 by Paar Physica
Test modus	• Creep test
Control parameters	<ul style="list-style-type: none"> • permanent shear force: 0,1 MPa • Temperature: +80°C

Additional quantifiable test results			
Sealant	creep deformation		type
	γ_{max}	γ_{visc}	
A	27 % 1,6 mm	5 % 0,3 mm	Visco-elastic
B	10 % 0,6 mm	1 % 0,06 mm	Visco-elastic
C	2 % 0,1 mm	0 %	elastic

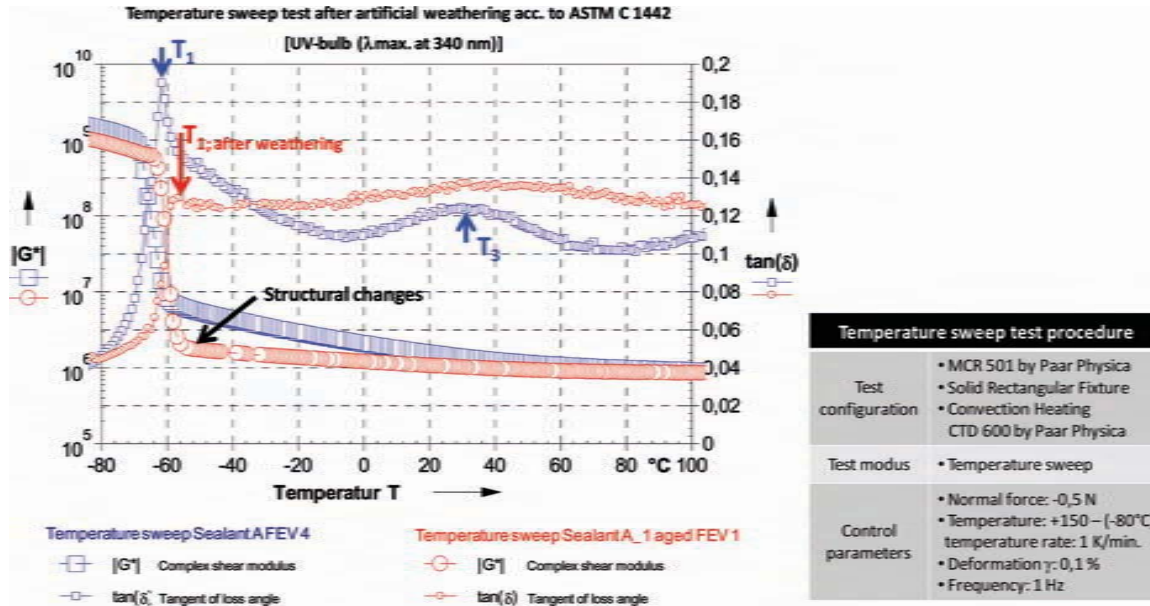


FIG. 16—Response of DMA traces to artificial weathering (temperature-sweep mode).

trace of $\tan\delta$ indicating changes of the inner network. In addition, Sealant A exhibits, after weathering, a shift of the low transition temperature T_1 to a 4°C higher value. The mechanical behavior of Sealant B, after 1300 h of weathering according to ASTM C 1442, is not affected (not shown in figure here).

The author recommends that in future studies the mechanical response of SSG sealants to superimposed artificial fatigue and ageing exposure within the dynamical spectrometer device itself should be evaluated. A first validation attempt in this direction was made in this study using superimposed independently controlled shear and tension loading in combination with temperature and UV loading as a simplified durability test mode on the three sealants. The sealants were subjected to:

- $\pm 10\%$ torsional deformation at a frequency (f) of 0.1 Hz to simulate effects of daily temperature changes acting on the sealant joint,
- a constant normal force of 3 N to simulate the effects of permanent (dead) loading,
- continuous UV-light exposure (λ_{\max} . at 365 nm) with 452 Wh/m², and
- constant temperature of + 80°C.

As can be seen from Fig. 17, Sealant A exhibited a considerable decrease in stiffness (50%) after 7200 load cycles that were meant to replicate daily temperature changes on the outside of a building. The behavior of parameter d (representing the specimen length) under this aging regime indicates permanent flow. Although the stiffness loss rate decreased already, after around 23500 load

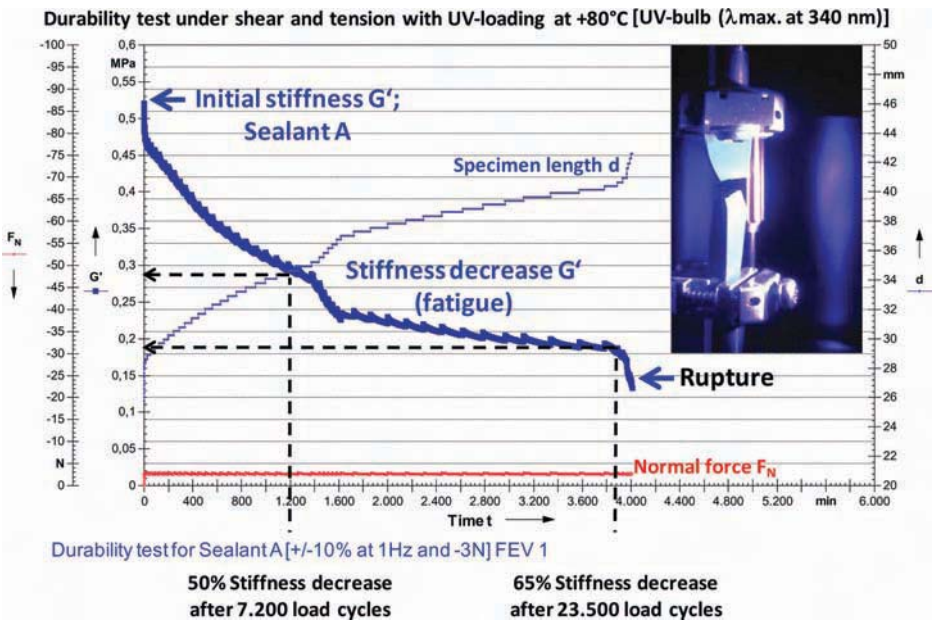
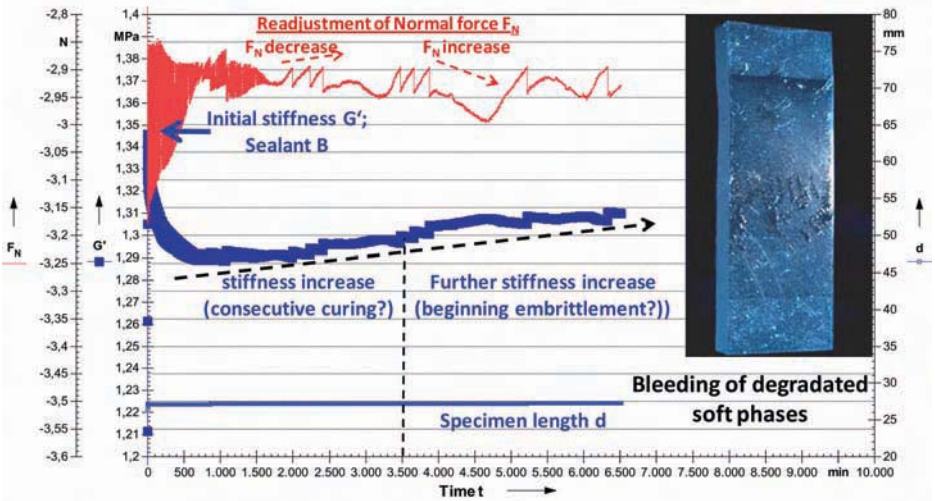


FIG. 17—Response of mechanical properties to superimposed loading (Sealant A).

Durability test under shear and tension with UV-loading at +80°C [UV-bulb (λ .max. at 340 nm)]



Durability test for Sealant B [+/-10% at 1Hz and -3N] FEV 1

FIG. 18—Response of mechanical properties to superimposed loading (Sealant B).

cycles, the remaining stiffness was only 35% of the initial value. The sealant was able to sustain in total 24000 load cycles before failing cohesively.

In contrast to Sealant A, Sealant B displayed much greater “durability” (see Fig. 18). After an initial stiffness decrease to adjust to the system tuning (to reach a balanced system state under loading), the stiffness steadily increased. Although not all structural processes are clarified, a subsequent curing is to be expected for the first test period (up to 3500 min) taking into account the results of the investigation of curing behavior. An explanation for the simultaneously occurring slight normal force decrease can be possibly a “wear-out” effect caused by fatigue, but this is compensated for, because of the normal force readjustment to 3 N. After more than 3500 min of loading time, a slight stiffness increase is correlated with increasing normal forces. This effect was interpreted as the beginning of an embrittlement of the cured sealant. This is also in agreement with the visual appearance indicating ageing effects by a shiny glazed specimen surface opposite to the UV source. After 39000 load cycles (daily temperature changes), no mechanical failure was detected. Although not all effects are, at this stage, fully evaluated, the dynamic-mechanical material test approach presented here provides an assessment of the sealants’ behavior under fatigue and ageing loading.

Proposed Approach for the Exploration of System Capability and Durability

Based on the fundamental knowledge identified in the dynamic-mechanical material analysis, the assessment approach can be consequently complemented by

an assessment tool able to validate capability and durability of the complete glazing system (glass-pane-sealant-frame) and its interaction with regard to its actual performance. Previous experiences with capability and durability performance assessment of pavement joints under load superposition are available as a general foundation for a practical adaptation of this approach on SSG systems [6–8,14]. Based on the needs and requirements, and taking into account the performance-related assessment concept, such a system test must demonstrate the following:

- the functional capability in terms of flexibility, cohesive and adhesive bond strength, indication of imperfections, and debonding,
- the durability in terms of fatigue strength and long-term cohesive and adhesive bond strength under superimposed mechanical and climatic loading,

the technical basis for the realization of this complex system testing approach will be a special adapted testing device (see Fig. 19).

The test facility includes a mechanical loading device to simulate quasi-static and/or dynamic horizontal and/or vertical deformations to emulate various axial and/or multi-axial stress conditions. The loading device is situated in a climate chamber able to apply a simultaneous simulation of the relevant climatic loads, i.e., temperature changes in the range -20 to $+60^{\circ}\text{C}$, rain, relative humidity in the range 40–95%, and UV irradiation with a wavelength range of 300–400 nm. Both loading devices (mechanical and climatic) are synchronized by a central control unit, thus allowing operation in single as well as coordinated, superimposed loading modes in numerous variations.

Summary and Outlook

A reflection of the given situation in material development, design, and use of SSG façades reveal the immediate need for better knowledge of material and system performance and durability. Complementary to the existing conventional approach, a coordinated dynamic-mechanical testing approach consisting of material and complex system tests is foreseen to improve the performance-oriented system design and durability prognosis. Based on preliminary material investigations on different sealants with a dynamic-mechanical spectrometer, the general potential of the approach was evaluated in this study. Based on the findings of this study, it appears possible to adapt this performance-related material test methodology to the field of SSG sealants. The various test results shown in this study demonstrate that the complex mechanical behavior of the sealant materials can be identified when exposed to specific load variations. The complex shear moduli are quantifiable. With it, a precondition for a subsequent numerical analysis and modeling seems to be given, because the knowledge of these parameters allows the use of modern tools, such as FEA, for the numerical design of glazings. The dynamic-mechanical test methodology also provides response to the materials structure, its technological behavior (extrusion, application), as well as to fatigue and ageing effects. Once the potential of the dynamic-mechanical material test methodology has been

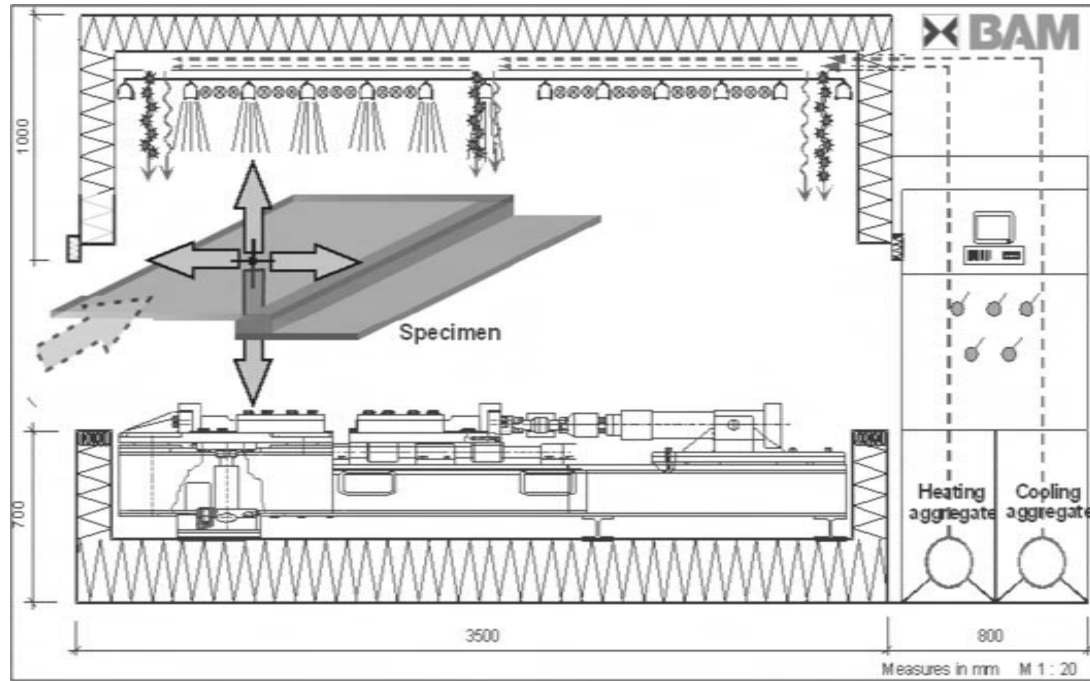


FIG. 19—System test device for complex loading.

further validated, it could also underpin the development of improved technical rules by building code authorities.

Acknowledgments

The writer would like to thank the German Federal Ministry of Economics and Technology (BMWi) for the support on this interesting research task, as well as our industrial cooperation partner for providing the sealant materials. The writer is especially indebted to our colleague Mr. Ch. Huth for conducting the specimen preparation and the DMA material tests under extreme time pressure.

References

- [1] EOTA Recommendation, 1999, "ETAG 002 Structural Sealant Glazing Systems, Part 1: Supported and Unsupported Systems," *Guideline for European Technical Approval for Structural Sealant Glazing Systems*, European Organization for Technical Approvals (EOTA), Brussels, Belgium.
- [2] Andriot, M., Chao, S. H., Colas, A., Cray, S., de Buyl, F., DeGroot, J. V., Dupont, A., Easton, T., Garaud, J. L., Gerlach, E., Gubbels, F., Jungk, M., Leadley, S., Lecomte, J. P., Lenoble, B., Meeks, R., Mountney, A., Shearer, G., Stassen, S., Stevens, C., Thomas, X., and Wolf, A. T., "Silicones in Industrial Applications," *Inorganic Polymers*, R. DeJaeger and M. Gleria, Eds., Nova Science Publishers, Hauppauge, NY, 2007, pp. 61–161.
- [3] Suppa, M., "Use of Silicone as Coating Material for Electronic Devices," *Plus*, No. 09, 2005, pp. 1609–1615.
- [4] Weller, B. and Nicklisch, F., "Bonding of Glass—Latest Trends and Research," *Proceedings of the 2010 Structures Congress*, ASCE American Society of Civil Engineers, Orlando, 2010, pp. 2545–2554.
- [5] Gordon, G., Lower, L., and Carbary, L. D., "Using Rheology Test Methods to Assess Durability of Cured Elastomers Undergoing Cyclic Deformation," *J. ASTM Int.*, Vol. 6, No. 3, DOI: 10.1520/JAI101975.
- [6] Recknagel, C., Pirskawetz, S., and Huth, C., "Material and System Investigations on Hot-Applied Plastic Compounds" (in German), *Research Report, German Highway Research Institute (BAST)*, Bergisch Gladbach, Germany, 2005, p. 147.
- [7] Recknagel, C., Pirskawetz, S., Huth, C., and Mews, O., "Material and System Investigations on Hot-Applied Elastic Compounds" (in German), *Research Report, German Highway Research Institute (BAST)*, Bergisch Gladbach, Germany, 2007, p. 220.
- [8] Recknagel, C., Pirskawetz, S., Huth, C., and Mews, O., "Material and System Investigations on Elastomer Joint Profiles" (in German), *Research Report, German Highway Research Institute (BAST)*, Bergisch Gladbach, Germany, 2009, p. 179.
- [9] Mezger, T. G., *The Rheology-Handbook*, 3rd ed., Vincentz Network, Hanover, Germany, 2011, p. 432.
- [10] Carbary, L., Bull, E., and Mishra, S., "Development of a Practical Method to Evaluate the Fatigue Properties of Structural Silicone Glazing Adhesives," *J. ASTM Int.*, Vol. 4, No. 1, DOI: 10.1520/JAI100403.
- [11] Anonymous, "Williams-Landel-Ferry Equation," http://en.wikipedia.org/wiki/Williams-Landel-Ferry_equation.
- [12] Ferry, J. D., *Viscoelastic Properties of Polymers*, 3rd ed., John Wiley & Sons, Hoboken, NJ, 1980, p. 672.

- [13] ASTM C 1442-11, 2011, "Standard Practice for Conducting Tests on Sealants Using Artificial Weathering Apparatus," *Annual Book of ASTM Standards*, ASTM International, West Conshohocken, PA.
- [14] Recknagel, C. and Pirskawetz, S., "Joint Sealing Systems for Pavements—A New Approach Towards a Performance Related Evaluation of Capability and Durability," *J. ASTM Int.*, Vol. 6, No. 3, 2009, DOI: 10.1520/JAI101961.

Christopher C. White,¹ Donald L. Hunston,² Kar Tean Tan² and Gregory T. Schueneman⁴

A Test Method for Monitoring Modulus Changes during Durability Tests on Building Joint Sealants

ABSTRACT: The durability of building joint sealants is generally assessed using a descriptive methodology involving visual inspection of exposed specimens for defects. It is widely known that this methodology has inherent limitations, including that the results are qualitative. A new test method is proposed that provides more fundamental and quantitative information about changes occurring in a sealant during durability testing. This test method utilizes a stress relaxation experiment to evaluate the non-linear viscoelastic behavior of sealants. In particular, changes in the time dependence of the apparent modulus can be observed and related to molecular changes in the sealant. Such changes often precede the formation of cracks and the ultimate failure of the sealant. This paper compares results obtained from the new test method and the currently used descriptive methodology.

KEYWORDS: sealant, durability, ASTM C719, ASTM C1519, stress relaxation, modulus

Manuscript received June 1, 2011; accepted for publication October 27, 2011; published online December 2011.

¹Engineering Laboratory, Materials and Construction Research Division, National Institute of Standards and Technology, 100 Bureau Dr., Stop 8615, Gaithersburg, MD 20899-8615 (Corresponding author), e-mail: christopher.white@nist.gov

²Engineering Laboratory, Materials and Construction Research Division, National Institute of Standards and Technology, 100 Bureau Dr., Stop 8615, Gaithersburg, MD 20899-8615.

Certain commercial products or equipment are described in this paper in order to specify adequately the experimental procedure. In no case does such identification imply recommendation or endorsement by the National Institute of Standards and Technology (NIST), nor does it imply that the item identified is necessarily the best available for the purpose.

Cite as: White, C. C., Hunston, D. L. and Tean Tan, K., "A Test Method for Monitoring Modulus Changes during Durability Tests on Building Joint Sealants," *J. ASTM Intl.*, Vol. 9, No. 2. doi:10.1520/JAI104090.

⁴USDA Forest Service, Forest Products Laboratory, One Gifford Pinchot Drive, Madison, WI 53726

Copyright © 2012 by ASTM International, 100 Barr Harbor Drive, PO Box C700, West Conshohocken, PA 19428-2959.

Introduction

Sealants are filled elastomers that are used commonly in structures in order to prevent moisture penetration through gaps, joints, and other openings. These structures span a wide range of diverse applications, including transportation vehicles and medical equipment. The greatest use of sealants, however, is in construction. Studies in the construction industry have indicated a 50% failure rate in less than 10 years and a 95% failure rate within 20 years after installation [1–3]. What makes these failures particularly detrimental is that sealants are often used in areas where moisture induced degradation is difficult to monitor and expensive to repair. Consequently, sealant failure is frequently detected only after considerable damage has occurred. In the housing market, premature failure of sealants and subsequent moisture intrusion damage significantly contribute to the $\$65 \times 10^9$ to $\$80 \times 10^9$ spent annually on home repair [4]. The environmental durability, therefore, is the most demanding requirement of a sealant, as it is the property that ultimately determines the long term service life.

Over the past few decades, extensive efforts have been devoted to investigating environmental effects on the long term durability of sealants and to investigating degradation mechanisms [5–8]. However, the accurate prediction of in-service performance in less time than required for field tests and tests on structures has remained an unsolved scientific issue. One of the main stumbling blocks to its solution is a lack of reliable methods for accurately quantifying the environmental degradation factors in the laboratory and field. Degradation measurements in the descriptive methodology usually involve visual evaluations of physical performance, including crack and chip size, chalking behavior, and color change. Although such a methodology can relate to a customer-perceived failure mode, it is qualitative and time consuming and provides little insight into the mechanisms leading to these macroscopic changes. This makes it difficult to develop models for accurately predicting sealant service life. An approach embedded in materials science could provide theoretical insight into the degradation mechanisms, help develop predictive models, and facilitate the establishment of a quantitative link between field and laboratory exposure results.

The limitations of descriptive methodology have prompted the sealant community to seek improvements in the testing of sealant materials. A recent paper [9] presented a new method that was developed in cooperation with the sealant industry and which offers a solution to some of the issues inherent to the current approach. In this new method, a stress relaxation measurement was employed that monitors temporal changes in stress for a sealant subjected to a fixed strain. From this information, an apparent modulus versus time curve is generated. The magnitude and time dependence of this apparent modulus are related to the molecular structure of the sealant. By monitoring how this modulus changes with exposure time in a degradation experiment, one can estimate changes in the molecular structure of the sealant. Changes in the modulus over time also provide crucial information about how a sealant responds to the stresses imposed by the expansion and contraction of a structure over the diurnal cycle.

In a recent ASTM round robin for ASTM C1519-10, “Standard Test Method for Evaluating Durability of Building Construction Sealants by Laboratory

Accelerated Weathering Procedures,” four sealant samples were subjected to a series of laboratory accelerated weathering procedures and then evaluated using the usual visual inspection methods. The purpose of this paper is to evaluate specimens from this round robin using the new test method and to compare these results against results obtained from conventional evaluations.

Experiment

Materials

The ASTM round robin utilized four sealants that are typical of commercial materials: a silicone, modified polyester, an acrylic, and polyurethane. Specimens were provided to different laboratories. Each laboratory exposed the specimens according to the ASTM C1519-10 protocol and evaluated them after exposure via visual inspection. The specimens were fabricated by curing the sealant between two metal beams in the geometry shown in Fig. 1. This is similar to the geometry specified in ASTM C719 [10]. The specimens were fabricated by one of the primary manufacturers of sealants and were arbitrarily identified by the letters A through D. Specimens of each type of sealant were obtained from one of the participants in the round robin. For each sealant, five replicate specimens were provided: two fresh specimens having no exposure history, and three specimens after exposure according to the round robin protocol.

The specimen geometry used here is a widely accepted industry standard; however, unlike the simple dog-bone geometry, the sealant is constrained where it is attached to the metal bars. Consequently, when stretched, the center region of the sealant can contract laterally, but the sealant adjacent to the metal bars cannot. This means that deformation is not uniform throughout the sample, and an apparent modulus calculated from these tests, E_a , will be different from that obtained in a simple tension test with a dog-bone specimen, E . It is customary to treat this difference by defining a parameter, S , known as the shape factor, where $E_a = S \times E$. As the goal for the test procedure developed in this work is for comparisons using a single geometry, these results will be presented in terms of E_a .

Characterization

Details of the new test method are described elsewhere [9]; briefly, it involves two steps: a preconditioning step and the property measurement step. In the

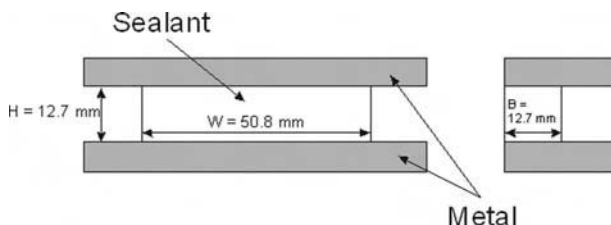


FIG. 1—Schematic illustration of the test geometry used (left side is front view, right side is cross-section).

test, the two metal beams containing the sealant specimen are pulled in tension in the direction perpendicular to the long axis of the specimen. The strain history is schematically shown in Fig. 2. In the first step, the specimens were subjected to two loading-unloading-recovery cycles. The motivation for this step is to quantify the Mullins effect and eliminate its influence in the subsequent characterization measurement. In order to do this, the maximum strain in the two cycles must be larger than any strain seen in the specimen's previous history, and the same maximum strain must be used whenever the procedure is conducted, so results can be compared. For the experiments here, a maximum tensile strain of 26% was employed. This strain level was chosen because it exceeded the typical test movements of $\pm 12.5\%$ and $\pm 25\%$ used in ASTM C719. In addition, 26% strain should not be large enough to introduce any damage into the specimen. The loading-unloading tests utilized a crosshead speed of 2.64 mm/min so that the total time under load (t_o in Fig. 2) was 150 s. In order to allow for viscoelastic recovery, the specimen was held at 0% strain for 1500 s ($10t_o$) between cycles and before the next step. The test procedure developed in Ref 9 assumes that there is complete or nearly complete recovery in the time period. The criterion was that the compressive stress required in order to maintain zero strain at the end of recovery be less than 1.5% of the maximum stress achieved during the tensile cycles. To evaluate the Mullins effect [9], the loading curves on the two cycles were compared, and the magnitude of the effect was defined as the fractional drop in stress between the first and second loading curves at a particular strain level λ_x

$$\text{Magnitude of Mullins} = \frac{\sigma_1(\lambda_x) - \sigma_2(\lambda_x)}{\sigma_1(\lambda_x)} \quad (1)$$

where σ_1 and σ_2 represent the stresses during the first and second loadings. At very low strains, the magnitude of the Mullins effect is difficult to determine because the experimental uncertainty is very high. In this range, small differences in the position of zero strain generate large differences in the Mullins effect. In contrast, as the strain approaches the maximum value achieved during the

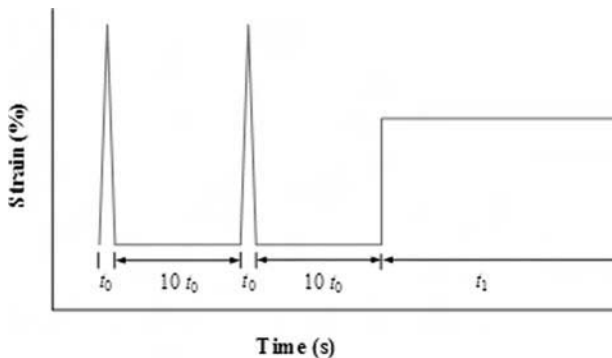


FIG. 2—Strain history used for Mullins cycles and stress relaxation tests.

loading cycle, the Mullins effect approaches zero. Between these extremes, however, there is a range of strains at which the magnitude of the Mullins effect remains relatively constant, changing by 10% or less. In the experiments here in which the maximum strain in the loading curves is 26%, the magnitude of the Mullins effect was determined at strains of 10%, 15%, and 20%.

Once the Mullins effect was quantified and eliminated, the viscoelastic properties of the sealant were measured in the second step of the procedure using a stress relaxation experiment (see Fig. 2). The specimens were loaded rapidly (70 mm/min) in tension to a maximum tensile strain of 18%, which was chosen arbitrarily between two limits, i.e., it must be significantly less than the strain level used in the Mullins cycles while not being so low that accurate measurements of strain and load become difficult. Once this strain level was attained, the specimen was held at that strain while the load was monitored as a function of time. The specimen reached the hold strain in just under 1 s. Data points during the first 5 s after loading commenced were ignored in order to eliminate confounding effects due to our inability to instantaneously load a specimen to the predetermined strain.

From the stress relaxation data, E_a was calculated using a relationship based on the statistical theory of rubberlike elasticity [9,11–13]

$$E_a(t, \lambda) = \frac{3L(t)}{WB(\lambda - \lambda^{-2})} \quad (2)$$

where:

W and B = width and breadth of the sealant (Fig. 1),

L = load,

t = time, and

λ = extension ratio, which is given by

$$\lambda = 1 + \frac{\Delta}{H} \quad (3)$$

where:

Δ = crosshead displacement, and

H = undeformed height of the sealant.

Results and Discussion

The results from the visual observations made in the ASTM round robin after exposures are as follows: Sealant B exhibited complete adhesive failure during the test, with separation primarily between the sealant and the metal beam (Fig. 3). Moreover, these specimens' dimensions exhibited permanent deformation as seen in Fig. 3. Sealant A did not fail, but it also exhibited permanent deformation. In addition, Fig. 4 shows that the metal beams were no longer parallel, suggesting that specimen loading might not have been symmetric. Other than the permanent deformation, however, sealant A showed no signs of

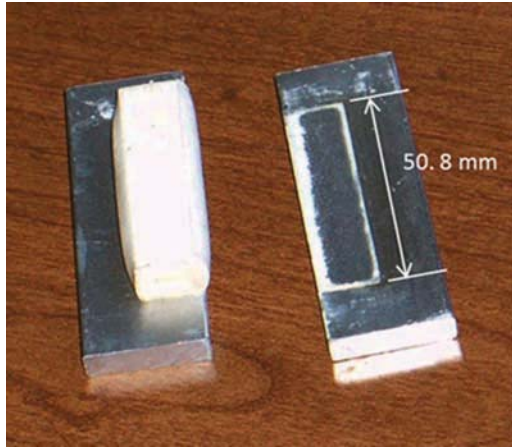


FIG. 3—Illustration of debonded sealant B.

cracking, debonding, or color change. Sealants C and D displayed no visual changes over the stress relaxation period.

During the Mullins cycles, all four sealants met the criterion for complete or nearly complete recovery. This was true despite the observation above that suggests sealants A and B might exhibit permanent deformation if t_o is sufficiently large. Figure 5 shows the average magnitude of the Mullins effect for two samples of each sealant determined at a strain of 15%. Average values from tests on the exposed samples are shown as the cross-hatched area in each bar (no exposed data are available for sealant B specimens because they failed during the exposure tests). Similar results were obtained at strains of 10% and 20%. Note first that sealants A and D show a larger Mullins effect than sealants B and C. This indicates that the network structures in A and D have more junction points that can be disrupted by strains of 26% than do those in sealants B and C. Tests on specimens after exposure show a Mullins effect that is much less than that observed for fresh specimens but well above zero. Two hypotheses could explain this observation, either when considered on their own or in combination. First, if in the exposure tests the maximum strain never reached 26%,

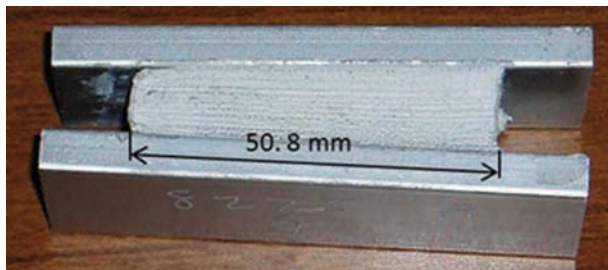


FIG. 4—Illustration of distorted sealant A.

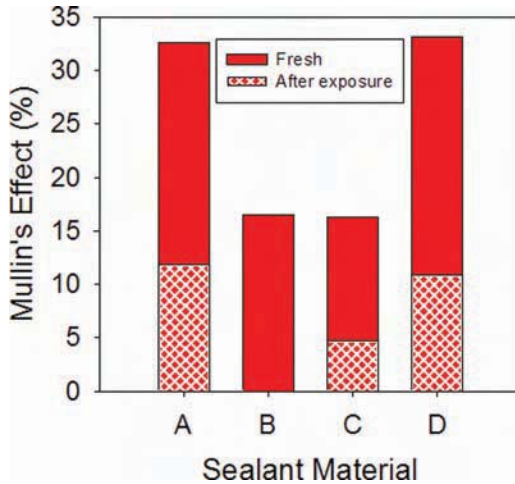


FIG. 5—Average magnitude of the Mullins effect for the two samples of each sealant, determined at a strain of 15%.

some Mullins effect would be expected in the characterization experiments. Second, a number of weeks passed between the exposure tests and the characterization experiments, and the specimens were under no load during this period. It has been shown [9] that many sealants recover (at least partially) some of the Magnitude of Mullins effect during such a period with no strain applied.

Figure 6 shows stress relaxation curves for all four fresh specimens. A wide variation in the stress relaxation modulus curves for the four sealants is apparent. Sealants A and D are virtually indistinguishable over the range of times

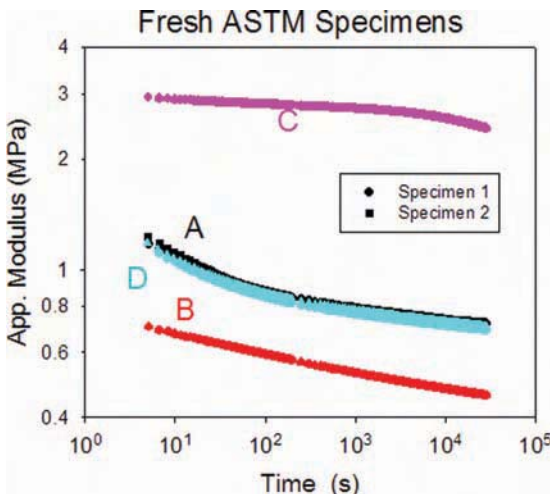


FIG. 6—Stress relaxation curves of fresh specimens of sealants A, B, C, and D.

tested. Relative to the range of modulus seen in previous sealant testing [9], sample B is near the soft end of the range, whereas sealant C is near the firm end. At very short times, sealants A and D display an upturn toward a glassy modulus, suggesting that they might have higher glass transition temperatures than sealants B and C. The curve for sealant C shows a slight downturn at long times, suggesting that flow-like behavior or a secondary relaxation mechanism might occur in these specimens over extended periods of time. Sealants A, C, and D show a clear rubbery plateau, whereas sealant B exhibits a continuous decrease in modulus through the rubbery zone. This decrease, combined with the relatively low modulus in sealant B, suggests its network structure might have fewer junction points than the networks in the other sealants.

All three sealant B specimens failed during the stress relaxation period, so it was not possible to characterize the behavior of this sealant over the specified stress relaxation period. It is worth noting, however, that the lack of a plateau in the curve shown in Fig. 7 for this sealant is consistent with the generation of a permanent deformation in the specimen that is held under load for some time. It would be interesting to perform diffusion studies to see whether the relatively low density of junction points in the network might facilitate migration of environmental species, such as water, into the specimen, because this could weaken the interface between the sealant and metal.

As noted above, the visual examination of the exposed C and D specimens revealed no visible changes in the physical appearance of these sealants. The characterization curves, however, show that molecular changes have occurred in these sealants. The stress relaxation behaviors after exposure are dramatically different, as shown in Figs. 7 and 8. Also included in these plots are the data from the tests on fresh specimens for comparison. The relaxation curves for sealant D shift down to approximately half of the values of the unexposed counterparts, though the shape of the relaxation curve remains unchanged. This means that the time-dependence of the apparent modulus is unaltered by exposure, at least in the range examined here. Although the precise mechanism

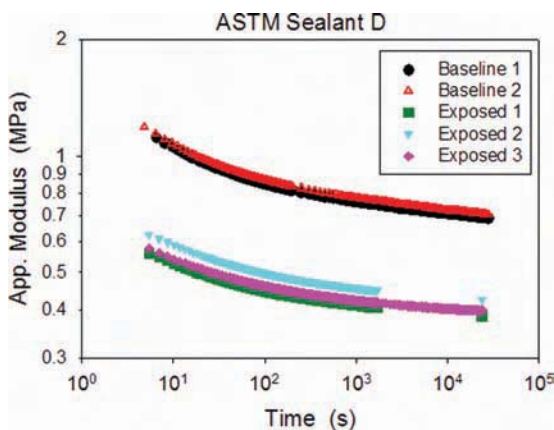


FIG. 7—Stress relaxation curves of fresh and degraded specimens of sealant D.

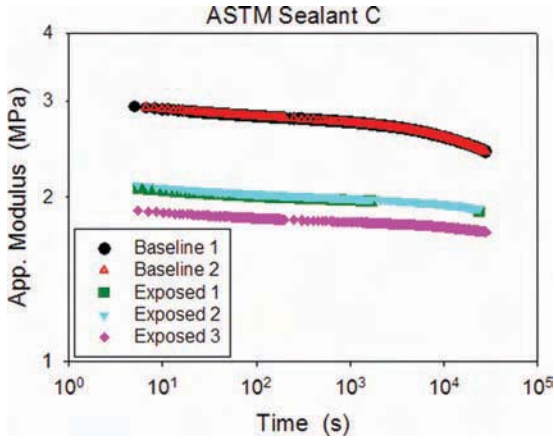


FIG. 8—Stress relaxation curves of fresh and degraded specimens of sealant C.

governing the decrease in apparent modulus remains ambiguous, the results support a view that structural changes after exposure are brought about by a reduction in the density of effective junction points in the network structure. Likewise, the magnitude of apparent modulus for sealant C decreases after exposure by about 30%. Although the shapes of the curves are similar, there is a less distinct downturn at long times than seen with the fresh sealants.

As stated above, exposure of sealant A produced no cracks, debonds, or color change, but some permanent deformation was present (Fig. 4). Two of the three exposed specimens were deformed to the point that further exposure was not possible. Results of experiments on the third specimen are shown in Fig. 9. As with sealants C and D, the relaxation behavior for this specimen shows a dramatic change after exposure. Specifically, a noticeable increase in apparent modulus and substantial change in curve shape are clearly evident. The plateau

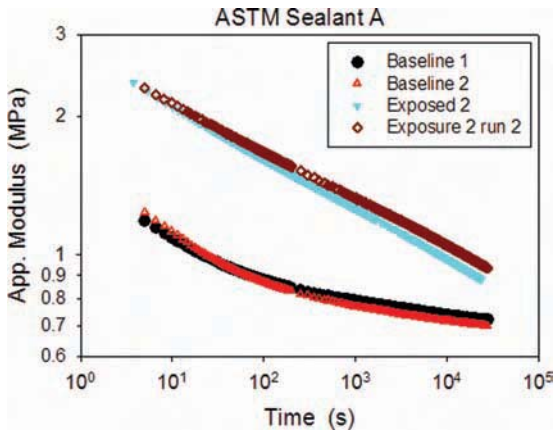


FIG. 9—Stress relaxation curves of fresh and degraded specimens of sealant A.

region at long times is completely absent. This change in the time dependence of the apparent modulus indicates that drastic structural modification has occurred in the exposed specimens. To ensure the reproducibility of this result, the characterization was performed for a second time, and the relaxation curves for the two runs are virtually identical (Fig. 9).

In order to test this result, attempts were made to forcefully return the two highly deformed specimens of sealant A to their original dimensions. Wedges and clamps were inserted in order to achieve the original shape, and the specimens were held in this way for several weeks. After the wedges and clamps were removed, the samples were allowed to set for several days. Some of the deformation returned, but not enough to make the resumption of testing possible. Stress relaxation measurements were then performed on the specimens, and the results are shown in Fig. 10. The new data show trends similar to what was found with the initial exposed sample: the apparent moduli showed an increase, and the curve shape changed significantly. Although the differences between the new curves and the curve for the first exposed specimen could be the result of sample-to-sample variation, it is far more likely that the differences are artifacts introduced by testing deformed specimens. Consequently, although tests on deformed specimens might be useful for showing general trends, quantitative comparisons should be avoided.

The relaxation curves for fresh sealants A and D are identical (see Fig. 6). Moreover, neither shows any cracking, debonding, or color change after exposure. The stress relaxation tests, however, show that the effect of exposure on the two sealants is completely different. Whereas sealant D exhibits a decrease in modulus with no change in curve shape, sealant A shows an increase in modulus and a dramatic change in curve shape (see Figs. 7 and 9). This result clearly demonstrates the different viscoelastic response of the sealants, which is not surprising given that their chemistries and formulations are different. This is

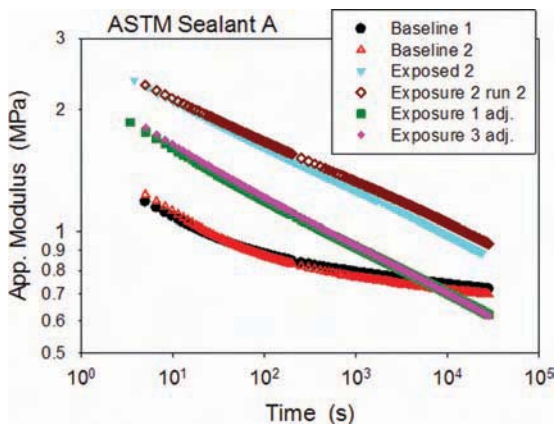


FIG. 10—Different stress relaxation curves obtained from forcing distorted degraded specimens of sealant A to return to their original dimensions. The data for fresh specimens are also included for comparison.

potentially important information that could not be obtained from conventional visual inspection.

Conclusions

A test method for assessing the durability of building joint sealants using a stress relaxation approach has been examined. Specimens of four commercial sealant materials that underwent exposure conditions according to ASTM C1519-10 as part of a round robin were obtained and utilized as model systems in order to compare this new test method with the current, descriptive methodology involving visual inspection for defects. The results here show that the new test method not only allows meaningful quantitative evaluation of sealant characteristics but also provides qualitative information about the molecular structure of the sealants. It has been shown that important additional information that is not provided by visual inspection can be obtained by using this test method. This is particularly evident in the results for sealants C and D, for which visual inspection fails to reveal any changes after exposure even though significant changes are detected by the stress relaxation measurements. Consequently, the results here indicate that the viscoelastic characterization provides a robust methodology for quantitatively evaluating the durability of building joint sealants.

Acknowledgments

The support from a NIST/industry consortium on Service Life Prediction of Sealant Materials is greatly appreciated. Participating companies include DAP, Degussa, Dow Corning, Kaneka Texas, SIKA, Solvay, Tremco, and Wacker Silicones.

References

- [1] Woolman, R., and Hutchinson, A., *Resealing of Buildings: A Guide to Good Practice*, Butterworth-Heinemann, Oxford, UK, 1994.
- [2] Grunau, E., "Service Life of Sealants in Building Construction," Research Report, Federal Ministry for Regional Planning, Building and Urban Planning, Bonn, Germany, 1976 (in German).
- [3] Chiba, R., Wakimoto, H., Kadono, F., Koji, H., Karimori, M., Hirano, E., Amaya, T., Sasatani, D., and Hosokawa, K., *Improvement System of Waterproofing by Sealants in Japan*, Japan Sealant Industry Association, Tokyo, Japan, 1992, pp. 175–199.
- [4] "Expenditures for Residential Improvements and Repairs—1st Quarter," *Current Construction Reports*, U.S. Census Bureau, Department of Commerce, Washington, D.C., 2002.
- [5] *Durability of Building and Construction Sealants and Adhesives*, STP 1453, A. T. Wolf, Ed., ASTM International, West Conshohocken, PA, 2004, pp. 385–398.
- [6] White, C. C., Tan, K. T., Hunston, D. L., and Williams, R. S., *Service Life Prediction of Polymeric Materials: Global Perspective*, J. W. Martin, R. A. Ryntz, J. Chin, and R. Dickie, Eds., Springer, New York, 2008, pp. 115–128.

- [7] Searle, N. D., and *Handbook of Sealant Technology*, K. L. Mittal and A. Pizzi, Eds., CRC Press, Boca Raton, FL, 2009, pp. 93–142.
- [8] Wolf, A. T., *Handbook of Sealant Technology*, K. L. Mittal and A. Pizzi, Eds., CRC Press, Boca Raton, FL, 2009, pp. 143–189.
- [9] White, C. C., and Hunston, D. L., “Characterizing the Non-Linear Viscoelastic Properties of Sealant Including the Mullins Effect,” *Polym. Eng. Sci.*, Vol. 48(12), 2008, pp. 2317–2328.
- [10] ASTM C719-93, 2010, “Standard Test Method for Adhesion and Cohesion of Elastomeric Joint Sealants Under Cyclic Movement (Hockman Cycle).”
- [11] Taylor, C. R., Greco, R., Kramer, O., and Ferry, J. D., “Nonlinear Stress Relaxation of Polyisobutylene in Simple Extension,” *J. Rheol.*, Vol. 20, 1976, pp. 141–152.
- [12] Ferry, J. D., *Viscoelastic Properties of Polymers*, 3rd ed., John Wiley & Sons, Inc., New York, 1980.
- [13] Ketcham, S. A., Niemiec, J. M., and McKenna, G. B., “Extension and Compression of Elastomeric Butt Joint Seals,” *J. Eng. Mech.*, Vol. 122, 1996, pp. 669–677.

Erratum for JAI104090, A Test Method for Monitoring Modulus Changes during Durability Tests on Building Joint Sealants, by Christopher C. White, Donald L. Hunston, Kar Tean Tan, published in The Journal of ASTM International (JAI), Volume 9, Issue 2, February, 2012.

The correct Author listing should be: Christopher C. White, Donald L. Hunston, Kar Tean Tan, and Gregory T. Schueneman⁴

⁴USDA Forest Service, Forest Products Laboratory, One Gifford Pinchot Drive, Madison, WI 53726

**FIELD EXPERIENCE
WITH SEALED JOINTS
AND ADHESIVE FIXATION**

Peter E. Nelson¹ and Emily R. Hopps¹

Moisture Sensitive Adhesives and Flooring Adhesive Failures

ABSTRACT: Over the last decade, changes in environmental government regulations have necessitated the reformulation of many historically durable adhesives used in the application of flooring materials. The most popular flooring adhesives traditionally used solvents containing volatile organic compounds (VOCs), but government-prescribed regulations that limit or restrict VOCs resulted in dramatic changes to most traditional flooring adhesives. Adhesives with VOC-containing solvents were replaced with water-based or 100% solids adhesive formulations. While these new formulations may reduce the environmental impact of new flooring installations, new adhesives are less durable and more susceptible to moisture-related deterioration. Within the past ten years more moisture-related flooring failures have occurred as adhesive systems have switched away from the proven VOC-containing technology to a newer, low VOC-compliant technology. If the concrete is not properly sealed or allowed to dry, the moisture inherent to concrete substrates can break down, re-emulsify, and dissolve moisture-sensitive flooring adhesives. Consequentially, applied flooring materials can delaminate, buckle, blister, and crack. This paper will compare the composition of newer moisture-sensitive flooring adhesives with that of their VOC-containing predecessors, and describe the properties of the adhesives that reduce overall durability. Case studies of flooring failures resulting from moisture-related deterioration of adhesives will be presented for various flooring materials including carpet tile, sheet vinyl, and vinyl composition tile flooring. Recommendations for repairing failed flooring and providing durable new flooring installations using moisture-sensitive adhesives will also be included.

KEYWORDS: adhesive, concrete, floor, VOCs, moisture

Manuscript received June 7, 2011; accepted for publication August 30, 2011; published online September 2011.

¹Simpson Gumpertz & Heger Inc., Waltham, MA 02453.

Cite as: Nelson, P. E. and Hopps, E. R., "Moisture Sensitive Adhesives and Flooring Adhesive Failures," *J. ASTM Intl.*, Vol. 9, No. 2. doi:10.1520/JAI104092.

Copyright © 2012 by ASTM International, 100 Barr Harbor Drive, PO Box C700, West Conshohocken, PA 19428-2959.

Introduction

Over the last few decades, widespread failures of many different floor finishes applied to concrete floor slabs have become more prevalent. Adhered flooring materials, such as sheet vinyl, vinyl composition tile, carpet, carpet tile, and rubber flooring frequently require repair or replacement early in their service life due to failures such as delamination, blistering, lifting, and cracking. Although there are many factors that contribute to the increase in adhered floor finish failures, a common thread in many of the failures is the durability of the adhesive material used to apply the floor finish to the concrete substrate. These durability issues can be traced back to changes in the flooring industry that began over twenty years ago.

Flooring Industry Changes

Changes in the flooring industry first began in 1989 with the United States Environmental Protection Agency's (EPA) Asbestos Ban and Phase-out Rule under the Toxic Substances Control Act (TSCA). The rule prohibits the manufacture, import, processing, and distribution of certain asbestos-containing products. Under the rule, the manufacture and processing of vinyl asbestos floor tile (VAT), one of the most popular floor finishes at the time, was to cease as of Aug. 1990. Although the United States Court of Appeals vacated and remanded most of the rule in Oct. 1991, making the manufacture of VAT technically allowable, VAT production has been phased out. The change from VAT to vinyl composition tile (VCT) signaled the start of a major change in the flooring industry [1-3].

At about the same time that the EPA was defining standards for the use of asbestos discussions to guide the reformulation of flooring adhesives to reduce volatile organic compound (VOC) emissions was underway. In 1990, the EPA received a citizen's petition filed under the TSCA. The petition focused on health concerns related to the emission of 4-phenylcyclohexene (4-PC) from newly installed carpet, carpet cushion, and carpet adhesive. Although the EPA denied the petition due to insufficient data, it formed the Carpet Policy Dialogue to support measures to reduce VOC emissions from carpet products. In 1991, the EPA completed the Carpet Policy Dialogue Compendium Report following a one-year effort by representatives from industry, public interest groups, government agencies, and the scientific community [4].

The Carpet Policy Dialogue resulted in a standardized test method to measure VOC emissions from carpet products and voluntary agreements from various carpet industry organizations to test their products for VOCs. Although manufacturers and industry organizations agreed to test and report to the public the amount of total VOCs in their products, the EPA did not establish maximum allowable VOC emission limits in the Carpet Policy Dialogue. Consequently, the South Coast Air Quality Management District (SCAQMD) of California established Rule 1168 for adhesive and sealant applications in April 1989. In February 1991, the SCAQMD established a VOC limit of 150 g/l for indoor carpet adhesives. Presently, the VOC limit stipulated by the SCAQMD

for most flooring adhesives, including indoor carpet, is 50 g/l [5]. The Carpet Policy Dialogue and regulations established by the SCAQMD in California drove the industry towards significant changes in the formulations of adhesives and other flooring products to reduce VOC emissions.

Regulations on VOCs in floor products became more stringent in 1998 when the EPA issued the National Volatile Organic Compound Emission Standards for Architectural Coatings under Section 183(e) of the Clean Air Act [6]. Under the standard, manufacturers and importers of architectural coatings (including floor coatings, concrete protective coatings, sealers, and stains) must limit the VOC content of specified coatings. Although VOC limits vary depending on the coating category, and adhesives are not explicitly mentioned as a subject coating, the standard has proved an incentive for the flooring industry to lower VOC product emissions and acted as motivation to reformulate products containing VOCs. Today, most flooring products available for commercial applications comply with the VOC limits established by SCAQMD. The use of VOC-containing products is strongly discouraged by such government-sponsored programs such as the U.S. Green Building Council's Leadership in Energy and Environmental Design (LEED) rating system.

Adhesive Chemistry and Moisture in Concrete Floors

Due to the numerous regulations developed over the last 20 years, flooring adhesives have been reformulated to reduce or eliminate VOCs. Most adhesive formulations include a binder, solvent, fillers, pigments, and additives. The primary source of VOCs in historical adhesive formulations is the solvent. The primary purposes of the solvent are to control viscosity during application, and when dissipated, facilitate the adhesive to setup and cure. Once the adhesive is applied, the solvent is not needed and evaporates into the air, which is necessary for completion of the chemical reaction of other components in the adhesive, resulting in cure. Historically, the solvents used in flooring adhesives have been organic liquids that typically contain VOCs. The evaporation of these VOC-containing solvents into the air during adhesive application is what compelled the reformulations under the various standards previously discussed.

However, these traditional VOC-containing adhesives had been tested and optimized over time, leading to proven, long-term durability. As the industry transitioned away from VOC-based solvent adhesives, new adhesive formulations were developed with either water-based solvents or without a dedicated solvent (i.e., 100% solids adhesives). Unfortunately, reformulating the adhesives has led to some unanticipated durability issues, especially those which are found with concrete substrate applications.

Concrete floor slabs are difficult substrates on which to apply floor finishes. Concrete inherently contains moisture. Water is an integral ingredient in all concrete, both for hydration of the cement and workability of the concrete during placement. The water that is not used for the hydration of the cement remains in the concrete after curing is complete and slowly dries to equilibrium with the surrounding environment when conditions are favorable for evaporation. Cured concrete can also reabsorb moisture from the surrounding environment, either

above or below the slab, after curing is complete. Ground water below slabs-on-grade or slabs-on-ground, rainwater and spills onto the concrete, and cleaning and maintenance procedures can all increase the amount of moisture in concrete floor slabs.

Concrete can take a very long time to dry. Many studies have been done to determine the drying time of concrete, and these studies have identified many variables that contribute to concrete's ability to dry. Even under the most ideal conditions, normal concrete can take several months to reach a moisture content that will not negatively affect floor adhesives. Once a floor finish with low permeability (e.g., most adhered resilient floor finishes) is applied to the concrete, moisture in the concrete can no longer dry into the ambient air provided that bottom side evaporation is not possible. Instead, the residual moisture in the concrete will tend to collect between the floor finish and the concrete. Depending on the moisture levels in the concrete, significant amounts of moisture can collect at this interface, where it is in direct contact with the adhesive.

Concrete also has a naturally high (alkaline) *pH*. The typical *pH* of freshly placed concrete is about 12 to 13. The *pH* of cured concrete will decrease over time through carbonation if it is exposed to the carbon dioxide in the air, but the *pH* of carbonated concrete is still around 9. Since the hydroxide ions that create the alkaline condition only exist in water, the high *pH* of concrete alone is not necessarily a concern. However, when the hydroxide ions are combined with the high levels of moisture that are potentially present in concrete floor slabs, the concrete becomes an unsuitable surface for floor finishes, especially those installed with the newer, water-based adhesives.

The most common flooring adhesives to come out of the new low- or VOC reformulations are water-based acrylic emulsions. Because these adhesives are designed with water as their solvent, they are susceptible to re-emulsification when exposed to water from other sources, such as moisture within a concrete floor slab. The degradation of the adhesive is commonly exacerbated by high *pH* levels and contact with very alkaline moisture from the concrete substrate. Because the older solvent-based adhesives did not have this inherent tendency to dissolve in water, they were much less susceptible to moisture and *pH* related deterioration.

The following case studies illustrate moisture- and *pH*-related degradation of water-based flooring adhesives.

Case Studies No. 1: Office Building

In 2006, the general rehabilitation of a 1970s office building included installation of new carpet and VCT on an existing concrete slab-on-grade. A few years after the rehabilitation work, the new carpet and VCT developed blisters, debonded, and the flooring adhesive turned soft and gummy intermittently throughout the building. The original slab-on-grade construction did not include a vapor retarder to prevent ground water-based vapor migration through the slab-on-grade. The original flooring system appeared to be VCT or VAT applied with older asphalt-based adhesives. Current conditions show as many as three layers of leveling compound and flooring adhesive have been

installed over the original asphalt flooring adhesives, which remain on the surface of the concrete slab. The newest flooring adhesive layer is the layer that is soft and gummy. Each time the floor was replaced, the loose debonded sections of the old floor adhesives and leveling layers were removed and another layer of leveling compound was applied. The condition of the older layers range from well bonded to having no bond, but none were soft and gummy like the most recent flooring application.

The moisture levels in the slab were measured according to ASTM F1869—Standard Test Method for Measuring Moisture Vapor Emission Rate of Concrete Subfloor Using Anhydrous Calcium Chloride [7], and the moisture vapor emission rate (MVER) ranged from 3.75 to 10.20 lb/1000 sq ft/24 h (lb). The floor adhesive manufacturer set a MVER limit of 5 lb, and the leveling underlayment installer set an MVER limit of 3 lb. The internal relative humidity (RH) levels, measured in accordance with ASTM F2170—Standard Test Method for Determining Relative Humidity in Concrete Floor Slabs Using in situ Probes using Protimeter MMS+ equipment [8], ranged from 58 to 93 %, although most of the results ranged from the mid-50s to the mid-60s. Although the flooring manufacturer did not specify internal concrete RH limits for their products in 2006, typical industry limits are 75 to 80 % RH.

Most current flooring industry standards and practice guides require removing the old layers of flooring material so the concrete bonding surface will be “permanently dry, clean, smooth and structurally sound.” Industry standards such as the Carpet and Rug Institute (CRI-104-2002) and the Resilient Floor Covering Institute (RFCI 1P#2) do not allow installation over older adhesives [9,10]. Although some manufacturers will allow new flooring installation over some existing flooring materials, new flooring adhesives should not be installed over asphalt adhesive because the new adhesive materials will likely not bond to the asphalt residue. Although the asphalt adhesive may provide some vapor-retarding properties, the older asphalt adhesive was discontinuous and ineffective serving as a moisture vapor migration layer. The practice of going over the older adhesive layers is a carryover from many older jobs when the new and old adhesives were of similar composition and compatible; hence, the observed discontinuous areas of original asphalt flooring adhesive and varying layers of older adhesive and underlayment. Consequently, what may have had limited successfulness many years ago is not working today.

However, the newer latex flooring adhesives turned soft and gummy while the residue of the older adhesives did not show the same level of moisture breakdown when exposed to the same level of moisture. Observation of the adhesive failure a few years after installation and only intermittently throughout the building indicates that the adhesive initially cured and provided acceptable adhesion, but later became soft and gummy after prolonged exposure to moisture. The rate of debonding and blisters increased with time. Sub-slab soil-based moisture diffused through the concrete slab, collected below the flooring, and caused the deterioration of the new adhesive and flooring system. No evidence that an initial cure of the adhesive was affected by the moisture was observed. Removal and replacement of the entire flooring system to the concrete base layer was recommended. Since the multiple layers of old adhesive

and underlayment did not provide a suitable substrate for the new flooring system, they should be completely removed before a moisture mitigation coating and the new floor system are applied.

Case Study No. 2: Hospital

Similar adhesive problems were identified in a new hospital facility in the Pacific Northwest constructed in 2003 and 2004. The majority of the floors in the facility consist of normal weight concrete slab-on-grade. Unlike the office building example, the new slabs were placed over a vapor retarder and a 2 in. thick compacted sand blotter layer. Floor finishes include VCT, various types of sheet vinyl, and carpet tile in the different areas of the hospital.

The maximum concrete moisture vapor emission rates (MVER) allowed by the various manufacturers of the floor finishes and adhesives was 3 lb measured in accordance with ASTM F1869. Tests performed on the new concrete before flooring was installed showed that actual moisture levels ranged from 4.8 to 7.6 lb. The pH levels on the concrete surface were low, ranging from 7 to 8. To address the elevated levels of moisture, the contractor installed a moisture mitigation coating on the surface of the slab prior to installation of the flooring. The product literature for the mitigation coating stated that it would reduce MVERs from up to 12 lb down to 3 lb. Following installation of the moisture mitigation coating, the finish flooring was installed during the last several months of construction.

A little over a year after construction was complete and the hospital became operational, problems with the floor were reported. The visual evidence of flooring issues with the sheet vinyl flooring includes ripples, bubbles, and liquids seeping from seams. Carpet tiles were easily removed from the floor, revealing wet and uncured adhesive. The VCT flooring exhibited cracking and lifting, especially aligning with joints in the concrete substrate. Additional moisture testing was performed following reports of issues with the flooring. At that time, reported MVERs ranged from 5.2 to 7.1 lb directly on the surface of the concrete. Tests conducted on the surface of the moisture mitigation coating ranged from 4.3 to 4.5 lb. The pH readings ranged from 7 to 10 directly on the surface of the concrete, and 6 to 7 on the surface of the moisture mitigation coating.

In an attempt to mitigate the problems, the contractor replaced the flooring in several areas of the hospital, such as installing new sheet vinyl in the operating rooms. The replacement protocol included removal of all existing floor materials, and shot blasting and grinding of the concrete slabs to achieve a rough concrete surface profile without any residue from the previous materials. A second moisture mitigation coating was then applied to the surface of the concrete slab, followed by the installation of a cementitious leveling underlayment and new sheet vinyl flooring. Shortly after installation of the replacement floor system, liquid-filled blisters appeared in the new flooring over the second moisture mitigation coating.

Moisture testing was performed subsequent to the formation of blisters in the replacement sheet vinyl. These MVER readings ranged from 11.6 to 5.8 lb. Internal concrete RH readings were collected in accordance with ASTM F2170

using a modified Protimeter MMS+ system. These readings ranged from 85 to 97%. The *pH* readings on the surface of the concrete ranged from 9 to 11. Samples of the compacted sand blotter layer between the concrete slab and vapor retarder were collected and were measured for moisture content. The typical moisture content of the sand blotter layer was about 3 to 6% by weight.

Additional testing to further understand the existing conditions was performed. Chemical analyses on the various adhesives, moisture mitigation coatings, and liquid from blisters were conducted. The results of these analyses showed that the first moisture mitigation coating was an emulsion-based product composed of agglomerates of acrylic, making it water-soluble and insufficiently dense to prevent or reduce moisture diffusion. The second moisture mitigation coating was also found to be an emulsion-based product (polyvinyl acetate) with a large amount of filler particles of titanium. These properties resulted in a mitigation coating that re-emulsified in the presence of water and allowed some vapor diffusion. Moisture vapor from the concrete and sand blotter layer migrated through the moisture mitigation coatings and degraded the adhesive. Adhesive degradation occurred with or without a moisture mitigation coating, and under four different types of flooring. Similar to the office building, we recommended complete removal of all existing floor materials, installation of an effective moisture mitigation coating, leveling underlayment, and finish flooring with their respective adhesives.

Recommendations

Moisture in concrete and moisture-sensitivity of current floor adhesives and coatings are an inherent difficulty in floor finish installations today. However, there are several key items that can be considered to improve the chances of a successful adhered finish floor installation. Concrete slabs on-grade or on-ground must be placed over an effective vapor retarder (or waterproofing membrane if required by the site conditions). The vapor retarder or waterproofing membrane will protect the concrete and floor finish from elevated levels of moisture present in the underlying soils. The authors agree with the requirements of American Concrete Institute (ACI) 302.2R (Guide for Concrete Slabs that Receive Moisture-Sensitive Floor Materials) regarding installation of a sand blotter layer between the concrete slab and vapor retarder [11], as was the case in Case Study No. 2. ACI 302.2R cautions against the use of a sand blotter layer when moisture-sensitive finishes are to be applied onto the slab. The intent of the blotter layer is to reduce the tendency of the slab to curl as it dries, but moisture that is entrapped in the blotter layer will likely diffuse through the concrete and cause the softening of the floor finish adhesive, producing similar deterioration to a floor slab without a vapor retarder.

Concrete slabs with an effective vapor retarder or waterproofing membrane could contain enough moisture at the time of flooring placement to cause adhesive deterioration. As discussed in the previous text, moisture is a main ingredient in concrete and the moisture must be allowed to dry to manufacturer-accepted levels before floor finish installation. Otherwise, moisture levels could be high as a result of ordinary water trapped in the concrete slabs. It is imperative to

perform moisture testing (ASTM F1869 and F2170) of the concrete slabs prior to flooring installation. The moisture tests should be performed by a certified tester once the building is enclosed and at operational temperature and humidity. As in Case Study No. 1, moisture testing of the existing slab must also recognize the time of year the floors are tested. When the slab system does not contain a vapor retarder, periodic testing over a longer period of time will be needed to determine the highest vapor drives as the moisture content changes with the seasons, level of the ground water, water vapor flow, and project location.

When moisture levels exceed flooring manufacturer's limits, installation of a topical moisture mitigation coating to protect the sensitive adhesives is recommended. As illustrated in Case Study No. 2, not all moisture mitigation coatings have proven successful. Selecting the appropriate moisture mitigation coating for a particular application and understanding the performance track record of selected products are important to the long-term durability of a flooring system. Given the increased sensitivity of these new low VOC adhesives to moisture, all concrete slabs-on-grade without an underlying vapor retarder should be covered with a moisture mitigation coating to account for the potential seasonal variability of concrete slabs in contact with soil when using these moisture-sensitive finishes. Installation of moisture mitigation coatings may also require the installation of a leveling underlayment (between the mitigation coating and the flooring adhesive). The underlayment will level the surface of the floor, which will likely require a rough profile by many reputable moisture mitigation coating manufacturers. The leveling underlayment will also serve as a blotter layer for the water-based acrylic floor adhesives. Without an absorptive material below the adhesive, the solvent water cannot evaporate to allow the adhesive to cure.

Many manufacturers have developed more moisture-tolerant adhesives that comply with current VOC limits. When moisture levels are borderline and a vapor retarder is present, upgrading to one of these adhesives may allow flooring installation without the need for application of a moisture mitigation coating. Confirming the compatibility of the adhesive with the rest of the floor system materials is critical to long-term performance. Evaluating the durability of the adhesive based on its track record in similar applications will help minimize the chances of moisture-related flooring failures.

References

- [1] 40 CFR Part 763, "Asbestos: Manufacture, Importation, Processing, and Distribution in Commerce Prohibitions; Final Rule," Environmental Protection Agency, Washington, D.C., July 12, 1989.
- [2] 40 CFR Part 763, "Asbestos: Manufacture, Importation, Processing, and Distribution in Commerce Prohibitions; Effects of Court Decision," Environmental Protection Agency, Washington, D.C., April 2, 1992.
- [3] 40 CFR Part 763, "Asbestos: Manufacture, Importation, Processing, and Distribution in Commerce Prohibitions," Environmental Protection Agency, Washington, D.C., Nov 5, 1993.
- [4] "Carpet Policy Dialogue Compendium Report," United States Environmental Protection Agency, Washington, D.C., Sept 27, 1991.

- [5] Rule 1168, 2005, "Adhesive and Sealant Applications," South Coast Air Quality Management District, Diamond Bar, CA.
- [6] 40 CFR Part 59, "National Volatile Organic Compound Emission Standards for Architectural Coatings," Environmental Protection Agency, Washington, D.C., Sept 11, 1998.
- [7] ASTM Standard F1869, 2011, "Standard Test Method for Measuring Moisture Vapor Emission Rate of Concrete Subfloor Using Anhydrous Calcium Chloride," ASTM International, West Conshohocken, PA, www.astm.org.
- [8] ASTM Standard F2170, 2009, "Standard Test Method for Determining Relative Humidity in Concrete Floor Slabs Using In Situ Probes," ASTM International, West Conshohocken, PA, www.astm.org.
- [9] CRI-104-2002, 2002, "Standard for Installation Specification of Commercial Carpet," Carpet and Rug Institute, Dalton, GA.
- [10] RFCI IP#2, 2005, "Recommended Installation Practice for Vinyl Composition Tile (VCT)," Resilient Floor Covering Institute, Rockville, MD.
- [11] American Concrete Institute, "Guide for Concrete Slabs that Receive Moisture-Sensitive Flooring Materials," *Report No. 302 2R-06*, American Concrete Institute, Farmington Hills, MI, 2006.

David Straup Slick,¹ Nicholas A. Piteo,² and Dean A. Rutila²

Case Studies of Adhesive and Rigid Insulation Board Failures due to Moisture in Low Sloped Roofing Assemblies

ABSTRACT: Foamed adhesives are used to join roofing assembly components to the roof substrate and to each other. A variety of performance problems with foamed adhesives as installed in roofing assemblies have led to assembly failures. We previously reported, in detail, four specific failure mechanisms caused by poor adhesive installation that we have observed, and we briefly note these failure mechanisms in order to maintain continuity as we expand on our earlier work. The focus of this paper is to report on other factors that also lead to adhesive and rigid insulation board performance problems, specifically, moisture contained within the roofing assembly and substrate, which can result in the failure of the roofing assembly. Similar substrate moisture issues occur in flooring assemblies; however, whereas the flooring industry continues to address moisture-related issues that lead to adhesive performance problems, the roofing and roofing adhesive industries have been less proactive regarding use, installation, and testing for assemblies with potential moisture-related issues. We present several case studies that illustrate excessive moisture in roofing assemblies or substrates as an issue that contributed to the adhesive failure of the roofing assembly. We also discuss the lessons to be learned from not addressing these issues at the onset of a project.

KEYWORDS: foamed, adhesive, insulation, moisture, roofing

Manuscript received June 15, 2011; accepted for publication November 9, 2011; published online March 2012.

¹Simpson Gumpertz & Heger Inc., 1828 L Street NW, Suite 950, Washington, DC 20036, e-mail: dslick@sgh.com

²Simpson Gumpertz & Heger Inc., 1828 L Street NW, Suite 950, Washington, DC 20036.

Cite as: Slick, D. S., Piteo, N. A. and Rutila, D. A., "Case Studies of Adhesive and Rigid Insulation Board Failures due to Moisture in Low Sloped Roofing Assemblies," *J. ASTM Intl.*, Vol. 9, No. 3. doi:10.1520/JAI104150.

Copyright © 2012 by ASTM International, 100 Barr Harbor Drive, PO Box C700, West Conshohocken, PA 19428-2959.

Introduction

A variety of performance problems with foamed adhesives as installed in roofing assemblies have led to assembly failures. We previously reported, in detail, four specific failure mechanisms caused by poor adhesive installation that we have observed [1], and we briefly note these failure mechanisms in order to maintain continuity as we expand on our earlier work. The focus of this paper is to report on other factors that negatively impact adhesive and rigid insulation board performance, specifically, moisture contained within the roofing assembly and substrate, which can result in failure of the roofing assembly. We present several case studies and a summary of hygrothermal computer modeling that exemplifies such roofing failures. We discuss the consequences of trapped moisture within the roofing assembly and its effect on roofing component adhesion. Similar substrate moisture issues occur in flooring assemblies; however, whereas the flooring industry continues to address moisture-related issues that lead to adhesive performance problems, the roofing and roofing adhesive industries have been less proactive regarding adhesive use, installation, and testing for assemblies with potential moisture-related issues.

Summary of Common Defects with Foamed Adhesive Application and Rigid Insulation Installation (as Previously Reported)

The use of foamed adhesives (defined in ASTM D907-08b [2] as adhesives with an apparent density that has been decreased by the presence of numerous gas-filled cells throughout the mass) is an established method for adhering roofing assembly components, including faced rigid cellular polyisocyanurate thermal insulation board as defined in ASTM C1289-10 [3] (insulation board), to the roof substrate and to each other within roofing assemblies. The proper design and installation of insulation board roofing assemblies are critical to the success of systems that rely on attachment with foamed adhesive. The detachment of insulation in service often contributes to roofing assembly failure, and defects related to roofing assembly design and insulation installation are often the root failure mechanism. Detached or poorly secured roofing assemblies cannot resist significant wind loads and are likely to be further damaged or destroyed by wind events well below the design wind pressures for the assembly.

Our recent investigations of failures of roofing assemblies that include foamed adhesive have revealed several distinct adhesion defects. These defects are independent of the type of roofing membrane and can be attributed to the application of the foamed adhesive, as well as to the placement of the insulation boards into the adhesive. These four distinct and common defects are improper foamed adhesive spacing and pattern, insufficient foamed adhesive quantity, inadequate insulation board to adhesive contact, and failure to maintain insulation board contact with the substrate. All of these defects reduce the uplift resistance of the roofing assembly and increase the likelihood of roofing detachment. In cases of partial failure in which the center of the roofing assembly becomes detached but the roofing assembly remains attached at the roof perimeter, these defects allow insulation movement and displacement, which can render the roofing assembly unserviceable.

Case Studies of Roofing Failures due to Moisture in Roofing Assemblies

Case 1: TPO Roofing Membrane Installation

We investigated the failure of a thermoplastic olefin (TPO) roofing membrane assembly at a four-building complex. The buildings consist of precast concrete exterior walls, cast-in-place concrete interior walls, and precast concrete roof planks with a concrete topping slab. Approximately one year after construction, the building owner observed inflated and billowing roofing membrane at two of the buildings, and at one of these buildings there was an irregular roofing surface from displaced insulation below the membrane. During our field work to investigate the failure, we observed occasional roofing membrane inflation and billowing at all structures; this was caused by internal building pressure (positive pressure) and pressure created by wind blowing across the roofs (negative pressure) (Fig. 1). Emergency retention bars installed over the roof surfaces reduced, but did not eliminate, the extent of the membrane inflation and billowing.

The typical roofing assembly consisted of, from exterior to interior, TPO roofing membrane, reportedly adhered with a polymer-based contact adhesive; multiple layers of paper-faced polyisocyanurate insulation that varied from 3 to 12 in. (7.62 to 30.48 cm) in total thickness, reportedly adhered with a one-component foamed adhesive; a 2 to 3 in. (5.08 to 7.62 cm) thick cast-in-place concrete topping slab; and approximately 6 in. (15.24 cm) thick precast concrete roof deck planks. Prior to any sample roof openings, we observed notable insulation board deformation reflected through the TPO membrane (Fig. 2). We made 29 sample openings and observed the following:

- At 29 of the 29 sample openings (100 %), as we peeled the membrane from the insulation board, some portion of the top insulation board facer experienced a cohesive failure and delaminated within itself (Fig. 3).



FIG. 1—TPO roofing membrane inflation and billowing.



FIG. 2—Notable insulation board deformation reflected through the TPO membrane.

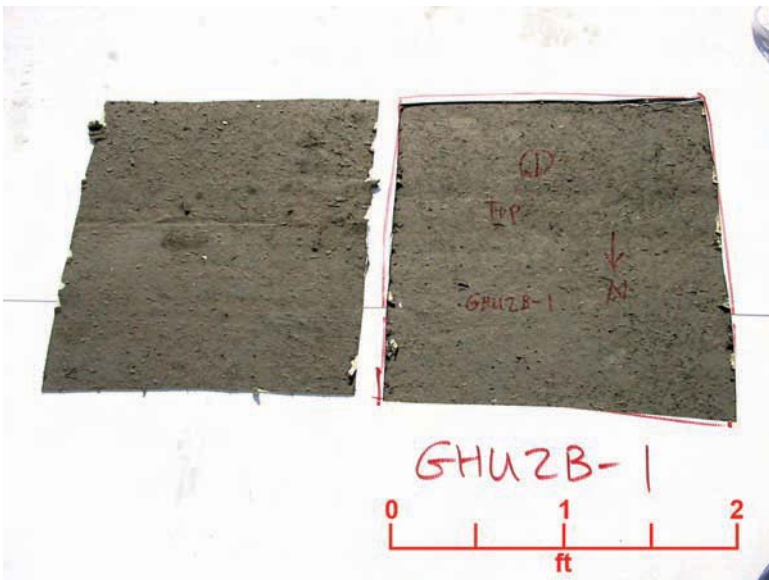


FIG. 3—Cohesive failure in the top insulation board facer found when removing the TPO roofing membrane.

- At 24 of the 29 openings (83 %), we observed moisture on the insulation board facers; we verified dampness or moisture with moisture-sensitive paper (Fig. 4). At 23 of the 29 sample openings (79 %), we observed moisture between the top layer of insulation and the TPO roofing membrane.
- At 25 of the 29 openings (86 %), we observed staining on the insulation board facers (Fig. 5).
- At 28 of the 29 openings (97 %), we observed apparent microbial growth on the insulation board facers (Fig. 6).
- At seven of the 29 openings (24 %), the insulation boards were displaced below the TPO membrane prior to our making our exploratory opening (Fig. 7).
- At eight of the 29 openings (28 %), the insulation boards were bowed or curled. At some of these openings, the edges of the tapered insulation board were curled up and no longer adhered to the insulation board below (Fig. 8). At seven of the eight openings with curled or deformed insulation (88 %), the insulation curling or deformation occurred at areas that were wet or which showed signs of previous moisture (i.e., stains or apparent biological growth).
- At five of the 29 roof openings (17 %), the concrete topping slab substrate was cracked. At three of these five locations, cracks occurred at openings adjacent to the parapet, and at two of these three locations we verified that the crack was above a joint in the hollow core precast concrete roof deck planks.

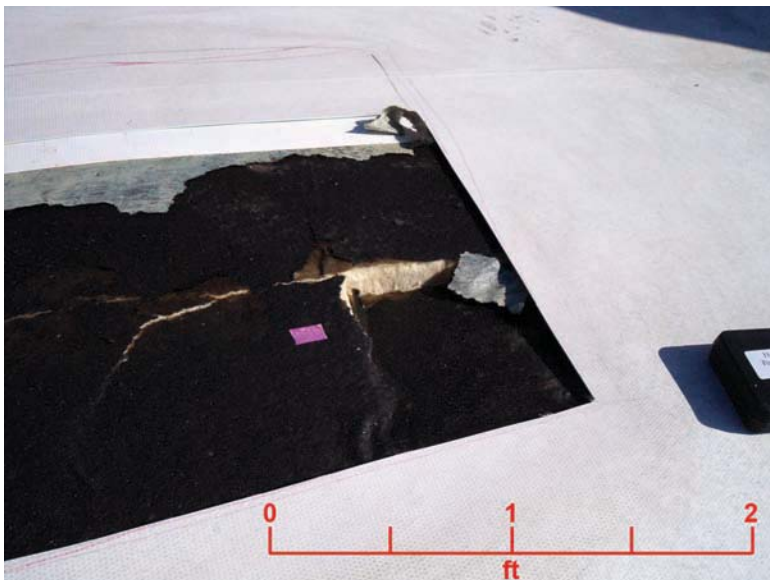


FIG. 4—Top insulation facer is wet, as indicated by moisture-sensitive paper that turns pink in the presence of moisture.



FIG. 5—Significant staining and signs of biological growth on the bottom layer of an insulation board facer.



FIG. 6—Apparent microbial growth on an insulation board facer.



FIG. 7—Displaced insulation boards within the roofing assembly below the TPO membrane.



FIG. 8—Curled-up edges of the insulation boards were no longer adhered to the insulation below.

We tested an insulation board sample in accordance with ASTM C1616 [4] and calculated a sample moisture content of 66.29 % (i.e., the sample was wet).

We measured the temperature and relative humidity of the concrete topping slab using a modified version of ASTM F2170 [5] (we had to limit the time between readings due to facility constraints), and after 24 h the average relative humidity of the topping slab was 75 % (relative humidity ranged between 58.6 % and 91.1 %).

Case 2: CSPE Roofing Membrane Installation

We investigated the failure of a chlorosulfonated polyethylene (CSPE) roofing membrane at three roof surfaces of a facility. Approximately one year after roofing membrane installation was completed, building facilities personnel observed inflated and detached roofing membrane and an irregular roofing surface from displaced insulation below the membrane.

During our field work, we determined that the typical roofing assembly consisted of, from exterior to interior, white CSPE roofing membrane, reportedly adhered with a one-component bonding adhesive; multiple layers of paper-faced polyisocyanurate insulation that varied from 2.5 to 7.5 in. (6.35 to 19.05 cm) in total thickness, reportedly adhered with a one-component foamed adhesive or a two-component polyurethane foamed adhesive; an approximately 3 in. (7.62 cm) thick composite cast-in-place concrete roof deck; and a steel roof deck with 3 in. (7.62 cm) deep flutes. We observed notable insulation board deformation reflected through the CSPE membrane prior to our making any sample openings. We made 30 sample openings in the roofing assemblies and noted the following:

- As we peeled the membrane from the insulation, we noted cohesive failure of the insulation board facer at 25 of 30 sample openings (83 %) and adhesive failure of the CSPE membrane at 17 (57 %) of the openings. Some openings exhibited both cohesive and adhesive failure.
- At 14 of 30 sample openings (47 %), we observed moisture on the insulation board facers; we verified dampness or moisture with moisture-sensitive paper.
- At 16 of 30 sample openings (53 %), we observed staining on the insulation board facers.
- At 15 of 30 sample openings (50 %), we observed apparent microbial growth on the insulation board facers.
- At six of 30 sample openings (20 %), the insulation boards were displaced below the CSPE membrane prior to our making our exploratory opening.
- At seven of 30 sample openings (23 %), the insulation boards were deformed (typically bowed or curled); at some openings, the edges of the insulation boards were curled up and no longer adhered to the insulation below.

We tested five insulation board samples in accordance with ASTM C1616 [4] and calculated that the insulation moisture content ranged from 3 % to 42 %, with an average of 10 % (i.e., the samples ranged from slightly wet to very wet).

We measured the temperature and relative humidity of the concrete topping slab using a modified version of ASTM F2170 [5] (we had to limit the time between readings due to facility constraints), and after 4 to 48 h the average relative humidity of the topping slab was 73 % (relative humidity ranged between 66 % and 85 %). We used these data to develop a hygrothermal model.

Case 3: EPDM Roofing Membrane Installation

We investigated the failure of an ethylene-propylene-diene rubber (EPDM) (ASTM D4637-10 [6]) roofing membrane and assembly. Approximately 1.5 years after roofing membrane installation was completed, building maintenance personnel observed detached roofing membrane.

During our field work, we determined that the typical roofing assembly consisted of, from exterior to interior, black EPDM roofing membrane adhered with an unidentified manufacturer's bonding adhesive; paper-faced polyisocyanurate insulation boards applied in one 2.5 in. (6.35 cm) thick layer, adhered with an unknown foamed adhesive; and a concrete roof deck of unknown thickness.

During our investigation, we made a total of ten sample openings. At five of ten sample openings (50 %), we noted moisture and apparent microbial growth within the roofing assembly. At several of these openings, we noted cohesive failure of the insulation board facer and adhesive failure of the EPDM membrane. Our investigation was focused on installing relative humidity probes to monitor the concrete roof deck moisture content. We measured the temperature and relative humidity of the concrete topping slab using a modified version of ASTM F2170 [5] (we had to limit the time between readings due to facility constraints). After 3 h, the relative humidity of the concrete roof deck at the wettest location was 98.9 %.

Summary of Hygrothermal Analyses Associated with Case Studies

For cases 1 and 2, we modeled the existing roofing system and performed hygrothermal analyses with the computer program WUFI Pro 4.2 [7] in order to simulate the impact of residual moisture within the cast-in-place concrete roof deck or topping slab on moisture condensation and accumulation potential within the roofing assembly, considering seasonal cyclic water vapor transmission through the assemblies.³ We did not hygrothermally model case 3. We used typical built-in moisture levels defined in the WUFI program for the various components of the roofing system for case 1. We input moisture levels similar to those that we measured in the field and during laboratory testing into the WUFI program for the various components of the roofing system for case 2. We used material property data, surface heat transfer coefficients, and boundary

³WUFI is a transient, one-dimensional hygrothermal model that includes moisture absorption and desorption in component materials and solar radiation and wind driven rain exposure.

condition temperatures from the American Society of Heating, Refrigeration, and Air Conditioning Engineers 2009 *Handbook of Fundamentals* [8] and the WUFI program database. We selected exterior climate data local to each project site from the WUFI database as the exterior boundary condition. We summarize our input and boundary parameters in Table 1. We used sine curves built into the WUFI model to model humidity and temperature transfer between the interior and exterior of the buildings for each case study.

We were not provided with the specific mechanical system operation parameters for temperature and humidity for either facility. For case 1, we performed our hygrothermal modeling with an interior temperature range of 65°F to 75°F (18.33°C to 23.89°C), with an average annual temperature of 70°F (21.11°C), and an interior relative humidity range of 35 % to 60 %, with an average annual relative humidity of 50 %, for our interior boundary conditions. For case 2, we performed our hygrothermal modeling with an interior temperature range of 70°F to 76°F (21.11°C to 24.44°C), with an average annual temperature of 73°F (22.78°C), and an interior relative humidity range of 30 % to 50 %, with an average annual relative humidity of 40 %, for our interior boundary conditions.

The case 1 simulation covered a four-year time frame in order to model conditions from building completion through the period during which the roofing insulation and membrane detachment occurred. The case 2 simulation covered both a 5- and a 10-year time frame from the time of our investigation forward. Case 2 also included roofing configurations with both CSPE and TPO roofing membranes. None of the simulations included a vapor retarder in the assembly.

The hygrothermal modeling showed that diffusive vapor transfer within both roofing systems from residual moisture within the concrete roof deck or topping slab and any residual moisture within other roofing system components (such as the insulation boards) would drive toward the building exterior during the initial heating season. The moisture drive would reverse and drive toward the building interior during the cooling season. The low permeability of the roofing membrane on the exterior side of the roofing assembly and the concrete topping slab over hollow core precast concrete roof deck or metal deck on the interior side of the assemblies prevents moisture from entering or exiting both systems.

In the models for both case 1 and case 2, residual moisture is trapped within the roofing assemblies and cycles through the assemblies with changes between heating and cooling seasons. The temperature within the roofing assemblies also varies with the heating and cooling season, and frequently reaches, or drops below, the dew point temperature for the environmental conditions within the roofing assembly. The cyclical moisture drive within the assemblies, combined with temperatures that are below the dew point, results in condensation and repeated wetting of the underside of the roofing membrane, organic insulation facers, and the concrete deck. Frequently wet materials lead to the reduced cohesive strength of the insulation facers; delamination of the insulation facers; biological growth within the roofing assembly; and weakened adhesive bond strength between the concrete topping slab and insulation board, between layers of insulation boards, and between the tapered insulation board

TABLE 1—Summary of WUFI model input and boundary parameters.

WUFI Input and Boundary Parameters	Case 1		Case 2	
	Average	Range	Average	Range
Concrete relative humidity, ^a %	75	58 to 91	73	66 to 85
Insulation moisture content, ^b %	66		10	3 to 42
TPO membrane permeability, ^c U.S. perms/metric perms	0.035/0.023		N/A	N/A
CSPE membrane permeability, ^d U.S. perms/metric perms	N/A	N/A	0.18/0.119	0.13 to 0.24/0.086 to 0.158

^aMeasured values based on a modified version of ASTM F2170 [5].

^bMeasured values based on ASTM C1616 [4].

^cValues based on manufacturer's literature using ASTM E96, Procedure B [10].

^dMeasured values based on ASTM E96, Procedure B [10].

and the roofing membrane. Additionally, moisture trapped within a roofing assembly, combined with roofing thermal cycles, also contributes to dimensional changes and bowing of the insulation boards, which places additional stress on the adhesive bond and wet insulation facers. Our field observations corroborated such insulation board bowing and loss of adhesive bond.

Our models showed that condensation within the roofing assembly was likely for both case 1 and case 2 for TPO and CSPE roofing membranes applied over a concrete substrate with no vapor retarder, which is consistent with our field observations of moisture, stains, and apparent mold growth. The failure of wet and deteriorated facers contributed significantly to the adhesive failure of the roofing assembly.

Moisture in the Roofing Assembly

Moisture trapped within a roofing assembly can be a significant cause of insulation board and membrane detachment in adhered roofing systems. Adhered roofing assemblies rely on adhesive to bond insulation boards to the substrate and to each other, and to bond the roofing membrane to the insulation. The organic facers on insulation materials make up a significant portion of the principal bonding surface within the assembly. Organic facers are sensitive to moisture, deteriorate when wet, lose cohesive strength, and can fail in service with minimal uplift pressure well below the designed uplift pressure for the assembly. Our empirical observations and computer modeling identified moisture within the roofing assembly as a primary cause of roofing failure in the three cases described above, as well as at numerous other buildings that we have investigated.

After placement, a concrete roof deck or topping slab slowly releases moisture as it cures and dries. Concrete must be allowed to sufficiently dry before roofing materials are installed in order to prevent detrimental residual moisture within the roofing assembly. Roof deck configurations often limit drying to the interior, and it can take months for concrete several inches thick to dry sufficiently through the concrete top surface to reduce the risk of roofing assembly failure due to trapped moisture. Our field measurements and computer modeling in the above-noted case studies indicated that the average relative humidity of the concrete roof deck substrates was likely higher than is acceptable prior to roofing assembly installation, and the concrete substrate was the primary source of residual moisture within each roofing assembly.

A vapor retarder installed on top of a roof deck limits vapor diffusion into the roofing assembly on roofs with significant seasonal periods with a vapor drive to the exterior (as in most of the United States). A properly selected and installed vapor retarder will limit the flow of residual moisture from a concrete deck into a roofing assembly, where it will become trapped after roofing membrane installation. The use of a vapor retarder also limits vapor diffusion into the roofing assembly from other sources. A vapor retarder might be required in order to separate roofing materials from sources of moisture or allow the installation of roofing materials over substrates with excess residual moisture to enable timely installation of the roofing assembly.

Other sources of moisture within the roofing assembly can have a negative effect on the performance of a roofing system. Case 3 included a leak into the assembly from a cooling tower, which increased moisture within the assembly and exacerbated the deterioration of the insulation facers and the loss of adhesion. Other sources of increased moisture in the roofing assembly can include leaks under the assembly during construction or the installation of wet roofing materials.

For case 1 and case 2, we also noted air flow into the roofing assemblies during our investigations. Although additional roofing assembly moisture load via vapor diffusion from the building interior through the roof deck was likely minimal, the moisture load and condensation potential within the roofing assembly likely increased from moisture-laden air from the building interior entering the roofing system. Consequently, in addition to a vapor retarder, a continuous air barrier might also be required as part of the roofing assembly (i.e., air seals at the building perimeter wall to roof deck transition, roof deck penetrations, etc.) in order to limit the flow of moisture-laden interior air into the roofing system. A continuous air barrier installed as part of the roofing assembly will also limit exterior air flow into the roofing system.

Each of the case studies presented above also included defects in the application of the insulation board adhesive that contributed to the roofing failures, as noted in our previous work. We concluded that both the moisture within the roofing assembly and insulation board adhesion defects were independently sufficient to cause detached insulation boards and roofing membrane. The resulting roofing assemblies were unable to resist reasonably anticipated wind forces, and they required repairs.

Design and Construction Considerations

A vapor retarder limits the passage of water vapor and might be required in order to separate the roofing assembly from substrates with excessive residual moisture or other sources of moisture that might enter the roofing assembly. Similarly, an air barrier might also be required in order to limit the infiltration of moisture-laden air into the roofing assembly. The roofing industry (including roofing system and roofing adhesive manufacturers, roofing designers, and roofing contractors) often does not provide sufficient project-specific direction regarding the requirement for a vapor retarder and/or an air barrier. Roofing assembly and roofing adhesive manufacturers' literature generally requires installation over a "dry" substrate, but manufacturers do not provide specific or practical criteria for evaluating concrete roof deck moisture content. Without defined and measureable criteria, the requirement for a "dry" substrate provides little guidance to control the risk of roofing assembly damage from residual moisture contained in the concrete roof deck. Common methods of concrete roof deck moisture testing, such as the "rubber mat test" (ASTM D4263 [9]), can falsely indicate a "dry" concrete substrate under some ambient test conditions and are unreliable as the sole evaluation of concrete moisture.

The issue of moisture in concrete roof decks is similar to moisture issues that must be considered when installing floor coverings on concrete substrates.

The flooring industry continues to refine maximum moisture threshold criteria and test protocols in order to help prevent catastrophic flooring failures resulting from moisture in concrete substrates that leads to adhesive failure. The roofing and roofing adhesive industries provide less definitive moisture criteria and test protocols for concrete roof decks. We suspect that this is driven, in part, by the impact of weather conditions, variable concrete mixes, and scheduling pressure for the contractor to quickly provide a weather-tight facility, limiting the amount of time that a roof substrate can be left exposed, and affecting the practicality of implementing more sophisticated and reliable test protocols. Flooring industry substrate moisture guidelines and standards for installation might provide guidance for the development of similar roofing guidelines and standards, but future roofing substrate moisture testing protocols must consider different field conditions and installation constraints in order for the protocols to be useful and practical. In our practice, we have attempted to correlate more sophisticated and reliable concrete substrate moisture testing with less invasive moisture testing techniques during roofing installation, but data collection is limited, because our field work is also constrained by the need to install or re-install roofing assemblies in order to maintain a weather-tight facility. We have found that we can relate relative humidity measurements on specific decks to surface moisture meters to establish a quick field test. However, even when re-roofing a concrete deck after a few years of service, a vapor retarder is often still required.

The roofing and roofing adhesive industries must develop guidelines or standards that provide more reliable and practical roof substrate moisture testing protocols to help roofing designers, roofing contractors, and building owners reduce the risk of installing roofing assemblies on wet substrates that lead to adhesive bond ineffectiveness and roofing assembly failure. If an acceptable substrate moisture content cannot be achieved, then the protocol should recommend the installation of a vapor retarder (and possibly an air barrier) directly above the roof substrate.

References

- [1] Slick, D. S., Piteo, N. A., and Rutila, D. A., "Case Studies of Foamed Adhesive Failures of Low Sloped Roofing Rigid Insulation Board," *Seventh Symposium on Roofing Research and Standards Development, Tampa, FL, November 2011*, ASTM International, Conshohocken, PA.
- [2] ASTM D907-08b, 2010, "Standard Terminology of Adhesives," *Annual Book of ASTM Standards*, Vol. 15.06, ASTM International, West Conshohocken, PA, pp. 1–12.
- [3] ASTM C1289-10, 2010, "Standard Specification for Faced Rigid Cellular Polyisocyanurate Thermal Insulation Board," *Annual Book of ASTM Standards*, Vol. 04.06, ASTM International, West Conshohocken, PA, pp. 1–8.
- [4] ASTM C1616-07e01, 2010, "Standard Test Method for Determining the Moisture Content of Organic and Inorganic Insulation Materials by Weight," *Annual Book of ASTM Standards*, Vol. 04-06, ASTM International, West Conshohocken, PA, pp. 1–2.

- [5] ASTM F2170-09, 2010, "Standard Test Method for Determining Relative Humidity in Concrete Floor Slabs Using In Situ Probes," *Annual Book of ASTM Standards*, Vol. 15-04, ASTM International, West Conshohocken, PA, pp. 1-5.
- [6] ASTM D4637-10, 2010, "Standard Specification for EPDM Sheet Used in Single-Ply Roof Membrane," *Annual Book of ASTM Standards*, Vol. 04-04, ASTM International, West Conshohocken, PA, pp. 1-5.
- [7] *WUFI Pro 4.2*. (2008). Fraunhofer Institute for Building Physics, Stuttgart, Germany.
- [8] American Society of Heating, Refrigerating, and Air-Conditioning Engineers, *2009 Handbook of Fundamentals*, American Society of Heating, Refrigerating, and Air-Conditioning Engineers, Inc., Atlanta, GA, 2009.
- [9] ASTM D4263-83, 2010, "Standard Test Method of Indicating Moisture in Concrete by the Plastic Sheet Method," *Annual Book of ASTM Standards*, Vol. 06-02, ASTM International, West Conshohocken, PA, pp. 1-2.
- [10] ASTM E96-10, 2010, "Standard Test Methods for Water Vapor Transmission of Materials, Procedure B," *Annual Book of ASTM Standards*, Vol. 04-06, ASTM International, West Conshohocken, PA, pp. 1-12.

PERFORMANCE UNDER SEISMIC LOADS

K. A. Broker,¹ S. Fisher,² and A. M. Memari³

Seismic Racking Test Evaluation of Silicone Used in a Four-Sided Structural Sealant Glazed Curtain Wall System

ABSTRACT: This paper presents the results of a study in which four-sided structural sealant glazing (SSG) insulating glass curtain wall units were subjected to cyclic racking test methods in accordance with AAMA 501.6 testing protocols. The test configuration included three side-by-side primary units and a corner unit. High-resolution cameras were utilized to capture instantaneous images during the racking test so that the displacement within the sealant joint could be captured and isolated from the displacement of the entire glazed unit. Drift capacity of the system in terms of glass attachment and sealant performance is reported in detail for different levels of racking displacements and boundary conditions. The overall behavior of the system is characterized, and specifically the sealant performance at a corner condition during racking drift is discussed. Additionally, expected strains in the sealant were calculated using a linear-elastic finite element model and were then compared with the strains the actual structural sealant joint underwent during system testing. Silicone sealant damage was evaluated using visual observation before and after cyclic racking. The paper discusses proposed acceptable sealant stress levels for seismic design and the durability of silicone used in the SSG system as compared to dry-glazed systems based on glass performance.

Manuscript received June 18, 2011; accepted for publication November 29, 2011; published online March 2012.

¹Dow Corning Corporation, 4742 Liberty Rd. S #346, Salem, OR 97302, e-mail: k.broker@dowcorning.com

²Bagatelos Architectural Glass Systems, Inc., 2750 Redding Ave., Sacramento CA 95820-2156, e-mail: sfisher@bagatelos.com

³Dept. of Architectural Engineering, Penn State Univ., 104 Engineering Unit A, Univ. Park, PA 16802, e-mail: memari@enr.psu.edu

Cite as: Broker, K. A., Fisher, S. and Memari, A. M., "Seismic Racking Test Evaluation of Silicone Used in a Four-Sided Structural Sealant Glazed Curtain Wall System," *J. ASTM Intl.*, Vol. 9, No. 3. doi:10.1520/JAI104144.

Copyright © 2012 by ASTM International, 100 Barr Harbor Drive, PO Box C700, West Conshohocken, PA 19428-2959.

KEYWORDS: racking test, seismic evaluation, structural sealant glazing, curtain walls, silicone, Finite Element Modeling

Introduction

There has been an ongoing effort at Pennsylvania State University to develop test data and behavior prediction of different types of glass attachment methods under seismic in-plane racking conditions. A thorough compilation of data and prediction approaches has been published encompassing mechanically captured two-sided and four-sided structural sealant glazing (SSG) designs. An industry need has been identified in particular to further this work to encompass the behavior of four-sided SSG curtain wall systems under seismic in-plane racking conditions. Four-sided SSG is a method of attaching glass to the aluminum mullions in curtain wall systems using only silicone sealants and no mechanically captured glazing pockets. This construction method has been used in the United States since 1971 with monolithic glass and since 1978 using insulating glass units [1]. Many buildings in high seismic zones of California were built employing four-sided SSG in the 1980s, with a proven history of success. Publications documenting glass damage (e.g., glass pieces falling out) in four-sided SSG construction after the Northridge earthquake in 1994 are not available, although one publication [2] mentions sealant damage in one building. In fact, according to EERI [3], most of the glass damage occurred in storefronts with large glass panes and that glazing systems with silicone sealant on one or more edges generally performed better than dry-glazed systems. Despite lack of evidence for poor seismic performance of four-sided SSG, building code officials in some areas, including the cities of Los Angeles and Irvine, noted that four-sided SSG was not explicitly recognized in the California Building Code or the International Building Code, and consequently the system has not been uniformly accepted in high seismic zones, in particular for healthcare facilities. Some recent research has addressed the topic of two-sided SSG [4,5], making it an easier system to present to building owners and building departments. Much of the existing data regarding four-sided SSG has been limited to a study in the 1990s by Zarghamee et al. [2], a recent study by Memari et al. [6], and many field history cases. There is still a significant need for better understanding of the seismic behavior of four-sided SSG systems. The need for further filling this gap in laboratory research and proving the performance of four-sided SSG has been felt for years. The research work in this paper intends to help fill this gap.

This paper will present actual seismic racking results on a full-scale curtain wall system mock-up that is of a design that would be expected to be installed in a real world project. The system was built by the California glazing subcontractor, Bagatelos Architectural Glass Systems, in cooperation with Dow Corning and tested at the Pennsylvania State University, using their dynamic racking test facility. The curtain wall system mock-up performance has been evaluated in accordance with AAMA 501.6 test protocols [7]. Additionally, this mock-up included a corner condition to address concerns about differential movement or interaction of adjacent glazing units to either side of a building corner. These results will be compared with the analytical results from a finite

element (FE) Model. Finally, this paper presents sealant test results, which show the modulus stability and durability of silicone sealants, making it one of the ideal choices of materials for the flexible anchorage system required to attach glass and perform satisfactorily in a seismic event.

Background

Four-sided SSG systems have been designed, since their inception, using the principles found in ASTM C-1401 [8]. The accepted maximum allowable stress in a sealant subjected to wind loading has been established as 20 psi (138 kPa). This was based on loading probabilities and the strength of sealants at the time ASTM C 1401 [8] was initially published. The probability of occurrence of the building code level design wind event in any one year is 0.02 (50-yr recurrence interval) [9], which corresponds to an effective load duration of 1 min, as discussed by Zarghamee et al. in 1996 [2]. The probability of occurrence of the building code level design seismic event in any one year is 0.002 (500-yr recurrence interval) [10], which corresponds to an effective loading duration of 1 s, per the Uniform Building Code as it existed in 1996 [11]. For these reasons, and the increased strength of sealants since the late 1970s, in 1996, Zarghamee proposed that 50 psi would be an acceptable maximum allowable level of sealant stress when designing for seismic loading [2]. The authors believe that based on the results generated by the present study, this proposed sealant maximum allowable design stress is reasonable and defensible for a four-sided SSG system in a high seismic zone.

As noted, two-sided SSG systems, which employ silicone for attaching two sides of the glass lite and mechanical gaskets to attach the opposite two sides, have been tested under racking conditions [4,5]. In these studies, two-sided SSG systems were compared to “dry glazed” systems, in which all four sides are mechanically captured with gaskets. Key conclusions from these works show that serviceability and drift capacities of two-sided SSG systems are significantly higher than their dry-glazed counterparts. Additionally, Memari et al. [5] noted by air leakage testing that both two-sided SSG and dry-glazed systems do leak air and that air leakage is increased after racking, even if the sealant sustains no visible damage. Based on the results of these studies, it can be assumed that a discontinuously sealed system with dry gaskets or sealant/gasket transitions will not maintain as high a serviceability performance level after seismic racking as compared to a continuously sealed system such as four-sided SSG. Data from actual buildings experiencing earthquakes has not yet been collected and published to conclusively prove this assumption and quantify the increased serviceability of a four-sided SSG system. However, a recent study on a four-sided SSG stick-built system [6] does confirm that a four-sided SSG system will have better overall seismic performance than a two-sided SSG and dry-glazed system. The authors of the paper presented here hope that the results of the research/testing discussed in the following sections will further address this issue in a meaningful way.

Research Program

The main objective of the research project discussed in this paper was to develop new experimental data to evaluate the behavior of structural silicone

under simulated seismic-induced deformation conditions. Although considerable tension and shear test data on structural silicone coupons is available, test data on a continuous sealant bead under four-sided SSG configuration is very limited. In particular, for the coupon test results to be more useful for application to assess seismic performance of structural sealants, some correlation needs to be developed between the continuous bead sealant behavior in a full-scale four-sided SSG mock-up under cyclic racking conditions and coupon tests on isolated short length sealant beads. Such full-scale racking test results can also help evaluate the proposed 50 psi (345 kPa) allowable sealant stress for seismic application. Another objective of the research was to use the results of full-scale testing to evaluate the accuracy of linear elastic FE modeling of the mock-up in predicting sealant deformation/stresses.

In designing the test mock-up configuration, it was important to note that in unitized systems, the corner condition poses the most unknown behavior, as most prior mock-up tests have considered only planar conditions. The reason for the importance of the corner condition has to do with the interaction of the two perpendicular panels at the corner, which leads to vertical shear transfer between the intersecting panels. Such vertical shear actually is expected to have more influence on the corner mullion especially if it is of a split mullion type. The test mock-ups were designed to evaluate the behavior of one type of unitized system developed by Bagatelos Architectural Glass Systems. It should be noted that unitized systems are custom designed and each designer will provide framing and connection details different from others. To develop a more complete understanding of the seismic response of the particular framing system developed by Bagatelos Architectural Glass Systems, the boundary condition of the vertical mullion stack joints was chosen as a variable. This allowed comparison of the behavior of a complete unitized system with sliding vertical mullions to the behavior of a system that emulated a stick-built condition with restrained vertical sliding. The details of the mock-up construction and boundary conditions are explained in the next section.

The racking tests followed the AAMA 501.6 [7] testing protocol that requires full-scale mock-ups be constructed and attached to a racking facility and be subjected to the pre-determined displacement cyclic history. In this study, the racking facility at the Pennsylvania State University, shown in Fig. 1 with a typical mock-up attached to the facility, was used. Mock-ups were attached to the sliding steel tubes of the facility. A computer-controlled actuator applies a given displacement at a given frequency (per the AAMA 501.6 test protocol) to the bottom sliding tube, and through the fulcrum arm, the top tube displaces an equal amount in the opposite direction. This motion simulates the drift a given story may experience during an earthquake. Each applied racking displacement step includes: a ramp-up period that builds within four cycles to the peak displacement at that step, four constant-amplitude cycles at the peak displacement, and a four-cycle ramp-down period. Each racking step increases in magnitude by 1/4 in. (6.4 mm) until facility capacity is reached (6 in. (152 mm) displacement) or complete mock-up failure occurs. Concatenation (joining) of the steps yields the AAMA 501.6 specified cyclic displacement protocol as shown in Fig. 2. The drift a specific building structure can be expected to experience

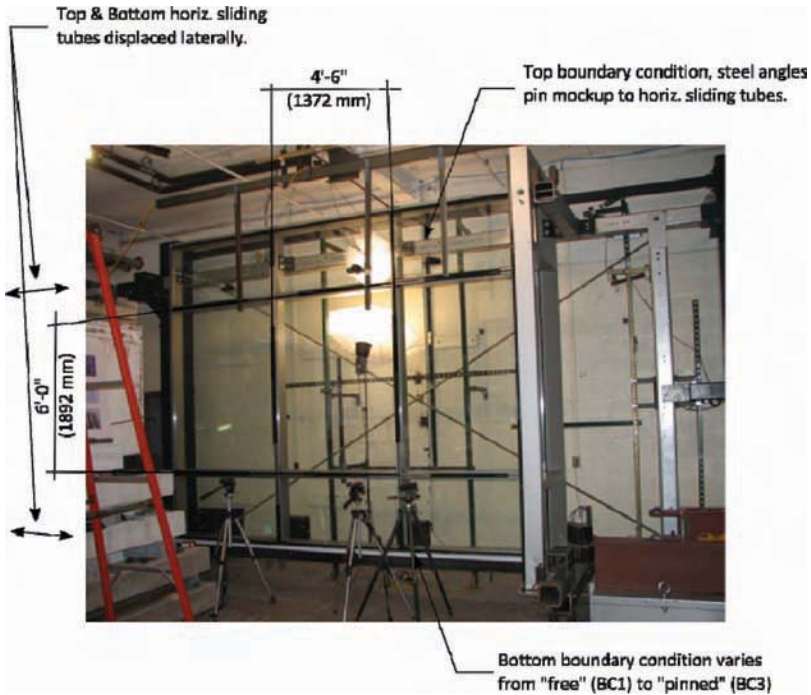


FIG. 1—Typical mockup mounted on the racking test facility.

during a design level seismic event is a function of the building primary lateral force-resisting system and the seismic ground motion expected to occur at the site. It is typical for building codes to restrict the buildings expected drift to between 1.25% and 2.00% of building story height.

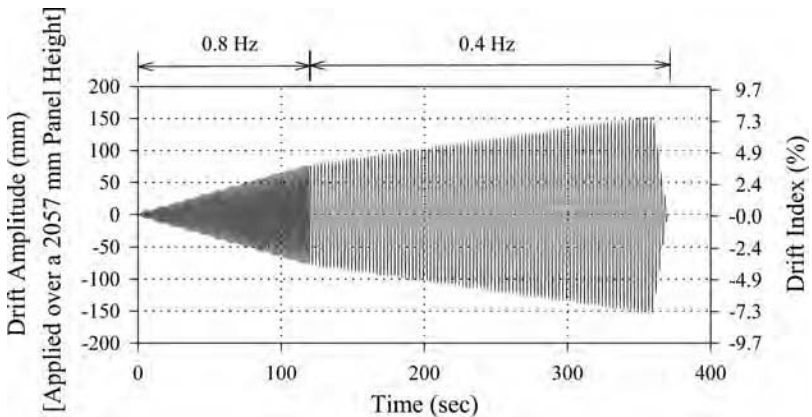


FIG. 2—Concatenated drift time history for AAMA 501.6 dynamic racking test.

Mock-up Construction/Testing Configurations

Three full-scale identical curtain wall mock-ups, including the corner section (three face units and one corner unit), were fabricated. The elevation and plan views are shown in Figs. 3 and 4. Details of the typical vertical mullion, corner vertical mullion, and typical horizontal mullion are shown in Figs. 5, 6, and 7. The structural sealant bead along the vertical mullion has a glue line thickness of 9/16 in. (14 mm) and a width of 9/16 in. (14 mm). The structural sealant bead along the horizontal mullion has a glue line thickness of 5/16 in. (8 mm) and a width of 9/16 in. (14 mm). Sealant joints were designed taking into consideration a typical wind load of 30–50 psf (1.4–2.4 kPa) and a maximum glass width of 5 ft. (1524 mm), yielding a required sealant bite of 7/16 in. (11 mm) using the commonly accepted “trapezoidal loading theory” for calculating sealant bite dimension based on windload (ASTM C 1401 [8]). The equation for calculating sealant bite for rectangular lites of glass, for windload conditions, is as follows:

$$\text{Sealant bite in inches} = \frac{\{0.5 \cdot \text{short span length (ft)} \cdot \text{windload (psf)}\}}{\{12 \text{ in./ft} \cdot \text{sealant design strength (20 psi)}\}}$$

$$\text{Sealant bite in mm} = \frac{\{0.5 \cdot \text{short span length (mm)} \cdot \text{windload (kPa)}\}}{\text{sealant design strength (138 kPa)}}$$

Although there is no published seismic sealant bite equation per se, it was good engineering judgment to increase the sealant bite as the curtain wall design

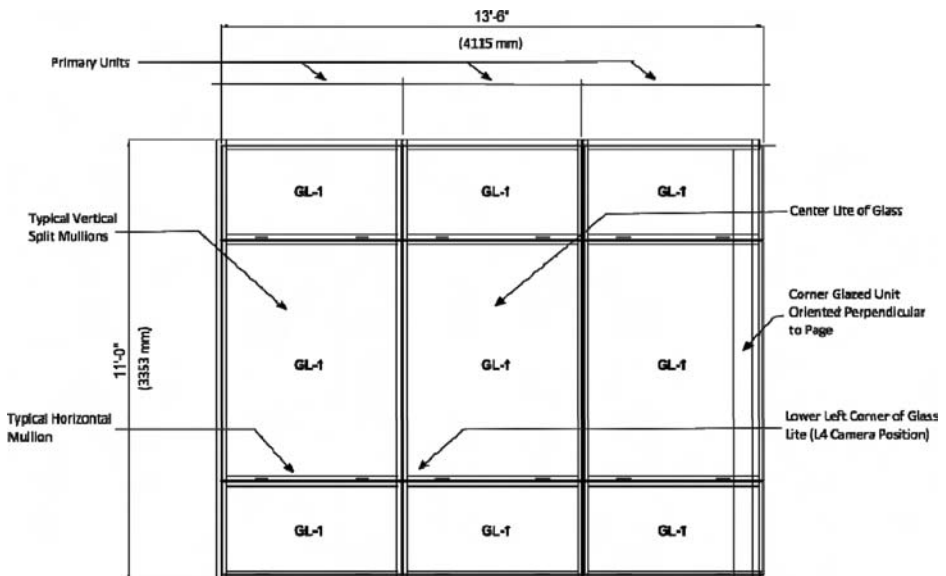


FIG. 3—Full curtain wall mockup elevation.

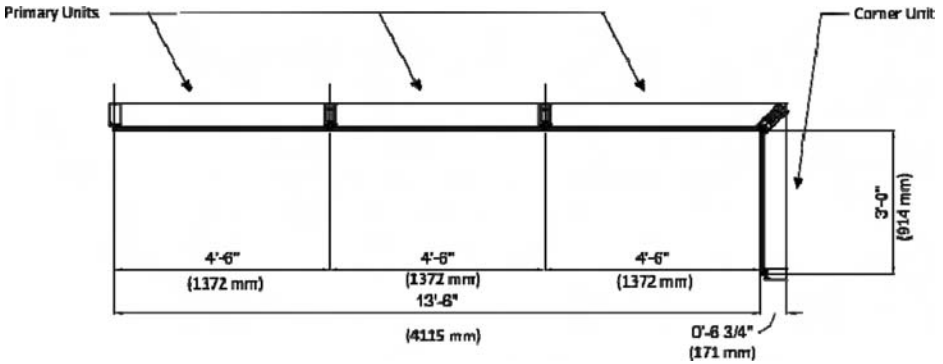


FIG. 4—Full curtain wall mockup plan.

allowed to provide a sealant thickness that could accommodate more shear deflection, while still maintaining a joint dimension that would typically be found in a real curtain wall design. Per industry standard structural glazing guidelines, sealant glue-line thickness is not to exceed the sealant width or “bite” (ASTM C1401 [8]), thus the resultant sealant thickness was 9/16 in. (14 mm) and 5/16 in. (8 mm) as noted above.

Three complete curtain wall mock-ups were constructed to have a repeatable system to test, while allowing for varying boundary conditions to be studied. The method by which the mullions are attached to the building can have a significant impact on the curtain wall performance independent of the glazing attachment method. For that reason it was decided to test these mock-ups in three distinct attachment configurations or boundary conditions. The three boundary conditions that were tested include: sway (boundary condition 1), rack with an allowance for vertical slip between vertical mullions (boundary

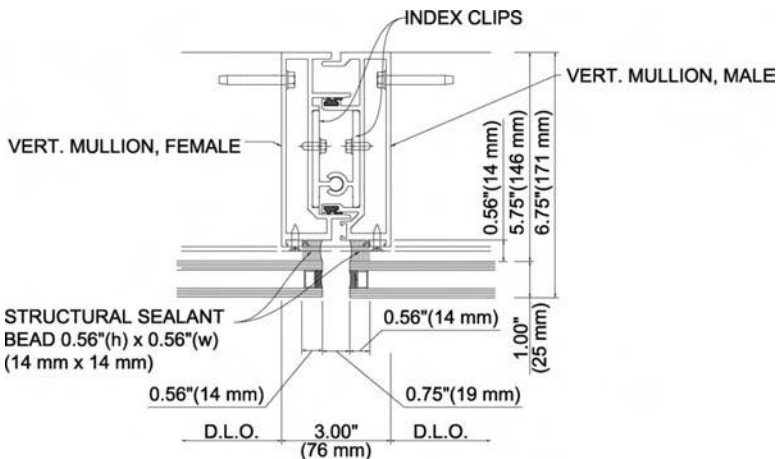


FIG. 5—Typical vertical split mullion.

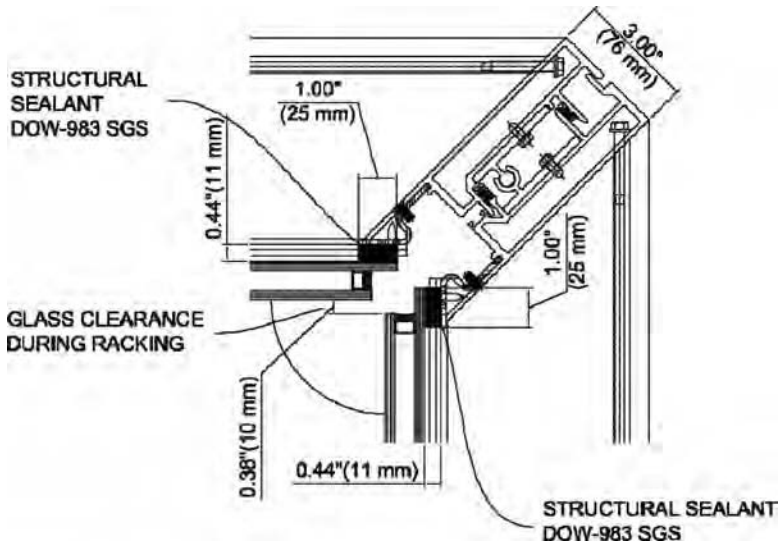


FIG. 6—Corner vertical split mullion.

condition 2), and rack (boundary condition 3). Refer to Fig. 8 for a description of these three boundary conditions.

Boundary condition 1, “sway,” is commonly referred to as a “unitized” curtain wall system. Curtain wall units in this type of system are typically fabricated one building story in height. As they are attached to the building, the bottom of the unit is “nested” into the top of the unit below. This “nesting” allows the units above and below each other to drift in-plane independently. The only source of restraint that is expected will likely come from the corner

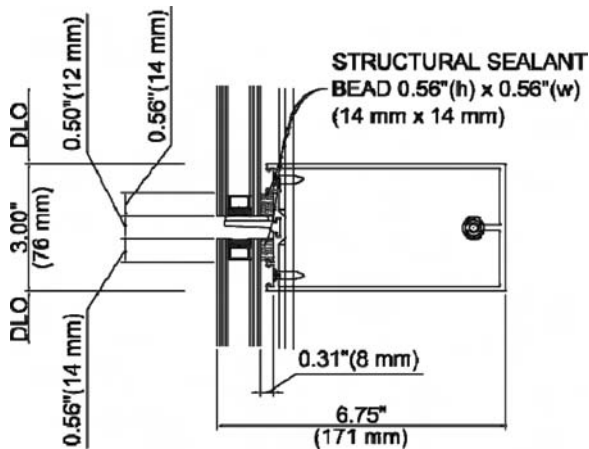


FIG. 7—Typical horizontal mullion.

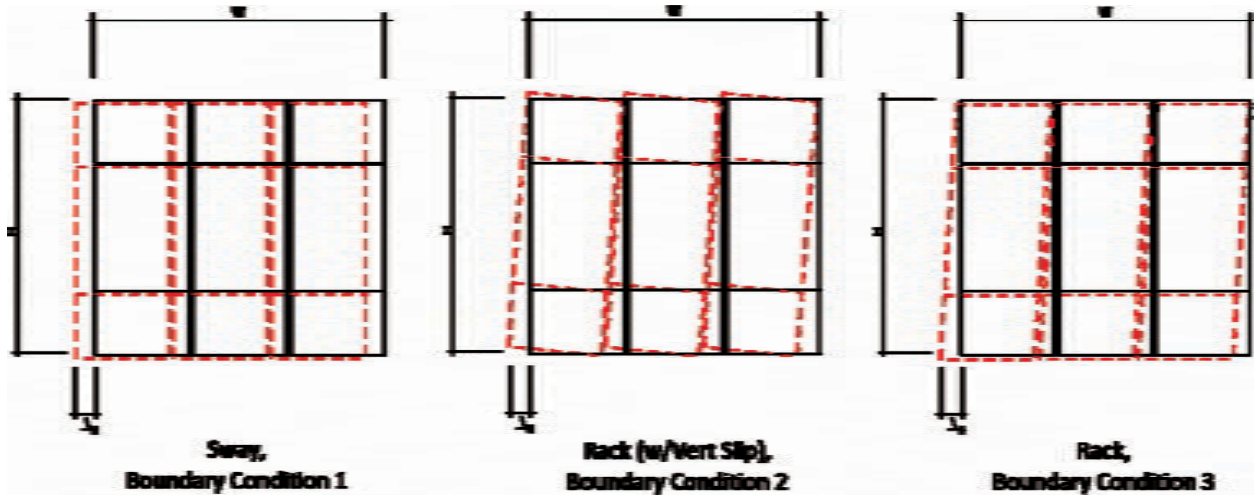


FIG. 8—Mock-up tested boundary conditions.

condition. Boundary condition 3, “rack,” is commonly referred to as a “stick-built” curtain wall system. In this type of system, the vertical mullions are attached to each building level to restrain movement of the mullion (with respect to the building structural system) in both the lateral (in the plane of the curtain wall) and transverse (normal to the plane of the curtain wall) directions. When the building displaces in a seismic event the vertical mullions will lean or rack with the building. Boundary condition 2, “rack with vertical slip,” is a hybrid attachment system. The vertical mullions are attached at each building level, and therefore rack as the building drifts. During this racking, the vertical male–female mullions are able to slip vertically slightly relative to each other. It is believed that this movement between the split vertical mullions will help to reduce some of the stress the sealant would normally experience during seismic racking behavior (boundary condition 3). It is therefore expected that this boundary condition will result in better performance than boundary condition 3.

Because the amount of sealant movement during boundary condition 1 is expected to be low (i.e., no sealant damage), it was assumed that it would be possible to test a second boundary condition (2 or 3) on the same physical mock-up unit. Many systems are attached such that sway is the primary expected movement during a seismic event. As the Zarghamee et al. [2] work attests to, sway does not allow much of the stress generated from the seismic movement to transfer to the glass-attachment system (regardless of its construction type). Boundary condition 3, “rack,” is expected to transfer the maximum amount of loading to the glass-attachment system, in this case, the silicone sealant on all four sides. This is the most severe case for a four-sided SSG system with regard to stress being transferred through the sealant. Boundary condition 2, “rack with vertical slip,” is expected to produce results somewhere in between boundary conditions 1 and 3.

Sealant Durability/Stress–Strain Graphs

The curtain wall systems were tested within 3 months after their construction. It must also be shown that the sealant system chosen for this application would perform equally as well after many years of weathering. There is extensive published work already available on the durability of silicone sealants [12–14]. As part of this research effort, some of that work has been updated and expanded to further illustrate the durability of silicone sealants. In particular, tensile adhesion samples were tested before and after weathering as well as shear adhesion samples. Cyclic testing, using AC45 criterion [15], to 50 psi (345 kPa) was also performed on sealants to show the effect of cyclical strain experienced during a seismic event.

The sealant that would generally be specified for curtain wall applications that are shop-fabricated is a high modulus, 25% movement capability, two-part quick curing 100% silicone sealant. Additionally, a high modulus, 50% movement capability, single-component 100% silicone sealant was tested so that a single-component sealant would also have documented results for its suitability. Single-component sealants are generally easier to work with in the field and may be used for reglazing or stick built/field installed units.

The tensile adhesion samples were constructed and tested to ASTM C1184 [16] criteria (Fig. 9). Per this criteria, the sample sealant dimension being tested is 2 in. (50 mm) long (left to right, Fig. 9) \times 1/2 in. (12.5 mm) deep (front to back in Fig. 9) \times 3/8 in. (9.5 mm) thick (top to bottom in Fig. 9). These are the same dimensions as for the shear sample, but the shear sample is pulled in the shear direction as shown in Fig. 10.

The movement rate for the pull testing was 0.5 in. (12.5 mm) per minute for both shear and adhesion samples in accordance with ASTM C1184 [16], Section 8.6. For the cyclical testing, tensile joints were prepared in the same configuration shown in Fig. 9. The graphs shown below in Figs. 11 and 12 summarize the tensile and shear testing results for the single-component and dual-component structural sealant, respectively. Based on the ultimate stress the sealants are capable of withstanding and the cyclical testing discussed below, 50 psi (345 kPa) is a reasonably acceptable stress level. Considering sealants are flexible materials, the behavior of the sealants from 0 to 50 psi (0–345 kPa) is very repeatable and the sealants in this range are behaving elastically as the cyclical testing discussed shows. The racking test results, discussed later, further validate the elastic behavior of the sealants in this stress range.

Seismic movement placed on the structural sealant bead attached to the inside of the glass lite primarily results in shear behavior. As documented by Zarghamee et al. [2], the shear modulus is approximately 1/4 that of tension. The ultimate strengths in either mode are very similar. For example, at 35 psi (241 kPa) in tension, the sealant strain is approximately 12% in tension and

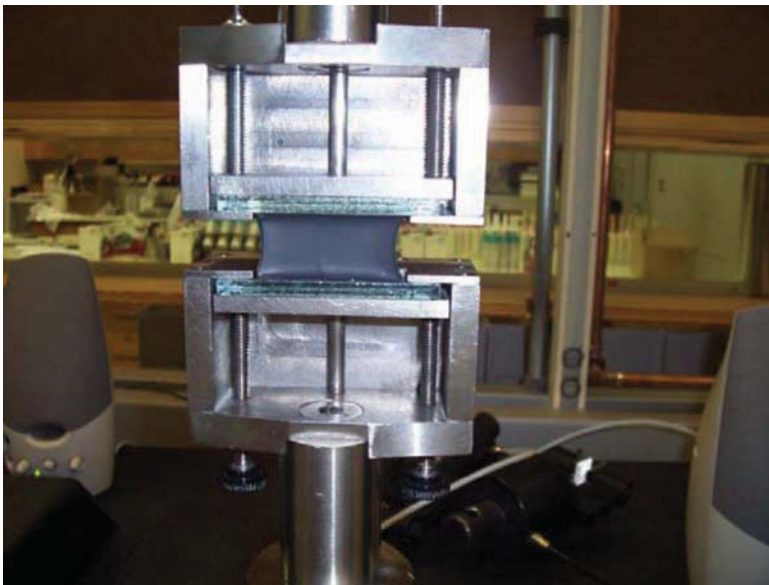


FIG. 9—Typical tensile adhesion sample set up as installed on a tensile testing machine.



FIG. 10—Typical shear adhesion sample set up as installed on a tensile testing machine.

50% in shear when examining Fig. 12 and the behavior of the dual-component sealant. At 35 psi (241 kPa) in tension for the single-component sealant (Fig. 11), the strain on the sealant is approximately 20% in tension and 70% in shear. This is actually favorable for seismic situations in that for a given strain or displacement during a seismic load, the associated stress on the sealant is lower in a shear mode than in a tensile mode. Therefore, using tensile data to design the sealant joint for seismic-induced stress is conservative when considering either a single- or dual-component sealant. Figure 12 also suggests that the behavior of the modulus varies with temperature in that the particular silicone tested at higher temperature shows higher modulus for the two-part sealant; such is not the case, however, for the one-part sealant as shown in Fig. 11. Although more softening of the modulus is generally expected with higher temperatures, the two-part sealant displays slightly different behavior but is within industry specification for silicone used in SSG systems, and some new test results are available in a recent report as well [17].

Per the testing method, the shear and tension results presented are based on pulling the sealant at a constant rate 0.5 in. (12.5 mm) per minute until

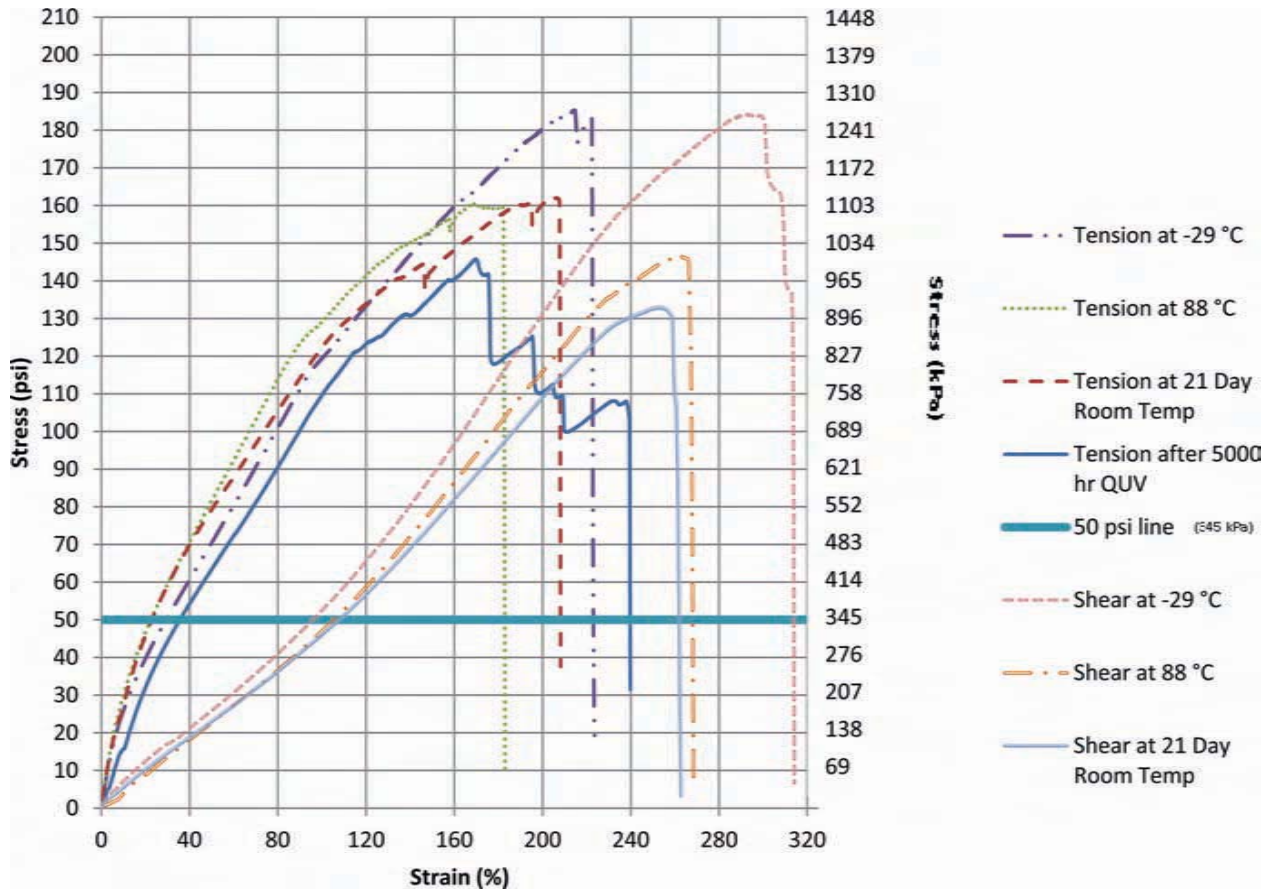


FIG. 11—Stress–strain curve for medium modulus one-part sealant as tested in both shear and tension, at various environmental conditions.

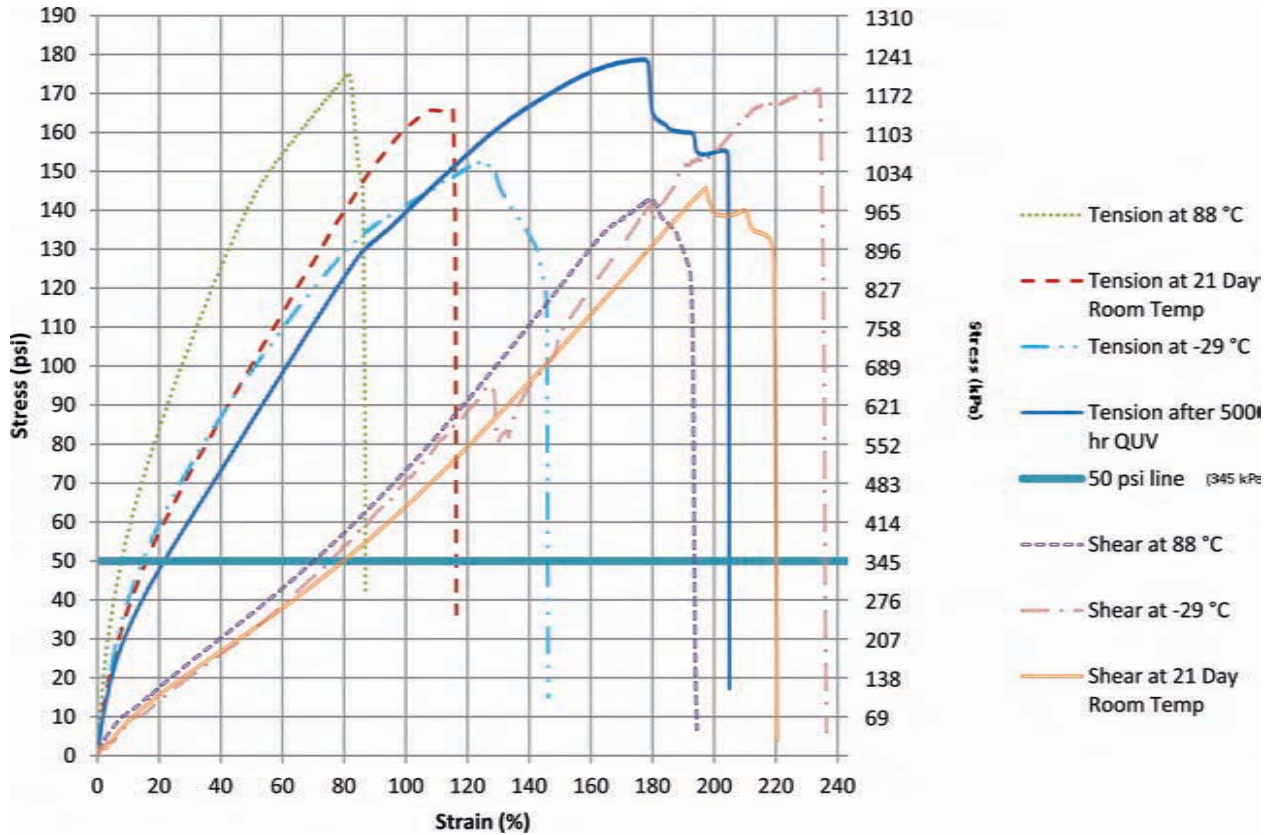


FIG. 12—Stress–strain curve for high modulus two-part sealant as tested in both shear and tension, at various environmental conditions.

destruction. During a seismic event, the sealant will be stressed to a lower level than its ultimate strength, but more likely in a cyclic manner. Consequently, it was proposed to simulate cyclical testing on a tensile adhesion joint to determine if there is any sealant softening after stressing the sealant repeatedly. Based on prior work [2], 50 psi (345 kPa) was chosen as the cyclic stress level. Samples were prepared and pulled to 50 psi (345 kPa), then allowed to relax, then pulled again to 50 psi (345 kPa) and allowed to relax for four cycles. On the fifth cycle, the samples were pulled to destruction. The strain rate for this testing was 1 in./min (25 mm/min) [15]. This testing was a variation of a standard tensile adhesion test method (ASTM C1135 [18]) and was carried out as new research to look specifically at the effect of a sealant repeatedly reaching 50 psi (345 kPa) in a short-term event. The ability of silicone sealants to withstand long-term cyclic movement due to thermal effects, from a durability standpoint, has already been addressed by an industry study in which sealants were cycled for 36|500 times, estimating 50 to 100 years of durability depending on the environment the silicone would be exposed to [19]. The intent of the shorter term cyclic testing completed here was to assess any effect on ultimate sealant tensile strength when sealants are purposefully pulled to 50 psi (345 kPa) during a short-term event such as an earthquake, versus a long-term cyclic stress such as thermal movement over many years. It is understood that during a seismic event that the number of cycles (including low and high amplitudes) will likely exceed five and an intermediate level of cycles could be considered for future sealant testing.

This cyclic testing was performed in tension, as it has been shown in this research and prior industry studies [20] that tensile testing provides conservative results relative to shear testing when evaluating design stresses for a sealant. It is understood that the results of cyclic testing in shear would provide valuable additional insight into sealant performance. As can be seen in Figs. 13 and 14, pulling either the 1- or 2-component sealant to 50 psi (345 kPa) repeatedly has very little effect on its ultimate strength. The cyclic testing was performed at room temperature, so the final result of the sample pulled to destruction can be compared to the room-temperature samples from the tensile adhesion testing referenced above. Five samples were cyclically pulled for each sealant, and the averages are presented in Table 1. One typical sample is depicted in the graphs for clarity.

The other important sealant properties to account for when considering seismic design are durability of the sealant and consistency of the sealant's strength and modulus properties over time, which can be seen in the 5000-h QUV exposure (accelerated weathering testing under ultraviolet light frequencies and condensation) and extreme temperature exposure conditions (Tables 2 and 3). The weathering criteria included low-temperature exposure (-29°C), high-temperature exposure (88°C), and 5000 hr QUV exposure, cycling from 8 hr at 60°C with ultraviolet (UV) exposure to 4 hr 50°C condensation. Modulus has been used here to indicate sealant stability across these conditions. The moduli reported have been calculated at 10% sealant strain. Young's modulus is calculated by taking the slope of a 0.2% offset trend line through the sealant stress-strain curve, from 0 to 10% strain in this case. Although peak stress may

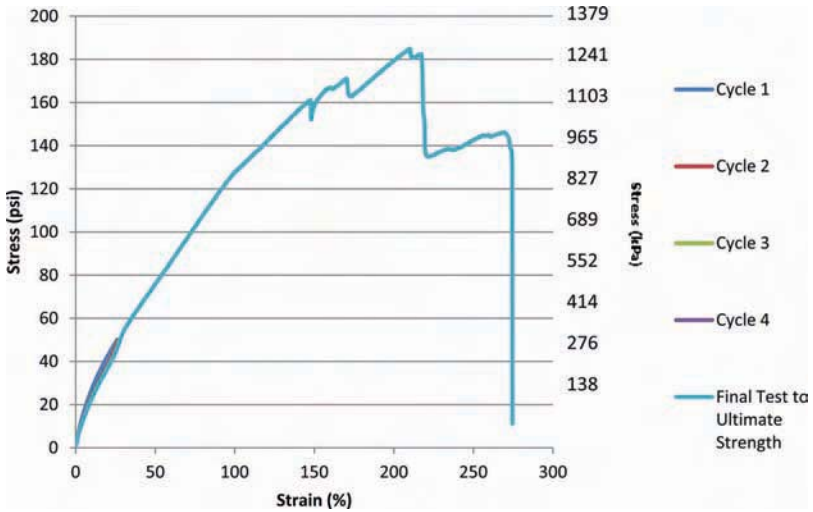


FIG. 13—Stress–strain curve for cyclical testing of one-component medium modulus sealant to 50 psi (345 kPa) with final test to ultimate strength.

fluctuate somewhat, if the modulus is remaining relatively stable, this indicates sealant durability. Results are presented in Tables 2 and 3 for both the two-component and single-component silicone sealants, as tested in shear and tension.

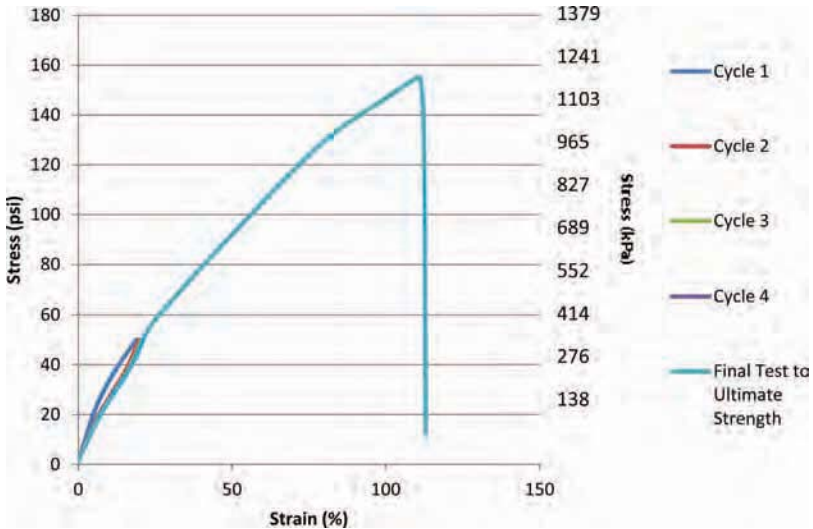


FIG. 14—Stress–strain curve for cyclical testing of two-component high modulus sealant to 50 psi (345 kPa) with final test to ultimate strength.

TABLE 1—*Sealant ultimate stress in tensile adhesion joint versus sealant ultimate stress after cyclical loading.*

Sealant	Ultimate Stress psi (kPa) of Single Pull Sample	Ultimate Stress psi (kPa) of Cyclically Pulled Sample
Single-component silicone at room temperature	160 (1103)	185 (1275)
Two-component silicone at room temperature	166 (1145)	149 (1027)

TABLE 2—*Summary shear data: 21-day room temperature (RT) cure (+ environmental exposures).*

Sealant	Ultimate Stress psi (kPa)	Ultimate Strain (%)	Young's Modulus psi (kPa)
Single-component silicone RT	133 (917)	253	45 (310)
Single-component silicone RT + 1 hr 88°C + 3 hr RT dwell	147 (1013)	262	47 (324)
Single-component silicone RT + 1 hr -29°C	184 (1268)	293	50 (345)
Two-component silicone RT	146 (1006)	198	71 (490)
Two-component silicone RT + 1 hr 88°C + 3 hr RT dwell	143 (986)	179	73 (503)
Two-component silicone RT + 1 hr -29°C	170 (1172)	228	65 (448)

TABLE 3—*Summary tensile adhesion data: ASTM C-1135 data, 21-day RT cure (+ environmental exposures).*

Sealant	Ultimate Stress psi (kPa)	Ultimate Strain (%)	Young's Modulus psi (kPa)
Single-component silicone RT	160 (1103)	191	231 (1592)
Single-component silicone RT + 1 hr 88°C + 3 hr RT dwell	160 (1103)	171	236 (1627)
Single-component silicone RT + 1 hr -29°C	185 (1275)	214	230 (1586)
Single-component silicone RT + 5000 hr UV exposure	145 (1000)	171	200 (1379)
Two-component silicone RT	166 (1144)	114	358 (2468)
Two-component silicone RT + 1 hr 88°C + 3 hr RT dwell	175 (1206)	81	399 (2751)
Two-component silicone RT + 1 hr -29°C	151 (1041)	128	364 (2510)
Two-component silicone RT + 5000 hr UV exposure	177 (1220)	179	401 (2765)

It is common that sealants are assumed to stiffen at cold temperatures and soften at high temperatures, but in general silicones are still more stable across a variety of conditions than other sealant chemistries [13]. In particular, the dual-component sealant represented in Fig. 12 actually displays tensile behavior opposite from what may be expected by some stiffening within a certain range of (environmental) high-temperature exposure; but the modulus is not significantly affected (Table 3) and the ultimate strength across all conditions is still well above 50 psi (345 kPa). It is a unique property of the sealant tested in this study but has posed no performance issue as the sealant has been used for structural glazing for many years in Europe and the United States. A recent test report [17] presents additional test data regarding this sealant behavior.

Additionally, sealant data is presented for 88°C exposure followed by a 3-hr room-temperature dwell time. As the focus of this paper is seismic behavior, the researchers found it very unlikely that a sealant in a construction project would come to an 88°C dwell time of 1 hr and simultaneously undergo a seismic event. However, the authors felt it was important to document any effects on the sealant if it had been exposed to a high-temperature event at some point prior to experiencing a separate seismic event. The important documented behavior is that the sealant can withstand high temperatures and return to its original performance.

The silicone sealants tested show modulus stability across both environmental conditions and cyclical testing. As further shown by this curtain wall rack testing, silicones provide the strength and flexibility to withstand significant seismic-induced movement. Furthermore, the weathering data presented here and in prior work substantiate that silicones provide the durability required for this stringent application.

Finally, the consistency of the results across all conditions, the high ultimate strength of the silicones, and the cyclic testing support the proposition made in 1996 [2] to employ a sealant design stress level of 50 psi (345 kPa) for seismic design.

Field-emission Microscopy Modeling Overview

Frequently on large projects, full-scale performance mock-ups testing protocols are required. Included in these testing protocols is the option to perform a static in-plane racking test AAMA 501.4 [21]. These performance mock-ups may not occur until a year or more after the curtain wall system has been designed. For dry-glazed mechanically captured or two-sided SSG systems whose performance is well documented in industry and research studies, this design and testing sequence is appropriate. For an essential service building (i.e., hospitals, police stations, etc.) with a four-sided SSG system, an AAMA 501.6 [7] test may be employed to prove the suitability of this design because the building will have more stringent serviceability requirements than non-essential construction. The results of the AAMA 501.6 racking test can confirm the design efficacy for actual seismic events. Because this is being used to prove the design, it must be conducted early in the design process. This adds cost to the project not only because of the addition of a second full scale mock-up test but also because a

physical mock-up must be constructed when not all of the design criteria has been established. It would be favorable in the future to be able to predict system performance without a full-scale curtain wall system being tested. To this end, a FE model of the full-scale mock-up tested as part of this research was created to compare and calibrate analytical results with the test results.

The FE model was constructed in a program called *Visual Analysis* by Integrated Engineering Software [22]. This FE modeling program focuses primarily on linear-elastic modeling of structures. Figure 15 shows an overall view of the completed model. The aluminum mullions (vertical and horizontal) are represented by two-node beam elements. Because the influence of the silicone sealant is expected to cause the glass lites to act as “shear” resisting elements, the moment restraints were released where the horizontal mullion beam elements attach to the vertical mullion beam elements. The stiffening influence of a nominal moment connection between the aluminum mullions is expected to be insignificant compared to the stiffening influence of the glass lites, which are attached to the aluminum mullions by the silicone sealant. The structural silicone sealant and the glass lites are represented by three- or four-node plate elements. Figure 16 shows close-up views of glass and sealant plate elements at glass corners. The appropriate linear-elastic material properties for all three materials were entered into the model. For the silicone sealant, the anisotropic and non-linear material behaviors cannot be accounted for in this specific FE modeling software. The Young’s modulus, E , of the silicone sealant was varied

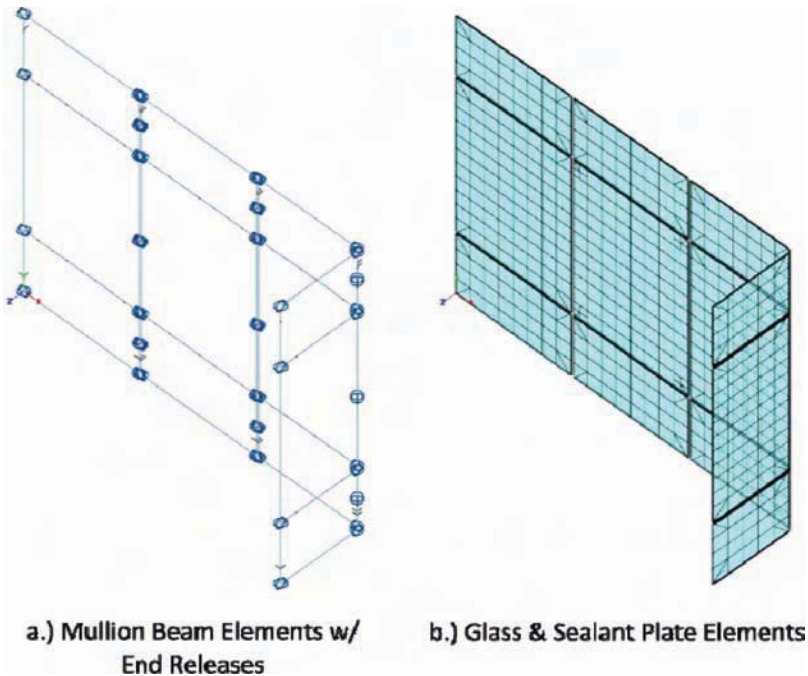


FIG. 15—FE model overall view.

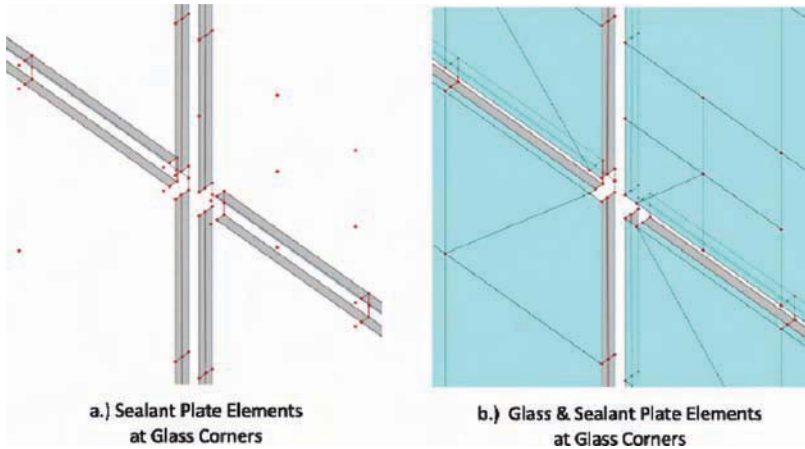


FIG. 16—FE model close-up view.

in separate runs of the model in an attempt to capture both the tension and shear behaviors of the sealant. This was only a rudimentary attempt to capture their effects. A more sophisticated FE software program would be needed to more fully integrate these non-linear sealant properties into the analysis. Additionally, as a result of these modeling limitations, the FE results will be compared only with the test results in the expected linear-elastic range of the sealant.

The FE modeling results presented here only correspond to boundary condition 3, “rack.” Once a good correlation/evaluation of the FE results has been established for this boundary condition as it relates to the corresponding physically tested boundary condition, the FE analysis of the remaining two boundary conditions can be pursued. For boundary condition 3, “rack,” both the top and bottom of the vertical mullions are attached to the testing apparatus with steel angles. In the FE software, these are represented by restraints in the X, Y, and Z directions. No rotational restraints are added at these support locations.

For the actual testing, movements in the mock-up specimens were measured at discrete displacement values. When trying to obtain analytical results from computer software that can be appropriately compared to testing results, it is important to simulate as closely as possible the actual test conditions. Therefore, the FE model was displaced to the same values that were measured in testing. Figure 17 shows a graphical representation of the displaced shape of the FE model at a given displacement. A close up of one of the glass lite intersections can be seen in Fig. 18. In both of these figures, the glass is represented by a “blue” color and the silicone sealant by a “grey” color.

The first step in evaluating the FE model is to review the overall results and determine if they generally correlate with the testing results and what might be considered to be appropriate behavior. From an overall view of the displaced model (Fig. 17), it is evident that the plate elements representing the glass lites are displacing and rotating rigidly. A close-up view of the glass lite intersection

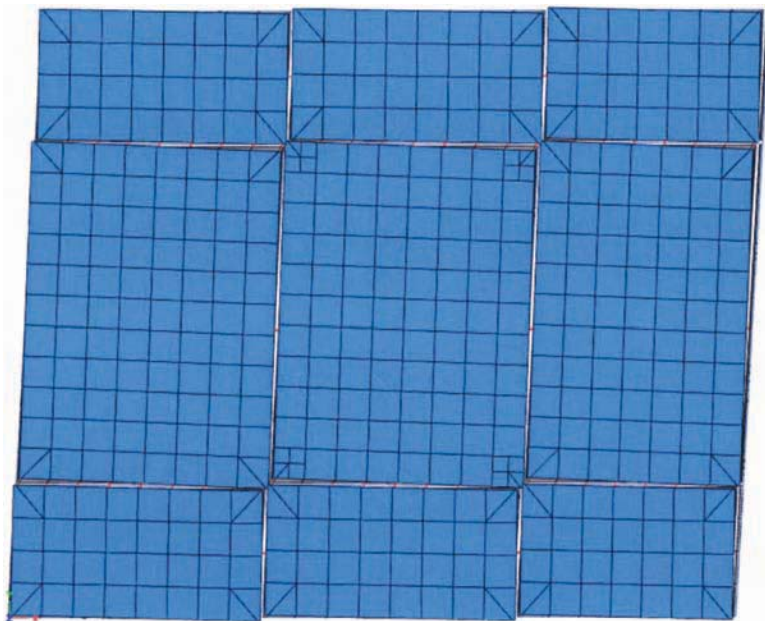


FIG. 17—FE model displaced shape.

(Fig. 18) also reveals that the silicone sealant is being stretched in an elastic manner. Figure 19 shows actual movement of the corners of the glass lite when the mock-up is in a similar displaced condition to the FE model view in Fig. 18. The FE model clearly demonstrates similar movement behavior to that of the actual test. Because the Young's modulus, E , of the glass is 10 100 ksi (69,637 MPa) and the E of the silicone sealant varies between 45 psi (310 kPa) in shear and 400 psi (2758 kPa) in tension (Tables 2 and 3) this type of result would be expected. The silicone sealant is substantially more flexible than the glass lites. The beam elements representing the aluminum mullions are not visible in either of the FE model views represented by Figs. 17 and 18. The aluminum mullion can be seen through the glass on the actual mock-up shown in Fig. 19. Because the strong and weak axis rotational df at each end of these elements are released (no moment) there is no resistance to lateral displacement from these elements in the FE model.

The next step in evaluating the FE model results is to calculate the elongation in the plates that represent the silicone sealant so that they can be compared with the test results. The elongation in the sealant is calculated based on the distance between two nodes that represent the front and back edges of the sealant, which attach a specific location on the glass lite to a corresponding location on the aluminum mullion. The difference in this distance before and after the model is displaced represents the relative elongation of the sealant for a given displacement.

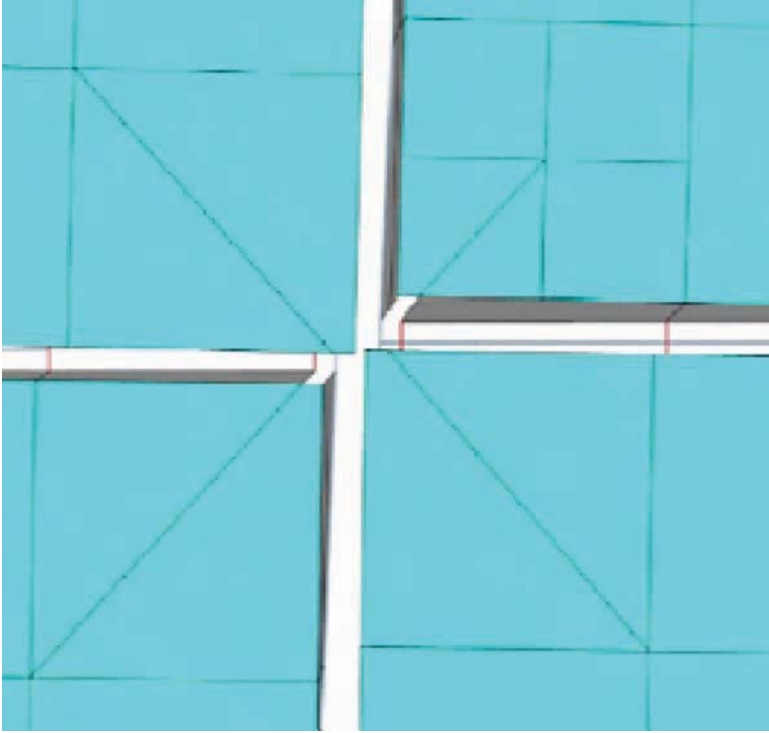


FIG. 18—FE close-up displaced shape at glass lite corners.

Discussion of the Racking Test Results

To put the overall tested displacements in context, it is important to discuss the maximum expected displacements/drifts the building code allows a structure to undergo/experience during a design level seismic event. Per ASCE 7-05 [9], the maximum allowed story displacement for an essential service building is 1.25% of the story height. For the tested mock-up, which is 11 ft (3353 mm) tall this corresponds to displacement of 1.65 in. (42 mm). The displacement before which glass fallout must not occur (ASCE 7, Ch 13 [9]) is: $\Delta_{\text{fallout}} \geq 1.25 \cdot I \cdot D_p$, where I is the importance factor, in this case 1.5, and D_p is the design displacement or the allowable displacement, in this case 1.65 in. (42 mm) and Δ_{fallout} is the drift associated with a piece of glass with an area of at least 1 in. (645 mm²) breaking away from the panel [2]. For this mock-up then, $\Delta_{\text{fallout}} \geq 3.10$ in. (79 mm), which means that if no glass fallout occurs prior to a displacement of 3.10 in. (79 mm), the mock-up has passed the ASCE 7-05 Δ_{fallout} criterion.

The focus of the results reported here will be from the 0–3 in. (0–76 mm) range, which captures performance of the system up to the displacement at which the code indicates that glass fallout, Δ_{fallout} , cannot occur. This also provides a range of results that can be correlated with the FE Model. Past 3 in. (76 mm) of movement, a non-linear model is probably more appropriate.

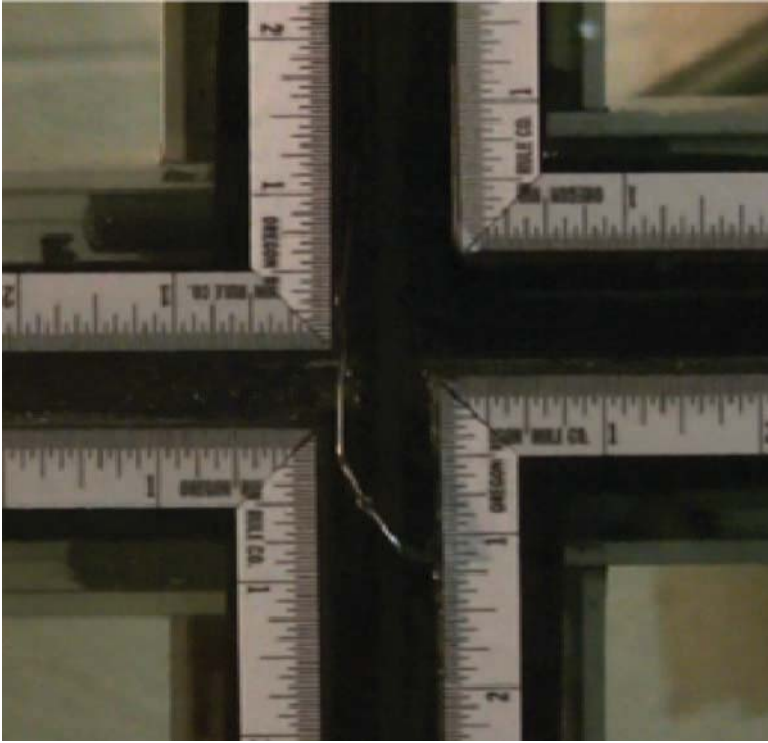


FIG. 19—Video still showing actual displaced shape at glass lite corners.

Boundary condition 1, “sway,” was tested all the way to 4 1/2 in. (114 mm) of displacement with no visible evidence of sealant damage (Fig. 20). The testing was stopped at this displacement because one of the index clips (Fig. 5) dislodged in the cavity between the male–female vertical mullions and wedged the vertical mullions apart. Testing beyond this point without removing and reinstalling the index clips would have resulted in additional damage to this mock-up unit making it unusable for a second boundary condition test. Boundary condition 2, “rack with vertical slip,” was tested all the way to 6 in. (152 mm) of displacement, which is the limit of the testing apparatus. The first signs of visible sealant damage/tearing occurred at 5 in. (127 mm) of displacement (Table 4). At 6 in. (152 mm) of displacement, the sealant around the perimeter of the center lite of glass showed approximately 15% damage/tearing. All of this sealant damage was cohesive with no evidence of adhesive failure. The center lite of glass (Fig. 3) was still firmly secured to the aluminum mullions and not in imminent danger of falling out. This system was tested well beyond the Δ_{fallout} criteria of 3.1 in. (79 mm), and did not result in any glass fallout even at 6 in. (152 mm) of displacement (Table 4). Therefore, by definition in the code, the “delta fallout” condition was exceeded. As delta fallout indicates the displacement level at which glass actually falls out during testing, the defined delta fallout then for

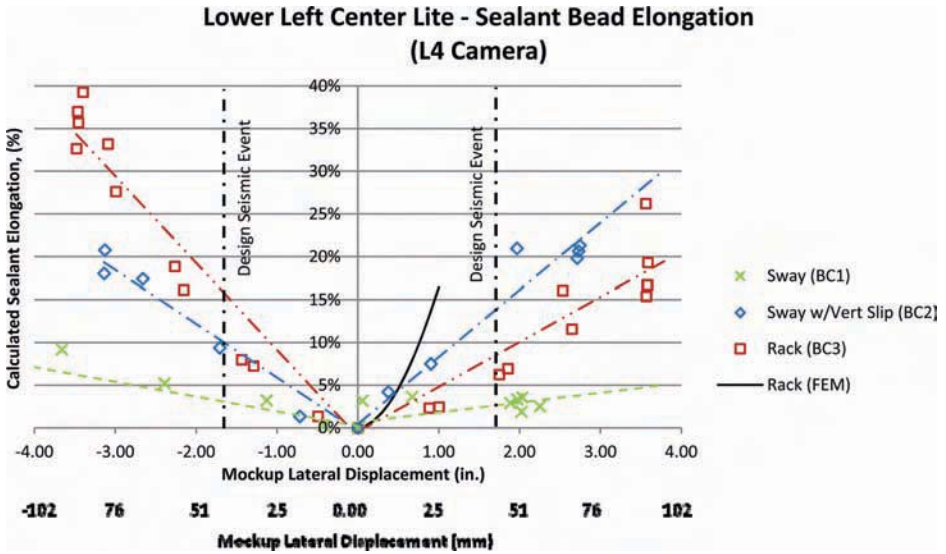


FIG. 20—Sealant elongation versus mockup displacement.

boundary condition 2 would be beyond 6 in, (152 mm). For boundary condition 3, minor visible sealant damage (one tear less than 1 in, (25 mm) in length) became evident at 4 in, (102 mm) of displacement. At 6 in, (152 mm) of displacement, there was complete sealant failure around the perimeter of the center lite of glass and it fell from the mock-up framing. The $\Delta_{fallout}$ criteria was again exceeded in this test, but as glass did fall out in this test, the delta fallout level would be referenced as 6 in, (152 mm) for boundary condition 3 (rack). With the center lite of glass completely disengaged from the mullions a full inspection of the sealant bead was possible both on the aluminum mullions and the broken lite of glass. This inspection revealed that the sealant damage was predominantly cohesive as we would want to see. There were some isolated locations that indicated localized adhesive failure but they amounted to less than 2% to 3% of the entire sealant bead, which secured the lite of glass to the aluminum mullions.

From analysis of the video footage, it can be determined that the sealant is elongating about 4% in boundary condition 1, “sway,” at a displacement of 3 in, (76 mm), well within its movement capability. As expected, in boundary

TABLE 4—Sealant damage at varying displacements and boundary conditions.

	Boundary Condition		
	BC1	BC2	BC3
Displacements at first sealant tear	N/A	5 in. (127 mm)	4 in. (102 mm)
Displacements at glass fallout	N/A	N/A	6 in. (152 mm)

condition 3, “rack,” the sealant undergoes greater movement, and from video analysis, the sealant in this condition strains approximately 15% at 3 in, (76 mm) displacement. In the hybrid condition, boundary condition 2, in which the vertical mullions are allowed to slip, the sealant elongates approximately 24% at 3 in, (76 mm) of displacement.

It was expected when the testing began that the sealant elongation for the hybrid condition (boundary condition 2), and subsequently any sealant damage noted would fall between the sway and rack conditions. The sealant performance results from visual inspection of sealant damage support this assumption, as sealant damage was not noted at all for the sway condition, and was noted at 4 in, (102 mm) for the rack condition. It follows then that sealant damage at any displacement between 4 in, (102 mm) and 6 in, (152 mm) would make sense for the hybrid condition. In fact, sealant damage was observed at 5 in, (127 mm) for the hybrid condition, exceeding the performance of the rack condition as expected, yet sustaining some damage not seen in the sway condition. Additionally at 6 in, (152 mm) of displacement there was approximately 15% of sealant tearing around the center lite for boundary condition 2, while 100% sealant tearing and glass fallout occurred on the same lite of glass for boundary condition 3, thus the racking results for boundary condition 2 again fell between the sway and rack condition. This is also supported by the hysteresis curves (Fig. 23). The load cell on the test apparatus requires less force to displace the mock-up an equivalent displacement with the sway (boundary condition 1) than for the racking (boundary condition 3).

In analyzing the sealant movement through video images, it was expected then that the elongation in the sealant for boundary condition 2 would be somewhere between 4% and 15%. However, in the analysis of the sealant movement through video images, the hybrid condition actually shows the sealant moving more—24%—than in the rack condition, which showed 15%. This does not correlate with the visual inspection of the sealant for damage; however, it may be within the bounds of error for the study given the cameras, images, and ruler methods required to arrive at these measurements.

The corner condition did not turn out to be a limiting factor on the overall system performance. For boundary condition 1, “sway,” the corner unit was the only significant source of restraint. Without the corner unit, it is likely that the strains in the sealant would have been even lower than those shown in Figs. 20 and 21. There was also no evidence of glass-to-glass contact where the primary and corner units joined (Fig. 6). The detailing of the glass lites at the corner allowed the glass lite on the primary unit to move past the edge of the corner unit glass lite. Glass-to-glass contact between the center lite and its surrounding lites of glass did not occur during the testing of boundary conditions 1 or 2. Glass-to-glass contact did occur while testing boundary condition 3 at around 5 in, (127 mm) of displacement.

Comparison of Racking Test versus FE Results

Because the silicone sealant is not directly visible in the video images (Fig. 19), another approach must be taken to calculate the elongation of the sealant. The

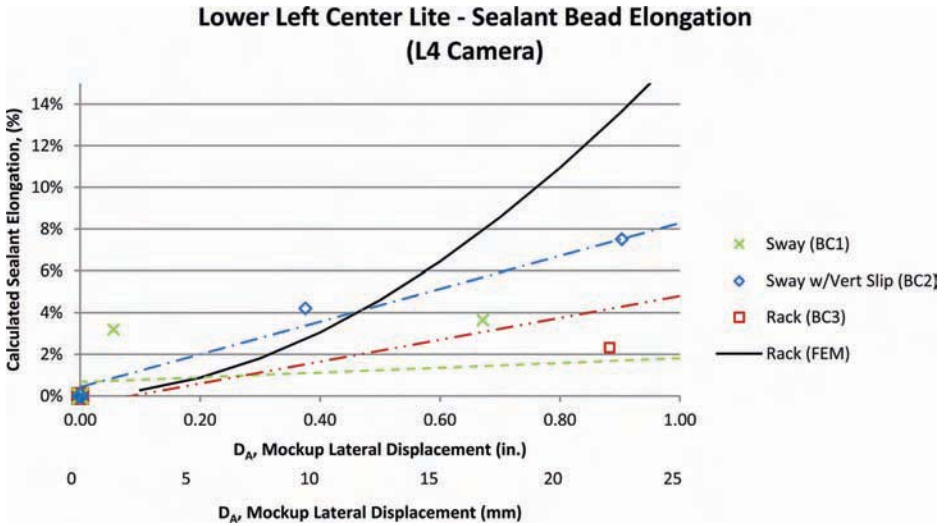


FIG. 21—Enlarged sealant elongation versus mockup displacement.

elements that are visible and measurable in the videos are the edge of glass and the intersection of the horizontal and vertical mullions behind the glass. Prior to beginning the mock-up testing, adhesive rulers were attached to each corner of the center glass lite and the surrounding glass lite corners (Fig. 19). Video cameras were located at each of the four corners of the center lite of glass. After the testing was completed, still images were extracted from the videos at known testing displacement values. These images were imported into a CAD program. Because the rulers adhered to the glass provide a known dimension, the still images were then scaled so that direct measurements could be taken from the images. By measuring the location of a corner of the glass lite (relative to the intersection of the mullions) from the initial condition and then at a known displacement, the relative movement in the horizontal and vertical directions of the corner of the glass lite can be calculated. Because the sealant is adhered to both the glass and the aluminum mullions, it must move the same amount. With this information we can calculate the elongation of the sealant at known displacements of the mock-up.

For this paper, the lower left corner of the center lite of glass (Fig. 3) was focused on. The two graphs (Figs. 20 and 21) show the elongation in the sealant bead at the corner of the glass as a function of the overall mock-up displacement. Calculated elongations for the same corner of the glass for all three tested boundary conditions are shown. In addition, the sealant elongation for the same corner of the glass lite for the “racked” boundary condition as predicted by the FE model is also shown.

There are a number of findings from these graphs to be discussed. To begin with, for a given displacement, the elongation in the sealant for boundary condition 1 (sway) is lower than for boundary condition 3 (rack). At a displacement

of 2 in, (51 mm), the sealant elongation in boundary condition 1 is 2.5 %, while the sealant elongation in boundary condition 3 is 10 % (Fig. 20). The sealant elongation in the hybrid condition, boundary condition 2, at the same displacement is 15 %. Although one would expect to see elongation for boundary condition 2 to be less than that of boundary condition 3, there were other factors that influenced such an outcome. These factors include failure of the index clips connecting the two parts of the split mullion resulting in rocking action of the panels, and lack of corner restraints during test on boundary condition 1.

The comparison between the sway and rack conditions, which were the two main boundary conditions for this study, yields useful sealant performance information, summarized in Table 5. Specifically, in the sway condition, very little strain is placed on the sealant, resulting in minimal stress being transferred through the sealant. In reviewing Fig. 12, it can be seen that 2.5 % strain would produce a sealant stress of approximately 5 psi (34 kPa). In the fully racked condition, at 10 % movement in the sealant, approximately 35 psi (241 kPa) stress in the sealant is generated, when taken in a worst case scenario assuming tensile behavior of the sealant. In comparing the sway condition to the rack condition at this 2 in, (51 mm) displacement, the stress on the sealant can be expected to be approximately seven times greater in the rack condition, up to 35 psi (241 kPa) in tension under racking.

In actuality, the stress generated falls somewhere between the shear and tensile conditions, and the shear stress at 2 in, (51 mm) of racking is only 7.5 psi (52 kPa). The sealant, as evaluated in either tension or shear, is well within its capability anywhere from the 7.5 psi (52 kPa) to 35 psi (241 kPa) bounded conditions given an ultimate strength of 133–149 psi (917–1027 kPa) in shear and tension, for the two-part sealant, respectively. In looking at the rack condition at the design displacement level of 3 in, (76 mm), the strain in the sealant is approximately 15 % (Fig. 20), resulting in a sealant stress of 15 psi (103 kPa) in shear and 45 psi (310 kPa) in tension (Fig. 12), again well within the sealant capability for this most stringent mode of testing. This analysis, summarized in Table 5, compares actual strains generated in the sealant per racking testing and calculates stresses in the sealant based on coupon testing (Figs. 11–14), which was carried out according to industry standard test procedures.

TABLE 5—Summary of mock-up displacements, sealant strains, and associated stresses.

Boundary Condition	Displacement (mm)	Actual Strain (per video analysis)	Correlated Sealant Stress	
			Range Shear	Range Tensile Stress
			Range, psi (kPa)	
Sway	1 (25)	1.8%	1–3 (7–20)	
Sway	2 (51)	2.5%	2–5 (14–34)	
Sway	3 (Δ_{fallout}) (76)	4.0%	5–15 (34–103)	
Rack	1 (25)	5.0%	7–17 (48–117)	
Rack	2 (51)	10.0%	7.5–35 (52–241)	
Rack	3 (Δ_{fallout}) (76)	15.0%	15–45 (103–310)	
FE model	1 (25)	15.0%	15–45 (103–310)	

It is understood that the strain rate during an actual seismic event is faster than the industry standard coupon test method pull rate of 0.5 in, (13 mm)/min. In fact, the equivalent strain rates experienced by the sealant beads on the mock-ups ranged from 2 in, (51 mm)/min up to 28 in, (711 mm)/min. These strain rates are a function of the test frequency (Fig. 2) and the boundary conditions (Fig. 8). As stress gauges cannot be installed in the sealant joint to take measurements during the racking testing, these stresses can only be estimated using FE modeling or stress strain graphs from the sealant coupon testing. The estimated stresses can then be validated by observing actual sealant performance and behavior on the mock-up after racking movement is induced.

The hysteresis curves, generated from the load sensor on the test apparatus, documented in Figs. 22 and 23, show very tight elastic behavior in the mock-up all the way up to a displacement of 3.00 in, (76 mm). While stresses in the sealant may be higher than predicted by the coupon testing, the overall performance of the sealant is comparable. Because, in general, faster loading rates result in materials showing higher strengths, it is expected that if the sealant coupons were pulled in shear at a higher strain rate, the resulting stress-strain curve for “fast” shear behavior would be steeper and probably closer to the tensile test curves presented here. Coupon shear testing at a higher strain rate would be a more direct correlation to sealant behavior in a racking testing and can be considered for future studies.

Finally, the FE modeling results show a more rapid increase in sealant elongation as the mock-up displacement is increased. Because this FE model is linear-elastic, it cannot accurately model the “softening” of the sealant with

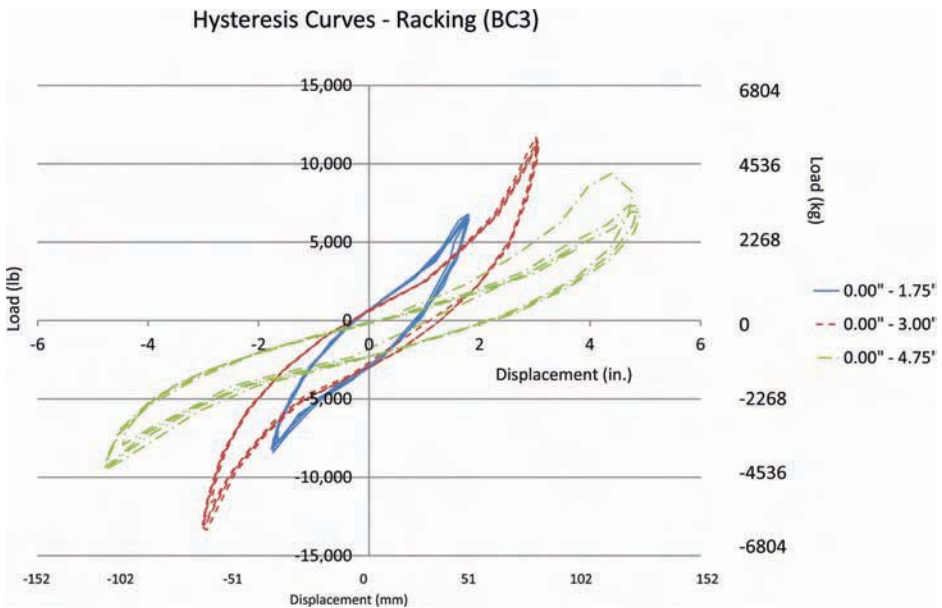


FIG. 22—Hysteresis curve racking boundary condition 3 (BC3).

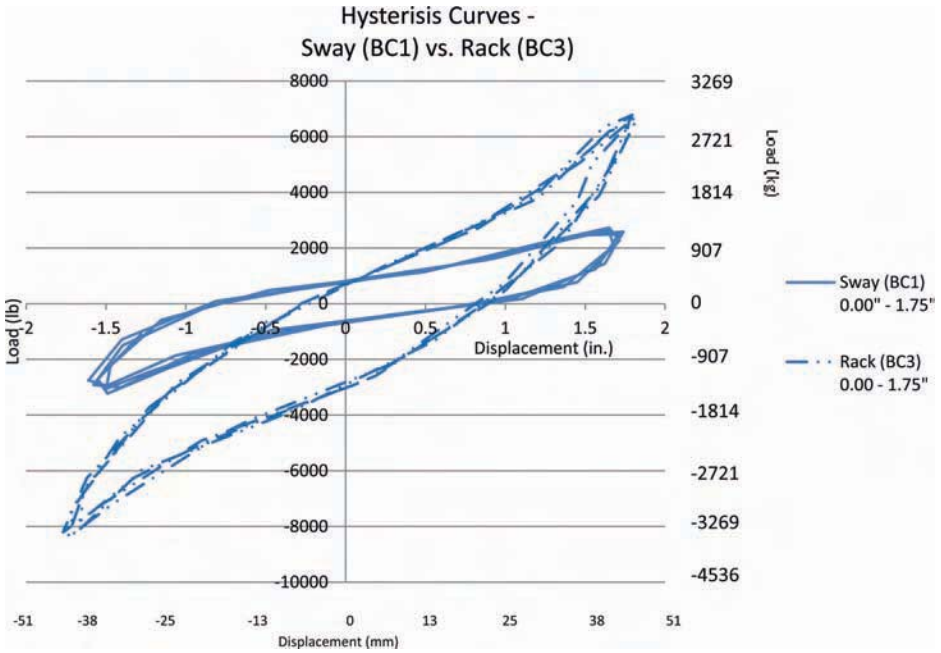


FIG. 23—Hysteresis curves sway (boundary condition 1) versus rack (BC3).

increased displacement. The “softening” of the sealant (reduction in modulus) with increase strain/stress is clearly illustrated in the hysteresis curve in Fig. 22. As the mock-up is cycled through larger displacements, the force required to reach a given displacement decreases. This “softening” behavior is also somewhat evident in the coupon test results (Figs. 13 and 14). Up to about 1 in. (25 mm) of mock-up displacement, the FE results follow the tested results for boundary condition 3. As displacements get larger, the FE results overestimate the actual sealant elongation as seen in the mock-up testing. This further documents that the FE modeling is a conservative approximation of the elongations in the sealant.

Summary and Conclusions

This study has provided new full-scale experimental data for the performance of a unitized four-sided SSG curtain wall system including the effects of a corner condition. The study has developed racking test data on continuous silicone sealant behavior and provided comparison with coupon test results and FE modeling results. When curtain walls are attached in such a manner that they are allowed to sway, as do fully unitized systems, the stress the sealant experiences at the allowable drift ratios per ASCE 7 are very minimal (well below 20 psi (138 kPa)). When curtain wall systems are required to rack, emulating stick-built conditions, sealant stress will be higher and sealant damage may occur at racking displacements beyond the seismic design drift level. However, at design displacement drift levels in a fully racking system, there should be no sealant

damage in a properly designed curtain wall system based on the results of this study. Also, the corner condition was shown not to be a limiting factor under racking movement. This is a key finding of this research because typical AAMA 501.6 testing does not require the inclusion of out-of-plane corner conditions.

This paper discusses the history of sealant design level stresses and supports the conclusions made in 1996, that 50 psi (345 kPa) is a reasonable design stress level for seismic events. The racking testing showed that the sealants can cycle up and down (in tension) to 50 psi (345 kPa) without adversely affecting the ultimate properties of the sealant. Based on coupon test results, this study also showed that the ultimate strength level of the sealants was only minimally affected by environmental conditions, including extreme temperatures and 5000 hr of QUV exposure. The silicone sealants are modulus stable across these environmental conditions. Also, by comparing tensile and shear stress values, this study shows that predicting curtain wall performance using tensile sealant design values is conservative when considering seismic-induced movement.

Silicone offers a flexible anchoring method when used on all four sides and, through curtain wall system racking testing, it has been shown to perform satisfactorily at high racking displacement, with acceptable damage levels that leaves the system still operable, as required by the building code. Coupon sealant test results on individual sealant samples show the long-term durability of silicones, as well as their suitability for use in seismic regions based on how they cyclically move and return without damage (sealant remains in an elastic deformation zone).

Finally, this study documents that linear elastic FE modeling is a valid way to conservatively predict the sealant stresses and system behavior, up to allowable drift levels, prior to implementing full physical racking tests (AAMA 501.4 or 501.6). By analyzing a FE model together with static racking testing (AAMA 501.4), system suitability for seismic areas can be acceptably predicted. Dynamic racking tests (AAMA 501.6) are very useful to new system technologies or new material verification and projects involving essential service structures.

Shear testing of sealant coupon samples at varying strain rates would produce stress-strain curves that would be meaningful and more readily comparable to actual seismic testing results. This should be considered for future work. Samples could be traditional "H piece" configurations to represent a sealant joint, or could be lap shear joints, or both to compare the effects of sealant joint configuration. Cyclic testing could be repeated at a higher number of cycles using the chosen joint design and a higher strain rate to more closely mimic actual seismic testing instead of correlating results through tensile testing. Furthermore, for follow-up studies, it is recommended that nonlinear FE modeling packages be used to more accurately predict the sealant behavior at higher strain levels.

References

- [1] Hilliard, J. R., Parise, C. J., and Peterson, C. O., Jr., *Structural Sealant Glazing, Sealant Technology in Glazing Systems, ASTM STP 638*, ASTM International, West Conshohocken, PA, 1977, pp. 67–99.
- [2] Zarghamee, M. S., Schwartz, T. A., and Gladstone, M., "Seismic Behavior of Structural Silicone Glazing," *Science and Technology of Building Seals, Sealants, Glazing*

- and *Waterproofing*, Vol. 6, ASTM STP 1286, J. C. Myers, Ed., ASTM International, West Conshohocken, PA, 1996, pp. 46–59.
- [3] Earthquake Engineering Research Institute (EERI), “*Northridge Earthquake Reconnaissance Report, Vol. 1*,” Earthquake Spectra, Supplement to Volume 11, EERI, Oakland, CA, 1995.
 - [4] Behr, R. A., “Seismic Performance of Architectural Glass in a Mid-rise Curtain Wall,” *J. Architect. Eng.*, Vol. 4, No. 3, 1998, pp. 94–98.
 - [5] Memari, A. M., Chen, X., Kremer, P. A., and Behr, R. A., “Seismic Performance of Two-Side Structural Silicone Glazing Systems,” *J ASTM Int.*, Vol. 3, No. 10, 2006, pp. 1–10.
 - [6] Memari, A. M., Kremer, P. A., and Behr, R. A., “Seismic Performance of Four-Sided Structural Sealant Glazing System,” *J. ASTM Int.* (in press).
 - [7] AAMA, 2009, “Recommended Dynamic Test Method for Determining the Seismic Drift Causing Glass Fallout from a Wall System,” Publication No. AAMA 501.6-09, American Architectural Manufacturers Association (AAMA), Des Plaines, IL.
 - [8] ASTM C1401, 2009, “Standard Guide for Structural Sealant Glazing,” *Annual Book of ASTM Standards*, ASTM International, West Conshohocken, PA.
 - [9] ASCE, 2006, “Minimum Design Loads for Buildings and Other Structures,” ASCE 7-05, American Society of Civil Engineers, Reston, VA.
 - [10] NEHRP, 2003, “Recommended Provisions for the Development of Seismic Regulations for New Buildings,” Building Seismic Safety Council, Washington, D.C.
 - [11] UBC, 1991, “Uniform Building Code Standards,” International Conference of Building Officials, Whittier, CA.
 - [12] Wolf, A. T., “Durability of Silicone Sealants,” *Durability of Building Sealants State-of-the-Art Report of RILEM TC 139-DBS*, A. T. Wolf, Ed., Rilem Publications, Bagneux, France, 1999, pp. 253–273.
 - [13] Bridgewater, T. J. and Carbary, L. D., “Accelerated Weathering and Heat Stability of Various Perimeter Sealants,” *Science and Technology of Building Seals, Sealants, Glazing and Waterproofing*, ASTM STP 1200, Jerome M. Klosowski, Ed., ASTM International, West Conshohocken, PA, 1992, pp. 45–63.
 - [14] Fedor, G. R., “Usefulness of Accelerated Test Methods for Sealant Weathering,” *Science and Technology of Building Seals, Sealants, Glazing, and Waterproofing, Second Volume*, ASTM STP 1200, J. M. Klosowski, Ed., ASTM International, West Conshohocken, PA, 1992, pp. 10–28.
 - [15] ICBO, 1991, “Acceptance Criteria for Type I Structural Silicone Glazing Sealant (Adhesive),” Report AC45, International Conference of Building Officials (ICBO) Evaluation Service, Inc., Whittier, CA.
 - [16] ASTM C1184, 2005, “Standard Specification for Structural Sealants,” *Annual Book of ASTM Standards*, ASTM International, West Conshohocken, PA.
 - [17] ATI, “Performance of Structural Silicone 983 SGS at Room Temperature vs High Temperature,” Test Report No. B2890.01-106-31, Architectural Testing Inc., York, PA, 2011.
 - [18] ASTM C1135, 2000, “Standard Test Method for Determining Tensile Adhesion Properties of Structural Sealants,” *Annual Book of ASTM Standards*, ASTM International, West Conshohocken, PA.
 - [19] Carbary, L. D., Bull, E. D., and Mishra, S. S., “Development of a Practical Method to Evaluate the Fatigue Properties of Structural Silicone Glazing Adhesives,” *J. ASTM Int.*, Vol. 4, No. 1, 2007, pp. 53–62.
 - [20] Shisler, F. W. III and Klosowski, J. M., “Sealant Stresses in Tension and Shear,” *Building Sealants: Materials, Properties, and Performance*, ASTM STP 1069, T. F. O’Conner, Ed., ASTM International, West Conshohocken, PA, 1990, pp. 95–107.

- [21] AAMA, 2009, "Recommended Static Testing Method for Evaluating Curtain Wall and Storefront Systems Subjected to Seismic and Wind Induced Interstory Drift," Publication No. AAMA 501.4-09, American Architectural Manufacturers Association (AAMA), Des Plaines, IL.
- [22] *Visual Analysis; v8.0.* (2011). Integrated Engineering Software, 519 E. Babcock St., Bozeman, MT 59715.

A. M. Memari,¹ S. Fisher,² C. Krumenacker,³ K. A. Broker,⁴
and R.-U. Modrich⁵

Evaluation of the Structural Sealant for Use in a Four-Sided Structural Sealant Glazing Curtain-Wall System for a Hospital Building

ABSTRACT: Cathedral Hill Hospital (the California Pacific Medical Center) is a 15-story building designed to be constructed in downtown San Francisco. The curtain-wall system for this building is primarily of unitized design employing a four-sided structural sealant glazing (SSG) system. This paper initially introduces the building and its curtain-wall design. Next, the summary of the results of full-scale racking tests on stick-built mockups of the curtain-wall system developed to evaluate the structural sealant performance are presented. Stick-built mockup, instead of unitized system, was chosen to initially evaluate the behavior of sealants under racking conditions. The mockups were designed to determine the behavior of the glass, framing, connections, and more importantly, the structural silicone under racking displacements following the AAMA 501.6 protocol. The test results (stress-strain relationships) on the structural sealant to determine tensile adhesion properties at selected temperatures and UV exposures are discussed and

Manuscript received June 18, 2011; accepted for publication January 2, 2012; published online April 2012.

¹Dept. of Architectural Engineering, Penn State Univ., 104 Engineering Unit A, University Park, PA 16802, e-mail: memari@enr.psu.edu

²Bagatelos Architectural Glass Systems, Inc., 2750 Redding Ave., Sacramento CA 95820-2156, e-mail: sfisher@bagatelos.com

³Smith Group, 301 Battery St., 7th Floor, San Francisco, CA 94111, e-mail: charles.krumenacker@smithgroup.com

⁴Dow Corning Corporation, 4742 Liberty Rd. S, #346, Salem, OR 97302, e-mail: k.broker@dowcorning.com

⁵Herrero Boldt, 633 Folsom St., 6th Floor, San Francisco, CA, 94107, e-mail: rmodrich@herrero.com

Cite as: Memari, A. M., Fisher, S., Krumenacker, C., Broker, K. A. and Modrich, R.-U., "Evaluation of the Structural Sealant for Use in a Four-Sided Structural Sealant Glazing Curtain-Wall System for a Hospital Building," *J. ASTM Intl.*, Vol. 9, No. 4. doi:10.1520/JAI104143.

Copyright © 2012 by ASTM International, 100 Barr Harbor Drive, PO Box C700, West Conshohocken, PA 19428-2959.

comparisons to the finite-element analysis results are presented. The wind load and seismic design of the sealants, including the finite-element modeling and analysis of a typical panel to evaluate the stresses in the structural sealants, are presented as well. The allowable stress issue in structural sealants for seismic design of four-sided SSG systems is discussed in light of the new information generated for this project.

Introduction

Cathedral Hill Hospital (the California Pacific Medical Center) is a 15-story building that has recently been designed and is to be constructed in downtown San Francisco. The curtain-wall system for this building is primarily of unitized design employing a four-sided structural sealant glazing (SSG) system [1]. The four-sided SSG system is referred to a system where the glass panes are attached to the glazing frame on all four sides using structural sealant. The four-sided SSG system is known to be a curtain-wall glazing system that offers opportunities for shop-glazed construction quality, some reasonable savings, and expedited erection and installation. The unitized system consists of a shop-glazed framing that has the glass panes attached to the framing in the shop and the panels are then assembled at the job site. In particular, horizontal stack joints are provided that accommodate in-plane sliding between vertically stacked panels, which meet at the horizontal stack joint. Although four-sided SSG systems have been used in high seismic regions, such systems have not been used for healthcare facilities in California. This healthcare facility project will be the first of its kind to use this glazing system type.

To ensure satisfactory seismic performance of the curtain-wall systems, ASCE 7-05 [2] adopted by the International Building Code, IBC [3], requires dynamic racking tests to be carried out on mockups of the curtain-wall systems according to AAMA 501.6 procedure [4] when three or more sides of the glass panes are not mechanically captured. Besides such ASCE 7-05 requirements for this project, performing this test was also a requirement established by the California Office of Statewide Health Planning and Development (OSHPD) early in the design process so that they could be assured that the four-sided curtain-wall system would perform satisfactorily on a California hospital. This test procedure is intended to determine the drift associated with glass fallout. ASCE 7-05 [2] requires the drift capacity of the curtain wall, represented by the glass fallout drift, sufficiently exceed the design drift determined based on structural analysis of the building.

Because the aluminum glazing frame sections for this project are custom designed and will be extruded after design documents have received preliminary approval from OSHPD, it was decided to carry out preliminary AAMA 501.6 racking tests on mockups constructed using available mullion sections with properties similar to the final sections that will be extruded later. The objective was to show satisfactory performance of a four-sided SSG system to help ensure that the conditional design document received approval. The final approval of the design documents will require racking testing associated with the AAMA 501.4 [5] testing protocols, of mockups constructed using the custom extruded sections.

The objective of this paper is to introduce the project, present the main results of the preliminary racking tests, discuss sealant properties, and finite-element modeling. In the following sections, some of the design and detailing aspects of the curtain-wall system and the AAMA 501.6 test method are explained. Then, the results of full-scale tests on preliminary mockups of the curtain-wall system carried out at Architectural Testing Inc. in York, PA are presented. The mockups were designed to determine the behavior of the glass, framing, connections, and more importantly, the structural silicone under racking displacements. The sealant coupon tests carried out by Dow Corning are discussed, and the results of the finite-element modeling of a typical panel to predict sealant stresses are presented.

Background

The majority of SSG construction is of the two-sided type, which commonly consists of attaching the two vertical glass pane edges to mullions using structural sealant, whereas the two horizontal edges are captured within glazing frame pockets using rubber gaskets based on typical dry-glazed construction practices. In four-sided SSG systems, all four sides of a glass pane are attached to the glazing frame using structural sealant [6,7]. Major guidelines for design, testing, and construction of SSG in the U.S. can be found in ASTM C1401-09 [1] and in Europe in ETAG 002 [8]. Because of the lack of a mechanical capture for the glass panes in four-sided SSG, one must rely heavily on the adhesion property of the sealant material to the glass and aluminum substrates. Although sealant manufacturers, curtain-wall designers, and glazing installers generally follow well-established standards, guidelines, and procedures for specifications, design, detailing, fabrication, and installation of four-sided SSG systems; nonetheless, some concerns about their seismic performance still exists. For this reason, full-scale mockup testing is necessary to establish satisfaction of the code's seismic provisions. Of course, such concerns in the past have been more about the shear deformation capacity of the structural sealant in stick-built curtain-wall systems. Recent experimental studies on racking test evaluation of two-sided and four-sided SSG curtain-wall systems [9,10] provide some insight to seismic performance of stick-built SSG systems.

Most of such concerns have been resolved recently through the use of unitized construction of four-sided SSG systems. Whereas in stick-built construction the glazing frame is usually continuous over multiple stories, and, therefore, the glazing panel will be forced to rack under story drift and subsequently transfer large strains to structural sealants, the unitized system is structurally discontinuous from story to story. This is accomplished through shop glazing and prefabricating the complete panels and simply attaching adjacent panels to one another through stack joints that easily allow sliding between panels, resulting in lower stresses in the structural sealant. As in stick-built designs, setting blocks are used to carry the dead load of the glass. For this project, typical stack joint details, as shown in the renderings of Fig. 1, are to be used.

For preliminary testing in this project, however, it was decided to investigate a worst-case scenario, which would mean a unitized system failing to

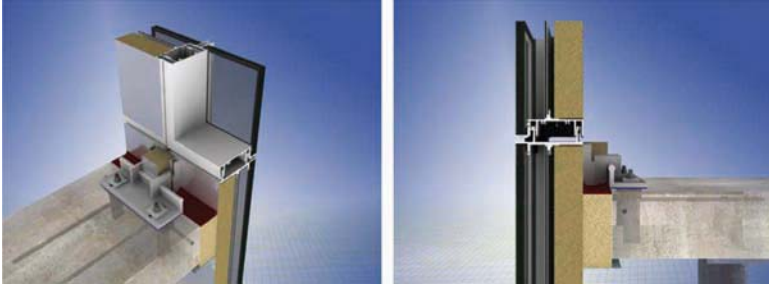


FIG. 1—Rendering of stack joints and anchor system for the unitized four-sided SSG system.

behave as intended and, in turn, to perform as a stick-built system by racking under in-plane story drift. The objective was to understand how the sealants perform under a racked frame condition. By showing that the performance of glass and sealants satisfied the intent of the code provision in a stick-built construction, there will be assurance that the system will perform satisfactorily under an actual unitized construction condition.

Description of the Building and the Curtain-Wall System

California Pacific Medical Center (CPMC) Cathedral Hill Hospital, a major hospital with 550 patient beds, is to be constructed in downtown San Francisco (Fig. 2). The building roof is 251 ft (76.5 m) above grade. The gravity-load-resisting system consists of concrete fill on metal decks, and steel beams, girders, and columns. The lateral-load-resisting system above grade consists of moment-resisting steel frames with supplemental viscous wall dampers, whereas that below grade includes reinforced concrete floor diaphragms and shear walls. The foundation is designed as reinforced concrete spread footings. The building is

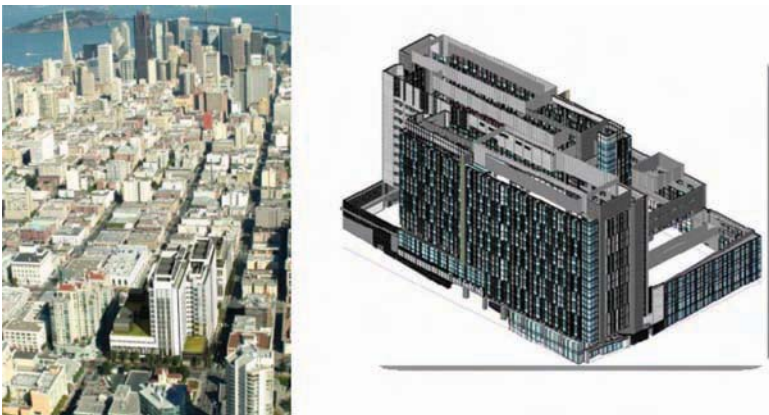


FIG. 2—Drawing of the building and its proposed location in San Francisco.

comprised of three main components: the podium, the tower, and the rooftop equipment and central plant. A significant portion (75%) of the exterior cladding system of the tower, levels 7–15 on the north and levels 3–15 on the south, is comprised of a four-sided SSG unitized curtain wall.

A unitized curtain-wall system involves building individual units in the shop, then shipping them to the project site, and finally attaching them to the building floor slabs at each level. The unitized panel for this building is typically an 8-ft, 4-in. (2540-mm) -wide by 14-ft (4267-mm) or 17-ft (5182-mm) -tall unit in the tower as shown in Fig. 3, or 17 ft (5182 mm) tall at the podium (floors 1–7) floors. There are three 8-ft, 4-in (2540-mm) panels and one 4-ft (1219-mm)-wide panel at each typical 29-ft (8839-mm) bay. All exterior glazing of the hospital are 1-in. (25.4-mm) -thick insulating glass units (IGU) consisting of two 0.25-in. (6.4-mm) panes of heat-strengthened glass with 0.5-in. (12.7-mm) air gap between. The IGUs are fully supported on all four sides by aluminum glazing frame members through structural silicone sealant. The factory coated

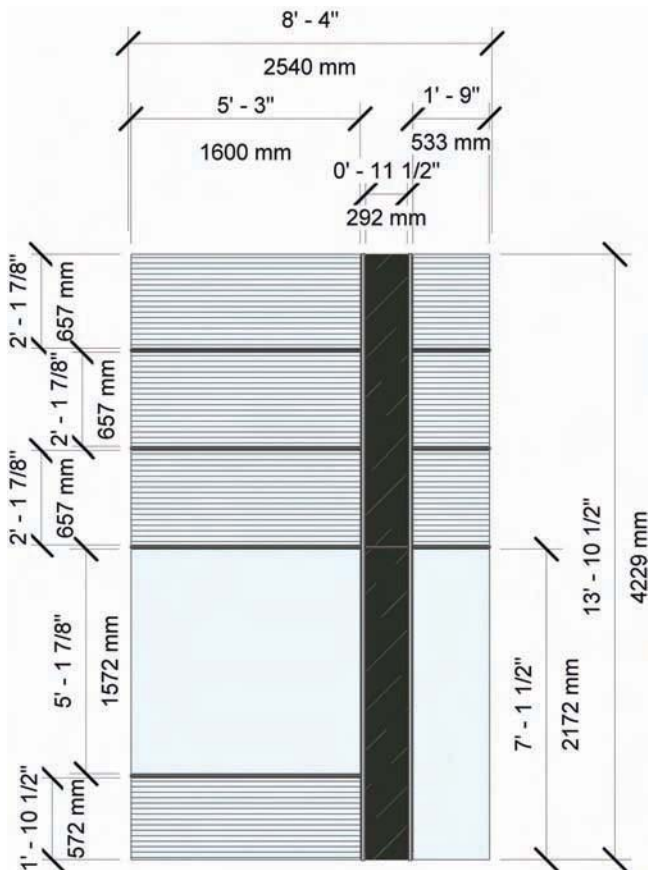


FIG. 3—Typical unitized curtain-wall panel.

finish on all extruded aluminum components of the curtain-wall system will be a two-part Kynar polyvinylidene fluoride (PVDF). PVDF [11] is a specialty resin plastic material in the fluoropolymer family and is used generally in applications requiring the highest strength, and resistance to solvents, acids, bases, and heat, and it is the premier finish for curtain-wall and window aluminum extrusions. Because four-sided SSG systems rely on a chain of adhesion, the adhesion of a factory-applied coating (PVDF) to an aluminum mullion must have an adhesion failure pull-off value in excess of the structural sealant's ultimate design strength. Laboratory testing has confirmed that the adhesion of a PVDF coating to an aluminum surface has an average pull-off strength of 215 psi (1482 kPa), which exceeds the maximum sealant tensile strength of 177 psi (1220 kPa).

There is a horizontal movement stack joint 7.75 in. (196.9 mm) above the top of the slab as shown in Fig. 1 at each floor accommodating lateral movement and vertical deflection. The stack joint that runs continuously around the full perimeter of the building is composed of two separate nested extrusions with air and water barriers. As shown in Fig. 1, there is a vertical stack movement joint at each side of the typical unit. There is some variation in the size of the glazing units, but this occurs at the east and west corner conditions referred to as day room areas. The mullions are 3 in. (76.2 mm) wide by 7 in. (177.8 mm) deep with 1 in. (25.4 mm) of insulating glass outboard. The vertical extruded aluminum fins project 1 in. (25.4 mm) from the face of the glass for both the intermediate mullions and vertical joint mullions, whereas the horizontal fins are flush with the face of the glass for intermediate mullions, but project 0.625 in. (15.9 mm) from the face of the glass for horizontal movement joint mullions.

The unitized curtain-wall system is connected to the building slab at the top of the two primary vertical mullions by a pair of vertical hook plates (two per panel) attached to the nesting vertical stack mullions just below the horizontal stack joint. These vertical plates are hooked onto an extruded aluminum bearing plate with serrated edges, which in turn is bolted to the cast-in Halfen channel anchors at the slab edge, as shown in Fig. 1. Additionally, the vertical hook plates will be mechanically fastened to this bearing plate once final alignment has occurred. The hook anchor plate incorporates height adjusting screws, which provide vertical alignment of the unit during installation. Slotted holes in the aluminum bearing plate allow for in-and-out alignment. The bottom (sill) horizontal mullion is mechanically engaged into the head mullion of the unit below (Fig. 4). The mechanical connection of the vertical stack mullions to the slab through the hook plates restrains the top of each unit from movement in the three translational component directions. The mechanical engagement of the sill to the head of the unit below restrains only the out-of-plane movement. Figure 4 shows typical details of the horizontal and vertical stack joints.

Structural Sealant Glazing Testing and Results for Seismic Work

Through the course of the project, data generated from ASTM C1135 [12] Standard Test Method for Determining Tensile Adhesion Properties of Structural Sealants was used to help develop the finite-element model and predict

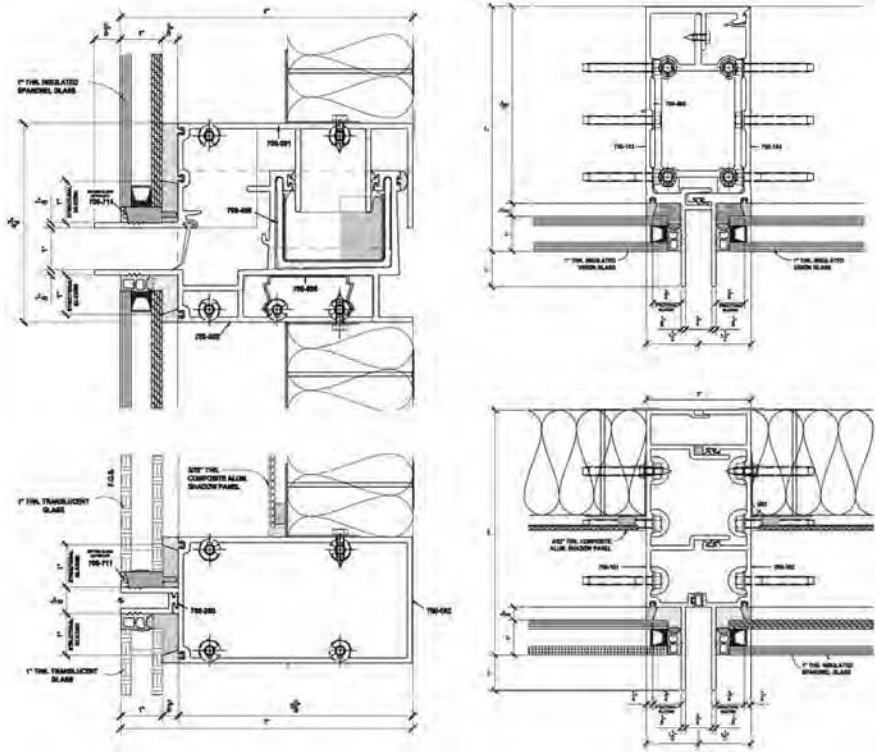


FIG. 4—Typical details of horizontal and vertical stack joints to be used on the building (SI unit conversion: 1 in. = 25.4 mm).

sealant behavior. Also the environmental conditions found in ASTM C1184 [13], The Standard Specification for Silicone Sealants, were applied and tested to demonstrate sealant durability.

The results of this testing generated stress–strain curves for the two sealants being utilized for the project, Dow Corning 983 Silicone Glazing Sealant (DC 983 SGS) and Dow Corning 995 Structural Silicone Sealant (DC 995). The two-part DC 983 SGS sealant is used for the in-shop glazing of the curtain-wall panels because of its quick setup time, allowing panels to be fabricated and subsequently moved to the job site after 24 h. Any field glazing or re-glazing required would be completed with the one-part DC 995 sealant, as it comes in packaging that is usable in the field, while still maintaining the high sealant strength necessary for the application.

A summary of the sealant properties for DC 983 SGS sealants and DC 995 sealants are shown in Figs. 5 and 6, respectively. Both of these graphs include the sealant properties when tested in tension per ASTM C1135 [12] criteria and sealant properties when tested in shear per AC 45 testing criteria [14]. The displacement (strain) rate for both tension and shear testing was 0.5 in. (12.7 mm) per minute according to ASTM C1184 [13]. In both tension and shear coupon

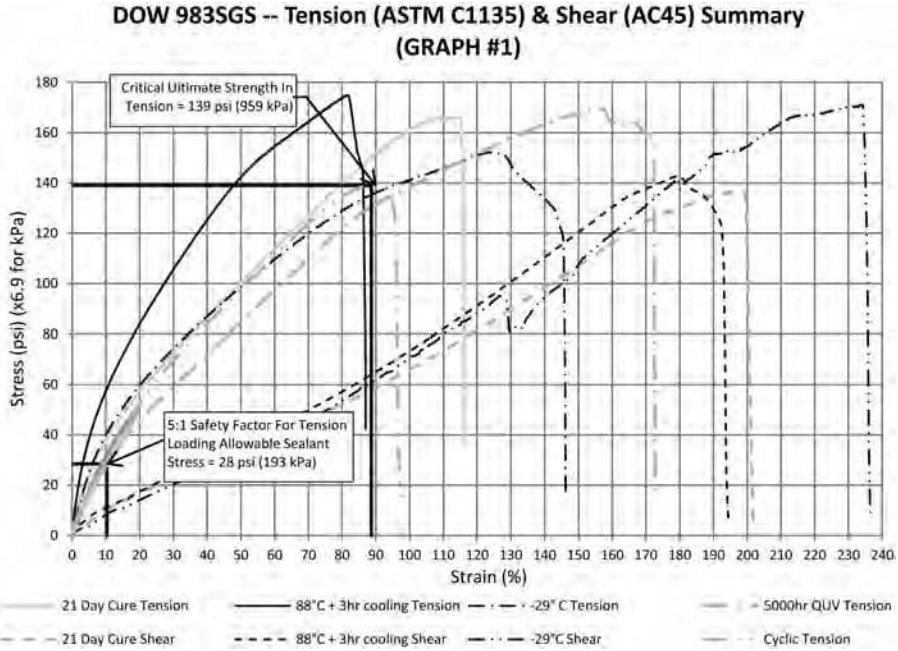


FIG. 5—Dow Corning 983 stress–strain curves.

tests, the failure was cohesive. Testing for both tension and shear were performed for a number of different environmental conditions. These graphs indicate a couple of key components of SSG sealant behavior performance. The first item that becomes apparent is that SSG sealants are much stiffer in tension than in shear. Based on the test results, the sealants are more than 4 times stiffer in tension than in shear. This is consistent with what is documented in ASTM C1401 [1] and supports the argument that it is conservative and appropriate to design SSG sealants based on the tested tension properties. A higher tension modulus will generate higher stresses in the sealants at a given strain. As an example, at approximately 10% strain, a bead of DC 983 SGS sealant would experience a 28-psi (193-kPa) stress if loaded in tension, but only about 10-psi (69-kPa) stress if loaded in shear. The second issue that the graphs illustrate is that whereas the overall ultimate stresses and strains the sealant can support are affected by different environmental conditions, there is much less variation in sealant behavior at allowable stress levels based on a 5:1 safety factor between those same variety of environmental conditions. Whereas ASTM C1401 documents the use of a 2.5:1 safety factor when originally establishing the 20-psi (138-kPa) allowable sealant stress in the 1970s and 1980s, OSHPD has requested a 5:1 safety factor for this project.

Although the SSG sealant bead will experience a combination of tension and shear behavior when subjected to seismic in-plane racking, to model sealants in finite-element analysis, the most conservative tensile sealant properties

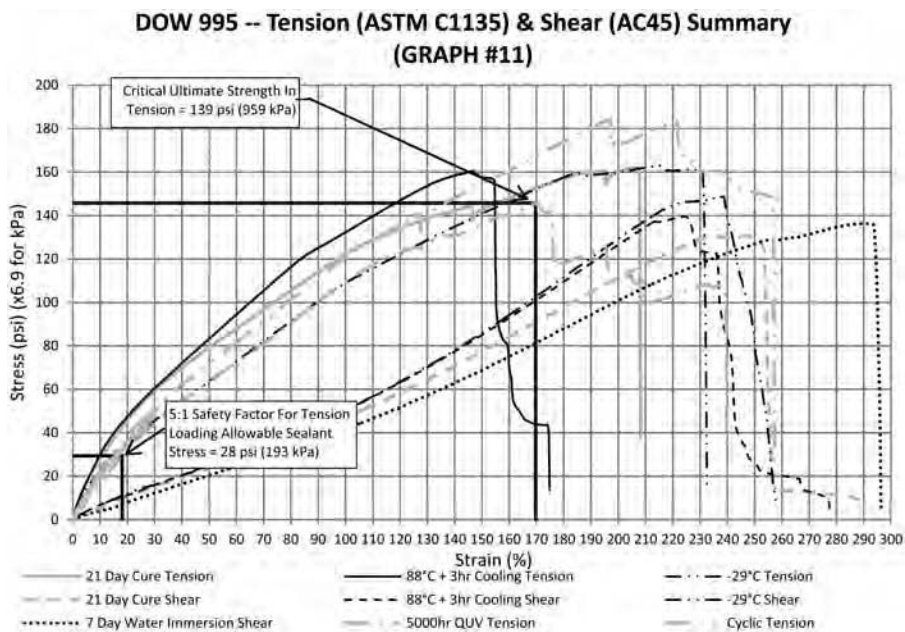


FIG. 6—Dow Corning 995 stress–strain curves.

were used. For DC 995 sealant, the most conservative results were obtained from the sample exposed to 5000 h of UV radiation, which is a simulation of accelerated aging, including the following cycles: 8 h UV at 60°C and 4 h condensation at 50°C. The sealant test data shown in Fig. 6 also includes shear testing data for comparison purposes and documents that the use of tension properties is conservative. For DC 983 SGS sealant, the most conservative results were obtained from a sealant sample that was cyclically tested in tension from 0 to 50 psi (0–345 kPa), and then pulled to failure, showing a 140-psi (965-kPa) ultimate strength (Fig. 5) after cyclic testing. The average across five samples cyclically tested was 149 psi (1027 kPa). The same cyclic testing was performed with DC 995 sealant, resulting in an ultimate strength average between five samples of 185 psi (1276 kPa). To be very conservative, it was chosen to use the 5000-h UV results at 145 psi (1000 kPa) instead of the cyclic testing data for DC 995 sealant.

Another aspect of structural sealant that needs to be determined for seismic analysis is deformability that is defined [2] as the ratio of the ultimate deformation to the limit deformation. The ultimate deformation is defined as “The deformation at which failure occurs and that shall be deemed to occur if sustainable load reduces to 80% or less of the maximum strength.” The limit deformation is defined as “Two times the initial deformation that occurs at a load equal to 40% of the maximum strength.” For DC 983 SGS sealant, the ultimate and limit deformations were obtained as 96% and 42%, respectively, giving the ratio of $96/42 = 2.3$. This ratio falls between 1.5 and 3.5 that according to ASCE 7-05 is

defined as limited deformability material. The ratio for DC 995 sealant referencing the 5000 h QUV curve is 1.9. Both these ratios define the sealants as limited deformability and per Table 13.5-1 [2]. Component amplification factor, $a_p = 2.5$ and component response modification factor, $R_p = 2.5$.

According to ASTM C719 [15], DC 983 SGS 2-part sealant is rated for 25% movement, whereas DC 995 SSS 1-part sealant is rated for 50% movement as allowable (serviceability) sealant strains for wind and thermal loading. ASTM 1401 [1] sets the allowable stress because of wind and thermal movement as 20 psi (138 kPa). This allowable stress is based on a SSG sealant with an ultimate strength of no less than 50 psi (345 kPa) or a 2.5:1 factor of safety against failure. Based on the sealant test results shown in Fig. 5 for DC 983 SGS sealant, this represents a safety factor of $140 \text{ psi (965 kPa)}/20 \text{ psi (138 kPa)} = 7.0:1$. Similarly, based on the sealant test data in Fig. 6 for DC 995 sealant, this represents a safety factor of $146 \text{ psi (1007 kPa)}/20 \text{ psi (138 kPa)} = 7.3:1$. Therefore, both sealant types meet the requirements of C1401 for using a 20 psi (138 kPa) allowable stress for wind and thermal loading. Based on consultation with Dow Corning, a proposed allowable sealant stress for seismic design is 50 psi (345 kPa). However, the building permit officials (OSHDP) requested a safety factor of 5:1 be adhered to for this specific project. Based on available sealant test results by Dow Corning, the most conservative condition is the cyclic tension testing of 983 SGS sealant at a strain rate of 0.5 in. (12.7 mm) per minute with an ultimate tensile strength of 140 psi (965 kPa), which results in an allowable stress of 28 psi (193 kPa) for seismic loading for a factor of safety of 5:1. Dow Corning 2-part DC 983 SGS sealant was chosen as the preferred sealant for shop glazing, whereas Dow Corning 1-part DC 995 sealant was chosen for field glazing. Typical properties for these sealant types are listed in Table 1.

Based on the curves generated in Figs. 5 and 6 the Young's modulus could be calculated at different ranges of sealant stress. The results are listed in Table 2. The modulus can change slightly depending on the stresses between which the slope of the curve is arrived at, but upon examination of Figs. 5 and 6, it can be seen that both sealants behave very linearly from 0 to 30 psi (207 kPa). Although 50 psi (345 kPa) is an industry-accepted level of sealant stress for seismic designs, this project limited the stress to be at a minimum 5:1 safety factor as requested by OSHDP. With an ultimate sealant strength of 140 psi (965 kPa), conservatively, the resultant design stress level is then 28 psi (193 kPa).

TABLE 1—DC 983 SGS and DC 995 sealant properties.

Properties	2-part DC 983 SGS	1-part DC 995
Tensile adhesion modulus (ASTM C1135)	300–800 psi (2069–5515 kPa)	175–325 psi (1207–2241 kPa)
Tensile strength (ASTM D412)	250 psi (1724 kPa)	350 psi (2413 kPa)
Movement capability (ASTM C719)	±25%	±50%
Durometer (ASTM C661)	40–50 Shore A	40 Shore A
Shear adhesion modulus (AC 45)	75 psi (517 kPa)	50 psi (345 kPa)

TABLE 2—*Dow Corning 983 SGS modulus and ultimate tensile properties.*

	Young's modulus, psi (kPa)	Ultimate strength, psi (kPa)
21-day room temperature	486 (3351)	165 (1138)
88°C elevated temperature	485 (3344)	146 (1007)
5000-h UV exposure	401 (2765)	170 (1172)

Additionally, seismic movement primarily results in shear stresses in the structural sealants. Based on tensile properties of uniform behavior, linear materials such as these two sealants can be used to develop equations and predict shear behavior. During the course of this study, the same dimension tensile adhesion joints were also tested in shear. As discussed earlier per test results and also shown by Zarghamee et al. in 1996 [16], the shear modulus is approximately 1/4 that in tension. The ultimate strengths in either mode are very similar. For example, as shown in Figs. 5 and 6, at 28 psi (193 kPa) in tension, the strain on the sealant is approximately 10% in tension and close to 40% in shear. This is actually favorable for seismic testing in that for a given strain or displacement during a seismic load, the associated stress on the sealant is lower in a shear mode than in a tensile mode. Thereby, the primary data by which this project was designed for, being tensile data, is a conservative approach.

The other important sealant properties to account for when considering seismic design are durability of the sealant and consistency of the sealant strength and modulus properties over time, which can be seen in the 5000 h QUV exposure and high-temperature exposure conditions. Upon review of these results, it can be seen that extended weathering has very little effect on silicone sealants, which is critical to long-term reliable seismic performance. The shear results are summarized in Table 3.

Hot, cold, and long-term weathering exposure conditions were tested to verify the consistency and durability of the silicone sealant properties. Although

TABLE 3—*Summary shear data; 21-day room-temperature (RT) cure (+ environmental exposures).*

Sealant	Ultimate shear stress psi (kPa)	Ultimate shear strain (%)	Young's modulus psi (kPa)
Dow Corning 995 RT	135 (931)	256	45 (310)
Dow Corning 995 RT + 1 h 88°C + 3 h RT dwell	140 (965)	225	47 (324)
Dow Corning 995 RT + 1 h -29°C	148 (1020)	244	50 (345)
Dow Corning 983 SGS RT	136 (938)	198	71 (490)
Dow Corning 983 SGS RT + 1 h 88°C + 3 h RT dwell	143 (986)	179	73 (503)
Dow Corning 983 SGS RT + 1 h -29°C	170 (1172)	232	65 (448)

silicone sealant durability is well documented in the industry, a quick overview of weathered sealant properties under tensile testing is summarized in Table 4.

SSG sealant is designed to transfer wind, thermal, and seismic loads and/or deformations through the glazing to the curtain-wall framing. For seismic design of building curtain-wall systems, to minimize racking-induced sealant shear stresses, and keep them within the allowable shear capacity, a unitized glazing system was chosen for the project. Within the unitized system, the silicone sealant remains adhered and absorbs stresses from building movements and wind load. When the silicone is adhered to the aluminum frame, it is then a part of an operating joint. Joint properties are tested per ASTM C1135 [12] and the resulting modulus of the system joint (not sealant alone) is 300–500 psi (2069–3448 kPa). The ultimate strength of such a joint is between 140–165 psi (965–1138 kPa) in tension and 135–170 psi (931–1172 kPa) in shear.

Discussion of the Finite-Element Modeling and Analysis

To predict the behavior of the mockup designed for this study before the actual testing, a finite-element model was developed and analyzed. The mockup detail that is discussed subsequently is shown in Fig. 7. The finite-element model was constructed in a program called Visual Analysis by Integrated Engineering Software [17]. This finite-element modeling program focuses primarily on linear-elastic modeling of structures. Figure 8 shows an overall view of the completed model. The aluminum mullions (vertical and horizontal) are represented by 2-node beam elements. Because of the flexibility of the silicone sealant at the perimeter of the glass lites, the glass panel is expected to act as shear-resisting elements, and, therefore, the moment restraints were released where the horizontal mullion beam elements attach to the vertical mullion beam elements. It is noted that the stiffening influence of a nominal moment connection between the aluminum mullions is expected to be insignificant compared to the stiffening influence of the glass lites, which are attached to the aluminum

TABLE 4—*Properties of weathered sealants under tensile testing.*

Sealant	Ultimate tensile stress psi (kPa)	Ultimate tensile strain (%)	Young's modulus psi (kPa)
Dow Corning 995 RT	162 (1117)	210	231 (1593)
Dow Corning 995 RT + 1 h 88°C	160 (1103)	146	236 (1627)
Dow Corning 995 RT + 1 h -29°C	162 (1117)	216	230 (1586)
Dow Corning 995 RT + 5000-h UV exposure	145 (1000)	171	200 (1379)
Dow Corning 983 SGS RT	165 (1138)	116	486 (3351)
Dow Corning 983 SGS RT + 1 h 88°C	146 (1007)	82	485 (3344)
Dow Corning 983 SGS RT + 1 h -29°C	151 (1041)	128	364 (2510)
Dow Corning 983 SGS RT + 5000-h UV exposure	170 (1172)	156	401 (2765)

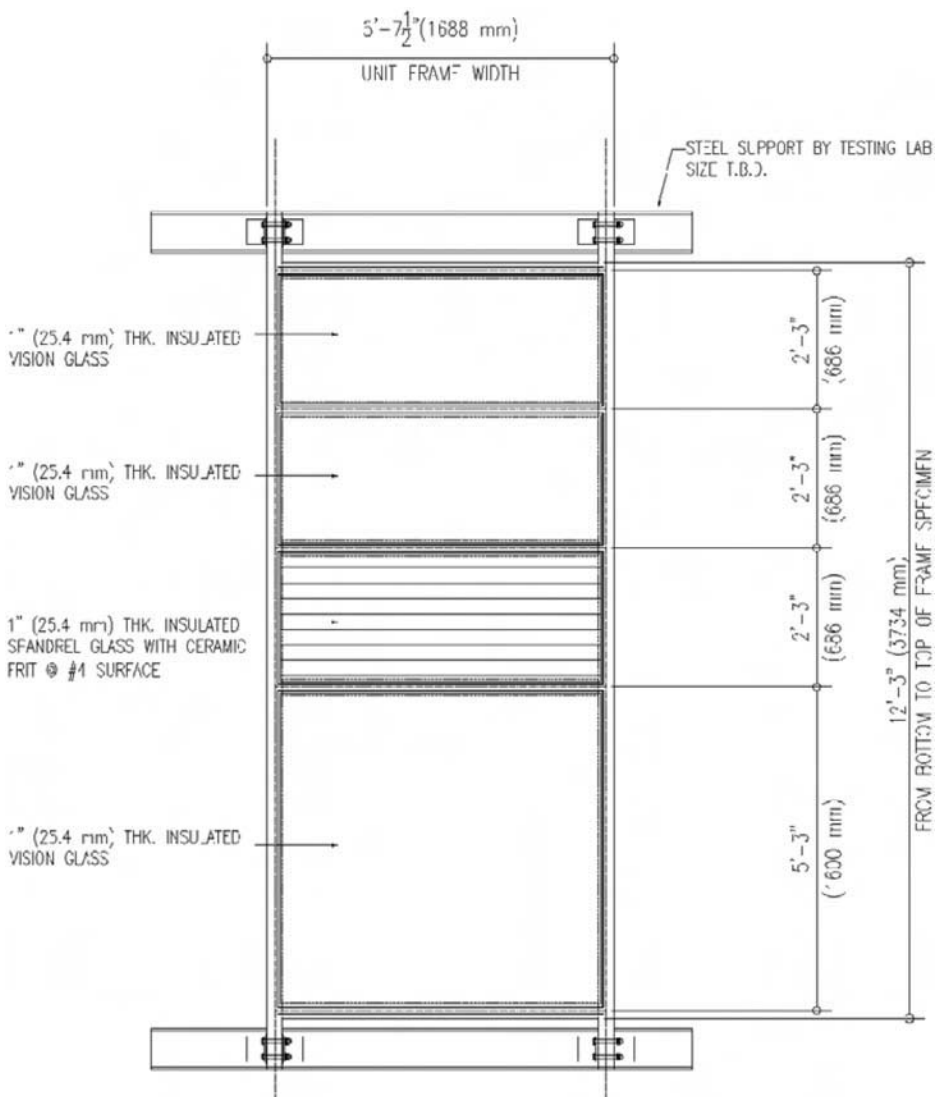


FIG. 7—Mockup designed for preliminary testing.

mullions by the silicone sealant. The structural silicone sealant and the glass lites are represented by 3- or 4-node plate elements. The appropriate linear-elastic material properties for all three materials were entered into the model. For the silicone sealant, the anisotropic and non-linear material behaviors cannot be accounted for in this specific finite-element modeling software. The Young's modulus, E , of the silicone sealant was varied in separate runs of the model in an attempt to capture both the tension and shear behaviors of the sealant. This was only a rudimentary attempt to capture their effects. A more

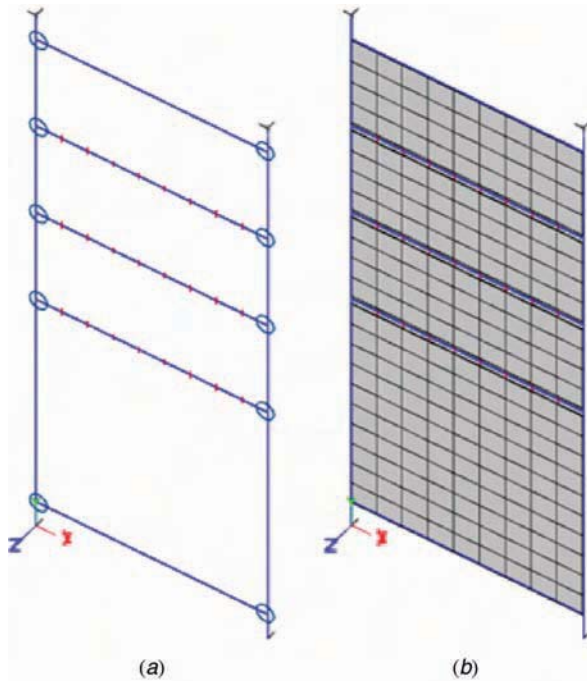


FIG. 8—Finite-element overall model view. (a) mullion beam elements with end releases, and (b) glass and sealant plate elements.

sophisticated finite-element software program would be needed to more fully integrate these non-linear sealant properties into the analysis.

For the actual testing, movements in the mockup specimens were measured at discrete displacement values. When trying to obtain analytical results from computer software that can be appropriately compared to testing results, it is important to simulate as closely as possible the actual test conditions. Therefore, the finite-element model was displaced to the same displacement values that were measured in testing. Figure 9(a) shows a graphical representation of the displaced shape of the finite-element model at a given displacement. Whereas the actual cyclic testing was carried out at frequencies of 0.8 Hz and 0.4 Hz, respectively, for displacements less than or equal to 3 in. (76.2 mm) and larger than 3 in. (76.2 mm), the finite-element analysis was carried out statically, which simulated a very slow loading rate. A close-up of one of the glass lite intersections can be seen in Fig. 9(b), where the movement of the panel below with respect to the upper panel at the horizontal stack joint is identified by the vertical line break at the bottom nodes of the upper panel. In both of these figures, the glass is represented by a “blue” color and the silicone sealant by a “grey” color.

The first step in evaluating the finite-element model is to review the overall results and determine if they generally correlate with the testing results and

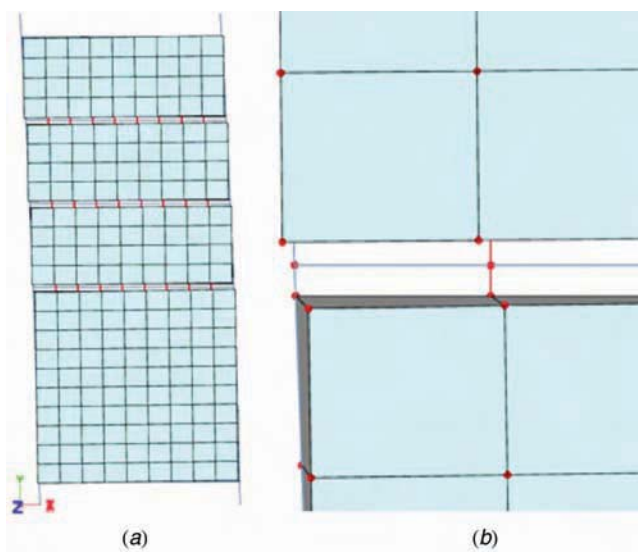


FIG. 9—Finite-element model displaced shapes: (a) overall displaced shape, and (b) close-up of displaced shape.

what might be considered to be appropriate behavior. From the overall view of the displaced model (Fig. 9(a)), it is evident that the plate elements, representing the glass lites, are displacing and rotating rigidly. The close-up view of the glass lite intersection (Fig. 9(b)) also reveals that the silicone sealant is being stretched in an elastic manner. The finite-element model clearly demonstrates similar movement behavior to that of the actual test. Because the Young's modulus, E , of the glass is 10100 ksi (69640 MPa), and the E of the silicone sealant varies between 45 psi (310 kPa) for shear and 400 psi (2758 kPa) for tension (Tables 2 and 3), i.e., substantially more flexible than the glass lites, this type of result would be expected. The beam elements representing the aluminum mullions are not visible in either of the finite-element model views represented by Fig. 9. Because the strong and weak axis rotational degrees of freedom at each end of these elements are released (no moment), there is no resistance to lateral displacement from these elements in the finite-element model. Comparison of the finite-element analysis result with mockup test results is described subsequently.

Discussion of Glazing System Design for Wind and Seismic Loads

The horizontal and vertical movement joints between each typical panel allow for movement and flexibility within the system. Individual unitized panels can sway independent of each other. Whereas some binding in the stack joint may occur, forcing the panels to rack slightly, they will not rack to the degree that a conventional stick system, firmly attached to each floor level, would. At the corners, the panels will be allowed to rock to accommodate the building drift. The

continuous horizontal fin, incorporated in the sill extrusion, carries the setting blocks and the dead load forces of the unit above. The horizontal joint is sized appropriately to accommodate slab edge deflection and thermal expansion within each window unit.

For wind loading (perpendicular to a given building elevation), the glass lites span in two-way action to their perimeter edges. Each of the four sides is adhered to the mullions with SSG sealant, which transfers all of this loading in either tension or compression. In tension under out-of-plane wind loading, the SSG sealant has an allowable capacity of 20 psi (138 kPa) [1]. Out-of-plane seismic loading is frequently much lower than wind loading and consequently not a governing load case. For the unitized system under study, the only in-plane restraint occurs at the head of the unit by means of the mechanical connections to the slab. The bottom (sill) of the unit is not restrained horizontally or vertically. Because in-plane restraint is not provided at the bottom of each unit, the primary mode of behavior for a unit caused by in-plane seismic loading is to sway. However, as shown in Fig. 4, adjacent vertical panels attached through the horizontal stack joint still will experience some in-plane resistance to movement because of the gaskets attaching the upper and lower sill mullions. Furthermore, for a hypothetical situation where for any reason the sway behavior fails and stack joints do not function as expected, the system would behave more like a stick-built system, i.e., it would rack. Racking here means that under in-plane lateral load at top of the panel, the panel will deform into a shape of a parallelogram. However, sway is the condition when the panel will slide in-plane at the horizontal stack joint keeping its rectangular shape. The racking condition will then require that each unit resist this loading either by frame action with each horizontal and vertical mullion connection resisting shear, tension, and moment, or the glass lites must act as shear-resisting elements with all stresses being transferred through the SSG sealant connecting the glass to the mullions. Whereas some moment can be transferred between the horizontal to vertical glazing frame member connections, this connection is primarily designed for direct shear and tension. The walls of aluminum mullions are typically thin (less than 0.125 in. (3.2 mm)) and, therefore, fairly flexible when subjected to moments resisted solely by screw fasteners between the members. The glass lites, however, present a relatively stiff element into the unit construction. This stiffness is tempered by the flexibility of the SSG sealant, the clearance between the edge of the glass, and the protruding fins of the mullions (Fig. 4).

For seismic design of four-sided SSG systems, it is essential to evaluate the maximum stresses experienced by the SSG sealant and make sure the sealant bead size is sufficient to keep stresses below the sealant allowable value. For this project, the sealant bead was originally sized to accommodate the maximum wind load on the largest lite of glass at just below the 20 psi (138 kPa) allowable. The typical sealant bead is 3/8 in. (9.5 mm) thick by 7/16 in. (11.1 mm) wide on the back face of the heat-strengthened glass lite (#4 surface). The SSG bead then wraps around the edge of the inside lite of glass to the #3 surface. The overall effective width for the L-shaped sealant bead is 5 in. (12.7 mm). The bead is Dow Corning 983 SGS two-part structural silicone sealant, which will be shop-installed. The structural sealant bead attaches the inboard lite of glass to the

aluminum mullion. All primary structural loads are transferred through the structural bead. For seismic loading, the allowable stress, based on a 5:1 safety factor requested by OSHPD, is 28 psi (193 kPa). Based on finite-element analysis of elastic models of the wall system, the sealant bead under in-plane seismic loading typically experiences stresses less than 20 psi (138 kPa) with few exceptions where the stresses reach approximately 24 psi (165 kPa).

The finite-element modeling performed indicates that the sealant stresses will remain below the 5:1 safety factor when the panel sways because of seismic loading. The results from the AAMA 501.6 testing discussed next have further shown that even when subjected to full racking, the SSG structural sealant beads perform adequately.

Discussion of the AAMA Test Protocol and Test Results

The AAMA 501.6 testing protocol requires that the mockup consist of what is determined to be the critical lites of glass. More specifically, the protocol requires test mockups to include those lites of glass in the curtain-wall system with the largest glass area, the thinnest glass, the most vulnerable glass type and glazing system type, the smallest glass-to-frame clearances, the smallest height-to-width ratio, and the largest drift index. It was determined that the patient room vision lite (5 ft, 2 in. \times 5 ft, 3 in. (1575 mm \times 1600 mm)) and the shadow box lite above (2 ft, 2 in. \times 5 ft, 3 in. (660 mm \times 1600 mm)) were the most critical lites to be tested. Figure 7 shows the mockup that was constructed for preliminary testing. The mockup is of stick-built type for this initial testing to cause the mockup to be racked and to determine the code required minimum delta fallout displacement (Δ_{fallout}). According to ASCE 7-05 [2], Δ_{fallout} shall be larger than the product of $1.25 I_p D_p$, where I_p is the important factor and D_p is the design relative story displacement (drift). For this project, and more specifically this mockup, the product of $1.25 I_p D_p$ was determined to be 3.75 in. (95.2 mm). This was the displacement that the mockup needed to reach under racking load without glass fallout to pass the test.

Because the curtain-wall system for this project is largely unitized and therefore de-coupled from movement in adjacent floors, testing to a racking displacement is conservative as the actual sway displacement will be less. There were four primary reasons why this decision was made. First, this was a preliminary test to assure OSHPD that a four-SSG system was safe enough to consider for an essential service building like a hospital. As such, it was necessary to establish that the system could perform beyond any drift that it was reasonably expected to experience under the design criterion. Secondly, OSHPD was concerned that while the primary mode of behavior for each unit was to sway, that there might be some friction or binding along the sill of the unit, which would force some level of racking to occur. Third, on this project, we have some punched windows that are completely framed into the metal stud system, which also supports the ACM panels and is designed to rack. While not required to fully rack because of the perimeter caulk joint and sliding head channel, these smaller windows will undergo more racking than the unitized units. Finally, the decision was made to construct the corner unitized units in an L-shaped

configuration to wrap the corners of the building. As such, these units would be required to undergo more racking than the typical unitized units. With all of these issues in mind, it was determined that the course of action that would most likely establish the performance capability of the system would be to rack the mockup.

With the mockup configuration testing method selected (rack, not sway), it was imperative that the glass, SSG bead size and type, and mullion paint (Kynar) be determined to exactly match what will be installed on the building. Sealant type, bead geometry, surfaces to be adhered to, and glass edge clearance all had to match what would be used on the project (Fig. 4) for the results of the testing to be considered valid for determining the performance of the final design. The resulting details for a horizontal and vertical section through the mullions for the preliminary mockup are shown in Fig. 10.

The AAMA 501.6 test can be used to validate a number of key design elements of the curtain-wall system including: adequacy/performance of the SSG structural sealant bead, adequacy of the glass edge clearance, drift associated with the first evidence of glass cracking (Δ_{cracking}), which is a serviceability limit state and drift associated with glass fallout (Δ_{fallout}), which is an ultimate limit state. Of course, the primary objective of the AAMA 501.6 test is to determine Δ_{fallout} .

According to AAMA 501.6 protocol, three replicates of a given mockup shall be tested on a dynamic racking test apparatus to determine the drift authoronding to glass fallout. For this project, the test apparatus was located at the ATI test facility in York, PA and is shown in Fig. 11 with a typical mockup mounted. Based on the AAMA 501.6 loading protocol, crescendo racking test consisting of a concatenated series of “ramp up” intervals and “constant magnitude” intervals each consisting of four sinusoidal cycles shall be applied to the specimen. The in-plane racking displacement steps between constant amplitude intervals shall be .25 in. (6.4 mm). The test shall be carried out at a frequency of 0.8 Hz for displacement amplitudes of 3 in. (76.2 mm) or less and at a frequency of 0.4 Hz for larger amplitudes. This means that for a displacement of 3 in. (76.2 mm) at 0.8 Hz, the displacement rate for top of the mockup would be 9.6 in. (244 mm) per second (576 in. (14630 mm) per minute). For the sealant, however, the strain rate is much lower as mentioned subsequently. Glass fallout drift (Δ_{fallout}) is defined as the drift corresponding to a piece of glass at least 1 in. [2] (645 mm²) in area breaking away and falling out of the mockup. For this project, the test was stopped after each step to inspect the specimen and, therefore, the concatenated displacement-time history used is shown in Fig. 12.

An important objective in these tests was to also determine the drift capacity of the structural silicone at glass fallout limit state. For this reason, as has been mentioned, the mockups were designed and attached to the test facility as stick-built systems. The mockups tested had dimensions of 5 ft, 7.5 in. (1715 mm) wide by 13 ft, 11 in. (4242 mm) high. Figure 13 shows one mockup on the test facility. The glass panels used in the mockups were 1 in. (25.4 mm) thick IGU for both vision and spandrel lite with ceramic frit. The glass type used was .25 in. (6.4 mm) thick heat strengthened.

The hysteresis, or load-displacement curves, for the mockup is shown in Fig. 14. There are four loading cycles shown in this figure, which authoronds to:

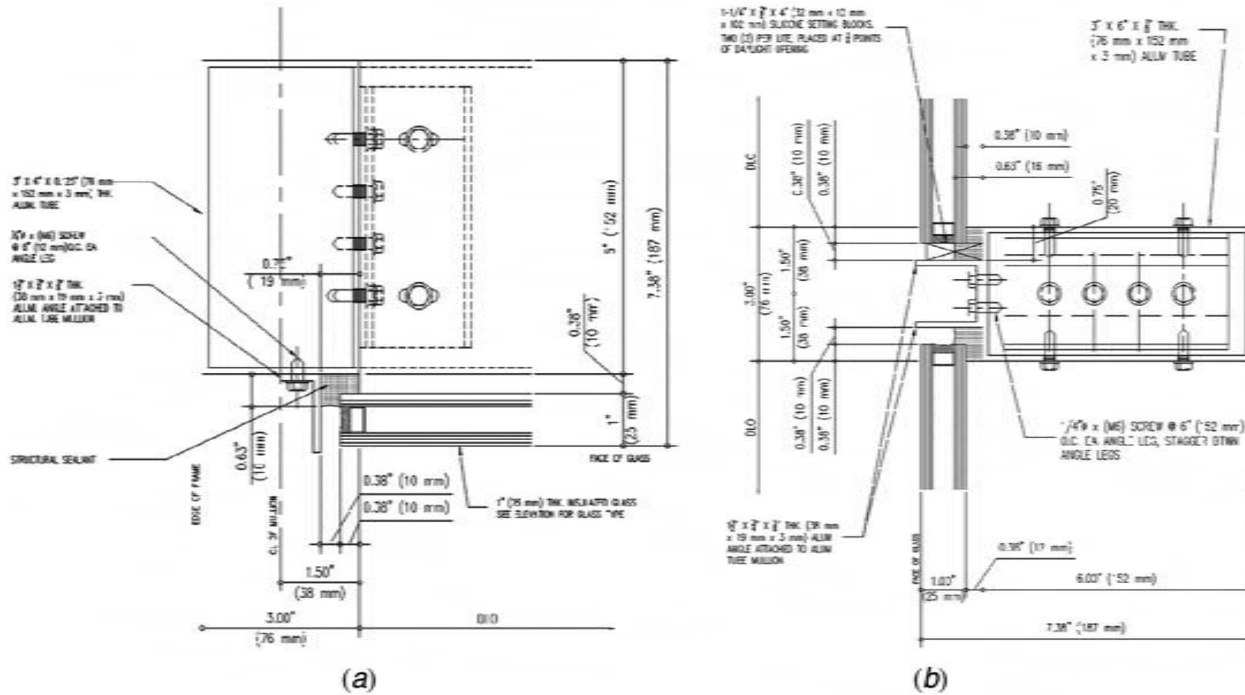


FIG. 10—Horizontal and vertical section details for the preliminary mockup: (a) vertical section, and (b) horizontal section.

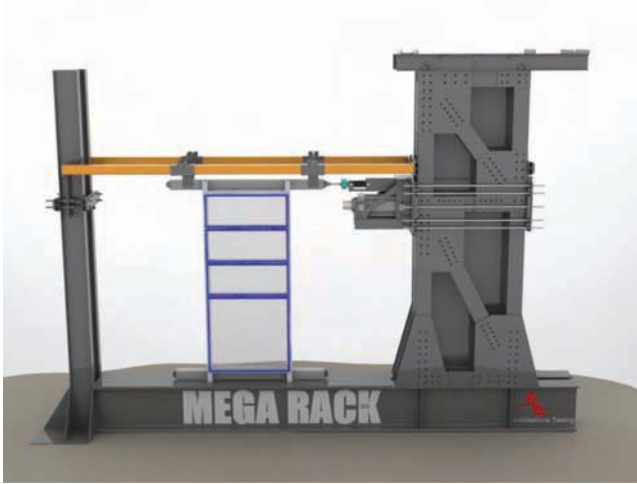


FIG. 11—ATI test facility for preliminary testing.

0–2 in. (0–50.8 mm), 0–3.75 in. (0–95.3 mm), 0–4.25 in. (0–108 mm), and 0–4.5 in. (0–114.3 mm) displacement levels. 2 in. (50.8 mm) displacement represents the design level seismic event for this building, i.e., 1.25% drift, whereas 3.75 in. (95.3 mm) represents the displacement that building code requires to be obtained without glass fallout. Both of these displacement cycles show very tightly spaced data. This indicates that there is very little strength loss in the silicone sealant as the mockup is cycled back and forth. The general slope of the 0–3.75 in. (0–95.3 mm) displacement cycle is less than that for the 0–2 in. (0–50.8 mm) displacement cycle. This indicates a softening of the silicone

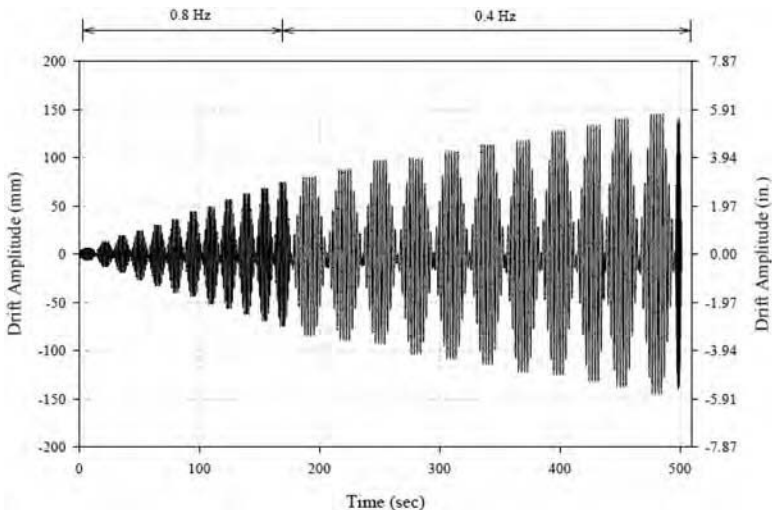


FIG. 12—Displacement-time history used for preliminary racking testing.

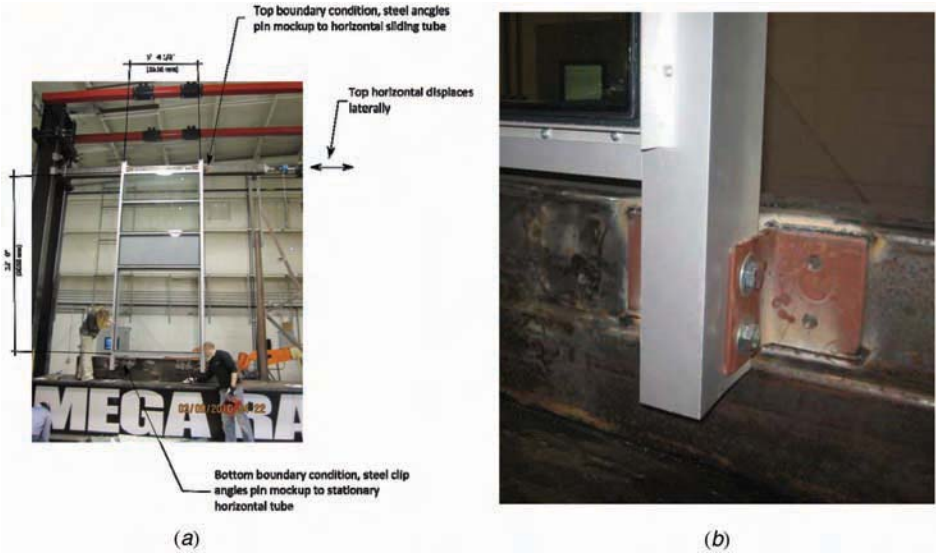


FIG. 13—One mockup on ATI facility. (a) entire mockup elevation, and (b) an enlarged view of one bottom boundary condition.

sealant resistance as it is cycled through larger displacement levels. This is consistent with the sealant test data (Figs. 5 and 6), which shows a reduction in the Young's Modulus as the elongation is increased. The sealant strain rate is a function of the actual sealant strain experienced at a given drift, the sealant bead thickness and the frequency of the racking. Based on a recent study [18], at a displacement of about 3 in. (76 mm) applied at a frequency of 0.4 Hz, the strain rate for a 9/16-in. (14-mm) -thick bead can vary between 2 in. (51 mm) per

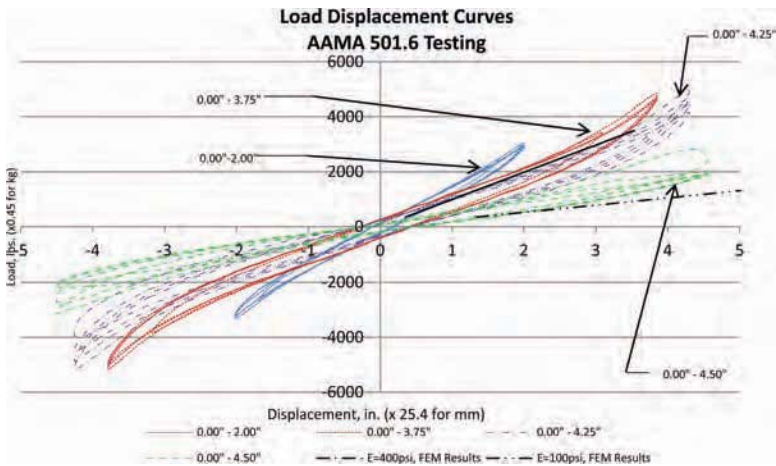


FIG. 14—Hysteresis curves (load displacement).

minute to 28 in. (711 mm) per minute. This strain rate is higher than the coupon strain rate of .5 in. (12.7 mm) per minute, but is closer to what would be expected to be experienced in an earthquake as the racking frequencies (0.8 Hz and 0.4 Hz) are representative of the natural (fundamental) frequencies of midrise buildings. It should be noted that, in general, materials show higher strengths at larger loading rates. This means that in an actual earthquake, it is expected that the sealants would show higher strength than what is shown by the coupon tests. Therefore, using coupon test results at lower strain rates is actually on the conservative side. The 0–4.5 in. (0–114.3 mm) displacement cycle represents the point at which the largest glass lite fell from the mockup. This data is represented by the color green and is more widely spaced than the previous displacement cycles. This wider spacing represents the strength loss as the sealant fails. The load-displacement cycle for 0–4.25 in. (108 mm) was included to show the performance of the sealant and mockup just prior to the cycle in which the glass fell out.

Overlaid on this data are two lines that represent the load-displacement data generated by the finite-element models. One of the lines represent the silicone sealant with a Young's modulus, $E = 400$ psi (2758 kPa), whereas the second one represents an $E = 100$ psi (690 kPa). A Young's modulus of 400 psi (2758 kPa) more closely represents the tension properties of the sealant (Table 4), whereas a Young's modulus of 100 psi more closely represents the shear properties of the sealant (Table 3).

According to ATI test report [19], the results show that no glass fallout occurred in any of the three mockups at the target drift of 3.75 in. (95.2 mm). The overall Δ_{fallout} for the mockup was reported to be 4.25 in. (108.0 mm) drift based on bottom vision lite fallout, which is 13% larger than the design drift of 3.75 in. (95.2 mm). As for sealant performance, minor sealant tear is reported on the exterior side at 3 in. (76.2 mm) drift and on the interior side at 3.75 in. (95.2 mm) drift. Figure 15 shows typical sealant tears at such drift levels. Therefore, as the test results indicate, at drifts close to the design drift, some sealant



FIG. 15—Typical structural sealant damage.

tearing occurred but not sufficient for any glass to become disengaged. The sealant tearing progressed at drifts beyond the design drift.

Conclusions

The conclusion from the test program is that even under the highly unlikely condition that the unitized system's stack joints do not function as designed and cause the curtain wall to rack as a stick-built system, this curtain-wall system satisfies ASCE 7-05 seismic provision of $\Delta_{\text{fallout}} \geq 1.25 I_p D_p$. Of course, because the final design will be of unitized construction, the glass fallout is certainly not expected to occur under the design drift. Based on the test results, one can conclude that the sealants are expected to experience some tear at drifts close to the target drift of 3.75 in. (95.2 mm) for a stick-built construction. However, for a unitized system wherein the stack joints allow the adjacent panels to slide past one another in a sway mode, structural sealant damage is not expected to occur at this target drift. The overall conclusion from the study is that four-sided SSG curtain-wall systems can be designed to satisfy the seismic provisions of the building code even in a stick-built construction system. However, because four-sided SSG systems are generally shop-glazed and mostly unitized system is employed, the seismic code provisions with respect to glass fallout are expected to be satisfied more readily and sealant damage (if any) is expected to be much less compared to stick-built systems.

References

- [1] ASTM C1401-09, 2009, "Standard Guide for Structural Sealant Glazing," *Annual Book of ASTM Standards*, ASTM International, West Conshohocken, PA.
- [2] ASCE 7-05, 2006, "Minimum Design Loads for Buildings and Other Structures," American Society of Civil Engineers, Reston, VA.
- [3] International Code Council (ICC), 2006, *International Building Code (IBC)*, ICC, Falls Church, VA.
- [4] AAMA 501.6-09, 2009, "Recommended Dynamic Test Method for Determining the Seismic Drift Causing Glass Fallout from a Wall System," American Architectural Manufacturers Association (AAMA), Des Plaines, IL.
- [5] AAMA 501.4-09, 2009, "Recommended Static Testing Method for Evaluating Curtain Wall and Storefront Systems Subjected to Seismic and Wind Induced Inter-story Drift," American Architectural Manufacturers Association (AAMA), Des Plaines, IL.
- [6] Dow Corning, 2006, "Structural Silicone Glazing from Dow Corning: Changing the Face of the World Cities," Dow Corning Corporation, www.dowcorning.com, pp. 1–12.
- [7] Dow Corning, 2007, Dow Corning Americas Technical Manual, <http://www.dowcorning.com/content/publishedlit/62-1112a-01.pdf?DCWS=Construction&DCWSS>.
- [8] ETAG, 1999, "Guideline for European Technical Approval for Structural Sealant Glazing Systems (SSGS)," *ETAG 002*, Amended October 2001, European Organization for Technical Approaches (EOTA), Brussels, Belgium.
- [9] Memari, A. M., Chen, X., Kremer, P. A., and Behr, R. A., "Seismic Performance of Two-Side Structural Silicone Glazing Systems," *J. ASTM Int.*, Vol. 3, No. 10, 2006, pp. 1–10.

- [10] Memari, A. M., Kremer, P. A., and Behr, R. A., "Seismic Performance of Four-Side Structural Sealant Glazing System," *J. ASTM Int.* (in press).
- [11] Kynar 500, "Kynar 500^R/Hylar 5000TM Pre-Finished Galvanized Steel Architectural Sheet & Coil," *Technical Information Sheet S723-RFS-284*, Firestone Building Products Company, 2011, <http://www.firestonebpco.com/templateFiles/includes/common/displayFile.ashx?fileId=8810>.
- [12] ASTM C1135-05, 2005, "Standard Test Method for Determining Tensile Adhesion Properties of Structural Sealants," *Annual Book of ASTM Standards*, ASTM International, West Conshohocken, PA.
- [13] ASTM C1184-05, 2005, "Standard Specification for Structural Silicone Sealants," *Annual Book of ASTM Standards*, ASTM International, West Conshohocken, PA.
- [14] AC 45, 1991, "Acceptance Criteria for Type I Structural Silicone Glazing Sealants (Adhesive)," International Conference of Building Officials (ICBO) Evaluation Services, Inc., Whittier, CA.
- [15] ASTM C719-93, 1993, "Standard Test Method for Adhesion and Cohesion of Elastomeric Joint Sealants under Cyclic Movement (Hockman Cycle)," *Annual Book of ASTM Standards*, ASTM International, West Conshohocken, PA.
- [16] Zarghamee, M. S., Schwartz, T. A., and Gladstone, M., "Seismic Behavior of Structural Silicone Slazing," *Science and Technology of Building Seals, Sealants, Glazing and Waterproofing, Vol. 6, ASTM STP 1286*, J. C. Myers, ed., American Society for Testing and Materials, Philadelphia, PA, 1996, pp. 46–59.
- [17] *Visual Analysis; v8.0.* (2011). Integrated Engineering Software, Bozeman, MT.
- [18] Broker, K. A., Fisher, S., and Memari, A. M., "Seismic Racking Test Evaluation of Silicone Used in a 4-Sided Structural Sealant Glazed Curtain Wall System," *J. ASTM Int.*, Vol. 9, No. 3, 2012.
- [19] ATI, "Preliminary Seismic Performance Testing of Four-Sided SSG Curtain Wall System," Test Report No. 97215.01-119-16, Architectural Testing, Inc., York, PA, 2010.

*Errol Bull*¹ and *Jorge Cholaky*²

A Review of the Behavior of Structural Silicone Glazing Systems Subjected to a Mega-Earthquake

ABSTRACT: Structural silicone glazed (SSG) curtain wall systems have offered architects and owners the ability to design a facade with unique aesthetic features since the 1970s. While their ability to durably withstand natural weathering and even high wind locations across the globe has been well established, their performance under seismic events is less well recorded. This paper presents a review of the performance of SSG systems following the 8.8 magnitude earthquake that shocked Chile in Feb 2010, which registered within the top five recorded in past history. Field reviews of existing low-, medium-, and high-rise buildings were inspected in the aftermath of the event to evaluate the performance of the different SSG variations of this system type (two-sided, four-sided, stick, unitized, among other variations) combined with other facade components such as: type of glazing, glass sizes, interstory drift, width of structural grid, slab/beam rigidity, etc.

KEYWORDS: structural silicone glazing, earthquake, SSG, high strain rate behavior of structural silicone, curtain wall systems, interstory drift

Introduction

Looking at structural silicone glazed (SSG) designs from the 1970s [1], 1980s [2], and 1990s [3] and beyond, one will mostly find a large variation on a theme: glass bonded to metal. SSG systems can encompass one-, two-, three-, and four-side bonded designs, with glass, metal (usually aluminum), and occasionally other materials. Yet, however variable, they are all conceptually similar whereas

Manuscript received June 24, 2011; accepted for publication March 23, 2012; published online May 2012.

¹ PE, Momentive Performance Materials, Waterford, NY.

² Ing., LCS Ingenieria, Santiago, Chile.

Cite as: Bull, E. and Cholaky, J., "A Review of the Behavior of Structural Silicone Glazing Systems Subjected to a Mega-Earthquake," *J. ASTM Intl.*, Vol. 9, No. 5. doi:10.1520/JAI104151.

Copyright © 2012 by ASTM International, 100 Barr Harbor Drive, PO Box C700, West Conshohocken, PA 19428-2959.

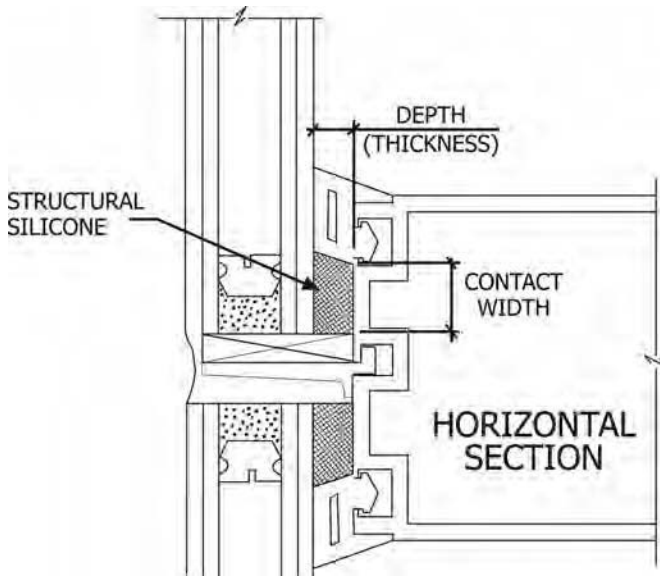


FIG. 1—SSG section detail.

glass or metal plates are bonded to a metal curtain wall part utilizing a structural silicone rubber adhesive as shown in Fig. 1. This silicone rubber adhesive acts as a flexible anchorage resisting wind pressures and at the same time absorbing translations and rotations due to imposed loads from: gusts, thermal expansions, and building movements (see Fig. 2). In an earthquake, in-plane rotation of inflexible glass would impart short-term shear strains of potentially large magnitude into the rubber. The most commonly used thickness of the structural adhesive in SSG systems is 1/4 in. (6.4 mm), far thicker than most “adhesives” in the traditional sense. That the adhesive in an SSG system has this thickness is what allows for the silicone rubber to stretch, rotate, and accommodate imposed strains. In a seismic event, the adhesive could experience displacements that may not have already been accommodated by the curtain wall system. Further, the commonly used 1/4-in. thickness can be increased to improve the in-plane flexibility of the system.

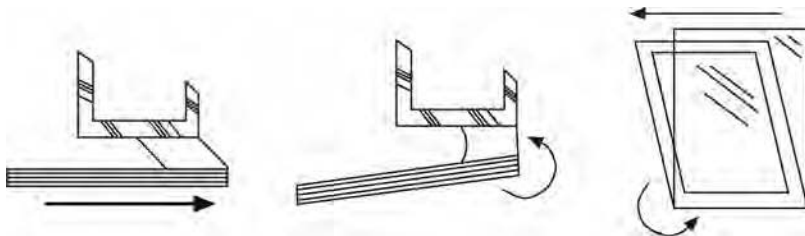


FIG. 2—Deformation through structural seals.

With respect to the in-plane deformation that an earthquake could place into a curtain wall system, it is not hard to imagine that a flexibly bonded assemblage (i.e., SSG) could offer improved performance over non-bonded curtain wall systems (“dry-glazed” or gasket-type systems that rely on compression or friction) when subjected to racking displacements from an earthquake. The bonded rubber adhesive would tend to “control” movements between parts, but on the other hand, could fail through shear if overstrained. Movements into a gasketed system would be more uncontrolled, and gaskets can be dislodged introducing yet additional uncontrolled movement between moving components. The thought here is that the uncontrolled movement would lead to an earlier collision between glass and metal, and thus breakage at an earlier stage in an event.

The ASTM C1401 industry guide on SSG [4] offers some commentary on performance of these systems and suggests that there are potential intrinsic benefits to using SSG systems in seismic regions, such as:

- (a) Controlling and in some cases eliminating breakage normally experienced during a small to moderate earthquake.
- (b) Minimizing the opportunity for glass to impact the metal glazing pocket surfaces, eliminating a primary cause of breakage (in four-sided SSG systems, the lite or panel is not captured in a metal glazing pocket).
- (c) Also, when a glass lite break does occur, the SSG system, because of continuous attachment of the glass edge, can retain much if not all of the broken glass, depending on glass type, and provided that the structural joint retains sufficient integrity.

Some of the ASTM suggestions above are supported by Penn State University (PSU) research studies via seismic simulations on two-side SSG systems where Memari et al. [5] conclude “that SSG systems can perform favorably in seismic events over conventional dry-glazed systems” with test results showing an approximately 65 % increase of cracking drift capacity (onset of glass cracks) when compared to a similarly sized and tested dry-glazed (non-SSG) system [5]. The research by PSU has identified that two-side SSG systems have improved serviceability and ultimate drift capacities than do dry-glazed (non-SSG) systems [6].

Additional research at PSU on four-side SSG systems [7] shows yet further improvement in drift capacities than does the two-side SSG research, concluding; “Comparison of four-side SSG system test results in this study with those of dry-glazed and two-side SSG in past studies shows that four-side SSG has higher cracking drift capacity than previously tested dry-glazed and two-side SSG by 146 % and 55 %, respectively. Moreover, the four-side SSG system has higher glass fallout capacity compared to dry-glazed and two-side SSG by 54 % and 13 %, respectively.” Additionally, “This study supports the commonly held notion in the industry that SSG systems, in general, and especially four-side SSG configurations are less vulnerable to glass damage in earthquakes. This notion is predicated upon the structural sealants being applied in accordance with silicone manufacturers specifications, and that silicone material properties have not deteriorated due to in situ weathering effects.”

SSG Design Considerations

According to building codes, curtain wall systems attached to the building structure are deemed “non-structural elements.” As with the superstructure of a building, these systems are also susceptible to damage from earthquakes, with glass fallout a life-safety hazard of significant concern. Curtain wall systems are designed around drift-based criteria, and system designers strive to create systems that utilize design elements to: control movements, improve drift capacities, and to minimize damage of the facade systems attached to these structures. Such accommodations can be in the form of: slotted connection holes [8], rounding of glass corners [9], interlocking unitized sub-frames, split mullions, movement accommodating frame-to-slab connections, and adhesively bonded glass and metal (SSG) including a properly selected structural silicone adhesive, which will be discussed more in-depth later.

An example of commonly used system in the Chilean market and in the buildings reviewed in this paper is the split-mullion type and are supported on a slide anchoring system as shown in Figs. 3 and 4. These systems offer movement accommodation via physical separation of interlinked components with typical accommodation ranges noted in Fig. 3. When seismic loads impose lateral displacement (interstory drifts) to the building, these de-linked components act along with slide-type supports to accommodate the displacements and in-plane rotation of glass relative to the supporting aluminum frame until the ranges are spent. At this point, the displacements will engage the structural seals by inducing in-plane transverse shear deformation with maximum strains occurring at corner locations. It is the corner locations that will be checked for silicone reaction. A more involved discussion involving the calculation of interstory drift and sealant shear strain is presented later.

Structural Silicone Considerations: Mechanical Properties

There are numerous structural silicone products sold in the global marketplace each with an individual mechanical property profile. To highlight to the reader the wide diversity of properties, we can take the examples of tensile adhesion strength coupled with elongation capacity. Figure 5 below shows recent laboratory test values of ultimate tensile adhesion strength (wider bars) and ultimate elongation value at maximum load (narrower bars) of 11 commercially available (at the time of this paper) structural silicone sealants. The specimen type was the “tensile adhesion” specimen as outlined in the ASTM C1135 Test Method for Determining Tensile Adhesion Properties of Structural Sealants [10], with one noted change in the specimen configuration: the thickness between bonded plates was changed from the test method default of 1/2 in. (12.7 mm) to 1/4 in. (6.4 mm), which more accurately reflects a real-life SSG application. Each graph represents an average of a minimum of ten specimens, all of which exhibited cohesive failure at rupture.

The 11 products represented in Fig. 5 are identified as follows:

1. Single-component, medium modulus silicone, manufactured in the U.S.
2. Single-component, high modulus silicone, manufactured in Europe.

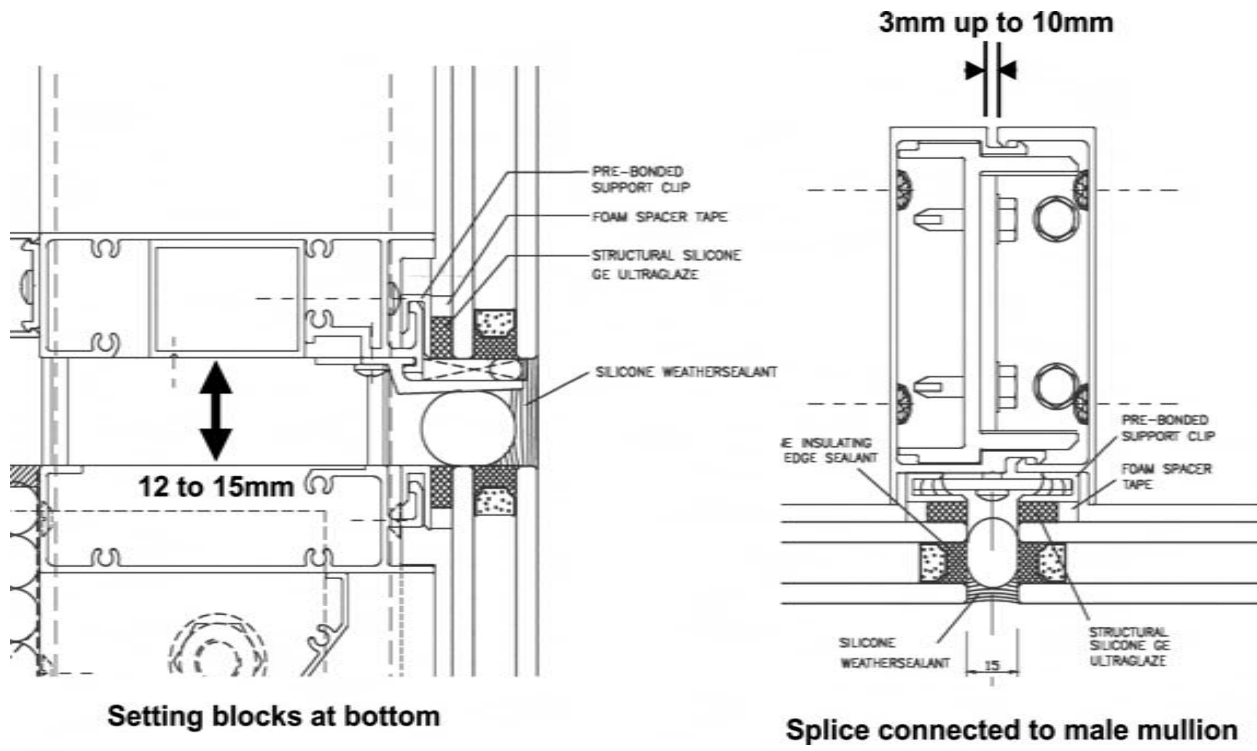


FIG. 3—Typical details of Chilean SSG systems.

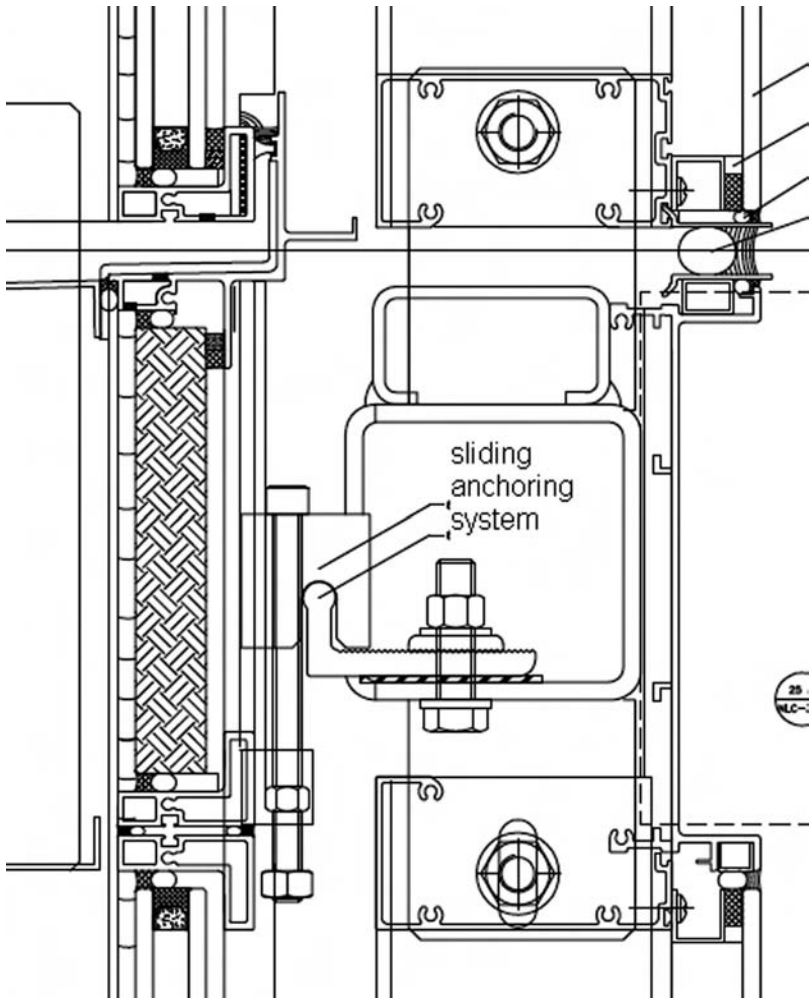


FIG. 4—Detail of sliding anchoring system.

3. Single-component, high modulus silicone, manufactured in the U.S.
4. Single-component, high modulus silicone, manufactured in Europe.
5. Dual-component, high modulus silicone, manufactured in the U.S.
6. Single-component, high modulus silicone, manufactured in Europe.
7. Single-component, medium modulus silicone, manufactured in U.S.
8. Single-component, high modulus silicone, manufactured in the U.S.
9. Dual-component, high modulus silicone, manufactured in the U.S.
10. Single-component, high modulus silicone, manufactured in the U.S.
11. Dual-component, high modulus silicone, manufactured in the U.S.

Looking at these two basic properties of any sealant, and comparing the extremes, one will recognize that product No. 11 is more than double the tensile

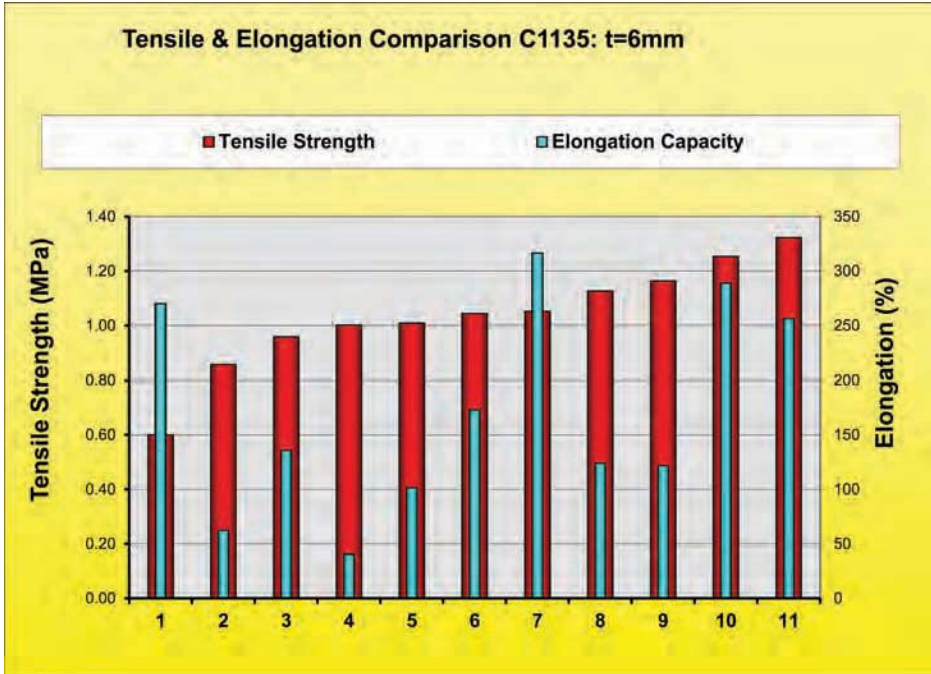


FIG. 5—Tension and % elongation comparison showing wide variability between products of these two measured properties.

strength of product No. 1. The values of the weakest versus the strongest are 0.60 MPa (87.1 psi) and 1.32 MPa (191.1 psi), respectively, the latter being 120 % stronger than the weaker. Regarding flexibility, one will find even wider variability within the group with the least flexible at 41 % and the most flexible 317 %, a 673 % difference. Such wide variation in mechanical properties will undoubtedly lead to performance differences when tested in some protective glazing applications. Protective glazing applications as defined by ASTM C1564 [11] include those subject to: earthquakes, hurricanes, windstorms, blasts, and other similar events.

When assessing the strength versus elongation profile of any given formulation, it is generally the case that filled rubber sealants attain physical strength at the cost of reduced flexibility. That is to say, the stronger the material, the stiffer and less flexible it becomes, and vice versa. Further, in these sealants, a given strain will result in higher stress in a stiff (less flexible) sealant and lower stress in a softer (more flexible) sealant. Arguably, it would be advantageous to lower the stresses imposed from strains imparted into a structural seal during a seismic event such that the sealant is not grossly overstressed leading to tearing or rupture of the sealant. Looking again at Fig. 5, some of the tested structural silicones possess a closer balance of these two properties with a combination of both high strength and high elongation capacity. In a material of this type, a

larger strain could be absorbed with a lower stress within the sealant when compared to others. This is interesting for consideration in protective glazing applications, which can impart larger strains (and subsequent stresses) into the system than do wind load and thermal expansion/contraction forces more typically seen in common SSG applications.

The shear strain behavior of a structural sealant is a reflection of its relative modulus, whereby a lower modulus structural sealant (medium modulus) will have more strain capacity than a stiffer less flexible (high modulus) structural sealant (capacity being point of rupture). The behavior of a structural glazing bead in shear has been previously reviewed by Kłowsowski and Wong [12]; however, the information in the Kłowsowski paper is relevant to testing on specimens at standardized (relatively slow) strain rates. An earthquake would impart shear strains into the structural seals at higher velocities than lab-tested rates. The test data presented below represents load-deformation values of a structural sealant tested at both standardized and higher strain rates.

Relatively High Strain Rate Behavior of Structural Silicone Sealants

In 2002, eight silicone sealant products were tested at GE's Global Research & Development Center on tensile testing equipment capable of producing relatively high crosshead speeds. The sealants were tested at different strain rates and different configurations (shear and tensile) to assess their material response characteristics under higher-than-typical strain rates in an effort to simulate atypical loadings (high wind events, seismic, blast, etc.), which impart energy into glazing systems differently than typical wind pressure loads. The study was useful to: (1) screen for formulations that provide the desired characteristics necessary to absorb the energy imparted into an affected glazing system, and (2) compare the mechanical properties of each formulation when pulled at a near-instantaneous strain rate (meters per second) versus the well-known mechanical properties of these products when pulled at a standardized (i.e., slow) strain rate (inches per minute).

The results of a two-part high modulus structural silicone from the 2002 testing is presented below as it is relevant to the topic of this paper. The data revealed increasing load and elongation values in both tension and shear as strain rate increases, and is reported in Table 1 and shown in Figs. 18–27. These findings are generally in agreement with Karpati's findings from 1972 [13]. Similar data has also been reported by Yarosh [14].

Resistance to Tear Propagation

In addition to a sealant's tensile adhesion strength and elongation capacity, its tear propagation resistance can play an important role under strain and repeat loading. Some structural silicone formulations propagate tears more readily than others and a product weak in this aspect would lead to a lower system drift capacity, as shear failure could occur earlier (assuming a tear site emerged in the structural seal during earthquake racking and was thus susceptible to

TABLE 1—High strain rate data in tension and shear.

High strain rate data for two-part high modulus structural sealant			
ASTM C1135 or C961 [15] test specimen with dimensions noted (see Figs. 16 or 17)	Strain rate, m/s (average values from ten specimens, each configuration and strain rate. All specimens failed cohesively)		
	0.00085 ^a	0.5	1.1
Tension C1135 , Newton (lb) 0.25 wide × 0.75 deep × 2 in. long (6.4 × 19 × 25 mm), see Fig. 16			
Max load—Newton (lb), % change [∅]	1192 (268)	1842 (414), 55 %↑	1975 (444), 66 %↑
Max stress—MPa (psi), % change [∅]	1.23 (179)	1.90 (276), 55 %↑	2.04 (296), 66 %↑
% Elongation at max load, % change [∅]	79	128, 62 %↑	145, 84 %↑
% Elongation at break, % change [∅]	99	184, 86 %↑	209, 111 %↑
Tension C1135 , Newton (lb) 0.5 wide × 0.5 deep × 2 in. long (12.7 × 12.7 × 50.8 mm), see Fig. 16			
Max load—Newton (lb), % change [∅]	743 (167)	1254 (282), 69 %↑	1383 (311), 86 %↑
Max stress—MPa (psi), % change [∅]	1.15 (167)	1.94 (282), 69 %↑	2.14 (311), 69 %↑
% Elongation at max load, % change [∅]	126	210, 67 %↑	230, 83 %↑
% Elongation at break, % change [∅]	141	254, 80 %↑	290, 106 %↑
Shear C961 , Newton (lb) 0.25 thick × 0.75 long × 1 in. wide (6.4 × 19 × 25 mm), see Fig. 17			
Max load—Newton (lb), % change [∅]	529 (119)	1058 (238), 100 %↑	1019 (229), 92 %↑
Max stress—MPa (psi), % change [∅]	1.10 (159)	1.6 (317), 99 %↑	1.6 (305), 92 %↑
% Elongation at max load, % change [∅]	112	153, 37 %↑	149, 33 %↑
% Elongation at break, % change [∅]	131	207, 58 %↑	

^aStandardized default strain rate of 2 in./min (50.8 mm/min) used in C1135 test method, [∅]percent change from standardized default strain rate.

propagate) than with a product more resistant to this action. This type of behavior may have possibly been exposed in a field inspection of a four-story four-sided SSG facade following the 1994 Northridge earthquake near Los Angeles, U.S. [8]. The building inspected was glazed and constructed in 1979–1980 utilizing an acetoxy cure structural silicone sealant, a recognized trait of which is lower resistance to tear propagation. Had a structural silicone with increased resistance to tear propagation been used in that design, it is possible that less damage to that curtain wall system may have occurred from the movements estimated and realized during that event.

The Guideline for European Technical Approval for Structural Sealant Glazing Kits (ETAG 002) [16] provides one measurement of this property. Section 5.1.4.6.4 of this guideline presents a method to assess “resistance to tearing,” which encompasses purposefully introduced cuts or “nicks” of defined dimension into the rubber of standardized specimens, see Fig. 6. These nicked specimens are then pulled to destruction on tensile-elongation equipment with the result of the test categorizing the product into one of two categories. Use category 1 represents a rubber that retained at least 75 % of un-cut control specimens, and use category 2 represents a rubber that retained at least 50 % but less than 75 % of un-cut control specimens. A rubber not retaining at least 50 % of controls does not meet the requirements of the document and may not be used in adhesively bonded SSG construction. Considering the above discussion regarding resistance to tearing, logic would suggest that a product that tests to the “use category 1” classification should bear consideration for seismic SSG designs.

Table 2 below shows the ETAG 002 tested category of several commercially available structural sealants as outlined in their respective ETA document.

From the information contained in Fig. 5 and Table 2, it is evident that there is sufficient variability in the tested mechanical properties of current commercially available structural silicone sealants and that some may be more appropriate for use in seismic regions than others. These highlighted properties of a structural sealant can play a more important role in the performance of SSG systems in seismic regions and product selection should be a consideration for use in such designs. In addition to the mechanical properties discussed, it

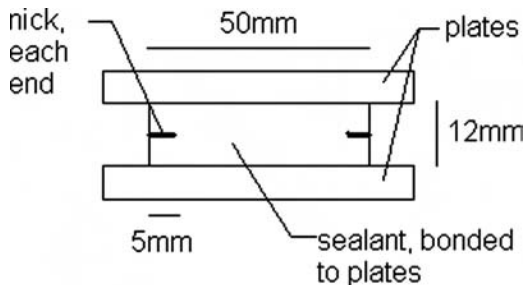


FIG. 6—Tear resistance specimen configuration and location of nicks.

TABLE 2—*Tear propagation use category per ETAG 002.*

Sealant type	Claimed movement class ^a	Availability	Use category
2-Component structural silicone	12	Americas, Asia, Europe	2
2-Component structural silicone	25	Americas, Asia	1
1-Component structural silicone	25	Euro, Asia	1
2-Component structural silicone	25	Americas	2
2-Component structural silicone	–	Europe, Asia	1
1-Component structural silicone	–	Europe	2

^aWhen tested to ASTM C719 [17].

goes without saying that adhesion quality and adhesive bond durability are equally important factors in the successful use of these systems.

Shear Strain Imposed into the Structural Silicone

Here we will use a real example from the earthquake (Isidora Foster building case study presented in more detail later in the paper) and make an estimate of the shear strain that could have been imposed into the structural sealant and compare this value to the shear strain capacity that could be expected of a two-part high modulus structural sealant when subjected to strain rates higher than those used in standardized tests (Table 1). Also recognize that in four-sided SSG systems, the glass will most closely rotate about its center of mass; therefore the drift is halved as it is split between opposing corners.

Consider first the worst-case scenario of the building where:

- (1) The maximum interstory drift allowed by code is reached a 33.9 mm (1.33 in.). See worst-case lateral displacement calculation on p. 14.
- (2) Assume no contribution of strain lowering from the frame anchoring and/or the curtain wall frame assembly.

In this scenario, the drift is imposed into the structural sealant and the shear displacement occurring at the location of highest strain (corners) is 16.9 mm (0.66 in.). Using trigonometry, the actual elongation experienced in the 6.4 mm (0.25 in.) thick bead is 18 mm (0.71 in.), which represents a 181 % shear strain. This value exceeds that which most, if not all, two-part high modulus structural silicones currently available could be expected to accommodate at a 6.4 mm (0.25 in.) thickness and at any strain rate. This is supported by the % elongation at maximum load values reported in Table 1. A shear strain of this magnitude would have manifested itself as failure through rupture and tearing of the structural seals at corner locations with possible dislocation of glass or fallout. Because this did not occur, it is reasonable to conclude that the curtain wall and anchoring system functioned properly to accommodate displacements from the event and the structural seals experienced strains lower than those at max load (strains after maximum load but before break of the specimen are associated with tearing of the rubber).

Now consider a more realistic scenario where:

- (1) A 9.2 mm (0.36 in.) actual interstory drift is used (this is the drift predicted to have occurred on the Isidora Foster building as estimated by finite element modeling taking into consideration soil conditions, nearby measured ground accelerations, and overall building response), and
- (2) assume no contribution of strain lowering from the frame anchoring and/or the curtain wall frame assembly.

In this scenario, the drift is imposed into the structural sealant and the shear displacement occurring at the location of highest strain (corners) is 4.6 mm (0.18 in.). Using trigonometry, the actual elongation experienced in the 6.4 mm (0.25 in.) thick bead is 7.9 mm (0.31 in.). This represents a 23 % shear strain, which is well below that which a two-part high modulus structural sealant can accommodate before damage to it occurs (reference values from Table 1 above).

Correlating this 23 % strain with a stress, we can derive from Fig. 24 (and the associated load-displacement data generated to make these curves) a stress of approximately 324–331 kPa (47–48 psi). However, Fig. 24 represents load-displacement curves generated using a very slow strain rate [the standardized strain rate of ASTM C1135; 50.8 mm/min (2 in./min)], which is not entirely relevant to the response of structural sealant from loading because of a seismic event. Considering the data generated at the higher tested strain rates, we can get another estimate of stress in the structural sealant. From Fig. 27, which superimposes the averages of the three tested rates in shear, it can be seen that the two faster rates closely parallel each other throughout most of the tested range. From these two faster strain rates, the associated stress at 23 % strain is in the range of 448–462 kPa (65–67 psi).

The stress estimates from the above scenarios must be tempered with the two following considerations:

- (1) Both scenarios assumed that the curtain wall and anchoring system did not contribute to reduce shear displacement into the structural seals, which is unlikely.
- (2) The faster strain rates used to derive the latter stress estimate are likely beyond what the structural sealant would experience in a seismic event.

Both of these considerations, taken alone or combined, would tend toward lowering the estimated stress ranges shown above. Regarding shear strain rates relative to seismic events, future work is of interest to better correlate SSG behaviour with lab and mock-up testing.

Actual SSG System Performance Post-Quake

The PSU research mentioned earlier was conducted using a single-component medium-modulus structural silicone (GE SCS2000) on “stick” built curtain wall units. The projects reviewed in this paper were constructed using a high modulus two-component structural silicone on “unitized” curtain wall systems. Unitized systems are currently the more prevalent assembly method for SSG systems, and are built in a factory and transported to the jobsite for modular

type installation by interlocking with adjacent units, while “stick” built systems are installed piece-by-piece on the job site.

Santiago is currently home to Latin America’s tallest tower (Torre Costanera at about 300 m) as well as several dozen towers exceeding 30 stories, many of them constructed with SSG curtain wall systems. Yet, considering the magnitude of the event and the extent of overall damage, there was reported favorable performance of modern buildings and facades. Several buildings with SSG facades were surveyed in the aftermath of the 2010 Chilean earthquake with most of them showing little or no damage even though the magnitude of the quake was the fifth largest in recorded history. To more completely assess the good performance observed of SSG systems post-quake, it is important to recognize the “behind the scenes” value of the Chilean Seismic Building Code, which is reviewed below.

Mega-Earthquake

Three and a half hours into Feb 27, 2010, a mega-earthquake with a moment magnitude (M_w) registering 8.8 on the Richter scale shook the central-south part of Chile. With its epicenter estimated at 43 km offshore and northwest of the locality of Cobquecura (see Fig. 7) and nearly 400 km southwest of Santiago, it produced 8.5 magnitude recordings in the greater Santiago city area; Chile’s capital, most populous city (population of around 6 million) and home to numerous tall glass facade buildings.

This “megathrust” earthquake occurred at the convergence of the Nazca (oceanic) plate with the South American continental plate at a depth of 35 km (21.7 miles) [source: Servicio Sismológico, University of Chile, www.sismologia.cl]. “Megathrust earthquakes occur at subduction zones at destructive plate boundaries (convergent boundaries), where one tectonic plate is forced under (subducts) another. Due to the shallow dip of the plate boundary, which causes large sections to get stuck, these earthquakes are among the world’s largest, with moment magnitudes that can exceed 9.0. Since 1900, all six earthquakes of magnitude 9.0 or greater have been megathrust earthquakes. No other type of known tectonic activity can produce earthquakes of this scale” [18].

Energy Release and Earthquake Characteristics

The event was recorded by 35 accelerographs situated at ground level covering the length of the 500 km (311 mile) rupture zone. Few megathrust earthquakes in the world have been as well recorded as this one. Table 3 presents peak ground accelerations (PGA) recorded at some of the accelerograph stations established and monitored by the University of Chile. A significant characteristic of the recorded accelerograms was the long duration of around 2.5 min [19], a relatively long ground shaking when compared to other earthquakes.

When comparing the frequency content of the Chile 2010 earthquake with others (like the Lolleo 1985 earthquake, in Chile) (Fig. 8), we see a greater relative importance of low frequency components (larger periods). This is evident



FIG. 7—The red circle indicates the epicenter of the earthquake near the small town of Cobquecura, in the Maule province. Santiago is shown upper right.

TABLE 3—Peak ground acceleration, PGA (g) recorded on Feb. 27 [19].

Station name	Maximum north-south acceleration	Maximum vertical acceleration	Maximum east-west acceleration
FCFM, center (greater Santiago)	0,165	0,138	0,163
Santiago, center (greater Santiago)	0,218	0,182	0,309
Maipu (greater Santiago)	0,561	0,240	0,478
Constitución (VIII region)	0,552	0,352	0,640
Angol (IX region)	0,928	0,281	0,681

as there was severe damage to non-structural elements (curtain walls excluded) in middle- and high-rise buildings (having larger periods) than evidenced in low-rise buildings.

Figure 9 reveals the response spectra of the recorded motions from Santiago station and shows acceleration measurements exceeding the values recommended by the current Chilean seismic code. These effects may have

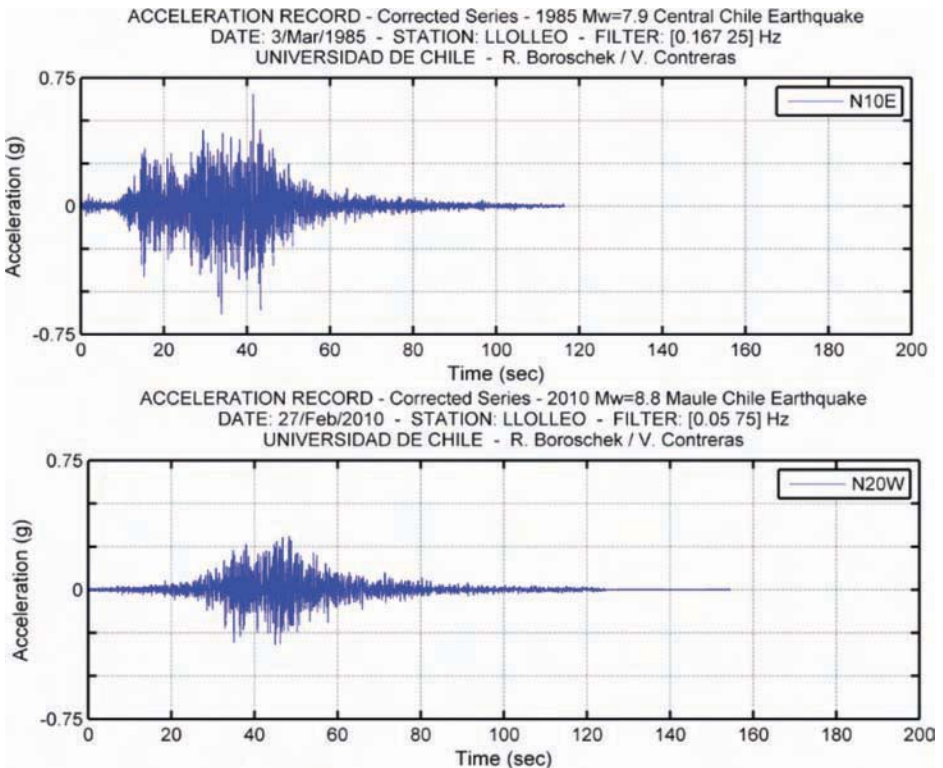


FIG. 8—Accelerograms from two stations, one in the 1985 Llolleo quake and one from the 2010 Maule quake [20].

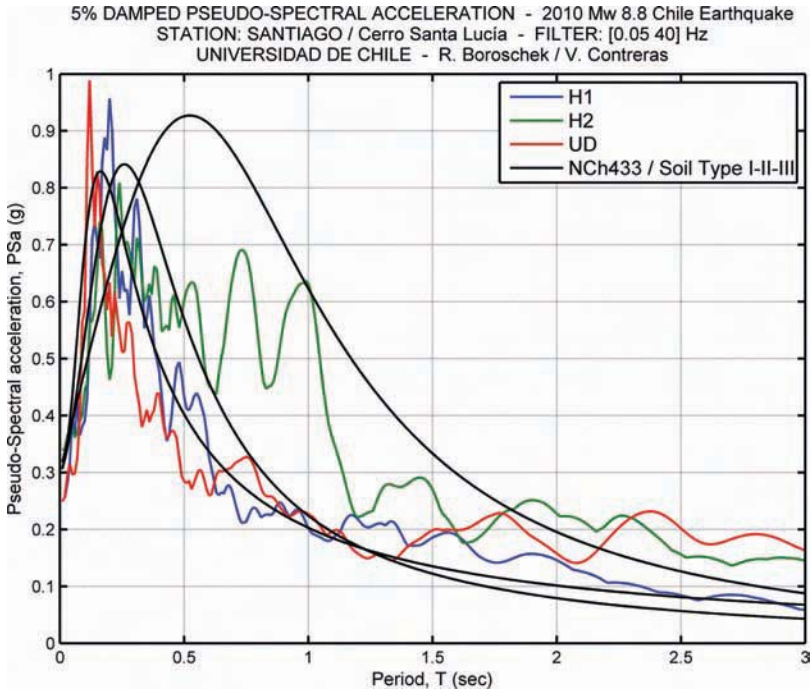


FIG. 9—Response spectra for Santiago Station [20].

contributed to the observed damage and structural failures in many high-rise buildings [20].

Building Rigidity and Interstory Drift

Buildings need to control movements that occur in the structure to prevent damage to the main elements as well as non-structural elements such as curtain walls and interior partitions. An important parameter used by the Chilean National Code NCh433.Of96 [21] (hereafter referenced as NCh433) to meet this objective is the interstory drift where restrictions are imposed for torsional effects and to overall building lateral displacements and interstory drifts. Section 5.9.2 limits displacement between centers of gravity to two per thousand of the interstory height and Section 5.9.3 limits the incremental displacement of any point on the floor of the building with respect to the centers of mass, to one per thousand of that height for a total allowed displacement of three per thousand.

Regarding these drift restrictions, Guendelman et al. presented the study “Perfil Bio-Sísmico de Edificios/Bio-seismic Profile of Buildings” [22]. This study performed a seismic review of reinforced concrete buildings which included 2262 actual buildings constructed in Chile. The study established a set of seismic indicators, whose values are compared with those considered

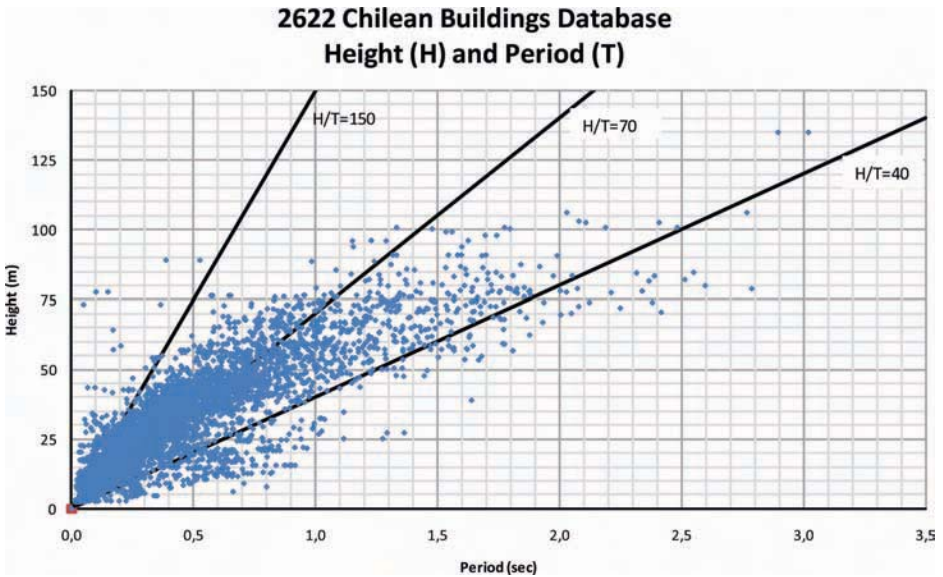


FIG. 10—Distribution of rigidity ratio H/T verified in 2262 buildings in Chile [22].

satisfactory according to general experience. Among the several indicators noted in the study, two are specifically interesting to understand the rigidity and deformation characteristics of buildings in Chile:

- (1) Total height/translational first mode period (H/T) index. This index, with dimensions of speed, has been considered a good estimate of the rigidity of a building. In general terms, it may be noted that values of H/T between 20 and 40 m/s identify flexible buildings, between 40 and 70 those of normal stiffness, and 70, to a maximum of 150, the rigid ones. Figure 10 shows all 2262 build rigidities superimposed.
- (2) Maximum interstory drift: Shown in Fig. 11 is the frequency distribution of the 2622 buildings reviewed. From Figs. 10 and 11, Guendelman et al. [22] found that a large majority of concrete buildings in Chile are more rigid when compared to other similar buildings in other countries. Furthermore, the Chilean code imposes demanding interstory drift restrictions. Both of these items likely contributed to the successful performance of those facades reviewed after this event.

Response Modification Factor

The NCh433 code defines values for the response modification factor, R^* . This factor is intended to reflect the energy absorption and dissipation characteristics of the resisting structure, as well as the practical experience on the seismic behavior of the different types of structures and materials used. The response modification factors are shown in Fig. 12.

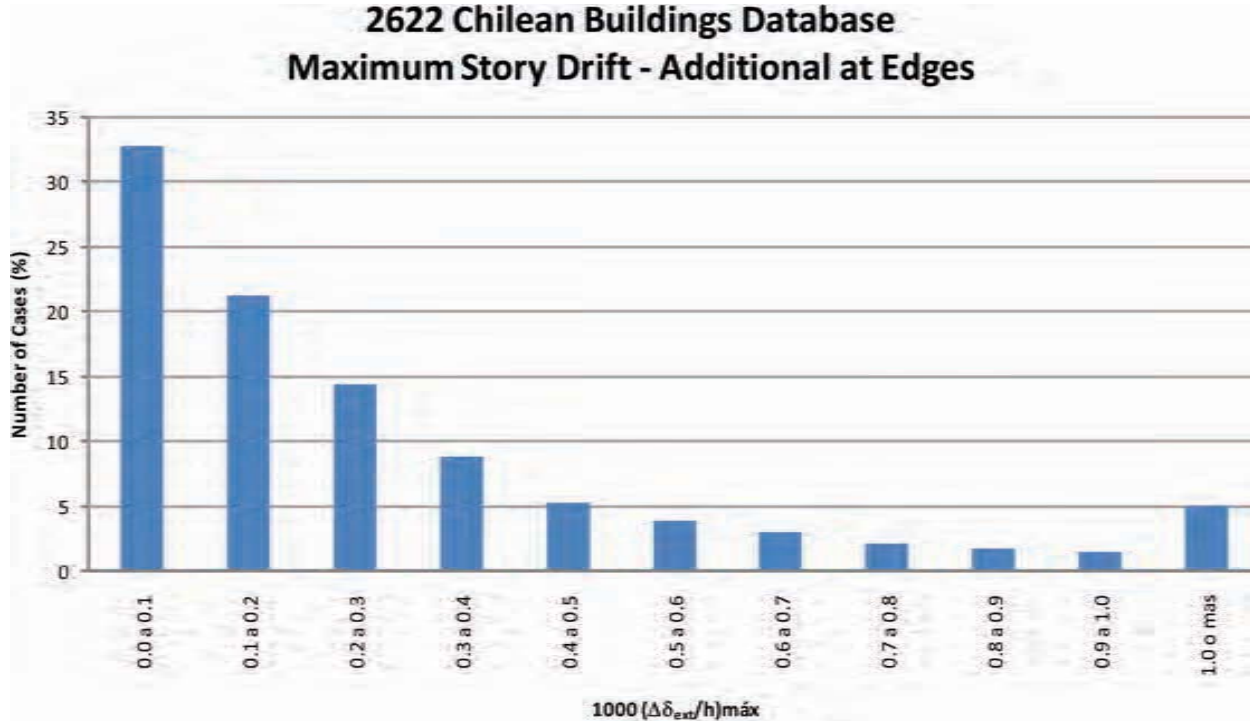


FIG. 11—Frequency distribution determined in 2622 buildings in Chile [22].

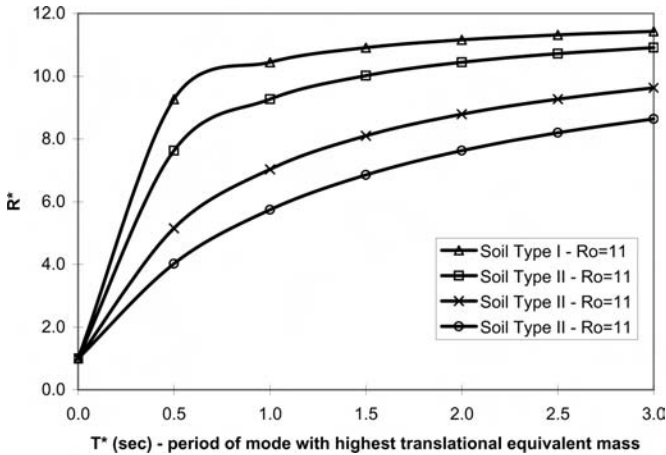


FIG. 12—(R^*) Response spectra modification factor [21].

Limitations on Base Shear Stress

NCh433 indicates the total shear that the building structure must accommodate at its base. In no case shall this base shear be less than $A_0IP/6g$, where I is the “importance” factor of the building; and P is the total weight of the building above the base level. Furthermore, the code states that if the calculated base shear stress is less than the above minimum, then interstory displacements must be multiplied by a factor so that the shear stress meets the stated value.

Structural and Seismic Review

Starting in 2003, the national building authorities require that building projects must be independently peer reviewed, from a structural perspective. Before construction can commence, the project drawings (architectural and structural) and specifications must be submitted for approval to the building department of the municipality where the site is located. Failure to comply with this requirement can result in sanctions imposed by the judiciary system.

These code provisions and seismic design requirements have proven beneficial to the built environment in Chile, and Rojas et al. [23] state: “The relatively good reported performance of modern structures in Chile can be attributed to the building codes and standards adopted by the country and the level of expertise of the design professionals.” Several buildings with favorable post-quake performance are described in Table 4.

Case Study of Interstory Drift on a Typical Building in Chile

Isidora Foster Building (Fig. 13)

Project overview: slender floor plan, 25 floors above grade, eight floors under grade, total height: 80 m (262 ft) above grade. Completed in 2004, location: El Golf area, Las Condes, Santiago.

TABLE 4—List of buildings reviewed post-quake that performed favorably.

Project name, location, and date	Height and width of frames	Glass configuration	CW type and silicone	Silicone beads	Anchoring system	Damage report during quake
Torre Parque Arauco location: Las Condes, Santiago two buildings, each with 22 floors above grade, completed 2009	Frame sizes: 600 × 3240 mm, 1200 × 3240 mm, 1800 × 3240 mm, total height 60 m above grade, setting blocks	IG units on vision and spandrel areas, clear annealed 6 mm/air space, 12 mm/clear annealed 6 mm	Unitized four-side SSG with pre-bonded subframe profile, structural silicone: two-part high modulus, ETAG use category 2	Structural bead 13.5 × 6 mm, weather-seal 18 × 6 mm	Anchored through splice connection fixed to the mullion male, 3 mm of horizontal expansion of male/female mullions and 12 mm vertical clearance for thermal expansion	Was reported to have suffered no damage during the earthquake
Nueva Las Condes (NLC 6&8) location: Las Condes, Santiago two buildings, each with 21 floors above grade, completed 2010	Frame size 1380 × 3300 mm, setting blocks at bottom	Vision and spandrel areas IG unit makeup: 6 mm/12 mm, AS/6 mm	Unitized four-side SSG, structural silicone: two-part high modulus, ETAG use category 2	Structural bead 13.5 × 6 mm, weather-seal 21 × 6 mm	Anchored through splice connection fixed to the mullion male, with 3 mm of horizontal expansion of male/female mullions, hanging from slab above	Was reported to have suffered no damage during the earthquake

TABLE 4—Continued

Project name, location, and date	Height and width of frames	Glass configuration	CW type and silicone	Silicone beads	Anchoring system	Damage report during quake
Valle Alegre Building location: Las Condes, Santiago two buildings, each with 11 floors above grade, completed 2010	Frame size 1300 × 3200 mm, Total height 37.8 m, setting blocks at bottom	Vision and spandrel areas IG unit makeup: 6 mm/12 mm, AS/6 mm with a horizontal aluminum decorative cap	Unitized four-side SSG with pre-bonded subframe profile, structural silicone: two-part high modulus, ETAG use category 2	Structural bead 13.5 × 6 mm, weather-seal 21 × 6 mm	Anchored through splice connection fixed to the mullion male, with 3 mm of horizontal expansion of male/female mullions and 12 mm vertical clearance for thermal expansion	Was reported to have suffered no damage during the earthquake
Clinica Indisa Building location: Providencia, Santiago one building with nine floors above grade, completed 2009	Frame size 1650 × 3100 mm with vision and spandrel areas, setting blocks at bottom	Vision area (2250 mm) IG unit makeup: 6 mm/12 mm, AS/5 mm spandrel area (850 mm), tempered monolithic of 6 mm	Unitized four-side SSG with exterior vertical reinforcing profile, structural silicone: two-part high modulus, ETAG use category 2	Structural bead 12 × 6 mm, weather-seal 15 × 6 mm	Anchored through splice connection fixed to the mullion male, hanging from slab above, 3 mm of horizontal expansion of male/female mullions	Was reported to have suffered no damage during the earthquake

TABLE 4—Continued

Project name, location, and date	Height and width of frames	Glass configuration	CW type and silicone	Silicone beads	Anchoring system	Damage report during quake
Clinica Santa María building location: Providencia, Santiago one building with nine floors above grade, completed 2008	Frame size 2000 × 3500 mm, with vision and spandrel areas, setting blocks at bottom	Vision area (1500 mm): IG unit makeup: 6 mm/12 mm, AS/6 mm, spandrel area (1000 mm): tempered monolithic of 6 mm	Unitized four-side SSG with pre-bonded subframe profile, structural silicone: two-part high modulus, ETAG use category 2	Structural bead 12 × 6 mm, weather-seal 15 × 6 mm	Anchored through splice connection fixed to the mullion male, hanging from slab above, 3 mm of horizontal expansion of male/female mullions	Was reported to have suffered no damage during the earthquake
Isidora Foster building location: Las Condes, Santiago one building with 25 floors above grade, completed 2007	Frame size 1600 × 3000 mm with vision and spandrel areas, setting blocks at bottom	Vision area: IG unit makeup 6 mm/12 mm, AS/6 mm, spandrel area: ACM panel	Unitized four-side SSG with horizontal profile (window wall between slabs, 20 mm of clearance), structural silicone: two-part high modulus	Structural bead 16.5 × 6 mm, weather-seal 20 × 6 mm, horiz. 15 × 6 mm vert.	Anchored using expansion bolts in the slabs	Was reported to have suffered no damage during the earthquake

TABLE 4—Continued

Project name, location, and date	Height and width of frames	Glass configuration	CW type and silicone	Silicone beads	Anchoring system	Damage report during quake
Isidora Magdalena building location: Las Condes, Santiago one building with 25 floors above grade, completed 2008	Frame size 1400 × 3000 mm with vision and spandrel areas, setting blocks at bottom	Vision area: IG unit makeup 6 mm/12 mm, AS/6 mm, spandrel area: ACM panel	Unitized two-side SSG with horizontal profile (window wall between slabs, 20 mm of clearance), structural silicone: two-part high modulus	Structural bead 16.5 × 6 mm, weather-seal 20 × 6 mm, horiz. 15 × 6 mm vert.	Anchored using expansion bolts in the slabs	Was reported to have suffered no damage during the earthquake
Magdalena con Riesco building location: Las Condes, Santiago one building with 25 floors above grade, completed 2009	Frame size 1200 × 3300 mm, setting blocks at bottom	Vision and spandrel areas, IG unit makeup: 6 mm/12 mm, AS/6 mm	Unitized four-side SSG with pre-bonded subframe profile, structural silicone: two-part high modulus	Structural bead 16.5 × 6 mm, weather-seal 20 × 6 mm, horiz. 15 × 6 mm vert.	Anchored through splice connection fixed to the mullion male, hanging from slab above with 3 mm of horizontal expansion of male/female mullions	Was reported to have suffered no damage during the earthquake

TABLE 4—Continued

Project name, location, and date	Height and width of frames	Glass configuration	CW type and silicone	Silicone beads	Anchoring system	Damage report during quake
Las Torcazas con Apoquindo building location: Las Condes, Santiago one building with 18 floors above grade, completed 2008	Frame size 1300 × 3200 mm, setting blocks at bottom	Vision and spandrel areas, IG unit makeup: 6 mm/12 mm, AS/6 mm, additional 250 mm glass to cover slab edge	Unitized four-side SSG with pre-bonded subframe profile, structural silicone: two-part high modulus, ETAG use category 2	Structural bead 16.5 × 6 mm, weather-seal 20 × 6 mm, horiz. 15 × 6 mm vert.	Mullion anchored with bracket to anchoring plate, hanging from slab above with 3 mm of horizontal expansion of male/female mullions, and 15 mm vertical clearance for thermal expansion	Was reported to have suffered no damage during the earthquake
Clinica BiCentenario building location: Las Rejas con Alameda, Santiago one building with 21 floors above grade	Frame size 1250 × 3500 mm, setting blocks at bottom	Vision area (3160 mm): IG unit makeup: 6 mm/12 mm, AS/6 mm, spandrel area (340 mm): 6 mm tempered monolithic	Unitized four-side SSG with pre-bonded subframe profile, structural silicone: two-part high modulus, ETAG use category 2	Structural bead 12 × 6 mm		Was reported to have suffered no damage during the earthquake (only 10 stories of curtain wall had been installed at the time of the earthquake)

TABLE 4—Continued

Project name, location, and date	Height and width of frames	Glass configuration	CW type and silicone	Silicone beads	Anchoring system	Damage report during quake
Diario del Sur building location: Concepción one building with three floors above grade, completed 2000	Facade modulation of 1000 mm, setting blocks at bottom	Vision and spandrel areas: AN monolithic 6 mm	Stick two-side SSG with horizontal fixation using a cap decorative profile, structural silicone: one-part	Structural bead 12 × 6 mm, weather-seal 14 × 6 mm, horiz. 15 × 6 mm vert.	Anchored through splice connection fixed to the mullion male, hanging from slab above with 3 mm of horizontal expansion of male/female mullions	Was reported to have suffered no damage during the earthquake
Reitz Building location: Viña del Mar one building with 13 floors above grade, completed 2009	Frame size 1420 × 3500 mm with vision and spandrel areas, setting blocks at bottom, total height: 45.5 m	Vision area (2250 mm): IG unit makeup: 6 mm/12 mm, AS/6 mm, spandrel area (850 mm): tempered monolithic of 6 mm	Unitized two-side SSG with horizontal profile (window wall between slabs, 20 mm of clearance), structural silicone: two-part high modulus, ETAG use category 2	Structural bead 16.5 × 6 mm, weather-seal 20 × 6 mm horiz. 15 × 6 mm vert.	Anchored through splice connection fixed to the mullion male, hanging from slab above, 3 mm of horizontal expansion of male/female mullions	Was reported to have suffered breakage of about 15 lites of glass. The glass was without polished edges

TABLE 4—Continued

Project name, location, and date	Height and width of frames	Glass configuration	CW type and silicone	Silicone beads	Anchoring system	Damage report during quake
CCU building location: Providencia, Santiago one building with 22 floors above grade, completed 2006	Frame size 1300 × 3200 mm, setting blocks at bottom	Vision and spandrel areas, IG unit make-up: 6 mm/12 mm, AS/6 mm with horizontal aluminum decorative cap	Unitized four-side SSG with pre-bonded subframe profile, structural silicone: two-part high modulus	Structural bead 12 × 6 mm, weather-seal 15 × 6 mm	Anchored through splice connection fixed to the mullion male	Was reported to have suffered no damage during the earthquake
Titanium Tower location: Las Condes, Santiago one building with 52 floors above grade, completed 2009	Frame size 1600 × 3650 mm, setting blocks at bottom, total height 192 m above grade	Vision and spandrel areas, IG unit make-up of 34 mm total thickness	Unitized four-side SSG with pre-bonded subframe profile, structural silicone: two-part high modulus	Structural bead 21 × 6 mm, weather-seal 14 × 6 mm	Anchored through splice connection fixed to the mullion male, hanging from above slab, anchoring system allows 25 mm movement on both sides and also horizontal male/female movement	Was reported to have suffered no damage during the earthquake. At that time, the tallest building in Chile with dampening devices to reduce 40 % drift

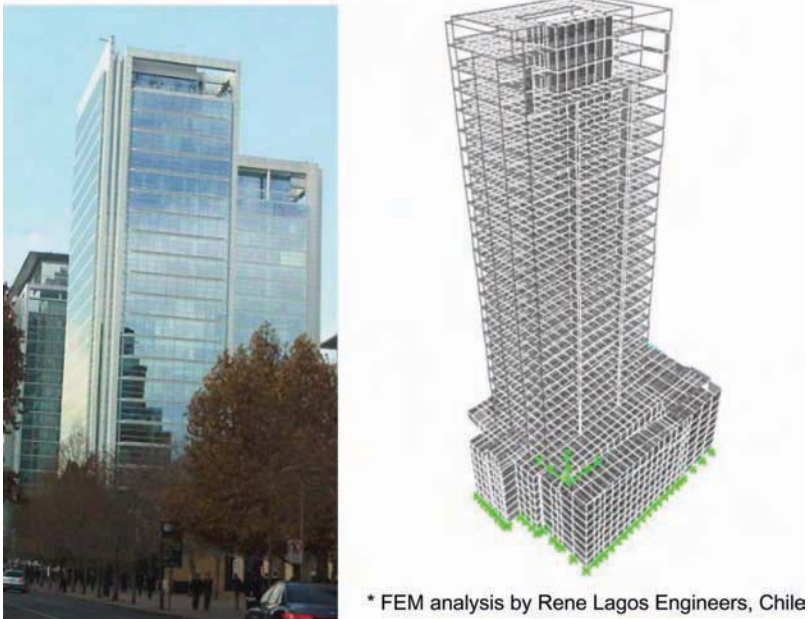


FIG. 13—*Isidora foster building.*

Description of curtain wall system:

- CW type: four-sided SSG system; window wall type, anchored between slab with about 20 mm clearance,
- CW area: 7000 m² (75,000 ft²),
- Interstory height: 3200 mm (10.5 ft), glass width: 1300 mm (4.3 ft),
- Glass type: IG units of AN 6 mm/12 mm, AS/AN 4 mm (vision and spandrel),
- Was reported to have suffered no damage during the earthquake.

Seismic conditions and characteristics of the building:

- Seismic zone no. 2: effective acceleration value $A_0 = 0.3$ g,
- Soil type II, $R_o = 11$,
- Fundamental period of the building, $T = 2.5$ s (courtesy René Lagos Engineers, Santiago),
- Response modification factor (R^*) = 10.6 (from Fig. 12, with $T = 2.5$ s and above soil and seismic zone conditions). However, to satisfy the base shear stress requirements mentioned previously, the calculated drift must be multiplied by R^* and divided by 3.0 to arrive at the actual estimated drift. Therefore, the final R^* value to use is $10.6/3 = 3.53$.

Lateral displacement calculation (worst case):

- Assuming the total interstory drift allowed by the NCh433 code = 3 ‰ (which is the sum of lateral displacement of 2 ‰ and torsional effect of 1 ‰),

- The calculated allowable interstory drift is then = 3 ‰ of 3200 mm = 9.6 mm (0.38 in.),
- And the actual interstory drift will be $9.6 \text{ mm} \times 3.53 = 33.9 \text{ mm}$ (1.33 in.),
- Considering that the four-sided SSG glass will rotate about its center of mass, we can calculate that the shear displacement at the location of highest strain (corner) is = 16.9 mm.

Lateral displacement calculation (from dynamic spectral analysis; courtesy René Lagos Engineers, Santiago):

- Calculated interstory drift ratio (drift/height) = 0.00081 (by FEM software),
- NCh433 calculated interstory drift = $0.00081 \times 3200 \text{ mm} = 2.6 \text{ mm}$ (with reduced seismic response spectra),
- Therefore, the actual interstory drift is $2.6 \text{ mm} \times 3.53 = 9.2 \text{ mm}$ (0.36 in.)

Summary Relative to Isidora Foster Building

The maximum allowable interstory drift according to NCh433 would be 33.9 mm (1.33 in.). If we compare the actual estimated drift value for this building (9.2 mm) with the maximum allowable (33.8 mm), we find significant reserve capacity.

Special Case Studies

MTS Building, Santiago (Fig. 14)

- Project overview: Completed in 2005, the building is situated in the Americo, Vespucio area and is a concrete and, steel framed structure with three floors. This building experienced a large, vertical displacement that induced structural and non-structural damages, including the SSG curtain wall. The building is situated in a zone with a special soil type that may have contributed to the high structural displacements.
- Performance during the earthquake: was reported to have suffered significant damages in ceiling, partition walls, and curtain wall during the earthquake. Damage included a strong upward thrust buckling vertical mullions and breaking glass. In Fig. 14, one can see glass retained by the structural silicone post-breakage.

IBM Building, Santiago (Fig. 15)

- Located in Providencia, this building is a two-sided vertical SSG “stick” system fabricated, by Cupples in 1982 (Fig. 15). There are eight stories with metal panels at the spandrel areas giving it a “strip” window look. This building is the first SSG design in the city and suffered no reported damage during the earthquake.



FIG. 14—*MTS building, retained glass.*



FIG. 15—*IBM building, 30 years old.*

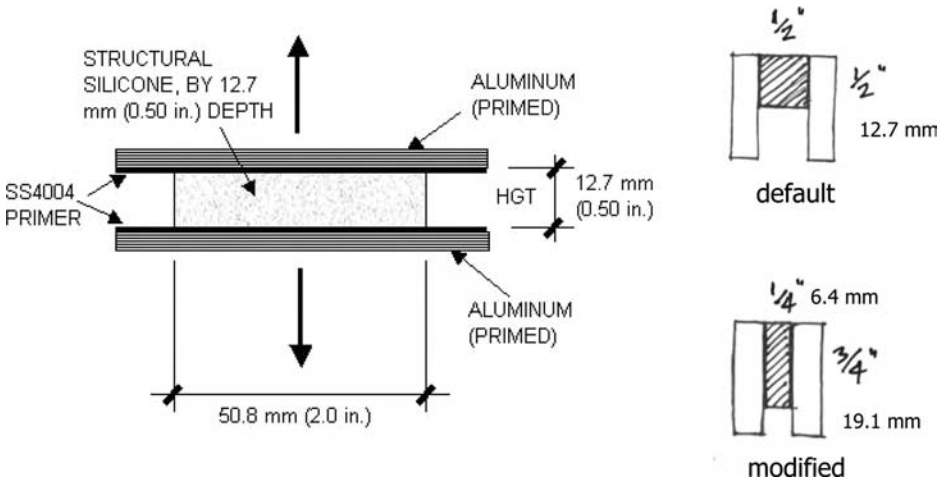


FIG. 16—ASTM C1135 tensile adhesion specimen; default and modified configuration.

Summary and Observations

- (1) The seismic performance of an SSG curtain wall alone cannot be treated as an isolated system as its performance depends upon its interaction with the super structure and the super structure’s response to an event. From this standpoint, the behaviour of many SSG systems in the vicinity of the event (2010 mega-earthquake) performed favorably with little or no damage. This is a result of the inherent flexibility of the split-mullion modern SSG curtain wall systems coupled with the

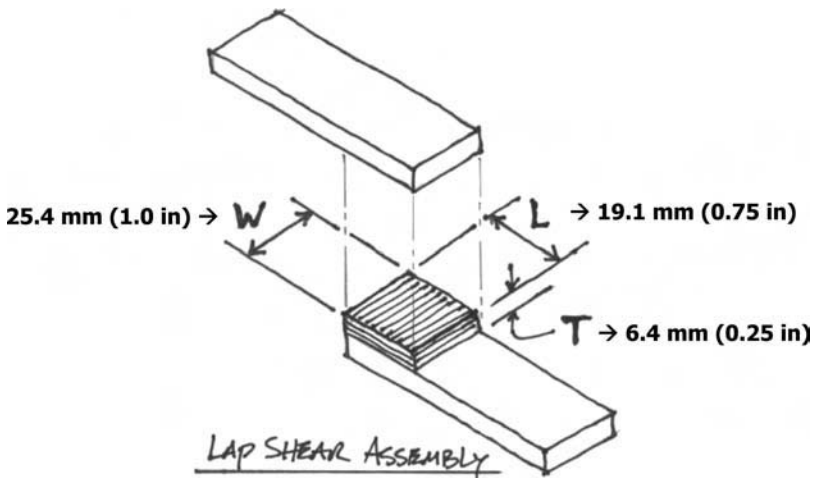


FIG. 17—ASTM C961 Lap shear specimen configuration (modified).

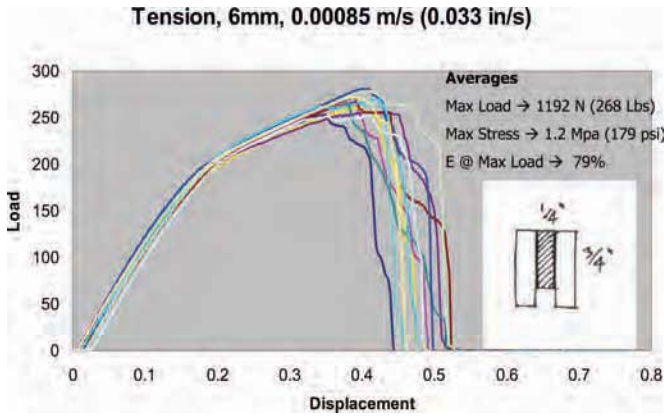


FIG. 18—Load displacement curves: standardized strain rate.

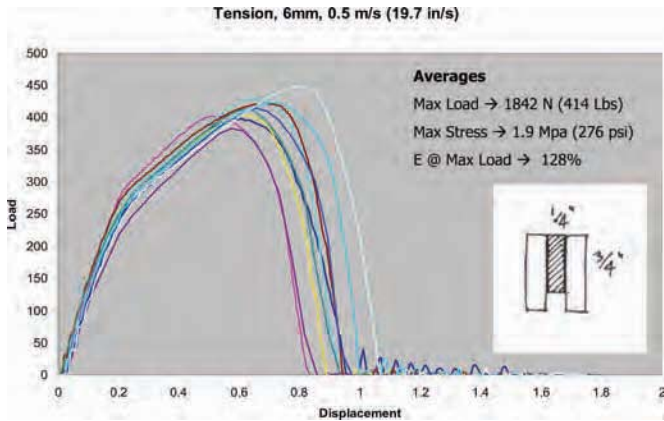


FIG. 19—Load displacement curves: high strain rate.

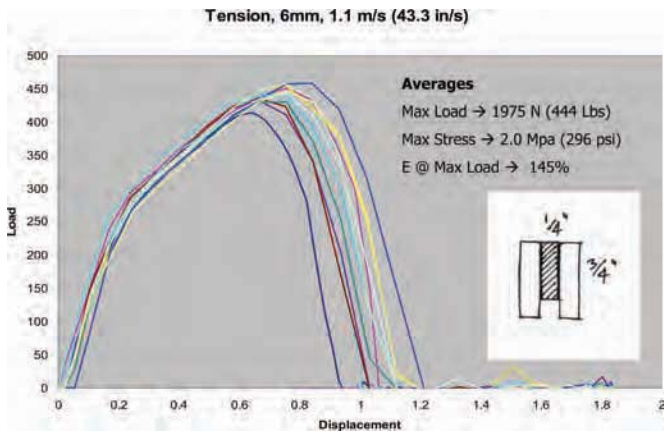


FIG. 20—Load displacement curves: highest strain rate.

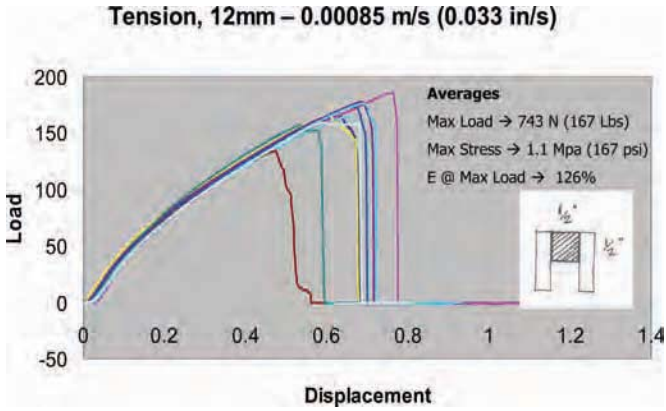


FIG. 21—Load displacement curves: standardized strain rate.

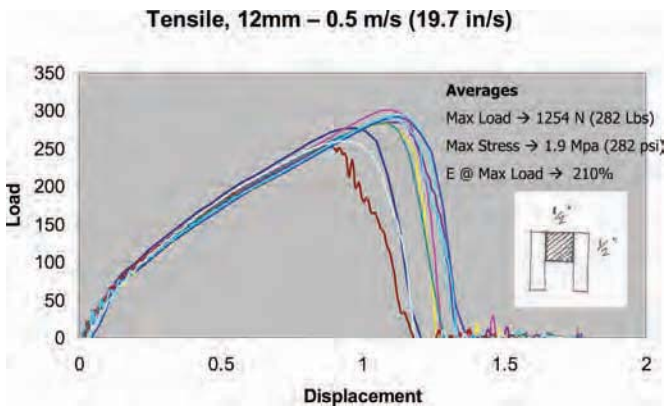


FIG. 22—Load displacement curves: high strain rate.

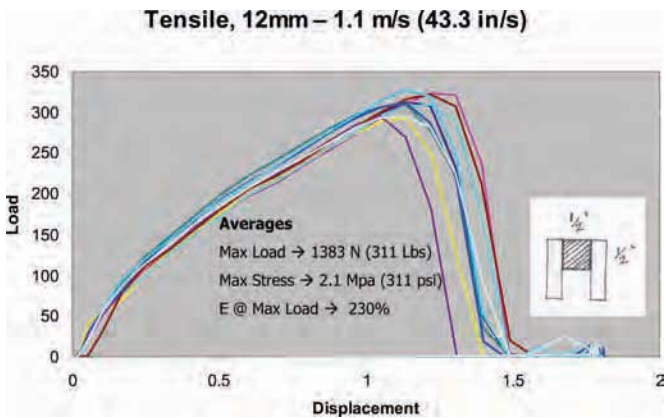


FIG. 23—Load displacement curves: highest strain rate.

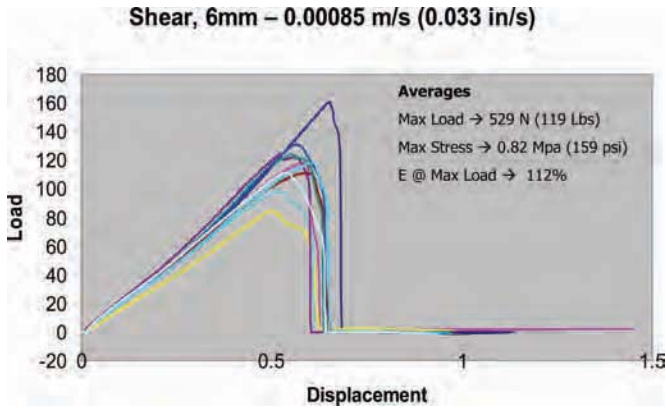


FIG. 24—Load displacement curves: standardized strain rate.

restrictions and requirements imposed on building structures in the national seismic code.

- (2) Of the buildings reviewed in this paper, both “stick” and “unitized” type and both two-side and four-side SSG systems performed favorably, including most of these without any reported damage, with one approaching 30 years of age.
- (3) All of the SSG projects reviewed in this paper that performed favorably utilized the 6.4 mm (0.25 in.) minimum thickness of the structural seal recommended by the ASTM C1401 industry guide. In SSG systems where there is no contribution from split mullions and sliding anchors,

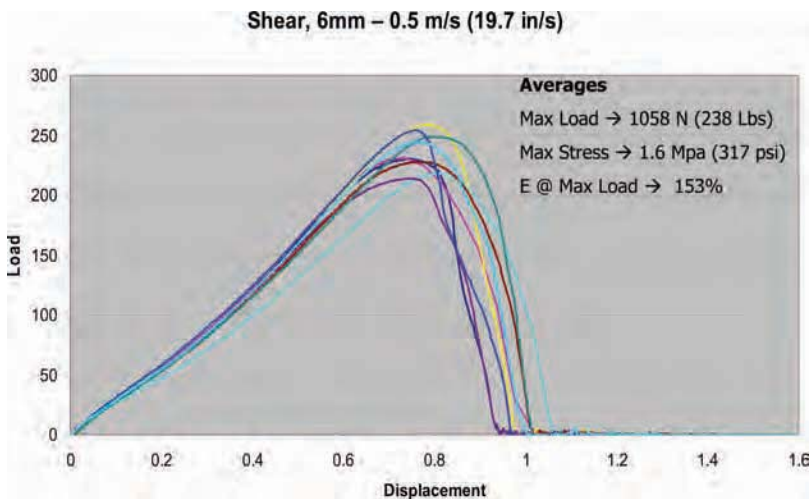


FIG. 25—Load displacement curves: high strain rate.

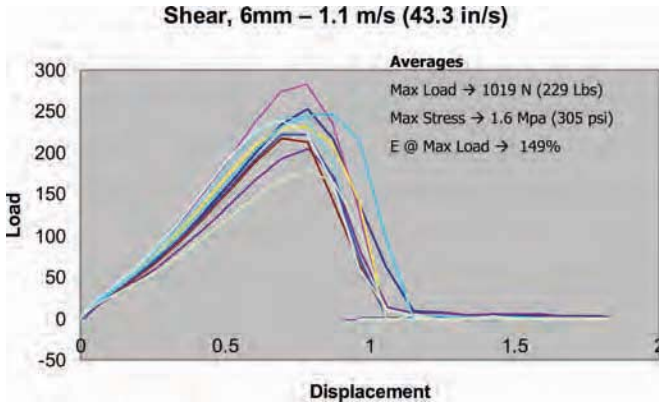


FIG. 26—Load displacement curves: highest strain rate.

the thickness of the sealant becomes more important in its ability to absorb lateral displacements from interstory drifts.

- (4) Shear stresses imposed into the structural silicone will vary according to the specific product utilized (high modulus versus medium modulus, etc.) but also according to the strain rate that the sealant is subjected to. Thus, SSG designers ought to carefully select the material for use in designs in seismic regions.
- (5) The majority of the buildings reviewed in this paper were designed and fabricated utilizing two-part high modulus shop applied structural silicone by three experienced companies in conjunction with proper technical support and overview. It is believed that the experience provided by these fabricators contributed to the success of the SSG systems reviewed.

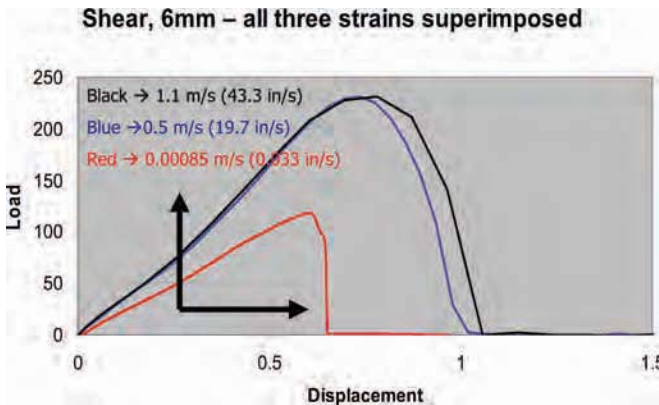


FIG. 27—Load displacement curves, all three strain rates superimposed.

- (6) The high rigidity and low interstory drifts of buildings imposed by the seismic code NCh433 contributes to reduced actual shear strains into structural seals when compared to building codes of outer countries.
- (7) Site review of a damaged SSG curtain wall (MTS Building) showed glass fragments retained by the silicone. This supports the ASTM notion that the structural seal and weatherseal can contribute to retaining broken glass during the event, minimizing fallout hazard to pedestrians (Fig. 14).

Acknowledgments

The writers thank the following contributors for their important input in this research: Tomás Guendelman, partner of IEC Ingenieros Ltda, Santiago, Chile, Rodolfo Saragoni, partner of SyS Ingeniería Ltda, Santiago, Chile, René Lagos, principal of René Lagos Ingenieros, Santiago, Chile, and KBE Curtain Wall Manufacturer, Santiago, Chile.

References

- [1] General Electric Company, Waterford, NY, U.S. Patent No. 4,092,812 (Aug 5, 1976).
- [2] Kawneer Company Inc., Norcross, GA, U.S. Patent No. 4,650,702 (Oct 15, 1985).
- [3] L. S. Skarpness, Glenwood, MN, U.S. Patent No. 6,581,354 (June 25, 1999).
- [4] ASTM C1401, 2009, "Standard Guide for Structural Sealant Glazing," *Annual Book of ASTM Standards*, ASTM International, West Conshohocken, PA.
- [5] Memari, A. M., Chen, X., Kremer, P. A., and Behr, R. A., "Seismic Performance of Two-Side Structural Silicone Glazing Systems," *J. ASTM Int.*, Vol. 3, No. 10, Paper ID JAI100407.
- [6] Memari, A. M., Chen, X., Kremer, P. A., and Behr, R. A., "Seismic Performance of Structural Silicone Glazing Systems," *Proceeding of the Symposium on Durability of Building and Construction Sealants and Adhesives*, Reno, NV, June 15–16, 2005.
- [7] Memari, A. M., Kremer, P. A., and Behr, R. A., "Seismic Performance of Stick-Built Four-Side Structural Sealant Glazing System and Comparison with Two-Side Structural Sealant Glazing and Dry-Glazed Systems," *J. ASTM Int.* (in press).
- [8] Zarghamee, M. S., Schwartz, T. A., and Gladstone, M., "Seismic Behavior of Structural Silicone Glazing," *Science and Technology of Building Seals, Sealants, Glazing, and Waterproofing*, Vol. 6, J. C. Myers, Ed., ASTM International, West Conshohocken, PA, 1996.
- [9] Memari, A. M., Kremer, P. A., and Behr, R. A., "Architectural Glass Panels with Rounded Corners to Mitigate Earthquake Damage," *Earthquake Spectra*, Vol. 22, 2006, pp. 129–150.
- [10] ASTM C1135, 2011, "Standard Test Method for Determining Tensile Adhesion Properties of Structural Sealants," *Annual Book of ASTM Standards*, Vol. 04.07, ASTM International, West Conshohocken, PA.
- [11] ASTM C1564, 2009, "Standard Guide for Use of Silicone Sealants for Protective Glazing Systems," *Annual Book of ASTM Standards*, Vol. 04.07, ASTM International, West Conshohocken, PA.
- [12] Klowsowski, J. M. and Wong, A., "Shear Component of a Structural Sealant Glazing Joint," *Science and Technology of Building Sealants, Glazing and Waterproofing*, ASTM International, West Conshohocken, PA.

- [13] Karpati, K. K., "Mechanical Properties of Sealants: II. Behavior of a Silicone Sealant as a Function of Rate of Movement," *J. Paint Technol.*, Vol. 44, No. 569, 1972, pp. 58–66.
- [14] Yarosh, K., Wolf, A., and Sitte, S. A., "Evaluation of Silicone Sealants at High Movement Rates Relevant to Bomb Mitigating Window and Curtainwall Design," *J. ASTM Int.*, Vol. 6, No. 2, 2009, Paper ID: JAI101953.
- [15] ASTM C961, 2011, "Standard Test Method for Lap Shear Strength of Sealants," *Annual Book of ASTM Standards*, Vol. 04.07, ASTM International, West Conshohocken, PA.
- [16] Guideline for European Technical Approval for Structural Sealant Glazing Kits (ETAG 002). Part 1: Supported and Unsupported Systems, http://www.ue.itb.pl/files/ue/etag/etag_002.pdf. (Last accessed May 8, 2012).
- [17] ASTM C719, 2010, "Standard Test Method for Adhesion and Cohesion of Elastomeric Joint Sealants under Cyclic Movement (Hockman Cycle)," *Annual Book of ASTM Standards*, Vol. 04.07, ASTM International, West Conshohocken, PA.
- [18] Wikipedia, http://en.wikipedia.org/wiki/Megathrust_earthquake (Last accessed May 8, 2012).
- [19] Saragoni, G. R., Lew, M., Naeim, F., Carpenter, L. D., Youssef, N. F., Rojas, F., and Schachter Adaros, M., "Accelerographic Measurements of the 27 Feb 2010 Offshore Maule, Chile Earthquake," *Struct. Des. Tall Spec. Build.*, Vol. 19, 2010, pp. 866–875.
- [20] Boroschek, R., Soto, P., and Leon, R., "Maule Region Earthquake, Feb 27, 2010," *Renadic Report Revision 2*, Faculty of Mathematics and Science, Civil Engineering Department, University of Chile, Oct 10, 2010.
- [21] NCh433.Of96, Instituto Nacional de Normalización, Earthquake Resistant Design of Buildings, Official Chilean Code, 1996.
- [22] Guendelman, B. T., Guendelman, B. M., and Lindenberg, B. J., 1997, "Perfil Bio-Sismico de Edificios," *VII Jornadas Chilenas de Sismología e Ingeniería Antisísmica y Primer Congreso Iberoamericano de Ingeniería Sísmica*, La Serena, Chile.
- [23] Rojas, F., Lew, M., and Naeim, F., "An Overview of Building Codes and Standards in Chile at the Time of the 27 Feb 2010 Offshore Maule, Chile Earthquake," *Wiley Online Library*, doi: 10.1002/tal. 676.

Andreas T. Wolf (Editor)

A Panel Discussion: ASTM Introduces C1736 Standard Practice for Non-Destructive Evaluation of Adhesion of Installed Weatherproofing Sealant Joints Using a Rolling Device

ABSTRACT: The panel discussion was originally conceived as a discussion on sealant warranty issues, but became a spirited conversation regarding the impact of the newly developed ASTM C1736 Standard Practice with participation by the panelists, ASTM C24 members, as well as presenters and guests of the international symposium. The panel consisted of three members of ASTM C24 committee, who had direct involvement with the creation, oversight, and/or passage of C1736, plus one panelist representing a sealant applicator. In order to provide context to the discussion, the editor has provided a short introduction to the topic.

Introduction

Considerable work has focused in the past on the deterioration of building joint sealants (see, for instance, information provided in the RILEM State-of-the-Art Report [1]), while less emphasis has been placed on understanding the consequences of seal failure, particularly in respect to water-tightness. Deficiencies in the water-tightness of weather seals in building envelopes may indeed be induced by the effect of weathering on sealants, as the climatic factors may cause the sealant to deteriorate by hardening, softening (reversion), cracking, or losing adhesion to the substrate. However, deficiencies that affect the water-tightness of weather seals may also come about from design faults or improper installation. Water penetrating into the joint and into the building envelope via these deficiencies may lead to deterioration of the building fabric or premature failure of the joint sealant or of other envelope components.

By the early 2000s, a practical means of assessing adequate sealant performance in the field in terms of the quality of the sealant-to-substrate bonding following initial installation as well as during inspections carried out over the life of the sealed joint had become of considerable interest in the construction community. Since 2003, ASTM has sponsored this “Durability of Building and Construction Sealants and Adhesives (DBCSEA)” Symposium Series. The need

for a field practice to facilitate the inspection of sealed joints such that the continuity of the seals can readily be determined was highlighted by various presentations during this symposium series. Work presented by Lacasse, Miyauchi, and Hiemstra at the 2008 symposium demonstrated that substantial amounts of water, i.e., up to several liters per minute, can be penetrate through very small interfacial “cracks” along the bond line of the sealed joint with the crack lengths ranging between 2 mm and 16 mm [2]. Not surprisingly, water readily enters open cracks along the sealant-to-substrate interface when the joint is extended; however, the study also demonstrated that water from wind-driven rain may penetrate through cracks of non-extended (apparently “closed”) joints. Loss of sealant adhesion in non-extended joints (and, even more so, in compressed joints) may not be detectable by simple visual inspection.

The most commonly used industry protocol to check joint sealant adhesion has been the destructive “pull test” procedure as described in ASTM Standard Practice C1521-09e1 for Evaluating Adhesion of Installed Weatherproofing Sealant Joints [3]. This method allows checking the adhesion of the sealant at discrete locations along the joints; however, it is not suited for the evaluation of the continuity of the seal.

In the 2003 Symposium of the DBCSA series, a method of in-field testing of sealed joints using a rolling device was presented [4]. Every symposium in the series thereafter has had one or more presentations on the topic of continuity of joint seals in terms of suitable inspection methods as well as consequences of failure. Putting words to action, in 2001, ASTM C24 Committee on Building Seals and Sealants began to look seriously at the rolling device methodology for consideration as a standard practice. Starting in 2008, work item WK21464 “Standard Practice for Non-Destructive Evaluation of Adhesion of Installed Weatherproofing Sealant Joints Using a Rolling Device” came under development by ASTM C24.30. By the time the 4th DBCSA Symposium began on June 16th, 2011, the committee had granted final approval for WK21464 just the day before, on June 15th, and subsequently gave it the designation ASTM C1736. ASTM C1736-11 Standard Practice for Non-Destructive Evaluation of Adhesion of Installed Weatherproofing Sealant Joints Using a Rolling Device has recently been published [5].

The ASTM C1736 Standard Practice describes a non-destructive evaluation procedure which induces a depression in the joint seal via a rolling device. Subjecting the sealant bead to a strain by moving the rolling device continuously over the sealed joint causes a stress on the bonding at the sealant-to-substrate interface that moves along the bond line. Controlling the amount of stress induced along the bond line allows an assessment of the quality of the adhesive bond of a joint seal in a particular installation. This practice, therefore, can be used to verify the continuity of building seals and its primary purpose is to reveal sealant adhesion anomalies that may affect air or water infiltration resistance or both of the sealed joint. It is expected that this practice will be used for quality control, forensic investigations, and repair programs. Users may include sealant manufacturers, consulting engineers and architects, test agencies, and construction contractors.

This paper is a summary of a panel discussion, originally conceived as a discussion on sealant warranty issues, but which evolved into a spirited conversation regarding the passage of C1736. The thematic thread that developed during

the discussion was what impact will this standard have on the industry, in the context of historical and current industry standard practice?

The following is a summary of that discussion, with C24 members, guests, and audience participation represented generically. The panel consisted of three members of ASTM C24 committee, who had direct involvement with the creation, oversight, and/or passage of C1736, plus one panelist representing a sealant applicator. One audience member represented a Consultant in the content and total amount of comment that was offered. For clarity, additional contributory comments and questions from audience members have been woven into the responses made by the panelists. Note that names, personal comments and issues, and all otherwise off subject material have been removed.

Panel Discussion

Development of C1736

C24 Representative #1—In the mid 1990's, ASTM committee C24 decided that the industry needed a Standardized Practice to evaluate adhesion of installed weatherproofing sealants. Such a practice would have applications in new construction for quality control, existing construction for service life evaluations, and in-field “forensic” determinations of air and water infiltration sources. The result of this effort was C1521, first published in 2002 [3].

C1521 contains both destructive and non-destructive methods to evaluate sealant adhesion. The non-destructive method only looks at small areas of the sealant installation, providing a snap-shot of the total. The later added (2008 revision to C1521) ‘continuous procedure using rolling devices’ can be used to obtain a larger picture of the installation. However, the committee decided an additional stand-alone Standard Practice was also needed for the rolling device method. With the passage of C1736, we now have two standards for in-field evaluation of adhesion of installed weatherproofing sealants.

C24 Representative #2—The committee did a good job of writing this new standard; there were enough “controversial” points of view that a really good standard was produced. The wisdom of the ASTM process shines through in it, because if it was left up to a single individual, or a group of individuals with like thinking, it would not be as balanced as it is; it is balanced due to the diversity of thought reflected within it.

C24 Representative #3—I have come to appreciate the high level of due diligence that ASTM provides, with all of the relevant stakeholders participating in the development and review process. Sometimes we wish that the process could go a little faster, but the net result is very good standards. In addition, once a standard is published, it will be reviewed once every seven or eight years to reconcile it with changes in the industry, and if needed, the standard will be adjusted to reflect those changes.

General Implications of C1736 for the Industry

C24 Representative #2—Rolling devices are able to provide information that goes well beyond the joint appearance; sometimes joints look bad on the surface, but are good underneath, and vice versa. Joint geometry, twisted backer rod, and other anomalies can be discerned when using these devices; but, the intent of the standard is focused on adhesion. Due to the high elastic recoverability factor of many performance sealants, complete bond line failure can exist and one would never know it by looking. The intent behind the methodology of C1736 is to facilitate complete and durable building seals.

Applicator—I am skeptical regarding the ability of this test method to reveal the entire picture; there are many factors that go into a wall design, and therefore many different problems that can develop. It is my position that the best place to put extra effort is into applicator education and training – applicator certification ideally – to prevent sealant problems in the first place. I am also apprehensive regarding potential mischief that could be dredged up from such testing, costing everyone unnecessary time and money. Therefore, those using this test methodology (of C1736) should have good knowledge, expertise, and intent when using it so as to prevent misuse.

Consultant—I have been using the screen roller procedure for at least 15 years, and it is the number one tool I use because I want to know everything that is going on in that sealant joint. I place a piece of easily removable painters' type masking tape alongside the joint that I wish to analyze; I have the roller in one hand, and a felt tip pen in the other. As I roll along spot to spot in the bead, where it pushes in easily, I put a mark indicating that the sealant is very thin; when I come to a spot where the roller does not push in, I indicate on the tape that the spot is hard, heavy, or thick; when adhesion has failed, I indicate that on the tape as a line showing where the failure starts and stops. When I am finished with a specific area, I put a label on the masking tape and take a picture of it, for the record and for future analysis. This provides information that can identify systemic problems when specific issues are found to be repetitive, or share commonality. While the standard is written as a test for adhesion, much more information can be derived from its' use. A screen roller combined with a good marking and data archive system form my number one diagnostic method when conducting sealant forensic analysis. I can teach and have taught others how to use this methodology in less than an hour.

Implications of the Use of This Practice

C24 Representative #2—C1736 has two main procedures; Section 7.3 is most appropriate to in-depth analysis by an expert; Section 7.4 is more tuned to 100% evaluation for continuity of joint seal. In some cases, systemic issues are the most important thing to determine, served well by expert analysis of a discrete area. At other times it may be critical to achieve continuity of seal, meaning a 100% test and repair becomes the preferred usage of the standard. Both of these

procedures have a focused purpose, and the new standard reflects the flexibility needed in the industry.

Applicator—I have a concern that this methodology could be used inappropriately to create more problems that it can resolve. For example, what is to prevent a building owner from taking his 20-year sealant warranty, commissioning a 100% analysis on the 19th year of the warranty period, and then go back to the warranty issuer with a demand for a new sealant installation? For another example, there are 20-year sealant warranties that have been written for substrates that has a 1-year warranty. How are these types of potential mischief and conflict to be resolved?

C-24 Representative #2—‘What is best for the building is what is best for everyone connected to it, whether they realize it or not’. For example, two 40-foot [12.192 m] lengths of metal panel wall sections spontaneously fell from a building during a wind storm. This building was 30 years old, standing in the dry air of the Sonoran Desert in Phoenix Arizona, yet when investigated, what was found was rust rot throughout the building façade, caused by failed sealant joints leaking water for 30 years. The danger came from the fact that the seal leaks went unrecognized because the building did not leak to the inside where folks could observe it. So, for 30 years the rust rot did damage with the building owner completely unaware. We need to make sure that seal systems are truly sealed for the sake of the building first, in the interest of the public health and welfare, and then we can figure out how to pay for it. Whatever the cost, we know it will be less than the cost of a human life.

C-24 Representative #1—I agree with The Applicator that training and education for failure prevention should come first. It has been my experience that all too often the applicator/mechanic does not know why he is told to do a certain procedure. The Applicator may ignore or modify a procedure out of simple preference or ignorance, not simply as a time saving measure. I have found that when applicators fully understand the why of a certain procedure, they become very motivated to do it the right way. Why does the joint design need a certain profile; why is there a need for bond breaker tape to prevent three sided adhesion; why is primer needed on this substrate but not on that one; when Applicators understand the whys’, they are most times very willing to comply with the procedural mandates. Education of field personnel to a high professional level is problem prevention; however, the fact that the testing of C1736 now exists should encourage better installation practices through better training. The two can peacefully coexist and promote each other.

C24 Representative #2—We have to remember that this is a field practice, not a laboratory test. All we are trying to do is find out whether or not we have adhesion, in a sampling or as continuity of seal in a 100% evaluation. Quantification of the results is called out in the reporting section 8 of C1736 as a ratio of failure against the total amount tested. This is written into the standard as a

protection to everyone involved. For example, when properly reporting results per the standard, a hypothetical 0.5% failure rate may occur. That may mean there are enough seal breaches to warrant a full scale test and repair program, because it can mean a considerable number of potential air and water leaks in a seal grid of miles of field applied sealant; but on the other hand, it also means that the sealant was applied at and is performing at the rate of 99.5%. This is not a negative for the sealant producer or installer; it is simply the as-built degree of total continuous seal achieved within the limits of human capability. When the adhesive failures are identified, they can be repaired without replacing the entire installation. For years we have been relying on a single bead of sealant to perfectly seal buildings, when that is simply not possible in the real world of construction, unless there is an accompanying 100% test program. Now, with the methods of this new standard, we have a mechanism to test and repair those unavoidable adhesive failures, meaning we can now produce truly sealed buildings with a single sealant bead.

Applicator—I see a potential danger that a pre-existing prejudice will be label all of the problems found as “applicator error”, and the whole industry will become litigious, with applicators taking the brunt of the cost and blame. I hope that the adversarial aspects of the industry can change so that we can all work together to resolve these problems without unduly placing the financial burden on applicators, sealant producers, and insurance policies.

The Future of C1736 and the Industry

C24 Representative #2—What we are hoping to achieve with the new standard is provide a venue where we can all work together to make litigation disappear, repair our infrastructure, and provide us all with better building seals that can allow structures to last longer. There is plenty of blame to go around for our collected industry past, starting with designs that require an impossible level of installation perfection. What we are trying to achieve with the new standard is provide a platform to fix buildings and move forward into the future.

C-24 Representative #1—Too often the initial installation is focused on aesthetics over function. We need to make sure buildings don’t leak first, and deal with aesthetics second, although looks are also very important. Education of both designers and applicators combined with field testing can achieve both goals.

Applicator—Perhaps a maintenance programs that looks at an installations once every five years or so could become common practice. I think that would be good for owners, applicators, and the industry at large. Right now there are specifications for maintenance inspections written into construction documents, and ASTM guides such as C1193 [6] that make such recommendations, but they are not being implemented industry wide.

C24 Representative #3—Every sealant producer has to recognize that the rolling device evaluation will, from this moment forward in time, be used more and more. Producers and façade designers have a responsibility to inform the owners what these evaluations will mean in terms of repair or replacement. There are many sealant installations that are twenty or thirty years old, and there is a growing number of ordinances mandating periodic façade inspections. New and improved standards can combine with mandates and expectations to propel the industry forward into the new century. If we combine our efforts as an industry, we can bring building seals into an unprecedented age of function and durability we once only dreamed about.

References

- [1] Wolf, A. T. (Ed.), *Durability of Building Sealants*, RILEM Report 21, RILEM Publications, Bagnex, France, 1999.
- [2] Lacasse, M. A., Miyauchi, H., and Hiemstra, J., “Water Penetration of Cladding Components – A comparison of Laboratory Tests on Simulated Sealed Vertical and Horizontal Joints of Wall Cladding”, in: *Durability of Building and Construction Sealants and Adhesives*, 3rd Volume, STP 1514, A. T. Wolf, Ed., ASTM International, West Conshohocken, PA, 2010, pp. 359–390.
- [3] ASTM Standard C1521-09e1, 2009, “Standard Practice for Evaluating Adhesion of Installed Weatherproofing Sealant Joints”, Annual Book of ASTM Standards, ASTM International, West Conshohocken, PA.
- [4] D. Huff, “Nondestructive Testing of Installed Weatherproofing Sealant Joints”, *Durability of Building and Construction Sealants and Adhesives*, STP 1453, A. T. Wolf, Ed., ASTM International, West Conshohocken, PA, 2005, pp. 335–345.
- [5] ASTM Standard C1736-11, 2011, “Standard Practice for Non-Destructive Evaluation of Adhesion of Installed Weatherproofing Sealant Joints Using a Rolling Device”, Annual Book of ASTM Standards, ASTM International, West Conshohocken, PA.
- [6] ASTM Standard C1193-09, 2009, “Standard Guide for Use of Joint Sealants”, Annual Book of ASTM Standards, ASTM International, West Conshohocken, PA.

Overview

Introduction

The Fourth ASTM International Symposium on Durability of Building and Construction Sealants and Adhesives (2011-DBCSEA) was held on June 16–17, 2011 in Anaheim, California. It was sponsored by the ASTM International Committee C24 on Building Seals and Sealants in cooperation with the International Union of Laboratories and Experts in Construction Materials, Systems and Structures (RILEM). The symposium was held in conjunction with the standardization meetings of the C24 Committee. With presentations from authors representing nine countries in North and South America, Europe, Asia, and Australia, the symposium was a truly international event.

As in the previous events of this symposium series, the 2011 symposium brought together architects, engineers, scientists – researchers and practitioners. One of the stated goals of the symposium was to transfer new ideas, gained from laboratory research and field work, to the study of sealant and adhesive durability and the development of new products and test methods. The symposium provided an excellent forum for international experts to share and compare their experiences, network with their peers, and exchange best practices with regard to the durability testing and assessment of building and construction sealants and adhesives. It also provided a platform for an expert panel discussion. The panel discussion was originally conceived as a discussion on sealant warranty issues, but became a spirited conversation regarding the impact of the newly developed ASTM C1736 Standard Practice with participation by the panelists, ASTM C24 members, as well as presenters and participants of the international symposium. Perhaps the greatest value of this series of symposia lies in the discussions occurring during these events and in the utilization of the resulting information.

The current series of ASTM symposia on Durability of Building and Construction Sealants and Adhesives is a continuation of tri-annual symposia which were inaugurated by the RILEM Technical Committee 139-DBS Durability of Building Sealants in 1994. Today, this continuing series of symposia provides the best scientific forum globally in the building and construction industry for peer-reviewed papers on all aspects of sealant and adhesive durability. Furthermore, data presented at those symposia over the past 17 years have been the single most important factor influencing ASTM International and ISO standards as well as RILEM technical recommendations related to construction sealant durability.

In several languages, such as Dutch, Finnish, Romanian or French, *sustainable* is translated as *durable*. This synonymous use of *durable* and *sustainable* is not surprising, as durability plays a key role in achieving

sustainable construction, because “one way of extending resource productivity is by extending the useful life of products” (DeSimone & Poppof, 1998). The increased utilization of sustainable construction practice, i.e., designing for durability by utilizing building science and life cycle analysis as its foundation, as well as mandatory government regulations, such as the European Construction Products Directive, have elevated the importance of the durability and service life performance of building and construction sealants and adhesives. All products, not just those involved in safety-critical applications, must demonstrate durability as part of their fitness for purpose assessment. Life cycle costing considerations increasingly drive investment decisions towards products and systems with longer service life cycles and lower maintenance costs.

Against a background of national and international efforts to harmonize testing and approval of building materials and structures, ASTM International and RILEM have been looking for ways of bringing together the experience of international experts active in the application and testing of building and construction sealants and adhesives.

As with most scientific disciplines, substantial advances often occur through a series of incremental steps, each contributing pieces of the puzzle, rather than in giant leaps. This is also the case for the papers presented at the Fourth International Symposium on Durability of Building and Construction Sealants and Adhesives (2011-DBCSEA). Many of the papers reflect progress reports on on-going research. At the 2011-DBCSEA symposium, we saw several examples of the steady progress being made by leveraging these scientific advances into a new generation of test methods as well as assessment practices.

This book contains twenty-three of the twenty-seven papers presented at the symposium as well as two papers submitted only for publication in the proceedings. It also contains an editorial summary of the panel discussion. The contributions condensed in this STP volume represent state-of-the-art research into sealant and adhesive durability and reflect the varying background, experience, profession, and geographic location of the authors. The following major themes are evident in this collection:

- Laboratory Testing and Specialized Outdoor Exposure Testing
- Factors Influencing the Durability of Sealed Joints and Adhesive Fixing
- Development of New Test Methods and Performance-Based Specifications
- Field Experience with Sealed Joints and Adhesive Fixing
- Performance under Seismic Loads

Overview of Papers

Below is a short overview of the papers published in this volume with regard to the above five categories.

Laboratory Testing and Specialized Outdoor Exposure Testing

Over the last decade, the use of fiber-reinforced polymer (FRP) composites as construction materials in structural engineering applications has grown substantially. Also known as advanced composite materials (ACMs), these materials have proven themselves to be especially valuable for use as main components in hybrid structural members. However, in order to fully capitalize on the high tensile strength of the FRP materials, an effective connection mechanism between the FRP and the conventional building material must be operational at the interface in order to achieve optimum performance of the hybrid structural members. **Chen** and **El-Hacha** in their paper investigate the bond performance between glass-fiber reinforced polymer (GFRP) plates and cast-in-place ultra-high-performance concrete (UHPC) using an epoxy-based adhesive filled with coarse silica sand aggregates. Both shear and tensile tests are conducted using three different types of epoxy adhesives. Analysis of the experimental data shows that the specimens bonded with the moisture tolerant epoxy adhesive intended for bonding of hardened concrete and steel performs the best.

The use of glass in the building industry is increasingly extended beyond its space-enclosing function to structural applications, such as in glass beams, glass columns or bracing façade elements. Recently, interest in I-shaped bonded hybrid steel-glass beams as transparent structural elements has grown. In these beams, steel flanges and glass are connected by a linear adhesive bond. The coupling between steel and glass substantially increases the flexural strength of the glass beams due to the shear forces being transferred via an adhesive bond. In their contribution, **Feldmann**, **Abeln** and **Preckwinkel** study the behavior of adhesive joints in hybrid steel-glass beams by means of simplified small scale tests. The results show that full-scale hybrid beams with butt splice bonded and U-bonded geometries are feasible using suitable load-bearing adhesives. However, careful design of the joints is required, taking the specific properties of the adhesive (brittleness, weather resistance, etc.) into consideration.

Autoclaved aerated concrete (AAC), also known as autoclaved cellular concrete (ACC) or autoclaved lightweight concrete (ALC), was invented in the mid-1920s in Sweden and has recently gained some reputation as a green building material, because of its thermal insulation property. In Japan, high-performance water-borne acrylic sealants are traditionally the sealant product of choice for use between ALC panels. While the degradation mechanisms

of acrylic sealants are well known, their resistance to outdoor weathering has not yet been fully investigated. **Miyauchi, Lacasse, Enomoto, Murata** and **Tanaka** study the long-term behavior of these sealants by on-site investigation of acrylic sealed external joints of ALC-clad buildings as well as by outdoor exposure testing of different types of acrylic sealants in three climate regions located in Japan. As expected, the aging of these sealants, as determined by the degree of surface cracking, depends on the local temperature and the respective degree of exposure to solar radiation. Also not surprisingly, joint configurations with two-sided sealant adhesion, installed in deep panel ALC cladding, are more reliable than three-sided adhesion joints used for thin panel ALC cladding in terms of the durability of the sealed joints installed in actual buildings. However, what does surprise is the substantial amount by which the elongation of the three-sided adhesive joint configurations decreases after five years outdoor exposure and the associated large number of sealed joints with ALC substrate failure.

The durability of sealed or bonded joints is dictated by many factors such as joint design, surface preparation, application, formulation, joint movement, and weather. **Schueneman, Hunt, Lacher, White** and **Hunston** attempt to address the link between formulation and weathering durability by monitoring changes in apparent modulus during exposure to outdoor weathering and cyclic strain. Cyclic movement is accomplished via custom built systems that apply cyclic strain. The conditions for simultaneous exposure to strain and weathering are chosen such as to simulate wood (cold compression) and concrete/metal (hot compression) construction materials. A key finding of their research is that changes in apparent modulus are primarily driven by underlying changes in compression set, a potentially critical contributor to stress in structures during rapid temperature changes.

In their paper, **Sitte, Brasseur, Carbary** and **Wolf** report on the preliminary evaluation of a novel transparent structural silicone adhesive (TSSA) developed for point fixing in glazing. The paper presents information on the durability and physical properties of the new material and suggests a methodology for deriving static and dynamic design strength values for the new material based on creep rupture experiments as well as nondestructive dynamic load experiments using the stress whitening phenomenon observed with this material as the limit state. The paper further discusses material characterization and hyperelastic modeling used in the finite element analysis based on finite strain theory.

The Institute of Building Construction at Dresden's Technical University is one of Europe's leading research facilities focused on the study of glass in buildings. **Weller** and **Vogt** describe some of the research activities carried out at this institute on bonded glass connections for load-bearing structures. Examples of the research covered are bonded point supports for overhead

glazing and for large photovoltaic modules subjected to high environmental loads, linear adhesive joints for hybrid steel-glass composite beams with good ductility and for glass fins with a reduced cross-section in minimized steel-and-glass facades, as well as bonded joints for photovoltaic facades and for an all-glass pavilion.

Further research at the same institute is highlighted in a paper by **Weller, Nicklisch, Prautzsch** and **Vogt** that outlines the testing and evaluation program used in the selection of adhesives for transparent bonded joints in all-glass load-bearing structures of two buildings located in Dresden and Grimma, Germany. The test and evaluation program designed by the institute led to individual approvals of these constructions by the German building code authority. The authors describe the various stages of this project from the evaluation of material properties of various adhesives to the optimization of the bonded joint geometry in order to achieve long-term integrity of the structures.

Recent years have seen a multitude of new sealant and adhesive products based on novel polymers, cure chemistries, and formulations being launched onto the market for which there is a lack of experience in terms of performance histories for similar products. An accurate service life prediction model is urgently needed for building sealants to greatly reduce the time-to-market of a new product and reduce the risk of commercializing a poorly performing product. A key element in any accelerated weathering test is the precise control of all environmental variables in the laboratory test apparatus in order to produce reliable weathering data that can be used to generate a predictive model. In their contribution, **White, Hunston, Tan, Filliben, Pintar** and **Schueneman** report on a systematic study investigating individual and synergistic impacts of four environmental factors (cyclic movement, temperature, relative humidity, and ultraviolet radiation) on the durability of a model sealant using a novel laboratory test apparatus. The apparatus not only allows precise control of the environmental factors, but it also permits in-situ characterization tests of the specimens.

Factors Influencing the Durability of Sealed Joints and Adhesive Fixing

While our understanding of the factors that determine the service life of sealed or bonded joints has progressed substantially over the past decades, there is still much research needed on the durability and reliability of novel structures, components or designs. Several papers at the symposium focus on this topic.

Bent or warped glass allows turning a typical glass-and-metal curtain wall design into an exciting, innovative architectural statement. Traditionally, curved glass is manufactured from float glass by heating it to a temperature above the softening point and then shaping the glass in a mould. Since this

technique is time and energy consuming and consequently relatively expensive, cold-bending has been developed as a more affordable alternative. In this glazing technique, flat glass panes are bent to the desired shape on a curved frame and then mechanically or adhesively attached to the frame. The cold-bending process implies that the glass becomes permanently subjected to bending stresses during its lifetime. Glass on contemporary curtain wall projects is mostly insulating glass which raises concerns about the longevity of cold bent insulating glass (IG) units, as the bending process induces a shearing action to both the primary and secondary edge-seals. While very little scientific information on this topic has been generated in the past, the number of building projects involving cold-bent insulating glass globally continues to increase rapidly. In their land-mark paper, **Besserud, Bergers, Black, Carbary, Mazurek, Misson** and **Rubis** describe testing protocols designated to determine the effect of cold-bending on the durability of the insulating glass unit as measured by argon retention, frost point change, and visual changes after aging. As part of the experimental protocol, first the bending behavior of a full size IG unit is assessed, which is then modeled to predict the stresses and strains on the primary and secondary seals. Small (standard) size IG units are then tested according to the ASTM E2188-10 and E2190-10 protocols while simultaneously subjecting them to an edge seal displacement in all three directions that induces equivalent stresses in the edge seal. Argon retention and frost point measurements are taken before and after the durability testing and results reported. The methodology developed in this research provides a strong foundation for future testing in the area of cold-bent IG unit durability.

Durable, reliable, and high strength adhesion of elastomeric sealants and adhesives to a variety of substrates is essential to a broad range of industries. In their paper, **Gutowski, Toikka** and **Li** discuss and experimentally verify the principles of engineering substrate surfaces through grafted connector molecules. The authors demonstrate that the incorporation of silicon-based and/or amine-terminated graft molecules such as silanes or polyethyleneimines, at the polymer interface, results in the formation of strong molecular links between a range of organic and metallic substrates and elastomeric sealants or adhesives, leading to significantly improved bonding. The technology has been successfully adopted by the global automotive industry for improving adhesion of a variety of adhesives and coatings to polyolefinic substrates.

The bonding of point-fixed supports for glazing has recently received increased attention, as in contrast to mechanical fixation, bonding of point supports offers a number of advantages, such as no or lower visibility of the supports from the exterior, a ‘smooth’ transfer of the load into the glass pane (avoiding stress peaks), and the elimination of drilling holes from the glass. Failure mechanisms under typical loading conditions and parameters that

affect failure probability, mode, or mechanism are the focus of ongoing investigations. **Hagl** studies the mechanical characteristics of degraded silicone-bonded point supports with axial geometry undergoing tensile loading. Tensile loading of bonded point supports is considered the critical load case, as dynamic loads, such as wind load, subject the adhesive to out-of-plane loads. In the paper, the following parameters are investigated in their effect on the durability of point supports bonded with a two-part adhesive: (a) incorrect mixing ratio of the adhesive components, (b) inhomogeneous mixing due to insufficient or improper mixing procedure, (c) fatigue degradation of the adhesive, and (d) local defects in the bond, e.g., caused by inclusion of bubbles or by partially failed adhesion. The main motivation for this kind of research is to strengthen the confidence of building code authorities in the durability of bonded designs.

As mentioned earlier, there is an increased interest in the cold-bending of glass in order to realize curved or warped glass façades. However, cold bending induces permanent stresses in the glazing structure, especially in the corner area of the glass units. Dynamic or static loads acting perpendicular to the glass surface, such as wind or snow loads, also cause high stresses in the corner area. **Hagl** and **Dieterich** present numerical results of a parametric study for pressure-loaded glass units with a focus on corner loads and stresses. The results show that the stress levels in the corner areas might exceed the design stress values used for sizing the bond geometry.

Blistering of sealed or bonded joints is as a form of degradation. Sometimes blistering is observed when exposure to direct sunlight occurs immediately after application of the sealant or adhesive on an unusually hot day. Often this case of blistering can be attributed to intrusion of air or moisture from voids within the substrate into the sealant or adhesive. While other causes of blistering exist, blistering driven by the diurnal variation in temperature is an important aspect of the degradation of sealed or bonded joints. The paper by **Hailesilassie** and **Partl** deals with the mechanism of asphalt blistering on concrete bridges. While the focus of their paper is on blistering in asphalt overlays, their findings are relevant to the sealant and adhesive industry. According to the authors, blistering is a major problem in asphalt covered concrete structures, such as multi storage parking buildings, built-up roofs, tunnels, pedestrian areas or concrete bridge decks. In this particular research, a linear viscoelastic finite element model is developed to simulate time dependent blister growth in the asphalt layer under uniformly applied pressure with and without temperature and pressure fluctuation. The finite element model simulation shows that the daily temperature variations may have a significant influence on blister growth in asphalt pavements. The authors conclude that temperature fluctuation has more influence on blister growth than fluctuation of the pressure inside the blister.

Joints may fail because of degradation of either cohesive or adhesive properties of the sealant or adhesive. Since silicone materials display excellent bulk durability, adhesive failure mode is the more likely cause of joint failure. Interfacial adhesion can be improved either by modifying the formulation of the sealant or adhesive or by modifying or treating the surface of the substrate, for instance, by plasma treatment or use of a primer. **Vandereecken** and **Maton** report on a comparative study evaluating the adhesion improvement observed for a two-part silicone adhesive on a variety of substrates either by applying a wet primer or the dry Pyrosil® flame treatment. Pyrosil® is a pyrolytic chemical pre-treatment process that forms an amorphous, nano-scale silicate layer on the treated surfaces. In this process, the targeted surface is treated with the front (oxidizing) section of a flame obtained by burning a silane, propane, and butane mixture in a pen-like torch. During the combustion process, the silane is oxidized to form SiO₂ nano-particles which cover the surface with an ultra-thin (20 - 40 nm) strongly adhering silica coating.

Development of New Test Methods and Performance-Based Specifications

The weatherability of construction sealants is a highly important performance criterion for the prediction of their aesthetic and functional service lives. Currently, the evaluation of a sealant's surface degradation is carried out mainly by qualitative visual assessment against pictorial references. **Enomoto, Ito** and **Tanaka** present information on the weatherability of construction sealants based on a recently developed test specimen design that allows simultaneous exposure of the sealant to forced compression and extension movement in a single specimen with cyclic movement and weathering carried out simultaneously. A quantitative method for the assessment of surface cracks is employed and the relationship between outdoor and accelerated weathering exposure is evaluated by using metrics that indicate the degree of surface cracking as a new semi-quantitative criterion of surface degradation.

Recently, ASTM International published a standardized methodology suitable for the evaluation of joint seal continuity, ASTM C 1736-11 Standard Practice for Non-Destructive Evaluation of Adhesion of Installed Weatherproofing Sealant Joints Using a Rolling Device. This standard practice was created under the jurisdiction of ASTM committee C 24 on Building Seals and Sealants, and the direct responsibility of Subcommittee 30 on Adhesion. It was approved shortly before the symposium on July 1, 2011. In his paper, **Huff** discusses some of the technical questions raised during the development of this standard.

Today there are fifty-nine completed buildings globally that stand over 300 meters tall, a height generally considered super-tall, and dozens more

are under construction or being planned. The trend towards super-tall buildings is driven by scarcity of available land, economic prosperity with dramatic population growth within the big cities, and high economic value of the super-tall buildings. Nowhere is the trend towards super-tall buildings more evident than in Asia, especially in China and South Korea, as well as in the Middle East. Structural silicone glazing is a curtain wall technique commonly used in South Korea and this glazing method is also considered for many of the future super-tall buildings. However, there is no industry-wide guideline or specification for structural silicone sealants in South Korea. In order to prepare for such a specification, **Jung, Hahn** and **Lee** report on a comparative evaluation of locally available structural silicone sealants that employs artificial weathering protocols adapted from various global industry standards, such as ASTM C1135 and EOTA ETAG 002. While silicones in general are known to have excellent resistance to weathering, some silicone products included in the study still show noticeable degradation of properties, since the weathering performance of a sealant is affected by its overall composition and not just by its polymer type.

The strength of autoclaved lightweight concrete (ALC) is evidently lower than that of traditional concrete. When movement occurs at a sealed joint between ALC panels, the sealant is required to deform without causing damage to the ALC substrate. However, there is currently not sufficient information permitting the selection of suitable sealants for ALC substrates. **Miyauchi, Lacasse, Murata, Enomoto** and **Tanaka** report on a study comprising both static and dynamic tests carried out to obtain an indication of the modulus of a sealant that can be expected to provide long-term performance when applied to an ALC substrate. Using two-part polyurethane sealants of different elastic modulus, the authors determine the relationship between shear and tensile stresses and the type of joint fracture. The results reveal that the ALC substrate is increasingly likely to fail when the sealant stress exceeds about 0.6-0.7 MPa.

The design criteria for structural silicone glazing (SSG) applications require adhesive systems that maintain their functionality for longer than twenty years in actual field installations. Silicone sealants have well demonstrated their ability to effectively and reliably perform in long-term exterior structural applications. The first-ever four-sided SSG facade, completed in 1971, is still operational today. Still, estimation of the service life of SSG systems based on accelerated testing is difficult, since, in principle, it is necessary to test to failure in order to allow service life prediction, which, for systems designed for long-term durability, imposes practical difficulties. Further complications arise during the transfer of information gained on small scale test specimens to the actual performance of SSG systems as a whole. In his paper, **Recknagel** makes an attempt at adapting dynamic-mechanical

material analysis for the performance characterization of structural silicone sealants. The results obtained are reported and discussed for three structural silicone sealants, and characterize their temperature-, deformation- and frequency-dependent behavior. The applicability of the dynamic mechanical material analysis approach and of its various complex test modes for the exploration of the technical performance and the estimation of fatigue life is evaluated for the three sealants investigated. The author intends to complement the dynamic-mechanical assessment methodology with suitable system tests on a section of a structural glazing system that will be subjected to a simplified load function representing the superposition of actual loads acting on the system. The technical fundamentals and the procedure proposed for the development of adequate system tests are discussed.

As already described for the Enomoto et al. paper, the durability of building joint sealants is generally assessed using a descriptive methodology involving visual inspection of aged specimens for defects. This methodology has inherent limitations and the results are qualitative in nature. **White, Hunston** and **Tan** propose a new test method that utilizes stress relaxation to evaluate changes in the viscoelastic behavior occurring in sealants during durability testing. In particular, changes in the time dependence of the apparent modulus can be observed and related to molecular changes in the sealant. According to the authors, such changes often precede the formation of cracks and the ultimate failure of the sealant. The paper compares results obtained with the new test method and the currently used descriptive methodology.

During the symposium, a panel discussion was held regarding the impact of the newly developed ASTM C1736 Standard Practice for Non-Destructive Evaluation of Adhesion of Installed Weatherproofing Sealant Joints Using a Rolling Device. The panel consisted of three members of ASTM C24 committee, who had direct involvement with the creation, oversight, and/or passage of C1736, plus one panelist representing a sealant applicator. Context to the discussion is provided by the editor, who has added a short introduction to the topic.

Field Experience with Sealed Joints and Adhesive Fixing

Over the last decade, changes in environmental protection regulations have necessitated reformulation of many historically durable adhesives used in the application of flooring materials. Solvent-borne adhesives with high content of volatile organic compounds (VOCs) were replaced with water-borne or 100% solids adhesive formulations. **Nelson** and **Hopps** suggest that these new environmentally friendly adhesives are less durable and more susceptible to moisture-related deterioration. If the concrete is not properly sealed or allowed to dry, the moisture permeating through or contained in

the concrete slab can re-emulsify moisture-sensitive flooring adhesives. Consequentially, applied flooring materials can delaminate, buckle, blister, and crack. The paper compares the properties of the newer moisture-sensitive flooring adhesives with those of their VOC-containing predecessors, and describes the properties of the adhesives that reduce overall durability. It also presents case studies of flooring failures resulting from moisture-related deterioration of adhesives for various flooring materials including carpet tile, sheet vinyl, and vinyl composition tile flooring.

Foamed adhesives are used to join roofing assembly components to the roof substrate and to each other. A variety of performance problems with foamed adhesives as installed in roofing assemblies have led to assembly failures. **Slick, Piteo** and **Rutila** present several case studies that illustrate excessive moisture in roofing assemblies or substrates as an issue that contributes to adhesive failure of the roofing assembly.

Performance under Seismic Loads

Buildings exposed to seismic loads pose a severe threat to life and safety of pedestrians as components of the cladding or curtain wall may fracture, dislodge, and fall down. The seismic performance of architectural glass installed in the fenestration section of curtain walls is of special interest, as glass is brittle and may crack, which increases the probability of catastrophic failure, culminating in the fallout of the entire unit. In light of the extensive use of architectural glass in seismically active geographies, anecdotal evidence suggests that the actual performance of glazing during earthquakes is relatively good, as only few serious casualties associated with curtain wall problems are reported. The U.S. National Institute of Building Sciences in their *Seismic Safety of the Building Envelope Report* (Arnold, 2009) attributes the relative good performance of glass and metal curtain walls to the inherent strength of glass, the flexibility of the framing assembly, the resiliency of the glass retention materials, and the relatively small size of the glass panels. However, historically the sizes of the glass panes have increased and novel methods of glass attachment, such as structural silicone glazing (SSG), have become commonplace. The fact that the load transfer between the glass and the framing system in a SSG curtain wall must occur through the sealant implies that the seismic response of SSG systems is most likely different from systems that are dry-glazed. Recent studies of the seismic performance of various SSG curtain wall configurations were focused on the identification of the failure limit states associated with glass in SSG assemblies. The seismic performance of curtain wall systems is generally assessed in dynamic racking tests on curtain wall mockups

In their paper, **Broker, Fisher** and **Memari** present the results of a study in which four-sided structural sealant glazing (SSG) insulating glass curtain

wall units were subjected to cyclic racking test methods in accordance with AAMA 501.6 testing protocols. The drift capacity of the system in terms of glass attachment and sealant performance is reported in detail for different levels of racking displacements and boundary conditions. The overall behavior of the system is characterized, and specifically the sealant performance at a corner condition during racking drift is discussed. The damage to the structural silicone sealant is evaluated using visual observation before and after cyclic racking. The authors discuss proposed acceptable sealant stress levels for seismic SSG design and present sealant test results, which show the modulus stability and durability of silicone sealants.

A law in California is mandating earthquake resistance of all hospitals by 2013. California Pacific Medical Center (CPMC) has been planning the new Cathedral Hill Hospital in Downtown San Francisco as a LEED Silver-rated building in conformance with this law. When complete, this 100,000 m², fifteen-story, 555-bed hospital will fill a whole city block. The curtain wall system for this building is primarily of a unitized design employing a four-sided structural silicone glazing system. In order to ensure satisfactory seismic performance of the curtain wall system for this project, dynamic racking tests were carried out according to AAMA 501.6 procedure. In their paper, **Memari, Fisher, Krumenacker, Broker** and **Modrich** discuss the results of these dynamic racking tests carried out on curtain wall mockups with regard to the behavior of the glass, framing, connections, and the structural silicone. Tensile stress-strain test results on the structural silicone sealant at selected temperatures and after ultraviolet (UV) light exposures are discussed, and comparisons to the finite element analysis results are presented. Finally, the allowable stress in seismic design of four-sided SSG systems is discussed in light of new information generated for this project.

The 8.8 Magnitude earthquake that shook Chile at 3:34 a.m. on Saturday, February 27, 2010, was one of the most devastating in the history of the country. The earthquake was felt in most parts of Chile, Argentina and some parts of Bolivia, southern Brazil, Paraguay, Peru and Uruguay. The earthquake was followed by hundreds of aftershocks, the strongest measuring from 6.0 to 6.9 on the moment magnitude scale. In their paper, **Bull** and **Cholaky** report on the state of SSG systems in low, medium and high-rise buildings that were inspected in the aftermath of the event.

Closure

As we publish this volume, I look forward to the next Symposium on Durability of Building and Construction Sealants and Adhesives (2014-DBCSA) and the associated flurry of papers in this dynamic industry. I encourage all readers to participate in the work of ASTM C24 committee, to attend the future symposia, and to contribute new papers. Your participation and feed-

back help to advance the industry and, as a result, we will all benefit from improvements to our built environment.

In closing, I would like to gratefully acknowledge the outstanding quality of the contributions made by the authors as well as the dedicated efforts of the 2011 session chairpersons, the peer reviewers, the staff of ASTM and AIP, and the Associate Editor of JAI, who all helped to make the 2011 symposium and the publication of the associated papers possible.

Andreas T. Wolf
Wiesbaden, Germany

AUTHOR INDEX

Index Terms

Links

A

Abeln, B. 26–46

B

Bergers, M. 205–242

Besserud, K. 205–242

Black, A. J. 205–242

Brasseur, M. J. 86–123

Broker, K. A. 473–504 505–528

Bull, E. 529–564

C

Carbary, L. D. 86–123 205–242

Chen, D. 3–25

Cholaky, J. 529–564

D

Dieterich, O. 286–307

E

El-Hacha, R. 3–25

Enomoto, N. 47–69 343–360 385–403

Index Terms

Links

F

Feldmann, M.	26–46		
Filliben, J. J.	177–201		
Fisher, S.	473–504	505–528	

G

Gutowski, W. S.	243–265		
-----------------	---------	--	--

H

Hagl, A.	266–285	286–307	
Hahn, K.	370–384		
Hailesilassie, B. W.	308–330		
Hopps, E. R.	447–455		
Huff, D. N.	361–369		
Hunston, D. L.	70–85	177–201	432–443
Hunt, C. G.	70–85		

I

Ito, A.	343–360		
---------	---------	--	--

J

Jung, J.	370–384		
----------	---------	--	--

K

Krumenacker, C.	505–528		
-----------------	---------	--	--

Index Terms

Links

L

Lacasse, M. A.	47–69	385–403
Lacher, S.	70–85	
Lee, H.	370–384	
Li, S.	243–265	

M

Maton, I.	331–340	
Mazurek, A.	205–242	
Memari, A. M.	473–504	505–528
Misson, D.	205–242	
Miyauchi, H.	47–69	385–403
Modrich, R.-U.	505–528	
Murata, S.	47–69	385–403

N

Nelson, P. E.	447–455	
Nicklisch, F.	152–176	

P

Partl, M. N.	308–330	
Pintar, A. L.	177–201	
Piteo, N. A.	456–470	
Prautzsch, V.	152–176	
Preckwinkel, E.	26–46	

Index Terms

Links

R

Recknagel, C.	404–431
Rubis, K.	205–242
Rutila, D. A.	456–470

S

Schueneman, G. T.	70–85
Sitte, S.	86–123
Slick, D. S.	456–470

T

Tanaka, K.	47–69	343–360	385–403
Tan, K. T.	177–201	432–443	
Toikka, G.	243–265		

V

Vandereecken, P.	331–340		
Vogt, I.	124–151	152–176	

W

Weller, B.	124–151	152–176	
White, C. C.	70–85	177–201	432–443
Wolf, A. T.	86–123		

SUBJECT INDEX

Index Terms

Links

A

<i>ABAQUS</i> TM	308–330		
accelerated exposure	343–360		
accelerated weathering	370–384		
acrylate	124–151		
adhesion	243–265	331–340	
adhesive	124–151	447–455	456–470
adhesive failure	370–384		
adhesive technology	26–46		
apparent modulus	70–85		
architectural design feature	205–242		
argon retention	205–242		
ASTM C719	432–443		
ASTM C1519	432–443		
ASTM C1736	361–369		
ASTM E2188	205–242		
ASTM E2190	205–242		
autoclaved lightweight concrete	47–69	385–403	

B

bent glass	205–242		
blister growth	308–330		
bond	3–25		
bonding design	266–285		

This page has been reformatted by Knovel to provide easier navigation.

Index Terms

Links

Building sealant

70–85

C

capability evaluation

404–431

closed-form solution

308–330

cold bent glass

205–242

286–307

compression set

70–85

concrete

447–455

construction

177–201

continuous sealant evaluation

361–369

corner load

286–307

creep

308–330

cured

361–369

curtain wall systems

529–564

curtain walls

473–504

cyclic loading

266–285

D

degradation

266–285

doubly curved glass

205–242

durability

47–69

70–85

243–265

331–340

343–360

432–443

durability evaluation

404–431

dynamic-mechanical testing

404–431

E

earthquake

529–564

epoxy

3–25

exposure testing

47–69

This page has been reformatted by Knovel to provide easier navigation.

Index Terms

Links

F

fibre reinforced polymers	3–25
film adhesive	86–123
finite-element method	308–330
Finite Element Modeling	473–504
floor	447–455
foamed	456–470
fracture	385–403

G

glass	3–25	124–151
glass fin	124–151	
glass frame	124–151	
glazing	86–123	

H

high strain rate behavior of structural silicone	529–564
hybrid beam	124–151
hybrid steel-glass beams	26–46

I

indirect tensile test	308–330
insulating-glass durability	205–242
insulation	456–470
interstory drift	529–564

Index Terms

Links

J

joint 361–369

K

Korea 370–384

M

master curve 308–330

material characterization 404–431

mechanical characteristics 404–431

metallic substrate 243–265

mixing ratio 266–285

model 177–201

modulus 177–201 385–403 432–443

moisture 447–455 456–470

molecular brushes 243–265

N

non-destructive evaluation 361–369

O

one part 370–384

organic substrate 243–265

outdoor aging 70–85

outdoor exposure 343–360

Index Terms

Links

P

performance assessment	404–431
photovoltaic facade	124–151
PIB durability	205–242
point fixing	86–123
polyethyleneimines	243–265
primers	331–340
Prony series	308–330

R

racking test	473–504
relaxation	308–330
rolling device	361–369
roofing	456–470

S

Sealant	47–69	177–201	343–360
	385–403	404–431	432–443
sealant failure in adhesion	361–369		
seismic evaluation	473–504		
Service Life Prediction	177–201		
shear	3–25		
sigmoidal function	308–330		
silica sand	3–25		
silicone	86–123	370–384	473–504
silicone adhesion	243–265		
silicone adhesive	266–285	286–307	
silicones	243–265	331–340	

Index Terms

Links

small- and large-scale tests	26–46		
SPHERE	177–201		
SSG	529–564		
Statistics	177–201		
strain cycling	70–85		
stress relaxation	432–443		
structural	86–123		
structural behavior	26–46		
structural glazing	26–46	266–285	286–307
	370–384	404–431	
structural sealant glazing	473–504		
structural silicone	205–242		
structural silicone glazing	529–564		
superimposed loading	404–431		
surface degradation	343–360		
surface engineering	243–265		
system test method	404–431		

T

tensile strength	370–384		
tension	3–25		
two part	370–384		

U

Ultra-High-Performance- Concrete	3–25		
----------------------------------	------	--	--

V

VOCs	447–455		
------	---------	--	--

Index Terms

Links

W

wall panel	47–69	385–403
warped glass	205–242	286–307
weatherability	343–360	